Universidade do Minho
Escola de Engenharia

Nima Azimi Resketi

Integrated experimental-analytical study of the durability of textile reinforced mortar composites for the strengthening of masonry

July 2025

Integrated experimental-analytical study of the durability of textile reinforced mortar composites for the strengthening of masonry
Nima Azimi Resketi
UMinho | 2025

Universidade do Minho
Escola de Engenharia

Nima Azimi Resketi

Integrated experimental-analytical study of the durability of textile reinforced mortar composites for the strengthening of masonry

Doctoral Thesis
Civil Engineering

Work concluded under the supervision of:
Prof. Daniel V. Oliveira
Prof. Paulo B. Lourenço
Prof. Katrin Schollbach

July 2025

DIREITOS DE AUTOR E CONDIÇÕES DE UTILIZAÇÃO DO TRABALHO POR TERCEIROS

Este é um trabalho académico que pode ser utilizado por terceiros desde que respeitadas as regras e boas práticas internacionalmente aceites no que concerne aos direitos de autor e direitos conexos. Assim, o presente trabalho pode ser utilizado nos termos previstos na licença abaixo indicada. Caso o utilizador necessite de permissão para fazer um uso do trabalho em condições não previstas no licenciamento indicado, deverá contactar o autor, através do RepositóriUM da Universidade do Minho.



Atribuição
CC BY

https://creativecommons.org/licenses/by/4.0/

Acknowledgements

First and foremost, my deepest gratitude goes to Professor Daniel Oliveira, my daily supervisor, whose unwavering support and guidance made this PhD possible. More than just a supervisor, he has been a model of integrity, kindness, and leadership. His trust in me, his scientific insight, and his encouragement to pursue international collaborations were pivotal throughout this journey. I am truly thankful for his availability, patience, and constant reassurance, especially during those moments when I doubted myself more than my results. I would also like to sincerely thank Professor Paulo B. Lourenço for believing in me and giving me the opportunity to be part of this research. His trust meant a great deal, and his support was fundamental, without it, completing this PhD would not have been possible. I carry deep respect for his role in shaping this work and my academic growth.

The majority of this research was conducted at the Department of Civil Engineering at the University of Minho. A significant part of my time (and soul) was spent in the LEST lab—immense thanks to Marco, the lab coordinator (you can finally exhale now—until my next project!). To Sr. Matos, the superhero technician who always had a solution, your support was invaluable. Thanks also to Luciano, César, and Carlos for their help during countless experiments. Special thanks to Dr. Rui Silva and Dr. Enrico Garbin for their guidance, discussions, and lifesaving interventions, and to Ana Fonseca, our secretary, for her constant support and warm smile. I am deeply grateful to Professor Katrin Schollbach from TU Eindhoven, who kindly supervised this thesis from the very beginning. Her openness and scientific guidance, especially when I was just discovering the microscopic world, were instrumental. Sincere thanks to Professor Jos Brouwers for hosting me at TU/e, and to Anneke and Harrie for their lab support. I also thank my TU/e friends—Hoss, Beatrice, Farbod, Marina, Leila, Winnie, Kaveh, Sahar, and Arman—for the laughs, coffees, and unforgettable memories.

At Politecnico di Milano, I was lucky to be welcomed by Professor Tommaso D'Antino, whose insights into modeling were incredibly valuable. A special mention goes to Veronica for her helpful input during the numerical modeling phase. Thanks also to colleagues and friends who made the Milan chapter much easier to survive: Angelo, Salah, Niki, and Luis.

None of this would have been meaningful without my family. To my Mum, Dad, and my beloved sister, Negar, thank you for your endless love, patience, and belief in me. Even from afar, your presence was always felt. You stood by me during the tough times and cheered me on even when you had no idea what "TRM" meant.

To my friends and fellow researchers, Zabih, Amir, Eduarda, Omid, Maryam, Salar, Annalaura, Mehdi, Momo, Luca, Dario, Francesca, Carolina, Daniel, Sajad, Carla, Simon, GiGi, and all those whose names I might have forgotten (please forgive the author's aging memory!), thank you for being part of this journey. Whether it was a conversation, a coffee, a weekend escape, or a lab panic moment, you contributed in more ways than you know.

A heartfelt note of gratitude also goes to Sarah, who over the last few months, supported me in ways that truly mattered. Your presence and help made the final stretch of this journey a lot lighter.

This PhD was funded by the Portuguese Foundation for Science and Technology (FCT, grant 2021.05328.BD), with additional support from the Erasmus+ project (2024-1-PT01-KA131-HED-000214341) and ISISE at the University of Minho. I also thank Mapei S.p.A. for providing materials, organizing scientific meetings, and for their collaboration, special thanks to Rossella Comensoli for making this connection possible.

And finally, "I want to thank me. I want to thank me for believing in me. I want to thank me for doing all this hard work. I want to thank me for having no days off. I want to thank me for never quitting. I want to thank me for just being me at all times". **Snoop Dogg!**

Statement of Integrity

I hereby declare having conducted this academic work with integrity. I confirm that I have not used plagiarism or any form of undue use of information or falsification of results along the process leading to its elaboration.

I further declare that I have fully acknowledged the Code of Ethical Conduct of the University of Minho.

Integrated experimental-analytical study of the durability of textile reinforced mortar composites for the strengthening of masonry

Abstract

The use of Textile-Reinforced Mortar (TRM) systems has emerged in recent decades as a promising solution for the strengthening of masonry structures, offering compatibility with heritage materials and favorable mechanical performance. However, despite the growing application of TRM in real structures, the understanding of its long-term durability under aggressive environmental conditions remains limited. In particular, the effects of acid attack, common in polluted or industrial environments, have received insufficient attention in the scientific literature. This doctoral thesis addresses this gap through a systematic investigation of the mechanical behavior and degradation mechanisms of TRM composites under both short-term loading and long-term environmental exposure.

The research began with an experimental evaluation of the short-term tensile response of TRM systems, examining the influence of fiber type, number of textile layers, and layer configurations. This was followed by an in-depth analysis of the creep behavior under sustained loading, providing insights into time-dependent deformation mechanisms. A preliminary durability campaign was then conducted under mild exposure conditions—saline, alkaline, and water immersion—to establish baseline degradation effects. The focus then shifted to severe acidic environments, where TRM specimens with lime-based mortars were exposed to sulfuric acid at different pH levels (1.5 to 3.0) and durations up to 6000 hours. Multi-scale analyses combining mechanical tests, microstructural characterization, and mineralogical assessment were employed to quantify degradation and to isolate the role of the mortar matrix in the aging process.

To interpret the observed changes, a chemo-mechanical damage model was developed, incorporating scalar degradation variables informed by experimental data. In parallel, a machine learning framework was implemented to predict the evolution of mechanical properties based on exposure conditions. The behavior of aged TRM composites was then studied through tensile and bond performance, highlighting the influence of acid severity. A cohesive material law (CML)-based analytical model was employed to simulate the bond–slip response under single-lap shear configurations, and predictive simulations were developed to estimate the global load–slip behavior of aged specimens. Overall, this thesis contributes to the knowledge on TRM durability by linking environmental degradation to mechanical and microstructural changes, and by proposing physically informed models for life prediction of TRM systems exposed to aggressive conditions.

Keywords: Acidic degradation; Bond–slip model; Chemo-mechanical modeling; Creep; Durability; Environmental exposure; Lime-based mortar; Long-term behavior; Machine learning; Textile-Reinforced Mortar.

Estudo integrado experimental-analítico da durabilidade de compósitos de argamassa reforçada com têxteis para o reforço de alvenaria

Resumo

A utilização de sistemas de Argamassa Reforçada com Têxteis (TRM: Textile-Reinforced Mortar) tem vindo a ganhar destaque nas últimas décadas como uma solução promissora para o reforço de estruturas de alvenaria, oferecendo compatibilidade com materiais históricos e um desempenho mecânico favorável. No entanto, apesar da crescente aplicação do TRM em estruturas reais, a compreensão do seu comportamento a longo prazo em condições ambientais agressivas permanece limitada. Em particular, os efeitos da degradação ácida, comum em ambientes industriais ou poluídos, têm sido pouco explorados na literatura científica. Esta tese de doutoramento visa colmatar essa lacuna através de uma investigação sistemática do comportamento mecânico e dos mecanismos de degradação de compósitos TRM, tanto em condições de carregamento de curto prazo como de exposição ambiental prolongada.

O estudo teve início com a avaliação experimental do comportamento à tração de sistemas TRM, analisando a influência do tipo de fibra, do número de camadas têxteis e da sua disposição. Seguiu-se uma análise aprofundada do comportamento à fluência sob carregamento sustentado, fornecendo informações relevantes sobre os mecanismos de deformação dependentes do tempo. Posteriormente, foi realizada uma campanha preliminar de durabilidade em ambientes moderados — imersão em água, soluções salinas e alcalinas — com o objetivo de estabelecer efeitos de referência. A investigação centrou-se depois em ambientes severamente ácidos, expondo espécimes de TRM com argamassas à base de cal a soluções de ácido sulfúrico com diferentes níveis de pH (entre 1,5 e 3,0) e durações até 6000 horas. Foram utilizadas análises multiescala, combinando ensaios mecânicos, caracterização microestrutural e avaliação mineralógica, para quantificar a degradação e isolar o papel da argamassa no processo de envelhecimento.

Com base nos resultados experimentais, foi desenvolvido um modelo de dano químico-mecânico, integrando variáveis de degradação calibradas. Paralelamente, foi implementado um modelo de aprendizagem automática para prever a evolução das propriedades mecânicas em função das condições de exposição. O comportamento dos compósitos envelhecidos foi também estudado através de ensaios de tração e de aderência, com destaque para a influência da intensidade ácida. Um modelo analítico baseado numa lei coesiva (CML – Cohesive Material Law) foi utilizado para simular a resposta aderência–deslizamento em configurações de ensaio de corte do tipo "single-lap", permitindo posteriormente a previsão do comportamento global de espécimes degradados. No seu conjunto, esta tese contribui para o conhecimento sobre a durabilidade do TRM, estabelecendo ligações entre a degradação ambiental, as alterações mecânicas e microestruturais, e propondo modelos fisicamente fundamentados para a previsão da vida útil de sistemas TRM expostos a condições agressivas.

Palavras-chave: Aprendizagem automática; Argamassa à base de cal; Argamassa Reforçada com Têxteis (TRM); Comportamento a longo prazo; Degradação ácida; Durabilidade; Exposição ambiental; Fluência; Modelação químico-mecânica; Modelo aderência–deslizamento..

Table of Contents

Acknowledgements iii

Statement of Integrity iv

Abstract v

Resumo vi

Table of Contents vii

List of abbreviations xii

List of figures xiv

List of tables xxii

Chapter 1 Introduction 1

1.1 Background and motivation 1

1.2 Research objectives and scope of the study 3

1.3 Outline of the thesis 4

Chapter 2 State of the art 7

2.1 Seismic vulnerability of masonry structures 7

2.2 Strengthening systems: history and emerging directions 8

2.2.1 FRP strengthening systems 8

2.2.2 TRM strengthening systems 9

2.3 Mechanical behavior of TRM systems 9

2.4 Long-Term loading behavior and creep 12

2.5 Durability of TRM: effect of environmental conditioning 13

2.5.1 Effect of alkaline exposure 14

2.5.2 Effect of saline environment 15

2.5.3 Effect of acidic exposure 16

2.6 Degradation mechanisms; capabilities of mineralogical tests 17

2.7 Mortar modeling 18

2.7.1 Machine learning approach 18

2.7.2 Chemo-mechanical modeling 18

2.8 Analytical and numerical modeling of bond behavior in TRM systems 20

2.9 Conclusion 21

Chapter 3 Characterization of TRM materials and composites 23

3.1 Introduction 23

3.2 Materials 24

3.2.1 TRM matrix 24

3.2.2 Textile meshes 24

3.2.3 Masonry substrate 25

3.2.4 Resin 26

3.3 Material characterization procedures....26
3.3.1 Mortar's flexural test....26
3.3.2 Mortar's compressive test....27
3.3.3 Mortar's elastic modulus test....28
3.3.4 Mortar's direct tensile test....29
3.3.5 XRD analysis....30
3.3.6 XRF analysis....30
3.3.7 TGA analysis....30
3.3.8 FTIR analysis....31
3.3.9 Optical Microscopy....31
3.3.10 SEM and EDX analysis....31
3.3.11 Bulk Density measurement....31
3.3.12 Open Porosity measurement....31
3.3.13 ICP Leaching analysis....31
3.3.14 Masonry unit's compressive test....32
3.3.15 Yarn's tensile test....32
3.3.16 Textile's tensile test....33
3.4 Yarn to mortar bond behavior....34
3.5 TRM to substrate bond behavior....35
3.6 TRM tensile behavior....36
3.7 Conclusion....38
Chapter 4 Short term performance of TRM under tension: Influence of test setup and layering....39
4.1 Introduction....39
4.2 Experimental program....40
4.2.1 Materials and Methods....40
4.2.2 Material characterization tests....41
4.2.3 TRM tensile testing....41
4.2.4 Gripping configurations....41
4.2.5 Textile arrangement and matrix effect....42
4.2.6 Testing procedures....43
4.3 Results and discussion....44
4.3.1 Material properties....44
4.3.2 Tensile behavior analysis....45
4.3.3 Overall TRM tensile behavior....46
4.3.4 TRM tensile behavior (TR setup)....48
4.3.5 Effect of number of layers....50
4.3.6 Comparison of setups....55
4.4 Conclusion....58
Chapter 5 Long-Term performance of TRM under creep....61
5.1 Introduction....61
5.2 Materials and characterization procedures....62
5.2.1 Bond Characterization tests....63

5.2.2 Creep tests 63
5.3 Results and discussion 66
5.3.1 Materials 66
5.3.2 Strength of single-lap shear specimens 68
5.3.3 Effect of specimens' curing time 69
5.3.4 Bond creep response 69
5.3.5 Discussion 76
5.4 Conclusion 76
Chapter 6 Long-Term performance of TRM under environmental aging: saline, alkaline, and acidic conditioning 79
6.1 Introduction 79
6.2 Sample preparation 80
6.3 Aging environments 81
6.3.1 Reference state 82
6.3.2 Dry condition 82
6.3.3 Water condition 82
6.3.4 Acidic condition 82
6.3.5 Alkaline condition 82
6.3.6 Saline condition 83
6.4 Mineralogical and chemical analysis 83
6.5 Testing overview 83
6.6 Results and discussion 84
6.6.1 Material properties 84
6.6.2 Pull-out behavior 95
6.6.3 Single-lap shear test 116
6.6.4 Comparison between the glass and the basalt TRM systems 139
6.6.5 Comparison on the different aging environments 140
6.7 Conclusion 141
Chapter 7 Multiscale analysis of TRM matrix aging in acidic environments: from experimental testing to chemo-mechanical and machine learning models 143
7.1 Introduction 143
7.2 Experimental program: durability campaign II 144
7.2.1 Materials 144
7.2.2 Aging method 146
7.2.3 Labeling schemes 147
7.3 Experimental results and discussion 147
7.3.1 Early age curing effect 147
7.3.2 Evolution of lime-based mortars during reference aging 148
7.3.3 Effect of acidic aging 151
7.3.4 Discussion on aging mechanism 154
7.4 Chemo-mechanical damage modeling 154
7.4.1 Damage modeling strategy 154

7.4.2 Damage model calibration and chemo-mechanical prediction....154
7.4.3 Model calibration and reference group validation....155
7.4.4 Extension of the damage model to aged mortars....156
7.4.5 Leaching-based chemo-mechanical prediction framework....162
7.4.6 Predictive evaluation using the chemo-mechanical model....163
7.4.7 Interpretation and integration....165
7.5 Machine learning-based modeling of flexural behavior....166
7.5.1 Model training and validation (XGBoost)....166
7.5.2 Predictive results and interpretation....169
7.5.3 Discussion....175
7.6 Conclusion....178
Chapter 8 Effect of acidic conditioning on TRM composites: experimental evaluation and mechanistic modeling of aging....181
8.1 Introduction....181
8.2 Experimental program....182
8.3 Experimental results and discussion....183
8.3.1 Mortar behavior overview....183
8.3.2 Grid performance....185
8.3.3 TRM tensile behavior....187
8.3.4 TRM pull-out behavior....195
8.3.5 TRM single-lap behavior....200
8.4 Analytical modeling of the bond interface in single-lap shear test....204
8.4.1 Definition of the rigid trilinear interfacial law $\tau(s)$....206
8.4.2 Identification of the τ–s law and CML calibration....207
8.4.3 Interfacial phases and model calibration....209
8.4.4 Scaling-Based Transformation Between CMLs:....219
8.4.5 Empirical Modeling of Interfacial Degradation Parameters....221
8.4.6 Discussion on the bond behavior modeling framework....223
8.5 Conclusion....223
Chapter 9 Conclusions and future research....225
9.1 Introduction....225
9.2 Experimental research....225
9.2.1 Main outcomes of the TRM tensile testing....225
9.2.2 Creep behavior of the TRM....226
9.2.3 Effect of mild aggressive environments....227
9.2.4 Acidic intensity and aging mechanism....228
9.3 Numerical modeling....229
9.3.1 Machine learning-based prediction of mortar degradation....229
9.3.2 Chemo-mechanical modeling of acidic damage in mortar....230
9.3.3 Numerical simulation of TRM bond behavior under shear....231
9.4 Suggestion for future works....231
9.4.1 Experimental durability assessment....231

9.4.2 Numerical modeling and predictive frameworks 232
9.4.3 Materials and system optimization 233
9.4.4 Performance-based design and service life prediction 233
REFERENCES 234

List of abbreviations

AR-glass	Alkali-Resistant Glass
$Ca(OH)_2$	Calcium Hydroxide
$CaCO_3$	Calcium Carbonate
CaO	Calcium Oxide
C-A-S-H	Calcium-Alumino-Silicate Hydrate
C-S-H	Calcium-Silicate-Hydrate
CDM	Continuum Damage Mechanics
CML	Cohesive Material Law
COV	Coefficient of Variation.
DIC	Digital Image Correlation
EDX	Energy Dispersive X-Ray Analysis
FEM	Finite Element Methods
FRCM	Fiber Reinforced Cementitious Matrix
FRP	Fiber-Reinforced Polymers
FTIR	Fourier-Transform Infrared Spectroscopy
GFRP	Glass Fiber Reinforced Polymer
H_2SO_4	Sulfuric Acid
ICP	Inductively Coupled Plasma
IMC	Inorganic Matrix Composites
ITZ	Interfacial Transition Zone
LOI	Loss Of Ignition
LVDT	Linear Variable Differential Transformer
ML	Machine Learning
NaCl	Sodium Chloride
NHL	Natural Hydraulic Lime
PBO	Poliparafenilene Benzobisoxazole
pH	Potential of Hydrogen
PSD	Particle Size Distribution
RF	Random Forest
RHA	Rice Husk Ash
RMSE	Root Mean Square Error
RSP	Recycled waste Slurry micro Powder
SEM	Scanning Electron Microscopy
SHAP	SHapley Additive exPlanations
SRG	Steel-Reinforced Grout
SSD	Saturated-Surface-Dry

TGA	ThermoGravimetric Analysis
TRC	Textile Reinforced Concrete
TRM	Textile Reinforced Mortar
XGBoost	Extreme Gradient Boosting
XRD	X-ray Diffraction
XRF	X-ray Fluorescence

List of figures

Figure 1 Out-of-plane displacement of a masonry wall observed during the 2017 Kermanshah earthquake in Iran. Such failure mechanisms contributed to significant casualties due to the widespread use of unreinforced masonry construction in the affected region [55].....8

Figure 2 Applied mechanical tests, as expressed in this paper: (a) mortar compression; (b) brick compression; (c) mortar flexural; (d) mortar elastic modulus; (e) TRM single-lap shear; (f) fiber pull-out [140]. 11

Figure 3 Configuration of the tensile test setup (glass-TRM specimen is shown) [7].....12

Figure 4 Schematic representation of the tensile response of a TRM composite, showing the three typical loading stages: uncracked, crack development, and crack stabilization [251] 21

Figure 5 Planitop HDM Restauro mortar (Mapei) used in this study: (a) the two components—liquid polymer and dry powder, and (b) the solid component (Part A) showing dispersed short fibers.....24

Figure 6 Textile reinforcements used in this study: (a) glass fiber mesh, (b) basalt fiber mesh, and (c) high-strength unidirectional steel mesh, with a detailed view of the steel cords shown in the magnified inset. 25

Figure 7 Extruded solid clay brick used as masonry substrate in TRM-related tests: (a) overall view of the brick unit; (b) detail of the sandblasted surface after two cycles of preparation to improve mortar adhesion. 26

Figure 8 Two-component epoxy resin (MapeWrap 31, Mapei) used in selected tests for impregnation and anchorage purposes. Component A (resin base) and Component B (hardener) were mixed prior to application. 26

Figure 9 Flexural test on a prismatic mortar specimen (40 × 40 × 160 mm^3) using a three-point bending configuration to determine the flexural strength according to EN 1015-11. 27

Figure 10 Compressive strength testing setups for mortar specimens: (a) independently cast cube specimen (50 × 50 × 50 mm^3); (b) half-prism from flexural test with a loading face of 40 × 40 mm^2; and (c) cylindrical specimen (⌀75 × 150 mm) tested following the elastic modulus test.....28

Figure 11 Elastic modulus test setup for cylindrical mortar specimens, showing the capping, actuator, and LVDT configuration used to record strain within the central third of the specimen.....29

Figure 12 Dog bone specimen used for the direct tensile strength test of mortar, utilized in the present study. 30

Figure 13 Compression test on a 50 × 50 × 50 mm^3 brick specimen used to evaluate the compressive strength of the masonry substrate, with lubricated Teflon sheets inserted between the loading platens. 32

Figure 14 Tensile strength test setup for single yarn specimens using the MTS Exceed® E44 electromechanical testing machine. 33

Figure 15 illustrates the experimental setup used for the tensile strength tests on textile meshes. (a) presents the MTS-based configuration used for certain glass specimens; (b) shows the hydraulic actuator system; and (c) provides a close-up of the central gauge region equipped with external instrumentation for strain measurement. 34

Figure 16 Test setup for pull-out tests showing the yarn anchored in resin, embedded in mortar, and instrumented with dual LVDTs for monitoring axial slip. 35

Figure 17 Single-lap shear test configuration showing TRM composite bonded to brick substrate with, LVDTs mounted on an omega-shaped aluminum piece, and setup within the hydraulic loading frame. 36

Figure 18 (a) Specimen preparation of TRM coupons reinforced with steel cords; (b) specimen preparation of TRM coupons reinforced with glass textile; (c) tensile test configuration showing the test setup. 37

Figure 19 Overview of the experimental program.....40

Figure 20 Schematic representation of TRM coupons and test setups: a) SF setup; b) MF setup; c) LF setup; d) TR setup. 42

Figure 21 Configuration of the tensile test setup (glass-TRM specimen is shown) 44

Figure 22 Stress-Strain curve for single-layer specimens for: a) MF_G_1L_10; b) MF_S_1L_10; c) SF_G_1L_10; d) LF_G_1L_10. 47

Figure 23 Crack distribution (failure location is indicated by a box) for single-layer specimens for representative samples of: a) MF_G_1L_10, b) MF_S_1L_10, c) SF_G_1L_10, and d) LF_G_1L_10. 48

Figure 24 Failure of coupons with TR setup: a) stress-strain behavior of TR_G_1L_10 with final crack distribution; b) stress-strain behavior of TR_S_1L_10 with final crack distribution, accompanied by failure location in the box; c) delamination of the interface of the steel fabric and matrix inside the gripping area. 49

Figure 25 SEM microscopy of MF_G_2L_10 before testing (unpolished surface). 51

Figure 26 Stress-Strain curves for multi-layer specimens with MF setup, for: a) MF_S_2L_10; b) MF_S_2L_15; c) MF_G_2L_10; d) MF_G_2L_15. 52

Figure 27 Crack distribution (failure location is indicated by a box) for multi-layer specimens with MF setup using DIC analysis, for representative samples of: a) MF_S_2L_10; b) MF_S_2L_15; c) MF_G_2L_10; d) MF_G_2L_15. 53

Figure 28 Stress-strain curves for multi-layer specimens with TR setup for: a) TR_G_2L_10; b) TR_G_2L_15; c) TR_S_2L_15. 54

Figure 29 final crack distribution (failure location marked with a box) for multi-layer specimens with TR setup using DIC analysis, for representative samples of a) TR_G_2L_10; b) TR_G_2L_15; c) TR_S_2L_15. 56

Figure 30 Average stress-strain curves for each group vs. bare textiles for: a) single-layer glass TRM; b) multi-layer glass TRM; c) single-layer steel TRM; d) multilayer steel TRM. 57

Figure 31 Comparison between the strength of each test setup and the textile's strength as the upper threshold for: a) glass-based TRM; b) steel-based TRM. 58

Figure 32 Overview of the experimental program presented in this chapter. 62

Figure 33 Configuration of the creep test on single-lap shear specimens: (a) overall view of the test setup; (b) detailed view of the specimen setup. 63

Figure 34 Creep testing setup for glass yarn: (a) Overview of the setup with weights applied for tensile loading; (b) Close-up view of the glass yarn and gripping mechanism used in the creep test. 64

Figure 35 Mechanical characteristics of mortars as affected by prolonged curing exposure in compressive and flexural strength tests. 66

Figure 36 Displacement vs. creep time diagram for the single glass yarn under creep loading. 67

Figure 37 Ultimate strength test results for single-lap shear samples: (a) envelope of the load-slip curve, including the average curve for samples at 90 days; (b) variation in peak load with increasing curing time. 68

Figure 38 Normalized ultimate strength versus curing time for flexural, compressive, and single-lap shear tests, showing the consistent growth trend across different test setups. 69

Figure 39 Creep loading results for single-lap shear specimens under 70% of the average ultimate strength at 90 days: (a) force-time and slip-time behavior over the entire test duration; (b) detailed force-time and slip-time behavior during the initial 14 days. 71

Figure 40 Creep loading results for single-lap shear specimens under 60% of the average ultimate strength at 90 days: (a) force-time and slip-time behavior over the entire test duration; (b) detailed force-time and slip-time behavior during the initial 14 days. 71

Figure 41 Creep loading results for single-lap shear specimens under 50% of the average ultimate strength at 90 days: (a) force-time and slip-time behavior over the entire test duration; (b) detailed force-time and slip-time behavior during the initial 14 days. 73

Figure 42 Creep loading results for single-lap shear specimens under 40% of the average ultimate strength at 90 days: (a) force-time and slip-time behavior over the entire test duration; (b) detailed force-time and slip-time behavior during the initial 14 days. 74

Figure 43 Creep loading results for single-lap shear specimens under 30% of the average ultimate strength at 90 days: (a) force-time and slip-time behavior over the entire test duration; (b) detailed force-time and slip-time behavior during the initial 14 days. 75

Figure 44 Flowchart of the experimental program 80

Figure 45 Schematic representation of curing of the samples. 80

Figure 46 (a) External view of the immersion tanks used for different aging conditions; (b) internal configuration showing TRM specimens arranged for exposure, illustrating the orientation and spacing maintained during the aging process. 81

Figure 47 Mechanical properties of mortars under dry and water condition conditions as a function of exposure time: (a) compressive strength; (b) flexural strength; (c) elastic modulus. 86

Figure 48 XRD patterns of mortar samples under different aging environments: unreacted, dry condition, water condition, alkaline, acidic, and saline. 87

Figure 49 Optical microscopy images of mortar specimens after 5000 hours under different conditions: (a) dry condition, (b) water condition, (c) acidic exposure, (d) alkaline exposure, and (e) saline exposure. 88

Figure 50 SEM micrographs of mortar samples under different exposure conditions: (a) dry condition, (b) water condition, and (c) acidic exposure. 89

Figure 51 TGA analysis of mortar samples aged under different environmental exposures: (a) weight loss versus temperature; (b) derivative weight loss versus temperature for dry condition, water condition, acidic exposure, alkaline exposure, and saline exposure. 89

Figure 52 Mechanical properties of mortars under increasing aging exposure time- effect of acidic environment: (a) compressive strength; (b) flexural strength; (c) elastic modulus 91

Figure 53 Mechanical characteristics of mortars exposed to three aging environments — effect of alkaline exposure: (a) compressive strength; (b) flexural strength; (c) elastic modulus.....93

Figure 54 Mechanical properties of mortars as a function of aging exposure time- effect of saline environment: (a) compressive strength; (b) flexural strength; (c) elastic modulus. 94

Figure 55 Load-slip curves of the pull-out test for the glass fiber in the DC environment, showing each individual specimen and the average curve for each group: (a) P_G_0; (b) P_G_DC_1000; (c) P_G_DC_3000; (d) P_G_DC_5000 96

Figure 56 Load-slip curves of the pull-out test for the glass fiber in the WI environment, showing each individual specimen and the average curve for each group: (a) P_G_WI_1000; (b) P_G_WI_3000; (c) P_G_WI_5000. 97

Figure 57 Pull-out performance of glass-based TRM under DC and WI conditions: (a) average load–slip response at the loaded end; (b) peak load; (c) debonding energy; (d) pull-out energy. 98

Figure 58 Load-slip curves of the pull-out test for the glass fiber in the AC environment, showing each individual specimen and the average curve for each group: (a) P_G_AC_1000; (b) P_G_AC_3000; (c) P_G_AC_5000. 99

Figure 59 Pull-out parameters of single glass-made TRM under different environmental conditions — effect of acidic exposure: (a) average load–slip response at the loaded end; (b) peak load; (c) debonding energy; (d) pull-out energy. 100

Figure 60 Pull-out parameters of single TRM glass yarn in different environments- effect of alkaline environment: (a) average load-slip response at the loaded end; (b) peak load; (c) debonding energy; (d) pull-out energy. 102

Figure 61 Load-slip curves of the pull-out test for the glass fiber in the AK environment, showing each individual specimen and the average curve for each group: (a) P_G_AK_1000; (b) P_G_AK_3000; (c) P_G_AK_5000. 103

Figure 62 Load-slip curves from the pull-out tests of glass fiber in saline environment, showing individual specimen results and the average curve for each aging duration: (a) P_G_SA_1000; (b) P_G_SA_3000; (c) P_G_SA_5000. 104

Figure 63 Pull-out parameters of single glass-based TRM in various environments; effect of saline environment: (a) average load-slip response at the load end; (b) peak load; (c) debonding energy; (d) pull-out energy.....105

Figure 64 Load-slip curves of the pull-out test for the basalt fiber in the DC environment, showing each individual specimen and the average curve for each group: (a) P_B_0; (b) P_B_DC_1000; (c) P_B_DC_3000; (d) P_B_DC_5000.....107

Figure 65 Load-slip curves of the pull-out test for the basalt fiber in the WI environment, showing each individual specimen and the average curve for each group: (a) P_B_WI_1000; (b) P_B_WI_3000; (c) P_B_WI_5000. 108

Figure 66 Pull-out parameters of basalt-based TRM under dry and water condition conditions: (a) average load–slip response of single basalt fiber; (b) peak load; (c) debonding energy; (d) pull-out energy.....109

Figure 67 Load-slip curves of the pull-out test for the basalt fiber in the AC environment, showing each individual specimen and the average curve for each group: (a) P_B_AC_1000; (b) P_B_AC_3000; (c) P_B_AC_5000. 110

Figure 68 Pull-out parameters of single basalt-based TRM in different environments- effect of acidic environment: (a) average load-slip response of single basalt fiber in pull-out test; (b)peak load; (c) debonding energy; (d) pull-out energy. 111

Figure 69 Load-slip curves of the pull-out test for the basalt fiber in the AK environment, showing each individual specimen and the average curve for each group: (a) P_B_AK_1000; (b) P_B_AK_3000; (c) P_B_AK_5000..... 112

Figure 70 Pull-out parameters of single basalt TRM yarn in different environments; effect of alkaline environment: (a) average load-slip response at the load end; (b) peak load; (c) debonding energy; (d) pull-out energy..... 113

Figure 71 Pull-out parameters of single basalt-based TRM in various environment; effect of saline environment: (a) average load-slip response at the loaded end; (b) peak load; (c) debonding energy; (d) pull-out energy. 115

Figure 72 Load-slip curves from the pull-out tests of basalt fiber in saline environment, showing individual specimen results and the average curve for each aging duration: (a) P_B_SA_1000; (b) P_B_SA_3000; (c) P_B_SA_5000. 116

Figure 73 Failure modes for the single-lap shear test according to CNR-DT 215 [308] 117

Figure 74 single-lap shear performance of glass-based TRM under dry and water conditions: (a) average load–slip response; (b) peak load; (c) debonding energy; (d) slip corresponding to peak load. 118

Figure 75 Load-slip curves of the single-lap shear test for the glass fiber in the DC environment, showing each individual specimen and the average curve for each group: (a) S_G_0; (b) S_G_DC_1000; (c) S_G_DC_3000; (d) S_G_DC_5000..... 119

Figure 76 Load-slip curves of the single-lap shear test for the glass fiber in the WI environment, showing each individual specimen and the average curve for each group: (a) S_G_WI_1000; (b) S_G_WI_3000; (c) S_G_WI_5000. 120

Figure 77 Load-slip curves of the single-lap shear test for the glass fiber in the AC environment, showing each individual specimen and the average curve for each group: (a) S_G_AC_1000; (b) S_G_AC_3000; (c) S_G_AC_5000..... 121

Figure 78 Single-lap behavior of glass-TRM in different exposure durations and mediums; effect of acidic environment: (a) average load-slip curve; (b) peak load; (c) debonding energy; (d) slip corresponding to peak load. 122

Figure 79 Load-slip curves of the single-lap shear test for the glass fiber in the AK environment, showing each individual specimen and the average curve for each group: (a) S_G_AK_1000; (b) S_G_AK_3000; (c) S_G_AK_5000..... 124

Figure 80 Single-lap behavior of glass-TRM in different exposure durations and mediums- effect of alkaline environment: (a) average load-slip curve; (b) peak load; (c) debonding energy; (d) slip corresponding to peak load. 125

Figure 81 Load-slip curves from the single-lap shear tests of glass fiber in saline environment, showing individual specimen results and the average curve for each aging duration: (a) S_G_SA_1000; (b) S_G_SA_3000; (c) S_G_SA_5000 126

Figure 82 Single-lap behavior of glass-TRM under various exposure durations and conditions; effect of saline environment: (a) average load-slip curve, (b) peak load, (c) debonding energy, (d) slip corresponding to peak load. 127

Figure 83 Load-slip curves of the single-lap shear test for the basalt fiber in the DC environment, showing each individual specimen and the average curve for each group: (a) S_B_0; (b) S_B_DC_1000; (c) S_B_DC_3000; (d) S_B_DC_5000. 129

Figure 84 Load-slip curves of the single-lap shear test for the basalt fiber in the WI environment, showing each individual specimen and the average curve for each group: (a) S_B_WI_1000; (b) S_B_WI_3000; (c) S_B_WI_5000 130

Figure 85 single-lap shear performance of basalt-based TRM under dry and water conditions: (a) average load–slip response; (b) peak load; (c) debonding energy; (d) slip corresponding to peak load. 131

Figure 86 Load-slip curves of the single-lap shear test for the basalt fiber in the AC environment, showing each individual specimen and the average curve for each group: (a) S_B_AC_1000; (b) S_B_AC_3000; (c) S_B_AC_5000. 132

Figure 87 Single-lap behavior of basalt-TRM in different exposure durations and mediums; effect of acidic environment: (a) average load-slip curve; (b) peak load; (c) debonding energy; (d) slip corresponding to peak load. 133

Figure 88 Load-slip curves of the single-lap shear test for the basalt fiber in the alkaline environment, showing each individual specimen and the average curve for each group: (a) S_B_AK_1000; (b) S_B_AK_3000; (c) S_B_AK_5000. 135

Figure 89 Single-lap behavior of basalt-TRM in different exposure durations and mediums; effect of alkaline environment: (a) average load-slip curve; (b) peak load; (c) debonding energy; (d) slip corresponding to peak load. 136

Figure 90 Load-slip curves from the single-lap shear tests of basalt fiber in saline environment, showing individual specimen results and the average curve for each aging duration: (a) S_B_SA_1000; (b) S_B_SA_3000; (c) S_B_SA_5000. 137

Figure 91 Single-lap behavior of basalt-TRM under various exposure durations and conditions; effect of saline environment: (a) average load-slip curve, (b) peak load, (c) debonding energy, (d) slip corresponding to peak load 138

Figure 92 Overview of the experimental program, of the present chapter. 145

Figure 93 Characterization of the mortar: (a) particle size distribution of the dry mortar; (b) FTIR spectra of unreacted mortar, and isolated short fibers; (c) XRD patterns of unreacted mortar with fibers; (d) SEM image showing the morphology of bundled short fibers. 146

Figure 94 Heat flow and cumulative heat release over 10 days. Sample 1 contains mortar part B; Sample 2 is mixed with water only. 148

Figure 95 Mechanical performance of mortar specimens during curing and aging phases: (a) prismatic compressive strength; (b) cylindrical compressive strength; (c) flexural strength; (d) cyclic elastic modulus. 149

Figure 96Physical properties of lime-based mortars in all environments: (a) bulk density and (b) open porosity evolution during curing and exposure. 150

Figure 97 Chemical and mineralogical test results on lime-based mortar samples exposed to climatic chamber and water immersion: (a) XRD patterns; (b) TGA thermograms. 150

Figure 98 Chemical and mineralogical test results on lime-based mortar samples exposed to different acidic immersion: (a) XRD patterns; (b) TGA thermograms; (c) optical microscopy for P15_6000 group showing altered zone. 152

Figure 99 SEM image of the P15-6000 mortar group, showing pores filled with calcite crystals. 152

Figure 100 Trilinear damage model for the unexposed reference group (E_C), compared against the experimental stress–strain envelope. 156

Figure 101 Stress–strain response of cylindrical specimens under compression: experimental envelope and numerical model for dry-conditioned samples aged (a) 1000 h; (b) 3000 h; and (c) 6000 h. 158

Figure 102 Stress–strain response of cylindrical specimens under compression: experimental envelope and numerical model for water-immersion samples aged (a) 1000 h; (b) 3000 h; and (c) 6000 h. 159

Figure 103 Stress–strain response of cylindrical specimens under compression: experimental envelope and numerical model for acidic solution with pH of 1.5 samples aged (a) 1000 h; (b) 3000 h; and (c) 6000 h. 160

Figure 104 Stress–strain response of cylindrical specimens under compression: experimental envelope and numerical model for acidic solution with pH of 2 samples aged (a) 1000 h; (b) 3000 h; and (c) 6000 h. 161

Figure 105 Stress–strain response of cylindrical specimens under compression: experimental envelope and numerical model for acidic solution with pH of 3 samples aged (a) 1000 h; (b) 3000 h; and (c) 6000 h. 162

Figure 106 Stress–strain response of selected exposure groups: individual tests, average curve, fitted trilinear model, and predicted chemo-mechanical model for (a) EM_C_P15_3000, (b) EM_C_P2_1000, (c) EM_C_P2_6000, and (d) EM_C_P3_3000. 164

Figure 107 XGBoost algorithm flowchart, depicting a series of consecutive decision trees, initial split (yellow), resulting predictions (green), and the adjustment of residuals (equations). 168

Figure 108 Histogram of the utilized experimental dataset. 169

Figure 109 Stress vs. displacement diagram for each individual specimens from the experiments for: (a) F_0 group; (b) F_DC_1000; (c) F_WI_1000; (d) F_AC_1000. 170

Figure 110 Results of XGBoost performance evaluation across various (a) cross-validation folds and (b) learning rates during Bayesian optimization for training and validation sets. 171

Figure 111 Comparative performance analysis of the XGBoost model representing (a) KDE for the training dataset, (b) KDE for the testing dataset, scatterplots of actual vs. predicted values for (c) training and (d) testing datasets. 174

Figure 112 SHAP summary plot of the most important input features for predicting stress values of mortar. 175

Figure 113 Variation of the flexural strength in different aging media from (a) experimental and (b) machine learning outputs. 175

Figure 114 Predicted Stress vs. displacement diagram for each individual specimens from the XGBoost output for: (a) F_0 group; (b) F_DC_1000; (c) F_WI_1000; (d) F_AC_1000. 177

Figure 115 Comparative analysis of experimental versus machine learning prediction of flexural strength for different environments (DC, WI and AC) at intervals of 1000, 3000, and 5000 hours of exposure. 178

Figure 116 An overview flowchart of the experimental campaign. 182

Figure 117 Variations in the mechanical properties of the textiles over exposure time under different aging environments: (a) Tensile strength variation across aging conditions; (b) Elastic modulus variation across aging conditions. 186

Figure 118 (a) Failure mode “a” in specimen T_C_RW_6000_2; (b) failure mode “b” in specimen T_C_RC_1000_2 187

Figure 119 Stress-strain curves of individuals and group average for: (a) T_C; (b) T_C_RC_1000; (c) T_C_RC_3000; (d) T_C_RC_6000; (e) T_C_RW_1000; (f) T_C_RW_3000; (g) T_C_RW_6000; (h) T_C_P15_1000; (i) T_C_P15_3000; (j) T_C_P15_6000; (k) T_C_P2_1000; (l) T_C_P2_3000; (m) T_C_P2_6000; (n) T_C_P3_1000; (o) T_C_P3_3000; (p) T_C_P3_6000. 189

Figure 120 Cracks properties: (a) average crack numbers; (b) average crack spacing. 192

Figure 121 Load-slip curves of individuals and group average for: (a) P_0; (b) P_RC_1000; (c) P_RC_3000; (d) T_RC_6000; (e) P_RW_1000; (f) P_RW_3000; (g) P_RW_6000; (h) P_P15_1000; (i) P_P15_3000; (j) P_P15_6000; (k) P_P2_1000; (l) P_P2_3000; (m) P_P2_6000; (n) P_P3_1000; (o) P_P3_3000; (p) P_P3_6000. 197

Figure 122 Pull-out parameters of single TRM glass yarn in different environments vs. exposure time: (a) average load-slip response at the load end; (b) peak load; (c) debonding energy; (d) pull-out energy. 198

Figure 123 Stress-slip curves of individuals and group average for: (a) S_0; (b) S_RC_1000; (c) S_RC_3000; (d) S_RC_6000; (e) S_RW_1000; (f) S_RW_3000; (g) S_RW_6000; (h) S_P15_1000; (i) S_P15_3000; (j) S_P2_1000; (k) S_P2_3000; (l) S_P2_6000; (m) S_P3_1000; (n) S_P3_3000; (o) S_P3_6000. 201

Figure 124 Single-lap behavior of glass-TRM in different exposure durations and mediums: (a) average stress-slip curve; (b) peak stress; (c) debonding energy; (d) slip corresponding to peak load. 202

Figure 125 (a) Single-lap shear setup with bonded length L; (b) differential free-body diagram illustrating internal forces and shear stress transfer through the interface. 205

Figure 126 Trilinear cohesive law with distinct elastic, softening, and residual frictional branches. 206

Figure 127 Calibrated rigid trilinear τ–s law for specimen S-RC-1000-1, showing elastic, softening, and frictional branches. 210

Figure 128 Distributions of τx, σx, and s(x) at the end of Stage I. 212

Figure 129 Distributions of τx, σx, and s(x) at the end of Stage II. 213

Figure 130 Distributions of τx, σx, and s(x) at the end of Stage III. 215

Figure 131 Distributions of τx, σx, and s(x) at the end of Stage IV. 216

Figure 132 Distributions of τx, σx, and s(x) at the end of Stage V. 217

Figure 133 Distributions of τx, σx, and s(x) at the end of Stage VI. 218

Figure 134 Global stress–slip curve for specimen GP79-1, showing transitions across all six loading stages with color-coded segments. 219

List of tables

Table 1 Literature summary on immersing specimens in acidic and water solutions. 17

Table 2 Detailed specification of test setups 43

Table 3 Results of material characterization test 45

Table 4 Test results on characterization parameters of different groups of coupons (CoV is given inside parenthesis) 46

Table 5 Specification of the single-lap shear test's sample in creep loading 65

Table 6 Detailed specification of test scheme 85

Table 7 XRF elemental composition of mortar samples subjected to different environmental exposures: dry condition, water condition, acidic exposure, alkaline exposure, and saline exposure. 90

Table 8 Elemental concentrations (ICP analysis) of the acidic and water immersion solutions after interaction with mortar specimens. Samples were collected before the second renewal cycle at one month of exposure. 153

Table 9 Model parameters for all aging environments 156

Table 10 Predicted versus experimental model parameters for selected exposure groups using the leaching-based chemo-mechanical model. 165

Table 11 Summary of the experimental database prepared for the machine learning model..... 169

Table 12 Hyperparameter tuning results of Bayesian optimization methods for the XGBoost model. 172

Table 13 Comparing performance metrics of machine learning models on training and testing datasets for stress prediction..... 173

Table 14 Characteristics of specimens tested 184

Table 15 Characteristics of specimens tested (continued from Table 14) 185

Table 16 Mechanical properties of the exposed textiles under different aging conditions 186

Table 17 Test results for characterization parameters of different coupon groups (CoV shown in parentheses) 190

Table 18 Test results on characterization parameters of different groups of coupons (continued from Table 17) 191

Table 19 Experimental slip–stress data and effective bond lengths for all specimen groups. 221

Table 20 Calibrated φ and ψ values with corresponding R^2 and τ predictions for aged groups. 221

Chapter 1 Introduction

1.1 Background and motivation

Masonry structures represent a substantial portion of the global built heritage, particularly in historical city centers and culturally significant sites across Europe and the Mediterranean region. These constructions, often characterized by low tensile strength and brittle behavior, are highly vulnerable to seismic actions, environmental degradation, and long-term aging phenomena. The preservation and continued use of such structures are of paramount importance not only for their architectural and historical value but also for societal, cultural, and economic reasons [1,2]. However, the structural deficiencies inherent to unreinforced masonry, when combined with increasing exposure to hazards such as earthquakes, moisture ingress, and pollution-driven deterioration, necessitate the application of compatible and effective strengthening interventions capable of enhancing structural safety while maintaining material and aesthetic compatibility [3].

Among the existing strengthening methods, FRPs have been widely employed due to their high strength-to-weight ratio and ease of application. Nevertheless, the use of organic matrices in FRP systems presents several drawbacks, particularly when applied to masonry substrates. Organic polymers are prone to moisture uptake, are chemically incompatible with porous and alkaline substrates, and exhibit sensitivity to ultraviolet radiation and thermal fluctuations. Furthermore, their long-term durability remains uncertain under aggressive environmental conditions, raising concerns regarding their suitability for conservation works in heritage structures [4,5]. These limitations have led to the emergence of TRM systems as an alternative solution over the past two decades. In TRM, the organic resin is replaced by an inorganic mortar matrix, improving compatibility, vapor permeability, and reversibility. As such, TRMs offer a more sustainable and technically coherent option for masonry strengthening, particularly in conservation-sensitive contexts [6].

The mechanical performance of TRM systems under short-term conditions has been extensively studied in the literature, with research focusing on direct tensile tests, bond performance, and flexural capacity of TRM-strengthened members. These investigations have established the critical role of the matrix–textile interface, textile configuration, and mortar type in defining the composite response. However, despite the growing volume of experimental and numerical studies, certain aspects of TRM behavior remain underexplored [7]. In particular, inconsistencies in test procedures, limited understanding of interfacial mechanisms, and the influence of component variability on system-level performance highlight existing knowledge gaps that warrant further systematic investigation. These issues become more prominent when the durability and time-dependent behavior of TRM systems are taken into account, which are critical to ensuring long-term effectiveness and serviceability [8,9].

The long-term performance of TRM systems, both under sustained mechanical loading and environmental exposure, remains insufficiently explored in current research. While numerous studies have focused on short-term mechanical improvements, limited attention has been given to time-dependent phenomena such as creep and chemical degradation. Sustained loading can induce progressive bond weakening and deformation at the textile–mortar interface, which may compromise structural efficiency over time [10]. Additionally, chemically aggressive environments, particularly acidic

exposure, pose significant risks to the integrity of lime-based and cementitious matrices. Acidic attack, often associated with atmospheric pollution or acid rain, leads to calcium leaching, matrix softening, and possible formation of expansive phases such as gypsum [11,12]. Historical evidence has shown that acid deposition caused extensive damage to masonry and concrete infrastructure, and similar environmental threats remain relevant in modern urban and industrial contexts. Despite these concerns, there is still a lack of standardized testing procedures and durability criteria for TRM systems under such exposures, highlighting the need for more comprehensive investigation into their long-term resistance [13,14].

While mechanical testing provides valuable insight into performance loss, it does not capture the underlying mechanisms of degradation that influence composite behavior. The evolution of material properties under environmental exposure is closely linked to changes occurring at the microstructural and mineralogical levels, including the formation of expansive phases, decalcification, and pore structure modification. Despite this, most investigations on TRM durability are limited to structural-scale assessments, often conducted by civil or structural engineers with minimal emphasis on chemical and mineralogical characterization. In this context, the present research integrates advanced characterization techniques, such as XRD, FTIR, SEM, TGA, and optical microscopy, to identify chemical alterations and correlate them with changes in mechanical performance [11,15]. This microstructural and mineralogical understanding is essential to decipher the actual degradation pathways, especially in porous lime-based matrices, where environmental interactions are highly pronounced.

In parallel, the increasing complexity of TRM systems and their interaction with diverse environmental exposures has highlighted the need for advanced data-driven tools to model degradation behavior. Machine learning techniques have demonstrated strong potential in this context, particularly for capturing nonlinear and multivariate relationships among parameters such as pH level, exposure duration, mechanical strength, and microstructural evolution. These methods enable the development of predictive models that can estimate performance loss with higher accuracy and adaptability compared to traditional regression-based approaches [16,17]. Moreover, machine learning can assist in identifying dominant variables influencing degradation and facilitate the interpretation of large experimental datasets that are otherwise difficult to analyze through classical statistical frameworks. When properly trained and validated, such models provide a powerful basis for anticipating long-term behavior under untested conditions and for optimizing design strategies in TRM applications exposed to aggressive environments.

In addition to data-driven tools, the use of analytical and numerical modeling remains essential for interpreting experimental results and simulating the behavior of TRM systems under various mechanical and environmental conditions. Analytical formulations, particularly those based on cohesive zone models, have been effectively used to describe the bond-slip response observed in single-lap shear and pull-out configurations. Trilinear cohesive laws, in particular, offer a simplified yet representative framework for capturing the progressive stages of bond degradation, including initial elastic response, peak interfacial strength, and post-peak softening behavior. These models enable the quantitative assessment of interfacial performance parameters, such as maximum shear stress, fracture energy, and slip capacity, which are critical for predicting failure modes and understanding the influence of matrix degradation or textile debonding. Furthermore, they provide a robust platform for parametric analyses aimed at evaluating the effects of different textile types, matrix compositions, and environmental exposures [18,19]. Numerical implementations of these models, often through finite element or discrete approaches, allow for more detailed simulations at the component or structural scale, thus supporting the design and optimization of TRM-strengthened systems. Such models are also valuable in the development of design guidelines, particularly when empirical data is scarce or when accelerated durability testing cannot fully capture long-term effects. Ultimately, the integration of analytical and numerical modeling into TRM research enhances the predictive capacity and reliability of strengthening

interventions, particularly in scenarios where environmental degradation and sustained loading are expected to interact [20,21].

The integration of experimental evidence, analytical formulations, and data-driven approaches offers a comprehensive framework for evaluating the long-term durability of TRM systems. Chemo-mechanical modeling, particularly when coupled with damage mechanics and degradation laws based on chemical leaching or matrix transformation, provides valuable insights into the progressive deterioration of mortar-based composites under aggressive environments. Such models enable the simulation of performance evolution by accounting for both mechanical and chemical influences, thus bridging the gap between material-level degradation and structural behavior [22,23]. This integrated perspective is essential for the development of reliable life-cycle assessments and performance-based design strategies, especially in applications where maintenance interventions are limited or infeasible. As TRM systems are increasingly used for the long-term protection of vulnerable masonry structures, a predictive understanding of their mechanical behavior under coupled environmental and mechanical stressors becomes indispensable.

1.2 Research objectives and scope of the study

The primary aim of this research is to advance the scientific understanding of TRM systems, with particular focus on their mechanical performance, long-term reliability, and degradation mechanisms under various environmental and mechanical stressors. To achieve this aim, a series of interconnected objectives have been established, addressing both experimental and modeling aspects at multiple scales. The scope of the study includes short-term and long-term mechanical characterization, environmental durability assessments, microstructural investigations, and the development of analytical, numerical, and data-driven models. The specific objectives are as follows:

Objective 1- To characterize the short-term mechanical behavior of TRM materials and systems under direct tension, compression, and bond-related loading conditions. This objective involves the systematic evaluation of mechanical performance through standardized tests on both matrix and composite levels. Particular attention is given to the tensile response of TRM, as it plays a critical role in determining the effectiveness of the strengthening system. Different textile types, reinforcement ratios, and configurations are assessed to define the mechanical parameters that govern the composite response under quasi-static conditions.

Objective 2- To investigate the long-term behavior of TRM systems subjected to sustained loading, with emphasis on creep performance. The influence of time-dependent deformation under constant load is evaluated using long-duration single-lap shear tests. Variables such as applied load level and matrix curing time are considered to understand the development of creep, its effect on interfacial bond integrity, and the implications for structural reliability over extended service periods.

Objective 3- To assess the durability of TRM composites under different chemically aggressive environments, including saline, alkaline, and acidic conditioning. A series of accelerated aging campaigns are conducted to evaluate the mechanical degradation and failure mechanisms induced by various chemical exposures. Pull-out, shear, and flexural tests are performed in conjunction with reference conditions to quantify the extent and nature of performance loss across exposure types and durations.

Objective 4- To elucidate the specific mechanisms of degradation under acidic conditions and their impact on mortar behavior. Acidic environments are studied in greater depth due

to their critical role in matrix deterioration. Specimens are exposed to varying pH levels and durations to investigate calcium leaching, strength reduction, and interfacial changes. The resulting trends inform the development of mechanistic understanding and predictive modeling strategies.

Objective 5- To explore the feasibility of applying machine learning techniques to predict durability performance based on environmental and material parameters. The study investigates the use of machine learning frameworks to model and forecast TRM degradation trends. By training models on experimental datasets involving exposure conditions and mechanical outcomes, key influencing variables can be identified, and predictive insights generated to support design and assessment.

Objective 6- To conduct microstructural and mineralogical analyses to support the interpretation of aging mechanisms. The integration of techniques such as XRD, TGA, SEM, FTIR, and optical microscopy allows the identification of mineral phase transformations, pore structure evolution, and chemical alterations within the matrix. These observations are correlated with mechanical test results to provide a multiscale understanding of material deterioration.

Objective 7- To develop analytical and numerical models for simulating the mechanical behavior of TRM under tensile and bond conditions. Analytical expressions and numerical implementations are established to describe the interface behavior observed in pull-out and single-lap shear tests. Cohesive zone models incorporating trilinear bond-slip laws are employed to simulate the local and global response of TRM systems, supporting parametric analysis and system optimization.

Objective 8- To implement a chemo-mechanical damage model for predicting mortar degradation under acidic exposure. A continuum damage mechanics framework is adopted to simulate the deterioration of mortar subjected to acid-induced aging. The model incorporates degradation laws based on leaching behavior and aims to capture the coupled evolution of mechanical and chemical properties over time, providing a basis for performance forecasting and life-cycle analysis.

Through these objectives, the research offers a comprehensive investigation into the performance and durability of TRM systems, spanning experimental characterization, degradation mechanism analysis, and predictive modeling. The study was conducted through an extensive experimental campaign supported by microscopic, chemical, and mineralogical characterization, and further complemented by analytical formulations, numerical simulations, and data-driven model development tailored to the observed degradation mechanisms. This integrated framework ensures a multiscale understanding of TRM behavior under both mechanical loading and environmental exposure, addressing current knowledge gaps and enabling improved long-term application in structural strengthening.

1.3 Outline of the thesis

This thesis is the result of a multiscale and multidisciplinary investigation into the mechanical behavior and durability of TRM systems for the strengthening of masonry structures. The research integrates experimental testing, chemical and microstructural analysis, as well as modeling approaches, both

numerical and data-driven, to address performance-related knowledge gaps at both material and system levels. The thesis is structured to reflect the sequential development of this investigation, beginning with a review of the scientific context, followed by short-term and long-term mechanical studies, environmental degradation assessments, and modeling frameworks aimed at prediction and interpretation. The work is organized into nine chapters. A brief summary of each chapter is provided below:

- **Chapter 1 – Introduction:** Introduces the research background and motivation, defines the objectives and scope of the study, and outlines the structure of the thesis.

- **Chapter 2 – State of the art:** Provides a literature review on the strengthening of masonry structures, with emphasis on the development and mechanical characterization of TRM systems. Special attention is given to long-term mechanical behavior and durability under environmental exposures, as well as current modeling strategies.

- **Chapter 3 – Characterization of TRM materials and composites:** Presents the mechanical and physical characterization of the individual constituents of the TRM system, including mortar matrices, reinforcing textiles, and their composite configurations. This chapter details the material properties obtained through various mechanical and microstructural tests on the mortars, as well as tensile tests on dry textiles and yarns. In addition, the mechanical characterization of the TRM composites is introduced to support subsequent performance evaluations.

- **Chapter 4 - Short term performance of TRM under tension: Influence of test setup and layering:** Investigates the tensile behavior of TRM composites under quasi-static loading across a range of configurations. The influence of test setup, gripping method, reinforcement ratio, and textile layering is assessed through direct tensile testing of multiple specimen configurations. The results provide insights into stress distribution, failure modes, and key parameters governing tensile performance, thereby defining the reference mechanical response of TRM systems prior to long-term or environmental exposure.

- **Chapter 5 – Long-term performance of TRM under creep:** Examines the creep behavior of TRM systems under sustained shear loading using a single-lap configuration. The influence of load level and curing age on long-term deformation is assessed through a 250-day experimental campaign.

- **Chapter 6 – Long-term performance of TRM under environmental aging: saline, alkaline, and acidic conditioning:** Presents the durability behavior of TRM composites subjected to saline, alkaline, and mildly acidic environments. Reference dry and water immersion conditions are included. Mechanical testing is complemented by microstructural and mineralogical analyses.

- **Chapter 7 – Multiscale analysis of TRM matrix aging in acidic environments: from experimental testing to chemo-mechanical and machine learning models:** Focuses on the degradation of lime-based mortar under sulfuric acid exposure. A multiscale approach is adopted, combining mechanical testing, chemical analysis, machine learning prediction, and chemo-mechanical damage modeling.

- **Chapter 8 – Effect of acidic conditioning on TRM composites: experimental evaluation and mechanistic modeling of aging:** Evaluates the mechanical performance of TRM systems aged under varying acidic intensities through tensile, pull-out, and shear tests. A numerical bond-slip model is developed to simulate interfacial degradation using a cohesive material law framework.

- **Chapter 9 – Conclusion and future research:** Summarizes the main findings of the research and proposes directions for future investigation, integrating the experimental and numerical outcomes at both the material and composite levels.

Chapter 2
State of the art

2.1 Seismic vulnerability of masonry structures

Masonry structures, integral to Europe's historical fabric, are still widespread globally today, particularly in developing nations and low-income regions [1,24–26]. These structures, often constructed using locally available materials such as stone, brick, and mortar, are highly vulnerable to environmental degradation and natural hazards. Environmental factors such as temperature, humidity cycles, sun exposure, and chemical agents contribute to progressive deterioration [27,28], while extreme events like earthquakes, floods, and strong winds pose immediate risks of structural failure [11,29]. A case study of the 2017 Kermanshah earthquake in Iran demonstrates that masonry structures remain one of the most commonly used systems in low- and middle-income regions [25,30,31]. Their popularity is mainly due to low material cost, ease of construction, and the availability of non-professional labor [32]. However, these structures often lack the ductility and integrity needed to withstand lateral loads. The strong bond between masonry units and mortar is critical for resisting such actions, as many of the failures can be traced to weaknesses at the brick–mortar interface [33]. Moreover, masonry walls are particularly vulnerable to both in-plane and out-of-plane failure mechanisms during seismic events, often leading to major structural damage or collapse [34–36]. One of the major issues observed during seismic events is the in-plane and out-of-plane displacement of masonry walls, attributed to the low ductility of both the mortar and the masonry units, as illustrated in Figure 1.

Lateral loads in masonry walls generally lead to diagonal cracking and horizontal shear failure along bed joints [37,38]. In these conditions, bond strength is a crucial parameter. The performance of the brick–mortar interface is influenced by several factors, including the surface texture, porosity, and pore size distribution of the masonry units [1,6]. Furthermore, the compressive load applied to the masonry structure can affect the interface behavior and bond quality [41,42]. Numerous experimental studies have investigated the bond strength between masonry units and mortars, employing a range of brick and block types [24, 27- 28]. Overall, the structural vulnerability of masonry systems, particularly during seismic events, is rooted in their low tensile strength, brittle behavior, and sensitivity to interface degradation. These limitations underscore the necessity for efficient retrofitting and strengthening strategies. In recent years, advanced materials such as FRP and TRM have emerged as viable solutions, offering improved compatibility, durability, and mechanical performance [4,5,46–54].



Figure 1 Out-of-plane displacement of a masonry wall observed during the 2017 Kermanshah earthquake in Iran. Such failure mechanisms contributed to significant casualties due to the widespread use of unreinforced masonry construction in the affected region [55].

2.2 Strengthening systems: history and emerging directions

The strengthening of structures, particularly masonry and concrete elements, has evolved significantly over recent decades. Traditionally, these interventions were carried out using steel jacketing, concrete overlays, or shotcrete layers, methods that, despite their effectiveness, often resulted in added mass, invasive application procedures, and incompatibility with heritage substrates. The demand for more sustainable, durable, and reversible solutions has driven the development of advanced composite systems, particularly in the context of seismic retrofitting and historic preservation. Among the most prominent of these systems are FRPs and the more recent one, TRMs [48,56–60]. These modern materials have progressively transformed the field of structural rehabilitation, offering improved performance in terms of mechanical efficiency, application ease, thermal compatibility, and durability under adverse environmental conditions. As the understanding of long-term behavior and interface mechanics continues to grow, particularly under cyclic and sustained loads, strengthening systems are increasingly designed not only to restore lost capacity but to enhance resilience and durability in a sustainable manner [13,19,32].

2.2.1 FRP strengthening systems

FRP systems have been extensively used for strengthening reinforced concrete and masonry structures due to their high tensile strength, corrosion resistance, and ease of application. These systems typically consist of high-strength fibers, such as carbon, glass, or aramid, embedded in a polymeric resin matrix [4,46–48,61]. Their widespread application includes flexural strengthening of beams, confinement of columns, and shear upgrading of walls. Despite their mechanical advantages, FRPs exhibit several limitations, particularly when used for heritage masonry applications [62–64]. The organic polymer matrix presents issues related to poor compatibility with mineral-based substrates, impermeability to water vapor, and significant degradation under elevated temperatures and ultraviolet radiation [7,65]. Additionally, reversibility, a key requirement in heritage conservation, is often not achievable with polymeric systems, which are difficult to remove without damaging the underlying structure. These

constraints have led to the emergence of mineral-based alternatives such as TRM systems, offering improved environmental, thermal, and chemical performance profiles while maintaining structural efficacy.

2.2.2 TRM strengthening systems

TRM, has emerged as a promising composite material for upgrading and strengthening concrete or masonry structures [7,66–68], and has gained significant attention as a composite material for strengthening and upgrading concrete or masonry structures [69]. TRM systems consist of a structural reinforcement fabric, typically composed of glass, basalt, carbon, PBO, steel, or other high-strength fibers, embedded in an inorganic matrix such as lime or cement [7,70]. This configuration offers several advantages over traditional FRP systems, including enhanced material compatibility with historic substrates, water vapor permeability, and improved fire resistance [63]. Despite the inherent brittleness of the inorganic matrix, its compatibility with existing building codes and extensive production and design expertise makes TRM a practical choice for structural rehabilitation.

The inorganic nature of the matrix allows for better integration with historic materials, reducing the risk of incompatibility issues that often arise with synthetic polymers [71–75]. Also, the porous nature of the matrix facilitates water vapor diffusion, enhancing compatibility with masonry by allowing the composite to exhibit similar thermal and mechanical behavior to the substrate. This characteristic is crucial for maintaining the breathability and moisture balance of historic structures, thereby preventing damage caused by trapped moisture and potential subsequent freeze-thaw cycles [75–77]. Additionally, they can be applied directly to irregular masonry surfaces without requiring additional mortar layers and can be easily replaced if necessary (thus, ensuring reversibility). The inorganic and porous nature of the matrix enhances compatibility with masonry by facilitating water vapor diffusion and exhibiting thermal and mechanical behavior similar to masonry while resisting typical polymer aging processes [24,51].

TRM composites exhibit pseudo-ductile behavior due to multiple cracking, rendering them suitable for seismic strengthening [78]. This behavior is influenced by the bond response between the textile and mortar, as well as the properties of both materials [11,79,80]. Additionally, the effectiveness of TRM composites relies on the bond properties between the composite and the substrate [81,82]. Hence, comprehending the bond behavior at various levels, including textile-to-mortar and TRM-to-substrate, under harsh environmental conditions, is crucial for developing durable strengthening solutions. Although extensive experimental and analytical research has delved into the mechanical characteristics of TRM composites, investigations into their durability are still quite limited [7,65,70,83]. External bonding exposes TRM to various environmental conditions, posing potential challenges to its performance. Despite prior studies addressing aspects of TRM durability, a knowledge gap persists due to inconsistent findings and incomplete exploration of the system's behavior. Consequently, the durability of TRM systems has emerged as a prominent concern in current research literature [84,85]. The recent extensive attention to the application of TRM in retrofitting masonry and concrete structures highlights its suitability as a strengthening system, particularly for vulnerable masonry systems [1,7].

2.3 Mechanical behavior of TRM systems

TRM is a composite material composed of textiles embedded into inorganic matrices [86–89]. Considering the frequent use of cement-based mortars, the acronym FRCM is also widely adopted in the literature [82,90,91]. Other terminologies such as TRC and SRG have been used depending on the matrix type and reinforcement configuration [92–96]. The advantages of TRM include low cost, high fire resistance, compatibility with masonry substrates, usability in moist or cold environments, and ease of application [62]. The mechanical behavior of TRM, is primarily influenced by the interaction between

fiber and matrix, as well as the quality of bond at the textile–mortar interface [5,97–99]. Due to the coarser particle size in inorganic mortars, complete impregnation of multifilament yarns is often limited. This results in partial engagement of filaments and uneven stress distribution during loading. The failure typically occurs via slippage among filaments, a phenomenon termed the "telescopic effect" [100], where outer filaments experience higher stresses than inner ones. Ongoing research continues to explore methods for minimizing this effect [101–103], and SEM analysis has proven valuable in assessing yarn impregnation.

Despite the widespread use of cement-based mortars, their limitations include brittleness, environmental impact, and incompatibility with historic masonry [55,104]. Lime-based and geopolymer mortars have been proposed as sustainable alternatives, offering better durability, mechanical behavior, and moisture permeability, though they typically provide lower compressive strength [105]. Given the variety of matrix types and textile reinforcements, the mechanical properties of TRM systems show significant variability [77,88,106], and are primarily governed by mortar properties rather than fiber strength alone [107]. TRM systems have been shown to enhance the tensile, flexural, and shear strength of masonry elements [21,78,83,108–114]. However, the knowledge base regarding their mechanical performance remains incomplete [107]. Research has been classified into tensile behavior, shear and bond properties, out-of-plane response, and pull-out mechanisms [83,105]. Debonding is a common failure mode, making tensile testing essential to quantify modulus of elasticity and interface bond characteristics [111]. Consequently, bond testing has been proposed for multilayer TRM to better understand these behaviors. A sample of common tests on TRM and its constituents are depicted in Figure 2.

Indeed, a wide range of factors influence the tensile response of TRM, including fiber type and treatment, mortar characteristics, specimen geometry, curing protocol, and loading configuration [97,108–111,115,116]. Fiber types studied include glass [110,117], basalt [77,115], PBO [89,118], carbon [109,119], steel [79,120] and Aramid [117,121]. Different test configurations (e.g., clamping [116,122,123] and clevis gripping [124,125]) have been employed. Research also indicates that textile performance in TRM cannot be directly inferred from individual fiber or mortar properties due to complex interface phenomena [98,126–128]. Several standards and guidelines have emerged, including CNR-DT200/2004 [129], CNR-DT215/2015 [130], AC434/2013 [131], ACI440/2010 [132], ACI549.4R/2013 [133], ACI549.4R/20 [134], ACI549.6R/20 [135], and RILEM TC 250-CSM [88]. However, these documents remain incomplete in addressing multilayer arrangements and complex failure mechanisms. Multi-layer TRM configurations have been explored to meet higher strength demands [63,90,115,122,136–138]. Studies have shown that increased layers may reduce ductility and promote premature debonding [102]. Failure typically manifests as fiber–matrix delamination, substrate detachment, or interlaminar separation [75,102,114,139].



Figure 2 Applied mechanical tests, as expressed in this paper: (a) mortar compression; (b) brick compression; (c) mortar flexural; (d) mortar elastic modulus; (e) TRM single-lap shear; (f) fiber pull-out [140].

DIC technique has also become a popular non-contact technique for tracking displacement and cracking in TRM specimens [102,141]. It provides full-field strain data, crack spacing, and load progression with high resolution. DIC studies have confirmed the influence of textile architecture on crack distribution and the critical role of reinforcement ratio [142,143]. According to ACI 549.6R-20 [135], the tensile behavior of TRM can be divided into three phases: (i) the uncracked mortar stage, (ii) crack initiation and propagation, and (iii) fiber-dominated response. However, identifying transitions between these stages using stress–strain plots is often problematic due to microcracking and filament rupture [123,136]. DIC offers a more precise means to identify these transitions and validate theoretical models (as can be seen in Figure 3). Test setups, specimen geometries, and gripping methods (rectangular vs. dumbbell; clevis vs. clamping) significantly affect the mechanical response of TRM [9,75,144]. Each method presents advantages and drawbacks. Clamping grips apply force laterally and require careful stress distribution, while clevis grips use pinned connections. Comparative studies have been conducted to optimize test procedures and reduce artifacts due to boundary conditions [111]. Round-robin campaigns and standardization efforts have emphasized clamping grip configurations with friction pads and stress distribution plates to improve reproducibility [75,119,145,146]. Recent studies continue to refine the reliability of tensile testing, DIC integration, and specimen preparation [143,147]. The current work builds on these efforts by experimentally assessing different TRM configurations, textile types (glass, steel), and test setups. A total of 84 specimens were tested under varied conditions, including strengthened grip zones and multi-layer assemblies. The DIC system was used in all cases to track cracking and strain evolution, enabling a comprehensive evaluation of TRM mechanical behavior. These

findings aim to further the understanding of TRM as a structural strengthening system and support the development of standardized testing procedures for both single and multi-layer applications.



Figure 3 Configuration of the tensile test setup (glass-TRM specimen is shown) [7]

2.4 Long-Term loading behavior and creep

Despite significant progress in understanding the short-term performance of TRM systems, their long-term mechanical behavior, particularly under sustained loading, remains insufficiently investigated. Among time-dependent phenomena, creep, the gradual deformation under constant load, is especially critical, as it may result in progressive displacement or failure if not considered in design [148,149]. This concern becomes more relevant when TRM is employed in load-bearing retrofitting applications, where continuous serviceability must be ensured [150]. While TRM generally has lower adherence to substrates compared to FRP, its mechanical properties are influenced by the bond behavior at the fiber-matrix interface and the individual properties of its components [97–99]. The relatively large particle size of inorganic matrices can prevent full impregnation of yarn filaments, causing a telescopic effect where outer filaments experience more stress, leading to asymmetrical stress distribution and slippage [100]. The effectiveness of TRM composites also relies heavily on the bond properties between the composite and the substrate [81,82]. Understanding this bond behavior at various levels, including textile-to-mortar and TRM-to-substrate, under harsh environmental conditions, is crucial for developing resilient strengthening solutions.

While extensive research has focused on the mechanical characteristics of TRM composites, investigations into their durability remain limited [11,151–153]. The external bonding of TRM exposes it to various environmental conditions, which may challenge its performance. Although some studies have addressed aspects of TRM long-term behavior including the durability of the system, a knowledge gap persists due to inconsistent findings and incomplete exploration of the system's behavior. Consequently, the long-term behavior of TRM systems has become a prominent concern in current research literature [11,152]. Despite the significant advancements in understanding the short-term performance, there remains a substantial gap in knowledge regarding their long-term behavior, especially under continuous loading, particularly in relation to creep. Creep, the time-dependent deformation under sustained load, is

a critical factor in the long-term performance of reinforced structures, as it can lead to progressive deformation and potential failure if not adequately accounted for [148,149]. This gap is particularly important for applications where TRMs are used in load-bearing elements, as the long-term reliability of these systems under sustained loads is crucial for ensuring structural safety [150].

There are very few studies that investigate the long-term mechanical behavior of TRM composite systems. Akbari Hadad and Nani in 2020 [154] examine the fatigue behavior of TRM-reinforced concrete beams, offering insights into TRMs' performance under cyclic loading conditions and emphasizing the importance of understanding their long-term durability. The study found that while TRMs can enhance the fatigue life of RC beams, their overall performance is highly dependent on the interaction between the fabric and matrix, as well as the specific loading conditions. Another significant study in the field, conducted by Bonati *et al.* in 2020 [155], provided valuable insights into the time-dependent deformation characteristics of TRMs using single-lap shear tests. The findings revealed that the creep behavior of TRMs is influenced by factors such as the type of textile used, the composition of the mortar matrix, and the environmental conditions to which the system is exposed.

Existing studies have demonstrated that TRMs exhibit a complex interaction between the textile and the matrix, which governs their overall creep response and long-term durability [11,154,155]. The insights from these studies highlighted the importance of understanding TRM creep performance, particularly the textile-mortar interaction under sustained loads, the impact of curing time, and environmental effects. Addressing these gaps is essential to achieving the key objectives of this research, which include developing reliable predictive models and establishing robust design standards that account for the long-term performance of TRMs under diverse loading scenarios. These findings underscore the necessity of advancing research in this area to ensure the safe and effective use of TRMs in structural applications.

2.5 Durability of TRM: effect of environmental conditioning

The long-term performance of TRM systems is influenced not only by their mechanical properties but also by their resilience under environmental exposures such as wet–dry cycling, freeze–thaw action, chemical aging, and high temperatures [13,14,156–158]. Among these, chemical exposures, particularly those involving aggressive substances like acids, alkalis, and salts, represent critical stressors that can compromise the durability of TRM composites. These exposures are especially relevant for retrofitted masonry structures located in polluted urban areas, coastal regions, or industrial environments where such agents are prevalent [159–164]. Various durability testing protocols have been adopted to simulate environmental conditions, including wet–dry cycling to replicate fluctuating humidity, freeze–thaw cycling to evaluate thermal resistance, and immersion in saline or alkaline solutions to assess chemical resistance. High-temperature exposure tests, which simulate fire or extreme heat scenarios, have also been performed [140,151,165–167]. Among these, chemical exposure conditions have recently attracted increasing attention due to their potential to significantly alter both the textile and the matrix. In particular, acidic environments have been noted for their aggressive effect on glass or basalt fibers, depending on matrix pH, solution concentration, and exposure duration [16,167].

Environmental exposure may also affect the bond behavior of TRM systems when applied to different substrates [153,168,169]. Given that bond performance governs stress transfer and overall structural behavior, these effects are particularly critical. Despite a growing body of research into the mechanical behavior of TRM composites, long-term durability remains a topic with significant gaps and inconsistent findings [11,29,170]. Factors such as moisture uptake, matrix shrinkage, and degradation of the fiber–matrix interface can lead to variations in performance over time. Therefore, additional studies are needed

to clarify and standardize test procedures and exposure conditions [94,153,170–172]. The chemical and mechanical properties of TRM systems depend on both constituent materials. Cement-based matrices dominate due to availability and strength, but lime- and geopolymer-based mortars are gaining traction for their lower environmental impact and improved compatibility with historic masonry [86–89]. Successful textile–mortar integration depends on full impregnation of the yarns, which ensures uniform stress transfer and mitigates premature failure [173]. Incomplete penetration of the matrix results in the so-called telescopic effect, leading to slippage and degradation of bond efficiency.

Experimental results have shown that key parameters like tensile strength, failure modes, and bond characteristics depend heavily on the textile type, mortar composition, and test configuration [105,107,174,175]. Testing protocols such as direct tension and bond strength tests are essential to evaluate the durability of TRM systems, while shear and out-of-plane testing of structural members provide insight into the global performance of strengthened elements [19,77,88,106]. Although research on TRM systems has advanced significantly, major gaps remain in the comprehensive understanding of their durability under realistic service conditions. Further work is required to consolidate existing findings and develop predictive frameworks capable of informing design and long-term assessment especially regarding the chemical agents.

2.5.1 Effect of alkaline exposure

Early investigations into the durability of fiber-reinforced cementitious systems under alkaline environments have emphasized the importance of matrix composition and interfacial behavior. Butler et al. [176] conducted a foundational study on TRC composites and found that high matrix alkalinity adversely affects the performance of glass-based reinforcement due to the development of solid phases at the fiber–matrix interface and on filament surfaces. Their results, supported by pull-out testing and microscopic analyses, indicated that the degradation mechanism is closely tied to the nature of the matrix. While this research focused on cement-based systems, such exposure conditions may pose different levels of threat in TRM systems. For example, lime-based matrices, which present lower pH values, may create a less aggressive environment for glass and basalt fibers. However, the environmental exposure of TRM systems, especially the impact on bond behavior with different substrates, remains a critical concern [153,168,169].

Subsequent studies expanded on these findings. Arboleda et al. [177] evaluated the mechanical behavior of TRM composites reinforced with PBO and other fabrics subjected to alkaline aging. Their results showed minimal deterioration and, in some cases, mechanical improvements, potentially due to extended curing. Although the alkaline pore environment is typically considered harmful to glass fibers, no degradation was reported for the fabric types used. Nobili [178], however, reported a reduction exceeding 50% in flexural strength and a 10–15% decline in tensile strength for lime-based TRM systems with glass reinforcement after alkaline and saline exposures, indicating that degradation may depend significantly on matrix-fiber compatibility. Rizzo et al. [27] observed that mortar specimens immersed in aqueous solutions exhibited a form of self-healing, with mechanical performance maintained or even enhanced due to delayed hydration. Calabrese et al. [152], in a more recent investigation, performed tensile testing on PBO TRM specimens using clamping-grip setups after exposure to alkaline solutions. Their results indicated only a limited reduction in tensile strength and a slight increase in cracking strength, again highlighting the role of ongoing hydration processes.

Nonetheless, despite these insights, the durability of TRM systems under alkaline environments remains an area requiring deeper exploration. Al-Lami et al. [29] emphasized the variability in experimental procedures across studies, which complicates comparisons and the generalization of results. Inconsistencies in findings, particularly those involving lime-based matrices, suggest that the

interaction between fiber and matrix, as well as composite-to-substrate bonding, must be further scrutinized. Calabrese et al. [152] also proposed defining environmental exposure coefficients specific to each composite system to improve predictive capability. Notably, most existing research has limitations in terms of exposure duration, matrix typology, and test comprehensiveness. Long-term campaigns incorporating lime-based mortars and both glass and basalt textiles under standardized alkaline, water-immersion, and dry conditions are still lacking, representing a significant gap in the literature [170].

2.5.2 Effect of saline environment

Despite substantial advances in understanding the mechanical properties of TRM composites, their long-term durability remains a critical research area with significant unresolved questions [11,29,170]. When TRM systems are externally bonded to masonry substrates, they are inherently exposed to environmental stressors such as moisture fluctuations, temperature variations, and chemical agents, including saline exposure. The latter is particularly relevant for structures located near coastal regions or in areas where salts are applied for food preservation or deicing purposes [153,179]. Saline degradation primarily arises from salt crystallization within the pore structure of masonry components. As chloride-rich solutions evaporate, salts crystallize and expand within the pores, exerting crystallization pressure that induces microcracking, accelerates material degradation, and compromises structural integrity [180]. This repetitive process leads to cumulative damage and reduces mechanical performance indicators such as compressive and tensile strengths, while simultaneously increasing porosity and water absorption [180,181].

Despite its relevance, the body of literature on the durability of TRM composites in saline environments is relatively limited. One of the earliest contributions was by Arboleda et al. [177], who tested carbon and PBO TRM specimens in cement-based mortar after 3000 hours of immersion in ocean water. Their findings revealed no significant performance deterioration. In 2016, Tedeschi et al. evaluated TRM using carbon textiles and lime-based mortar subjected to drying cycles in 10% Na_2SO_4 solution; pull-off tests indicated no meaningful correlation between adhesion strength and accelerated aging [182]. Donnini [153] reported a strong reduction in tensile capacity for TRM made with glass fabric and lime-based mortar exposed to 3.5% NaCl in wet-dry cycles. In another study by Donnini et al. [168], TRM systems made with carbon fabric and cementitious mortar were subjected to 1000 hours of immersion in a saline solution (2.45% NaCl + 0.41% Na_2SO_4 at 40°C). Results from tensile, pull-off, and double shear tests showed a variable response depending on the fabric coating. Franzoni et al. [24] studied steel-fabric-reinforced TRM using lime-based mortar subjected to wet-dry cycles in a combined 2% NaCl + 8% Na_2SO_4 solution, reporting no significant degradation apart from steel corrosion. In contrast, Alatawna et al. [179] observed an increase in tensile strength after aging TRM samples composed of carbon fabric and cementitious mortar in saturated NaCl solutions, suggesting negligible degradation. Bertolli et al. [183] recently conducted single-lap shear tests on TRM systems made with glass fabric and cementitious mortar after wet-dry cycling in 10% Na_2SO_4 solution, identifying a slight reduction in peak bond strength.

These findings reflect the current fragmentation of research in this area, with varying outcomes that can largely be attributed to non-uniform testing standards and experimental setups. Conditioning protocols differ widely, with references to AC 434-13 (2013), CSLLPP (2022), JSCE_E 549-2000, ASTM E2098, ETAG 029, GB/T 50082-2009, and ASTM D7705 [184–188], many of which were not specifically developed for TRM systems. These inconsistencies include variations in curing conditions, saline solution composition, exposure duration, and test methods (tensile, pull-off, or shear), making it challenging to draw generalizable conclusions. The lack of standardized saline environments, combined with disparate definitions of reference conditions for lime- or cement-based mortars, further complicates the interpretation of results. In several studies, the long-term effect of saline aging was evaluated solely

by comparing samples aged for fixed durations to unaged controls, without continuous monitoring or systematic aging protocols [32,179,189–194].

2.5.3 Effect of acidic exposure

Among various environmental stressors, acidic exposure represents one of the most chemically aggressive and structurally detrimental conditions for TRM systems, particularly when lime-based mortars are employed. Acid rain, urban pollution, and industrial emissions can result in low-pH environments that initiate or accelerate degradation processes within masonry and TRM-reinforced structures. Unlike other chemical agents, acids, particularly sulfuric acid (H_2SO_4), can directly dissolve calcium-based phases within mortars and react aggressively with fiber coatings, leading to compound degradation mechanisms at both material and interfacial levels [195–198]. Although considerable progress has been made in understanding TRM mechanical behavior, the long-term durability of these systems under acidic conditions remains underexplored and is marked by highly variable findings. Only a limited number of studies have systematically investigated this topic, and existing protocols vary widely in terms of solution composition, exposure duration, and test configuration, making direct comparison of results difficult [195,199,200]. In some cases, marginal improvements in strength have been reported, possibly due to continued hydration or surface densification effects [195,199,200]. However, other studies have shown substantial degradation, especially in systems containing glass textiles or poorly protected fiber–matrix interfaces [195]. These contradictory results highlight the need for standardized testing and better mechanistic understanding of acid-induced damage.

Acidic environments are particularly catastrophic for lime-based mortars due to their high calcium carbonate content, which undergoes dissolution in low-pH conditions, weakening both the matrix and its adhesion to embedded reinforcements. Reactions involving C-S-H decalcification and gypsum formation further disrupt the microstructure and compromise mechanical performance [195–198]. At the composite level, bond degradation between the textile and mortar is frequently observed due to telescopic effects, reduced frictional resistance, and microcracking at the interface. Textile performance is also contingent upon chemical composition and surface treatments; while basalt fibers typically exhibit higher chemical resistance, glass textiles tend to degrade more rapidly in acidic environments, particularly under long-term exposure [201,202].

A summary of selected studies investigating TRM performance under acidic exposure is provided in Table 1. For instance, a study by Donnini et al. [161,203] tested carbon textiles in lime-based mortar after immersion in hydrochloric acid at pH 2.5 for 1000 hours and observed marginal tensile strength losses. Similarly, other investigations evaluated the performance of AR-glass and PBO textiles in cementitious matrices under sulfuric and hydrochloric acid exposure, with divergent outcomes based on matrix composition and textile type [29,94,114]. These investigations confirm that matrix and textile degradation must be evaluated concurrently to fully understand composite behavior.

Table 1 Literature summary on immersing specimens in acidic and water solutions.

Ref.	Textile	Matrix	Solution	Duration [hr.]	Post-exposure tests
[199]	Carbon	Lime-based	acid (HCl, pH = 2.5)	1000	Tensile
[195]	AR-E-glass	Cement	acid (H_2SO_4)	1440	Tensile
[200]	AR-glass, carbon, PBO, basalt, and steel	Cement	acid (HA, pH = 2.5)	1000	Tensile
[204]	PBO	Cement-based	Water	96-1776	Single-lap shear and flexural
[205]	PBO and carbon	Cement-based	Water	1000 and 3000	Tensile and pull-off

To model acid rain effects and environmental deterioration, immersion in sulfuric acid has been adopted as an accelerated aging protocol in several studies, including the present one. As sulfuric acid is a principal component of atmospheric acidification, its use enables relevant and repeatable simulation of acid attack phenomena. The interaction of acidic solutions with the microstructure of hardened mortar has been further studied using microstructural and mineralogical testing methods, which provide insight into phase changes, elemental leaching, and microcracking under acid-induced stress [147,206,207]. These techniques are crucial in visualizing deterioration patterns and quantifying chemical transformations, thus complementing mechanical test outcomes. Despite their promise in structural strengthening, TRM composites are still susceptible to tensile and bond degradation in harsh environments. Tensile testing using clamping grips has emerged as a preferred method for evaluating TRM systems, enabling accurate stress transfer and minimizing slippage artifacts [11,199,200]. These tests help determine key parameters such as tensile strength, elastic modulus, and cracking behavior. In recent studies, bare textiles have also been subjected to tensile testing to assess coating degradation and evaluate their compatibility with different matrices [75,119]. Nevertheless, the lack of long-term experimental data, particularly for lime-based systems exposed to strong acids, underscores the urgent need for further research.

2.6 Degradation mechanisms; capabilities of mineralogical tests

Durability loss in masonry structures, especially in lime-based mortars, arises primarily from the interaction between the material and its exposure environment. Acidic deposition, sulfate attack, salt crystallization, carbonation, and freeze–thaw cycles are among the key agents triggering physical and chemical transformations within the mortar matrix. Among them, the acid-induced degradation is particularly detrimental due to its capacity to dissolve calcium-bearing phases, reduce cohesion, and promote cracking. Understanding these mechanisms requires not only mechanical testing but also a robust microstructural and mineralogical analysis framework. Techniques such as XRD, FTIR, SEM, TGA, and ICP analysis provide critical insights into mineralogical transformations, phase depletion, porosity evolution, and ion exchange reactions [151,208,208–212] . For instance, SEM imaging enables visualization of pore coarsening and microcracking, while TGA quantifies mass losses associated with portlandite and gypsum decomposition. The use of XRD assists in identifying crystalline phases, indicating the extent of carbonation or gypsum formation, whereas ICP analysis detects calcium leaching and trace ion diffusion. Collectively, these methods allow researchers to relate the mechanical degradation of mortars to specific chemical changes, thus enabling predictive durability assessments [15,213,214].

2.7 Mortar modeling

Mortar modeling plays a pivotal role in predicting the mechanical performance and long-term durability of TRM systems, particularly under aggressive environmental exposures. Recent advances have enabled the use of both machine learning and chemo-mechanical approaches to simulate the complex behavior of lime-based mortars. Machine learning offers data-driven insights for predicting strength and stiffness, while chemo-mechanical modeling provides a physically grounded framework to link chemical degradation processes to mechanical deterioration. Together, these methodologies support the development of accurate, scalable, and experimentally validated models for the assessment and design of durable masonry strengthening systems.

2.7.1 Machine learning approach

ML approaches have recently been explored to model and predict the mechanical performance of mortar-based materials under various environmental conditions. These data-driven methods enable the interpretation of complex and nonlinear relationships between input parameters (e.g., composition, curing time, environmental exposure) and mechanical outcomes (e.g., compressive and flexural strength) [215–218]. Particularly in acidic environments, where traditional modeling is challenged by the multivariate nature of chemical degradation, ML models can provide accurate short-term predictions. Previous studies applied ensemble methods such as Random Forest (RF) and XGBoost to predict the mechanical behavior of mortars incorporating recycled aggregates, biochar, and fibers, showing high precision and robustness [219–221]. For example, SHAP analysis in one study highlighted a negative correlation between RSP replacement and compressive strength, while others emphasized the critical influence of textile tensile strength on TRM performance [222]. In the present investigation, a dataset comprising flexural strength of lime-based mortars aged in sulfuric acid environments was modeled using XGBoost, revealing how pH level, exposure time, and mortar composition influence strength development. Despite the predictive power of ML, its use is inherently limited to the observed data range and cannot replace experimental validation, particularly for long-term deterioration. Therefore, ML is best applied in combination with experimental data, offering a complementary tool for forecasting degradation trends and supporting restoration strategies in historic masonry structures [16,223–225].

2.7.2 Chemo-mechanical modeling

Despite the widespread use of lime-based mortars in TRM systems, their long-term performance under aggressive acidic environments remains insufficiently investigated. While TRM systems have been widely studied under mechanical loading and standard environmental conditions, their behavior in acidic environments, common in urban and industrial settings due to acid rain or contaminated groundwater, has received limited attention [11,12,226]. This knowledge gap is especially critical given that acidic exposure induces complex degradation phenomena in cementitious composites, including the dissolution of portlandite, calcite, and potentially C_3S, as well as the decoupling of amorphous pozzolanic phases and the evolution of the pore network [227]. These transformations compromise both the chemical and mechanical stability of the material.

At the material level, the aforementioned degradation mechanisms result in increased porosity, reduced cohesion, and a decline in stiffness. One of the most critical chemical reactions in this context is the formation of gypsum ($CaSO_4 \cdot 2H_2O$) due to the interaction of sulfuric acid with calcium-bearing phases. This reaction generates expansive pressures, causing internal cracking and accelerating mechanical deterioration [228–230]. Multiple analytical techniques have consistently confirmed these transformations, highlighting mineralogical alterations and morphological degradation induced by acidic exposure [12]. Calcium leaching and ion exchange must therefore be understood not as isolated

mechanisms but as integral contributors to the broader deterioration process, as they destabilize hydration products and disrupt the microstructural framework, further aggravating performance loss [229,231].

The mechanical performance of lime-based mortars under acidic conditions has been shown to be highly sensitive to both the intensity and duration of exposure [229]. While short-term exposure to mildly acidic environments may initially result in strength gains due to pore filling by secondary mineral phases such as gypsum, prolonged exposure typically leads to embrittlement, crack propagation, and a substantial decline in load-bearing capacity [229]. Although many studies have documented mechanical performance losses, few have paired such analyses with quantitative microstructural or mineralogical assessments, limiting the understanding of the degradation mechanisms involved [214]. This underscores the necessity of integrative methodologies that combine chemical diagnostics with mechanical testing in order to develop reliable predictive models. To this end, recent investigations have employed advanced microstructural techniques, to examine chemically induced degradation in mortars, particularly under sulfuric acid exposure [15,213,214]. These analyses have revealed the depletion of portlandite and accumulation of gypsum, alongside localized damage phenomena such as pore coarsening and interfacial cracking, especially in reinforced mortars [59,147,206]. TGA profiles confirm mass loss in regions associated with portlandite and gypsum decomposition, providing further verification of chemical deterioration [11]. Nonetheless, these methods predominantly offer post-exposure insights and do not facilitate forward-looking predictions of mechanical performance. As such, a physically grounded chemo-mechanical model is required to quantitatively link chemical degradation to mechanical response and to forecast the behavior of lime-based mortars under diverse environmental exposures [16,214].

Continuum damage mechanics has increasingly been adopted as a robust modeling framework for simulating the progressive mechanical deterioration of cementitious materials under environmental stressors. In the context of lime- or blended-matrix mortars, CDM-based approaches have proven effective in capturing nonlinear stress–strain behavior driven by quasi-brittle fracture and chemically induced damage [232,233]. Trilinear models are particularly useful in this context, as they allow for the distinct representation of elastic, hardening, and softening phases, which are characteristic of the mechanical response of lime-based mortars. Notably, the work by Cui et al. [234] demonstrated the potential of CDM formulations in simulating stiffness degradation and strength loss in cement mortars subjected to sulfate and acidic environments. These models typically integrate experimental findings into phenomenological laws that evolve with exposure duration or chemical severity, thereby facilitating long-term performance prediction.

Despite this progress, most existing models have focused on cement-rich mortars and general sulfate attack, with relatively few tailored to lime-based mortars subjected to acidic conditions [16,235,236]. Furthermore, only a limited number of these models incorporate microstructural evidence in a systematic manner, which hampers their physical validation. In response, recent studies have explored the integration of chemical degradation indicators—such as porosity evolution, leaching indices, and mineralogical transformations—into mechanical modeling schemes [237,238]. This chemo-mechanical coupling is particularly relevant for lime-based mortars, where degradation is driven not only by mechanical stress but also by chemically induced processes such as binder decalcification and expansive gypsum formation. Several recent efforts have advanced multi-physics chemo-damage models for cementitious materials exposed to sulfate and chloride environments, demonstrating that phase changes significantly impact stiffness and strength [239,240]. However, such models often remain computationally intensive and are predominantly calibrated on Portland cement-based systems [241]. The absence of direct validation using microstructural data further limits their applicability to lime-based mortars, which exhibit different degradation patterns due to their high porosity, low clinker content, and

susceptibility to carbonation [242]. These limitations underscore the need for dual-scale modeling approaches that explicitly link microscale degradation processes with macroscale mechanical performance.

2.8 Analytical and numerical modeling of bond behavior in TRM systems

The accurate modeling of bond behavior in TRM systems is essential for understanding the composite action and load transfer mechanisms between the textile and the surrounding matrix. A wide range of analytical and numerical models has been developed to simulate the interface behavior, enabling better prediction of structural response, especially under complex loading or degradation scenarios. These models are typically formulated based on the principles of equilibrium, compatibility, and constitutive relationships that govern the shear stress–slip response at the textile–matrix interface [20,22,243]. Analytical models often rely on cohesive zone laws to characterize the bond-slip relationship through simplified, yet representative, constitutive equations. Among these, the bilinear and trilinear bond-slip laws are widely employed to approximate the local shear transfer mechanisms along the bonded interface [18,244–247]. Early models assumed constant bond stress or idealized elastic behavior, which provided only limited accuracy. More refined approaches incorporate piecewise linear or exponential cohesive laws, accounting for the distinct loading stages observed experimentally: an initial elastic phase, followed by peak load attainment and subsequent softening. These analytical models provide closed-form or semi-analytical solutions for local field variables such as slip, shear stress, and axial stress along the embedment length, under assumptions of uniform bonding, perfect alignment, and simplified boundary conditions [248].

A prominent development in this regard is the trilinear cohesive law, which distinguishes between three distinct phases: a rigid-elastic initial response, an elastic-softening transition, and a fully softening post-peak behavior, as can be seen in Figure 4. Each stage corresponds to different levels of damage propagation and interface degradation. Through this formulation, models can predict stress and slip distribution profiles along the bond length, as well as the onset and progression of interface failure. These models have been particularly useful in explaining the experimental results obtained from pull-out, single-lap shear, and tension stiffening tests. Numerical simulations, particularly those based on FEM, have offered greater flexibility in modeling the complex interactions within TRM systems. Interface elements incorporating cohesive laws have been widely adopted to simulate debonding and crack propagation. Numerical models also allow the inclusion of nonlinearities, variable material properties, complex geometries, and environmental effects. For instance, degradation due to aging, temperature, or chemical exposure can be simulated by updating the bond-slip parameters, such as initial shear strength, maximum shear stress, slip at peak stress, and ultimate slip, using experimentally derived degradation laws [18,19,29,114,244,249,250].

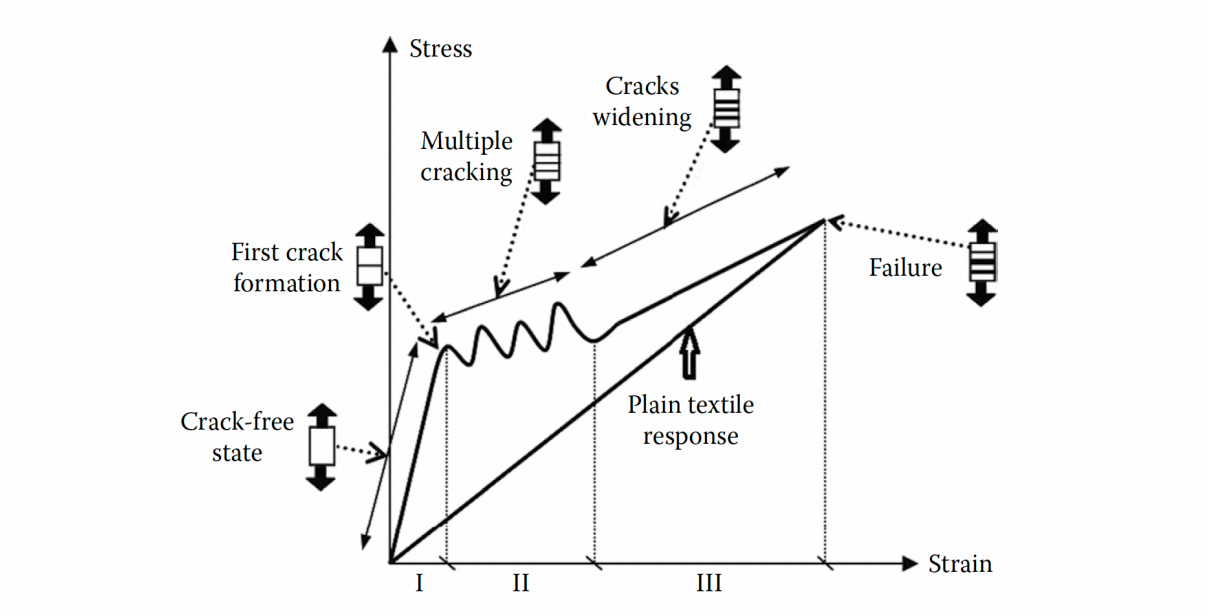

Figure 4 Schematic representation of the tensile response of a TRM composite, showing the three typical loading stages: uncracked, crack development, and crack stabilization [251]

Recent developments also include aging-sensitive models where the bond-slip law evolves as a function of environmental parameters. In such models, the cohesive parameters are modified based on leaching data, microstructural alterations observed through SEM or XRD, or loss of mechanical strength observed in aged specimens. These coupled models represent an important step toward simulating the long-term performance of TRM systems under aggressive exposure, such as acidic or saline environments. In summary, analytical and numerical models of the textile–matrix bond behavior in TRM systems have evolved significantly, ranging from simplified cohesive laws to advanced multiscale simulations incorporating environmental degradation. These modeling strategies are crucial for interpreting experimental results, guiding material selection, and designing interventions for masonry strengthening. By integrating mechanical, mineralogical, and chemical insights into these models, a more comprehensive and predictive understanding of TRM performance can be achieved [244,247,252–256].

2.9 Conclusion

This chapter provided a comprehensive state-of-the-art review concerning TRM systems, beginning with a broader perspective on masonry structures and their associated challenges. Initially, the focus was placed on the vulnerability of unreinforced masonry, particularly under seismic and environmental loads, and the need for strengthening interventions. A critical overview of traditional and modern strengthening techniques was presented, outlining the evolution from conventional retrofitting methods to more advanced composite-based solutions. In this context, TRM emerged as a promising technology due to its mechanical efficiency, compatibility with masonry substrates, and suitability for heritage conservation.

The discussion then shifted to the short-term mechanical performance of TRM systems, emphasizing the key parameters governing bond behavior, tensile strength, and cracking mechanisms. The applicability of TRM across various structural scenarios was reviewed, and its interaction with lime-based mortars was highlighted given their relevance for historical preservation. Following this, the chapter transitioned into durability considerations and long-term performance, introducing creep behavior and chemical degradation as critical concerns for sustainable TRM design. In particular, the lack of systematic studies on TRM under sustained loads and environmental aging was emphasized, indicating a significant research gap. Among environmental degradation factors, acidic exposure was identified as a particularly

aggressive and prevalent mechanism, especially in polluted urban and industrial regions. The detrimental effects of acid attack on mortar and the composite interface have been well-documented in broader cementitious literature; however, the specific degradation mechanisms in TRM systems remain largely unexplored. This underlines the need for focused investigations into the aging phenomena affecting TRM durability.

In parallel, numerical and computational modeling approaches were examined as powerful tools for simulating degradation and interpreting experimental findings. Despite the growing number of studies on mechanical modeling of TRM systems, interdisciplinary integration with chemical degradation data remains limited. The coupling of microstructural diagnostics and mineralogical tests, such as XRD, SEM, and TGA, with mechanical models offers new opportunities to characterize and predict material deterioration more accurately. In this regard, chemo-mechanical modeling appears particularly promising, offering a framework that integrates chemical deterioration mechanisms with mechanical performance loss. By embedding degradation laws into analytical or numerical models, such approaches can potentially simulate the long-term behavior of TRM systems under aggressive conditions. This multidimensional strategy not only enhances predictive capabilities but also lays the groundwork for performance-based design of more durable reinforcement systems. In the following chapters, these concepts will be further explored through experimental investigations on TRM systems subjected to long-term loading and aggressive environmental exposures, with a particular focus on creep behavior and acid-induced degradation.

Chapter 3
Characterization of TRM materials and composites

3.1 Introduction

A comprehensive understanding of the long-term behavior of Textile Reinforced Mortar systems requires a systematic characterization of their short-term performance under well-defined and controlled conditions. Before assessing the influence of environmental or sustained loading effects, it is essential to establish standardized test protocols and accurately characterize the constituent materials, interface systems, and the composite configuration itself. This chapter is dedicated to presenting the materials, experimental methods, and mechanical testing setups adopted throughout this research, with a focus on establishing a robust methodological framework to be employed in subsequent experimental campaigns. The characterization process commenced with the selection of a commercial lime-based mortar as the matrix, combined with two types of textile reinforcements, glass and high-strength steel, representing a range of mechanical and morphological properties. Extruded clay bricks were employed as the masonry substrate for interface-related testing. A structural epoxy resin was introduced in selected setups to improve anchorage conditions, facilitate gripping during tensile testing, and reduce the likelihood of premature failure near the boundaries. Material-level characterization of the matrix included compressive strength, flexural strength, elastic modulus, and direct tensile strength testing, all performed on standardized prismatic or dog-bone specimens to ensure reproducibility.

In parallel, mechanical tests were carried out on the reinforcing yarns and textile meshes to determine their tensile capacity and deformation behavior. Bond performance between the reinforcement and matrix was investigated through pull-out and single-lap shear test configurations, designed to simulate stress transfer mechanisms and failure modes at different interfaces. These configurations were carefully selected and refined based on literature guidance and adjusted to suit the specific reinforcement types and specimen geometries used in this research. Additionally, the preparation and configuration of direct tensile tests for TRM composites are introduced in this chapter. Overall, this chapter serves as a foundational methodological reference for the experimental investigations that follow. By defining the testing procedures and materials used in a consistent and transparent manner, it supports the reproducibility of results and enables future comparisons across different aging environments, mechanical stress conditions, and reinforcement strategies explored in subsequent chapters.

3.2 Materials

3.2.1 TRM matrix

A commercial mortar, Planitop HDM Restauro, manufactured by Mapei, was used as the TRM matrix in all experimental campaigns conducted in this study. This mortar is a ready-mixed, two-component system composed of Part A (solid component, can be seen in Figure 5a, b) and Part B (liquid component, Figure 5a). According to the technical data sheet provided by the manufacturer, the mortar is formulated using natural hydraulic lime, eco-pozzolan, sand, special additives, short fibers, and synthetic polymers dispersed in water. The mixing proportion follows a ratio of 25 kg of Part A to 4.75 kg of Part B, with an optional 0 to 2 kg of additional water per full bag. However, to maintain consistency in all casted mortars, no extra water was added, and only Part A was mixed with Part B in all test specimens.



(a) (b)

Figure 5 Planitop HDM Restauro mortar (Mapei) used in this study: (a) the two components—liquid polymer and dry powder, and (b) the solid component (Part A) showing dispersed short fibers.

3.2.2 Textile meshes

Three types of textile meshes were used: glass, basalt, and steel. These reinforcements were supplied by Mapei and selected based on their mechanical properties, compatibility with the TRM system, and intended structural applications. The glass and basalt reinforcements were woven biaxial fabric meshes designed to be alkali-resistant. The glass mesh (Mapegrid G220) consisted of yarns with an area per unit width of 35 mm^2/m in both directions, a mesh size of 25 mm × 25 mm, and a total weight of 250 g/m^2. The basalt fabric (Mapegrid B250) had a mesh size of 6 mm × 6 mm, a total weight of 250 g/m^2, and a yarn cross-sectional area of 0.2432 mm^2. A unidirectional steel reinforcement (GeoSteel G600, from Kerakoll) was also utilized. This mesh was made of ultra-high-strength galvanized steel cords with a cross-sectional area of 0.538 mm^2 per cord, arranged at a density of 1.57 cords/cm, and had an overall weight of 670 g/m^2. Each steel fiber was constructed by twisting five individual wires together—three straight filaments wrapped by two filaments at a high twist angle, forming a uniform and mechanically efficient cord. The three textile types used in this study are illustrated in Figure 6.

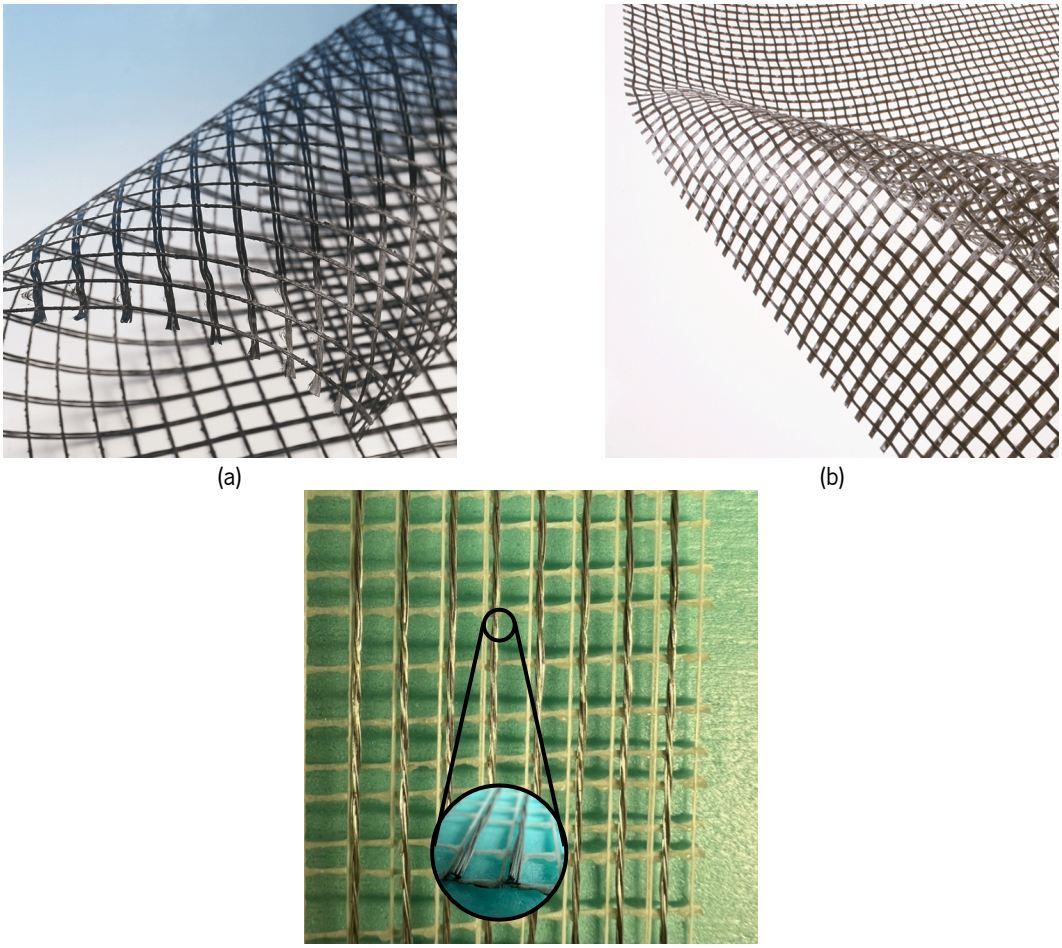

(a) (b)

(c)

Figure 6 Textile reinforcements used in this study: (a) glass fiber mesh, (b) basalt fiber mesh, and (c) high-strength unidirectional steel mesh, with a detailed view of the steel cords shown in the magnified inset.

3.2.3 Masonry substrate

Extruded solid clay bricks were used as the masonry substrate in selected experimental tests aimed at evaluating the bond behavior of the TRM system. The bricks had nominal dimensions of 200 × 100 × 50 mm^3 and were incorporated into the experimental setup to simulate real strengthening applications on masonry structures. To enhance the interaction between the mortar matrix and the brick surface, one face of each unit was subjected to two cycles of sandblasting prior to casting. This surface treatment was intended to increase roughness and promote mechanical interlock at the interface, thereby improving adhesion quality and consistency across specimens. An overall view of the brick unit and the sandblasted surface are shown in Figure 7.



(a) (b)

Figure 7 Extruded solid clay brick used as masonry substrate in TRM-related tests: (a) overall view of the brick unit; (b) detail of the sandblasted surface after two cycles of preparation to improve mortar adhesion.

3.2.4 Resin

A two-component epoxy-based resin (MapeWrap 31) was used in selected tests to enhance the bond performance and increase stiffness where required. This medium-viscosity, solvent-free epoxy resin was specifically developed for impregnation in dry-system applications. The resin consisted of two pre-measured components: Part A (resin) and Part B (hardener), which had to be mixed together before use. After mixing, the resin remained workable for approximately 40 minutes at 23°C. The two components of the MapeWrap 31 resin system are shown in Figure 8.



Figure 8 Two-component epoxy resin (MapeWrap 31, Mapei) used in selected tests for impregnation and anchorage purposes. Component A (resin base) and Component B (hardener) were mixed prior to application.

3.3 Material characterization procedures

3.3.1 Mortar's flexural test

The flexural performance of the mortar was evaluated through three-point bending tests on prismatic specimens with nominal dimensions of 40 × 40 × 160 mm³. These tests were conducted in accordance with the EN 1015-11B standard [257], which outlines procedures for determining the flexural strength of hardened mortars. Each specimen was positioned horizontally with a span length appropriate for its geometry, and a central point load was applied using a 25 kN hydraulic actuator. The test was carried

out under displacement control at a constant rate of 0.005 mm/s to simulate quasi-static loading conditions. This method enabled the identification of the initial cracking load and the flexural strength, which are essential for understanding the crack resistance and load distribution behavior of the matrix under bending stresses. After failure, each specimen was halved and subsequently used for compressive strength testing, as described in Section 3.3.2. The test configuration is shown in Figure 9, which displays a specimen under loading between support points during the bending procedure.



Figure 9 Flexural test on a prismatic mortar specimen (40 × 40 × 160 mm³) using a three-point bending configuration to determine the flexural strength according to EN 1015-11.

3.3.2 Mortar's compressive test

Compressive strength tests were conducted on three types of mortar specimens, selected according to the specific requirements of each experimental campaign. The first category comprised independently cast cubic specimens with nominal dimensions of 50 × 50 × 50 mm³, intended to provide consistent and reliable compressive strength data. The second type included halves of prismatic beams (40 × 40 × 160 mm³) that were previously tested in flexure, allowing for subsequent compressive testing on the undamaged portions of the fractured prisms. These halves offered a loading face of 40 × 40 mm², enabling comparative evaluation across specimen geometries. The third type consisted of cylindrical specimens with a nominal size of ⌀75 × 150 mm, tested immediately following the elastic modulus test as described in Section 3.3.3. The use of different geometries ensured a flexible yet comprehensive assessment of compressive strength throughout the experimental program.

To mitigate boundary effects and frictional restraint at the contact interfaces during loading, two Teflon sheets coated with lubricant were placed at both ends of the specimens. All compressive tests were carried out in displacement control at a constant rate of 0.005 mm/s using a hydraulic actuator with a 50 kN capacity. The procedure adhered to the ASTM C109 standard [258], ensuring the repeatability and comparability of results. The test setups for each specimen type are shown in Figure 10, where (a) displays a cube specimen, (b) illustrates a half-prism derived from flexural testing, and (c) shows a cylindrical specimen subjected to axial compression after the elastic modulus test.



Figure 10 Compressive strength testing setups for mortar specimens: (a) independently cast cube specimen (50 × 50 × 50 mm³); (b) half-prism from flexural test with a loading face of 40 × 40 mm²; and (c) cylindrical specimen (⌀75 × 150 mm) tested following the elastic modulus test.

3.3.3 Mortar's elastic modulus test

The elastic modulus of the mortar was evaluated using cylindrical specimens with dimensions of 75 mm in diameter and 150 mm in height. These tests aimed to determine the static modulus of elasticity under uniaxial compression, an essential property for assessing the stiffness of TRM systems. The testing procedure was carried out in accordance with the EN 12390-13 [259], which prescribes the use of cyclic loading–unloading sequences within the elastic range of the material to capture its reversible deformation behavior. Given the non-destructive nature of this method, each specimen was tested at different curing stages, allowing for the observation of stiffness development over time.

Prior to testing, the specimen ends were carefully capped using an epoxy adhesive to ensure uniform load distribution and minimize the risk of local crushing or eccentric stress during testing. The axial load was applied using a 50 kN hydraulic actuator, and the cyclic protocol defined in the standard was followed. To measure axial deformations, three LVDTs with a range of 5 mm were mounted symmetrically along the central third of each specimen. This arrangement ensured precise strain measurements while reducing the influence of boundary effects. The stress–strain data obtained from these tests were used to determine the tangent modulus in the linear portion of the loading curve. The complete test configuration is illustrated in Figure 11, which shows the cylindrical specimen placed within the testing frame, including the actuator, capping layer, and LVDT instrumentation used for data acquisition.

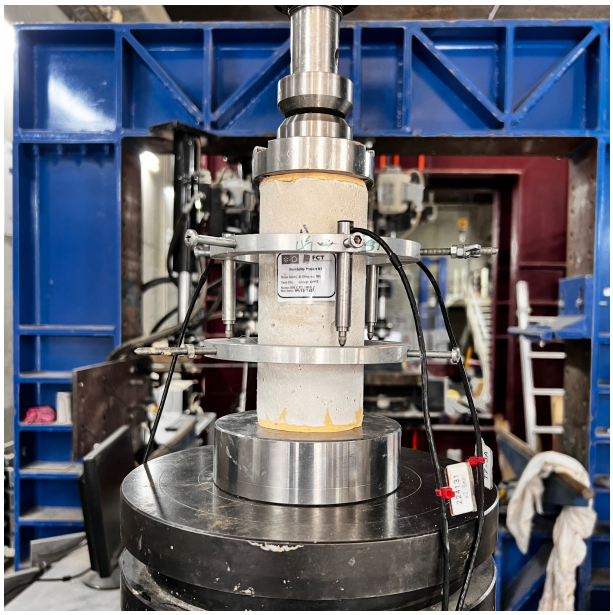

Figure 11 Elastic modulus test setup for cylindrical mortar specimens, showing the capping, actuator, and LVDT configuration used to record strain within the central third of the specimen.

3.3.4 Mortar's direct tensile test

The direct tensile strength of the mortar was assessed by means of uniaxial tension tests conducted on dog bone-shaped specimens, designed according to ASTM C307-18 [260]. This test aimed to evaluate the tensile behavior of the matrix under direct tensile loading and to complement the flexural and compressive strength assessments presented earlier in this chapter. The geometry of the specimens was specifically tailored to promote failure within a central gauge section, thereby ensuring reliable measurement of tensile properties. Each specimen consisted of a total length of 150 mm, featuring two widened gripping ends and a reduced central neck section to encourage fracture away from the clamping zones. The neck region had a rectangular cross-section with dimensions of 50 mm in length and 10 mm in width, and a thickness matching the casting mold (typically 10 mm), resulting in a gauge section of 10×10 mm^2. This narrowed geometry helped to concentrate tensile stresses within the central region and minimize stress concentrations at the transition zones.

The tensile tests were performed using a 50 kN servo-hydraulic actuator under displacement-controlled conditions at a rate of 0.005 mm/s, consistent with the rate employed in other quasi-static tests. Specimens were clamped using flat steel end plates, ensuring symmetrical alignment to prevent eccentric loading. The alignment and load application system were carefully adjusted to ensure axial loading through the specimen's centroidal axis. Load–displacement data were recorded and converted to engineering stress–strain curves based on the geometry of the necked section. The test setup and a representative failure mode of the mortar specimen are illustrated in Figure 12, where the characteristic

cracking in the neck region can be observed, confirming the effectiveness of the specimen design and alignment.



Figure 12 Dog bone specimen used for the direct tensile strength test of mortar, utilized in the present study.

3.3.5 XRD analysis

XRD analysis was conducted using a Bruker D6 PHASER diffractometer equipped with a Co-Kα radiation source, operating at 40 kV and 30 mA. Specimens were first pulverized using a ball-milling machine to ensure homogeneity and proper crystallographic resolution. Prior to analysis, hydration was halted by immersing the milled mortar samples in isopropanol for 24 hours, followed by drying at 70°C until constant mass. Measurements were conducted over a 2θ range of 10° to 90°, with a step size of 0.05° and a dwell time of 2 seconds per step. This analysis facilitated the identification of mineralogical changes such as decalcification and the formation of secondary phases.

3.3.6 XRF analysis

To determine the elemental composition of the unreacted mortar, XRF was performed using a PANalytical Epsilon 3 spectrometer. Prior to testing, the samples underwent a LOI process at 1050°C for 4 hours to quantify volatile components. The residue was then mixed with XRF-grade wax in a 1:2 ratio and pressed into pellets under 30 tons (approximately 294.2 kN) of force. This test was essential for quantifying the initial oxide composition of the mortar and for verifying material consistency.

3.3.7 TGA analysis

TGA was carried out on ~100 mg of powdered mortar samples using a NETZSCH TG 209 F3 Tarsus instrument. A heating rate of 10°C/min was applied from room temperature to 950°C under a nitrogen atmosphere to avoid oxidative reactions. The high-resolution top-loading design and micro-furnace allowed for detection of small mass losses corresponding to specific dehydration, decarbonation, and sulfate decomposition phases. This technique was used to monitor thermal stability and the evolution of hydration and carbonation products.

3.3.8 FTIR analysis

FTIR was performed using a Varian 670-IR spectrometer, operating in the 400–4000 cm^{-1} range at 1 cm^{-1} resolution. Powdered samples were analyzed after undergoing hydration stoppage and drying procedures. The FTIR spectra provided information on the chemical transformations of functional groups, particularly those associated with calcium hydroxide, calcium carbonate, and sulfate compounds. Peak shifts in the carbonate (CO_3^{2-}) and sulfate (SO_4^{2-}) regions indicated the influence of environmental exposure, especially under acidic conditions.

3.3.9 Optical Microscopy

Following mechanical testing, selected cross-sections were prepared for optical microscopy to visualize surface-level alterations and degradation fronts. Samples were embedded in low-viscosity Epofix epoxy mixed with methyl ethyl ketone and processed under vacuum using a CitoVac unit. After curing for 24 hours, specimens were polished using a Struers Tegramin-30 machine. Imaging was performed with a Zeiss microscope and Axiocam 305 color camera, enabling qualitative assessment of surface degradation and matrix integrity.

3.3.10 SEM and EDX analysis

For more detailed microstructural and compositional analysis, SEM was carried out using a Phenom Pharos G2 system. Embedded and polished specimens were gold-coated to reduce surface charging. SEM enabled the identification of cracks, fiber-matrix interfacial zones, and morphological changes, while EDX provided localized elemental composition. This dual approach was particularly valuable in identifying sulfur-rich and decalcified zones under acidic exposure.

3.3.11 Bulk Density measurement

The bulk density of flexural specimens was determined immediately after removal from the climatic chamber. No additional surface cleaning was performed due to controlled ventilation. Density was calculated from the specimen mass and geometric dimensions. This ensured consistency in evaluating potential mass changes due to aging and environmental conditioning.

3.3.12 Open Porosity measurement

Open porosity was measured on fractured halves of specimens using the procedure defined in EN 1936:2006 [261]. Samples were vacuum saturated in water, weighed submerged, then in SSD and dry conditions. The porosity was calculated based on the mass difference and provides insight into the extent of pore connectivity and saturation, particularly in the context of degradation due to prolonged environmental exposure.

3.3.13 ICP Leaching analysis

The aging solutions in which the mortar specimens were immersed were analyzed using ICP spectroscopy in accordance with ISO 11885:2007 [262]. Solutions were filtered to eliminate solid particles and tested for concentrations of leached elements. Results, expressed in mg/kg of solution, reflected the intensity of chemical degradation and dissolution. Elements analyzed included sodium (Na), potassium (K), calcium (Ca), magnesium (Mg), aluminum (Al), iron (Fe), chloride (Cl^-), sulfate (SO_4^{2-}), and nitrate (NO_3^-). These data were used to correlate leaching behavior with environmental exposure type and mechanical performance loss.

3.3.14 Masonry unit's compressive test

The compressive strength of the brick units used as substrates in TRM applications was evaluated through standardized tests conducted on cut specimens. To achieve dimensional consistency with the mortar cube tests, each brick sample was trimmed into 50 × 50 × 50 mm³ cubes. This allowed for direct comparison between the mortar and masonry compressive performance while minimizing geometry-related variability. The same boundary and loading conditions as the mortar cubes were applied to the brick samples to ensure experimental consistency across materials. As with mortar specimens, two Teflon sheets and a thin lubricant layer were inserted between the specimen faces and the compression platens to minimize interface friction and ensure uniform stress distribution during testing.

Compressive strength tests were conducted using a 50 kN hydraulic actuator under displacement control with a constant rate of 0.005 mm/s. This approach enabled stable loading and precise detection of failure onset. The results obtained from these tests provided essential information regarding the strength compatibility between the mortar matrix and the masonry substrate, which directly influences the reliability of TRM systems applied in real-world strengthening contexts. The experimental configuration for these tests is illustrated in Figure 13, which shows the loading setup and alignment of a representative brick specimen.



Figure 13 Compression test on a 50 × 50 × 50 mm³ brick specimen used to evaluate the compressive strength of the masonry substrate, with lubricated Teflon sheets inserted between the loading platens.

3.3.15 Yarn's tensile test

The tensile performance of individual yarns used in TRM systems was evaluated through uniaxial tensile tests performed under displacement-controlled conditions. These tests were aimed at determining the ultimate tensile strength, strain at failure, and elastic modulus of the reinforcement yarns. Each specimen was anchored at both ends using metallic gripping plates bonded with a two-component epoxy adhesive (MapeWrap 31) to ensure effective load transfer and to prevent premature failure at the gripping zones. This anchoring technique was applied uniformly to all specimens for consistency across measurements. All tests were carried out using an MTS Exceed® E44 electromechanical universal testing machine, equipped with an integrated optical extensometer. This system enabled accurate and continuous recording of force and displacement throughout the test. The displacement was monitored over a 100 mm gauge length centered on the specimen. The tests were executed under displacement control at a constant rate of 0.005 mm/s, in accordance with protocols established in relevant literature and

standardized testing guidelines. This ensured consistent loading conditions and allowed for direct comparison of mechanical performance across different yarn types. From the recorded force–displacement curves, the stress–strain behavior of each yarn was computed. These data were subsequently used to calculate the tensile strength and elastic modulus of the materials under investigation. The experimental configuration for the yarn tensile strength test is illustrated in Figure 14, which shows the mounted specimen, gripping system, and testing apparatus.

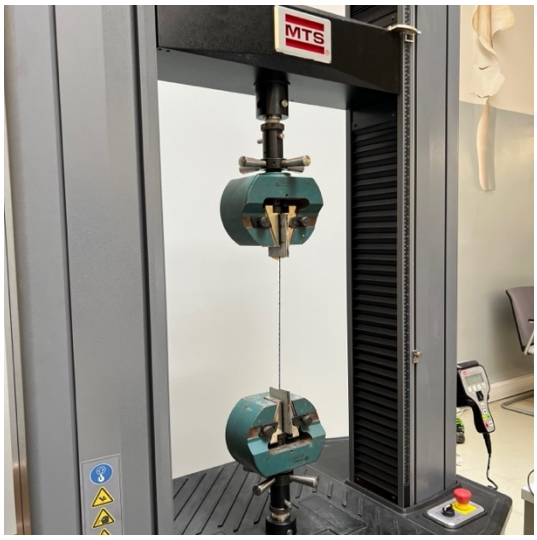

Figure 14 Tensile strength test setup for single yarn specimens using the MTS Exceed® E44 electromechanical testing machine.

3.3.16 Textile's tensile test

In addition to individual yarn tests, the tensile strength of textile meshes was assessed through direct uniaxial tensile tests, which enabled characterization of the collective mechanical behavior of the reinforcement under axial loading. These tests provided critical insights into the tensile capacity, strain at failure, and elastic modulus of the textiles as composite fabrics, while capturing the influence of mesh architecture, yarn interaction, and distribution. Textile specimens were prepared by cutting rectangular strips containing multiple longitudinal yarns—typically three yarns for the glass textile and up to nine for the basalt mesh, depending on the type. To ensure reliable anchorage and prevent slippage or premature failure at the gripping zone, the extremities of each specimen were bonded to gripping plates using the MapeWrap 31 epoxy resin. This anchoring method was applied uniformly across all specimens to standardize boundary conditions and facilitate consistent stress transfer.

All tensile tests on textile meshes were conducted under displacement control at a constant rate of 0.005 mm/s, following the same methodology adopted for single yarn testing. Two different testing systems were employed based on availability and experimental logistics. The first system involved the use of a 50 kN hydraulic actuator, equipped with an external LVDT spanning a gauge length of 100 mm for displacement measurement. The second configuration utilized the MTS Exceed® E44 electromechanical testing machine, paired with an optical extensometer to monitor deformation with high precision. The obtained force–displacement curves were converted into stress–strain data, from which the tensile strength and modulus were determined based on the initial linear portion of the response.

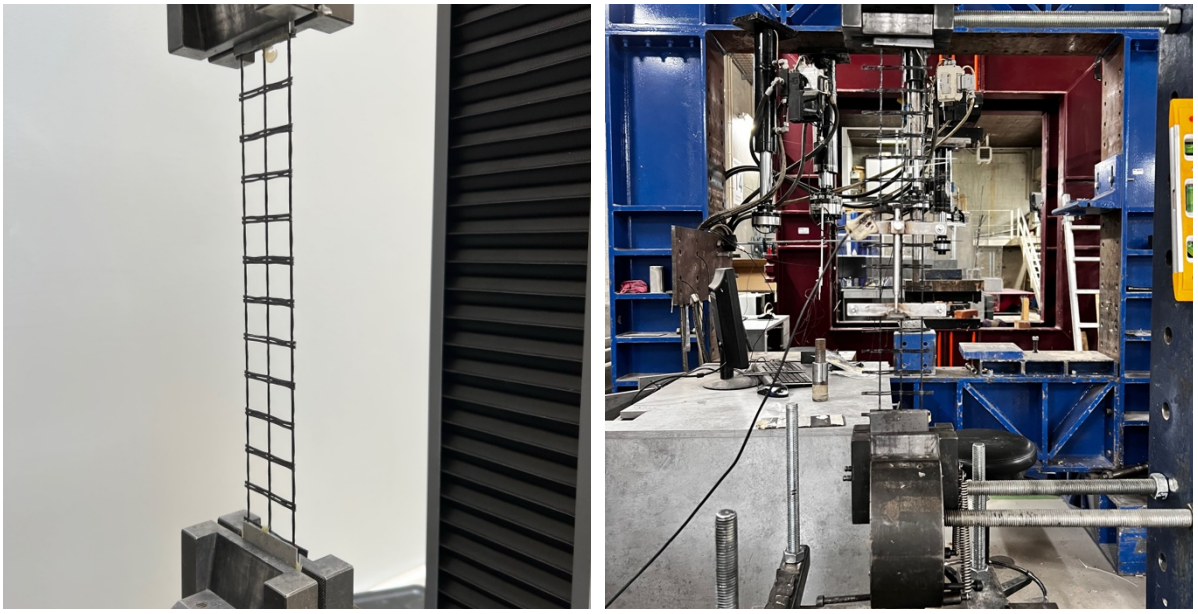

(a) (b)



(c)

Figure 15 illustrates the experimental setup used for the tensile strength tests on textile meshes. (a) presents the MTS-based configuration used for certain glass specimens; (b) shows the hydraulic actuator system; and (c) provides a close-up of the central gauge region equipped with external instrumentation for strain measurement.

3.4 Yarn to mortar bond behavior

The bond behavior between the fiber yarns and the mortar matrix was evaluated through direct pull-out tests, aiming to quantify the interfacial adhesion and load transfer efficiency within the TRM system. These tests served to characterize the mechanical interaction between the yarn and surrounding mortar, which significantly influences the composite's stress distribution and overall performance. Test specimens were prepared by embedding a single yarn longitudinally into a prismatic mortar block, while the free end of the yarn was securely anchored in a prefabricated resin block. This setup ensured consistent stress transmission and eliminated premature failure or slippage at the clamping interface. The adopted methodology was aligned with established protocols in the literature, particularly those emphasizing the use of rigid resin anchorage to isolate interfacial slip within the bonded length [263].

The embedded length of the yarn within the mortar was maintained at 50 mm for both glass and basalt fiber systems. This value was selected based on prior studies on glass TRM systems [264] and verified through preliminary testing for basalt, which demonstrated a comparable bond–slip response and effective load development within the same embedment length. All pull-out specimens were cured under the same environmental conditions adopted for other material characterization tests to ensure uniformity across the experimental campaign.

Pull-out tests were conducted using a 25 kN capacity hydraulic actuator under displacement-controlled conditions at a constant rate of 0.016 mm/s, to preserve quasi-static loading. Relative displacement between the yarn and mortar was measured using two LVDTs symmetrically positioned on opposite sides of the resin block. This configuration enabled accurate recording of axial slip and minimized eccentricity during loading. The failure modes, including yarn pull-out, matrix cracking, and fiber rupture, were visually observed and recorded for further interpretation of the interface failure mechanism. The experimental configuration adopted in this study is illustrated in Figure 16, which shows a representative pull-out specimen with clearly visible resin anchorage, yarn embedment, and LVDT arrangement for axial slip measurement. The image aids in conveying the geometric arrangement and boundary conditions applied during testing, which are crucial for interpreting the bond performance of TRM constituents.



Figure 16 Test setup for pull-out tests showing the yarn anchored in resin, embedded in mortar, and instrumented with dual LVDTs for monitoring axial slip.

3.5 TRM to substrate bond behavior

The bond performance between textile reinforcement and masonry substrate was further examined through single-lap shear tests, which aimed to simulate shear loading conditions and evaluate the mechanical integrity of the TRM system under monotonic displacement. This method focused on identifying the bond strength, load transfer characteristics, and failure mode—particularly distinguishing fiber rupture from debonding behavior. An effective bond length of 100 mm was adopted for both glass and basalt textiles, as previously recommended in the literature [263]. The specimen geometry and preparation were adapted to facilitate compatibility with testing equipment and instrumentation, ensuring that failure occurred within the bonded region. To stabilize instrumentation and improve data accuracy, resin blocks were cast over the first 50 mm of the textile's free end before mortar application. This measure also allowed precise installation of the displacement measurement system. Curing conditions

were kept consistent with those applied in the pull-out tests. In the days preceding the test, the exposed textile was further impregnated with resin to minimize premature failure outside the bonded zone. Gripping plates were applied as an additional safeguard against stress concentrations during clamping. Three yarns were used for glass textiles and nine for basalt specimens to account for differences in mesh architecture and to provide comparable mechanical behavior.

Material-specific reinforcement strategies were necessary due to the mesh size and different failure tendencies. For basalt textiles, resin coating alone over the free length was sufficient to avoid early failure. For glass textiles, which possess a coarser mesh and less confinement, additional strengthening was performed by wrapping the external portion of the textile with a basalt mesh and applying resin by forming a hybrid anchorage system to ensure failure occurred within the bonded zone. Prior to testing, a thin layer of epoxy was applied to the brick surface contacting the reaction frame to ensure load uniformity and prevent out-of-plane rotation. Displacement monitoring was achieved using two LVDTs affixed to an omega-shaped aluminum piece adhesively bonded to the resin block and brick surface. This configuration enabled accurate relative displacement measurement across the bond interface and helped detect any asymmetrical deformation. Specimens exhibiting rotation exceeding 5% were excluded to maintain data consistency. Tests were conducted under displacement control using a 50 kN hydraulic actuator at a constant rate of 0.005 mm/s. This procedure ensured quasi-static conditions and consistency with the tensile and pull-out tests. A representative photograph of the single-lap shear test setup is shown in Figure 17, which highlights the specimen configuration, resin-impregnated textile, LVDTs, and omega-shaped displacement sensor.

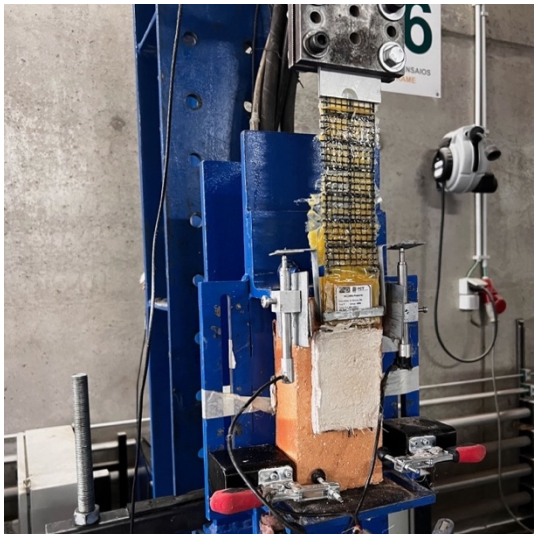

Figure 17 Single-lap shear test configuration showing TRM composite bonded to brick substrate with, LVDTs mounted on an omega-shaped aluminum piece, and setup within the hydraulic loading frame.

3.6 TRM tensile behavior

The uniaxial tensile behavior of the TRM system was investigated through direct tensile tests on composite coupons fabricated using the lime-based mortar and various textile reinforcements described earlier. These tests were aimed at characterizing the stress–strain response, cracking development, and failure mechanisms of TRM under direct tension parameters central to assessing the structural efficiency of composite strengthening systems. All specimens were cast in molds with fixed dimensions of 600 mm in length and 70 mm in width, with a nominal thickness of 10 mm, unless otherwise specified. The casting process was performed in two stages to ensure uniform textile positioning and adequate mortar compaction. As shown in Figure 18a, the casting began with the placement of the first mortar layer,

which covered approximately half the total thickness of the specimen. This layer served as a bedding platform for the textile, which was carefully positioned over the fresh mortar, ensuring precise alignment and avoiding any twisting or folding of the yarns. For TRM made with steel cords, special attention was given to maintaining the unidirectional arrangement and tension of the cords prior to the application of the second mortar layer. Once aligned, the second mortar layer was added, and the surface was leveled using a spatula to produce a consistent cross-section throughout the specimen. A similar preparation sequence was followed for TRM specimens with glass textile reinforcement, as depicted in Figure 18b.



(a)



(b)



(c)

Figure 18 (a) Specimen preparation of TRM coupons reinforced with steel cords; (b) specimen preparation of TRM coupons reinforced with glass textile; (c) tensile test configuration showing the test setup.

After casting, specimens underwent a controlled curing regime to promote consistent hydration and minimize shrinkage-related defects. For the first 24 hours, molds were covered with plastic sheeting. Thereafter, specimens were kept under saturated cloth and wrapped in plastic for an additional two days. Following demolding, the curing continued for seven days under moist conditions inside sealed plastic bags. These initial curing steps were consistently applied across all specimens, while extended curing conditions such as ambient exposure time and temperature were adjusted depending on the particular objectives of each experimental campaign.

To ensure reliable load application during testing, steel end plates measuring 70 mm × 100 mm were bonded to the free ends of each specimen five days before testing using a two-component epoxy adhesive.

These plates served as mechanical anchors, providing a uniform gripping surface and minimizing the likelihood of premature failure at the clamping region. The testing setup for the tensile coupons is presented in Figure 18c, which illustrates the complete configuration, including clamping system, alignment, and end anchorage application. This preparation and testing methodology facilitated consistent mechanical characterization of TRM systems under direct tensile loading. Nonetheless, as highlighted in the literature, several factors, such as the textile orientation, number of reinforcement layers, and gripping configuration can influence the mechanical response, especially in the post-cracking stage. These effects warrant detailed investigation, which forms the basis of the extended experimental program presented in the subsequent section.

3.7 Conclusion

This chapter presented a comprehensive overview of the materials, configurations, and testing methodologies adopted for the short-term mechanical characterization of TRM composites. The objective was to establish a consistent and reproducible framework for evaluating the mechanical behavior of TRM systems under quasi-static loading, serving as the foundation for subsequent experimental campaigns. A commercial lime-based mortar was characterized through compressive, flexural, elastic modulus, and direct tensile strength tests. The tensile behavior of textile yarns and grids, comprising high-strength steel and glass, was also evaluated to assess their standalone mechanical contribution. Additionally, bond-related tests, including pull-out and single-lap shear configurations, were introduced to explore the interaction between reinforcement and matrix, and between TRM and masonry substrates, respectively. Specimen preparation procedures, gripping methods, and mold geometries were described in detail, including specific anchorage techniques used to prevent premature failure and ensure uniform stress distribution.

By this chapter the test setups and preparation protocols detailed herein were designed to minimize variability, facilitate comparative analysis, and reflect field-relevant conditions. These methods will be employed in later chapters to investigate both the short-term mechanical response and the long-term durability of TRM systems under varied environmental and loading scenarios. Herein, the subsequent chapter builds directly upon the methodological basis established here by presenting the experimental results of the tensile test campaign. The influence of gripping strategy, textile configuration, and mortar thickness on the tensile behavior of TRM composites will be analyzed in depth, offering new insights into failure mechanisms, load transfer, and stress distribution under direct tension.

Chapter 4
Short term performance of TRM under tension: Influence of test setup and layering

4.1 Introduction

The experimental study presented in this chapter aims to characterize the uniaxial tensile behavior of TRM composites under short-term monotonic loading. Building upon the test setup and specimen preparation procedures described in Chapter 3, the present Chapter explores the influence of key parameters that govern the mechanical response of TRM systems in direct tensile test. In particular, the role of test configuration, namely the gripping method, as well as the number of textile layers and the thickness of the mortar matrix, are examined with a view to evaluating their effect on tensile strength, cracking behavior, and failure mechanisms. Recognizing the significant variability observed in the literature regarding TRM tensile test results, this study focuses on reducing experimental uncertainty by adopting a standardized methodology while systematically varying critical parameters. The comparison between configurations that transfer load directly through the textile and those relying on mortar clamping is central to this analysis. The influence of these configurations on stress distribution, strain localization, and crack propagation is addressed through a comprehensive parametric program involving both steel and glass textile reinforcements.

In total, thirteen distinct TRM configurations were fabricated, tested and studied in this chapter, resulting in a dataset of seventy-eight tensile coupons. Each configuration was designed to isolate the influence of a particular parameter while maintaining consistency in curing regime, material formulation, and specimen geometry. The experimental approach also included reinforcement of the free textile portion with epoxy resin to minimize premature failure near gripping zones, as well as the use of end plates for better alignment and stress transfer. By doing so, the study aimed to capture the intrinsic mechanical behavior of the TRM system and to identify the most reliable testing practices for material characterization. The results reported in this chapter are expected to inform both experimental protocols and numerical calibration efforts for modeling TRM systems. Furthermore, the findings serve as a foundation for understanding short-term composite behavior, which is an essential prerequisite for the long-term durability analyses discussed in the subsequent chapter.

4.2 Experimental program

The experimental phase focused on a series of direct tensile tests performed on TRM specimens reinforced with steel and glass textiles. The aim was to assess how variations in test configuration and the arrangement of reinforcement layers influence the mechanical behavior of the composite. To explore these parameters, multiple specimens were prepared using commercially available materials, while maintaining consistent specimen geometry and curing procedures across all groups. Two types of textile reinforcement, namely steel and glass textiles were considered, and various configurations were tested by modifying the number of textile layers and the method of load application. Particular attention was given to distinguishing between setups where loading was applied directly through the textile and those where load transfer occurred via the surrounding mortar. This allowed for a targeted comparison of the influence of clamping approach on stress distribution, cracking, and failure progression. Additional information regarding the configuration of the specimens and instrumentation is provided in Figure 19, which supports the visual understanding of the test arrangements and variables considered in this study.

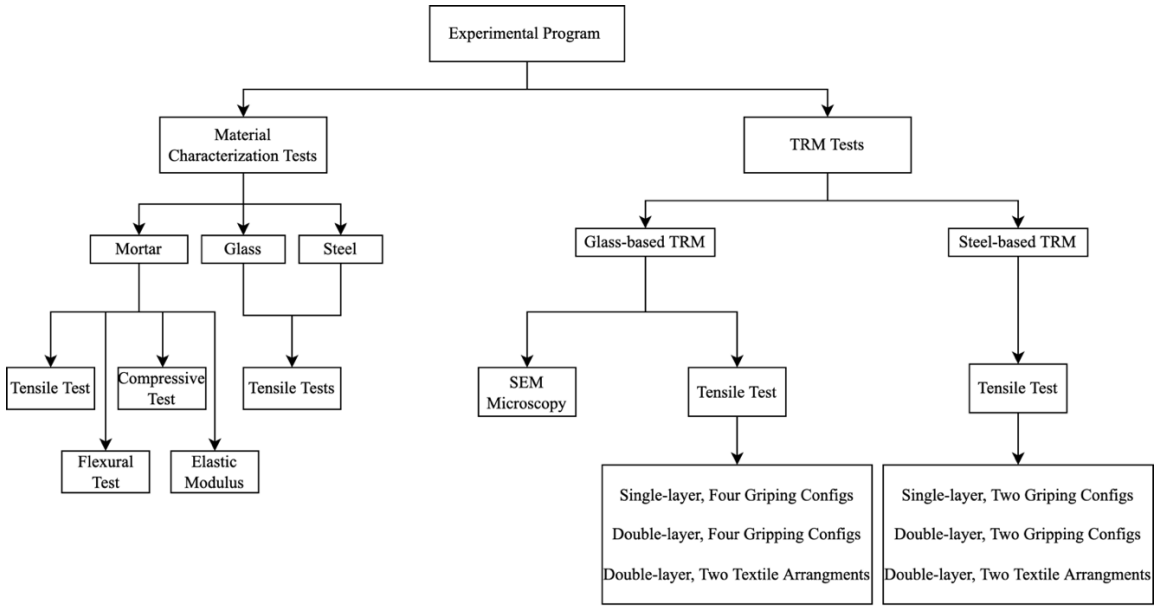

Figure 19 Overview of the experimental program

4.2.1 Materials and Methods

The composite specimens used in this phase of the experimental program were prepared by embedding textile reinforcements in a commercial hydraulic lime–cement–pozzolan mortar, whose compressive strength, flexural strength and elastic (dynamic) modulus were determined in the material characterization phase. Two types of textile reinforcement were employed: a bidirectional alkali-resistant glass fabric and a unidirectional galvanized steel mesh. Prior to composite fabrication, both textiles were characterized by direct tensile tests on the bare fibers. For the TRM specimens, fabricated by casting the mortar over the textile layers, uniaxial tensile tests were conducted to capture the full stress–strain response, and the fracture surfaces were examined by SEM. All of these test methods are described in detail in Chapter 3. A uniform curing regime was adopted for all composites. Specimens were demolded 72 hours after casting, then kept moist under wet cloths and plastic sheeting for seven days to promote hydration and minimize shrinkage. Thereafter they were stored at 15 °C ± 5 °C and 65 % ± 10 % RH for an additional 83 days before testing. This protocol was applied consistently across all batches to ensure that differences in mechanical behavior reflect only textile configuration and test setup, not variations in curing.

4.2.2 Material characterization tests

The mechanical behavior of the mortar used in the experimental campaign was evaluated by determining its flexural strength, compressive strength, elastic modulus, and direct tensile strength, following the procedures outlined in Section 3.3. Prismatic, cubic, cylindrical, and dog bone specimens were used, corresponding to the geometries and methods described previously. A total of six specimens were tested for each configuration to ensure result reliability and reduce variability in the mechanical property assessment.

All tests were conducted using a 50 kN capacity hydraulic actuator. Flexural and compressive strength tests were performed under force-controlled conditions, while elastic modulus and direct tensile strength evaluations were carried out under displacement control. For elastic modulus testing, three LVDTs with a 5 mm range were positioned along the middle third of each cylindrical specimen to capture axial deformation. The direct tensile test on mortar was executed using dog bone specimens, and loading was applied at a constant displacement rate of 0.005 mm/s to allow precise identification of the cracking point and tensile resistance.

In addition to mortar characterization, tensile strength tests were also conducted on the reinforcing textiles. Both single yarns and mesh segments consisting of three yarns were tested for the steel cords and glass fibers. These tests were performed according to standard procedures applicable to yarn and the textile assessments.

4.2.3 TRM tensile testing

Monotonic direct tensile tests were carried out on TRM composite specimens to investigate the influence of loading configuration and textile arrangement on the tensile behavior of the system. A total of 78 specimens were prepared and divided into thirteen groups to allow for systematic comparison between different setups and reinforcement configurations. The specimens were produced with standardized dimensions of 600 mm in length and 70 mm in width across all groups. All samples underwent consistent casting and curing procedures, followed by 90 days of conditioning under controlled laboratory conditions (20 ± 5°C and 70 ± 5% RH) as described in Section 4.2.1. Two principal load application strategies were considered in this study: one in which the tensile load was applied directly to the textile reinforcement, and another where the force was transferred through the mortar matrix. These contrasting approaches were used to evaluate their respective influence on stress transfer mechanisms, cracking evolution, and failure mode in TRM composites.

4.2.4 Gripping configurations

To examine the effect of test configuration on tensile response, four distinct gripping setups were employed, grouped into two broader categories based on how the tensile load was introduced into the specimen. In the first category, the force was applied directly to the textile reinforcement (designated as SF, MF, and LF), while in the second, the load was transferred through the mortar matrix (TR). Each configuration was designed to explore different aspects of boundary conditions and load path uniformity. These setups allowed for comparative analysis of cracking behavior, tensile strength, and strain distribution across varying reinforcement and anchorage conditions. The arrangement and geometry of each configuration are illustrated in Figure 20, which provides a visual reference for the experimental layouts used in this study.

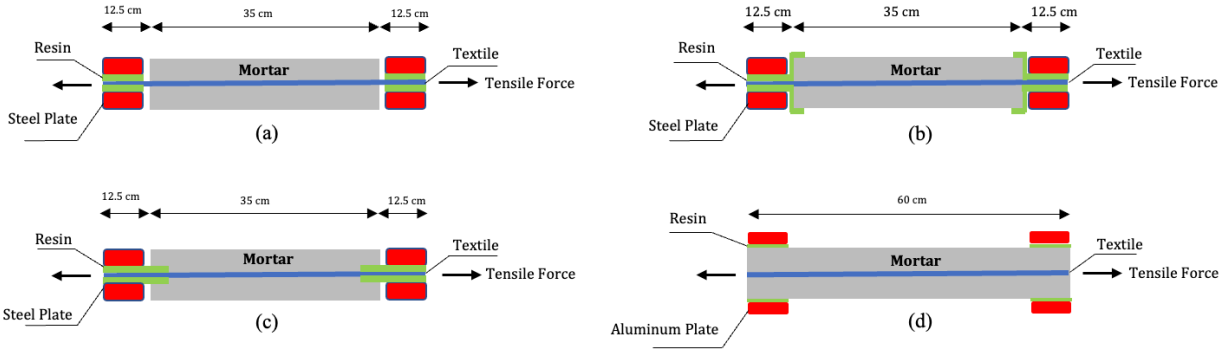

Figure 20 Schematic representation of TRM coupons and test setups: a) SF setup; b) MF setup; c) LF setup; d) TR setup.

In the first configuration, designated as SF, the tensile load was applied directly to the bare textile without any resin treatment at the ends (Figure 20a). This configuration has been introduced in earlier research with satisfactory results [63] and served as the baseline for comparison in the current study. Building upon the SF setup, two additional configurations were developed to improve stress transfer in the unbonded zones by reinforcing the textile ends. The second configuration, referred to as MF, involved impregnating both the mortarless fabric and the initial 5 mm of the adjacent mortared zone with a commercial epoxy resin, as previously proposed in similar experimental campaigns [265]. This was applied symmetrically to both ends of the specimen (Figure 20b), resulting in a locally stiffened region intended to enhance continuity between the reinforcement and the gripping system. The third configuration, designated as LF, followed a similar approach, with resin impregnation applied before casting, covering both the free fabric and a short portion of the mortared segment (Figure 20c). This treatment was intended to prevent stress concentration at the textile–mortar interface and to maintain better load alignment during testing [65]. In all three configurations (SF, MF, and LF), the central 350 mm of the specimen was embedded in mortar, and the tensile load was applied directly to the textile.

A fourth configuration, labeled TR, was implemented to assess the tensile response when the load is transferred through the mortar layer rather than the textile itself. In this setup, the full 600 mm length of the specimen was used, with 125 mm on each end clamped inside the grips (Figure 20d). This approach followed recommendations in the literature for improving load uniformity and replicating real application conditions more closely [7,266]. All four configurations were tested using the same mechanical gripping system to maintain consistency across specimens. While resin impregnation at the ends offers advantages such as improved stress continuity and crack distribution control, it also introduces potential drawbacks including increased local stiffness and variability in application quality. The comparative analysis of these configurations enabled a detailed evaluation of their respective benefits and limitations in the tensile testing of TRM composites.

4.2.5 Textile arrangement and matrix effect

In addition to testing configuration, the influence of textile arrangement and mortar thickness was also investigated to assess their contribution to the tensile behavior of TRM composites. Two different configurations were considered for specimens incorporating multiple textile layers. In the first configuration, two textile plies were embedded centrally within the mortar thickness, placed directly on top of each other without any separation. The overall mortar thickness in this case was maintained at 10 mm, consistent with the single-layer reference specimens. In the second configuration, an internal separation of 5 mm was introduced between the textile plies by increasing the total mortar thickness to 15 mm. This internal spacing created a distinct mortar interface between layers, allowing for an

examination of how vertical distribution affects stress transfer, matrix impregnation, and confinement of the reinforcement.

These two arrangements were expected to generate different mechanical responses due to variations in bonding, cracking behavior, and stiffness development across the thickness of the specimen. The comparison between them provided valuable insight into how textile stacking strategies influence the structural performance of TRM in multi-layer applications. To systematically track the experimental parameters, a consistent specimen notation was used. Each specimen was designated as S_T_L_TH_R, where "S" identifies the test setup type (i.e., SF, MF, LF, or TR), "T" refers to the type of textile reinforcement (glass or steel, indicated as G or S), "L" denotes the number of textile layers (1 or 2), and "TH" refers to the total mortar thickness (10 mm or 15 mm). For instance, a specimen labeled MF_G_1L_10 corresponds to a glass textile with the MF configuration, one textile layer, and a mortar thickness of 10 mm. The complete list of specimen groups and configurations is summarized in Table 2.

Table 2 Detailed specification of test setups

Group name	Specimen name	Type of fiber	TRM thickness [mm]	Mortar length [mm]	Number of textile layers	Gripping type
GP1	MF_S_2L_10	Steel	10	350	2	MF
GP2	MF_S_1L_10	Steel	10	350	1	MF
GP3	MF_S_2L_15	Steel	15	350	2	MF
GP4	TR_S_1L_10	Steel	10	600	1	TR
GP5	TR_S_2L-15	Steel	15	600	2	TR
GP6	SF_G_1L_10	Glass	10	350	1	SF
GP7	MF_G_2L_15	Glass	15	350	2	MF
GP8	MF_G_1L_10	Glass	10	350	1	MF
GP9	MF_G_2L_10	Glass	10	350	2	MF
GP10	LF_G_1L_10	Glass	10	350	1	LF
GP11	TR_G_1L_10	Glass	10	600	1	TR
GP12	TR_G_2L_15	Glass	15	600	2	TR
GP13	TR_G_2L_10	Glass	10	600	2	TR

4.2.6 Testing procedures

Five days prior to testing, steel or aluminum plates were bonded to both ends of the specimens using epoxy resin to ensure uniform stress distribution and to minimize the risk of slippage during load application. These plates were applied either on the textile reinforcement or directly on the mortar, depending on the gripping configuration of each setup. The aim was to facilitate stable mechanical engagement with the gripping system and reduce premature failures at the contact interface. All tests were conducted under displacement-controlled conditions at a constant loading rate of 0.005 mm/s, following established recommendations in the literature [265]. A hydraulic actuator with a load capacity of 50 kN was employed for all tests. Testing was continued until either a crosshead displacement of 20 mm was reached, or a significant load drop occurred, accompanied by visible rupture or failure of one or more yarns. Mechanical clamps were used to grip the specimens at both ends throughout the tests.

Displacement measurements were recorded using two LVDTs, each with a 20 mm range, mounted on the left and right sides of the specimen. These LVDTs captured the relative axial displacement between

the gripping zones. Additionally, DIC was employed to track the surface strain field using a stochastic speckle pattern applied to the specimen surface. Images were captured at a frequency of 0.2 Hz, with camera settings set to ISO 400, shutter speed 1/200 s, and aperture f/5.6. The full test setup, including the LVDT configuration and DIC system, is shown in Figure 21. Stress–strain responses derived from these tests are presented in Section 4.3. Strain was calculated by dividing the average displacement measured by the two LVDTs by their gauge length, while stress was computed using the effective cross-sectional area of the textile reinforcement.

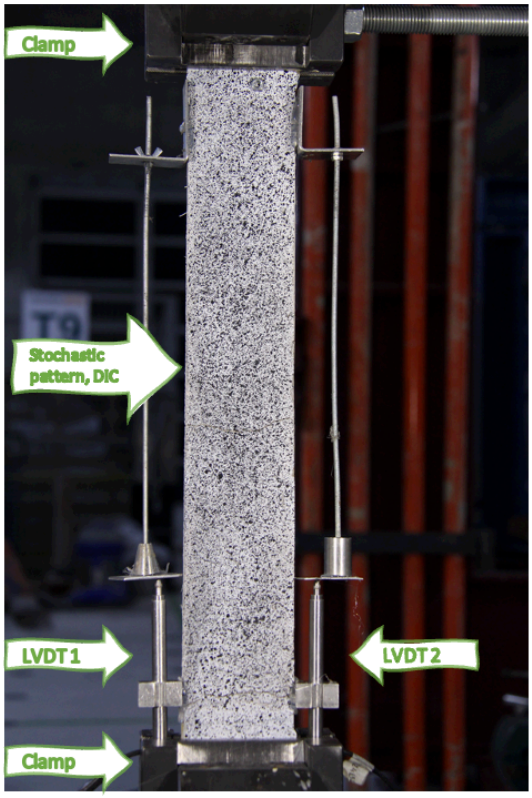

Figure 21 Configuration of the tensile test setup (glass-TRM specimen is shown)

4.3 Results and discussion

4.3.1 Material properties

The average values obtained from the material characterization phase are summarized in Table 3. These include the mortar's mechanical properties, as well as the tensile performance of the textile reinforcements at both yarn and fabric levels. The tensile strength of the mortar was 2.15 MPa as measured from the flexural test, whereas the direct tensile test using dog bone specimens yielded a significantly lower value of 0.77 MPa. This reduction in tensile capacity is consistent with trends reported in the literature, where direct tensile strength is typically lower than flexural strength due to differences in stress distribution and crack propagation [267–269].

The tensile strength results of both single yarns and mesh specimens are reported for the glass and steel textiles. While the elastic modulus values for the textiles were adopted from previous experimental campaigns [270], the tensile strength values were obtained within the scope of this study. A slight reduction in strength and a higher coefficient of variation (CoV) were observed in mesh tests compared to single yarns. This is attributed to non-uniform load sharing among the yarns in the mesh, which is a known limitation in fabric-level tensile tests [271]. Table 3 provides the complete overview of these

properties, including mean values and associated CoVs, ensuring a comprehensive understanding of the variability inherent in the tested materials.

Table 3 Results of material characterization test

Test Type	Value [CoV in percentage]
Mortar elastic modulus (GPa)	12.5 (8)
Mortar compressive strength (MPa)	11.2 (15)
Mortar flexural strength (MPa)	2.15 (17)
Mortar tensile strength (MPa)	0.77 (16)
Single glass yarn tensile strength (GPa)	1.12 (3)
Glass fabric tensile strength (three-yarn mesh) (MPa)	1.02 (13)
Single glass yarn elastic modulus (GPa) [270]	66.0 (5)
Single steel cord tensile strength (GPa)	2.98 (2)
Steel fabric tensile strength (ten-cords) (GPa)	2.91 (5)
Single steel cord elastic modulus (GPa) [270]	189 (8)

4.3.2 Tensile behavior analysis

The tensile behavior of TRM composites typically exhibits a three-stage response: the uncracked linear-elastic phase, the crack formation stage, and the post-cracking or crack stabilization phase [251,272]. These stages were identified and evaluated using the digital image correlation (DIC) technique, which enabled precise detection of crack initiation, propagation, spacing, and distribution [51,75,86,135]. The onset of cracking was defined by the appearance of the first visible crack in the DIC data, corresponding to the stress–strain pair (σ_I, ε_I). Crack stabilization, marking the transition into the final post-cracking stage, was identified at the point where no additional cracks developed, denoted as (σ_{II}, ε_{II}). These thresholds were used to segment the stress–strain response into three linear regions, each characterized by a distinct modulus: E_1 for the uncracked phase, E_2 for the stage following the first crack, and E_3 for the stabilized cracking phase.

In addition to the stiffness parameters, the ultimate tensile strength of the composite (ft) and its associated strain ε(ft) were also determined. The calculated parameters provided a comprehensive view of the tensile response of each configuration and served as the basis for evaluating the influence of textile type, layer arrangement, and test setup. The full set of parameters derived from the tensile tests is presented in Table 4.

Table 4 Test results on characterization parameters of different groups of coupons (CoV is given inside parenthesis)

Group name	E_1 [GPa]	E_2 [GPa]	E_3 [GPa]	ε_1 [%]	ε_{fi} [%]	ε (f_f) [%]	σ_1 [GPa]	σ_{fi} [GPa]	f_f [GPa]	Average number of cracks	Average crack spacing [mm]
MF_S_2L_10	781 (59)	207(11)	126(24)	0.02(57)	0.73(61)	1.92(3)	0.09(49)	1.48(53)	3.09(1)	4	122
MF_S_1L_10	917(33)	189(11)	152(13)	0.02(62)	0.66(12)	1.71(7)	0.15(18)	1.38(18)	2.96(5)	11	44
MF_S_2L_15	1107(24)	210(6)	148(3)	0.01(42)	0.24(15)	1.93(3)	0,13(32)	0.60(13)	3.09(1)	3	79
TR_S_1L_10	1297(22)	212(15)	124(59)	0.00(32)	0.00(47)	0.00(35)	0.14(24)	0.46(24)	0.60(24)	8	32
TR_S_2L_15	951(24)	214(7)	141(34)	0.02(28)	0.13(32)	0.31(41)	0.13(11)	0.38(22)	0.57(11)	3	77
SF_G_1L_10	2905(94)	38(11)	38(20)	0.02(53)	1.16(14)	1.51(8)	0.27(8)	0.71(12)	0.82(3)	2	105
MF_G_2L_15	1063(46)	28(66)	50(13)	0.06(135)	0.73(46)	1.42(4)	0.27(17)	0.49(37)	0.85(5)	8	59
MF_G_1L_10	1090(27)	59(26)	42(13)	0.02(44)	0.59(40)	1.26(6)	0.18(23)	0.52(27)	0.80(7)	6	74
MF_G_2L_10	573(58)	29(83)	49(18)	0.06(43)	0.97(37)	1.56(4)	0.24(12)	0.59(34)	0.88(8)	17	28
LF_G_1L_10	1864(50)	48(90)	55(30)	0.03(68)	0.54(20)	1.04(30)	0.44(42)	0.68(10)	1.01(14)	6	43
TR_G_1L_10	2492(32)	32(69)	33(44)	0.09(67)	1.00(35)	1.47(21)	0.37(26)	0.62(6)	0.74(5)	15	19
TR_G_2L_15	92(31)	3(29)	4(11)	0.16(46)	9.30(28)	12.0(23)	0.14(43)	0.37(36)	0.49(29)	4	61
TR_G_2L_10	1148(21)	24(23)	26(61)	0.00(54)	0.01(65)	0.02(59)	0.14(34)	0.32(32)	0.50(15)	1	-

* CoV is given inside parentheses

4.3.3 Overall TRM tensile behavior

The overall tensile response of single-layer TRM composites reinforced with glass and steel textiles was examined across three gripping configurations: SF, MF, and LF. The corresponding stress–strain diagrams are presented in Figure 22. As summarized in Table 4, both material types showed relatively low scatter at higher strain levels, with most specimens reaching failure at comparable strain values. This consistency was more pronounced in steel-based TRM specimens, likely due to the more homogeneous nature and superior mechanical properties of the steel cords, including higher tensile strength and reduced susceptibility to local imperfections. For steel-based TRM specimens, the clear identification of the three loading stages was challenging—particularly in the MF configuration—where the transition between Stage I (elastic) and Stage III (crack stabilization) appeared nearly continuous. The absence of a distinct Stage II (crack formation) is attributed to the higher reinforcement ratio of the steel system, which likely promoted early stress redistribution and reduced crack propagation visibility in the global response.

In the MF configuration, Figure 22c shows a smoother and more gradual load drop at the transition into Stage II compared to the SF setup. Digital image correlation (DIC) observations confirmed that cracks initiated earlier and developed more uniformly in the MF specimens. This early initiation and distributed cracking are indicative of improved interaction between textile and mortar, leading to a more reliable tensile response. Notably, the transition to Stage III began at approximately 77% of the ultimate strength in SF specimens, while in both MF and LF configurations, this transition occurred around 50%. This behavior suggests that the matrix in the SF configuration contributed less to stress redistribution, with the reinforcement absorbing most of the load until failure.

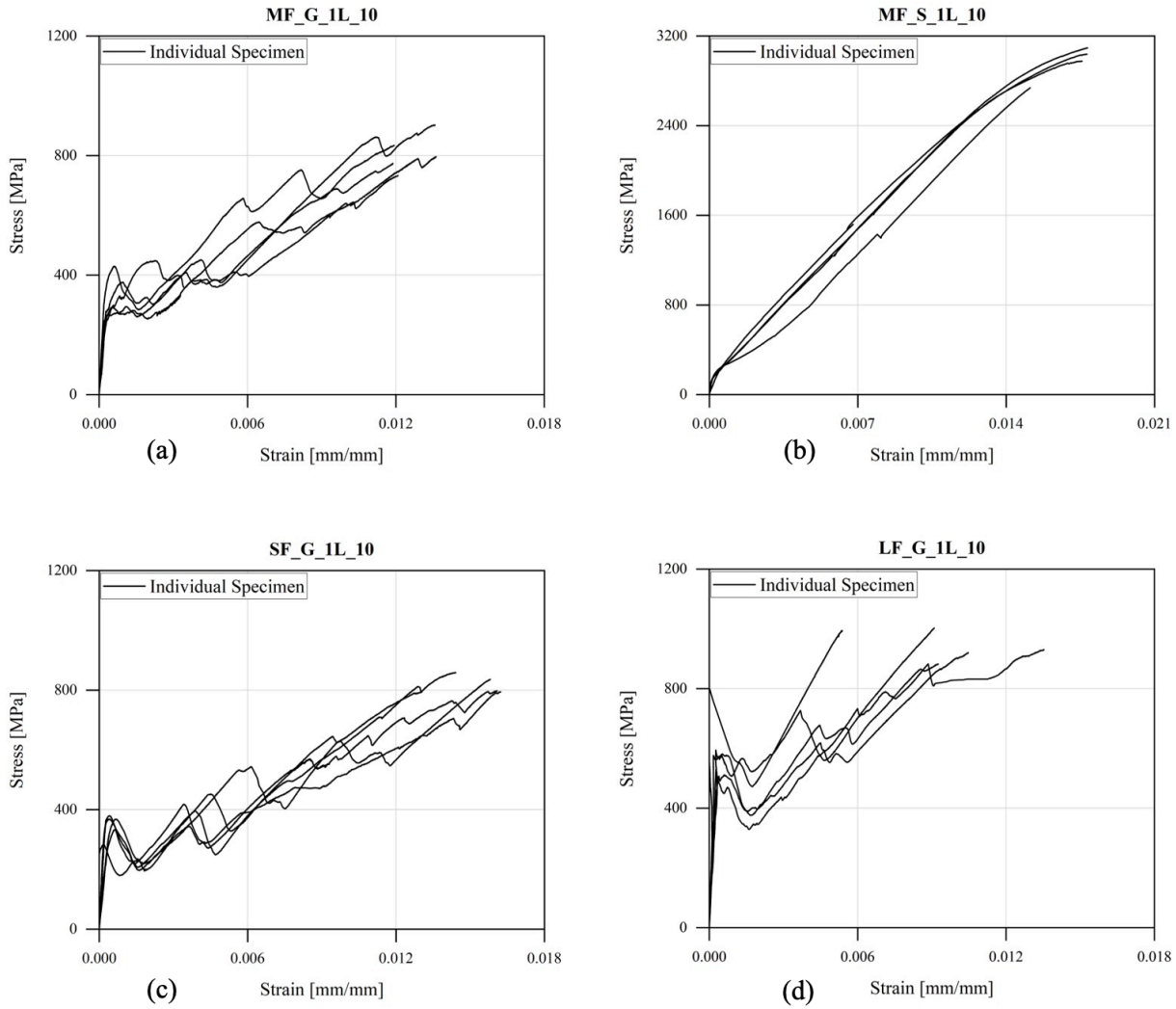

Figure 22 Stress-Strain curve for single-layer specimens for: a) MF_G_1L_10; b) MF_S_1L_10; c) SF_G_1L_10; d) LF_G_1L_10.

Elastic modulus comparisons in Stage III, shown in Table 4, reveal that this value was approximately 59%, 65%, and 86% of the bare textile's modulus for the SF, MF, and LF setups, respectively. These reduced values are attributed to interfacial degradation or insufficient impregnation of filaments within the textile roving [87], which compromises load transfer efficiency between mortar and reinforcement. In terms of peak strength, glass-based TRM specimens in the SF and MF groups reached values close to 800 MPa, corresponding to approximately 78% of the dry fiber strength. The LF configuration, however, exhibited an average strength of approximately 1008 MPa, nearly 98% of the dry fiber's capacity. Despite this improved performance, visual observations during failure (Figure 22d) indicated that some LF specimens experienced initial cracking at the boundary between the resin-impregnated textile and the mortar. This phenomenon was likely caused by the stiffness mismatch, producing localized stress concentrations. Consequently, failure in approximately half of the LF specimens initiated in this region, while the remaining specimens failed due to fiber rupture at central cracking locations.

Cracking patterns observed at failure are shown in Figure 23. On average, two major cracks formed in each LF specimen, with a mean spacing of approximately 105 mm. The first crack typically occurred 120 mm from either end of the specimen, indicating good load distribution. Although the LF setup offered the highest load capacity, some limitations were observed, including cracking outside the mortar region and premature failures near the mortar initiation zone. Unlike the SF and MF configurations, where cracks

were centrally distributed and spaced consistently, LF specimens occasionally developed a dominant crack outside the centerline.

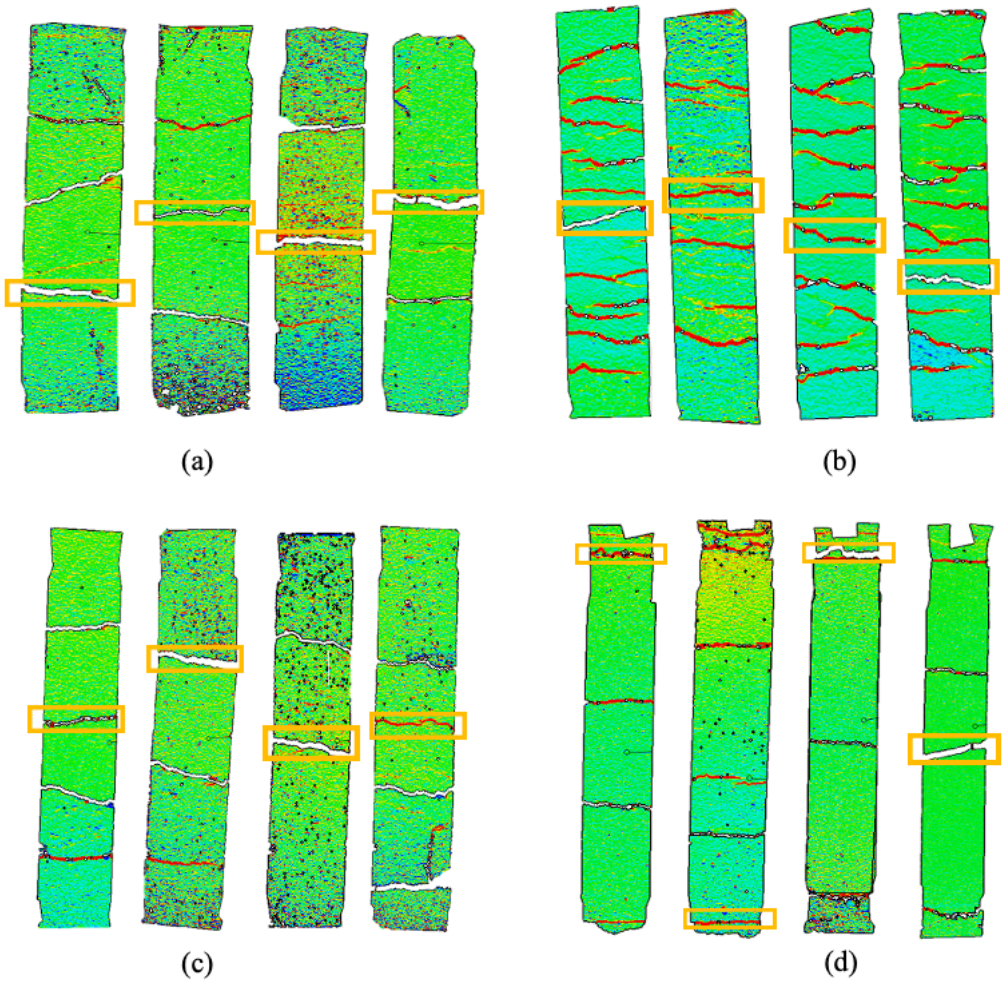

Figure 23 Crack distribution (failure location is indicated by a box) for single-layer specimens for representative samples of: a) MF_G_1L_10, b) MF_S_1L_10, c) SF_G_1L_10, and d) LF_G_1L_10.

In SF and MF specimens reinforced with glass textiles, the average number of cracks was three, with crack spacing of approximately 77 mm and 79 mm, respectively. The first visible crack in both configurations formed at a distance of approximately 100 mm from the specimen edge, suggesting uniform stress transfer and effective interaction between the mortar and textile. In contrast, steel-reinforced MF specimens exhibited significantly higher cracking density, averaging eight cracks with a spacing of 32 mm. The first cracks in this group appeared approximately 45 mm from the specimen extremities. This enhanced cracking behavior is attributed to the finer mesh size, higher ductility, and greater tensile strength of the steel reinforcement. Failure in steel-based TRM specimens was characterized by explosive rupture of fibers, consistently resulting in complete specimen collapse. This abrupt failure mechanism underscores the higher energy absorption capacity and sharper failure transition associated with steel reinforcement.

4.3.4 TRM tensile behavior (TR setup)

The tensile response of TRM specimens tested under the TR configuration—where the tensile load is transferred through the mortar—showed clear differences in behavior depending on the reinforcement

type. For glass-based TRM specimens, a dominant crack consistently developed near the gripping region (Figure 24a), attributed to stress concentration induced by the direct force transfer at the matrix level. The failure mode for these specimens was governed by fiber rupture, occurring either near or slightly inside the grip region. The three typical tensile response stages—elastic, crack development, and crack stabilization—were identifiable in the corresponding stress–strain curves (Figure 24a). In contrast, steel-based TRM specimens exhibited a markedly different failure mechanism. As shown in Figure 24b and Figure 24c, the failure was characterized by multiple fine cracks followed by the delamination of the steel cords from the mortar within the gripping zone. Importantly, fiber rupture was not observed in any of the steel-reinforced specimens. The observed delamination and grip-zone failure suggest that the 100 mm gripping length used in this configuration was insufficient for the required bond transfer, especially for steel fabrics. This observation aligns with previous findings highlighting the longer bond length required for high-strength, low-deformability reinforcements such as steel [273].

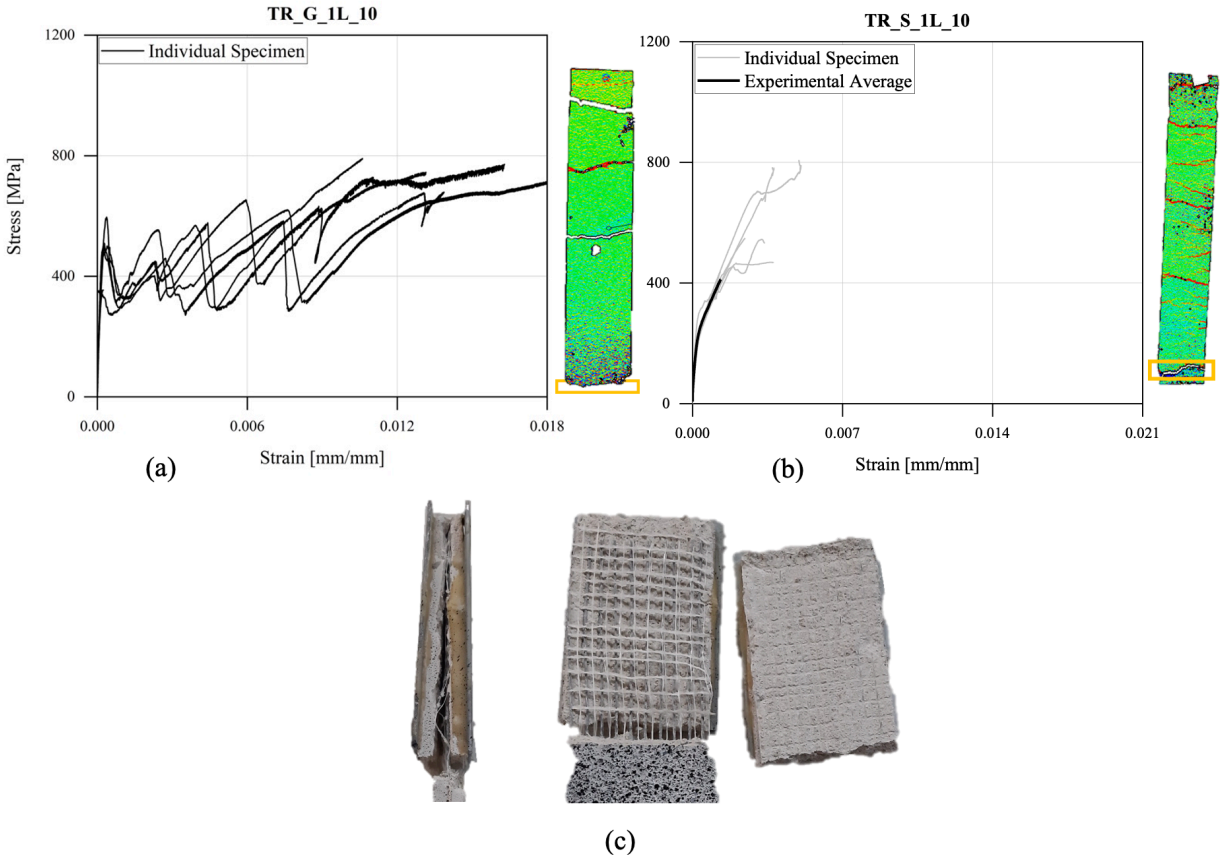

Figure 24 Failure of coupons with TR setup: a) stress-strain behavior of TR_G_1L_10 with final crack distribution; b) stress-strain behavior of TR_S_1L_10 with final crack distribution, accompanied by failure location in the box; c) delamination of the interface of the steel fabric and matrix inside the gripping area.

The stress–strain response of steel-based TRM under the TR configuration featured a linear elastic region followed by a nonlinear progression, reflecting the progressive debonding at the textile–matrix interface rather than fiber failure. The absence of a distinct crack development stage further confirms the premature delamination failure mode. These findings also emphasize the critical importance of maintaining consistent and adequate clamping force. As previously reported in the literature [274], any variation in the grip pressure during loading can significantly compromise result consistency and reduce the reliability of recorded mechanical performance.

The tensile strength values for TR specimens are provided in Table 4. On average, the glass-based TRM specimens reached a tensile strength of 745 MPa, approximately 73% of the strength of the corresponding dry textile. For steel-based specimens, the average tensile strength was 598 MPa, equivalent to only 20% of the dry mesh capacity. This limited strength utilization reflects the early onset of interfacial debonding and confirms that the gripping configuration was suboptimal for capturing the full potential of the steel TRM system. Despite these limitations, the failure mode—fiber rupture near the grip zone for glass TRM and delamination without rupture for steel TRM—is consistent with earlier research that accepts localized failure near the gripping region as a valid outcome, albeit with caution [75,91,111].

4.3.5 Effect of number of layers

The influence of incorporating a second textile layer into TRM composites was investigated for both glass- and steel-based systems by employing two different layer arrangements. In multilayer TRM configurations, particularly those constructed with dry mesh textiles, one of the primary concerns is the non-uniform penetration of mortar across the yarn cross-section. This issue becomes more pronounced in the absence of interlayer spacing, as inadequate mortar flow between layers can compromise both the impregnation and the interfacial bond behavior. To assess this effect, two configurations were studied: one in which two textile plies were embedded with zero spacing between them while maintaining a total mortar thickness of 10 mm (denoted 2L_10), and another in which a 5 mm mortar layer separated the two textiles, resulting in an overall thickness of 15 mm (2L_15). In the 2L_10 configuration, the tight spacing between textile layers can potentially hinder full mortar penetration, leading to localized weak zones. Conversely, the 2L_15 arrangement allows a thin intermediary mortar layer between plies, which facilitates more uniform impregnation and interaction, thus approximating the mechanical performance of a well-impregnated single-layer specimen. Figure 25 presents a scanning electron microscopy (SEM) image of a specimen cast with the 2L_10 configuration. While a slight reduction in mortar penetration was observed at the immediate contact interface between the two textile layers, no significant differences in impregnation quality were found across the remainder of the fabric cross-section. This suggests that although layering influences mortar flow, the overall distribution of the matrix around the yarns remained sufficiently homogeneous.

The subtle differences between the 2L_10 and 2L_15 configurations were primarily attributed to factors related to casting workmanship and textile curvature, which can be affected by packaging and pre-application handling. Minor irregularities in layer spacing were more apparent in the 2L_10 configuration, leading to local variations in interfacial distance and potentially altering stress distribution. Additionally, the absence of hydrophobic treatments in the textile surface facilitated the infiltration of mortar slurry into the fibers, which likely promoted better bonding but also contributed to a more active role of the textile in the hydration process of the surrounding matrix. Overall, while the inclusion of an interlayer mortar thickness improved consistency in fabric impregnation, the 2L_10 configuration still demonstrated sufficient penetration in most regions, with only localized areas of reduced interface quality.

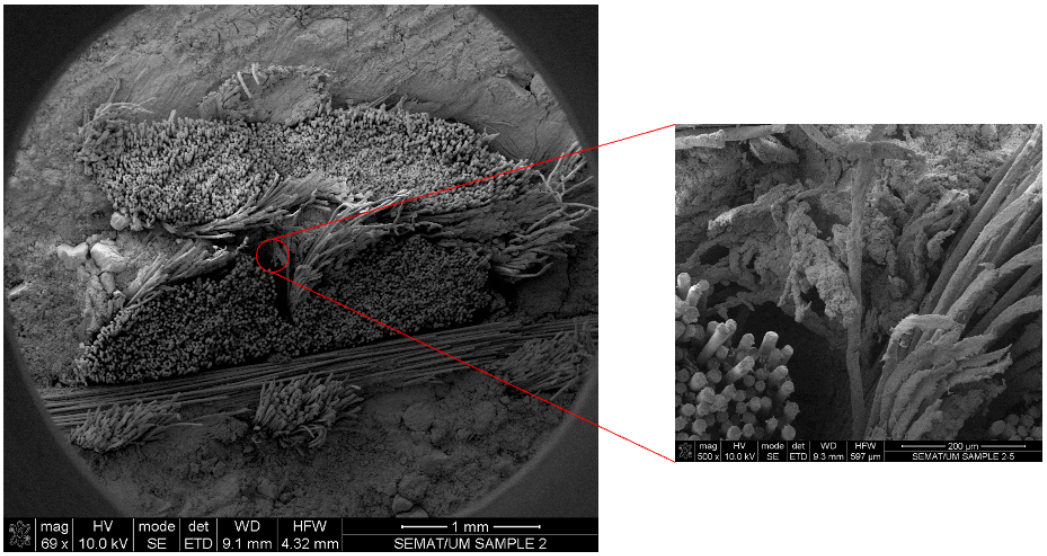

Figure 25 SEM microscopy of MF_G_2L_10 before testing (unpolished surface).

4.3.5.1 Layer's effect on MF setup

The effect of increasing the reinforcement ratio through the addition of a second textile layer was assessed for both glass- and steel-based TRM specimens using the MF gripping configuration. The stress–strain responses and cracking patterns of the multilayer specimens are illustrated in Figure 26 and Figure 27, respectively. Compared to single-layer configurations, a noticeable reduction in data scatter was observed in the multilayer specimens. This trend aligns with expectations, as increasing the textile ratio typically induces a more linear, tendon-like behavior, analogous to that observed in reinforced concrete elements. Among the tested configurations, the 2L_15 specimens—those with a middle mortar layer separating the textiles—exhibited improved bonding conditions and more uniform stress transfer. The presence of the intermediary mortar layer in this arrangement enhanced the composite action by facilitating better impregnation around the fabric edges and between the layers. In contrast, the 2L_10 configuration, with no separation between layers, was more sensitive to interfacial inconsistencies, resulting in reduced bond efficiency and increased variability in mechanical response. These differences were attributed to the diminished capacity for stress redistribution in the absence of adequate mortar separation.

Table 4 summarizes the ultimate tensile strength of each configuration. The results indicate a slight increase in capacity for all double-layer specimens relative to their single-layer counterparts, with the most significant improvement observed in the 2L_15 group. For glass-based TRMs, the tensile strength reached 86% and 83% of the dry textile's ultimate strength for MF_G_2L_10 and MF_G_2L_15, respectively. For the steel-based systems, the values were 104% and 103% for MF_S_2L_10 and MF_S_2L_15, suggesting near-complete utilization of the reinforcement capacity. These findings confirm that the MF setup provided adequate stress distribution and confinement, allowing both fabric types to perform near their maximum tensile potential. The results further suggest that increasing the reinforcement ratio in the MF configuration did not substantially alter the shape of the stress–strain curve, nor the mechanical efficiency of the system.

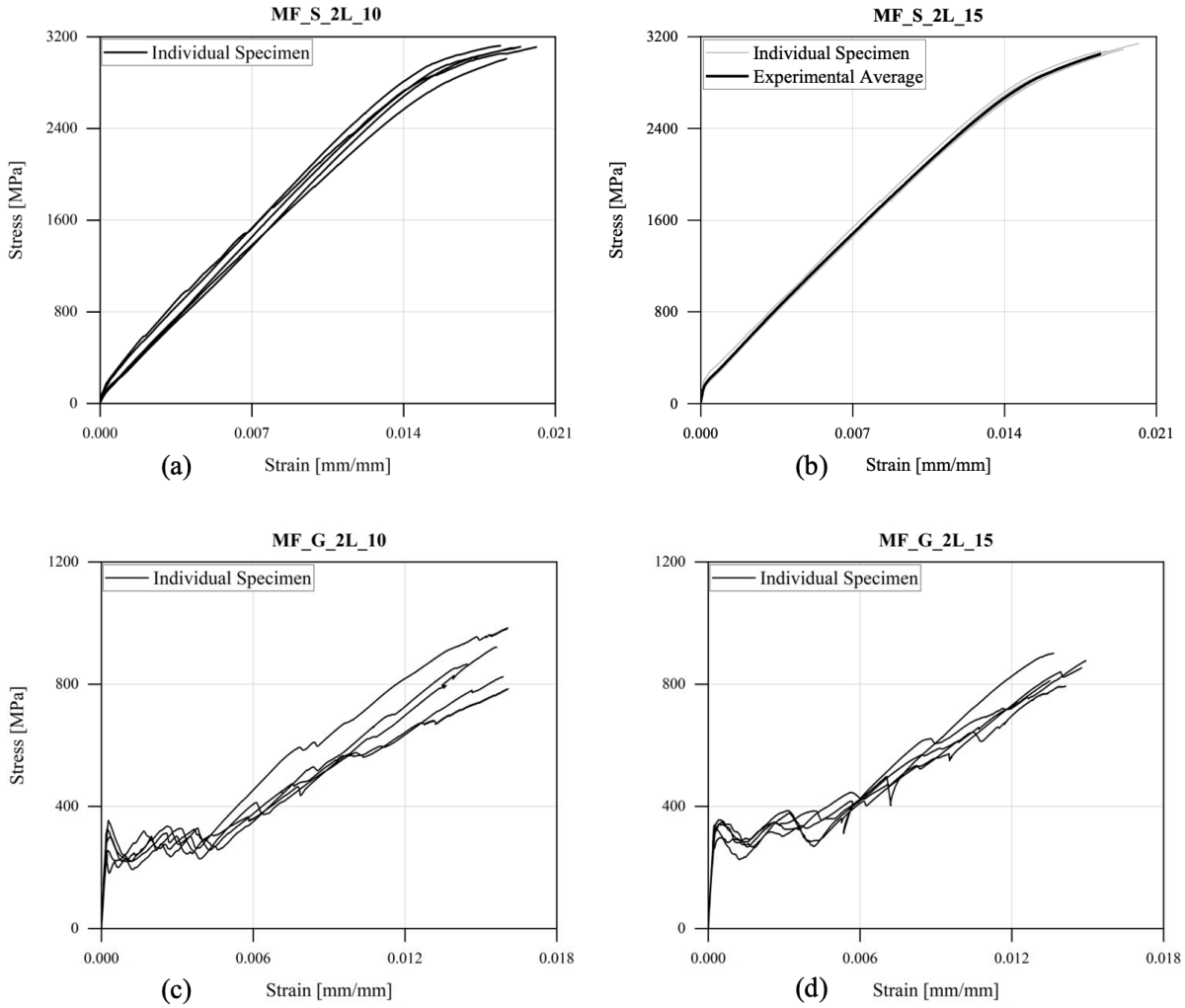

Figure 26 Stress-Strain curves for multi-layer specimens with MF setup, for: a) MF_S_2L_10; b) MF_S_2L_15; c) MF_G_2L_10; d) MF_G_2L_15.

Cracking patterns at failure, shown in Figure 27, support these observations. For steel-based specimens, the number of cracks changed from an average of eight in single-layer specimens to six in 2L_10 and fifteen in 2L_15 specimens. The increased crack density in the latter indicates improved stress redistribution due to the additional mortar layer. Moreover, cracks in the 2L_15 specimens appeared more uniformly distributed, often accompanied by a mix of wide and fine cracks. Failure of these specimens was typically explosive and more intense than observed in single-layer configurations, reflecting the higher stored energy and composite stiffness. In glass-based specimens, the average number of cracks increased modestly from three in single-layer specimens to four in the double-layer configurations. In MF_G_2L_15 specimens, a dominant crack consistently formed near the center of the specimen, while MF_G_2L_10 specimens exhibited a more dispersed cracking pattern within the middle third of the gauge length, similar to that seen in MF_G_1L specimens (refer to Figure 23). The central cracking in MF_G_2L_15 is likely a result of the middle mortar layer resisting differential sliding between the two textile layers, thereby concentrating tensile stresses in the center region. This localized interaction between the reinforcement and the middle matrix layer contributed to the formation of the major crack at that location

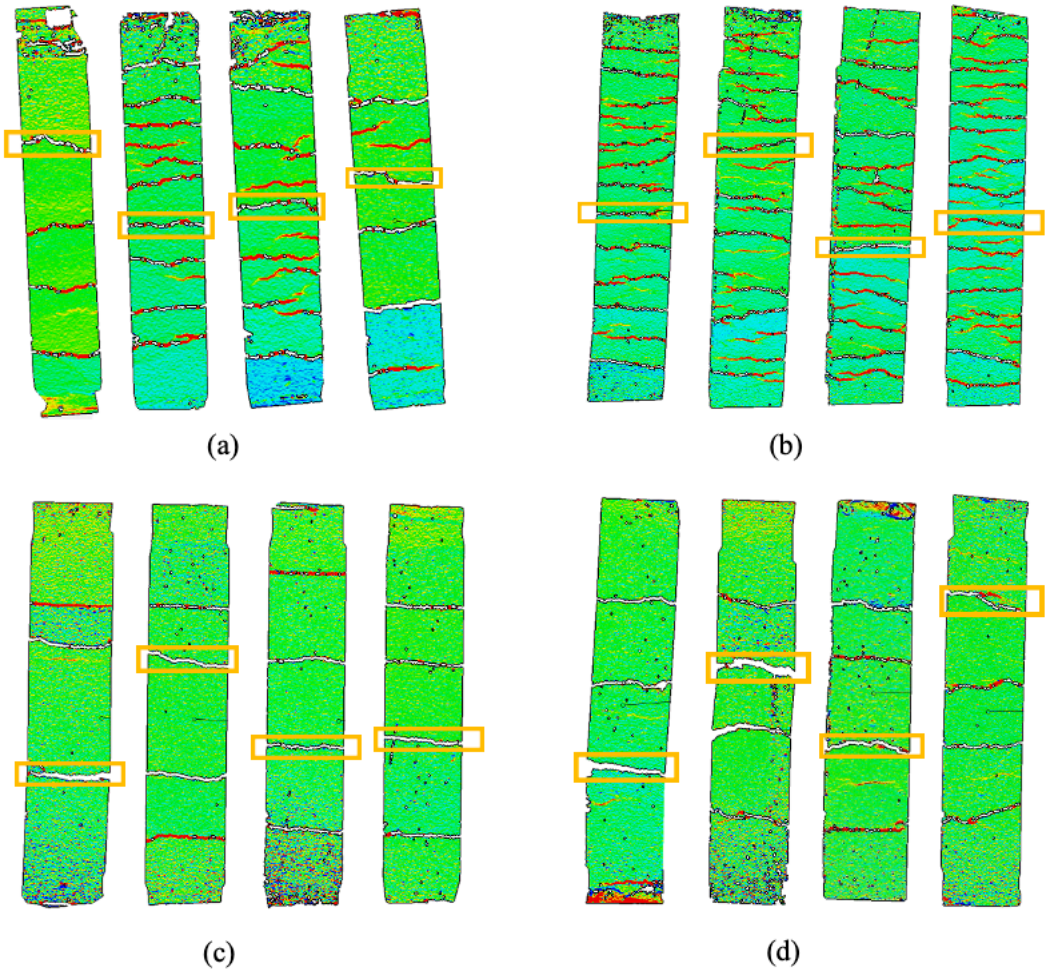

Figure 27 Crack distribution (failure location is indicated by a box) for multi-layer specimens with MF setup using DIC analysis, for representative samples of: a) MF_S_2L_10; b) MF_S_2L_15; c) MF_G_2L_10; d) MF_G_2L_15.

4.3.5.2 Layer's effect on TR setup

The influence of the number of textile layers on the tensile performance of TRM composites was also evaluated using the TR setup for both glass yarns and steel cords. Stress–strain curves are shown in Figure 28, while failure patterns and cracking behavior are presented in Figure 29. When comparing TR_G_2L_10 and TR_G_2L_15 specimens, it was observed that the 2L_15 configuration exhibited lower data scatter, suggesting a more consistent performance, likely due to improved matrix continuity and reduced interfacial frictional effects between layers. Despite this, a significant reduction in tensile strength was recorded for double-layer glass TRM specimens in comparison to their single-layer counterparts. On average, the ultimate tensile strength decreased by approximately 40%, highlighting the adverse impact of increased reinforcement ratio on the TR setup. This reduction was attributed to the occurrence of major cracks near the gripping region, often leading to detachment and sliding of fibers within the grip zone. These premature failure modes limited the load transfer capacity of the system and prevented full engagement of the textile reinforcement. Conversely, the steel-based TRM specimens demonstrated relatively stable tensile behavior, with no substantial reduction in strength observed across single- and double-layer configurations. The consistent response of the steel-based TRMs was associated with unchanged failure mechanisms and stable fiber–matrix interaction, even with an increased textile ratio.

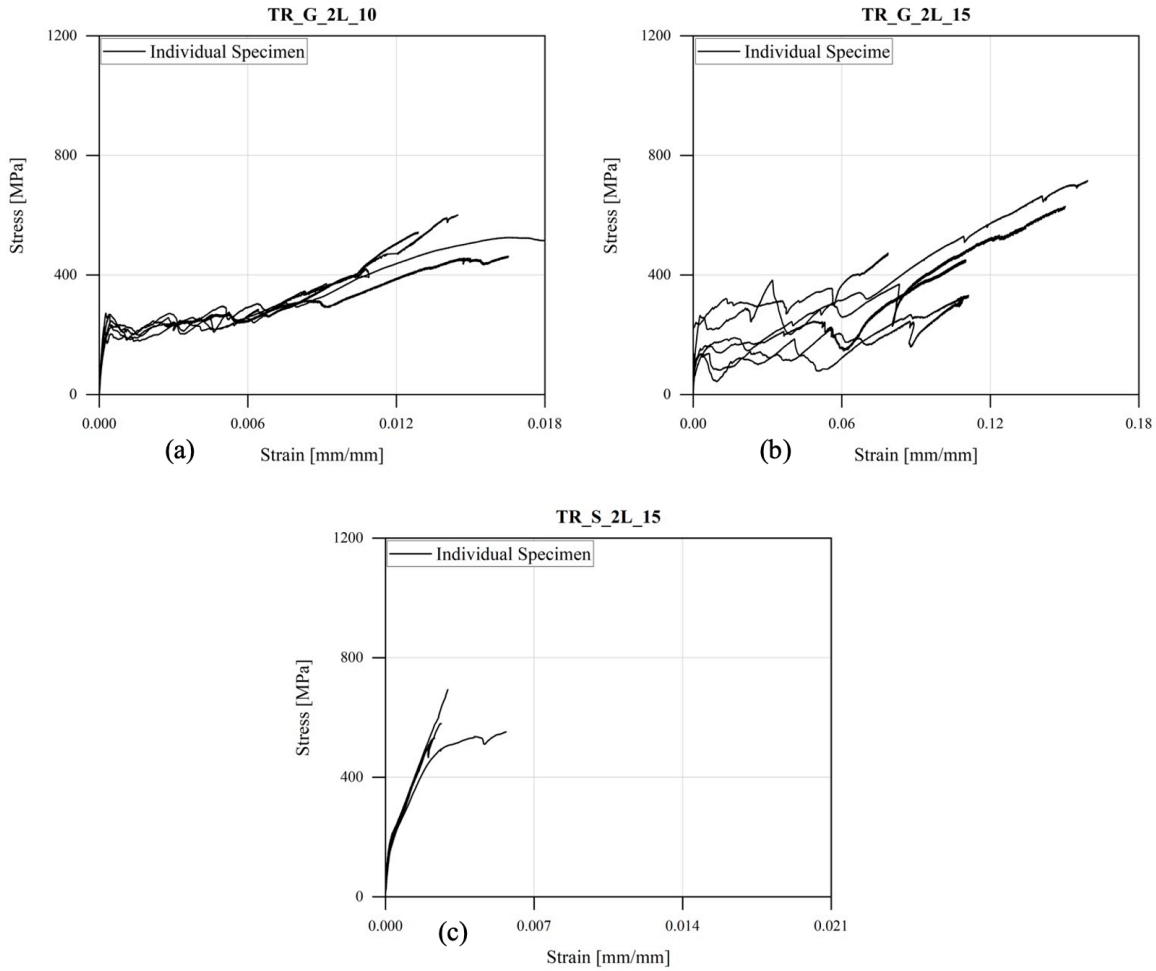

Figure 28 Stress-strain curves for multi-layer specimens with TR setup for: a) TR_G_2L_10; b) TR_G_2L_15; c) TR_S_2L_15.

In glass TRM specimens, a shift in cracking behavior was evident when transitioning from single- to double-layer configurations. The cracks, which were previously centered in the midspan of single-layer specimens (as in Figure 23a), tended to form closer to the gripping regions in double-layer specimens. This phenomenon was particularly pronounced in the TR_G_2L_10 group, where cracks typically developed within 15 mm of the clamping ends, often leading to fiber slippage and matrix detachment. The mechanical response was thus governed by localized failures that prevented uniform crack development and compromised the stress distribution along the specimen length.

The TR_G_2L_10 specimens achieved only 46% of the ultimate capacity of the corresponding bare textile, further demonstrating the setup's inability to ensure full load transfer. An average of eight small cracks with a mean spacing of 59 mm was recorded, though these cracks remained relatively narrow. The textile, rather than promoting crack widening as expected, acted primarily as a bridging element with limited engagement in load bearing. This ineffective stress redistribution resulted in an increase in the number of small cracks without significant crack opening, consistent with a non-uniform load path induced by premature interfacial failures. In the case of TR_G_2L_15 specimens, the reduced volumetric reinforcement ratio relative to TR_G_2L_10 yielded a more favorable cracking pattern and stress distribution. Cracks initiated at both specimen ends, yet at slightly greater distances from the grips (average of 25 mm). An average of six cracks with a spacing of 74 mm was observed. Despite this improvement, the ultimate strength remained low, reaching only 44% of the bare textile's capacity. Compared to the single-layer TR_G_1L configuration, which achieved 67% of the dry textile capacity, the response of the double-layer specimens in the TR setup was clearly inferior. These findings highlight a

pronounced sensitivity of the TR setup to reinforcement ratio and gripping conditions, particularly for composites made with glass fabrics.

Steel-based TRM specimens, such as TR_S_2L_15, exhibited cracking near the grip zones but without significant deterioration in ultimate strength. Detachment and sliding of the steel cords within the matrix were observed; however, the inherent strength and continuity of the steel cords mitigated further reductions in mechanical performance. As the mortar–fiber bond deteriorated, stress transfer was reduced, limiting the formation of localized macrocracks and leading instead to a dense network of microcracks. The inability to transform these microcracks into dominant failure cracks illustrates a compromised bond mechanism in this setup, although the effect on tensile capacity remained less critical than for the glass-based systems. Overall, these results confirm that the TR setup is highly sensitive to both textile configuration and reinforcement ratio. The presence of a second textile layer amplifies the likelihood of premature failure near the grip and interferes with uniform crack propagation, particularly in glass TRMs. The inability to fully develop the expected three-stage tensile response in these configurations further underscores the limitations of the TR setup when applied to multi-layer systems.

4.3.6 Comparison of setups

A comparative evaluation of the different tensile test configurations applied in this study, TR, SF, MF, and LF setups—was conducted with respect to multiple performance indicators, including ultimate tensile capacity, multi-stage stress–strain behavior, cracking pattern, failure mode, and the location of cracks relative to the gripping area. The comparison included both single-layer and multi-layer TRM specimens to assess the reliability and reproducibility of each setup across varying reinforcement ratios. The TR setup, which transfers tensile loads through the mortar, exhibited notable limitations, particularly as the reinforcement ratio increased. Figure 30 illustrates that in TR specimens, cracks increasingly formed near the gripping area, where premature failure was frequently observed. This behavior is attributed to insufficient mortar strength in the gripping zone, resulting in detachment of the textile from the matrix and, in some cases, crushing of the mortar under clamping pressure. Such behavior compromised the ability of the setup to reliably capture the tensile response of the composite. While increasing the gripping length could theoretically mitigate this stress concentration, doing so would require impractically long specimens for typical laboratory environments.

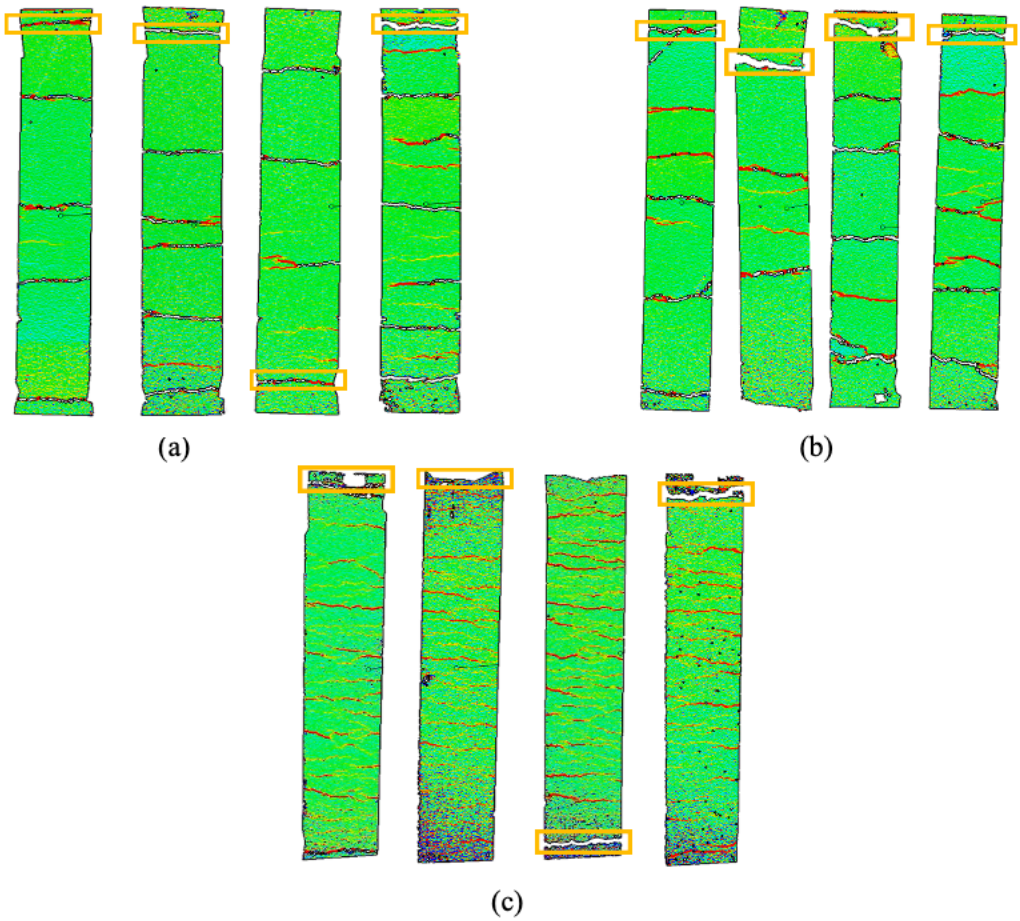

Figure 29 final crack distribution (failure location marked with a box) for multi-layer specimens with TR setup using DIC analysis, for representative samples of a) TR_G_2L_10; b) TR_G_2L_15; c) TR_S_2L_15.

Moreover, the performance of the TR setup was highly sensitive to the magnitude and consistency of the clamping force. Without standardized control over this parameter—preferably through calibrated hydraulic gripping systems—the reproducibility of results becomes uncertain. This limitation has not been adequately addressed in previous studies [75,275,276], yet this investigation reinforces the need for such control when using the TR configuration. The average stress–strain curves plotted in Figure 30 for single- and multi-layer TRMs highlight a clear decline in strength for TR specimens as the reinforcement ratio increases. The premature localization of failure near the gripping region further emphasizes the challenges associated with this setup. Accordingly, the TR configuration appears less suitable for reliably assessing the tensile performance of TRMs, especially in multi-layer applications.

In contrast, the SF, MF, and LF setups where the tensile load is applied directly to the textile demonstrated more stable and reinforcement-ratio-independent performance. Among these, the MF setup emerged as the most consistent and reliable. As shown in Figure 31, the MF setup provided a balanced representation of the composite response, capturing all stages of behavior while maintaining similarity to the tensile response of the bare textile, particularly in the third stage. Furthermore, the MF setup maintained high strength values regardless of reinforcement ratio, especially in steel-based composites, where the double-layer configuration approached the ultimate capacity of the dry textile (Figure 31).

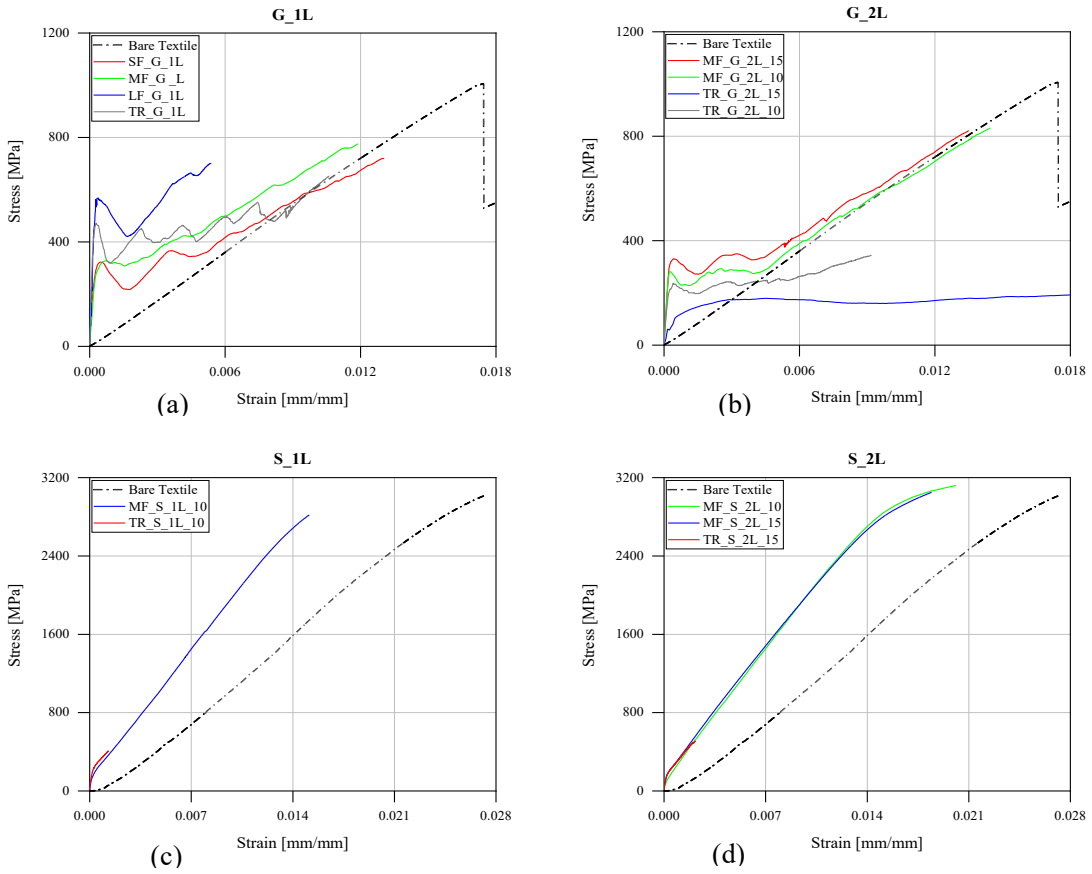

Figure 30 Average stress-strain curves for each group vs. bare textiles for: a) single-layer glass TRM; b) multi-layer glass TRM; c) single-layer steel TRM; d) multilayer steel TRM.

The SF setup also offered reasonable performance but exhibited two primary limitations. First, the bare textile in the gripping region is vulnerable to damage during transportation and testing, which can affect repeatability. Second, due to limited mortar continuity near the grips, the setup may under-represent composite interaction and confinement, particularly in brittle systems like glass-based TRMs. These concerns are reflected in the crack formation and stress–strain behavior observed in Figure 30. The LF setup, while achieving high strength values, revealed shortcomings in composite interaction. The long epoxy-impregnated textile segment resulted in a more tendon-like response, reducing the participation of the mortar and the characteristic composite behavior. Stress concentration issues near the epoxy–mortar transition was also observed, limiting the uniformity of stress distribution. Figure 31 further supports these conclusions by illustrating the comparative strength of each setup relative to the tensile capacity of the dry textile. For steel-based TRMs, the MF setup consistently achieved the highest performance, while glass-based specimens exhibited some reduction due to damage mechanisms such as telescopic fiber movement and frictional degradation. Nevertheless, among all tested methods, the MF setup best captured the expected tensile behavior, offered resilience across reinforcement ratios, and maintained structural fidelity throughout all stages of the tensile response.

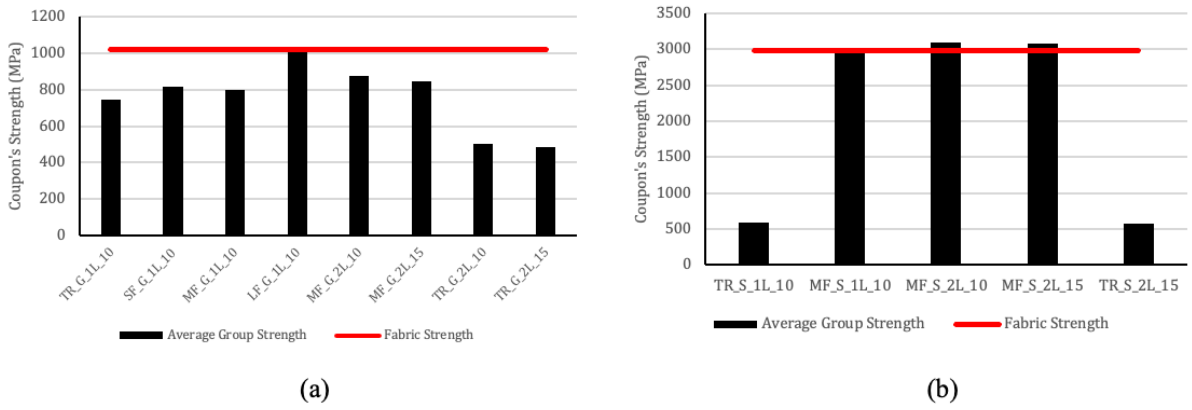

Figure 31 Comparison between the strength of each test setup and the textile's strength as the upper threshold for: a) glass-based TRM; b) steel-based TRM.

4.4 Conclusion

The tensile behavior of thirteen different groups of TRM composites containing glass and high-strength steel fabrics embedded into a lime-based mortar was studied in this paper. The tensile behavior of TRM coupons was performed using two main gripping methods, i.e., gripping mortar and gripping textiles. The effect of the addition of textile layers, their arrangement, and the mortar thickness in different setups were critically assessed. Based on results obtained from 78 tensile coupons and material characterization tests on each constituent, the following conclusions can be drawn:

- Based on the findings and comparing criteria such as load-carrying capacity, crack location, and failure pattern, it is advisable to apply the load directly onto the textile, rather than on the mortar. High setup dependency on the reinforcement ratio, presence of cracks near the grips, stress concentration at the edge of clamping plates, and delamination of mortar and textile inside clamps are the main drawbacks of clamping the mortar.
- While applying the load to the textile in a tensile TRM test, it is recommended to clamp the textile directly by impregnating the bare textile section with resin. Based on the results, considering the hardness of textiles and the penetration depth, it is possible to have a capacity near to the strength of bare fabrics. Results showed that clamping textiles directly without impregnation of the bare textile increases unwanted damage and scatter of results.
- Application of resin for impregnating the bare textile portion is highly recommended due to its significant benefits. Firstly, it effectively minimizes unwanted damage to the fabric during testing, particularly those resulting from the weight of the samples. By impregnating the textile with resin, the fabric's integrity is preserved, ensuring more accurate and reliable test results. Secondly, the use of resin contributes to a more uniform stress distribution across the samples, enhancing the load transfer from the textile to the composite system. This results in an improved mechanical performance and increased overall structural integrity.
- The behavior of multilayer TRM by assuming a suitable gripping system is independent of the reinforcement ratio. Results showed that the application of a small layer of mortar between the plies produces a favorable effect on decreasing the scatter of results.

- In theory, a trilinear stress-strain diagram is expected for each TRM composite tensile test type. Due to several reasons, like initial cracks and their development, stress-strain diagrams could be masked and made undetectable. The inability to identify these stages in previous research[75] may be due to the adoption of an incorrect detection method. The authors propose to use the DIC method for better precision in detecting each stage due to its ability to detect crack initiation and propagation stages.

Despite the limitations inherent in any experimental study, the findings reported here contribute valuable insight into the characterization of TRM under short-term loading conditions. However, it must be acknowledged that TRM composites are often used in structural strengthening scenarios where exposure to environmental degradation, long-term loading, and chemical attack are inevitable. These conditions can significantly alter the mechanical and interfacial behavior of TRM systems over time. Therefore, a short-term assessment, while necessary, is not sufficient for fully validating the use of TRM in structural applications. The next chapter will address this critical gap by focusing on the long-term performance and durability of TRM systems, particularly under environmental exposures and extended time-dependent loading. The durability-driven behavior, aging mechanisms, and resistance to degradation will be explored to complement the findings reported in this chapter and to provide a more complete basis for the practical implementation of TRM in the field.

This page is left blank on purpose

Chapter 5
Long-Term performance of TRM under creep

5.1 Introduction

Chapter 4 established the foundational mechanical properties of TRM systems by evaluating the response of both constituent materials and the composite under direct loading conditions. Parameters such as compressive and flexural strength of the mortar, as well as the tensile capacity of the textile reinforcement, were systematically characterized to provide a basis for subsequent investigations involving structural performance. However, the long-term behavior of TRM composites under sustained loading has received limited attention in the literature, despite its significance for applications involving permanent mechanical demand. In particular, creep deformation, the gradual development of strain under constant stress, poses critical implications for bond performance and overall structural integrity in TRM-strengthened elements. The time-dependent nature of this phenomenon may compromise the effectiveness of reinforcement systems, especially at the matrix–textile interface where load transfer is concentrated.

To address this gap, the present chapter investigates the creep response of TRM composites using an experimental campaign based on single-lap shear testing. The study integrates material-level and composite-level evaluations to assess the influence of sustained shear loading on long-term deformation. A commercially available lime-based mortar and glass textile reinforcement were employed throughout the test program. The mechanical behavior of the matrix was monitored through compressive and flexural strength testing at various stages of curing, while the tensile response of the textile was evaluated under both instantaneous and prolonged loading conditions. Present chapter explores the long-term creep behavior of TRM composed of glass fibers using single-lap shear tests across diverse loading conditions and durations. This section comprehensively details the materials used, the specimen preparation processes, and the testing methodologies implemented. Additionally, Figure 32 presents a schematic overview of the experimental protocol to facilitate clearer understanding and comprehension.

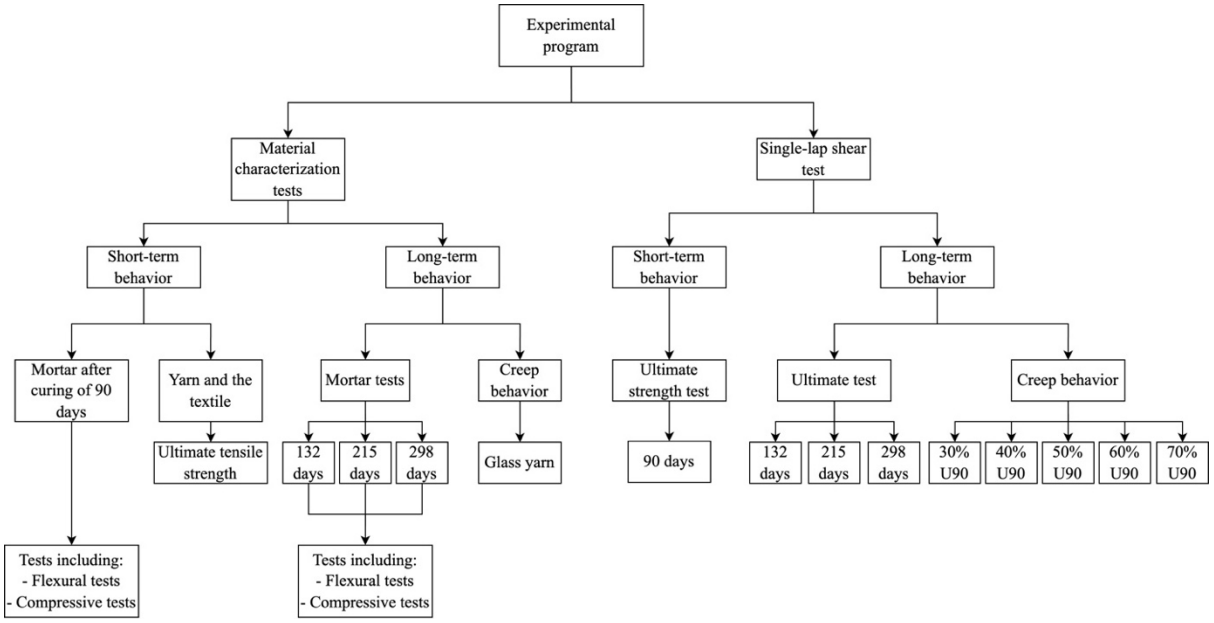

Figure 32 Overview of the experimental program presented in this chapter.

5.2 Materials and characterization procedures

The TRM system employed in this investigation consisted of a commercially available hydraulic lime-based mortar and an alkali-resistant glass textile, both previously described and characterized in Chapter 3. Material characterization tests, including compressive, flexural, and tensile evaluations of the mortar and textile constituents, were also conducted as reported in Chapter 3 and served to support the interpretation of the long-term results. As shown in Figure 32, the experimental program was structured into two main phases: (i) determination of ultimate strength and material properties at a reference curing age, and (ii) evaluation of long-term creep performance under sustained loading. Single-lap shear specimens were prepared using the lime-based mortar and glass textile described in Chapter 3, and were cured under controlled laboratory conditions of 20 ± 5 °C temperature and 65 ± 10% relative humidity. The reference curing period was fixed at 90 days, based on prior findings indicating the stabilization of mechanical properties beyond this duration. The average shear strength obtained at this age (U90) was adopted as the baseline for all subsequent creep loading levels. To evaluate the evolution of material and composite behavior over time, supplementary tests were conducted at extended curing durations of 132, 215, and 298 days. These tests included flexural and compressive strength assessments of the mortar, as well as single-lap shear bond tests on TRM specimens at the same ages. This approach enabled the assessment of strength gain due to curing and facilitated a more accurate interpretation of creep test results by accounting for the influence of aging on mechanical performance.

The average ultimate load obtained from the single-lap shear tests at the selected reference age was denoted as U90 and used to define the sustained loading levels for the creep campaign. Specifically, long-term tests were carried out at five different load levels: 30%, 40%, 50%, 60%, and 70% of U90. Due to the limited capacity of the creep test setup, which allowed for five specimens to be loaded simultaneously, the campaign was carried out in sequential batches. A given specimen remained under load until either mechanical failure occurred or the maximum test duration of 250 days was reached. This time frame was selected as a practical limit based on laboratory constraints and resource availability. For specimens that survived the full duration, the residual load-bearing capacity was subsequently determined by increasing the applied load until failure. In addition to the composite-level testing, long-

term tensile tests were also performed on the glass yarn reinforcement at 80% of its ultimate tensile strength, in order to evaluate potential differences in creep susceptibility at the reinforcement level.

5.2.1 Bond Characterization tests

The single-lap shear specimens were prepared following established protocols provided in Chapter 3, featuring a standardized bond length of 100 mm, following the established procedures by past investigations [11,263,277] as depicted in Figure 33b. The curing procedures after casting were consistent with those used for material characterization tests. To ensure the integrity of the textile and prevent premature failure in the unbonded areas, a resin block covering the entire length of the textile was prepared a few days before casting the samples (also Figure 33b). Following the curing period, and shortly before testing, gripping plates were attached to both ends of the samples to ensure proper load transmission between the testing machine and the specimens. The single-lap shear specimens were constructed using grids comprising three longitudinal yarns of glass. Before testing, the top surface of the single-lap specimens, which was in contact with the steel substrate frame, was leveled using epoxy to ensure uniform stress distribution and minimize the risk of sample rotation. LVDTs were placed on both sides of an omega-shaped aluminum piece, which was adhered to the resin block and brick. For ultimate strength testing, single-lap specimens were subjected to displacement-controlled conditions at a rate of 0.005 mm/s using the same 50 kN hydraulic actuator employed for the compressive and tensile tests.

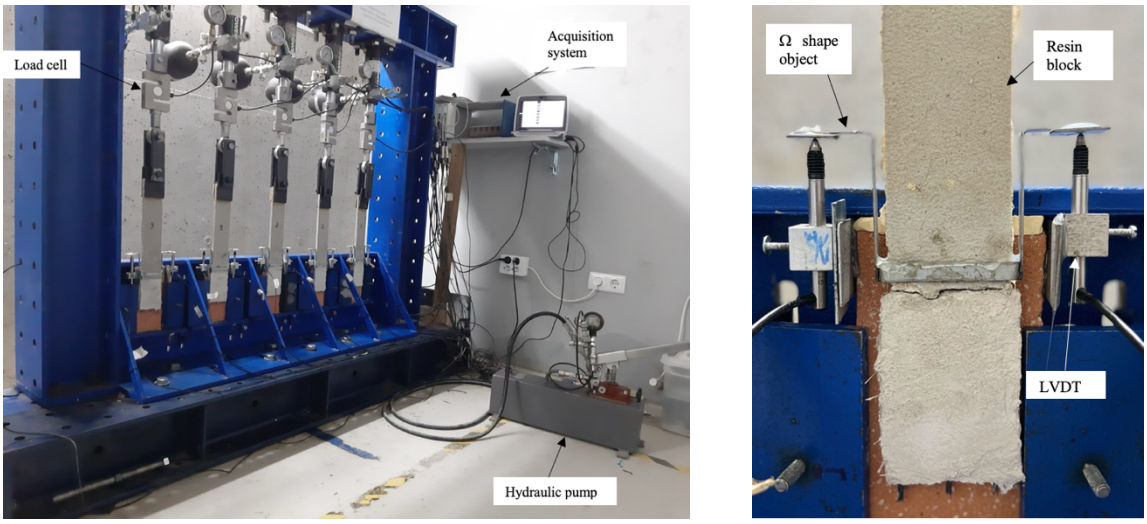

(a) (b)

Figure 33 Configuration of the creep test on single-lap shear specimens: (a) overall view of the test setup; (b) detailed view of the specimen setup.

5.2.2 Creep tests

Creep tests were conducted on both single yarn and single-lap shear test specimens. All tests were performed in a climatic chamber under controlled conditions, maintaining a constant temperature of 20°C and 80% relative humidity. As shown in Figure 33 and Figure 34, the test setups were placed next to each other within the same environment.

5.2.2.1 Yarn creep tests

To evaluate the behavior of the glass yarn under creep conditions, two yarn specimens were tested under a load corresponding to 80% of their tensile capacity, which was measured as 1.12 kN in a previous study [7]. This corresponds to a load of 0.896 kN. This load level was chosen because it is higher than all the load levels considered in the creep bond tests, ensuring that any potential creep displacement

could be fully captured. The initial assumption was that no significant creep displacement would occur at this load level, making it a suitable choice for understanding the yarn's behavior and its role within the composite system. A machine capable of mechanically applying tensile load to the yarn using arms and weights was employed. Elongation of the yarn was measured with an LVDT, as shown in the accompanying photo. A single yarn with a free length of 10 cm was used for these tests, and the gripping area was impregnated with resin inside a mold to maintain the yarn's integrity and prevent crushing at the gripping points. Throughout the testing period, the clamps were visually inspected to ensure no slipping occurred between the resin-impregnated yarn and the clamping system. The tests were conducted over a duration of 300 days, utilizing the same data acquisition system and frequency as the single-lap shear tests, allowing for a comprehensive assessment of the yarn's behavior under sustained loading conditions.

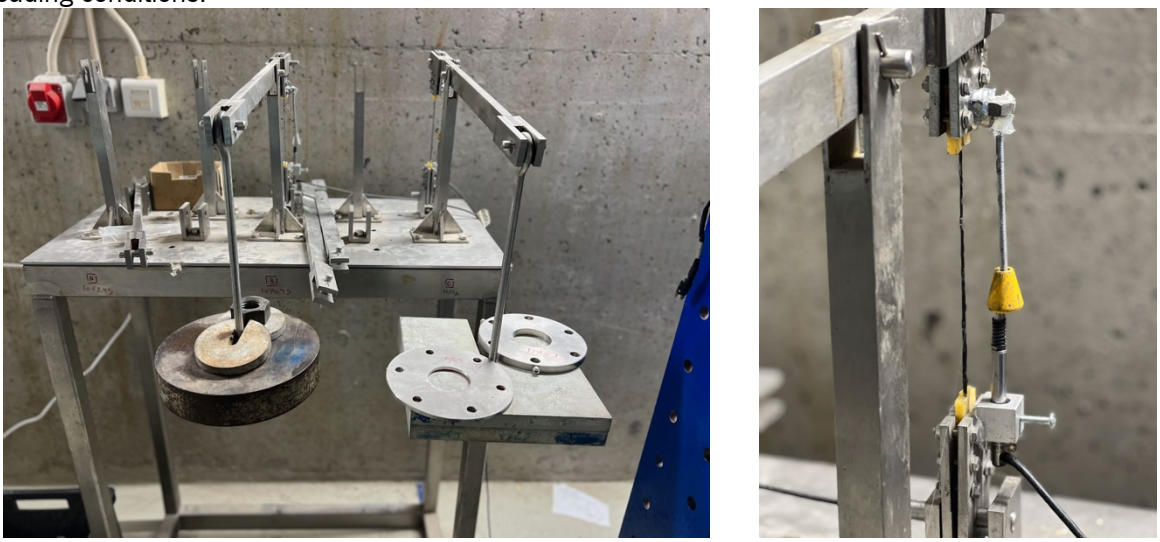

(a) (b)

Figure 34 Creep testing setup for glass yarn: (a) Overview of the setup with weights applied for tensile loading; (b) Close-up view of the glass yarn and gripping mechanism used in the creep test.

5.2.2.2 Bond creep tests

For the bond creep test, a specially designed frame was placed in the climatic room. The frame could accommodate five single-lap specimens, which were subjected to different loading conditions using a hydraulic pump, in a setup developed by previous researchers [277], also visible in the photo. Since the loading process was manual, care was taken to apply the load gradually to avoid dynamic loading effects. The loading phase for each specimen took approximately 10-15 minutes to reach the designated load level. Load corrections were performed as needed to account for any load reduction, with adjustments being made hourly on the first day and then daily based on the load level and the specimen's condition. Data acquisition was conducted at a frequency of 2 Hz, collecting three different data points for each specimen: two from the LVDTs and one from the load level, which was kept as constant as possible. After the completion of testing for each specimen, it was replaced with another specimen pre-cast and stored in the curing room, allowing for testing at different load levels.

Table 5 provides detailed information on each conducted test, including the measured parameters. The specimens are labeled using the notation SX.Y, where "X" represents the slot number where the specimen was mounted, and "Y" indicates the sequence of the sample in that slot. Three different age indicators are noted: A_0 (the curing age, which is the specimen's age at the start of the creep test), A_c (the creep age, representing the duration the specimen was subjected to creep loading), and A_t (the total age of the specimen at the time of test termination, which is the sum of the curing and creep ages). Additionally, two key parameters used in this table are S_{Peak} and $S_{Ultimate}$, which represent the days it took for

the specimen to reach the average peak slip, and the ultimate slip, respectively, as observed in the ultimate single-lap shear test after 90 days of curing. These parameters are important benchmarks, as they provide a reference for the displacement criteria at failure in the ultimate strength test, helping to assess the progression of creep displacement relative to these critical limits.

Table 5 Specification of the single-lap shear test's sample in creep loading

Force Level	Specimen	A_0 (Curing age)	A_c (Creep age)	Status	A_t (total age)	Maximum Load (kN)	S_{Peak} (day)	$S_{Ultimate}$ (day)
0.6 kN	S2.1	350	250	Terminated	600	2.67	Didn't meet	Didn't meet
	S3.1	350	250	Terminated	600	2.79	Didn't meet	Didn't meet
0.8 kN	S4.1	100	101	Failed	201	-	5	7
	S5.1	115	119	Failed	234	-	19	23
	S5.2	240	250	Terminated	490	2.57	15	17
	S.4.3	235	250	Terminated	485	2.51	36	42
1.0 kN	S1.0	90	250	Terminated	340	2.35	2	3
	S2.0	90	250	Terminated	340	2.63	12	14
	S1.1	350	236	Failed	586	-	4	7
1.2 kN	S3.0	90	250	Terminated	340	2.50	7	9
	S4.2	220	11	Failed	231	-	0	1
1.4 kN	S.5.0	90	11	Failed	101	-	0	1

Based on the initial results of the ultimate single-lap shear tests at 90 days, 2 kN was determined as the average load-bearing capacity of the specimens, referred to as U90. A total of 12 single-lap shear specimens were subjected to creep loading and are reported here. The creep testing campaign began with five specimens: two tested at 50% of U90, two at 60% of U90, and one at 70% of U90. The minimum creep load was set at 0.6 kN, which is above the elastic limit of 0.42 kN determined from specimens tested after 90 days of curing, as shown in Table 5. According to Table 5, the specimen subjected to 70% of U90 failed after 11 days of loading and was subsequently replaced with another specimen tested at 40% of U90. Similarly, the specimens tested at 60% of U90 experienced premature failure due to a hydraulic system malfunction and were also replaced with specimens loaded at 40% of U90. The decision to reduce the load level was influenced by the significant slip observed in specimens SP.1.0 and SP.2.0, which were tested at 50% of U90.

The specimens in slots 4 and 5, tested at 40% of U90, failed after 101 and 119 days, respectively. Given this unexpected behavior, an additional specimen was mounted in slot 5 at the same 40% loading level. In slot 4, after the failure of the first 40% U90 specimen, a new specimen (S4.2) was tested at 60% of U90, but it also failed after 11 days. This prompted the testing of another specimen (S4.3) at 40% U90 to further investigate this loading level's behavior. Specimens SP.1.0 and SP.2.0, which were tested at 50% of U90, withstood the creep load for 250 days, at which point the tests were concluded based on the predefined termination age. Following the completion of these tests, slot 1 was used to test another specimen at 50% of U90, while specimen S2.1 was tested at 30% of U90. Additionally, specimen SP.3.1 was tested at 30% of U90 after the conclusion of the test under 60% of U90. Overall, the campaign involved testing 12 different specimens under various creep loading conditions, providing valuable insights into their long-term behavior under sustained loads.

5.3 Results and discussion

This section presents and analyzes the results obtained from the experimental campaign, beginning with the material characterization of the mortar, examining its behavior over time, and assessing the creep behavior of the glass yarn. Following this, the single-lap shear tests are discussed, starting with the ultimate strength results and the influence of extended curing time on their performance. Subsequently, the study delves into the creep behavior of the single-lap specimens under various loading stages, offering comparative analysis and potential justifications for the observed behaviors. The initial mechanical properties of the glass textile and yarns, including their ultimate tensile strength, were measured in a previous study [7]. The tensile strengths were reported as follows: glass yarn at 1120 MPa and glass fabric (3 yarns) at 1020 MPa. These baseline values provide a reference for interpreting the performance of the materials under sustained loading conditions. By integrating these aspects, this section aims to provide a comprehensive understanding of the material properties and the long-term behavior of TRMs under continuous loading, offering insights into their potential applications and limitations in structural reinforcement.

5.3.1 Materials

Figure 35 illustrates the results of material characterization tests on the mortar, plotted against increasing curing time. The average values of each test group are represented by dots, with error bars indicating the variability within each group. These are connected across different curing ages by a trend line to demonstrate the overall progression. As shown in Figure 35a, both the compressive and flexural strengths of the mortar exhibit a similar trend, with both increasing as curing time progresses. Specifically, the compressive strength shows a significant increase of 55% when curing time extends from 90 days to 298 days. The flexural strength also follows this trend, with a 49% increase over the same period.

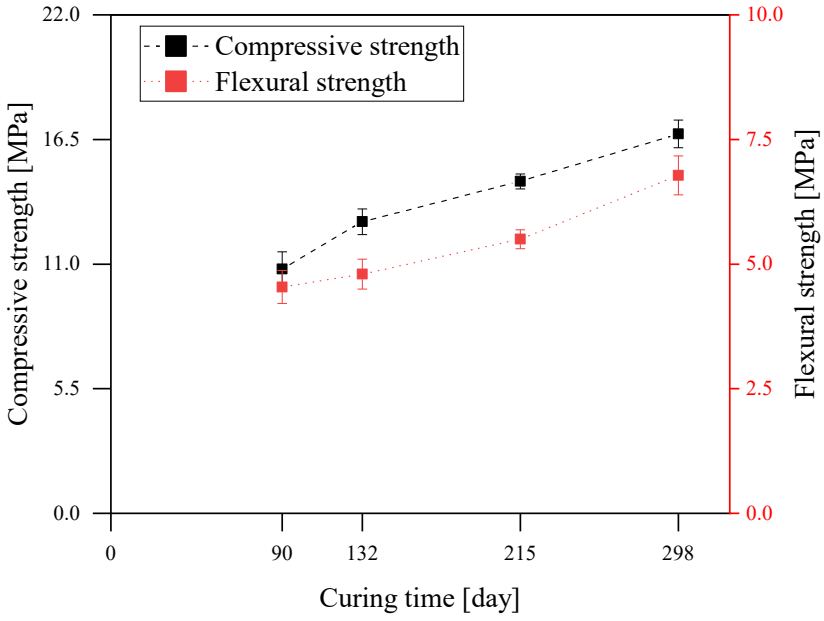

Figure 35 Mechanical characteristics of mortars as affected by prolonged curing exposure in compressive and flexural strength tests.

This observed behavior can be attributed to the ongoing hydration and carbonation process and microstructural development within the mortar as observed in the previous study [11,166]. As curing

progresses, the formation of additional hydration and carbonation products enhances the bonding between the aggregate and the matrix, contributing to increased compressive and flexural strengths.

5.3.1.1 Creep behavior of single glass yarn

Figure 36 illustrates the displacement behavior of two individual glass yarn samples subjected to 80% of their load-carrying capacity over a period of 300 days. The displacement-time curves of yarn 1 and yarn 2 exhibit typical creep behavior characterized by an initial rapid increase in displacement followed by a slower, more stable phase, and eventually a secondary acceleration towards the end of the test period. This behavior is indicative of the viscoelastic nature of the glass yarns, where immediate deformation occurs under load due to the elastic response, followed by time-dependent deformation or creep as the material undergoes further stress relaxation and molecular rearrangement under sustained load [10]. In the early stages, both yarns demonstrate a steep increase in displacement, with yarn 1 showing a slightly higher initial displacement than yarn 2. This initial phase, typically referred to as primary creep, suggests that the yarns experience significant internal strain as the fibers adjust to the applied load. The rate of displacement slows down during the secondary phase, indicating that the yarns have entered a more stable creep phase where the internal fiber structure is resisting further deformation. However, yarn 2 shows a more pronounced secondary creep phase, maintaining a relatively steady displacement rate until approximately 275 days. In contrast, yarn 1 begins to show signs of accelerated creep earlier, around 225 days, suggesting variability in the material properties or slight differences in loading or environmental conditions between the two yarns.

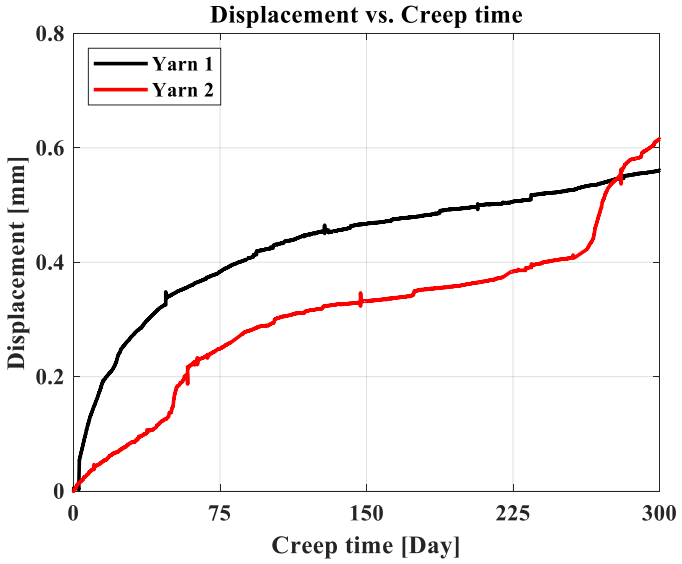

Figure 36 Displacement vs. creep time diagram for the single glass yarn under creep loading.

As the test progresses beyond the 225-day mark, both yarns exhibit a noticeable increase in displacement rate, entering what is commonly referred to as tertiary creep. This phase is characterized by a rapid increase in deformation, often leading to material failure [278,279]. The earlier onset of tertiary creep in the yarn 1 compared to the yarn 2 may indicate that yarn 1 is more susceptible to long-term degradation under sustained load, possibly due to microstructural weaknesses or higher initial damage accumulation. By the end of the 300-day period, both yarns show significant displacement, with Yarn 2 eventually catching up to and slightly surpassing the displacement observed in Yarn 1. This could be attributed to variations in the creep resistance of the individual yarns, potentially influenced by factors such as fiber orientation, initial microstructural flaws in filaments that might have effects on the performance over time [280]. The data from this creep test is critical for understanding the long-term performance and reliability of glass yarns in TRM applications, particularly in their ability to maintain

structural integrity under prolonged loading conditions. Additionally, the observed yarn displacement highlights the contribution of the textile itself to the overall displacement in composite systems. In the creep bond tests, the slipping of the yarn within the mortar is a major factor influencing the total displacement. In fact, understanding the inherent creep behavior of the yarn, gives the possibility of better differentiating between the creep deformation caused by the mortar-textile interaction and the one by the intrinsic properties of the yarn. This differentiation is essential for accurately interpreting the creep bond test results and improving the design and optimization of TRM systems for long-term applications.

5.3.2 Strength of single-lap shear specimens

Figure 37a provides a detailed depiction of the load-slip response for glass-TRM specimens subjected to single-lap shear testing after 90 days of curing. The figure includes the envelope curve derived from six individual tests and an average curve, offering a representative view of the behavior of these specimens under such conditions. To ensure data reliability, the study adhered to previously established acceptance criteria [11], excluding samples that exhibited premature failure or excessive rotation of the omega-shaped object. Overall, the load-slip response of the glass-TRM specimens can be broadly categorized into three distinct phases: the elastic (linear) phase, the nonlinear hardening phase, and the post-peak phase, as considered in the previous research [263].

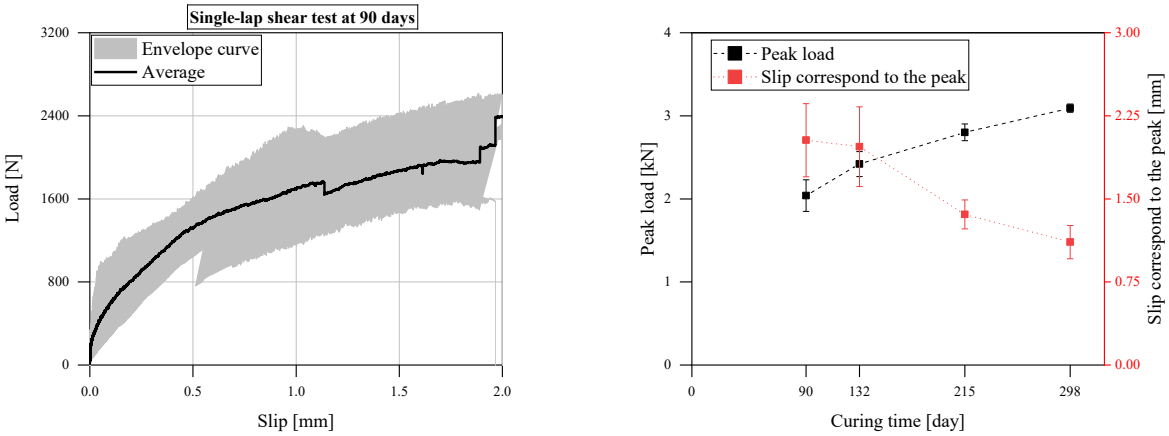

Figure 37 Ultimate strength test results for single-lap shear samples: (a) envelope of the load-slip curve, including the average curve for samples at 90 days; (b) variation in peak load with increasing curing time.

By the initial loading stage, the load-slip response is linear which reflects elastic behavior with proportional load increase and slip. This behavior is indicative of an intact bond between the glass textile and the mortar matrix. As loading progresses, a nonlinear hardening phase emerges, marked by micro-cracking within the mortar matrix and textile-matrix interface, and progressive sliding of the textile. Despite these damages, the composite continues to carry additional load due to the textile reinforcement bridging cracks and redistributing stresses. Upon reaching the peak load, the system enters the post-peak phase, where load decreases with increasing slip. If failure occurs through matrix detachment, the post-peak phase exhibits a brittle, rapid loss of load capacity [11]. Conversely, yarn rupture leads to a less abrupt decline, with the peak load determined by the tensile strength of the yarns.

The observed behavior in this study, characterized by a mix of fiber rupture and fiber sliding, can possibly be attributed to changes in mortar properties due to hydration and carbonation . This carbonation enhances matrix stiffness and mechanical interlock between the textile and mortar, leading to a higher initial stiffness and peak load capacity. Figure 37b further elaborates on the influence of curing time on peak load, showing a trend of increasing peak load with extended curing time. This trend is consistent with the results observed in compressive and flexural strength tests of the mortar. The 50%

increase in peak load as curing progresses could possibly be attributed to the impact of prolonged curing on the mechanical properties of TRM composites. The observed combination of initial high stiffness followed by brittle failure emphasizes the need to consider the effects of simultaneous curing and aging before and during the creep test by considering parameters like hydration and carbonation, when evaluating the long-term performance of TRM-reinforced structures.

5.3.3 Effect of specimens' curing time

The comparison of curing effects on the ultimate strength of flexural, compressive, and single-lap shear tests is presented in Figure 38. The graph illustrates the ultimate strength of each test normalized by its respective ultimate strength at 90 days, allowing for a direct comparison of their trends over time. The results reveal that all three test setups follow an almost similar growth pattern, indicating consistent improvements in the mechanical properties of the TRM composite system with extended curing time. The flexural and compressive tests show steady growth, reflecting the gradual enhancement of the mortar matrix's mechanical properties due to the prolonged curing period. The single-lap shear test results also exhibit a comparable trend, by suggesting that the bond strength between the mortar and the textile similarly benefits from extended curing. However, a slight divergence is observed in the behavior of the flexural test compared to the compressive and single-lap shear tests. This deviation could be attributed to the presence and influence of short fibers within the mortar matrix, which contribute to crack bridging and load redistribution under flexural stresses. The observed consistency across different testing setups underscores the robustness of the material under varying load conditions.

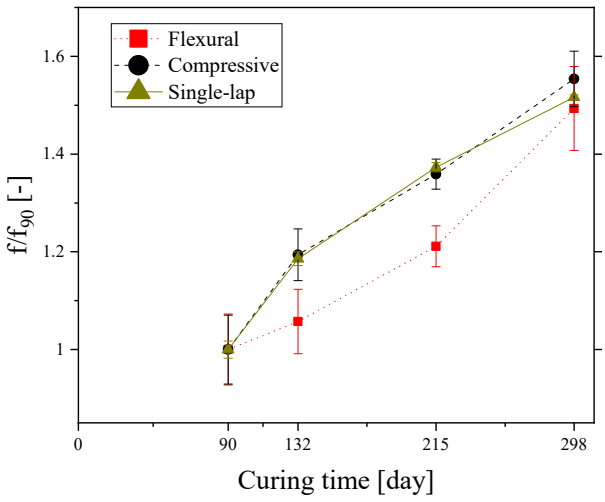

Figure 38 Normalized ultimate strength versus curing time for flexural, compressive, and single-lap shear tests, showing the consistent growth trend across different test setups.

5.3.4 Bond creep response

This section presents the results of creep loading tests on 12 single-lap shear specimens, evaluated under various loading levels and curing ages. For clarity in analysis, the results were categorized based on their respective creep loading levels (U90). The data were analyzed using two primary graphs. The first graph illustrates slip versus creep time for the entire duration of the tests, providing insights into the initial displacement, as well as potential secondary and tertiary creep stages. To maintain clarity, load versus creep time is not included in this graph since the load levels were consistent across the tests. The second graph displays force versus creep age, alongside slip versus creep age, during the initial 14 days of loading. This graph allows for a detailed examination of the initial slippage of the specimens and

provides a closer look at the secondary creep behavior. Given that the hydraulic system required more frequent load corrections at the beginning of the loading phase, these two sets of data are combined using a secondary axis to better visualize their relationship. Finally, the section concludes with a comprehensive discussion of the overall findings from all the conducted tests, integrating insights from the different loading scenarios and their implications for the creep behavior of the tested TRM specimens.

5.3.4.1 70% U90 (1.4 kN)

Figure 39 illustrates the force versus creep time and slip versus creep time for a single-lap shear specimen tested at 70% of U90. The graphs depict both the entire duration of the test and a detailed view of the initial two days. Only one specimen was tested at this load level due to its early failure (after 11 days) and the high maintenance demands required to sustain the load, which posed logistical challenges. In Figure 39a, the force and slip behavior over the 11-day period is shown. The force required frequent adjustments to maintain the target load, averaging five corrections per day, with no significant reduction in the adjustment frequency over time. This frequent need for adjustment is due to the hydraulic system's nature; any displacement in the specimen causes a reduction in the hydraulic pressure and the applied load consequently, necessitating continuous corrections, especially given the significant slippage observed in the samples. The slip, measured by two LVDTs, steadily increases throughout the test, demonstrating typical primary creep behavior, where the bond between the fiber and the matrix gradually weakens, leading to increased slippage under sustained load. However, as the test progresses, the rate of slip accelerates, particularly towards the end, suggesting the onset of secondary or even tertiary creep just before failure. This acceleration indicates that the material was approaching its failure point, with the bond between the textile and the matrix deteriorating under the sustained high load.

Figure 39b focuses on the initial two days of the test. During this period, the specimen exhibits a significant amount of slip, even though the applied force remains relatively constant. This behavior suggests that the bond between the textile and the mortar is undergoing initial adjustments under load, which is typical in creep tests where materials rapidly adjust to the applied stress. The slip behavior in the first two days shows a rapid initial increase, followed by a slight deceleration, indicating that the specimen may be entering a transient, more stable phase of creep. However, due to the high load level (70% of U90), this stable phase is short-lived, as indicated by the specimen's ultimate failure within 11 days. The frequent need for load adjustments, coupled with the rapid increase in slip, underscores the challenge of maintaining a stable creep condition at such a high load level. The specimen's early failure suggests that the material's ability to resist sustained high loads is compromised, likely due to microstructural degradation or progressive bond failure between the glass textile and the mortar matrix, compounded by potential damage to the outer filaments of the glass yarn from friction with the mortar.

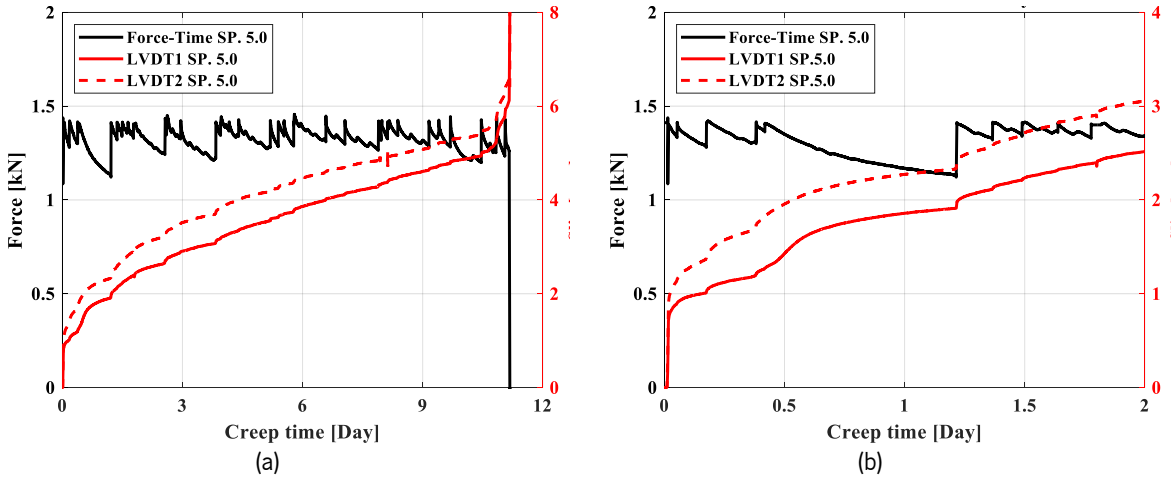

Figure 39 Creep loading results for single-lap shear specimens under 70% of the average ultimate strength at 90 days: (a) force-time and slip-time behavior over the entire test duration; (b) detailed force-time and slip-time behavior during the initial 14 days.

5.3.4.2 60% U90 (1.2 kN)

Figure 40 illustrates the creep behavior of two single-lap shear specimens, SP.3.0 and SP.4.2, under 60% of the average ultimate strength at 90 days (U90). Specimen 3.0, with a curing age of 90 days (A_0) based on Table 5, shows a progressive increase in slip over the 250-day creep period (Figure 40a). The graph shows a steady increase in slip, indicating a typical primary creep phase where the bond gradually weakens under sustained load. During the initial 14 days of the test (Figure 40b), the force remains relatively stable, but the slip gradually increases, reflecting the internal adjustments within the material under load. The absence of one LVDT for this specimen limits the precision of the slip measurement, but the available data still indicates significant slippage early on, corresponding to the material's continued adjustment and stress redistribution. The creep behavior observed in this specimen aligns with the known characteristics of glass yarns under sustained load, where the yarns themselves contribute to the overall deformation through their intrinsic creep properties. The values for S_{peak} at 7 days and $S_{ultimate}$ at 9 days for SP.3.0 suggest that the specimen reached the displacement equivalent to its peak and ultimate load relatively early showing a rapid degradation of the bond between the textile and the mortar.

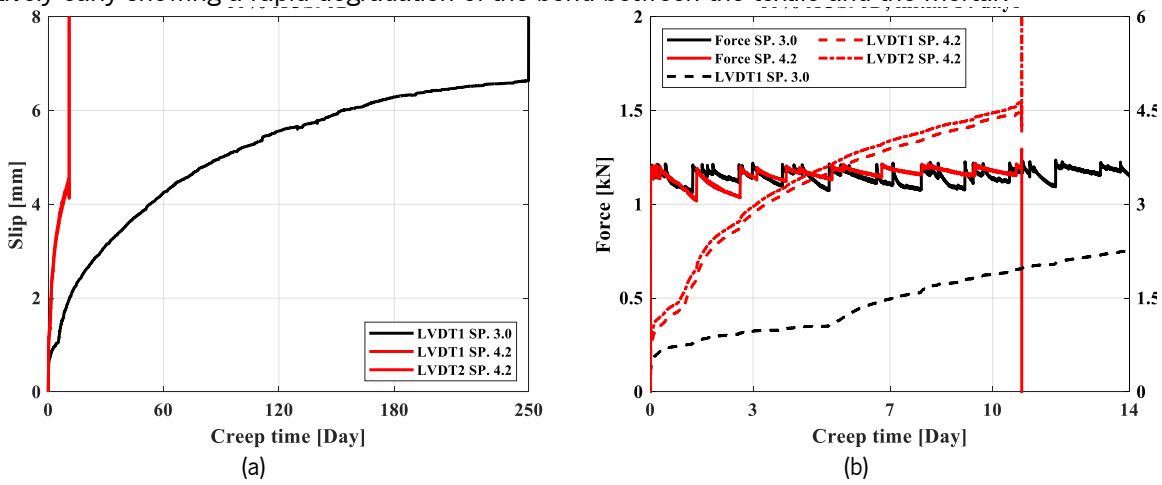

Figure 40 Creep loading results for single-lap shear specimens under 60% of the average ultimate strength at 90 days: (a) force-time and slip-time behavior over the entire test duration; (b) detailed force-time and slip-time behavior during the initial 14 days.

Specimen 4.2, with an A_0 of 220 days, presents a different creep behavior possibly due to its more advanced matrix development. The extended curing period resulted in higher compressive and flexural strengths, indicating a more mature and robust bond, and possibly a higher deflection capacity between the textile and mortar. The slip increased rapidly in this case, leading to an early failure after 11 days of

creep loading, might suggest that even with improved matrix properties, the applied load was sufficient to induce significant microstructural damage and bond degradation. In the initial 14 days by the Figure 40b, SP.4.2 shows a more pronounced increase in slip compared to SP.3.0, despite having a higher initial strength. This rapid slip increase can be attributed to the internal stresses and potential micro-cracking within the matrix that could have occurred during the extended curing period. The S_{peak} and $S_{ultimate}$ values of 1 day indicate that the specimen reached critical slip thresholds almost immediately under load, further emphasizing the material's sensitivity to sustained high loads, despite its initial strength.

Considering both specimens at the same time, the two specimens, having differences in curing age significantly influenced the creep response. SP.3.0, with its shorter curing period, displayed a steady creep response but reached critical slips earlier. In contrast, SP.4.2, despite its longer curing time and stronger matrix, exhibited a rapid slip increase leading to early failure, suggesting that prolonged curing might lead to brittleness or other microstructural issues under high sustained loads. The presence of secondary creep behavior, especially in SP.4.2, is evident from the rapid slip increase after a short initial period, indicating that the material quickly moved from primary to secondary creep, and then into tertiary creep, leading to failure. This behavior is consistent with the glass yarn's known creep characteristics, where the fibers themselves contribute to the overall deformation under sustained stress.

5.3.4.3 50% U90 (1.0 kN)

Figure 41 presents the creep behavior of the three tested specimens under 50% of U90. Both SP.1.0 and SP.2.0 have a curing age of 90 days, which, based on earlier material characterization tests, suggests a partially matured mortar matrix. However, as indicated in the compressive and flexural strength tests, the mechanical properties of the mortar at this curing stage are still developing, which influences the bond strength between the glass textile and mortar. The slip versus creep time graphs for SP.1.0 and SP.2.0 show a steady increase in slip over the 250-day testing period, consistent with primary creep behavior where the bond between the textile and the matrix gradually weakens under sustained load. The graphs indicate that the specimens undergo significant deformation, with slip increasing progressively without abrupt failures. This behavior aligns with the expectation that a 50% loading level, while inducing noticeable creep, does not immediately threaten the integrity of the bond.

During the initial 14 days as shown in Figure 41b, both specimens display an almost stable force, indicating that the hydraulic system maintained the load effectively. However, the slip increased gradually, with an initial rapid slip transitioning into a more stable secondary creep phase. This indicates that the bond was adjusting under sustained load, redistributing stress across the textile and mortar matrix. The absence of tertiary creep suggests that the material's structural integrity was not immediately compromised, even though gradual degradation was occurring. After reaching the 250-day limit, both SP.1.0 and SP.2.0 were subjected to increased load levels to determine their maximum load capacities post-creep. SP.1.0 reached a maximum load of 2.35 kN, while SP.2.0 achieved 2.63 kN. These values are lower compared to the original ultimate strength test results at a similar age, indicating some loss of load-bearing capacity due to the prolonged creep loading. This reduction can be attributed to the accumulated microstructural damage within the matrix and the interface between the textile and mortar, which likely weakened over time.

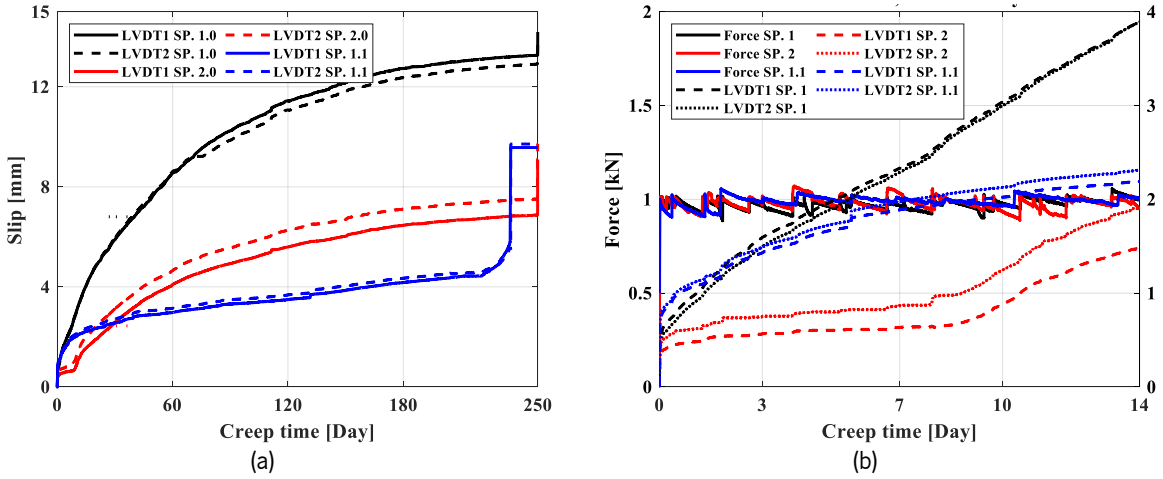

Figure 41 Creep loading results for single-lap shear specimens under 50% of the average ultimate strength at 90 days: (a) force-time and slip-time behavior over the entire test duration; (b) detailed force-time and slip-time behavior during the initial 14 days.

Specimen 1.1, with a curing age of 350 days, exhibited different creep behavior due to the development of the matrix strength. The extended curing time resulted in higher initial compressive and flexural strengths, which would generally enhance the bond between the textile and mortar. However, despite this stronger bond, SP.1.1 failed after 236 days of the creep loading, suggesting that even an over-cured matrix is susceptible to sustained load degradation over time. The initial 14-day analysis of SP.1.1 shows less slip compared to SP.1.0 and SP.2.0, reflecting the stronger bond from longer curing. However, the secondary creep phase is still evident, with slip gradually increasing until failure. The failure at 236 days, despite the specimen's mature state, indicates that the sustained load eventually overcomes even a well-developed bond, leading to microstructural failures, possibly because of increased fragility of the matrix and eventual rupture. It is important to note that since the glass yarn did not fail even after 300 days of creep loading at 80% of its load capacity, the failure observed in the specimens cannot be attributed solely to the behavior of the fiber.

Comparing these three specimens, the data reveals a clear relationship between curing age and creep behavior. SP.1.0 and SP.2.0, with shorter curing periods, exhibited more pronounced creep deformation, reflecting ongoing matrix development and a relatively weaker bond. In contrast, SP.1.1, which had a longer curing period, showed reduced initial creep but eventually failed under prolonged load, highlighting that extended curing improves resistance but does not completely prevent creep failure. Regarding the S_{peak} and $S_{ultimate}$ values based on Table 5, SP.1.0 and SP.2.0 reached these critical slips relatively early (within 12 to 14 days), while SP.1.1, despite its stronger initial bond, failed after 236 days, probably due to the secondary creep dominating these specimens' behavior in which gradually degrading the bond until failure. The glass yarn's intrinsic creep behavior also contributes to the overall creep deformation observed. While the yarn alone might not account for all the slip observed, it does play a significant role, particularly as the bond between the textile and mortar degrades over time.

5.3.4.4 40% U90 (0.8 kN)

Figure 42 presents the creep behavior of the four tested specimens under 40% of U90. Specimens 4.1 and 5.1, underwent to creep loading with curing age of 100 days and 115 days respectively, exhibited relatively early failures under 40% U90 creep loading. The slip versus creep time graph for these specimens shows a progressive increase in slip, with a notable acceleration before failure, indicating the onset of tertiary creep. Meanwhile, SP.4.1 failed after 101 days, while SP.5.1 failed after 119 days. The earlier failure of these specimens indicates that their matrices, while more cured than some earlier tested specimens, were still susceptible to significant degradation under sustained load, likely due to the incomplete development of long-term bond strength between the textile and mortar. During the initial 14

days as shown in Figure 42b, the force remains relatively stable, but the slip increases gradually, showing an early stage of secondary creep. The consistent increase in slip with time, followed by a more rapid slip, suggests that secondary creep transitioned into tertiary creep, which finally led to a failure. This behavior is consistent with the anticipated response of a partially matured mortar matrix, which gradually loses its load-bearing capacity under prolonged stress.

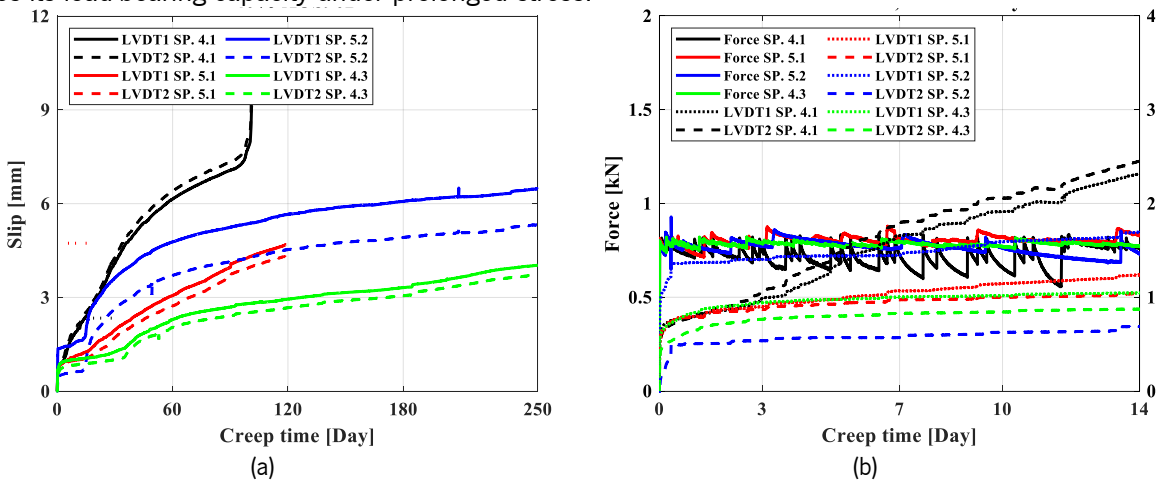

Figure 42 Creep loading results for single-lap shear specimens under 40% of the average ultimate strength at 90 days: (a) force-time and slip-time behavior over the entire test duration; (b) detailed force-time and slip-time behavior during the initial 14 days.

Specimens 5.2 and 4.3, with curing ages of 240 days and 235 days respectively, show a different behavior due to their extended curing times. Both specimens reached the 250-day limit without failure, indicating a significantly improved resistance to sustained loads compared to SP.4.1 and SP.5.1. After the creep test period, the load levels were increased to measure their maximum load capacities, reaching 2.57 kN for SP.5.2 and 2.51 kN for SP.4.3. These values are somewhat reduced compared to the initial ultimate strength and suggest that while the matrix was more developed, some degradation still occurred under the prolonged loading conditions. In the initial 14 days, SP.5.2 and SP.4.3 demonstrate relatively stable slip behavior with no significant acceleration, indicating that these specimens primarily experienced primary and secondary creep without transitioning into tertiary creep. The prolonged curing time allowed the mortar matrix to develop stronger bonds with the textile, reducing the rate of slippage under sustained load.

The overall creep behavior observed in these specimens under this load level reflects the complex interplay between the matrix's curing age, the load level, and the inherent properties of the glass yarn. The failure of SP.4.1 and SP.5.1 suggests that even at 40% U90, specimens with less curing time might be considered vulnerable to bond degradation and creep failure. In contrast, SP.5.2 and SP.4.3, with longer curing times, showed much greater resistance to creep, confirming the importance of curing in enhancing the bond strength. Regarding the values of S_{peak} and $S_{ultimate}$, SP.4.1 and SP.5.1 reached critical slips relatively quickly, indicating their rapid progression through creep stages, while SP.5.2 and SP.4.3 did not reach these critical slips within the 250-day test period, showing a more stable creep behavior. Moreover, it should be noted that the possible damage to the outer filaments of the glass yarn due to friction with the mortar matrix could have contributed to the reduced strength and increased slippage over time. As the outer filaments degrade, the overall load-bearing capacity of the yarn decreases, leading to increased slip and eventually failure, particularly in specimens with less curing time where the bond between the textile and mortar is weaker.

5.3.4.5 30% U90 (0.6 kN)

Figure 43 shows the creep behavior of the four tested specimens under 30% of U90. According to the graphs provided, Specimen SP.2.1, with a curing age of 350 days, shows a stable creep behavior under

the creep loading. Both Specimens 2.1 and 3.1 have curing ages of 350 days. According to the material characterization test results up to 298 days, there was a noticeable enhancement in the mortar's properties, such as compressive and flexural strength, which would contribute to the resistance against creep deformation. The slip versus creep time graphs for both SP.2.1 and SP.3.1 show minimal slip throughout the 250-day testing period, suggesting that the matrix provided strong resistance to creep deformation. The initial 14-day analysis as shown in Figure 43b shows stable force readings with only slight increases in slip while reflecting a robust bond between the textile and mortar that effectively resists sustained loading. The data indicates that primary creep was the dominant phase for both specimens, with no significant progression into secondary or tertiary creep. After the 250-day test period, both specimens were terminated by increasing the load until failure. SP.2.1 showed a maximum load capacity of 2.67 kN, and SP.3.1 showed a maximum load capacity of 2.79 kN, demonstrating that these specimens maintained their structural integrity despite the prolonged creep loading considering the strength growth observed by ultimate strength tests during the period of 298 days. These post-creep load capacities, while slightly reduced compared to their original strengths, are consistent with the expectation that the material's properties improve with curing time but may continue to evolve, potentially affecting long-term performance as seen in other studies for curing periods extending beyond one year [281].

The consistency in performance between SP.2.1 and SP.3.1 highlights the significant impact of curing age on creep resistance. The extensive curing time allowed both specimens to develop strong bonds between the textile and mortar, effectively resisting deformation even under sustained load. The minimal slip observed suggests that the specimens primarily experienced primary creep, with no significant transition into secondary or tertiary creep, probably due to an enhanced strength, the load level was below the elastic range of the system. The S_{peak} and $S_{ultimate}$ values in Table 5 also confirm that neither specimen reached critical slip thresholds during the test period, indicating that the 30% loading level was within the material's capacity to maintain bond integrity. The glass yarn's intrinsic creep behavior, which showed minimal displacement under similar conditions, also likely contributed little to the overall deformation observed, given the relatively low load levels. The absence of significant tertiary creep behavior in either specimen, coupled with their high post-creep load capacities, indicates that the material retained its structural integrity and did not undergo significant microstructural damage. Additionally, the potential damage to the outer filaments of the glass yarn due to friction with the mortar was likely minimized under this lower load level, contributing to the stable performance observed.

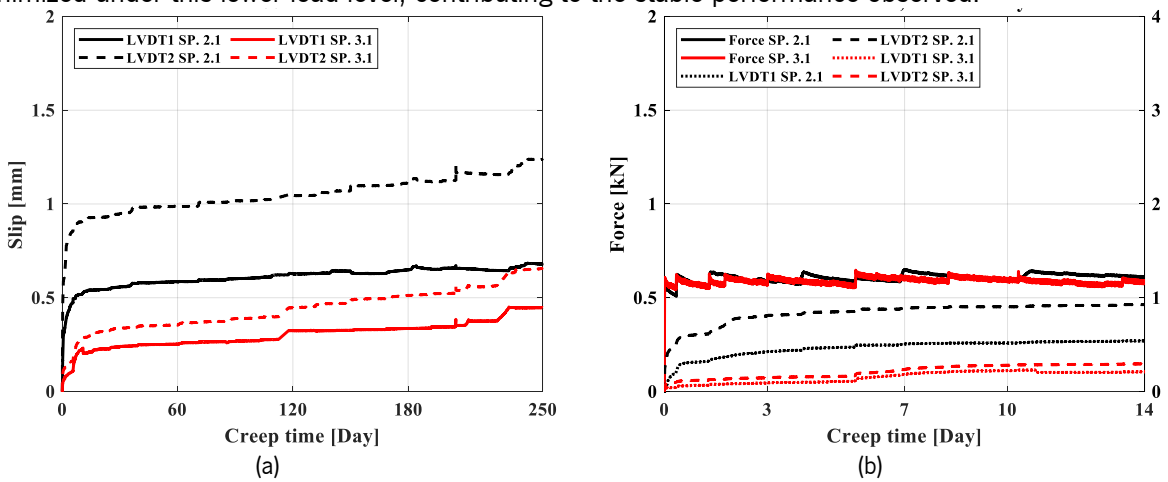

Figure 43 Creep loading results for single-lap shear specimens under 30% of the average ultimate strength at 90 days: (a) force-time and slip-time behavior over the entire test duration; (b) detailed force-time and slip-time behavior during the initial 14 days.

5.3.5 Discussion

The comprehensive analysis of the creep behavior in single-lap shear tests across different load levels ranging from 30% to 70% of the average ultimate strength at 90 days reveals critical insights into the performance of TRM under sustained loads. The results show a complex interaction between curing age, load level, and the inherent properties of both the mortar matrix and the glass yarns. The creep behavior across the various load levels reveals a clear trend, as expected, in which higher load levels lead to more rapid and pronounced creep deformation, with early transitions into secondary and tertiary creep phases. At 70% of U90, the specimens exhibited early failure, with significant slip and rapid displacement increase, indicating that the bond between the glass textile and the mortar matrix was unable to withstand the high sustained load over time. This early failure is likely due to microstructural degradation within the mortar and the progressive bond failure between the textile and the matrix, and the occurence of progressive damage. As the load level decreases, the creep behavior becomes more stable. At 60% of U90, specimens with longer curing times demonstrated better resistance to creep, though early critical slips and transitions to secondary creep were still observed. At this load level, the results highlight the importance of considering the combined effects of load and curing age, as even well-cured specimens showed signs of rapid creep progression under sustained high loads.

The behavior under 50% of U90 further supports the observation that lower load levels reduce the rate and extent of creep deformation. Specimens at this load level exhibited gradual degradation under sustained load, with the extent and rate of creep deformation closely tied to the curing age. Specimens with longer curing times demonstrated enhanced resistance to creep, maintaining their structural integrity over the testing period, while those with shorter curing times showed earlier onset of critical slips and a greater loss of structural integrity. At 40% and 30% of U90, the specimens demonstrated significantly better creep performance with lower slip. Specimens under 40% load showed that longer curing times lead to enhanced resistance to creep, with only minimal degradation observed in their post-creep load capacities. Under 30% load, the specimens exhibited excellent stability, with no significant transitions into secondary or tertiary creep phases. This suggests that at lower load levels, the mortar matrix and the bond with the textile are sufficiently robust to resist long-term deformation, especially when adequate curing time is provided.

The curing age also plays a pivotal role in determining the creep resistance of TRM systems. The analysis shows that as the curing time increases, the mortar matrix develops enhanced mechanical properties, including compressive and flexural strengths, which in turn improve the bond strength with the glass textile. Specimens with longer curing times consistently exhibited better resistance to creep across all load levels, with less pronounced slip and more stable load-bearing capacities. The interplay between load levels and curing age is also important in determining the overall creep performance of TRM systems. High levels of loading significantly challenge the bond strength between the textile and mortar, leading to earlier failure and more pronounced creep behavior. In contrast, at lower load levels, even specimens with shorter curing times exhibit sufficient resistance to creep, though longer curing periods consistently result in better performance.

5.4 Conclusion

The objective of this chapter was to assess the behavior of TRM systems under sustained loading, employing a single-lap shear configuration to investigate the influence of curing time and applied load levels on long-term performance. The experimental program incorporated compressive, flexural, and elastic modulus tests on the mortar at selected curing durations, as well as shear bond tests on TRM specimens to determine the load-bearing capacity. In addition, tensile creep tests were conducted on dry

glass yarns and TRM specimens subjected to different fractions of their average capacity over a 250-day period. The main findings are summarized as follows:

- The creep performance of the TRM system was significantly influenced by both the applied load level and the curing age of the mortar matrix. Higher load levels led to accelerated deformation and premature failure, particularly in specimens with limited curing. In contrast, lower sustained loads and longer curing durations contributed to long-term structural integrity.
- The results confirmed that increasing curing time enhanced the mechanical properties of the mortar, including compressive and flexural strengths. However, potential aging effects beyond typical curing durations must be considered for long-term applications, highlighting the importance of accounting for extended material evolution in the design of TRM systems.
- Specimens loaded at levels exceeding 60% of their reference capacity (U90) experienced substantial creep deformation and early failure, attributed to progressive bond degradation and microstructural damage in the matrix. These outcomes reinforce the challenges associated with maintaining bond integrity under sustained high stress.
- At lower creep load levels (30–40% of U90), TRM specimens exhibited greater stability and resistance to deformation. Those with longer curing periods retained favorable post-creep capacity and showed minimal slip, even after prolonged loading durations, underscoring the benefits of sufficient matrix maturation.
- The tensile creep behavior of the glass yarn contributed minimally to overall deformation under the tested conditions. Nonetheless, the potential for mechanical degradation of outer filaments due to frictional interaction with the surrounding mortar should be considered in long-term durability assessments, particularly at higher load levels.
- The interdependence between applied load and curing maturity emerged as a critical parameter in the mechanical behavior of TRM systems. Appropriate balancing of these factors is essential to ensure adequate resistance to creep-induced degradation and to preserve structural performance over time.
- The outcomes of this chapter highlight the necessity of investigating durability-related degradation mechanisms in chemically aggressive environments, where the combined effects of sustained loading and chemical exposure—such as acidic, alkaline, and saline conditions—may accelerate deterioration. In particular, the evolution of the matrix–textile interface under such exposures is expected to further influence mechanical performance and serviceability. These interactions are comprehensively addressed in the subsequent chapter.

This page is left blank on purpose

Chapter 6
Long-Term performance of TRM under environmental aging: saline, alkaline, and acidic conditioning

6.1 Introduction

TRM composites are increasingly recognized for their suitability in retrofitting masonry and reinforced concrete structures, particularly where compatibility with historical materials and minimally invasive intervention techniques is essential. Although their short-term mechanical performance has been well established under controlled laboratory conditions, the durability of TRM systems under long-term environmental exposure remains less understood. Real-world TRM-strengthened structures are subjected to a range of environmental stressors, including chloride-laden aerosols in coastal areas, alkaline leachates from adjacent concrete elements, and mildly acidic rain or industrial emissions, that can critically affect their interfacial behavior and structural integrity [178,282,283]. The present study addresses this issue through a controlled experimental program designed to simulate degradation processes induced by three chemically active aging environments: saline, alkaline, and acidic. To enable comparative evaluation, two additional reference conditions, dry storage and water condition were included. These five environments were selected to reflect the range of typical exposures encountered in field applications. The primary focus of the study is the assessment of bond degradation at the fiber-matrix interface, as this is a key determinant of TRM mechanical performance and energy dissipation capacity.

The testing protocol incorporates both mechanical and microstructural evaluations. Pull-out and single-lap shear tests were performed to quantify changes in bond strength, debonding energy, and failure mechanisms in TRM specimens fabricated with either glass or basalt textiles. Parallel mechanical testing on the mortar matrix, combined with complementary microstructural and mineralogical analyses, including XRD, SEM, TGA, and optical microscopy provided additional insight into the physical and chemical changes affecting the system over time. Figure 44 presents a flowchart outlining the structure of the experimental program. The chart summarizes the exposure environments, aging durations (1000, 3000, and 5000 hours), and the series of tests conducted at each stage, including those on textile, mortar, and TRM composites. This visual framework clarifies the experimental methodology and contextualizes the data presented in the following sections.

The findings of this chapter aim to establish a baseline understanding of TRM durability under mild environmental aggression. Special attention is drawn to the pronounced vulnerability of TRM systems in acidic media. This observation supports the motivation for the focused investigation on acid-induced degradation mechanisms, presented in the subsequent chapter, which examines TRM performance under intensified acidic exposure and extended aging durations.

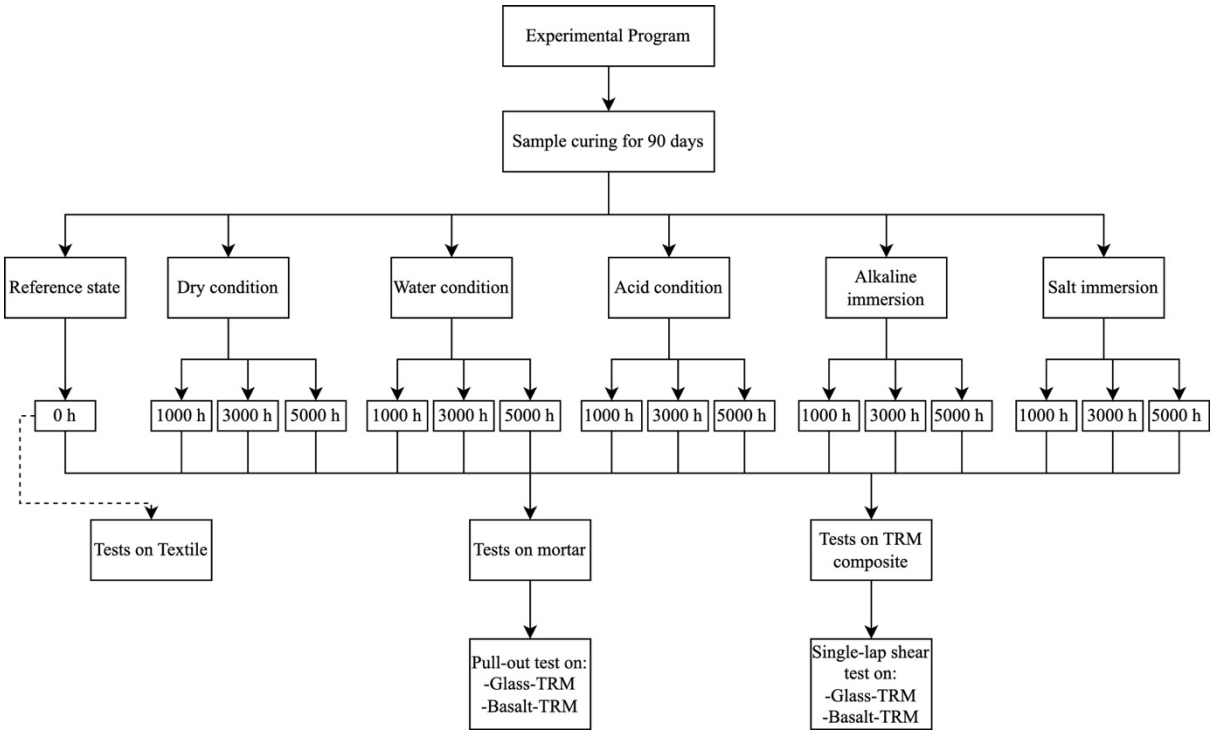

Figure 44 Flowchart of the experimental program

6.2 Sample preparation

Two different types of textile grids (i.e., glass and basalt) and the lime-based mortar as well as clay bricks as introduced earlier have been utilized. Various material characterization tests, encompassing compressive, flexural, and elastic modulus assessment, were carried out for mortar considering the three aging environments and all aging exposures. Simultaneously, direct tensile tests were executed only on unaged yarns and textiles. It is worth noting that the aging time is counted from the end of the curing period (90 days) when specimens are exposed to the three aging conditions, as substantiated by prior research [7,65], see also Figure 45.

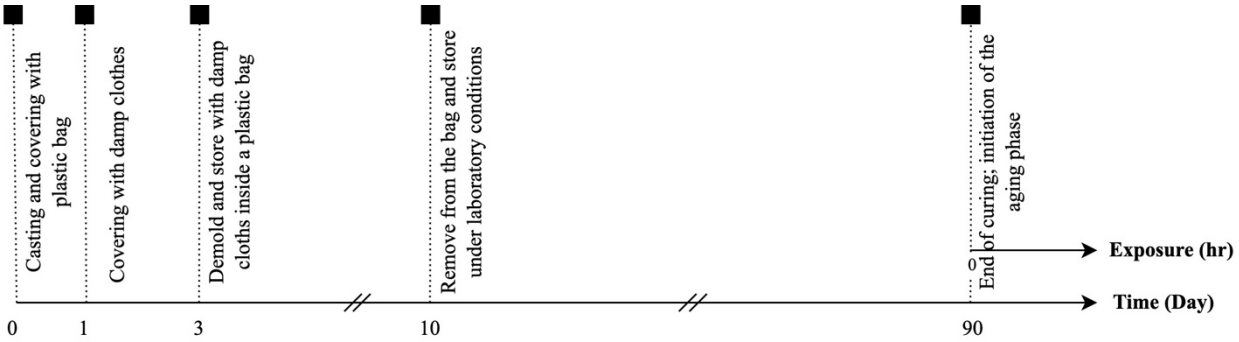

Figure 45 Schematic representation of curing of the samples.

Chapter 3 illustrates the material characterization tests conducted in this chapter, specifically the mortar compressive test, mortar flexural test, mortar elastic modulus, and brick compressive tests, respectively. It is noteworthy that the exposed, untreated surfaces of mortar samples underwent rectification at the end of the curing process to attain a surface roughness consistent with that of other surfaces and to ensure uniformity in aging boundaries. Brick samples were likewise positioned within tanks alongside mortar specimens to be subjected to identical conditions as the mortar. For specimens subjected to dry conditions, testing was conducted under ambient conditions, whereas immersed specimens were assessed under SSD conditions. The testing protocol for SSD conditions entailed removing samples from water 15 minutes before testing and wiping off any excess of surface moisture.

6.3 Aging environments

The durability performance of TRM composites was assessed under controlled exposure to five distinct and standard aging environments, selected to simulate commonly encountered conditions in real-world applications. These environments included a dry condition, water condition, and three chemically aggressive media: acidic, alkaline, and saline solutions. Additionally, a reference group was defined to represent the unaged state of the material immediately after the completion of the curing period. The purpose of this environmental conditioning was to isolate the effects of each aging mechanism on the physical, chemical, and mechanical properties of both the mortar matrix and the composite interface.

A consistent methodology was employed across all exposure scenarios to ensure comparability. All immersion-based exposures were conducted at a regulated temperature of 20 °C using closed-lid tanks equipped with a water circulation system to ensure homogeneity of the solution. The solid-to-solution ratio was fixed at 1:4 to minimize concentration variability caused by leaching. To further mitigate changes in chemical composition over time, the solutions were renewed after 1000 and 3000 hours of exposure. As shown in Figure 46, the aging system consisted of custom-designed tanks where specimens were uniformly distributed and submerged under controlled conditions. For dry and reference conditions, storage was carried out under ambient laboratory conditions. Across all environments, specimens designated for composite performance testing and microstructural characterization were treated simultaneously and under identical protocols. This section outlines the aging parameters for each condition, beginning with the unaged reference state.



(a) (b)

Figure 46 (a) External view of the immersion tanks used for different aging conditions; (b) internal configuration showing TRM specimens arranged for exposure, illustrating the orientation and spacing maintained during the aging process.

6.3.1 Reference state

The reference condition represents specimens tested directly after the curing phase, without exposure to any external environmental conditioning. These samples serve as the baseline for comparison, providing insight into the initial mechanical and microstructural performance of the TRM systems. All reference specimens were cured under laboratory conditions for 90 days prior to testing to ensure full hydration and mortar hardening. No additional environmental exposure was applied beyond the curing period.

6.3.2 Dry condition

Specimens assigned to the dry condition were stored in a controlled laboratory environment with a temperature of 20°C ± 5°C and relative humidity of 65% ± 10%. This exposure condition was intended to simulate indoor or sheltered structural applications where TRM systems are not subjected to direct environmental attack. No moisture ingress, chemical interaction, or external loading was applied during this period. The dry condition serves both as a practical reference and as a contrast to immersion-based environments, particularly in terms of the absence of ionic transport or matrix dissolution.

6.3.3 Water condition

To simulate a neutral wet condition, specimens were fully immersed in tanks containing distilled water. The water condition environment was maintained at a constant temperature of 20°C using a temperature regulation system, and water pumps were used to ensure uniform fluid circulation. This exposure condition aims to replicate service environments such as groundwater contact or general moisture exposure without chemical aggressiveness. The distilled water was replaced after 1000 and 3000 hours to control the accumulation of leached ions from the mortar, ensuring consistency in testing conditions. The immersion depth was sufficient to fully submerge all composite specimens and mortar samples intended for material characterization.

6.3.4 Acidic condition

Acidic aging was conducted using a sulfuric acid solution prepared with 95–97% purity sulfuric acid supplied by Chem-Lab. The solution was adjusted to a target pH of 3.0, in accordance with protocols established in previous studies involving GFRP [284]. A fixed solid-to-solution ratio of 1:4 was maintained, and specimens were fully immersed in closed-lid tanks. The temperature was regulated at 20°C, and water pumps ensured continuous circulation of the solution. To counteract pH variation due to leaching and ongoing acid-base reactions, the solution was renewed after 1000 and 3000 hours of exposure, and the pH was adjusted twice weekly through the addition of fresh acid. This condition was specifically selected to provide a basis for the detailed acidic durability campaign described in the subsequent chapter.

6.3.5 Alkaline condition

For alkaline exposure, specimens were immersed in a calcium hydroxide solution with an initial pH of 12.6, corresponding to a concentration of 0.16%. This solution simulates the high-pH environment typical of freshly cast concrete or cementitious surroundings. The aging procedure adhered to the same temperature and circulation control parameters used in other immersion environments, with a constant temperature of 20°C and active circulation to maintain uniformity. The solid-to-solution ratio was kept at 1:4, and the alkaline solution was renewed after 1000 and 3000 hours to prevent saturation with leached species. Composite specimens and mortar samples were fully submerged throughout the exposure period.

6.3.6 Saline condition

A 3.5% NaCl solution was used to replicate marine-like conditions commonly encountered in coastal and offshore structures. The salt solution, prepared with NaCl of 99.7% purity (Chem-Lab), was maintained at 20°C using a temperature regulator and circulated uniformly by water pumps. The fixed solid-to-solution ratio of 1:4 was again applied. Similar to the other immersion-based conditions, the saline solution was replaced after 1000 and 3000 hours to minimize the effects of material leaching and maintain a consistent chloride concentration. Full immersion was ensured for all composite specimens and material characterization samples. The exposure durations, ranging from 1000 to 5000 hours, were selected to capture intermediate and extended aging behaviors over progressive degradation stages and are in alignment with practices established in previous experimental studies [27,153].

6.4 Mineralogical and chemical analysis

To comprehensively evaluate the degradation mechanisms affecting the TRM system under various aging environments, a suite of mineralogical and chemical characterization techniques was employed. These analyses were designed to capture both compositional changes in the mortar matrix and alterations at the microstructural level, thereby enabling a mechanistic interpretation of observed macroscopic performance losses. Techniques such as XRD, XRF, TGA, and FTIR, as described in Chapter 3, were used to identify phase transformations, chemical dissolution, and reaction products. Microscopic examinations, including optical microscopy and scanning electron microscopy coupled with EDX, facilitated the assessment of physical deterioration and elemental redistribution. Additionally, measurements of bulk density and open porosity provided insight into pore structure evolution, while ICP analysis of the aging solutions quantified the extent of ionic leaching during exposure. Together, these methods offer a multi-scale perspective on the environmental aging behavior of TRM composites.

6.5 Testing overview

Six specimens were prepared for each test configuration to ensure statistical reliability and reproducibility. The experimental matrix included compressive strength tests (C), flexural strength tests (F), elastic modulus evaluations (E), direct tensile tests on textiles (T), and bond behavior assessments through both pull-out (P) and single-lap shear (S) tests. To facilitate systematic tracking and identification, each specimen was labeled using the standardized notation T_F_A_D_I, where “T” denotes the test type (C, F, E, T, P, or S), “F” identifies the textile type (G for glass, B for basalt), “A” indicates the aging environment (DC, WI, AC, AK, or SA), “D” specifies the aging duration in hours (0, 1000, 3000, or 5000), and “I” represents the specimen number within each group (from 1 to 6). For instance, the label P_G_AK_5000_2 refers to a pull-out specimen fabricated with glass textile, subjected to alkaline exposure for 5000 hours, and identified as the second specimen in that group. Similarly, S_B_SA_3000_5 denotes a single-lap shear specimen reinforced with basalt fibers and exposed to saline conditions for 3000 hours, being the fifth sample in that series.

All specimens underwent identical curing conditions as expressed in section 6.2, prior to exposure and were handled in parallel across all stages of the experimental campaign to minimize batch variability. The use of a unified coding system and consistent procedures ensured traceability and comparability across different test types and environmental scenarios. A visual representation of specimens immersed in the water tank during aging is provided in Figure 46, while detailed information regarding each test group is summarized in Table 6.

6.6 Results and discussion

This section presents the experimental outcomes obtained from mechanical and material characterization of TRM mortar samples subjected to various environmental aging conditions. The primary focus is placed on the degradation trends and phase transformations induced by prolonged exposure to mild aggressive environments, namely acidic, saline, and alkaline media. To facilitate meaningful interpretation of results, two reference conditions, dry storage and water condition were incorporated as comparative baselines. These reference media provide essential contrast for isolating the effects of chemically active exposure, especially in terms of physical durability, pore structure alteration, and strength development. The discussion is structured to first address the bulk material properties of the mortar matrix, followed by an in-depth assessment of bond-related performance through pull-out and single-lap shear tests.

6.6.1 Material properties

The mechanical response of the mortar matrix under different exposure environments was evaluated through compressive strength, flexural strength, and elastic modulus tests. These parameters are critical for understanding the intrinsic changes in the mortar microstructure and their contribution to the composite system's overall performance. The use of DC and WI conditions as baseline environments is grounded in both practical relevance and scientific reasoning [11,16,140,151,165–167]. The dry condition reflects sheltered in-service applications where carbonation and pozzolanic activity dominate the long-term behavior [285–289]. In contrast, water condition serves as a neutral wet condition that facilitates continued hydration while eliminating the influence of chemical reactants, thereby serving as a useful benchmark for identifying chemically induced degradation mechanisms [288–290].

The interpretation of results across the three chemically active environments, acidic, saline, and alkaline was performed in relation to the corresponding DC and WI reference groups. All mechanical property graphs for each exposure type include these baselines to support direct visual and statistical comparison. In addition, mineralogical and microstructural analyses, including XRD, XRF, TGA, SEM and optical microscopy, are used to corroborate the observed mechanical behavior.

Table 6 Detailed specification of test scheme

Specimen's Name	Specimen's type	Fabric Type	Aging Medium	Aging Time**
C_0	Compressive	-	Dry condition	-
C_DC_1000				1000 h
C_DC_3000				3000 h
C_DC_5000				5000 h
F_0	Flexural	-	Dry condition	-
F_DC_1000				1000 h
F_DC_3000				3000 h
F_DC_5000				5000 h
E_DC_DA*	Elastic Modulus	-	Dry condition	-
				1000 h
				3000 h
				5000 h
T_G_DC	Tensile	Glass	Dry condition	-
T_B_DC	Tensile	Basalt	Dry condition	-
C_WI_1000	Compressive	-	Distilled water	1000 h
C_WI_3000				3000 h
C_WI_5000				5000 h
F_WI_1000	Flexural	-	Distilled water	1000 h
F_WI_3000				3000 h
F_WI_5000				5000 h
E_WI_DA*	Elastic Modulus	-	Distilled water	1000 h
				3000 h
				5000 h
C_AC_1000	Compressive	-	Acidic solution	1000 h
C_AC_3000				3000 h
C_AC_5000				5000 h
F_AC_1000	Flexural	-	Acidic solution	1000 h
F_AC_3000				3000 h
F_AC_5000				5000 h
E_AC_DA*	Elastic Modulus	-	Acidic solution	1000 h
				3000 h
				5000 h
C_ AK _1000	Compressive	-	Alkaline solution	1000 h
C_ AK _3000				3000 h
C_ AK _5000				5000 h
F_ AK _1000	Flexural	-	Alkaline solution	1000 h
F_ AK _3000				3000 h
F_ AK _5000				5000 h
E_ AK _DA*	Elastic Modulus	-	Alkaline solution	1000 h
				3000 h
				5000 h
C_SA_1000	Compressive	-	Saline solution	1000 h
C_SA_3000				3000 h
C_SA_5000				5000 h
F_SA_1000	Flexural	-	Saline solution	1000 h
F_SA_3000				3000 h
F_SA_5000				5000 h
E_SA_DA*	Elastic Modulus	-	Saline solution	1000 h
				3000 h
				5000 h
P_G_0	Pull-out	Glass	Dry condition	-
P_G_DC_1000				1000 h
P_G_DC_3000				3000 h
PL_G_DC_5000				5000 h
P_B_0	Pull-out	Basalt	Dry condition	-
P_B_DC_1000				1000 h
P_B_DC_3000				3000 h
P_B_DC_5000				5000 h
P_G_WI_1000	Pull-out	Glass	Distilled water	1000 h
P_G_WI_3000				3000 h
P_G_WI_5000				5000 h
P_B_WI_1000	Pull-out	Basalt	Distilled water	1000 h
P_B_WI_3000				3000 h
P_B_WI_5000				5000 h
P_G_AC_1000	Pull-out	Glass	Acidic solution	1000 h
P_G_AC_3000				3000 h
P_G_AC_5000				5000 h
P_B_AC_1000	Pull-out	Basalt	Acidic solution	1000 h
P_B_AC_3000				3000 h
P_B_AC_5000				5000 h
P_G_AK_1000	Pull-out	Glass	Alkaline solution	1000 h
P_G_ AK _3000				3000 h
P_G_ AK _5000				5000 h
P_B_ AK _1000	Pull-out	Basalt	Alkaline solution	1000 h
P_B_ AK _3000				3000 h
P_B_ AK _5000				5000 h
P_G_SA_1000	Pull-out	Glass	Saline solution	1000 h
P_G_SA_3000				3000 h
P_G_SA_5000				5000 h
P_B_SA_1000	Pull-out	Basalt	Saline solution	1000 h
P_B_SA_3000				3000 h
P_B_SA_5000				5000 h
S_G_0	Single-lap	Glass	Dry condition	-
S_G_DC_1000				1000 h
S_G_DC_3000				3000 h
S_G_DC_5000				5000 h
S_B_0	Single-lap	Basalt	Dry condition	-
S_B_DC_1000				1000 h
S_B_DC_3000				3000 h
S_B_DC_5000				5000 h
S_G_WI_1000	Single-lap	Glass	Distilled water	1000 h
S_G_WI_3000				3000 h
S_G_WI_5000				5000 h
S_B_WI_1000	Single-lap	Basalt	Distilled water	1000 h
S_B_WI_3000				3000 h
S_B_WI_5000				5000 h
S_G_AC_1000	Single-lap	Glass	Acidic solution	1000 h
S_G_AC_3000				3000 h
S_G_AC_5000				5000 h
S_B_AC_1000	Single-lap	Basalt	Acidic solution	1000 h
S_B_AC_3000				3000 h
S_B_AC_5000				5000 h
S_G_ AK _1000	Single-lap	Glass	Alkaline solution	1000 h
S_G_ AK _3000				3000 h
S_G_ AK _5000				5000 h
S_B_ AK _1000	Single-lap	Basalt	Alkaline solution	1000 h
S_B_ AK _3000				3000 h
S_B_ AK _5000				5000 h
S_G_SA_1000	Single-lap	Glass	Saline solution	1000 h
S_G_SA_3000				3000 h
S_G_SA_5000				5000 h
S_B_SA_1000	Single-lap	Basalt	Saline solution	1000 h
S_B_SA_3000				3000 h
S_B_SA_5000				5000 h

* Due to the non-destructive nature of elastic modulus tests, the same specimens were tested at different ages.

6.6.1.1 Effect of dry and water condition

The mechanical performance of specimens aged under dry and water condition conditions provided insight into the hydration and carbonation mechanisms of lime-based mortars in the absence of chemically aggressive exposure. As shown in the mechanical characterization plots (Figure 47), compressive strength increased linearly with time under DC conditions, with values rising from initial curing up to 5000 hours. This strength development is primarily attributed to ongoing pozzolanic activity and carbonation, which promote matrix densification. In contrast, WI specimens exhibited a peak in compressive strength at 3000 hours, followed by a decline at 5000 hours. The initial increase is linked to sustained hydration, while the subsequent decrease is attributed to calcium leaching and reduced availability of calcium ions, which compromises the stability of C-S-H gels.

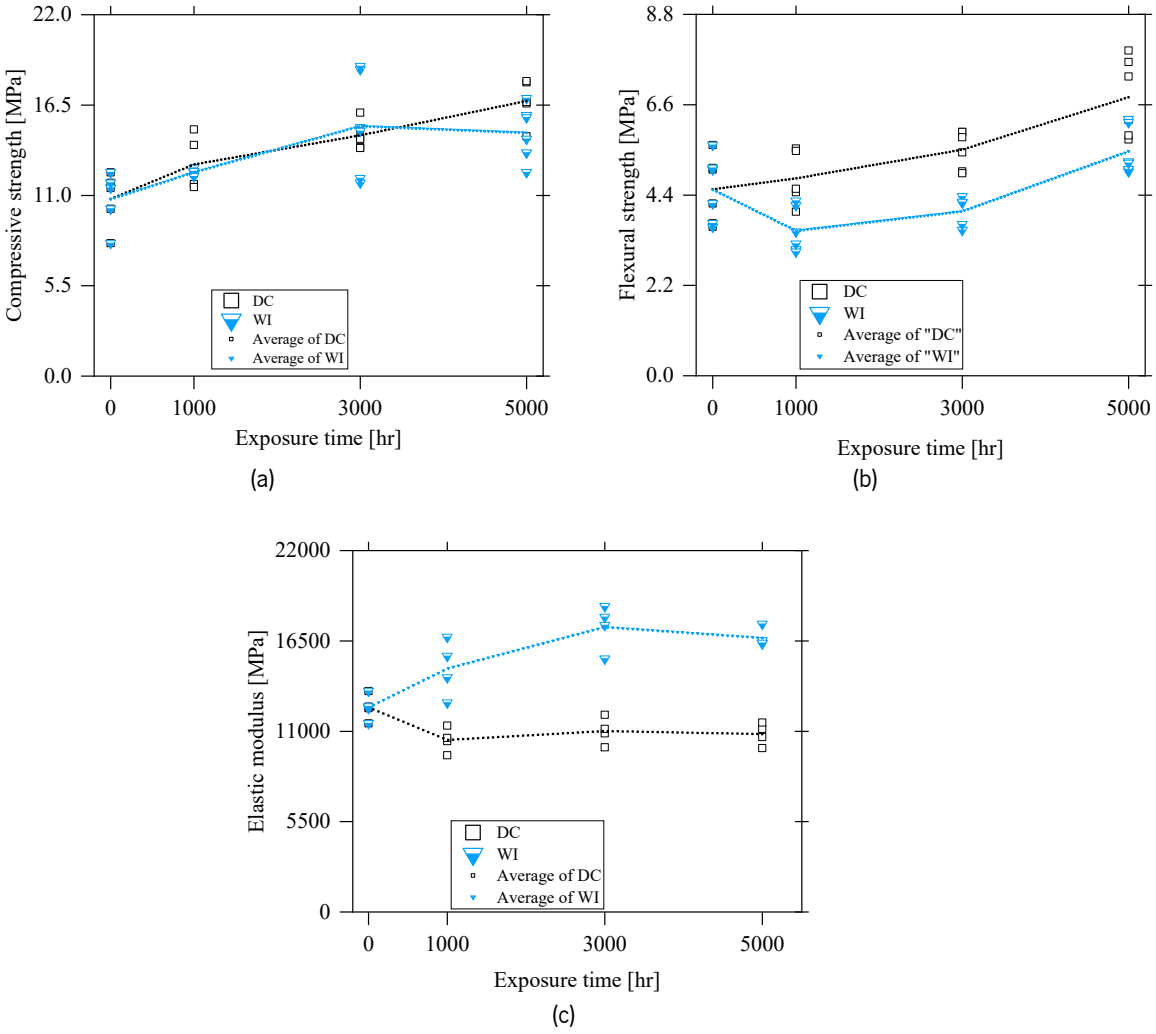

Figure 47 Mechanical properties of mortars under dry and water condition conditions as a function of exposure time: (a) compressive strength; (b) flexural strength; (c) elastic modulus.

Flexural strength under dry conditions followed a similar trend to compressive strength, with a near-linear increase over the entire aging period. This improvement is interpreted as the result of continuous matrix densification and increased cohesion between the mortar components. Conversely, WI specimens displayed an initial drop in flexural strength at 1000 hours, likely caused by water-induced reduction in fiber-matrix friction due to wet conditions [159,291]. Nonetheless, strength increased again after prolonged immersion, possibly due to internal hydration and the contribution of short fibers bridging

microcracks. These fibers, more effective in dry conditions, experienced reduced pull-out resistance under saturated conditions, as also observed in the reduced flexural modulus for WI compared to DC.

The XRD patterns (Figure 48) revealed quartz and calcite as the main crystalline phases in both DC and WI samples, confirming the mineralogical stability of the mortar in the absence of chemically active species. Gypsum formation, observed in other environments, was absent in both DC and WI, supporting the visual evidence that no aggressive sulfate reaction occurred. Minor differences in peak intensity were noted, potentially indicating subtle differences in the degree of carbonation between the two conditions.

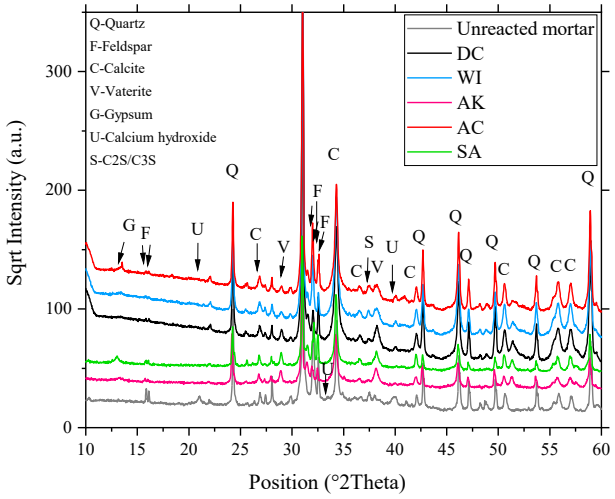

Figure 48 XRD patterns of mortar samples under different aging environments: unreacted, dry condition, water condition, alkaline, acidic, and saline.

Optical microscopy (Figure 49) further illustrated the homogeneity of the mortar matrix across both conditions, with a well-distributed aggregate-paste interface and no visible signs of chemical degradation. However, WI specimens appeared slightly more porous, which correlates with the observed reduction in strength at later ages. These findings were corroborated by SEM analysis (Figure 50), which indicated high porosity in both samples but no severe matrix disintegration. Importantly, SEM imaging highlighted limited fiber-matrix adhesion and exposed short fibers embedded in the matrix, which, while not contributing significantly to mechanical strength, provide insight into the internal morphology and reinforcement distribution.

Thermogravimetric analysis (Figure 51) showed mass loss peaks associated with portlandite decomposition around 400°C and calcite decomposition above 600°C for both environments. In DC samples, a slightly more pronounced weight loss at higher temperatures was observed, consistent with greater carbonation. The WI sample displayed lower peak intensity, supporting the interpretation that prolonged condition inhibited carbonation due to CO_2 limitations and favored the dissolution of hydration products, including portlandite.

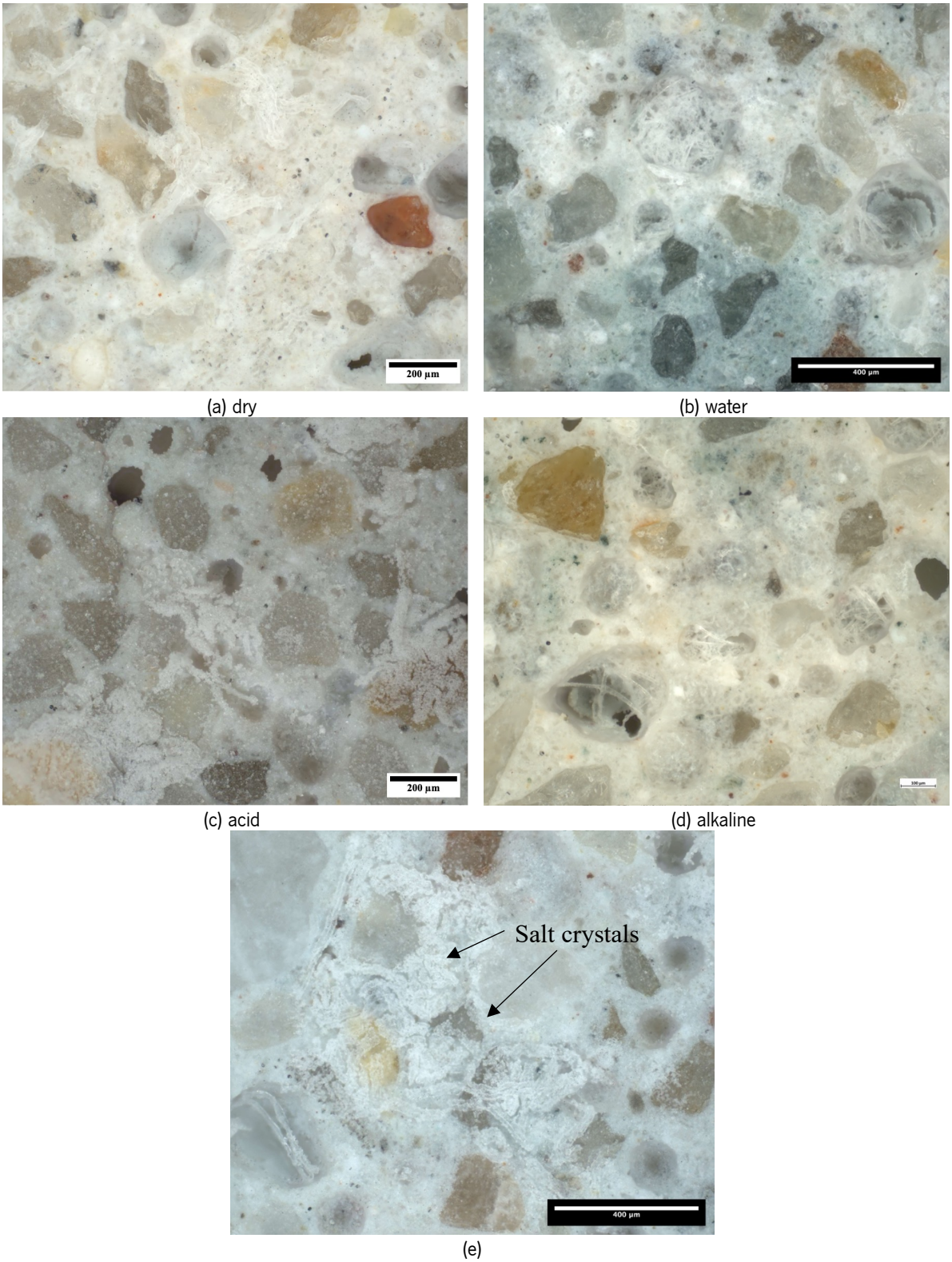

Figure 49 Optical microscopy images of mortar specimens after 5000 hours under different conditions: (a) dry condition, (b) water condition, (c) acidic exposure, (d) alkaline exposure, and (e) saline exposure.

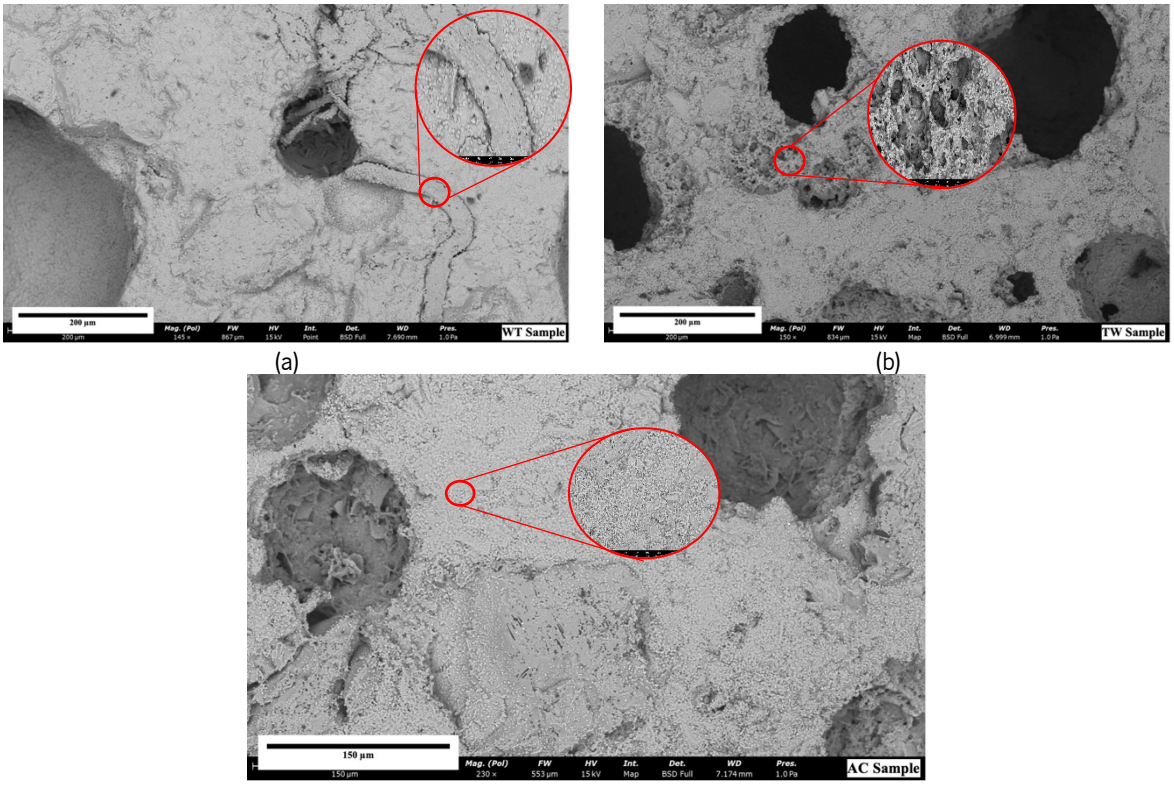

Figure 50 SEM micrographs of mortar samples under different exposure conditions: (a) dry condition, (b) water condition, and (c) acidic exposure.

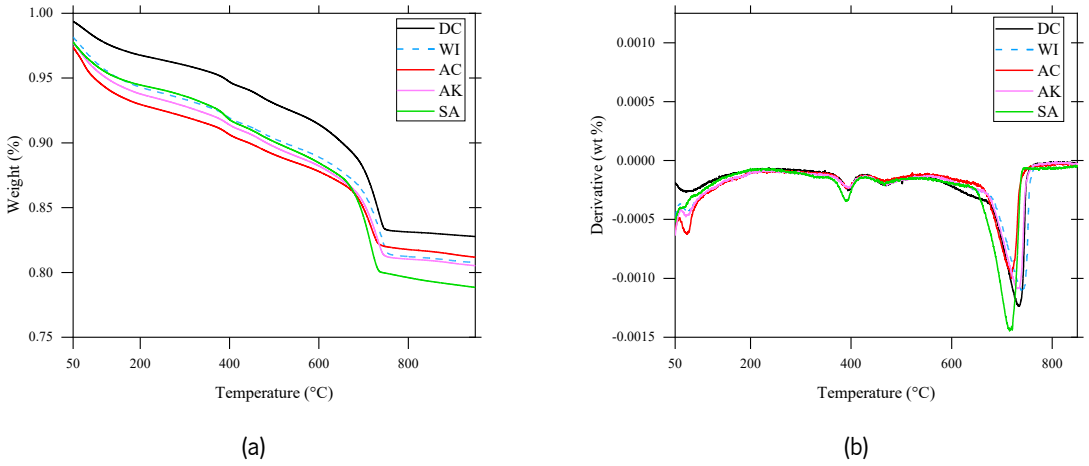

Figure 51 TGA analysis of mortar samples aged under different environmental exposures: (a) weight loss versus temperature; (b) derivative weight loss versus temperature for dry condition, water condition, acidic exposure, alkaline exposure, and saline exposure.

XRF results (Table 7) confirmed the predominance of SiO_2 and CaO, associated with quartz aggregate and hydrated lime phases, respectively. Interestingly, the WI sample showed an unexpectedly high CaO content. However, this anomaly is likely an artifact of fused bead preparation, as it was not supported by a corresponding increase in loss on ignition (LOI), which would otherwise suggest greater $CaCO_3$ content. The similarity in LOI values across the two conditions suggests comparable levels of carbonation, with slight differences potentially related to differences in pore saturation and leaching.

Table 7 XRF elemental composition of mortar samples subjected to different environmental exposures: dry condition, water condition, acidic exposure, alkaline exposure, and saline exposure.

Compound	WT (%)	TW (%)	AC (%)	AK (%)	SA (%)
SiO2	47,93	34,55	47,81	46,24	46,19
CaO	24,68	37,42	22,48	25,00	24,76
Al2O3	5,35	2,98	6,49	4,67	5,09
MgO	1,87	1,29	1,84	1,97	2,20
Fe2O3	0,81	2,14	0,75	0,77	0,55
SO3	0,69	0,69	1,01	0,63	0,59
K2O	0,63	0,75	0,81	0,71	0,65
TiO2	0,22	0,73	0,23	0,27	0,22
In2O3	0,19	0,00	0,17	0,00	0,00
ZrO2	0,14	0,43	0,14	0,15	0,13
Cr2O3	0,08	0,18	0,06	0,05	0,02
PdO	0,07	0,00	0,05	0,00	0,00
MnO	0,04	0,11	0,05	0,05	0,04
SrO	0,04	0,12	0,04	0,04	0,04
CuO	0,00	0,01	0,00	0,00	0,00
ZnO	0,00	0,01	0,00	0,00	0,00
LOI	17,27	18,59	18,08	19,45	19,51

Collectively, these results demonstrate that while both DC and WI environments maintain the mineralogical stability of lime-based mortar, differences in mechanical performance arise from the interplay of hydration, carbonation, and leaching phenomena. Dry conditions favor carbonation and progressive matrix densification, while water condition supports early hydration but leads to calcium loss and microstructural weakening over extended durations. These findings establish a robust baseline for assessing the additional impact of acidic, saline, and alkaline environments discussed in subsequent sections.

6.6.1.2 Effect of acidic condition

The exposure of mortar specimens to AC environments produced distinct trends in mechanical degradation and mineralogical transformation, particularly at longer durations. The mechanical performance, as shown in the compressive, flexural, and elastic modulus results (Figure 52), revealed a characteristic peak in all three properties around 3000 hours of exposure, followed by a marked decline at 5000 hours. This behavior contrasts with the steady gains observed under dry conditions and the less pronounced drop in performance under water condition. The initial increase in strength may be attributed to continued hydration and carbonation processes in the early exposure stages, while the subsequent deterioration is likely the result of sulfate-induced damage mechanisms, most notably the formation of expansive gypsum phases [292].

The compressive strength under acidic exposure demonstrated a trend similar to that of water condition, with comparable values up to 3000 hours, but a steeper decline thereafter. The flexural strength followed a similar trajectory, maintaining a near-linear increase until 3000 hours before plateauing. Unlike the water-immersed samples, however, the AC specimens did not exhibit an initial strength loss, suggesting that the acidic environment may have initially promoted densification through hydration, before sulfate accumulation led to microstructural weakening. The elastic modulus also showed a peak at 3000 hours, consistent with the interpretation that a more compact matrix was initially formed before the onset of chemical degradation. Microstructural and mineralogical observations further support this interpretation. Optical microscopy (Figure 49c) indicated the presence of newly formed white crystalline deposits in the AC specimens, which were not observed in water-immersed counterparts.

These were interpreted as gypsum or other sulfate compounds formed through the reaction between sulfuric acid and calcite phases in the mortar. This is corroborated by the XRD patterns (Figure 48), which, although similar across environments in terms of dominant phases (quartz and calcite), show distinct gypsum peaks in the AC sample [293]. The presence of gypsum, a softer phase than calcite has important implications for long-term mechanical integrity, as its formation is typically associated with volumetric expansion and microcrack propagation.

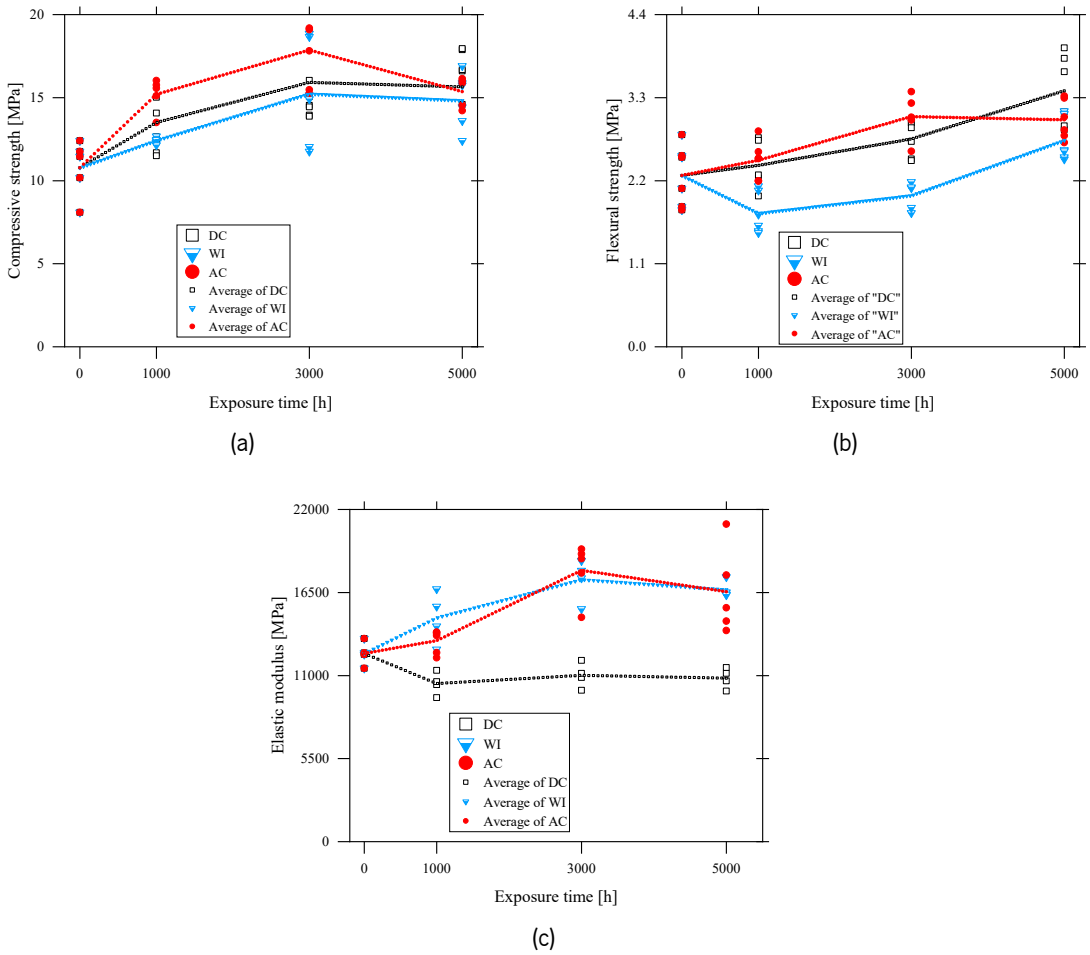

Figure 52 Mechanical properties of mortars under increasing aging exposure time- effect of acidic environment: (a) compressive strength; (b) flexural strength; (c) elastic modulus

SEM imaging (Figure 50) revealed a high overall porosity in the mortar, with no abrupt morphological differences between environments. However, the AC sample displayed poor fiber-matrix adhesion, which may have contributed to the deterioration of flexural performance by reducing the effectiveness of fiber bridging across microcracks [281]. The short fibers visible in the SEM images, while not structural textiles, may still influence local crack arrest mechanisms and serve as indicators of matrix-fiber interaction quality. The XRF analysis (Table 7) identified a slightly elevated SO_3 content in the AC samples, consistent with the incorporation of sulfate species, though the values were lower than expected. This is likely due to thermal decomposition of sulfates during fused bead preparation at high temperatures, a known limitation of XRF analysis under such conditions. Nonetheless, the data align with the mineralogical observations from XRD and the thermal behavior from TGA. TGA and DTG analysis (Figure 51) further confirmed the presence of gypsum in the AC samples. A mass loss peak near 100°C, absent in the DC and WI conditions, was associated with dehydration of $CaSO_4 \cdot 2H_2O$. Additional

decomposition events at 400°C and above 600°C corresponded to portlandite and calcite phases, respectively. The lower peak intensities in the AC group beyond 3000 hours suggest partial decomposition or transformation of the mortar's calcium phases due to acid attack, further supporting the interpretation of chemical degradation through gypsum crystallization [294]. Generally, acidic aging, in mortar was found to initially enhance the mechanical performance of the mortar, likely through hydration-induced matrix densification. However, beyond 3000 hours, the aggressive chemical environment facilitated the accumulation of sulfates and formation of expansive gypsum phases, which led to strength deterioration and stiffness reduction. These findings are supported by the mechanical test results, microstructural observations, and mineralogical data, and collectively point to gypsum-related decay as the dominant degradation mechanism in acidic environments.

6.6.1.3 Effect of alkaline condition

Exposure of the mortar to alkaline environments produced a distinct response in mechanical behavior, primarily governed by the activation of pozzolanic reactions and modification of hydration kinetics. As shown in Figure 53, the compressive strength of specimens immersed in alkaline solution increased significantly during the early stages of exposure, with a peak at 1000 hours. This early strength enhancement was greater than that observed for dry or water-immersed specimens over the same interval, suggesting that the elevated pH environment facilitated rapid formation of hydration products. Between 1000 and 3000 hours, strength gains persisted at a reduced rate, eventually reaching values comparable to the dry condition by 5000 hours. The enhanced mechanical performance in early-age alkaline exposure is attributed to accelerated formation of calcium-alumino-silicate hydrate ($C-A-S-H$) gels. The lime-based mortar used in this study contained hydraulic constituents such as $Ca(OH)_2$, calcite, and dicalcium silicate (C_2S), along with pozzolanic materials and silicate aggregates. In the alkaline medium, the dissolution of $Ca(OH)_2$ was limited, maintaining a high local calcium concentration that favored the pozzolanic reaction. This led to the rapid generation of $C-A-S-H$, which contributed to matrix densification and mechanical strengthening [295–297].

Flexural strength followed a similar trace (Figure 53b), reaching elevated values at early aging stages and maintaining relatively stable performance through to 5000 hours. This stability contrasts with the slight late-age reduction observed in compressive strength, likely due to fiber-matrix bond degradation. The alkaline solution may have induced mild chemical attack on the short fibers present in the mortar, thereby compromising their role in microcrack bridging and toughness enhancement. Nevertheless, no significant loss of flexural stiffness was observed, as evidenced by the elastic modulus trends in Figure 53c, which showed a consistent increase throughout the exposure period. This observation indicates that, at the macro-scale, the matrix retained adequate structural integrity.

Mineralogical transformations under alkaline conditions were investigated using TGA analysis, as illustrated in Figure 51. Compared to dry-stored specimens, alkaline-aged samples exhibited higher mass loss in the temperature range associated with the decomposition of $C-A-S-H$ gels (~70–100°C), suggesting the formation of additional hydrated phases [298]. At higher temperatures (~800°C), the dry-stored sample showed slightly greater weight loss due to the decomposition of carbonates, indicating more extensive carbonation relative to the alkaline-aged counterpart. These findings confirm that pozzolanic reactions dominated the early-stage matrix evolution in alkaline exposure, while carbonation was more prevalent in the dry condition [287,296]. The interplay between hydration, pozzolanic activity, and carbonation was further supported by observations of strength trends. The plateau in compressive and flexural strength after 3000 hours, despite a continued increase in stiffness, suggests a stabilization of chemical activity. This may be explained by the saturation of available reactive phases and potential microstructural weakening at the fiber-matrix interface due to persistent high pH. In contrast to the monotonic increase observed in the dry condition, and the strength decline noted under acidic or saline

exposure, alkaline aging initially promoted mechanical enhancement, followed by performance stabilization [11,299–303]. Overall, the alkaline condition demonstrated a beneficial influence on early mechanical properties due to accelerated pozzolanic reactions and hydration. However, its long-term effects appear to stabilize, potentially limited by fiber degradation and the exhaustion of reactive constituents. When compared to the dry and water-condition environments, the alkaline medium offered superior early-age performance, with comparable or slightly reduced strength by the final aging stage. These observations suggest that while alkaline environments may not induce aggressive deterioration, their capacity to improve long-term performance may be constrained by microstructural stability and fiber durability.

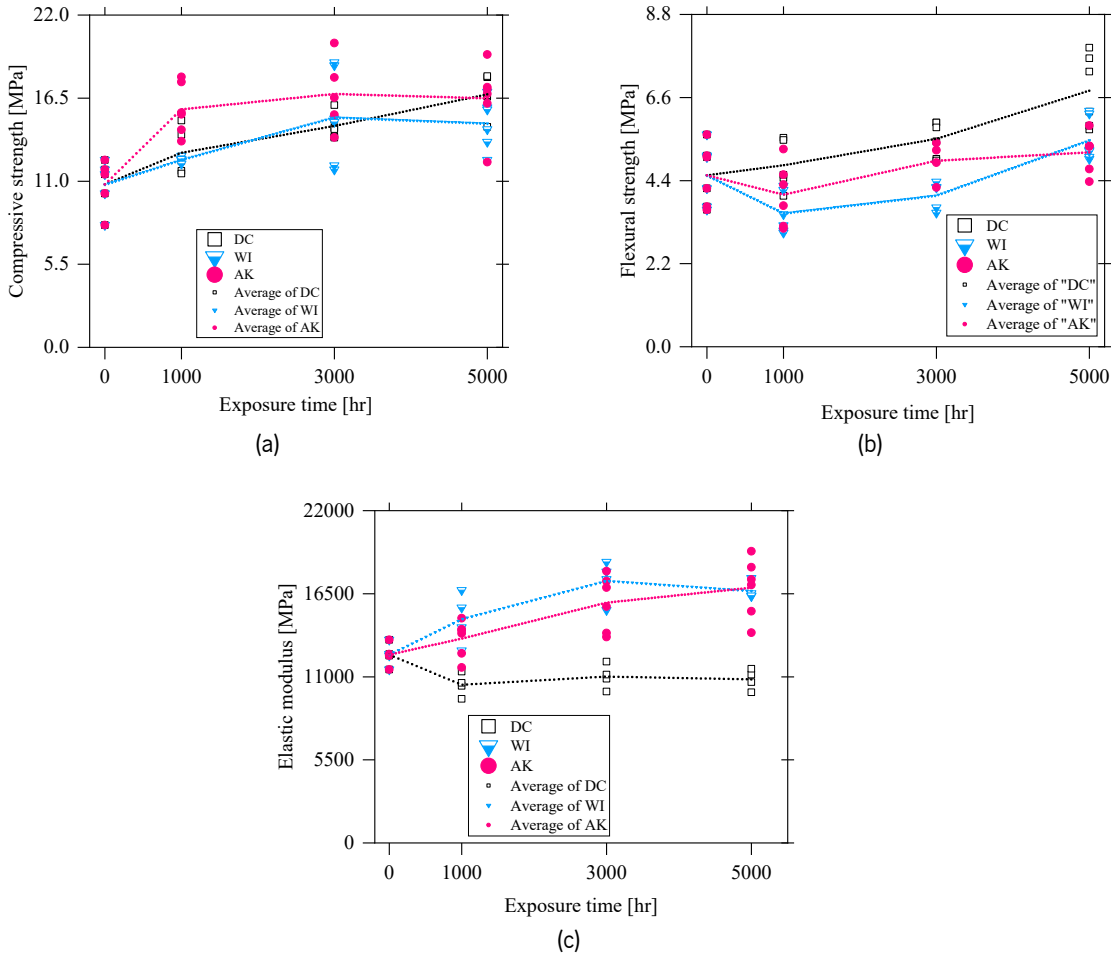

Figure 53 Mechanical characteristics of mortars exposed to three aging environments – effect of alkaline exposure: (a) compressive strength; (b) flexural strength; (c) elastic modulus.

6.6.1.4 Effect of saline condition

The exposure of the lime-based mortar to a saline environment led to a distinct pattern in mechanical performance, initially characterized by enhancement followed by deterioration at extended durations. As shown in Figure 54a, compressive strength progressively increased up to 3000 hours of immersion, with a noticeable decline observed between 3000 and 5000 hours. This trend, while somewhat mirrored by specimens stored under water condition, was more pronounced under saline aging. The early-stage strength improvement can be attributed to the synergistic action of hydration and limited pozzolanic reactivity, which were likely accelerated in the presence of chloride ions [304]. These ions are known to promote early-age cement hydration reactions, particularly affecting the Portland cement constituents within the mixed binder system [305].

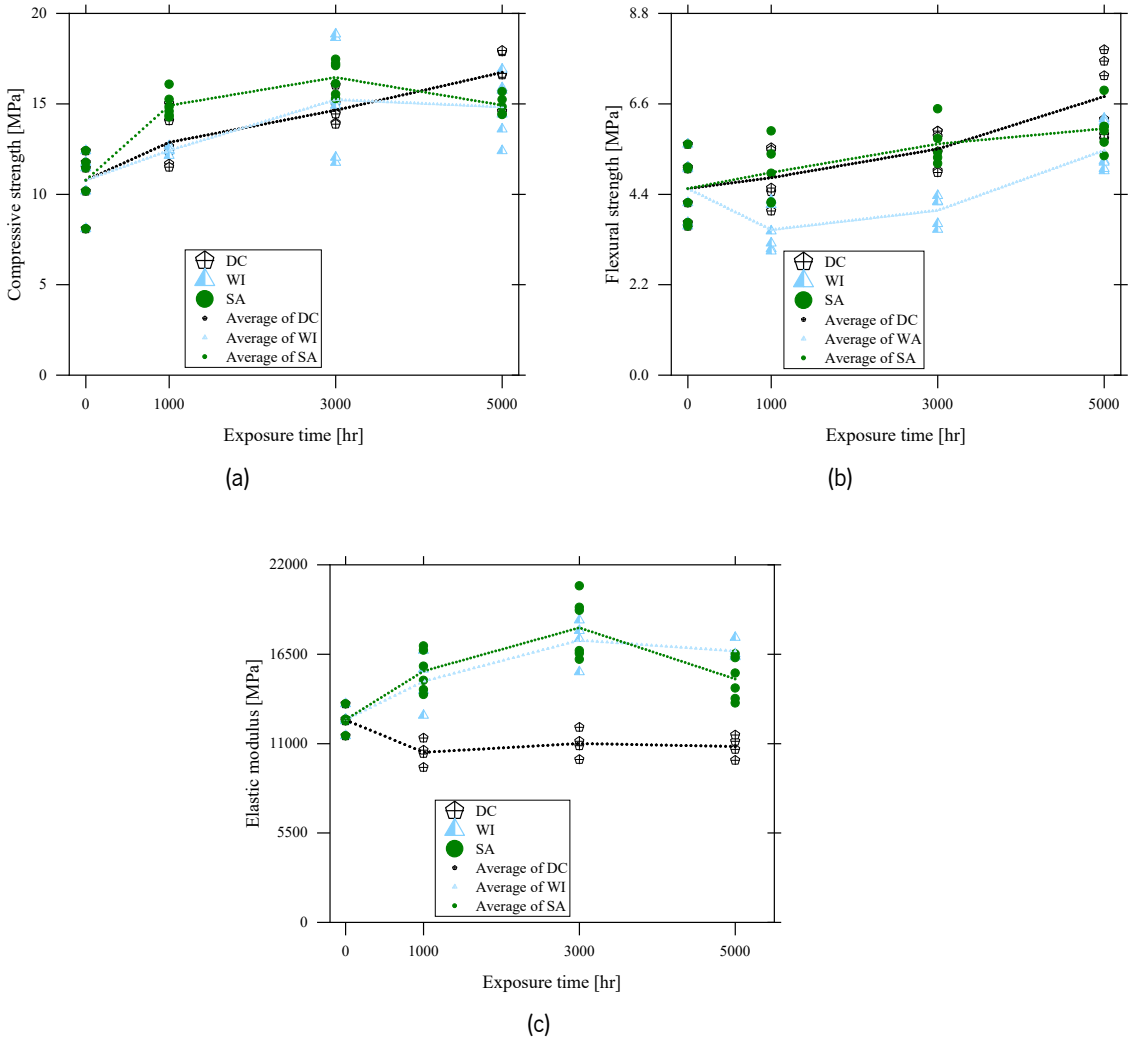

Figure 54 Mechanical properties of mortars as a function of aging exposure time- effect of saline environment: (a) compressive strength; (b) flexural strength; (c) elastic modulus.

The flexural strength data (Figure 54b) followed a comparable evolution. A marked increase was observed at early ages, particularly within the first 1000 hours of exposure, which may be linked to the combined effects of continuous hydration and densification of the matrix microstructure. However, flexural strength began to decline after 3000 hours. This performance decay is presumed to result from progressive chloride-induced degradation mechanisms, such as the leaching of calcium-bearing phases, a decrease in pH, and the precipitation of salts within the pore structure. These factors likely disrupted the fiber-matrix interface, reducing the contribution of short fibers in bridging cracks and resisting flexural loads [159,291]. This hypothesis is substantiated by the elastic modulus results (Figure 54c), which demonstrated an initial increase in stiffness, followed by a plateau and slight reduction after 3000 hours. This mechanical response suggests that the saline exposure initially enhanced the overall packing density and matrix continuity. However, prolonged immersion likely triggered ionic mobility and microstructural instability, undermining stiffness and strength. While the DC specimens exhibited a steady increase in stiffness and strength, the saline-aged mortars revealed a more complex degradation trajectory, influenced by competing hydration, leaching, and salt crystallization mechanisms.

XRD analysis, as depicted in Figure 8, revealed the presence of crystalline gypsum in the saline-aged samples after 5000 hours of exposure. The identification of gypsum, a softer and expansive phase,

indicates the formation of salt-related products within the matrix. Although not predominant at early ages, this phase was clearly detectable at extended durations, marking the onset of secondary degradation due to ionic exchange between the matrix and saline solution. These findings are corroborated by the optical microscopy results shown in Figure 9. While WI showed relatively clean pore structures, saline-aged samples exhibited white salt crystals embedded within the matrix, particularly after 5000 hours. The localized crystallization of salts within the pore network suggests ionic accumulation and subsequent precipitation under saturated conditions. This effect not only promotes pore blockage but also increases internal stress concentrations, potentially initiating microcracking and reducing the mechanical capacity of the mortar over time. Overall, the exposure to saline environments induced a two-phase behavior in the mortar. During early exposure, mechanical properties improved due to enhanced hydration and microstructural compaction. However, the long-term presence of chloride ions led to leaching, gypsum formation, and pore crystallization, which collectively contributed to degradation. Compared to the reference conditions of dry storage and water condition, the saline-aged mortars showed higher early-age mechanical performance but poorer long-term durability, underscoring the need for careful assessment of TRM systems exposed to marine or deicing salt environments.

6.6.2 Pull-out behavior

In the context of bond evaluation of the TRM, a series of pull-out tests were conducted to evaluate the bond degradation in specimens incorporating glass and basalt fiber textiles. The resulting data allow a comparative assessment of environmental impacts on interfacial performance, with specific emphasis on chemical compatibility, fiber degradation, and changes in matrix integrity. The bond performance was characterized by analyzing key parameters derived from the load-displacement curves of the pull-out tests. These include the peak load, which indicates the maximum interfacial resistance before failure; the debonding energy, defined as the area under the load-displacement curve up to the peak load, representing the energy required to initiate fiber-matrix separation; and the pull-out energy, which corresponds to the energy dissipated through post-peak fiber sliding until complete disengagement. These parameters collectively describe the efficiency and robustness of the load-transfer mechanism across the fiber-mortar interface. By integrating mechanical and visual assessments, the pull-out results provide insight into the durability of the fiber–matrix interface under realistic aging scenarios. The comparative analysis of glass and basalt-based TRM systems under each exposure condition enables a deeper understanding of fiber-specific vulnerabilities and matrix interactions, which are critical for optimizing composite design and predicting service-life performance in aggressive environments.

6.6.2.1 Glass-based TRM

6.6.2.1.1 Effect of dry and water condition

The pull-out performance of glass-based TRM systems under DC and WI conditions demonstrates a time-dependent evolution in fiber–matrix interaction, as illustrated in Figure 55-Figure 57. These two environments, consistent with those identified as reference baselines in previous sections, represent contrasting aging mechanisms: carbonation-induced matrix densification in dry conditions and hydration-driven mineralogical evolution under water condition. The bond behavior was evaluated using four key parameters: average load–slip response, peak load, debonding energy, and pull-out energy. The effective bond length adopted in the pull-out tests was approximately 50 mm, in accordance with established values for both glass and basalt yarns [11,263]. Displacement during testing was tracked using LVDTs to ensure accurate deformation measurements.

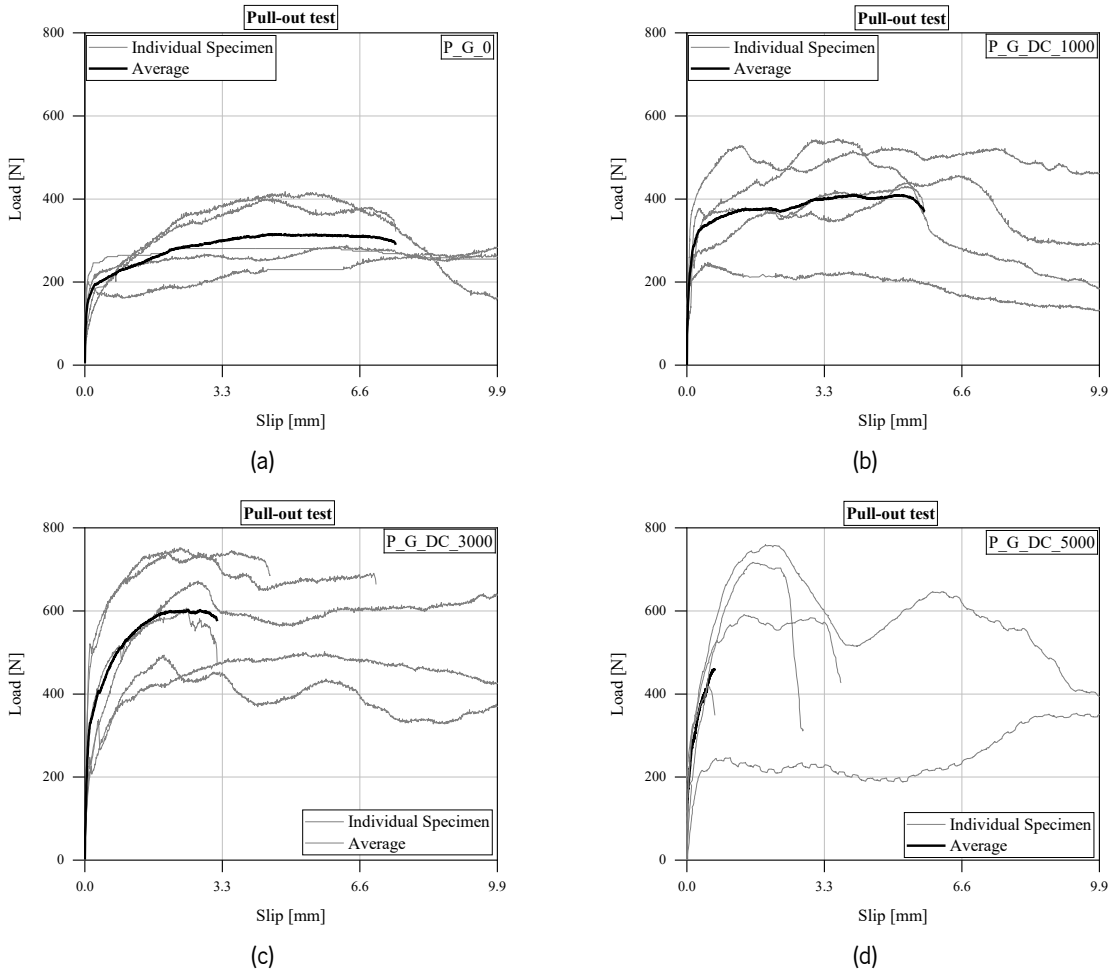

Figure 55 Load-slip curves of the pull-out test for the glass fiber in the DC environment, showing each individual specimen and the average curve for each group: (a) P_G_0; (b) P_G_DC_1000; (c) P_G_DC_3000; (d) P_G_DC_5000

Figure 55 and Figure 56 presents the individual load–slip curves for all tested specimens in each group, where individual responses are shown in gray and the group average in black. These curves highlight the typical three-phase response: an initial linear segment associated with elastic interfacial behavior, a nonlinear segment reflecting slip-hardening or softening due to progressive friction and microcracking, and a post-peak sliding stage governed by frictional dissipation along the fiber–mortar interface [263]. The presence of these stages across nearly all specimens emphasizes the consistency in interface mechanics despite aging. As shown in Figure 57a, both DC and WI exposures led to initial enhancements in bond strength, dry conditions promoted matrix densification via carbonation, whereas water condition encouraged further $C-S-H$ formation. Across all tests, the dominant failure mode was fiber slippage, and no systematic increase in fiber rupture was observed with prolonged aging, indicating that the fiber–matrix interface retained sufficient mechanical integrity under both exposure conditions.

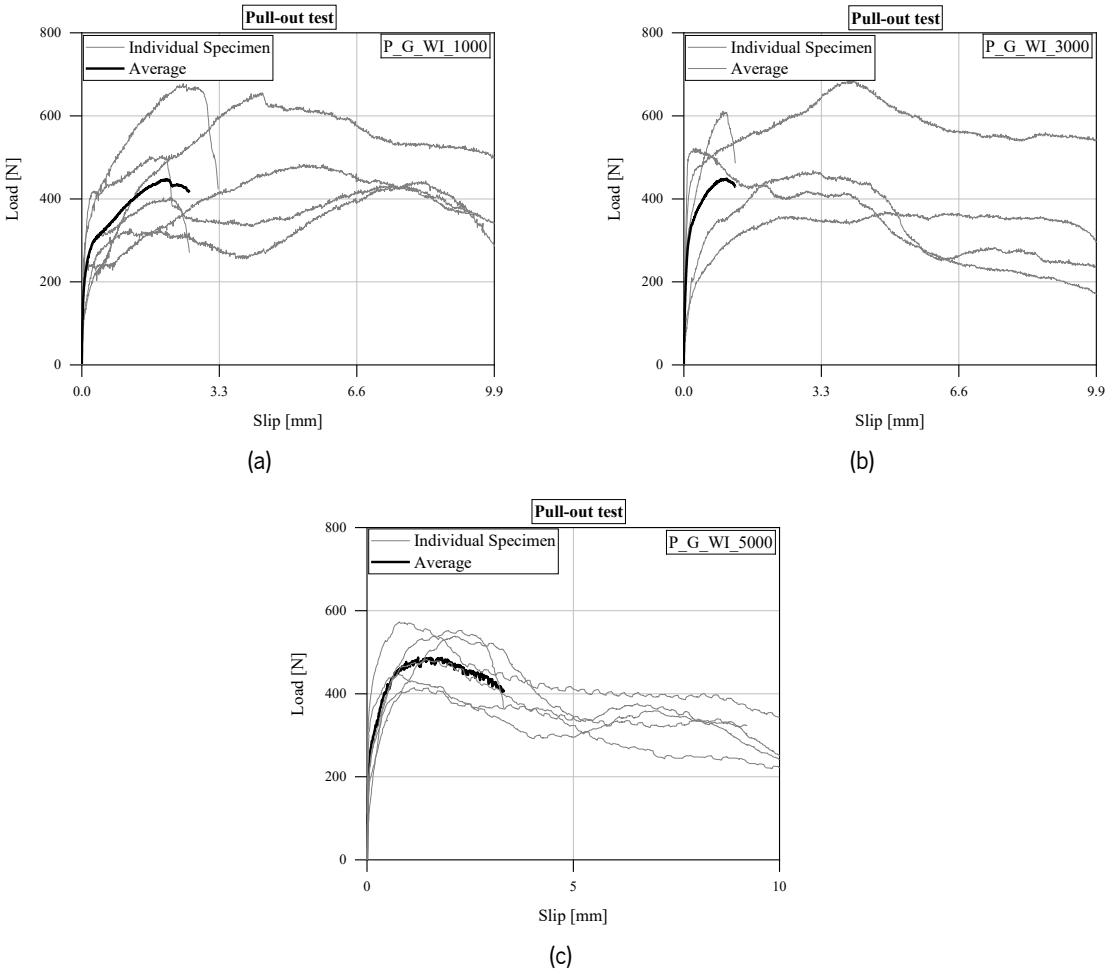

Figure 56 Load-slip curves of the pull-out test for the glass fiber in the WI environment, showing each individual specimen and the average curve for each group: (a) P_G_WI_1000; (b) P_G_WI_3000; (c) P_G_WI_5000.

The observed peak load evolution (Figure 57b) further supports this interpretation. In DC conditions, an increase in peak load was noted up to 3000 hours of exposure, after which stabilization occurred. This suggests that carbonation, which was confirmed through the mineralogical and TGA analysis in Section 6.6.1, enhanced the matrix density and surface hardness, thus improving interfacial grip. However, the plateau beyond 3000 hours implies a saturation of this effect, where further carbonation does not significantly alter the interfacial friction or bonding capacity. For the WI samples, a similar increase in peak load was observed until 3000 hours, attributed primarily to continued hydration of reactive phases such as dicalcium silicate and the formation of $C-S-H$ gels. The decline in peak load at 5000 hours suggests that prolonged water exposure may have led to calcium leaching and weakening of the interfacial bond, as previously observed in the mechanical strength degradation discussed in Section 5.6.1. The variation in debonding energy (Figure 57c) reflects the energy required to initiate the separation of the yarn from the matrix. In dry conditions, debonding energy increased significantly up to 3000 hours, mirroring the trend observed in the peak load and corresponding to carbonation-enhanced surface roughness and mechanical interlock. A slight decrease at 5000 hours indicates the onset of interfacial degradation, possibly due to microcracking or embrittlement of the matrix surrounding the fibers. In water-immersed specimens, debonding energy also peaked at 3000 hours and remained relatively stable afterward, suggesting that the beneficial effects of hydration on matrix integrity and interfacial bonding were limited by progressive saturation and potential deterioration of fiber-matrix adhesion over time.

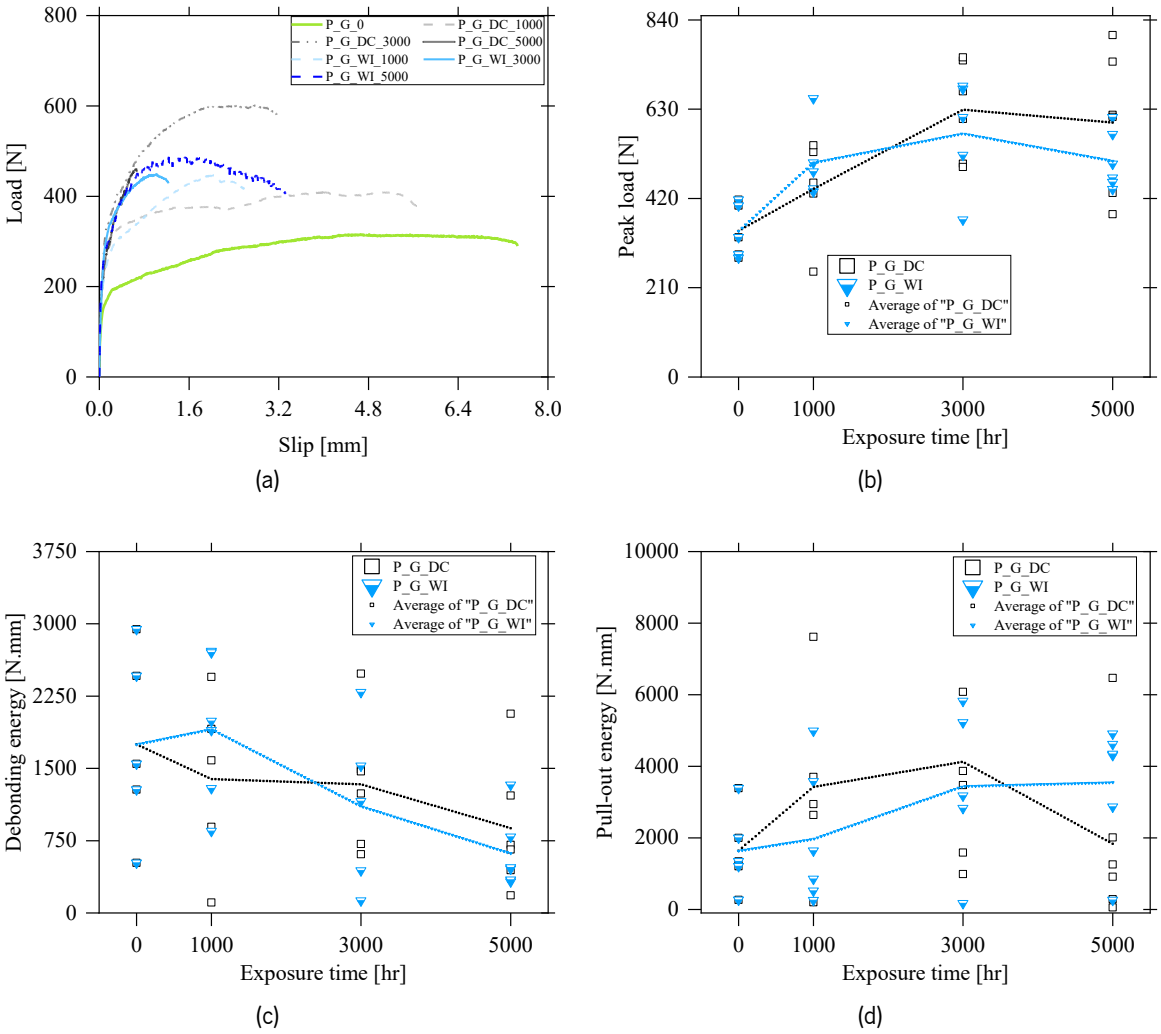

Figure 57 Pull-out performance of glass-based TRM under DC and WI conditions: (a) average load–slip response at the loaded end; (b) peak load; (c) debonding energy; (d) pull-out energy.

The pull-out energy (Figure 57c d), which accounts for the total work done during the complete extraction of the fiber, including post-peak sliding is especially sensitive to changes in interfacial friction and matrix ductility. Under DC conditions, pull-out energy showed a consistent increase until 3000 hours, aligning with the development of frictional resistance due to densification and improved matrix stiffness, also shown by previous research [281]. A marginal decline at 5000 hours suggests that while the matrix continues to strengthen, the energy dissipation capacity at the interface may be compromised by the reduced ability to deform plastically around the yarns. Water condition induced a similar pattern, with energy increasing up to 3000 hours due to progressive hydration, followed by a stabilization or slight drop associated with matrix saturation and leaching-induced weakening. These observations collectively highlight that both DC and WI environments promote interfacial bond enhancement up to a critical exposure time, beyond which chemical or microstructural degradation mechanisms begin to dominate. The failure modes further confirm the nature of the bond degradation observed during testing. Under both DC and WI exposures, the predominant failure mechanism was fiber slippage, with occasional partial ruptures noted. These observations suggest that the interfacial bond strength generally remained below the tensile capacity of the yarns throughout the test duration. This behavior contrasts with that observed in alkaline-aged specimens, where fiber rupture became more prevalent, indicating enhanced interfacial bonding. Overall, the pull-out response of glass-based TRM under dry and water condition conditions

exhibited a transient improvement in bond characteristics, which appeared to stabilize after 3000 hours and slightly decline with extended exposure. These findings highlight the significance of environmental control in TRM applications, particularly when glass fibers are used in lime-based composite systems.

6.6.2.1.2 Effect of acidic condition

The pull-out performance of glass-based TRM subjected to acidic exposure exhibited distinctive behavioral patterns in comparison to the reference environments. As shown in Figure 58, which presents both individual and average load–slip curves, the acidic condition induced a progressive degradation of interfacial bond behavior with increasing exposure duration. The individual curves clearly demonstrate variability in the response, yet consistently indicate a reduction in slip-hardening and bond stiffness over time. Across all acidic aging groups, fiber slippage was the predominant failure mode, suggesting that the interfacial bond strength remained lower than the tensile capacity of the yarns. However, instances of partial rupture were intermittently observed, particularly at intermediate exposure durations, potentially reflecting localized improvements in matrix–fiber adhesion.

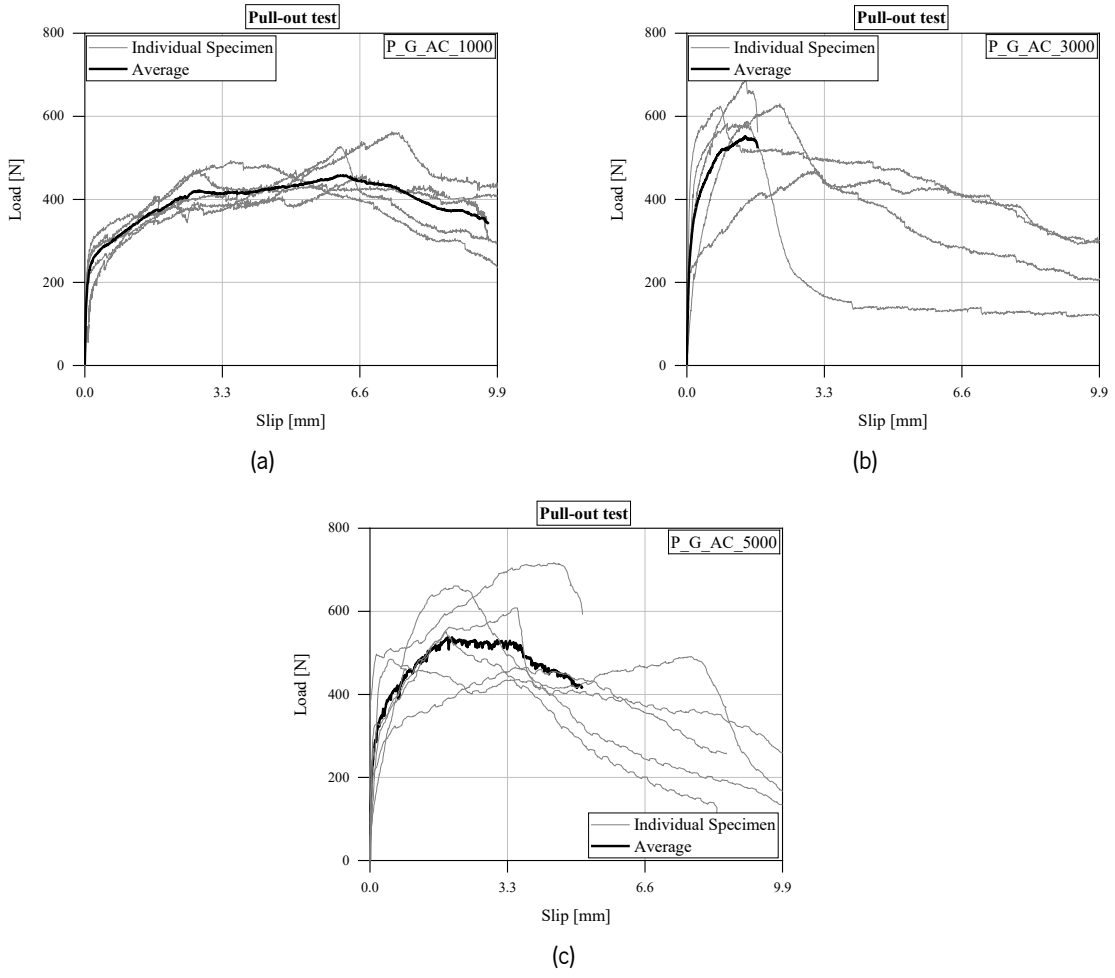

Figure 58 Load-slip curves of the pull-out test for the glass fiber in the AC environment, showing each individual specimen and the average curve for each group: (a) P_G_AC_1000; (b) P_G_AC_3000; (c) P_G_AC_5000.

At the 1000 hours of aging, the G_AC_1000 group exhibited a notably flattened load–slip response, with limited hardening and reduced interfacial stiffness compared to dry and water-immersed specimens. This trend is attributed to acid-induced matrix degradation mechanisms such as decalcification and sulfate attack. The formation of gypsum, as confirmed by XRD and TGA results (refer to Figure 48 and Figure 51), supports the interpretation of a chemically weakened ITZ [306]. Complementary observations

from optical microscopy and SEM further revealed matrix softening and microcracking, which are likely to contribute to premature debonding and increased slip deformation under tensile loading.

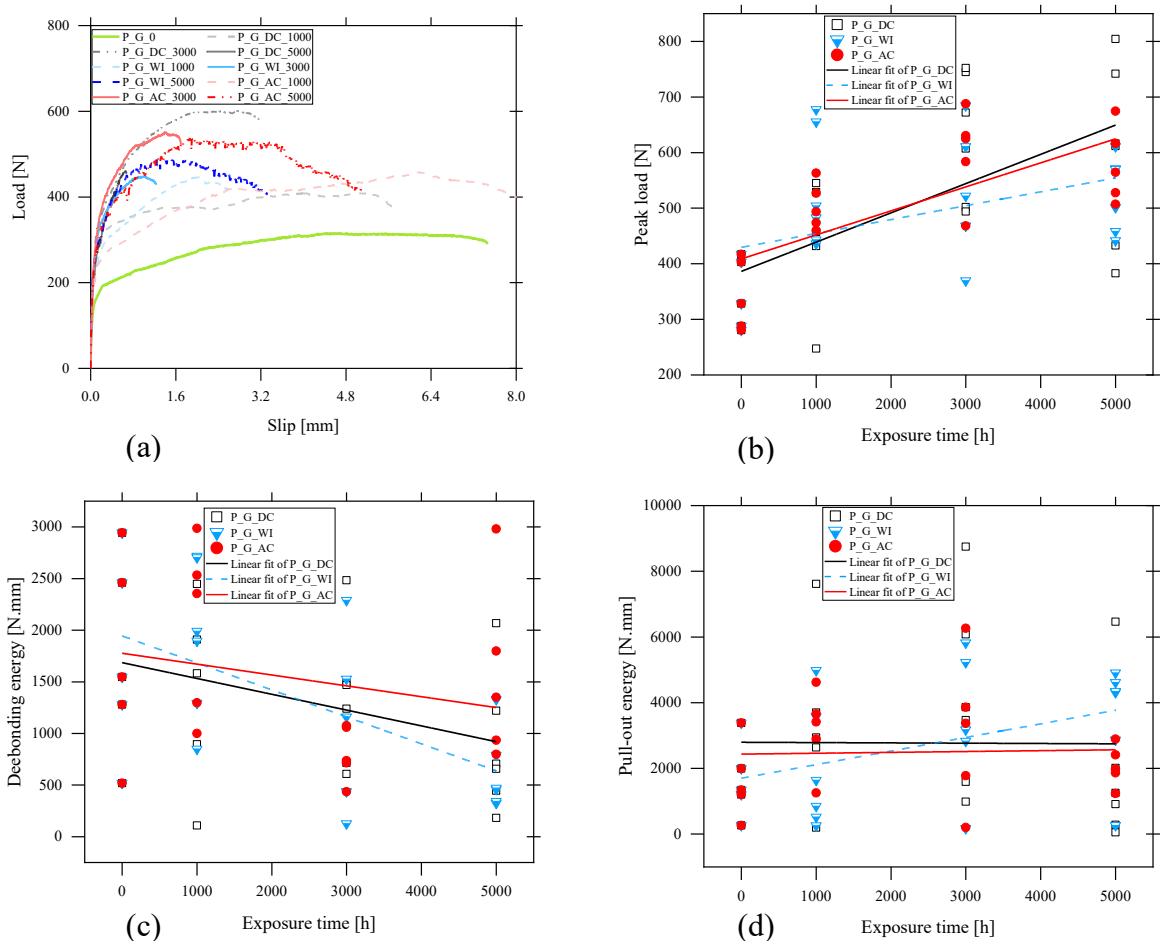

Figure 59 Pull-out parameters of single glass-made TRM under different environmental conditions — effect of acidic exposure: (a) average load–slip response at the loaded end; (b) peak load; (c) debonding energy; (d) pull-out energy.

At 3000 hours of acidic exposure, a partial recovery of the pull-out response was observed in the G_AC_3000 group. The increase in peak load relative to earlier exposure suggests that hydration and limited carbonation may have temporarily offset the progressive chemical degradation. This is in agreement with the concurrent mechanical strength results, which indicated a peak in compressive and flexural strength at this aging duration. Nevertheless, the diminished strain-hardening region and the relatively reduced post-peak energy dissipation still signal a weakening of the overall bond integrity. The interfacial bond, while temporarily enhanced, remained vulnerable to chemical shrinkage and further sulfate interaction, reducing its capacity for sustained energy dissipation during the sliding phase. At 5000 hours, the acidic deterioration mechanisms became more dominant, as evident in the G_AC_5000 group. The load-slip curve flattens significantly, with a diminished initial stiffness and suppressed hardening response, indicating a loss of both mechanical interlock and frictional resistance [137,270]. The peak load shows only a marginal improvement over earlier exposure but is lower than the corresponding value in the dry condition at the same exposure time. This reflects the balance between minor strength gains in the matrix and major bond deterioration at the fiber–mortar interface. The

observed reduction in pull-out energy at this stage suggests that the residual capacity for frictional sliding has also diminished, likely due to increased porosity, loss of cohesion, and microstructural disintegration.

Quantitative trends further substantiate these observations. As shown in Figure 59b, the peak load in acidic-aged specimens displays a slightly positive slope over time, though lower in magnitude compared to dry and water-immersed counterparts. More critically, Figure 59c demonstrates a pronounced reduction in debonding energy with increasing exposure time, particularly beyond 3000 hours. This trend implies that although the peak load may remain stable or slightly improve, the energy required to initiate interfacial failure progressively declines due to chemical weakening and softening effects. This decoupling of peak load and debonding energy behavior points to a fragile and deteriorated interface increasingly susceptible to early-stage failure. Finally, Figure 59d depicts the variation of pull-out energy with exposure time. Unlike the water-immersed specimens, which showed a positive trend, the pull-out energy in acidic-aged samples remained nearly constant with a slight downward trend, reflecting the compromised ability of the system to dissipate energy after peak load. This trend, combined with evidence from SEM and XRF analyses, underscores the role of interfacial degradation mechanisms, particularly gypsum formation, sulfate-induced swelling, and microcrack propagation in diminishing the durability and bond effectiveness of glass TRM systems under acidic environments. Collectively, these findings highlight the vulnerability of glass–mortar interfaces to long-term acid exposure, which must be addressed through material selection and protective strategies in aggressive service conditions.

6.6.2.1.3 Effect of alkaline condition

The alkaline environment induced a distinct evolution in the pull-out response of glass-based TRM, with a trend toward enhanced bond performance up to an intermediate exposure duration, followed by indications of interfacial deterioration. The average load–slip curves presented in Figure 60 illustrate this progression, showing that alkaline-aged specimens developed greater initial stiffness and improved post-peak stability compared to the reference environments. The response retained the characteristic triphasic behavior typical of TRM systems: an initial linear elastic stage, a slip-hardening segment, and a post-peak sliding plateau. These stages reflect the progressive engagement of frictional and mechanical interlock mechanisms at the mortar–fiber interface.

To provide a more complete view of the bond behavior, Figure 61 presents the individual load–slip curves alongside the average response for each exposure group. These curves clearly capture the variability among specimens and confirm the presence of the three-stage response in nearly all tests. The visual coherence between individual and average curves reinforces the reliability of the observed trends and supports the interpretation of enhanced bonding at specific aging durations. Failure mode analysis confirmed a transition in the mechanical behavior of the interface. Unlike the predominantly fiber slippage observed under dry and water-immersed conditions, specimens subjected to 3000 hours of alkaline exposure exhibited complete fiber rupture across all samples, indicating a bond strength exceeding the tensile capacity of the yarn. For the 1000- and 5000-hour exposures, partial decline to fiber slippage was recorded in some specimens, suggesting that the bond improvement was transient and potentially reversible as a function of prolonged exposure. This behavior may reflect the evolution of the interfacial chemistry, where initial pozzolanic reactivity enhances matrix cohesion, but long-term leaching or secondary phase formation could weaken the fiber–matrix interaction.

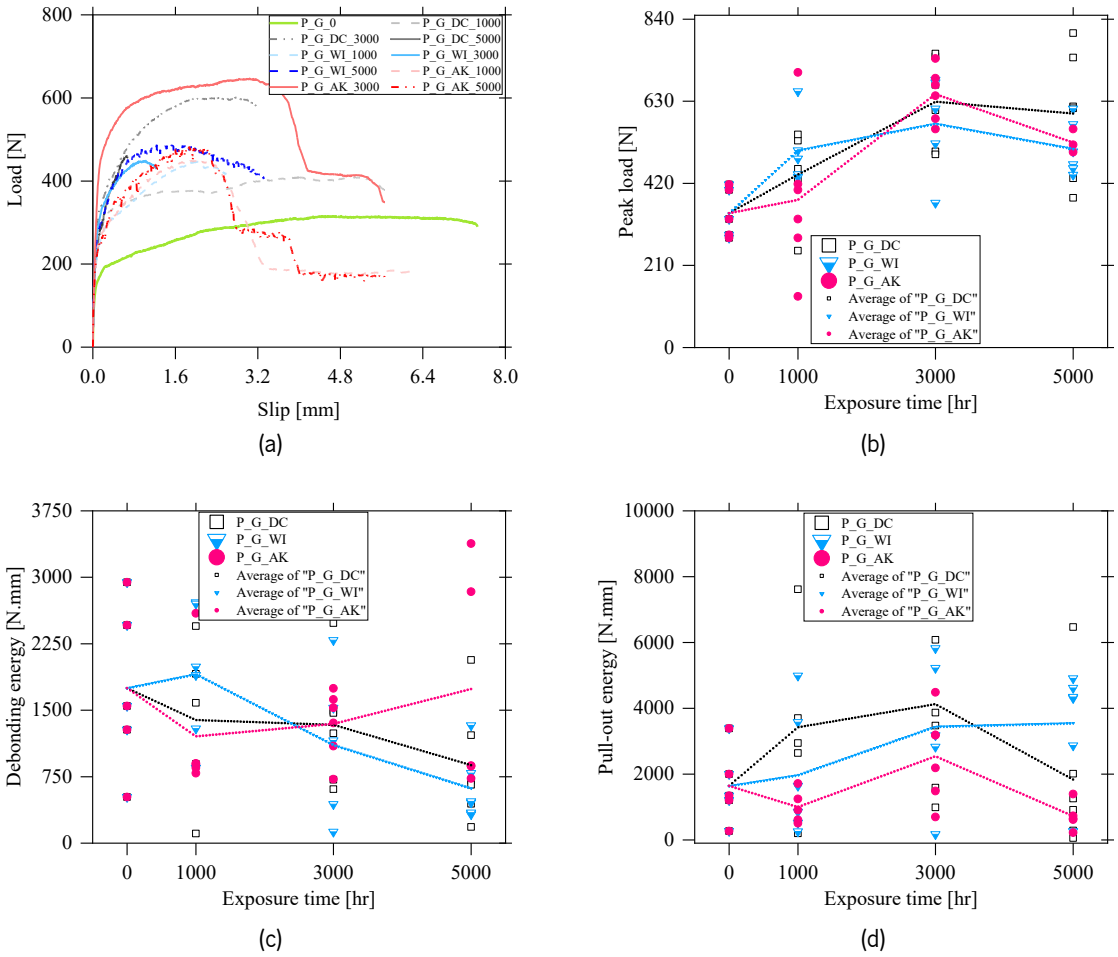

Figure 60 Pull-out parameters of single TRM glass yarn in different environments- effect of alkaline environment: (a) average load-slip response at the loaded end; (b) peak load; (c) debonding energy; (d) pull-out energy.

The quantitative analysis of the peak load, shown in Figure 60b, confirms the superior performance at 3000 hours, where the maximum bond strength was achieved. This aligns with the peak observed in compressive and flexural strength tests, attributed to enhanced hydration and pozzolanic reactivity fostered by the alkaline solution. The elevated pH environment is known to promote the formation of additional $C-A-S-H$ gels, which contribute to a denser microstructure and improved matrix continuity. However, the decrease in peak load at 5000 hours suggests a threshold beyond which continued exposure leads to adverse effects, such as leaching of alkali-soluble phases or the formation of expansive byproducts that compromise bond integrity. Debonding energy, as presented in Figure 60c, exhibits a consistent trend with the peak load results. A maximum value is recorded at 3000 hours, reflecting the highest energy demand to initiate interfacial failure. This enhancement is consistent with the formation of a chemically stable and mechanically interlocked interface, reinforced by the products of ongoing pozzolanic reactions. The subsequent reduction at 5000 hours implies a weakening of the bond, potentially driven by microcracking, reduced frictional resistance, or chemical shrinkage. These effects may disrupt the continuity of the ITZ, reducing its ability to sustain increasing load transfer at the onset of slippage.

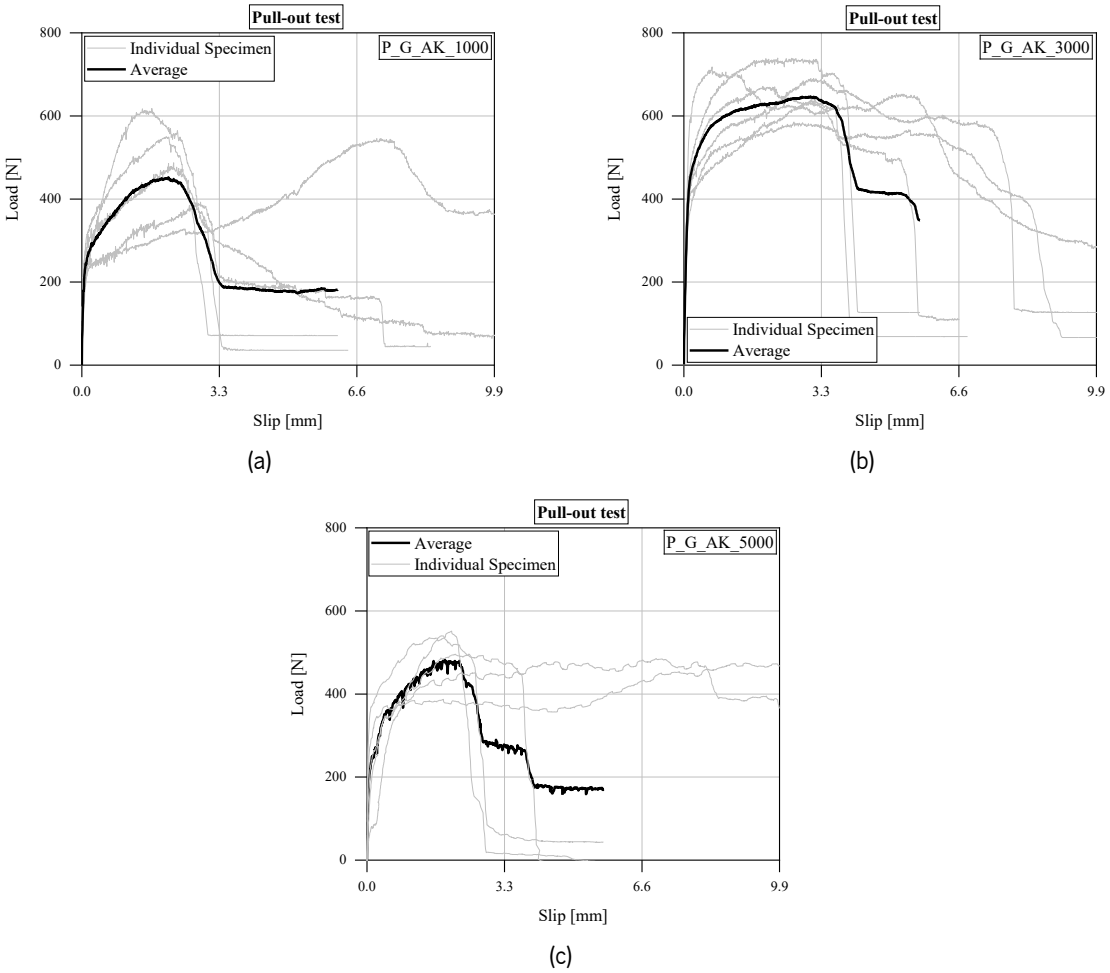

Figure 61 Load-slip curves of the pull-out test for the glass fiber in the AK environment, showing each individual specimen and the average curve for each group: (a) P_G_AK_1000; (b) P_G_AK_3000; (c) P_G_AK_5000.

Similarly, Figure 60d indicates that pull-out energy, representing the area under the load–slip curve after peak load, peaked at 3000 hours and declined thereafter. This parameter is particularly sensitive to the integrity and frictional behavior of the fiber to mortar interface during the post-peak phase. The reduced pull-out energy at 5000 hours may result from a combination of microstructural weakening and the onset of fiber slippage, as also reflected in the change in failure modes. While the matrix properties may remain mechanically sound, as suggested by concurrent strength testing, the interfacial degradation diminishes the system's ability to dissipate energy through sustained frictional interaction. Altogether, the alkaline environment demonstrated a favorable influence on the glass TRM bond performance up to an intermediate duration of exposure, with significant gains in peak load, debonding energy, and total pull-out energy at 3000 hours. These findings are consistent with the simultaneous mineralogical observations of pozzolanic activity and matrix densification. However, prolonged exposure beyond this critical window appears detrimental to the durability of the interfacial bond, emphasizing the need for optimized exposure durations and material compatibility in alkaline-prone service conditions.

6.6.2.1.4 Effect of saline condition

The influence of saline exposure on the pull-out response of glass-based TRM systems exhibited a non-linear evolution shaped by the interplay between early hydration enhancement and long-term interfacial degradation. The detailed behavior of individual specimens under each aging duration is presented in Figure 62, which illustrates the full set of load–slip curves along with the corresponding average response. These curves reveal distinct triphasic behavior and provide insights into variability

within the experimental groups, confirming the presence of three main stages: initial linear bonding, slip-hardening, and post-peak frictional sliding. The average load–slip curves depicted in Figure 63 further highlight the influence of exposure duration. At 1000 hours, the TRM specimens exhibited reduced pre-peak stiffness relative to the dry and water-immersed references, indicating early-stage weakening of the mortar–fiber bond. Nonetheless, a moderately extended post-peak region was recorded, which may be attributed to short-term benefits from chloride-induced hydration that temporarily enhanced interfacial ductility and frictional resistance. By 3000 hours, a significant improvement was observed in both pre-peak and post-peak response, suggesting favorable contributions from continued hydration and possible pozzolanic effects stimulated by chloride ions.

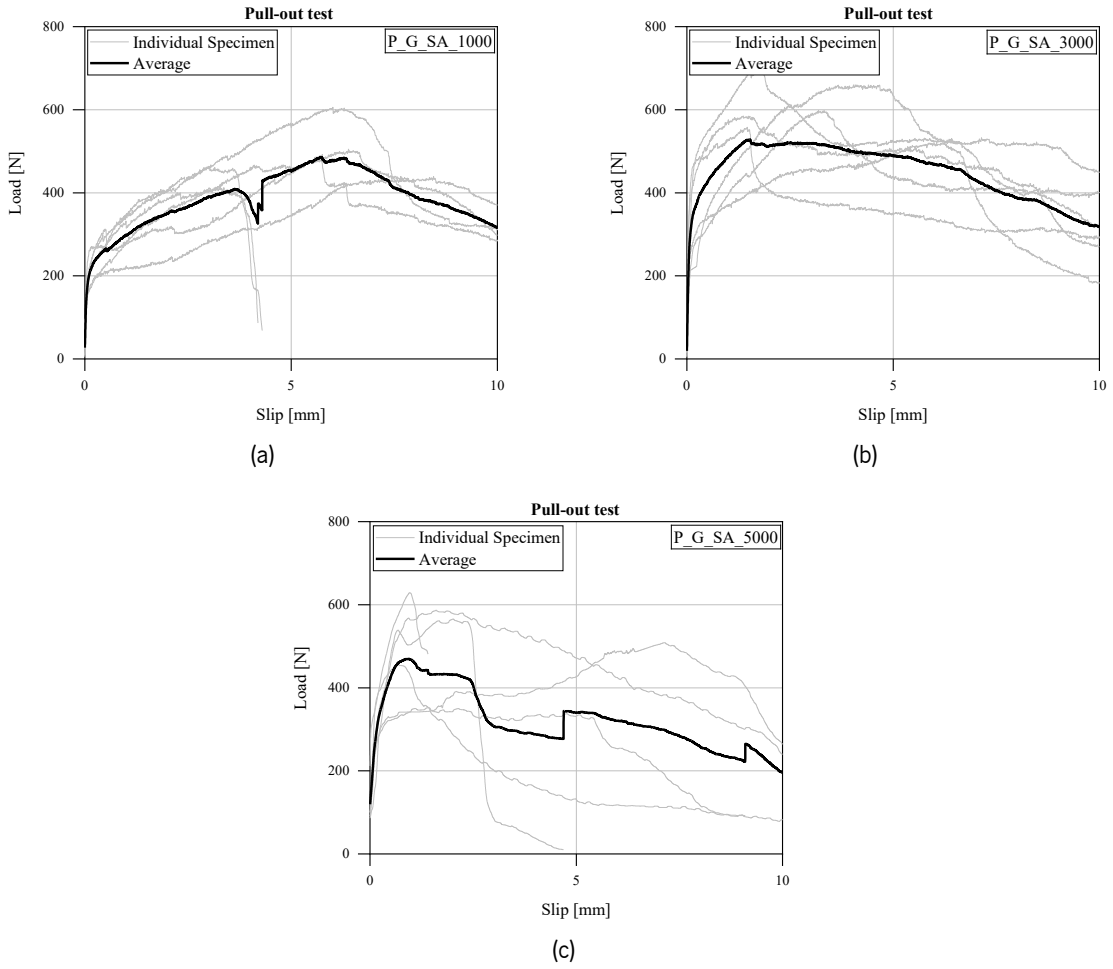

Figure 62 Load-slip curves from the pull-out tests of glass fiber in saline environment, showing individual specimen results and the average curve for each aging duration: (a) P_G_SA_1000; (b) P_G_SA_3000; (c) P_G_SA_5000.

However, at 5000 hours of saline exposure, this positive trend reversed. The average curve demonstrated reduced stiffness and a sharper post-peak decline, indicative of pronounced interfacial degradation and diminished bond strength. These findings reflect the dual role of saline exposure: initially accelerating beneficial hydration processes but ultimately promoting deleterious effects such as leaching, salt crystallization, and microcracking at the fiber–mortar interface. The increased variability among specimens observed at this stage also supports the hypothesis of localized degradation mechanisms, driven by heterogeneous chloride transport and chemical instability of the interfacial transition zone.

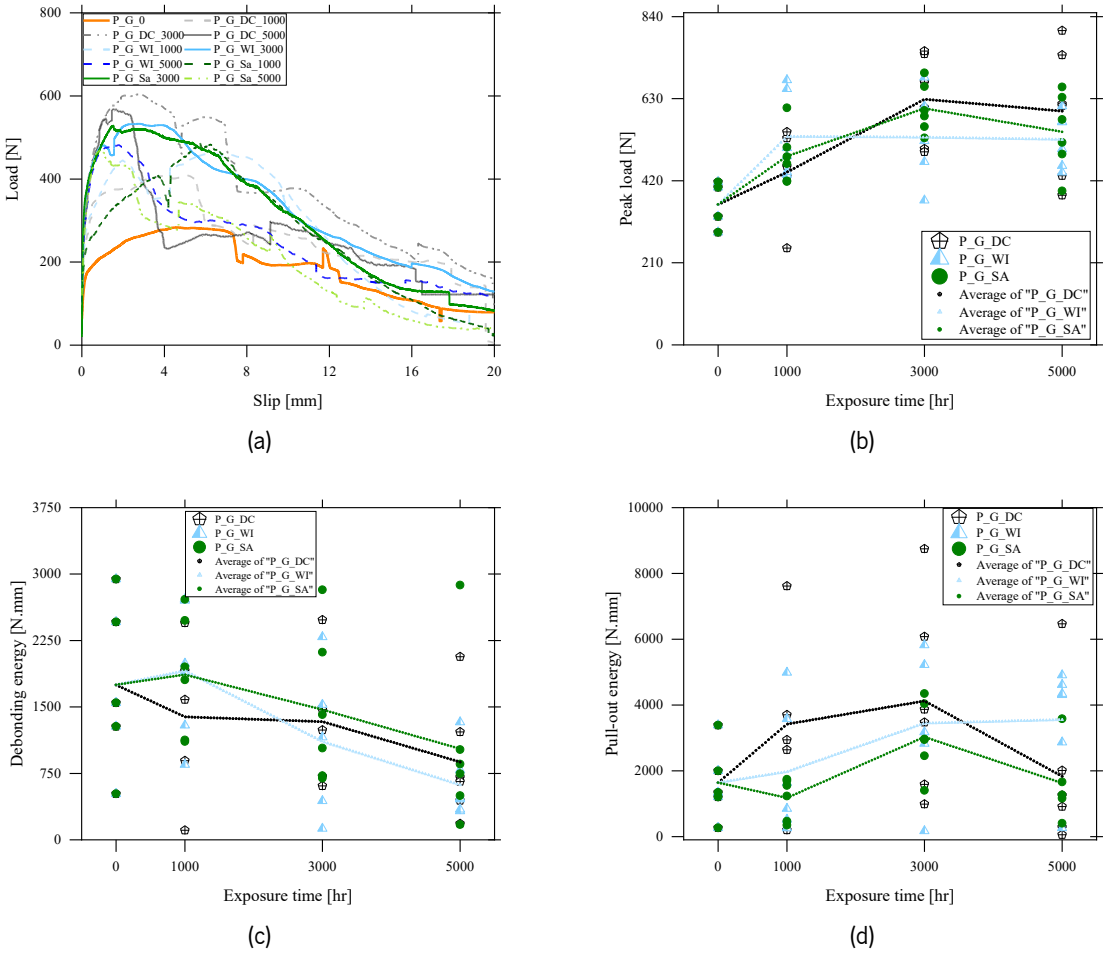

Figure 63 Pull-out parameters of single glass-based TRM in various environments; effect of saline environment: (a) average load-slip response at the load end; (b) peak load; (c) debonding energy; (d) pull-out energy.

Figure 63b illustrates the peak load values across exposure durations. A moderate increase in peak load was observed up to 3000 hours, indicating an improved interface likely due to the chloride-accelerated hydration and densification of the matrix. However, at 5000 hours, a marked decline was observed, suggesting the onset of chemical degradation at the fiber–mortar interface. This behavior may be attributed to calcium leaching and the precipitation of expansive salts such as calcium chloroaluminates, which generate internal stresses and microcracking, thereby compromising the load transfer mechanism. The decline beyond 3000 hours marks the turning point where the detrimental effects of prolonged chloride exposure outweigh the initial benefits. In comparison to the relatively stable trend in WI specimens, the observed decay in peak load under saline exposure underscores the heightened chemical vulnerability of the glass–mortar bond in such environments [289].

The debonding energy trends, shown in Figure 63c, further substantiate this interpretation. A progressive decline in the energy required to initiate failure was noted with increasing exposure, most prominently in the saline-aged specimens. This reflects the gradual weakening of the interfacial zone due to increased porosity, salt crystallization, and microstructural disruption, leading to lower energy thresholds for fiber debonding. The reduction in debonding energy under saline conditions can be associated with both chemical and physical degradation mechanisms, including loss of cohesion in the mortar and chemical alterations at the yarn–matrix interface [307]. These results are coherent with mineralogical findings that identified salt-related crystalline phases and microstructural evidence of internal deterioration.

In contrast to the monotonic decline of debonding energy, the pull-out energy presented in Figure 63d exhibited a more complex trend. An initial reduction at 1000 hours, followed by a peak at 3000 hours and a subsequent decline at 5000 hours, was observed. The increase at 3000 hours corresponds to the improved post-peak frictional interaction due to matrix densification and increased contact area. However, beyond this stage, the degradation of the interfacial zone and matrix cohesion diminishes the energy dissipation capacity during pull-out. The scattering in the pull-out energy data is partly attributed to variability in failure modes, as slippage allows for extended post-peak response, while rupture terminates the curve abruptly. The inclusion of all failure types within each group amplifies this variability, yet the overarching trend remains evident. Overall, the saline environment imposed a dual influence on the bond performance of glass-based TRM systems. While short-term exposure activated hydration and densification, improving bond parameters up to 3000 hours, prolonged exposure led to degradation mechanisms that eroded the interfacial integrity. The combined analysis of load-slip behavior, failure modes, and energy dissipation confirms the susceptibility of glass–mortar interfaces to long-term saline attack, necessitating further investigation for durability design in chloride-rich environments.

6.6.2.2 Basalt-based TRM

6.6.2.2.1 Effect of dry and water condition

The pull-out behavior of basalt-based TRM systems in dry and water condition conditions revealed distinct trends associated with the chemical stability of basalt fibers and the evolving microstructural characteristics of the mortar matrix. As illustrated in Figure 64 and Figure 65, individual load–slip curves (in gray) alongside the average response (in black) display the characteristic triphasic behavior of TRM systems and highlight the variability in bond performance among specimens. The corresponding average load–slip responses are also presented in Figure 66a, indicating an overall enhancement in bond performance over time under dry conditions, while water condition induced a more subdued evolution in the bond properties.

Under dry exposure, the progression of carbonation and continued hydration appeared to substantially improve the interfacial properties, leading to a gradual and consistent increase in the peak load, as shown in Figure 66b. The load–slip curves for the DC environment exhibited the steepest initial slopes and the highest peak loads at 5000 hours, confirming the beneficial effect of prolonged curing under ambient conditions. This increase was accompanied by an extended post-peak region, suggesting enhanced frictional resistance and energy dissipation. Visual inspection suggested that the failure mechanism under dry conditions tended toward fiber rupture, indicative of a strong fiber–matrix bond. This robust interaction is likely promoted by the higher stiffness and rougher surface texture of basalt fibers, which favor mechanical interlock with the carbonated mortar.

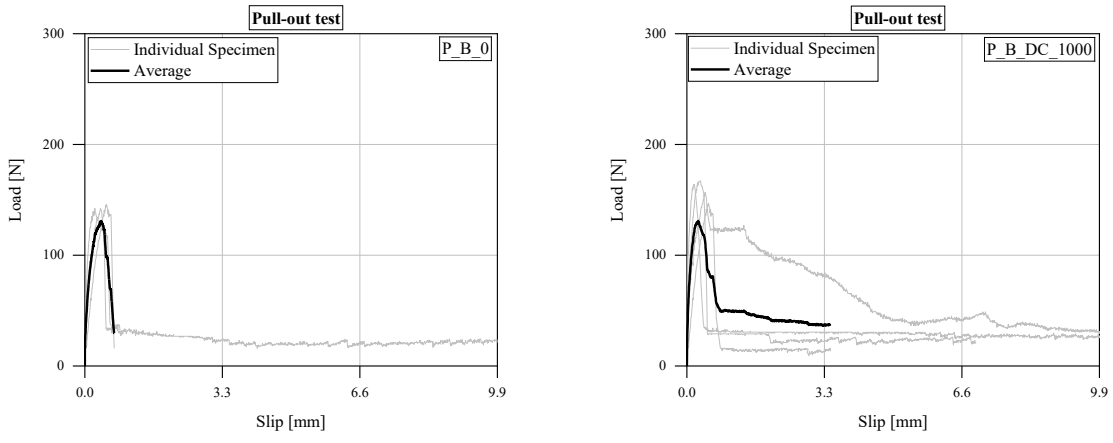

(a) (b)

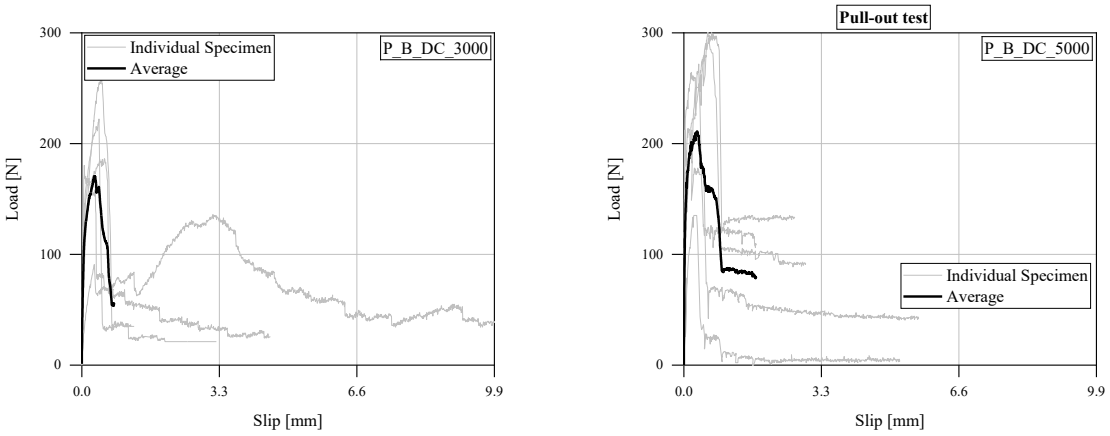

Figure 64 Load-slip curves of the pull-out test for the basalt fiber in the DC environment, showing each individual specimen and the average curve for each group: (a) P_B_0; (b) P_B_DC_1000; (c) P_B_DC_3000; (d) P_B_DC_5000.

The evolution of peak load in Figure 66b confirms these contrasting trends. A steady increase in peak load was observed in dry specimens over the full duration, whereas WI specimens showed a slight decline from 0 to 3000 hours, followed by a modest recovery at 5000 hours. This non-monotonic behavior indicates a temporary bond weakening due to saturation effects, followed by partial recovery as hydration products stabilize the matrix. The overall lower peak load values in the WI condition underscore the limited interfacial development in the absence of carbonation. The debonding energy values presented in Figure 66c reflects the energy required to initiate interfacial failure and further emphasize the influence of environmental exposure. In DC specimens, debonding energy increased until 3000 hours and slightly declined at 5000 hours, corresponding to a potential transition in the dominant failure mechanisms or microstructural maturity. The WI specimens, however, exhibited a noticeable drop at 1000 hours, likely due to SSD testing conditions that reduced frictional resistance. The values then stabilized, suggesting a balance between ongoing hydration and interfacial softening.

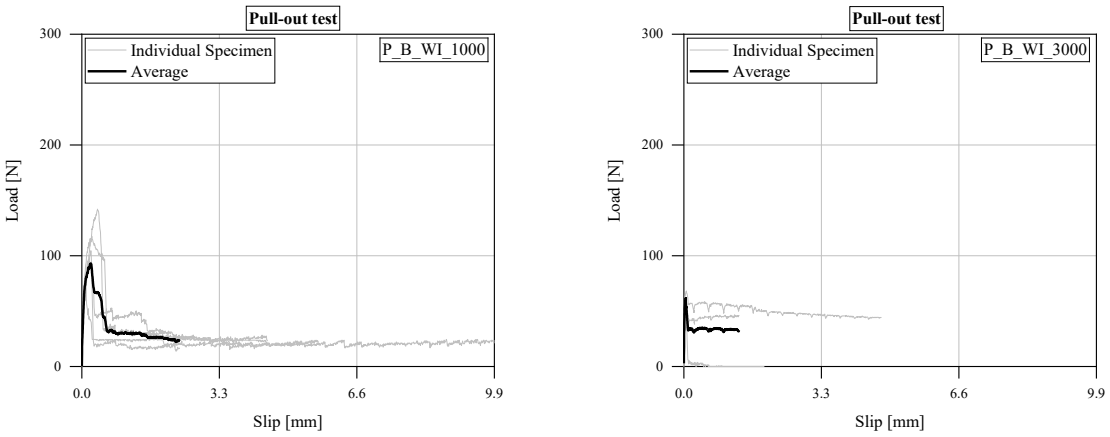

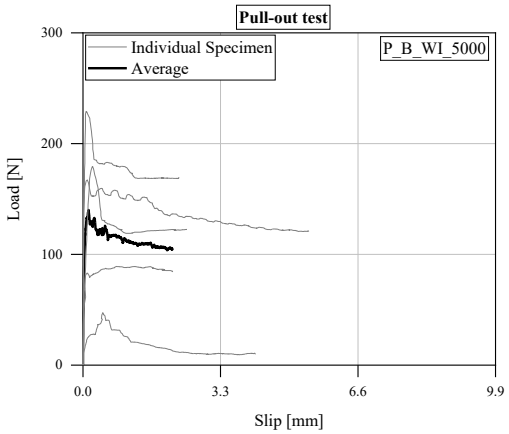

(c)

Figure 65 Load-slip curves of the pull-out test for the basalt fiber in the WI environment, showing each individual specimen and the average curve for each group: (a) P_B_WI_1000; (b) P_B_WI_3000; (c) P_B_WI_5000.

Pull-out energy trends in Figure 66d, capturing the energy dissipated post-peak until complete fiber extraction, revealed a more complex response. All groups exhibited an initial increase up to 1000 hours, with the DC specimens showing continued growth up to 5000 hours, reaching the highest recorded values. This reflects the contribution of prolonged carbonation and densification of the ITZ. In WI specimens, the pull-out energy improved steadily until 5000 hours, though the rate of increase was lower, reflecting the limited enhancement in interfacial friction under saturated conditions. The overall pull-out behavior of basalt-based TRM in dry conditions was characterized by progressive strengthening of the fiber–mortar interface due to continued carbonation, higher mechanical interlock, and predominant fiber rupture, indicative of a robust and durable bond. Conversely, water condition introduced a moderating influence on bond development, with moisture-induced softening and potential calcium leaching compromising the ITZ. Despite the inherent chemical stability of basalt fibers in aqueous environments, the absence of carbonation and the effects of saturation ultimately led to inferior bond parameters in WI conditions relative to DC. These findings highlight the superior performance of basalt TRM systems under ambient curing and the challenges posed by continuous water exposure in long-term durability scenarios.

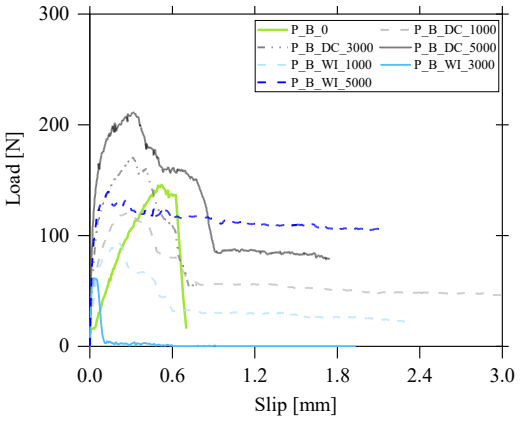

(a)

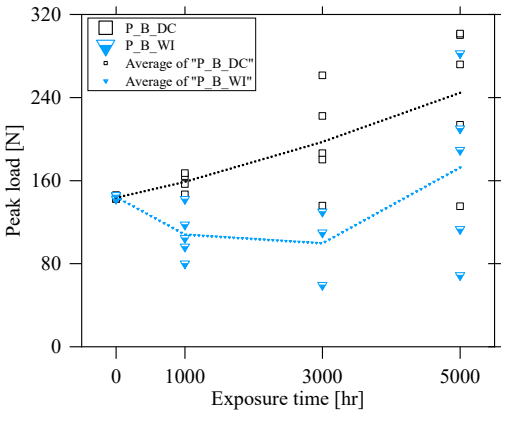

(b)

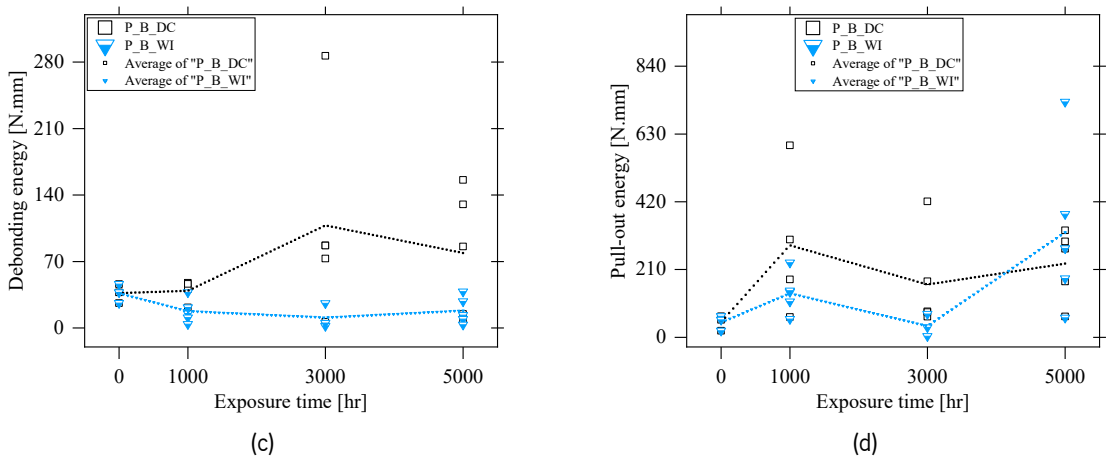

Figure 66 Pull-out parameters of basalt-based TRM under dry and water condition conditions: (a) average load–slip response of single basalt fiber; (b) peak load; (c) debonding energy; (d) pull-out energy.

6.6.2.2.2 Effect of acidic condition

The pull-out response of basalt-based TRM specimens subjected to acidic aging conditions exhibited a complex interplay between interfacial degradation, fiber strength, and matrix compatibility. As shown in Figure 67, the individual load–slip responses and the corresponding average behavior across different exposure durations illustrate the variability and consistency in bond degradation trends. These responses reinforce the interpretation of a progressive decline in interfacial performance with extended exposure. The average load–slip curves presented in Figure 68a further emphasize this behavior, revealing three distinct failure stages: an initial linear phase corresponding to elastic interfacial response, followed by a nonlinear transition governed by progressive debonding, and culminating in a sharp post-peak drop during the dynamic failure stage. In contrast to the glass-based TRM specimens, no significant strain-hardening behavior was observed, and the post-peak response was consistently abrupt. This pattern indicates a brittle failure mode dominated by fiber rupture and rapid loss of load transfer capability in the degraded interface.

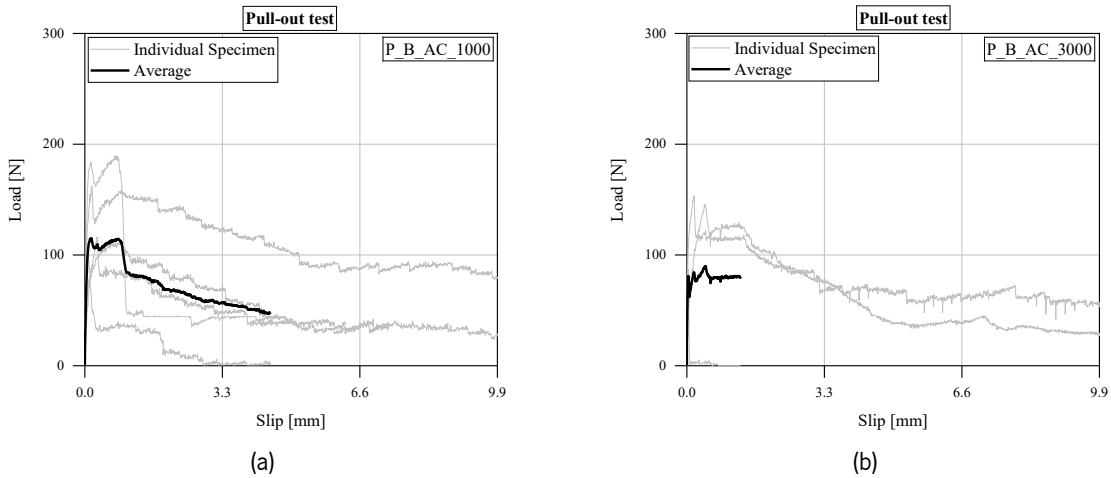

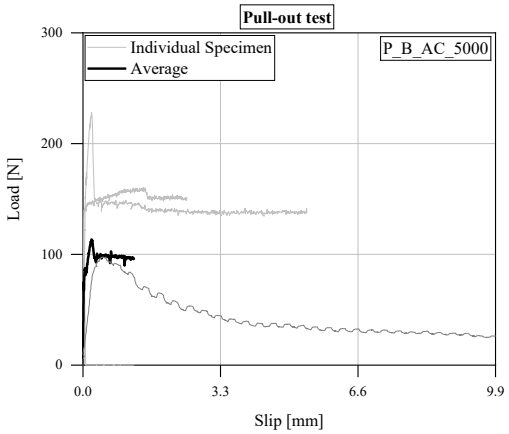

(c)

Figure 67 Load-slip curves of the pull-out test for the basalt fiber in the AC environment, showing each individual specimen and the average curve for each group: (a) P_B_AC_1000; (b) P_B_AC_3000; (c) P_B_AC_5000.

Among the acidic-aged groups, the initial behavior of specimens aged for 1000 hours (B_AC_1000) displayed the highest initial stiffness and load-bearing capacity compared to later exposure durations. Interestingly, this group was the only one to exhibit a combination of fiber slippage followed by rupture, suggesting that the fiber–matrix interface had not yet undergone substantial chemical degradation and retained partial ductility. As the exposure period increased to 3000 hours (B_AC_3000), a pronounced weakening in bond strength was observed, evidenced by a flatter load–slip curve and earlier onset of failure. The performance partially recovered at 5000 hours (B_AC_5000), but not to the levels initially recorded at 1000 hours. This non-monotonic behavior implies a dynamic interaction between initial degradation of the interface due to gypsum formation and later stabilization processes that may include secondary hydration or pore refinement. Nevertheless, the absence of strain-hardening and consistently brittle post-peak behavior across all acidic-aged groups indicated an overall deterioration in bond quality under sulfuric acid exposure.

The evolution of peak load with exposure time, shown in Figure 68b, indicates a positive trend across all environments, with the steepest increase occurring under acidic conditions. This suggests that despite progressive interface weakening, the peak load capacity continued to increase, potentially due to delayed strength gain in the matrix or densification of the mortar surrounding the embedded fiber. This phenomenon may also reflect a transition in failure mechanisms from interfacial sliding to abrupt rupture, driven by increased mechanical interlock and accumulated internal stresses. In contrast, the trend in debonding energy (Figure 68c) exhibited a clear decline for acidic specimens, in stark opposition to the positive trends recorded for dry and water-immersed specimens. This indicates a deterioration of the interface's energy-absorbing capacity under acidic conditions, most likely caused by the dissolution of calcium-bearing phases, chemical shrinkage, and the development of expansive products such as gypsum that disrupt the continuity of the ITZ [137,270]. The decoupling of increasing peak load and decreasing debonding energy further reinforces the brittle nature of failure observed under acid exposure.

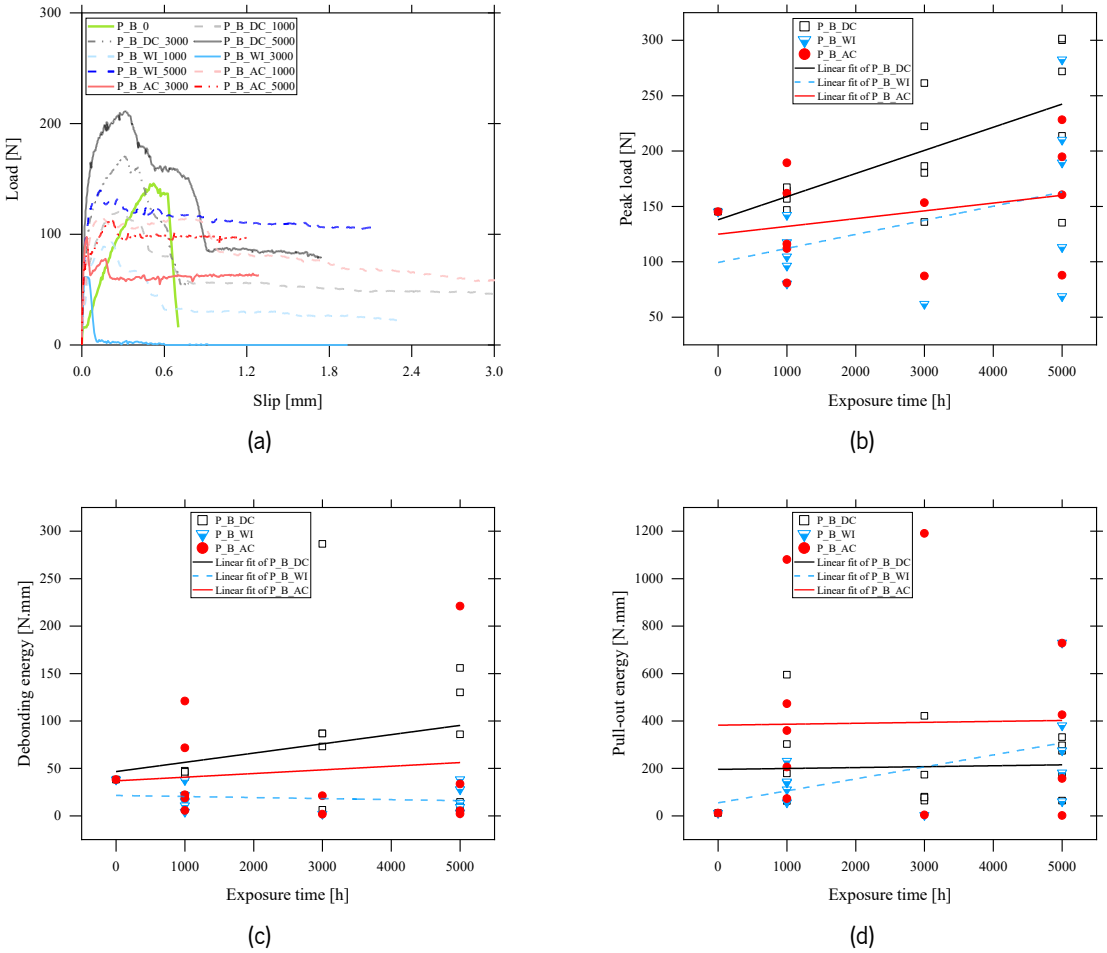

Figure 68 Pull-out parameters of single basalt-based TRM in different environments- effect of acidic environment: (a) average load-slip response of single basalt fiber in pull-out test; (b)peak load; (c) debonding energy; (d) pull-out energy.

The pull-out energy trends presented in Figure 68d was less reliable for interpretative purposes due to the prevalence of fiber rupture, which yields minimal post-peak sliding and thus low pull-out energy values. Nonetheless, these results were included for completeness and comparative analysis. As stated, the pull-out energy values for fiber rupture cases are inherently small and subject to greater scatter due to sensitivity to localized defects and the stochastic nature of failure propagation. Overall, the acidic environment induced a distinctive degradation pattern in basalt-based TRM systems, marked by reduced energy dissipation capacity and brittle fracture behavior. While the increasing peak load trend suggests some matrix strengthening over time, the declining debonding energy and the predominance of rupture-based failure mechanisms indicate a progressively fragile interface. This is consistent with mineralogical and microstructural observations pointing to gypsum crystallization and loss of calcium phases under acidic exposure. Compared to dry and water condition conditions, the acidic medium was found to be more detrimental to the bond integrity of basalt fibers, emphasizing the critical need for environmental resistance considerations in TRM design for chemically aggressive settings.

6.6.2.2.3 Effect of alkaline condition

The influence of alkaline aging on the bond behavior of basalt-based TRM was assessed through pull-out testing across different exposure durations. As shown in Figure 69, the individual load–slip response along with the averaged behavior provide insight into the variability and consistency of interfacial performance across the aging timeline. These results confirm that while individual specimens may exhibit some dispersion, the overall bond behavior remains coherent, particularly around the 3000-hour mark.

The average load–slip response in Figure 70a demonstrates that alkaline conditions led to a robust interfacial bond characterized by high initial stiffness, elevated peak loads, and relatively gradual post-peak decay, particularly after 3000 hours of exposure. This behavior reflects an efficient interfacial load transfer facilitated by favorable microstructural changes, such as enhanced hydration and pozzolanic reactions induced by the presence of calcium hydroxide in the alkaline medium. These reactions contribute to the formation of $C-A-S-H$ phases, which improve the matrix density and the chemical affinity with basalt fibers.

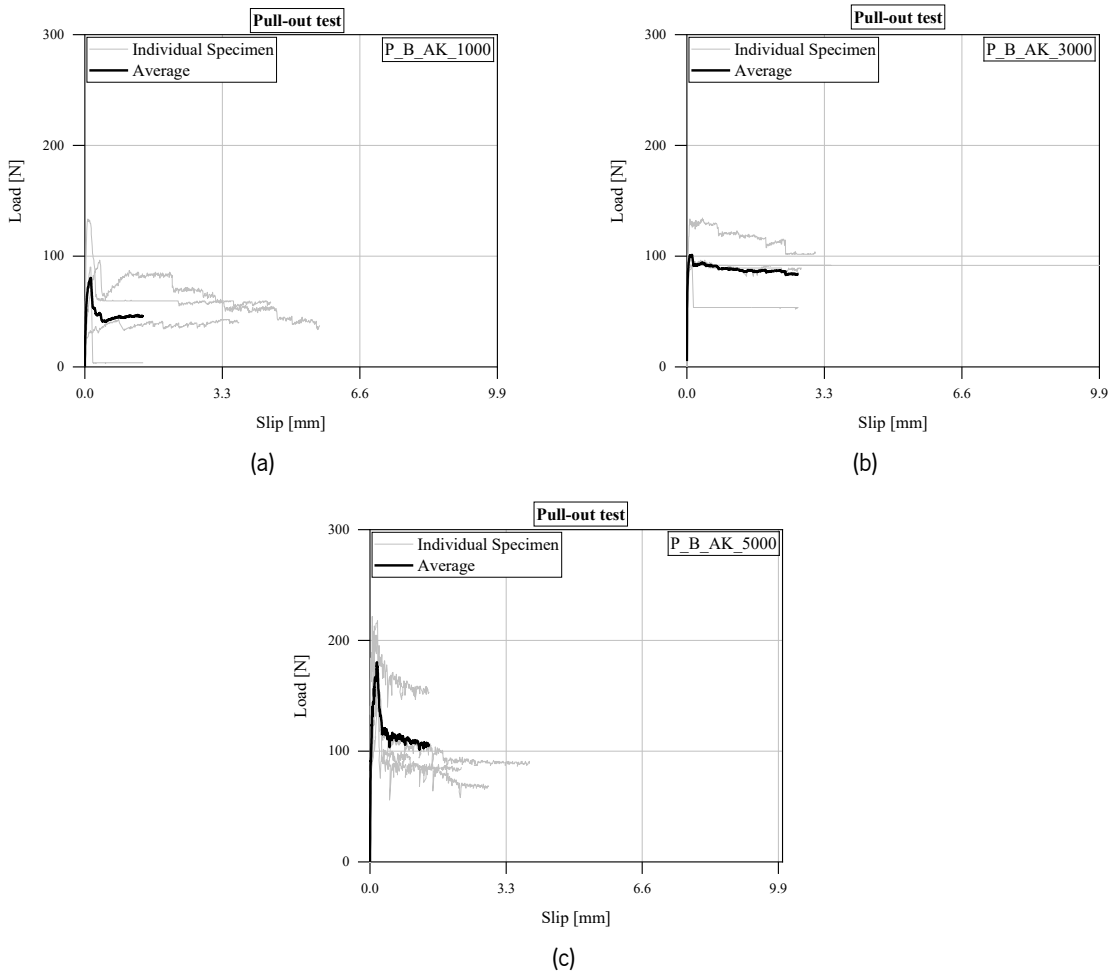

Figure 69 Load-slip curves of the pull-out test for the basalt fiber in the AK environment, showing each individual specimen and the average curve for each group: (a) P_B_AK_1000; (b) P_B_AK_3000; (c) P_B_AK_5000.

The trend in peak load across exposure times, depicted in Figure 70b, confirms that the highest bond strength occurred at 3000 hours of alkaline exposure, with only a slight reduction observed at 5000 hours. This plateauing behavior, while still reflecting high bond performance, suggests the onset of minor degradation mechanisms. The chemical stability of basalt fibers in alkaline environments appears sufficient to preserve the integrity of the fiber–matrix interface, even at longer durations. The sustained high peak loads observed through 5000 hours underline the suitability of basalt textiles for use in alkaline environments, especially when optimal curing and exposure conditions are maintained. Compared to dry and water-immersed groups discussed in prior sections, the alkaline-aged specimens consistently outperformed in terms of peak load, affirming the additional contribution of pozzolanic activity in improving fiber–matrix bond quality.

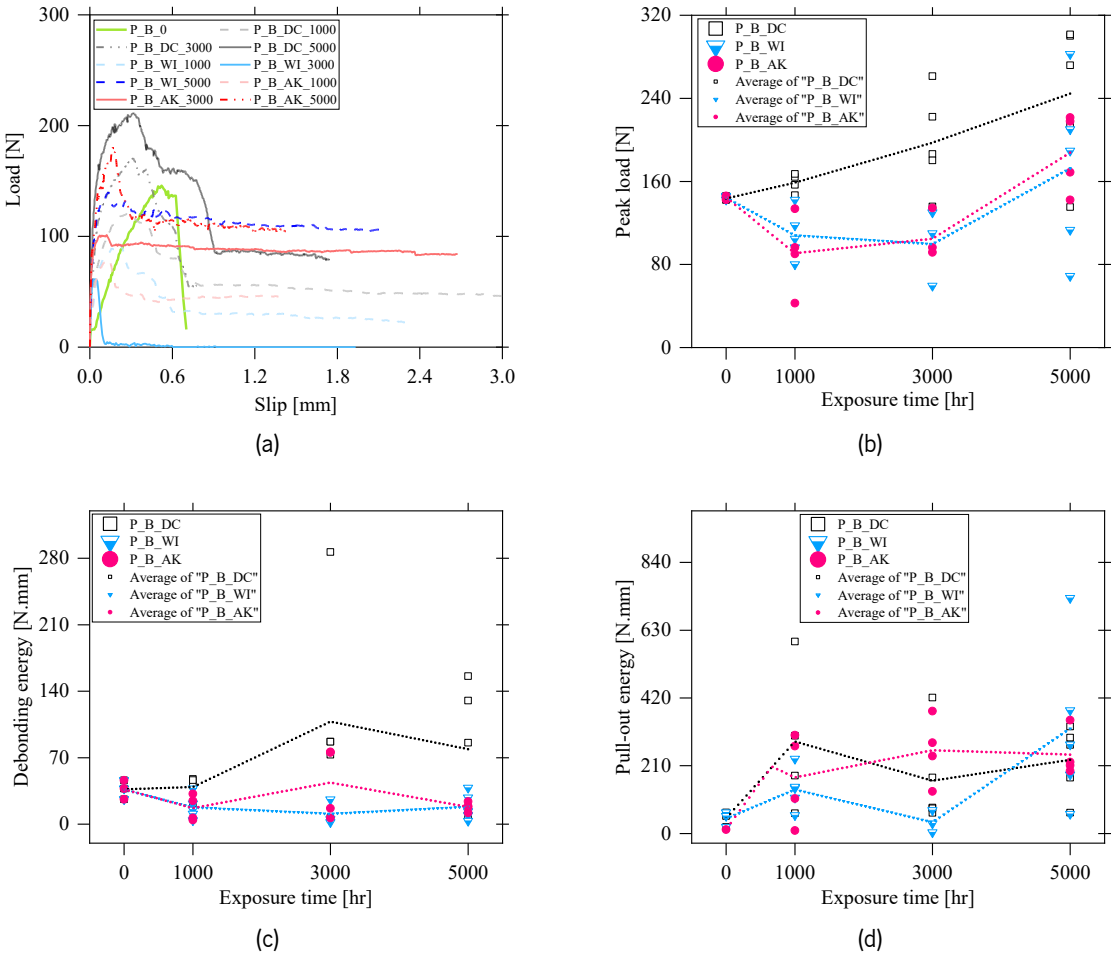

Figure 70 Pull-out parameters of single basalt TRM yarn in different environments; effect of alkaline environment: (a) average load-slip response at the load end; (b) peak load; (c) debonding energy; (d) pull-out energy.

Debonding energy trends, shown in Figure 70c, further corroborate the peak load behavior. Energy absorption up to the peak point increased with exposure duration and peaked at 3000 hours, indicating enhanced energy dissipation during the initial interfacial debonding. The subsequent slight decline in debonding energy at 5000 hours may be attributed to microstructural fatigue or local chemical degradation of the mortar or the fibers, though this reduction remains relatively minor. The elevated modulus and surface roughness of basalt fibers contribute significantly to their mechanical interlock with the matrix, a mechanism that becomes more effective with microstructural densification induced by pozzolanic and hydration reactions. These findings align with trends observed in the compressive and flexural strength measurements of the aged mortar, which also exhibited optimal values around 3000 hours of alkaline exposure.

The pull-out energy, which quantifies the total energy dissipated from the peak load until failure, is depicted in Figure 70d. It was observed that specimens exposed to alkaline conditions reached their maximum pull-out energy at 3000 hours, followed by a modest reduction at 5000 hours. This temporal evolution reflects a balance between interfacial strengthening via hydration reactions and eventual onset of degradation phenomena, such as fiber embrittlement or ITZ weakening. Despite the slight decrease beyond the optimal exposure time, the overall pull-out energy remained higher than that of specimens aged in water or dry conditions, demonstrating the resilience of the basalt–mortar interface in alkaline environments. The collective results from load–slip curves, peak load, and energy parameters reveal a favorable bond development in basalt-based TRM systems aged in alkaline solutions. The optimal

performance at 3000 hours indicates a beneficial synergy between mortar densification and fiber compatibility, with basalt's inherent chemical resistance contributing to sustained bond strength. While longer exposure may introduce minor degradation, the overall robustness of the bond under alkaline aging supports the applicability of basalt TRM in environments characterized by high alkalinity, especially where prolonged exposure is anticipated. These findings reinforce the strategic selection of fiber types based on anticipated environmental conditions to ensure long-term TRM performance.

6.6.2.2.4 Effect of saline condition

The pull-out behavior of basalt-based TRM subjected to saline aging exhibited complex interactions between the fiber–mortar interface and the evolving microstructure under chloride-rich conditions. The average load–slip responses presented in Figure 71a, along with the corresponding individual curves shown in Figure 72, reveal a moderately favorable performance at early exposure durations, particularly at 3000 hours. The sharpest load–slip response was recorded between 1000 and 3000 hours, primarily attributed to the accelerating effect of chloride ions on early hydration reactions, which led to enhanced matrix densification and improved interfacial bonding. However, a performance plateau followed by a slight reduction in bond quality was observed at 5000 hours, suggesting that extended saline exposure may introduce long-term degradation mechanisms such as microcracking, salt crystallization, and leaching-induced weakening of the ITZ. Compared to water condition, the saline environment initially appeared less detrimental to bond development, likely due to the early hydration benefits associated with chloride exposure. Nevertheless, these benefits were not sustained over time, revealing the progressive vulnerability of the bond interface to chemical degradation.

The peak load evolution shown in Figure 71b further supports these observations. A minor increase in peak load was recorded from 0 to 3000 hours, reflecting temporary bond enhancement through chloride-accelerated hydration. However, a subsequent decline in peak load at 5000 hours was detected, suggesting progressive deterioration of the fiber–matrix interface. This trend is consistent with previous findings in saline-aged cementitious systems, where chloride ingress promotes the formation of expansive compounds and leaching of calcium, thereby compromising the structural cohesion of the matrix. The less severe decrease compared to water-immersed specimens may be attributed to the relatively stable chemical nature of basalt fibers in chloride environments, which can partially resist long-term deterioration.

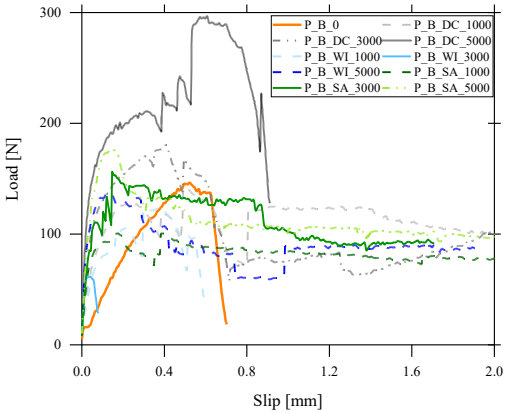

(a)

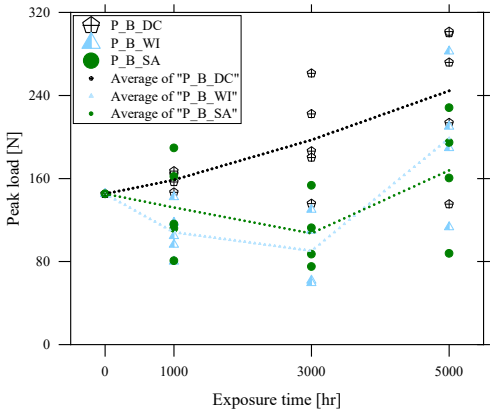

(b)

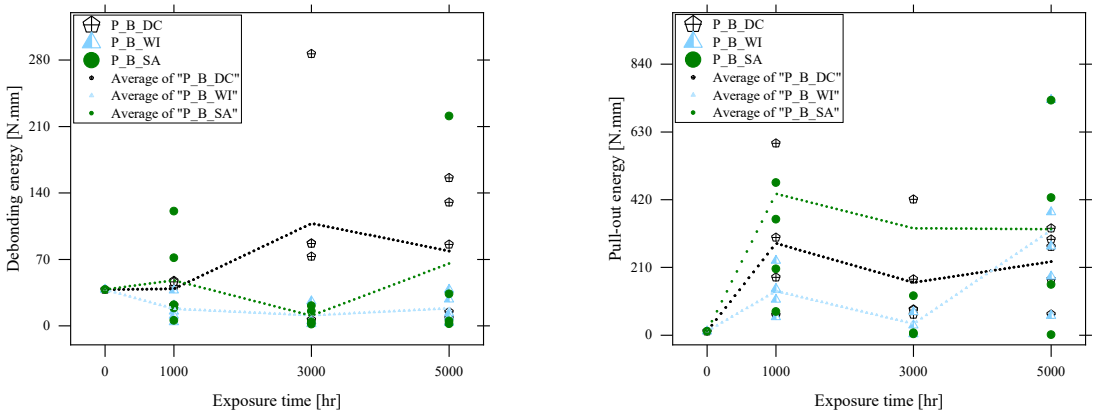

Figure 71 Pull-out parameters of single basalt-based TRM in various environment; effect of saline environment: (a) average load-slip response at the loaded end; (b) peak load; (c) debonding energy; (d) pull-out energy.

Debonding energy trends illustrated in Figure 71c exhibits more variability. Initially, from 0 to 1000 hours, the saline specimens showed negligible change, suggesting a short-term stabilization effect of chloride ions. However, a reduction in debonding energy was recorded at 3000 hours, potentially linked to increased microstructural damage and reduced interfacial toughness. Interestingly, a minor recovery at 5000 hours was observed, although this behavior deviates from typical long-term degradation patterns and may reflect localized densification or experimental variability rather than a systemic recovery. This ambiguity underscores the sensitivity of debonding energy measurements to interfacial heterogeneities and test configuration, especially when bond failure involves rupture rather than continuous slippage.

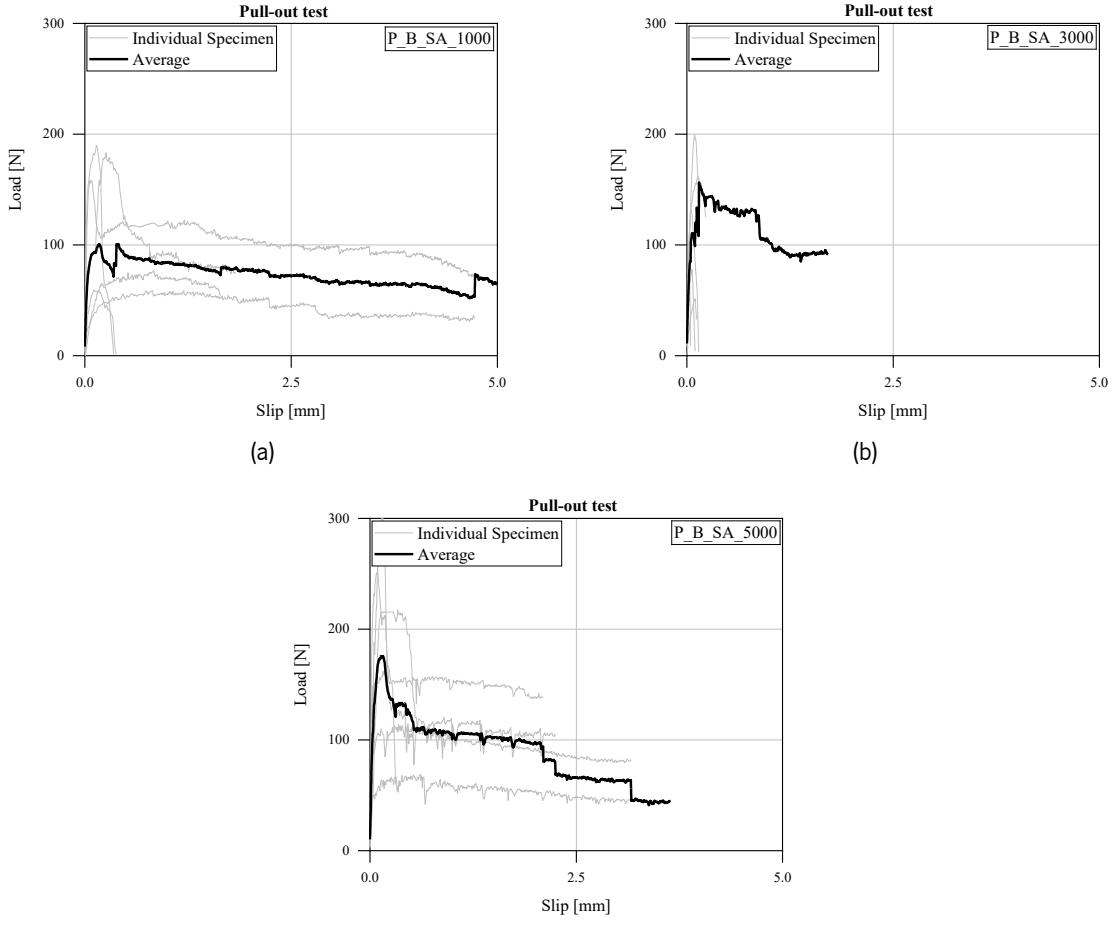

(c)

Figure 72 Load-slip curves from the pull-out tests of basalt fiber in saline environment, showing individual specimen results and the average curve for each aging duration: (a) P_B_SA_1000; (b) P_B_SA_3000; (c) P_B_SA_5000.

The pull-out energy data depicted in Figure 71d reinforce the complexity of the degradation process. Between 0 and 1000 hours, the saline-aged specimens demonstrated the highest increase in post-peak energy among all environments, likely due to pore filling and reduced porosity from early hydration. However, from 1000 to 3000 hours, a decline in pull-out energy was observed, pointing to a weakening of the mechanical interlock and loss of frictional resistance across the interface. At 5000 hours, the downward trend continued, contrasting with the partial recovery seen in dry and water-immersed samples. This persistent decline reflects cumulative damage to the fiber–matrix interface, possibly exacerbated by salt crystallization within pores and the formation of expansive chloride-bearing compounds, both of which induce internal stresses and impair energy dissipation capacity during fiber extraction.

Failure mode observations indicated that fiber rupture remained the dominant mechanism across all saline exposure durations, with no consistent shift toward fiber slippage. This outcome confirms the general robustness of the basalt–mortar interface, likely enhanced by the mechanical interlock provided by the fiber's rough surface and high elastic modulus. However, the relatively low slip range consistently observed in basalt specimens, compared to glass may also reflect the influence of their finer cross-sectional geometry and the increased sensitivity of single-yarn configurations to local defects. While the failure mechanism remained stable, the evolving bond characteristics and reduced energy dissipation capacity observed at later stages suggest a progressive weakening of the interface under extended saline exposure. In summary, saline aging of basalt-based TRM resulted in an initial improvement in bond behavior due to accelerated hydration, followed by a progressive decline beyond 3000 hours. The interplay between chloride-driven densification and delayed matrix degradation emphasizes the dual role of saline environments. Although basalt fibers exhibit chemical stability in such conditions, the fiber–mortar interface remains susceptible to microstructural and chemical disruptions, which can compromise long-term durability.

6.6.3 Single-lap shear test

The single-lap shear test was employed to assess the bond performance of TRM composites under various environmental exposures by characterizing the load-slip behavior between the composite system and the substrate. This test setup, in which the bonded length was designed to be twice the effective bond length of the textile, allows a comprehensive evaluation of the mechanical response under direct shear, without engaging strain-hardening effects beyond the peak load. The analysis focused on key parameters, namely the peak load, debonding energy (defined as the area under the load-slip curve up to the peak), and the slip corresponding to the peak load. Failure modes were also monitored and classified in accordance with the CNR-DT 215 standard into Mode "C" (debonding at the interface) and Mode "F" (tensile rupture of the textile) [308]. These classifications are illustrated in Figure 73, which provides representative examples of failure modes observed during testing across different exposure conditions.

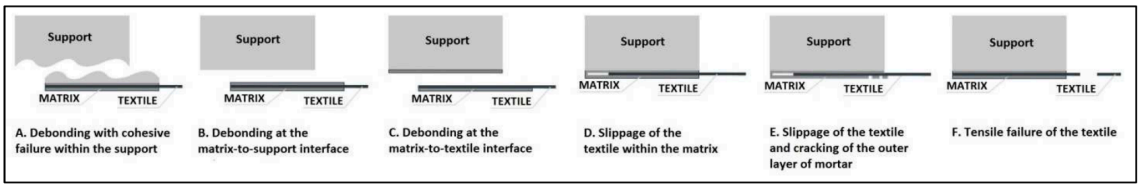

Figure 73 Failure modes for the single-lap shear test according to CNR-DT 215 [308]

Given the complexity of the test configuration and the interaction among different interfaces (fiber–mortar and mortar–substrate), these parameters provide insights into the degradation or enhancement of the bond with aging. Due to the sensitivity of this configuration to rotation and stress distribution, only those tests meeting strict reliability criteria, acceptable omega-profile rotation and failure away from bare textile regions, were retained. The behavior across different aging conditions was examined through group-averaged load-slip curves, with supporting data presented as peak load evolution, debonding energy trends, and slip at maximum load. These parameters collectively inform the changes in bond integrity, energy absorption, and system ductility induced by environmental exposure.

6.6.3.1 Glass-based TRM

6.6.3.1.1 Effect of dry and water condition

The single-lap shear response of glass-based TRM specimens subjected to dry and water condition conditions revealed a progressive evolution in load transfer and failure behavior with increasing aging duration. Figure 74a presents the average load–slip curves for each group, capturing the characteristic three-stage response: an initial linear phase corresponding to elastic bonding, a nonlinear hardening stage associated with interfacial sliding and progressive damage, and a post-peak phase governed by the dominant failure mechanism. To further illustrate the consistency and variability within each group, Figure 75 and Figure 76 displays the individual load–slip curves alongside the average response. The individual curves, plotted in gray, highlight the reproducibility of the triphasic behavior across specimens, with the average curve shown in black. In both DC and WI environments, the evolution of the response curve indicates that aging notably enhanced interfacial stiffness and increased peak load values, particularly after prolonged exposure, reflecting improved matrix consolidation through carbonation and hydration mechanisms, respectively.

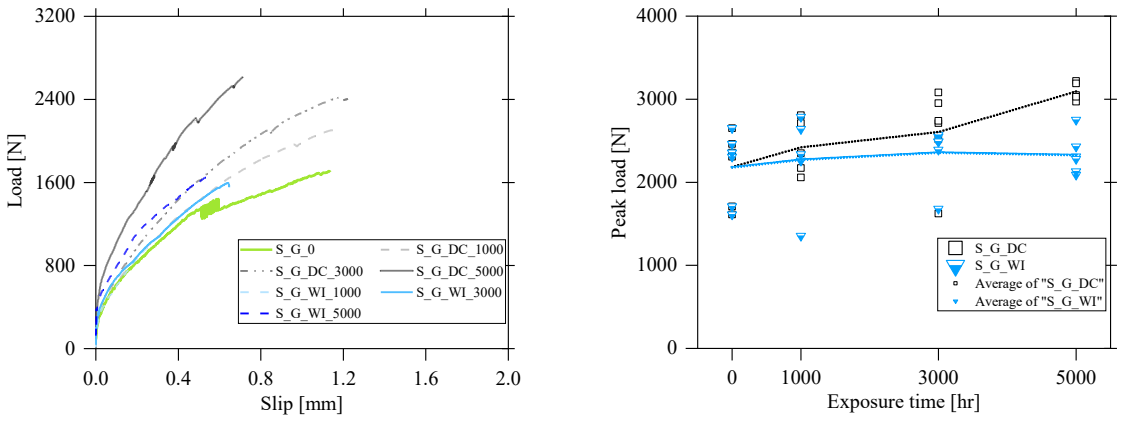

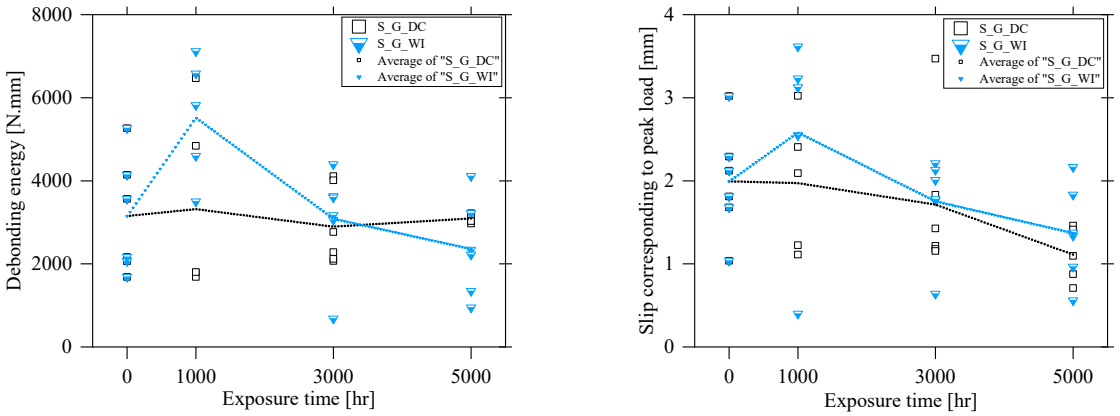

Figure 74 single-lap shear performance of glass-based TRM under dry and water conditions: (a) average load–slip response; (b) peak load; (c) debonding energy; (d) slip corresponding to peak load.

Under dry conditions, the specimens exhibited a continuous increase in peak load and stiffness from age zero to 5000 hours, consistent with matrix densification driven by carbonation and progressive hydration. Tensile rupture was consistently observed as the dominant failure mode, suggesting that both the fiber–mortar and mortar–substrate interfaces exceeded the tensile capacity of the textile, indicative of a fully developed bond. Notably, the slope of the initial linear phase increased with exposure time, reflecting improved interfacial stiffness. The post-peak response also evolved with aging: while strain-softening behavior was present in S_G_DC_0 and S_G_DC_1000, indicating energy dissipation post-yarn failure, this response was no longer observed in S_G_DC_3000 and S_G_DC_5000, where failure occurred abruptly after the peak. This transition is likely associated with reduced system ductility, as further evidenced by the decrease in slip at peak load (Figure 74d).

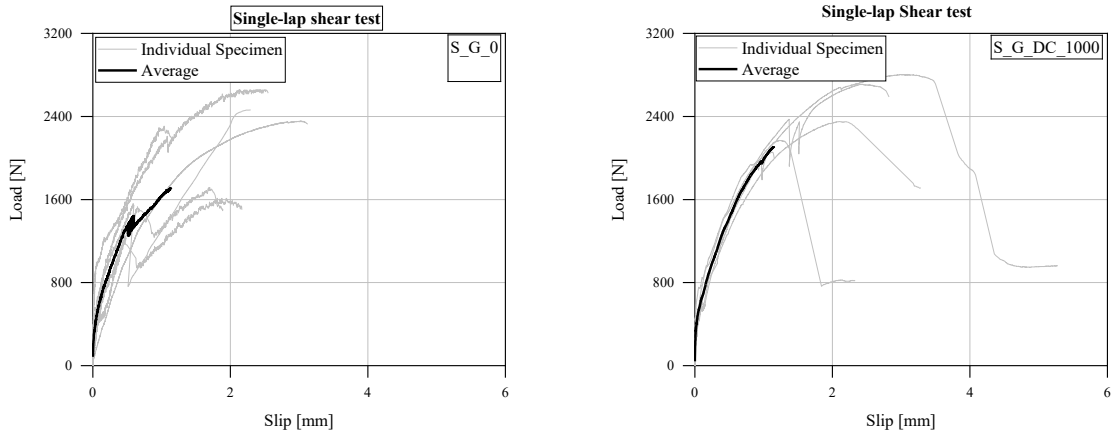

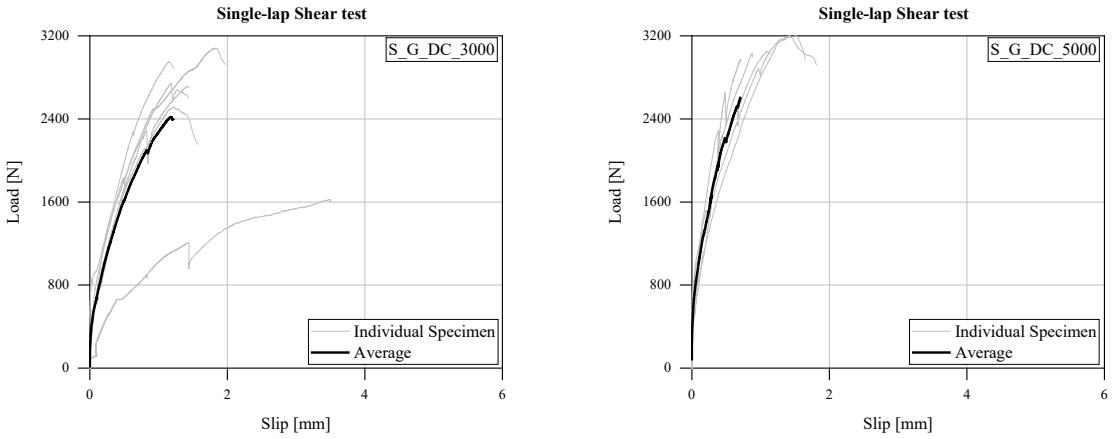

(c) (d)

Figure 75 Load-slip curves of the single-lap shear test for the glass fiber in the DC environment, showing each individual specimen and the average curve for each group: (a) S_G_0; (b) S_G_DC_1000; (c) S_G_DC_3000; (d) S_G_DC_5000.

In water condition, the load-slip response exhibited a similar but less pronounced trend. Peak load increased with exposure duration, reaching near the tensile limit of the bare textile by 5000 hours (Figure 74b), which confirms sustained hydration-induced matrix strengthening. However, the failure mode became slightly more variable, with some specimens showing signs of debonding at the mortar–substrate interface, particularly at longer exposure durations. These occurrences point to localized weakening likely caused by prolonged saturation and leaching effects. The average load-slip curves for WI samples maintained their nonlinearity up to 3000 hours, with visible strain-softening after peak. At 5000 hours, however, the behavior transitioned to a more brittle failure with reduced ductility, as evidenced by a lower slip at peak and the absence of a significant post-peak phase. This trend is consistent with observations from pull-out tests and mechanical characterization results, where extended condition diminished the energy dissipation capacity despite continued strength gains.

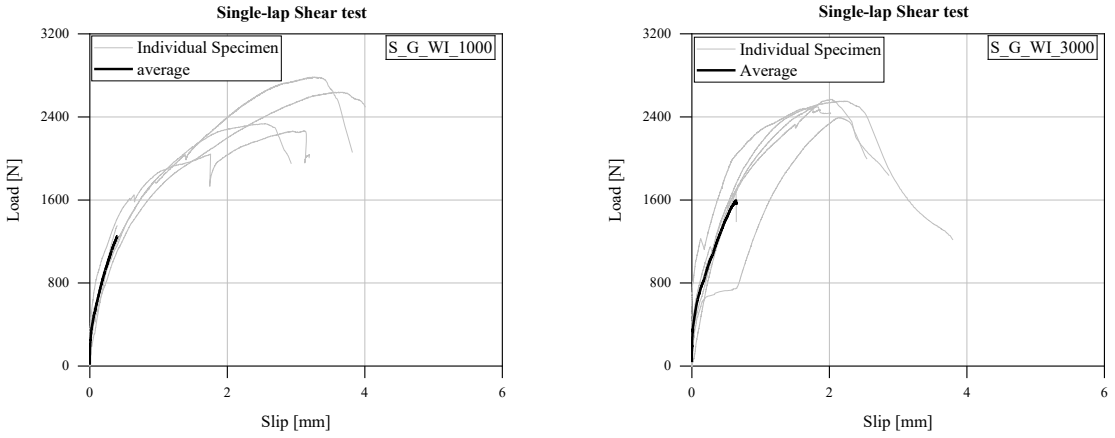

(a) (b)

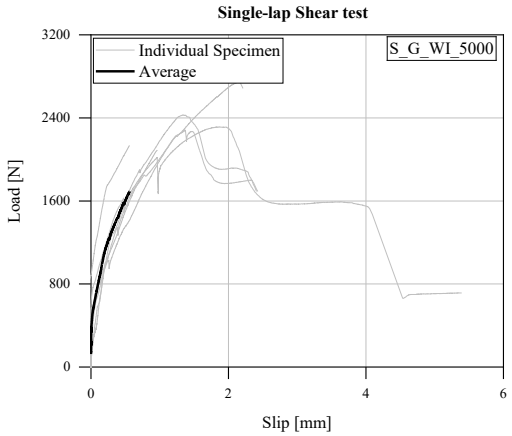

(c)

Figure 76 Load-slip curves of the single-lap shear test for the glass fiber in the WI environment, showing each individual specimen and the average curve for each group: (a) S_G_WI_1000; (b) S_G_WI_3000; (c) S_G_WI_5000.

Debonding energy trends further elucidate the influence of aging. As shown in Figure 74c, the energy absorbed up to peak load declined slightly with exposure time in DC specimens, consistent with reduced ductility and a stiffer, more brittle interface. In contrast, WI specimens experienced a more significant drop in debonding energy, particularly beyond 1000 hours. This behavior reflects a dual effect: while hydration enhances bond strength, continuous water exposure also leads to increased porosity and potential microstructural damage near the interface. The steeper decline in debonding energy in WI relative to DC underscores the importance of moisture management in maintaining long-term bond performance. Overall, the single-lap shear test results confirm the positive impact of aging under dry conditions, promoting bond strength and stiffness at the expense of ductility. In water-immersed specimens, gains in strength were accompanied by a reduction in energy absorption and an increased likelihood of interfacial failure. These findings align with the microstructural and mineralogical analyses, which demonstrated hydration and carbonation effects in the dry and water environments, respectively, and reinforce the understanding of how environmental aging modifies the mechanical response and failure modes of TRM systems.

6.6.3.1.2 Effect of acidic condition

To better illustrate the variability and consistency within each aging group, Figure 77 presents the individual load–slip responses of glass-based TRM specimens subjected to acidic conditions, alongside their corresponding average curves. These individual plots highlight the distinct phases of the bond behavior and reveal specimen-to-specimen variations in terms of stiffness, peak load, and post-peak characteristics, particularly under long-term exposure. The aging of glass-based TRM specimens in acidic environments induced substantial changes in the single-lap shear response, particularly influencing the post-peak behavior and energy dissipation characteristics. As presented in Figure 78a, the average load-slip curves for specimens immersed in sulfuric acid solution reveal a transition in mechanical behavior with increasing exposure time, marked by a shift from strain-softening toward a more brittle failure mechanism. This evolution in response was directly associated with the microstructural and chemical degradation of the fiber–mortar interface, as supported by mineralogical observations and mechanical characterizations discussed earlier.

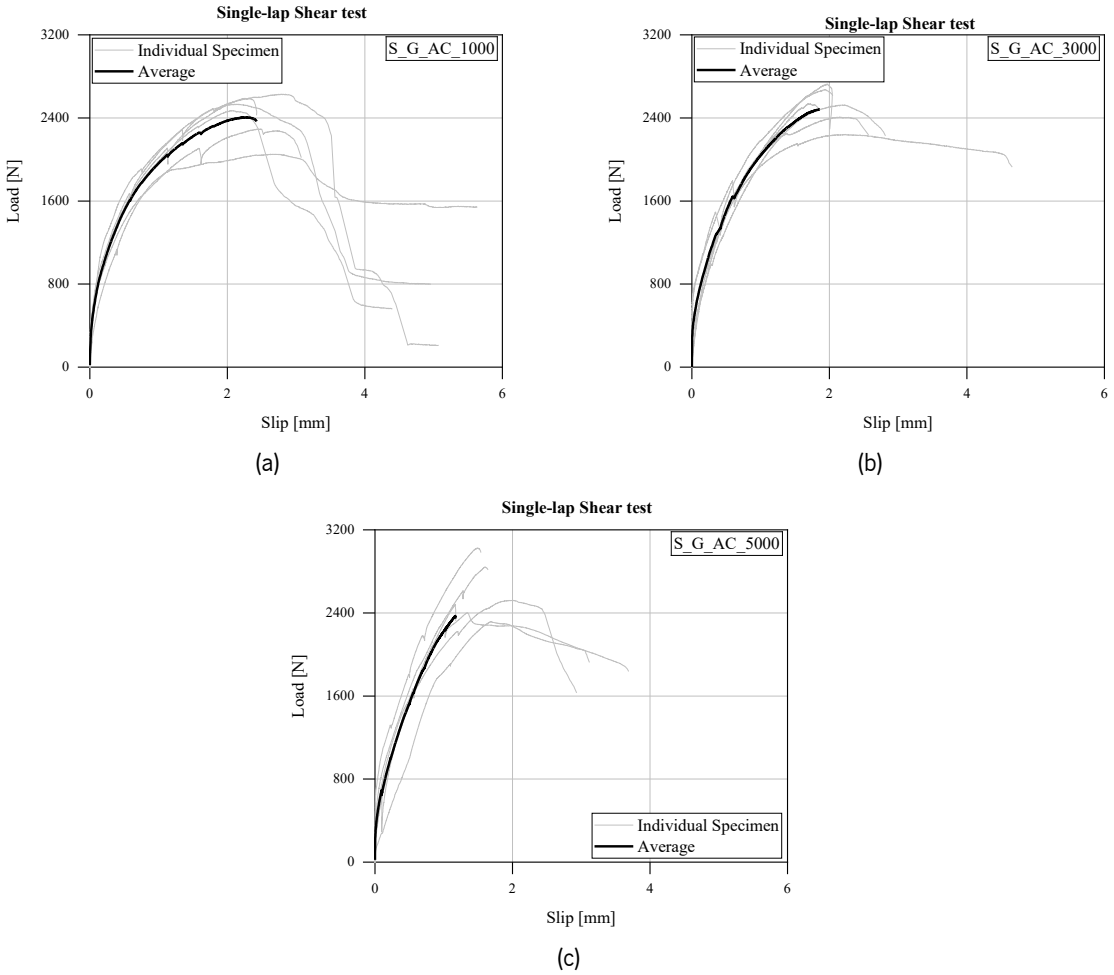

Figure 77 Load-slip curves of the single-lap shear test for the glass fiber in the AC environment, showing each individual specimen and the average curve for each group: (a) S_G_AC_1000; (b) S_G_AC_3000; (c) S_G_AC_5000.

At 1000 hours of exposure, specimens displayed a nonlinear hardening phase followed by a softening behavior post-peak, indicative of partial energy dissipation prior to failure. This phase suggested that, at early ages, the acidic environment had not yet critically damaged the interfacial bond, allowing a degree of plastic sliding of the fibers within the mortar. This behavior may be attributed to the early-stage hydration benefits still prevailing in the presence of moisture, albeit in a mildly acidic medium. However, the presence of gypsum, as confirmed by XRD and TGA analyses, may have already begun to impair the mortar microstructure and the integrity of the ITZ.

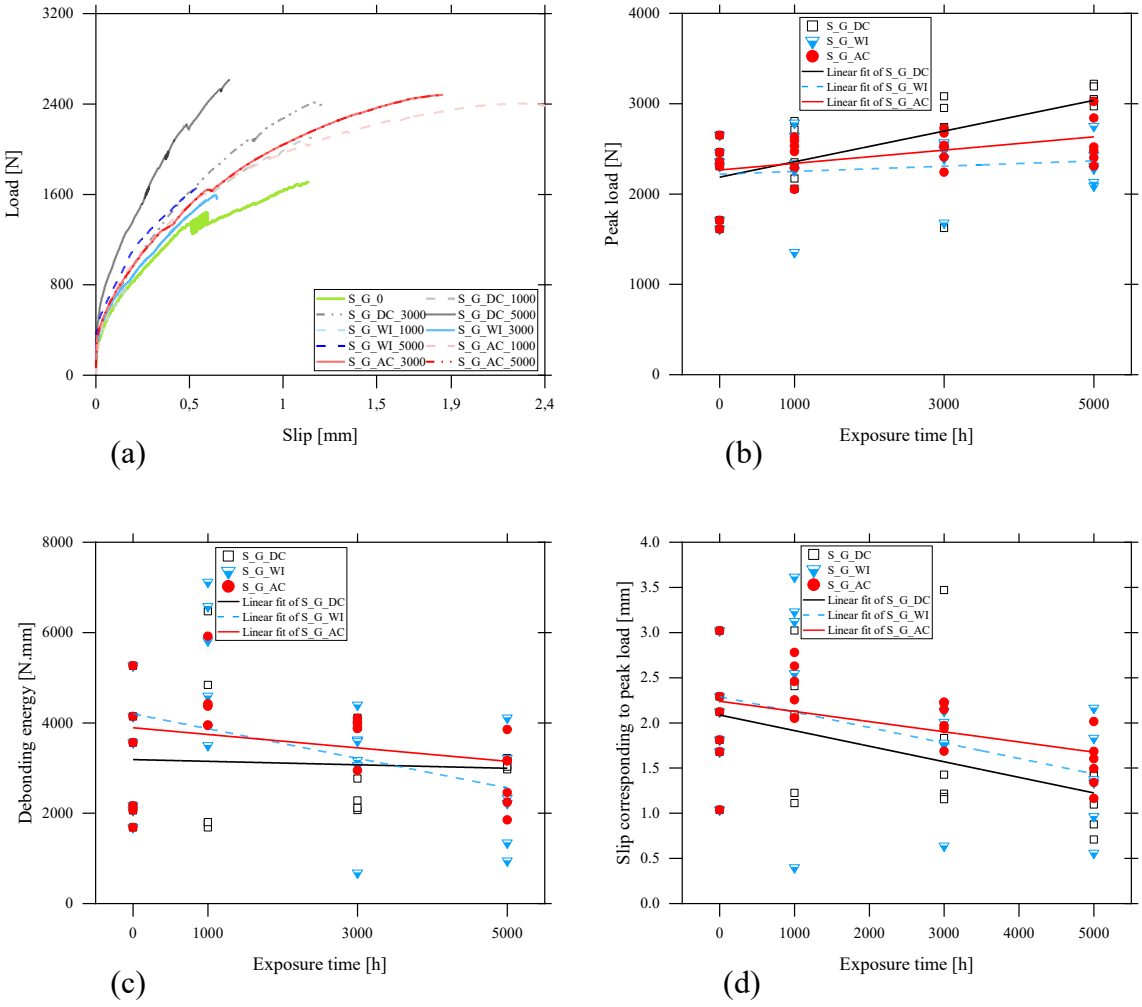

Figure 78 Single-lap behavior of glass-TRM in different exposure durations and mediums; effect of acidic environment: (a) average load-slip curve; (b) peak load; (c) debonding energy; (d) slip corresponding to peak load.

As exposure time increased, a notable transformation was observed. In the specimens aged for 3000 and 5000 hours, the nonlinear hardening phase shortened considerably, and failure occurred abruptly following the peak load, with minimal slip and energy absorption after peak. This brittle behavior is indicative of reduced ductility and compromised bond performance. The absence of strain-softening in these later stages reflects a progressive weakening of the fiber–mortar interface, likely due to increased gypsum formation and the accumulation of microcracks within the matrix. The load-slip curve steepness prior to peak also diminished, suggesting a loss in interfacial stiffness compared to earlier exposure stages. The corresponding trends in peak load, as depicted in Figure 78b, revealed a moderate increase with exposure time, although not as pronounced as observed under dry conditions. This limited strength development suggests that the degradation effects induced by acidic exposure gradually counteracted the early-stage benefits from continued hydration. Although tensile rupture of the fibers remained the prevailing failure mode across all specimens, the mechanical capacity of the TRM system appeared to approach a plateau, constrained by the progressive weakening of the fiber–mortar interface.

Debonding energy trends, presented in Figure 78c, showed a continuous decline with increasing exposure duration in the acidic environment. This parameter, representing the energy absorbed by the system up to peak load, decreased more steeply than in dry-aged specimens, confirming the loss of interfacial toughness. The steep negative slope suggests that gypsum-induced matrix damage and

chemical shrinkage reduced the ability of the mortar to sustain energy absorption during progressive fiber sliding. These findings align with prior research linking acid-induced mineral transformations to weakened mechanical behavior. The slip corresponding to peak load (Figure 78d) decreased consistently with aging, further reinforcing the observation of increased system brittleness. Reduced slip values imply a more abrupt failure process, corroborating the visual and mechanical evidence of interface deterioration. The earlier transition from ductile to brittle failure in acidic-aged samples, compared to those aged in water condition, highlights the dual role of the acidic environment: while it initially sustains hydration reactions, it concurrently initiates chemical decay mechanisms that compromise long-term performance. In summary, the acidic exposure condition resulted in a degradation-dominated response in glass-based TRM systems during single-lap shear testing. Despite initial strength retention, long-term immersion in sulfuric acid solution induced significant reductions in debonding energy, ductility, and post-peak resistance, leading to a brittle failure mechanism governed by interfacial damage. These outcomes are consistent with the broader mechanical and microstructural findings presented in previous sections and underline the critical impact of aggressive chemical aging on the structural reliability of TRM systems.

6.6.3.1.3 Effect of alkaline condition

The exposure of glass-based TRM specimens to alkaline environments introduced significant modifications in their single-lap shear response, particularly in terms of interfacial stiffness, peak load capacity, and failure behavior. Figure 79 presents the individual load–slip responses for all alkaline-aged specimens, highlighting the variability in curve shape and post-peak behavior across different aging durations. These individual results consistently exhibited the characteristic three-phase response, initial linear, nonlinear hardening, and post-peak, though with notable differences in slope and ductility depending on the exposure period. As shown subsequently in Figure 80a, the corresponding average load-slip curves consolidate this behavior and further confirm that all groups adhered to the typical profile observed in TRM shear testing. Specifically, the initial segment reflected elastic adhesion at the fiber–mortar interface, followed by a nonlinear region governed by progressive sliding and bond degradation, and culminating in a post-peak stage dictated by the dominant failure mode. Across all exposure durations, failure consistently occurred through yarn rupture, indicating that the bond strength at the interface exceeded the tensile capacity of the textile throughout the aging period.

At early exposure times, specifically at 1000 hours, the specimens exhibited an enhanced initial stiffness and peak load compared to water-immersed counterparts, a response attributable to accelerated pozzolanic reactions promoted by the alkaline solution. The presence of calcium hydroxide in the environment likely facilitated the formation of additional $C-(A)-S-H$ phases at the interface, which in turn densified the matrix and enhanced mechanical interlocking between the glass yarns and the mortar. This interfacial densification is reflected in the steeper slope of the initial load-slip response and the elevated peak load observed at this age. Between 1000 and 3000 hours, the bond strength remained relatively stable, as indicated by minimal changes in peak load and consistent load-slip behavior. This plateau in performance suggests that the beneficial effects of pozzolanic reactivity reached a saturation point, beyond which the matrix no longer exhibited significant gains in interfacial cohesion. The observed stabilization corresponds with the trends seen in the pull-out tests and mechanical characterization data, wherein mortar compressive and flexural strengths showed limited improvement beyond 3000 hours. Post-peak behavior in these specimens became more abrupt with time, hinting at a gradual transition toward brittleness, likely due to the onset of microstructural changes or the formation of expansive reaction products over extended exposure periods.

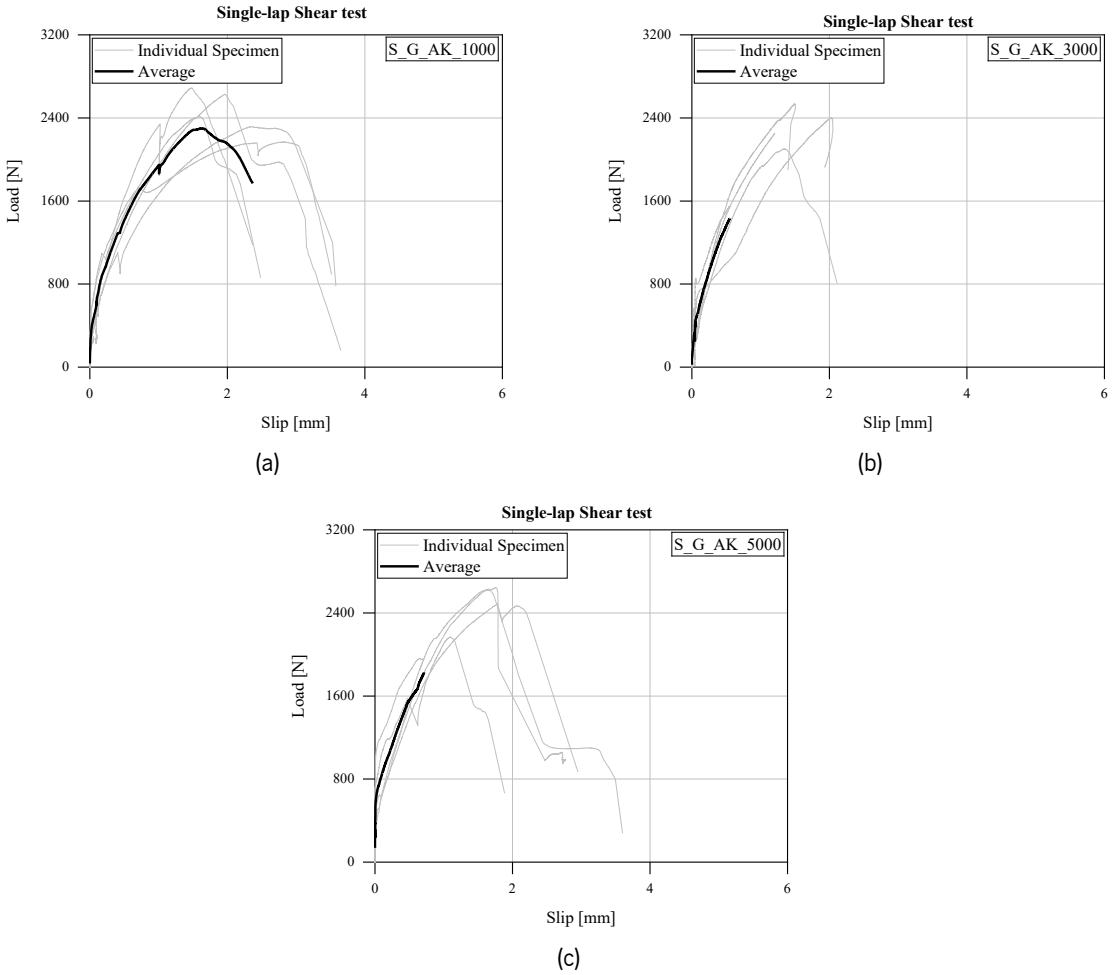

Figure 79 Load-slip curves of the single-lap shear test for the glass fiber in the AK environment, showing each individual specimen and the average curve for each group: (a) S_G_AK_1000; (b) S_G_AK_3000; (c) S_G_AK_5000.

As reported in Figure 80b, the peak load under alkaline exposure reached its maximum at 1000 hours and was maintained with only marginal variation up to 3000 hours before stabilizing. This trend reflects the early enhancement from the pozzolanic reactions and the subsequent microstructural equilibrium. Compared to dry conditions, which displayed continuous strength gains due to carbonation, the alkaline-aged specimens demonstrated slightly lower peak loads, although still superior to those observed in water-immersed samples. This comparative behavior underscores the dual role of alkaline exposure in promoting early interfacial strengthening while also introducing the potential for long-term deterioration. Debonding energy trends (Figure 80c) further illustrate the influence of the alkaline environment. The maximum debonding energy was observed at 1000 hours, followed by a gradual decline over time. This decline is attributed to the gradual emergence of microcracks and the weakening of the ITZ, reducing the system's ability to absorb energy during progressive yarn pull-out. The observed pattern aligns with previous findings in pull-out testing, where bond performance peaked early under alkaline exposure before tapering due to cumulative degradation. When compared to the dry and water-immersed environments, the alkaline specimens maintained intermediate debonding energy values, suggesting that the matrix retained a partially densified structure despite some degradation.

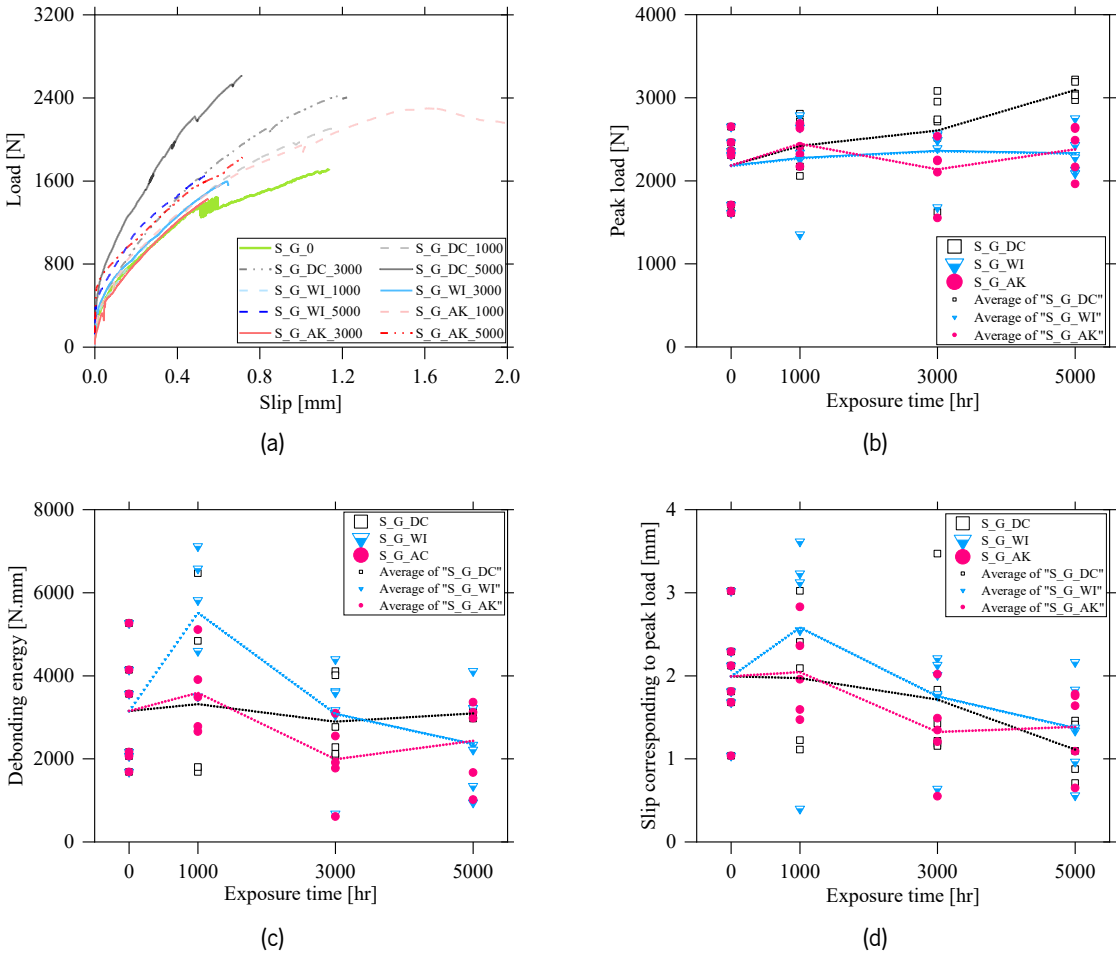

Figure 80 Single-lap behavior of glass-TRM in different exposure durations and mediums- effect of alkaline environment: (a) average load-slip curve; (b) peak load; (c) debonding energy; (d) slip corresponding to peak load.

Slip corresponding to the peak load, presented in Figure 80d, decreased with increasing exposure time, especially between 0 and 1000 hours, and then stabilized. This behavior reflects the stiffening of the interfacial bond due to early pozzolanic activity, which limited the extent of deformation prior to failure. The decreasing trend in slip indicates a transition from a more ductile to a stiffer and potentially more brittle system over time. When juxtaposed with water-immersed specimens, which exhibited more gradual reductions in slip, the alkaline-exposed specimens revealed a faster loss in ductility, albeit maintaining higher bond strength. This is corroborated by the overall steeper slope of the load-slip curve in alkaline-aged specimens compared to those in wet environments. In general, the alkaline aging condition of glass-based TRM systems produced a pronounced early-age enhancement in interfacial bond strength, largely driven by pozzolanic reactivity and matrix densification. This improvement was most evident at 1000 hours and was sustained through 3000 hours of exposure. Beyond this duration, the benefits appeared to plateau, with indications of minor degradation. The observed trends in load-slip behavior, peak load, debonding energy, and slip at peak load collectively suggest that while alkaline environments initially improve TRM bond performance, prolonged exposure may introduce a transition toward reduced ductility and potential long-term vulnerability.

6.6.3.1.4 Effect of saline condition

The exposure of glass-based TRM systems to saline environments induced a complex and time-dependent influence on their single-lap shear behavior, as evidenced by the evolution of mechanical and energy dissipation parameters. Figure 81 illustrates the individual load–slip responses of saline-aged

specimens, where the typical three-phase behavior, elastic rise, nonlinear hardening, and post-peak decline which can be consistently identified across all repetitions. Despite slight variability in slip capacity and peak sharpness, the overall response pattern remains coherent, indicating a stable bond mechanism. As shown in the average curves presented in Figure 82a, the general trend confirms the characteristic progression: an initial linear phase driven by elastic bonding, a nonlinear segment associated with progressive interfacial debonding and textile sliding, and a post-peak phase defined by failure through fiber rupture. Failure was consistently governed by Mode F beyond 1000 hours of exposure, confirming that the mortar-to-substrate and mortar-to-textile interfaces retained sufficient integrity to fully mobilize the tensile capacity of the reinforcement.

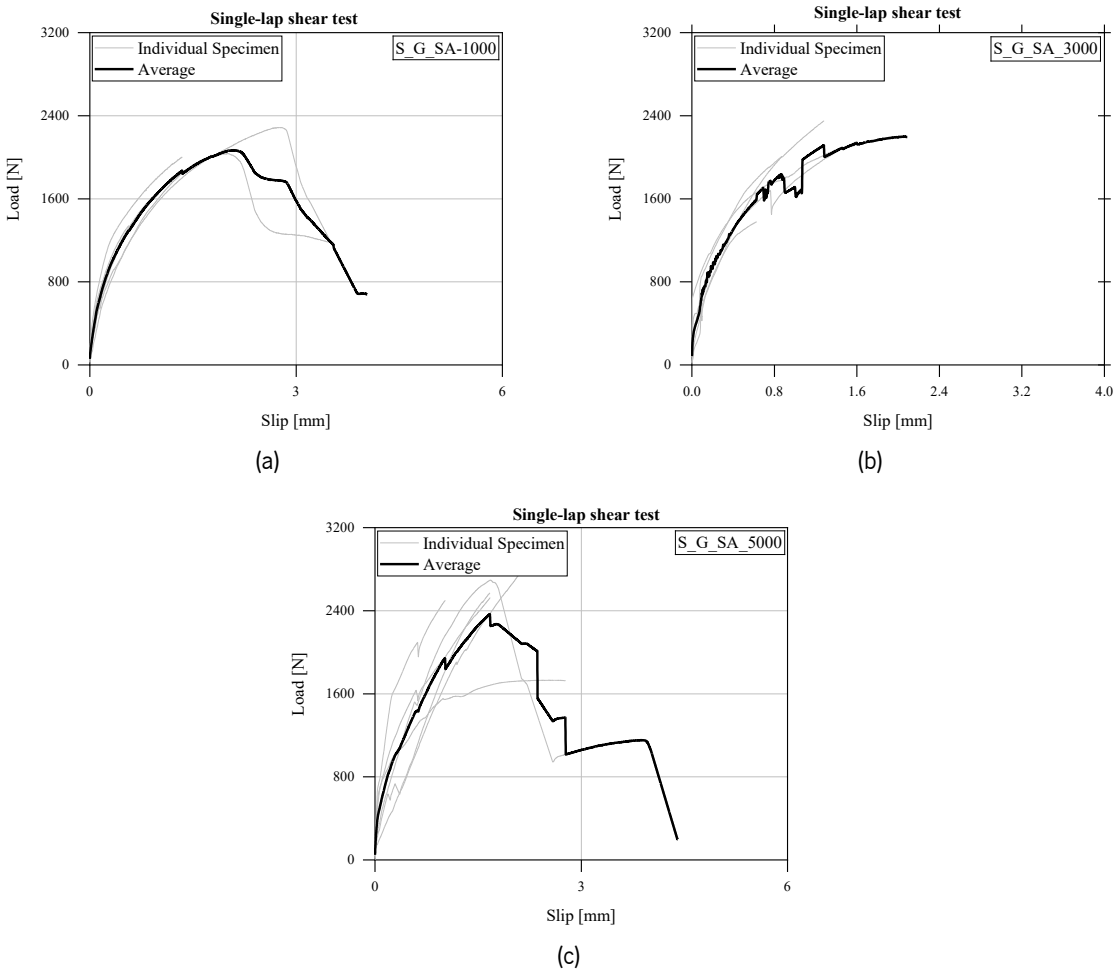

Figure 81 Load-slip curves from the single-lap shear tests of glass fiber in saline environment, showing individual specimen results and the average curve for each aging duration: (a) S_G_SA_1000; (b) S_G_SA_3000; (c) S_G_SA_5000

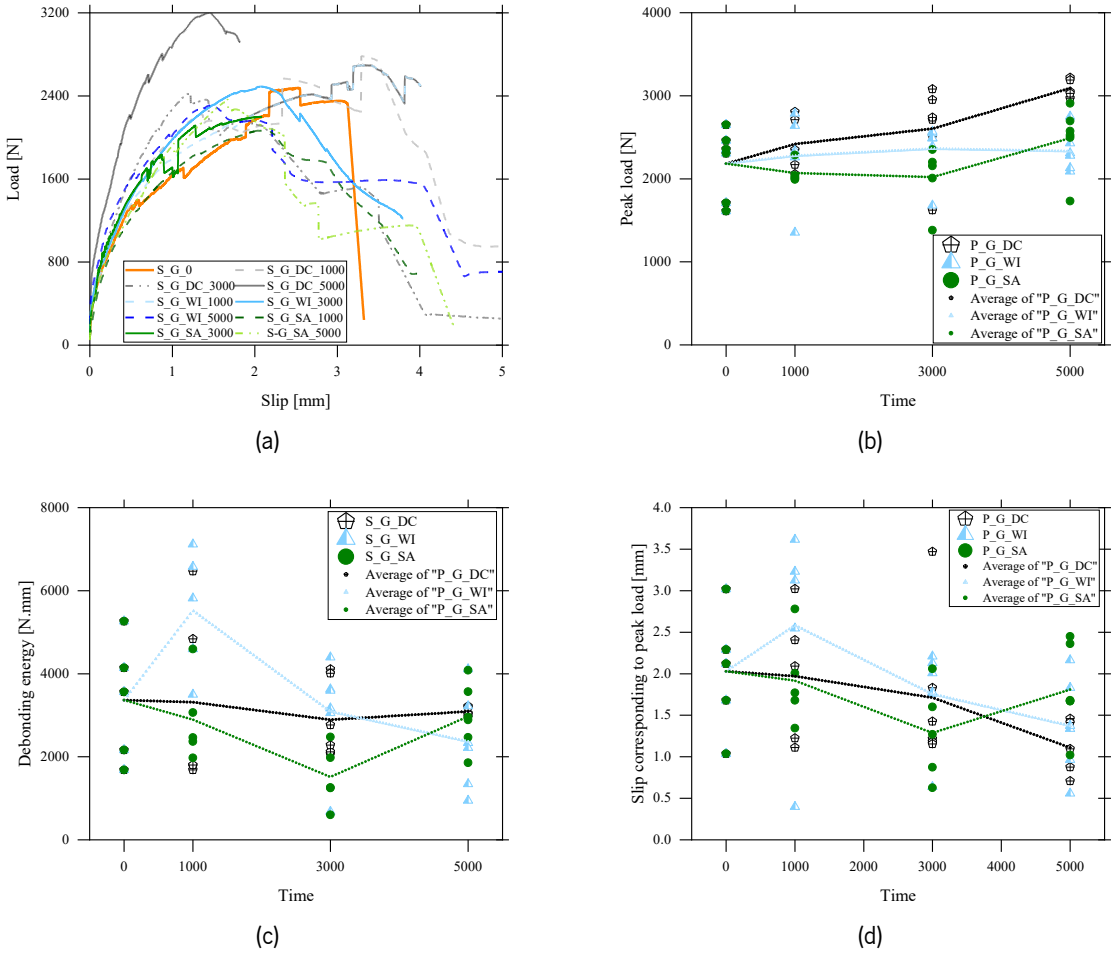

Figure 82 Single-lap behavior of glass-TRM under various exposure durations and conditions; effect of saline environment: (a) average load-slip curve, (b) peak load, (c) debonding energy, (d) slip corresponding to peak load.

Up to 3000 hours of exposure, a gradual increase in the stiffness of the initial linear portion of the load-slip curve was observed, reflecting bond enhancement likely associated with chloride-induced acceleration of hydration reactions within the mortar matrix. This behavior is consistent with the microstructural development typically promoted by chloride presence, leading to denser hydration products and improved interfacial contact. However, at 5000 hours, a noticeable decline in the slope of the initial phase occurred, pointing toward the onset of deterioration mechanisms, such as salt crystallization or matrix softening, which compromised interfacial stiffness. This trend aligns with the findings from pull-out tests and microstructural analyses, which revealed the formation of salt-related compounds and localized porosity growth in the mortar matrix after prolonged saline exposure. Figure 82b illustrates the progression of peak load with increasing exposure time. In contrast to the dry (DC) and water condition (WI) specimens, the saline-aged specimens maintained a relatively constant peak load up to 3000 hours, followed by a measurable increase at 5000 hours. This deviates from the trend observed in the pull-out test, where peak load typically peaked earlier before declining due to long-term degradation. A potential explanation for this divergence lies in the influence of the fired clay brick substrate employed in the single-lap configuration. The substrate may have partially absorbed chloride ions or impeded their transport to the critical interfacial zones, thereby attenuating their short-term chemical effects. This substrate-mediated behavior likely contributed to a delayed manifestation of chloride-induced degradation or, conversely, a more gradual enhancement of the bond through controlled hydration, ultimately yielding a higher peak load at extended exposure.

The corresponding debonding energy values, shown in Figure 82c, provide further insight into the TRM system's capacity for energy absorption prior to failure. For the SA specimens, a reduction in debonding energy was observed up to 3000 hours, followed by a partial recovery at 5000 hours. This temporal dip is indicative of transient bond weakening, possibly due to microcracking or localized interfacial defects, which reduce the efficiency of energy transfer at the mortar-textile interface. The subsequent recovery may reflect delayed densification effects, or again, a buffering effect provided by the substrate's porosity and chemical interaction with the saline solution. Comparatively, WI specimens exhibited an initial rise at 1000 hours, likely linked to hydration gains, but declined thereafter as saturation-induced softening and leaching effects took hold. DC specimens, on the other hand, exhibited minimal variation, reinforcing the role of carbonation as a stabilizing mechanism in dry environments.

Figure 82d displays the evolution of slip corresponding to the peak load. For the saline-aged groups, slip values remained below those of DC and WI specimens up to 3000 hours, reflecting increased interfacial stiffness but also reduced ductility. The limited deformation capacity at these stages is consistent with a more brittle failure mode, as might result from chloride crystallization and subsequent disruption of the bond structure. At 5000 hours, however, slip values increased, surpassing those of the other groups. This late-stage recovery may reflect complex interactions between the mortar and the clay brick substrate, potentially involving delayed chloride ingress or a redistribution of internal stresses, which permitted additional deformation prior to failure. These trends are in agreement with the observations from pull-out testing, where an initial enhancement in bond performance was followed by progressive degradation in the mechanical response. In summary, saline exposure introduced an evolving pattern of interfacial behavior in glass-based TRM specimens subjected to single-lap shear testing. Initially, chloride-driven acceleration of hydration enhanced bond stiffness and strength, but with prolonged exposure, signs of matrix and interface degradation became apparent. The unusual recovery of peak load and slip capacity at 5000 hours highlights the potential mitigating effect of the fired clay substrate in buffering chloride transport and delaying degradation mechanisms. These findings underscore the importance of substrate characteristics in evaluating the long-term performance of TRM systems exposed to aggressive environments.

6.6.3.2 Basalt-based TRM

6.6.3.2.1 Effect of dry and water condition

The single-lap shear response of basalt-based TRM specimens subjected to dry and water condition conditions exhibited distinct behaviors in terms of stiffness development, peak load attainment, energy dissipation, and failure mechanisms. Figure 83and Figure 84 presents the individual load–slip curves for these two reference environments, highlighting the consistency of the three-phase progression. While some scatter is evident, particularly in post-peak behavior, the general response pattern confirms the reliability of the bond mechanism under both dry and immersed conditions. As shown in the averaged curves in Figure 85a, specimens stored in dry conditions demonstrated a progressive increase in the slope of the linear portion with aging, reflecting a steady enhancement in interfacial stiffness. This behavior is attributed to continued hydration and carbonation processes that promote matrix densification and improved fiber-to-mortar bonding. Notably, the DC specimens showed increasingly abrupt post-peak failure with age, consistent with a transition from ductile to brittle failure as the matrix became stiffer over time.

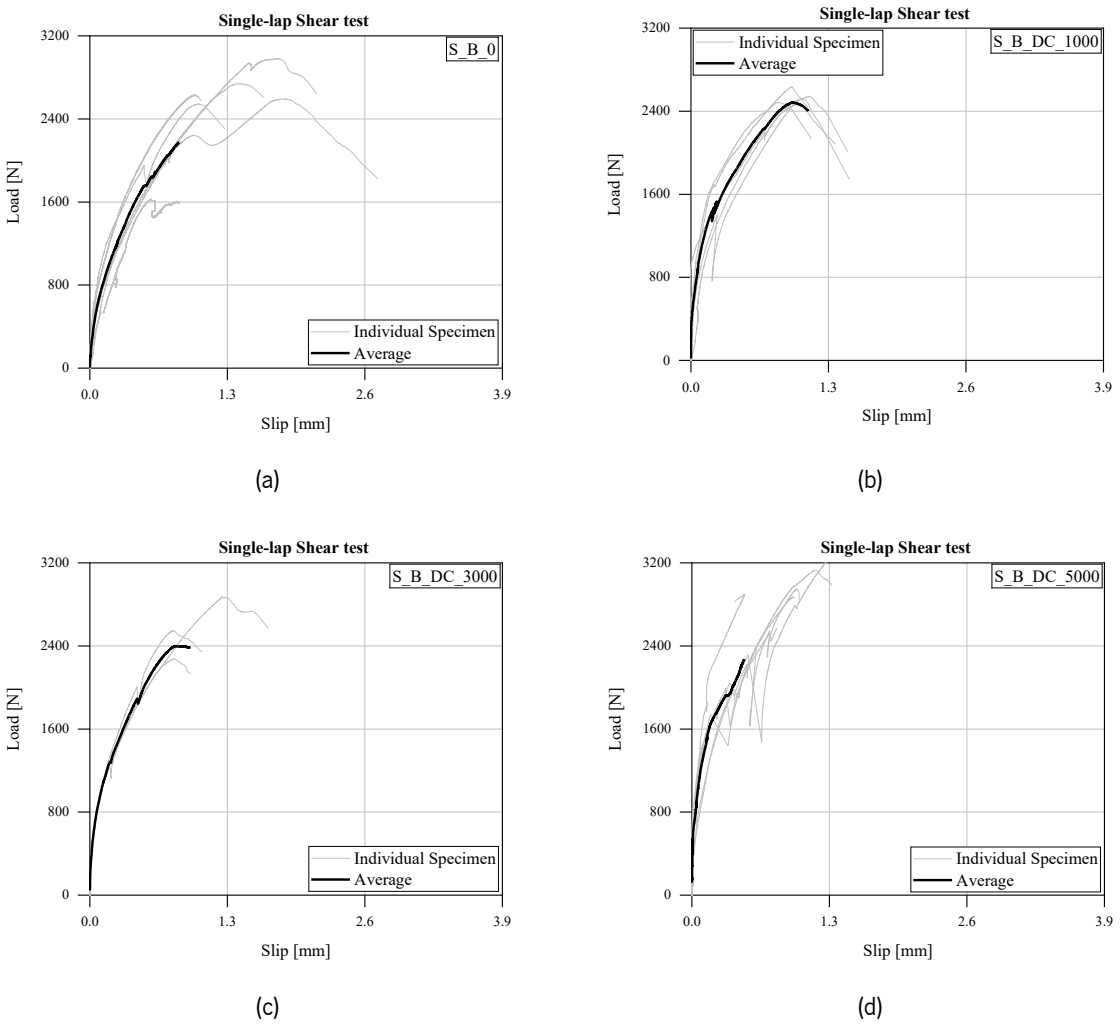

Figure 83 Load-slip curves of the single-lap shear test for the basalt fiber in the DC environment, showing each individual specimen and the average curve for each group: (a) S_B_0; (b) S_B_DC_1000; (c) S_B_DC_3000; (d) S_B_DC_5000.

In contrast, the behavior of specimens aged in WI was characterized by a reduction in the linear stiffness at early aging durations, followed by a stabilization trend. The most significant drop was recorded at 1000 hours, suggesting an early-stage weakening of the bond due to water-induced softening of the mortar matrix. This interpretation is further supported by the observation of lower peak loads and decreased slip values at peak load in WI specimens compared to their dry-stored counterparts. The persistent presence of water in the WI condition likely impeded full matrix curing and may have facilitated the leaching of calcium hydroxide, both of which are detrimental to bond integrity. Nonetheless, after 3000 hours, the WI specimens reached a relatively stable performance state, implying that long-term immersion does not lead to progressive degradation but rather a plateau in mechanical characteristics.

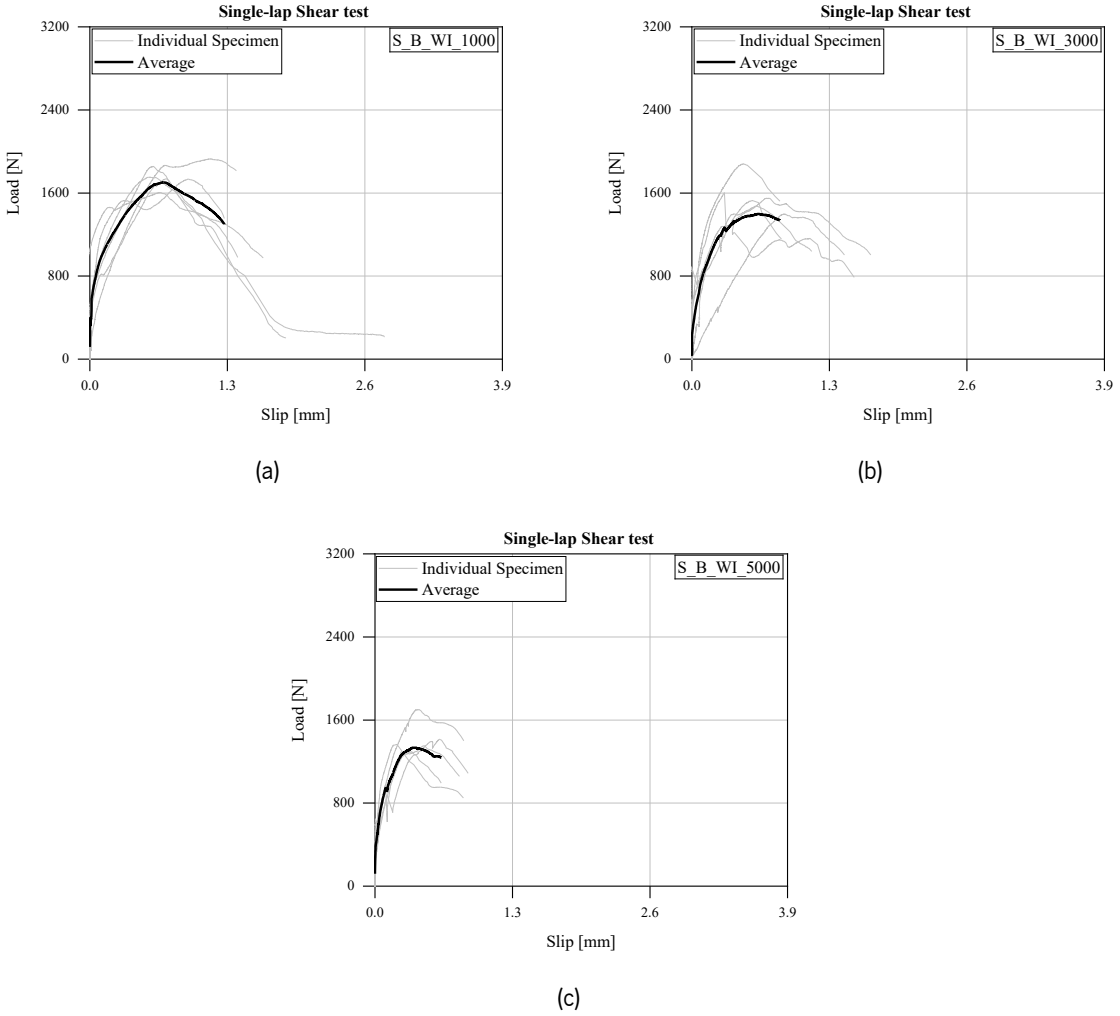

Figure 84 Load-slip curves of the single-lap shear test for the basalt fiber in the WI environment, showing each individual specimen and the average curve for each group: (a) S_B_WI_1000; (b) S_B_WI_3000; (c) S_B_WI_5000

Figure 85b illustrates the temporal evolution of peak load across exposure durations. In the dry condition, peak load values increased steadily, reaching their maximum at 5000 hours. This increase reflects a strengthening of the interface, consistent with the enhanced stiffness observed in the initial loading phase. Conversely, the WI specimens displayed a rapid reduction in peak load at 1000 hours, followed by a plateau, indicating a relatively inert behavior in later stages. The results point to the deleterious effect of early moisture ingress, which compromises the fiber-mortar interaction, although subsequent hydration may have helped prevent further deterioration. The lower peak loads for WI specimens relative to the dry group throughout the aging process further confirm the negative influence of continuous saturation on interfacial bond strength.

Debonding energy, shown in Figure 85c, quantifies the energy required to reach the peak load and is derived from the area under the load-slip curve up to the maximum point. For DC specimens, debonding energy remained generally stable with slight fluctuations, aligning with the consistent mechanical enhancement through carbonation. For WI specimens, an initial drop at 1000 hours was followed by a near-constant trend, consistent with the early weakening and subsequent stabilization observed in the peak load data. The convergence of debonding energy values for DC and WI groups at 5000 hours highlights the limited ability of hydration alone to match the interfacial toughness achieved via

carbonation. This behavior is in accordance with the mineralogical analysis of the matrix, which indicated greater densification and cohesion under dry conditions.

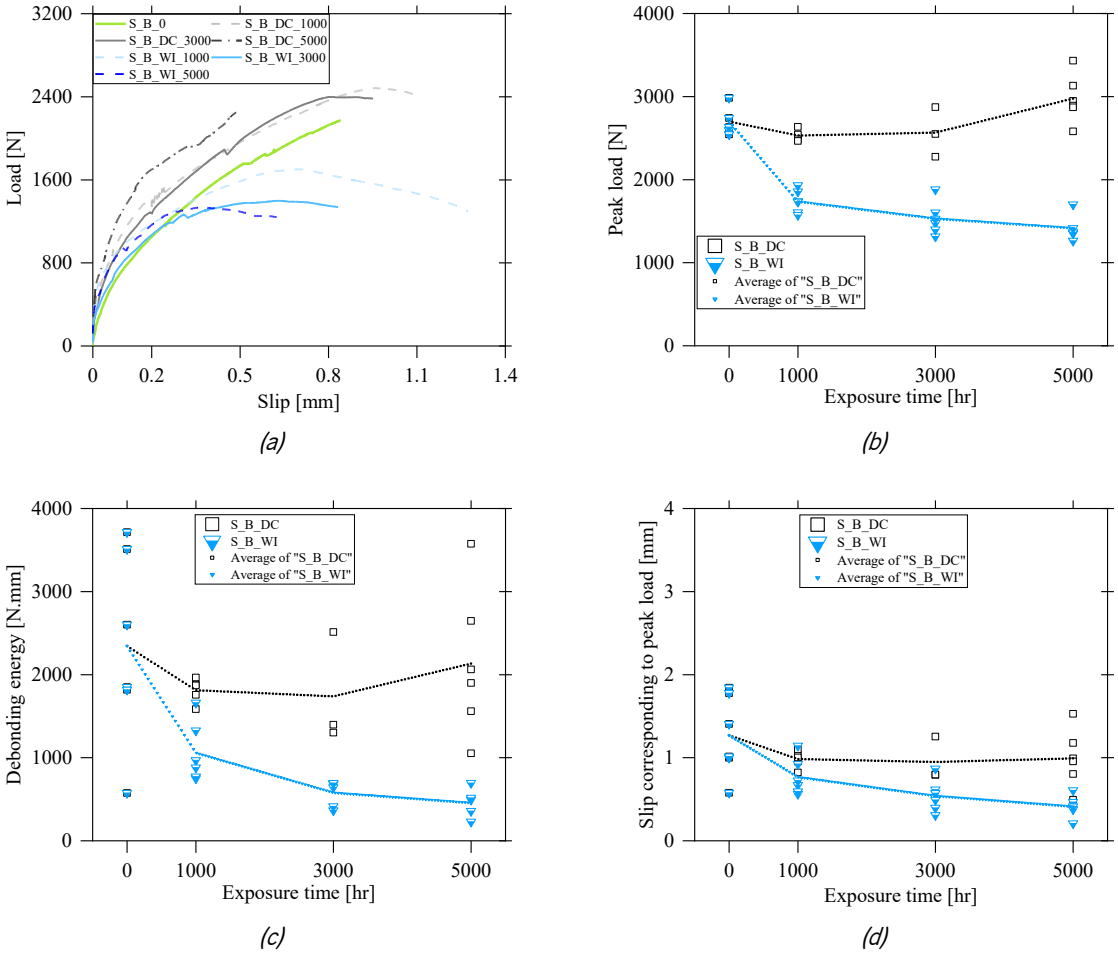

Figure 85 single-lap shear performance of basalt-based TRM under dry and water conditions: (a) average load–slip response; (b) peak load; (c) debonding energy; (d) slip corresponding to peak load.

Figure 85d presents the slip corresponding to peak load for all exposure conditions. A decreasing trend in slip was observed for both environments, though the rate of decrease was steeper for WI specimens. This reduction in deformability implies an evolution toward more brittle failure with increasing exposure time, particularly under water condition. The lower slip values of WI specimens are indicative of reduced ductility at the interface, most likely due to compromised mortar cohesion and increased susceptibility to premature crack propagation. Regarding failure modes, visual inspection confirmed that the predominant mode across both conditions was fiber rupture near the loaded end, preceded by fiber sliding. This suggests that even in the presence of environmental aging, the tensile strength of the basalt fiber was effectively mobilized, and interfacial detachment was not the dominant failure pathway. However, the brittle nature of failure was more evident in the WI specimens, especially at extended exposure times. In general, dry curing conditions supported a progressive enhancement in bond strength and energy dissipation through continued hydration and carbonation, while water condition introduced early-stage softening effects that limited mechanical gains. The observed differences in stiffness, peak load, and slip confirm the detrimental role of prolonged moisture exposure in undermining the long-term durability and ductility of basalt-based TRM systems.

6.6.3.2.2 Effect of acidic condition

The influence of acidic exposure on the bond behavior of basalt-based TRM systems in single-lap shear testing revealed a progressive degradation of the mechanical response with increasing aging time. Figure 86 presents the individual load–slip curves for specimens aged in acidic environments, alongside their corresponding average responses. Despite the observed variability, especially in the post-peak region, all specimens exhibited the characteristic three-stage response: an initial linear phase reflecting the elastic behavior and interfacial adhesion, a nonlinear hardening segment linked to microcracking and progressive sliding at the bond interface, and a post-peak decline governed by either fiber rupture or interface debonding. The average curves, shown in Figure 87a, confirmed a consistent reduction in both linear slope and peak load with prolonged exposure. This trend highlights the detrimental impact of acidic aging on interfacial stiffness and bond integrity, likely due to matrix softening, decalcification, and chemical attack on the fiber–mortar transition zone.

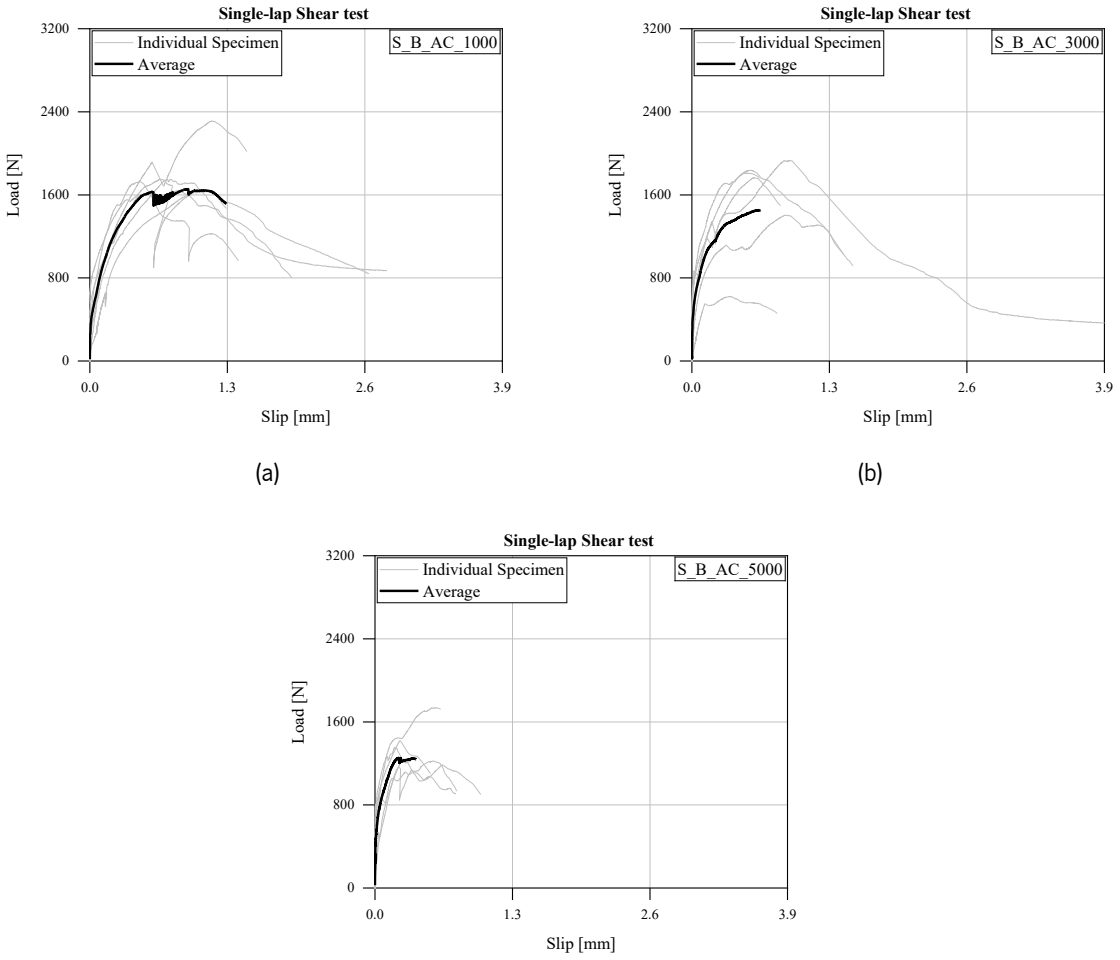

Figure 86 Load-slip curves of the single-lap shear test for the basalt fiber in the AC environment, showing each individual specimen and the average curve for each group: (a) S_B_AC_1000; (b) S_B_AC_3000; (c) S_B_AC_5000.

Compared to dry-cured specimens, which exhibited continuous improvement in linear stiffness and strength, the acidic-aged groups experienced more severe declines, especially after 3000 and 5000 hours of exposure. The load-slip behavior evolved from a relatively ductile response with an extended strain-softening phase to a more brittle profile with a shortened post-peak segment. This transition is indicative of chemical degradation mechanisms such as leaching of alkaline components, microcrack development due to expansive by-products (e.g., gypsum formation), and potential embrittlement of the

interface zone. The steeper negative trend in peak load with time in the acidic condition, as seen in Figure 87b, further substantiates the accelerated degradation rate of the bond system compared to water-immersed specimens, confirming the higher aggressiveness of acidic attack.

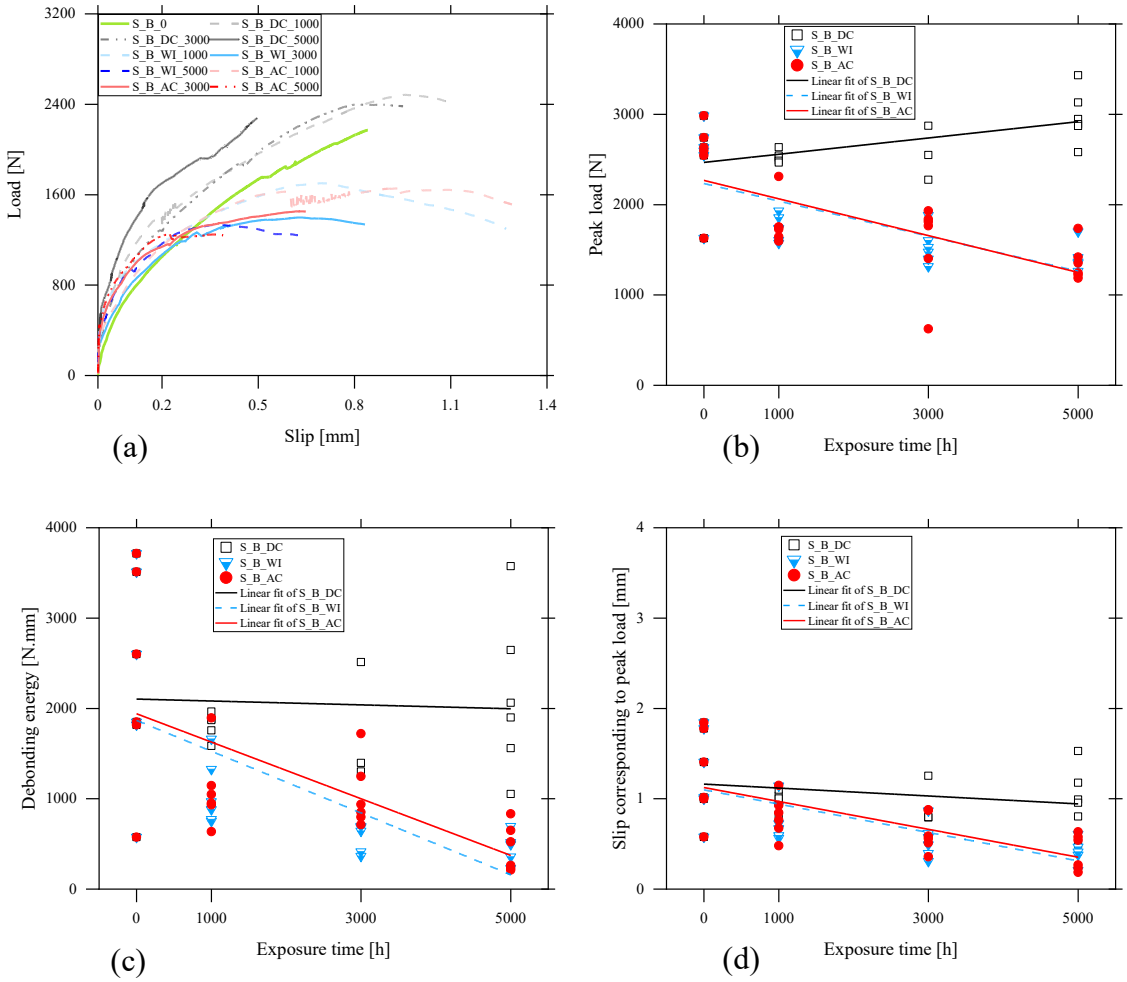

Figure 87 Single-lap behavior of basalt-TRM in different exposure durations and mediums; effect of acidic environment: (a) average load-slip curve; (b) peak load; (c) debonding energy; (d) slip corresponding to peak load.

Debonding energy, depicted in Figure 87c, showed a consistent decline with aging time in acidic conditions. This reduction corresponds to the decreasing capacity of the system to absorb energy prior to failure, supporting the interpretation that interfacial degradation was the primary driver of performance loss. The similarity in the declining slope of debonding energy between acidic and water condition conditions suggests that moisture ingress and associated chemical reactions are the dominant deteriorative mechanisms. However, the steeper decline in peak load for acidic specimens emphasizes the amplified impact of low pH environments.

The slip corresponding to peak load, presented in Figure 87d, also followed a decreasing trend for acidic-aged specimens. This behavior indicates a reduction in ductility and the capacity for energy dissipation through deformation, which may be attributed to progressive fiber-matrix bond weakening and an increased tendency for abrupt failure. The reduced slip values are consistent with the microstructural findings showing superficial damage and darkening of the mortar matrix in acidic-exposed specimens, possibly linked to the increased exposure of embedded fibers and local embrittlement near the interface.

Visual inspection of the tested specimens revealed no major signs of structural collapse or deep matrix spalling after 5000 hours of acidic exposure. However, superficial degradation was observed in the form of surface discoloration and more visible fiber outlines, suggesting that chemical weathering was primarily concentrated near the external layers. The absence of widespread cracking or substrate detachment indicates that acid-induced deterioration in lime-based mortars may be localized, with expansive reaction products likely confined to the near-surface zone, thus limiting the extent of internal damage. In conclusion, prolonged exposure to an acidic environment led to a clear deterioration in bond quality and mechanical response of basalt-based TRM under single-lap shear loading. The observed reductions in stiffness, peak load, debonding energy, and slip highlight the vulnerability of the system in aggressive environments, particularly when compared to the more stable performance observed in dry conditions. The mechanical degradation trends align with those reported in the pull-out tests and are corroborated by mineralogical observations, confirming the susceptibility of basalt TRM systems to acidic aging mechanisms.

6.6.3.2.3 Effect of alkaline condition

Figure 88 displays the individual load–slip responses of basalt-based TRM specimens exposed to alkaline environments, overlaid with the corresponding average curves. The consistent shape of individual responses reinforces the reliability of the observed trends and supports the interpretation of interfacial evolution under alkaline exposure. The mechanical response of basalt-based TRM systems exposed to an alkaline environment was investigated through single-lap shear testing, and the resulting average load–slip behavior, peak load, debonding energy, and slip at peak load are shown in Figure 89. The results reveal that specimens subjected to alkaline aging exhibited intermediate bond performance, positioned between those observed for dry and water condition conditions. As shown in Figure 89a, the average load–slip curves consistently displayed the typical triphasic response consisting of an initial linear elastic segment, a nonlinear hardening regime, and a post-peak phase. For alkaline-aged specimens, the slope of the initial linear phase was steeper than that of the water-immersed counterparts, indicating a stiffer bond interface, but it remained lower than the dry-cured specimens, which benefited from extensive carbonation.

This intermediate stiffness can be attributed to the enhanced pozzolanic activity induced by the alkaline solution, in which calcium hydroxide present in the mortar reacted with the silica-rich basalt fibers to produce additional $C-(A)-S-H$ phases. This contributed to a denser and more chemically integrated interfacial zone, improving the mechanical interlock and bond continuity. As a result, the initial stiffness and bond strength were increased relative to water-immersed specimens. However, due to the absence of full carbonation and the potential onset of microstructural degradation at prolonged exposure, the maximum values observed remained below those achieved under dry conditions. Post-peak behavior in alkaline-aged specimens also reflected a semi-brittle response, characterized by a sharper decline than the water-immersed specimens but less abrupt than in the dry condition. This is indicative of a transitional failure mechanism where chemical enhancement is counteracted by evolving damage mechanisms over time. Figure 89b illustrates the variation of peak load with exposure time. The data reveal that specimens aged in alkaline solution reached their highest peak load at 1000 hours, after which the values remained stable up to 3000 hours and subsequently plateaued. This behavior reflects the early strength gains attributed to pozzolanic reactions, followed by stabilization as the reaction products saturated the available reactive sites at the interface. The pattern is consistent with the trends observed in pull-out testing, supporting the hypothesis that the alkaline environment promotes early bond enhancement, which eventually reaches a steady-state performance. Comparatively, peak loads in alkaline conditions remained consistently higher than those in water condition but lower than in dry-cured specimens, underscoring the combined but non-dominant effects of pozzolanic reactions and limited carbonation.

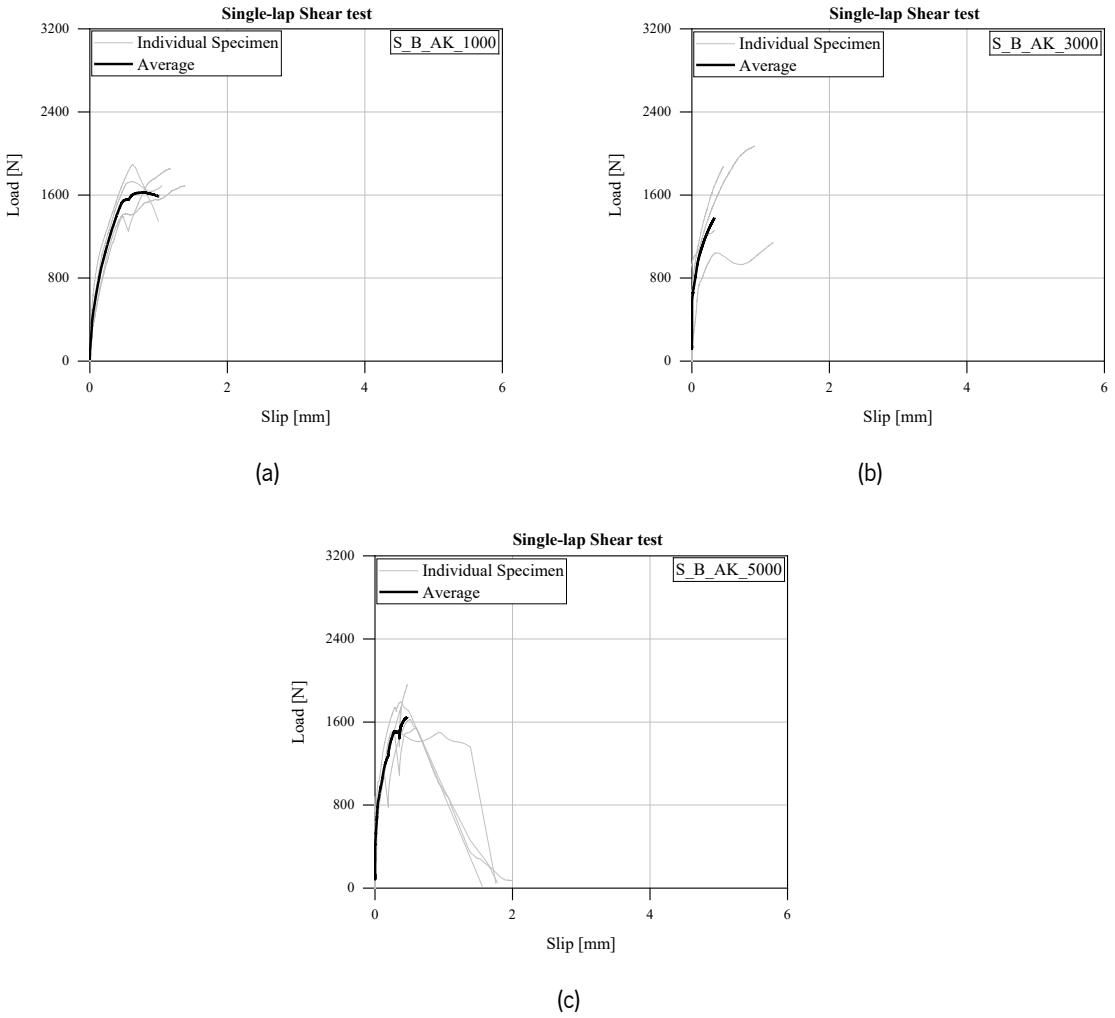

Figure 88 Load-slip curves of the single-lap shear test for the basalt fiber in the alkaline environment, showing each individual specimen and the average curve for each group: (a) S_B_AK_1000; (b) S_B_AK_3000; (c) S_B_AK_5000.

Debonding energy, shown in Figure 89c, followed a similar trend to the peak load. An initial increase was observed at 1000 hours, followed by a gradual decrease with extended exposure. The initial gain in energy absorption capacity may be attributed to improved chemical bonding and microstructural densification, whereas the later decline can be associated with the progressive development of microcracks and possible degradation of the fiber-mortar interface. This reflects a potential shift from chemically dominated enhancement mechanisms to deterioration-driven performance loss, especially as the system remains exposed to high alkalinity. While the energy absorption in alkaline conditions was superior to that in water condition, it remained below the stable and sustained values recorded in dry conditions. This again confirms the transitional nature of alkaline exposure effects, balancing initial strengthening with long-term susceptibility to chemical fatigue.

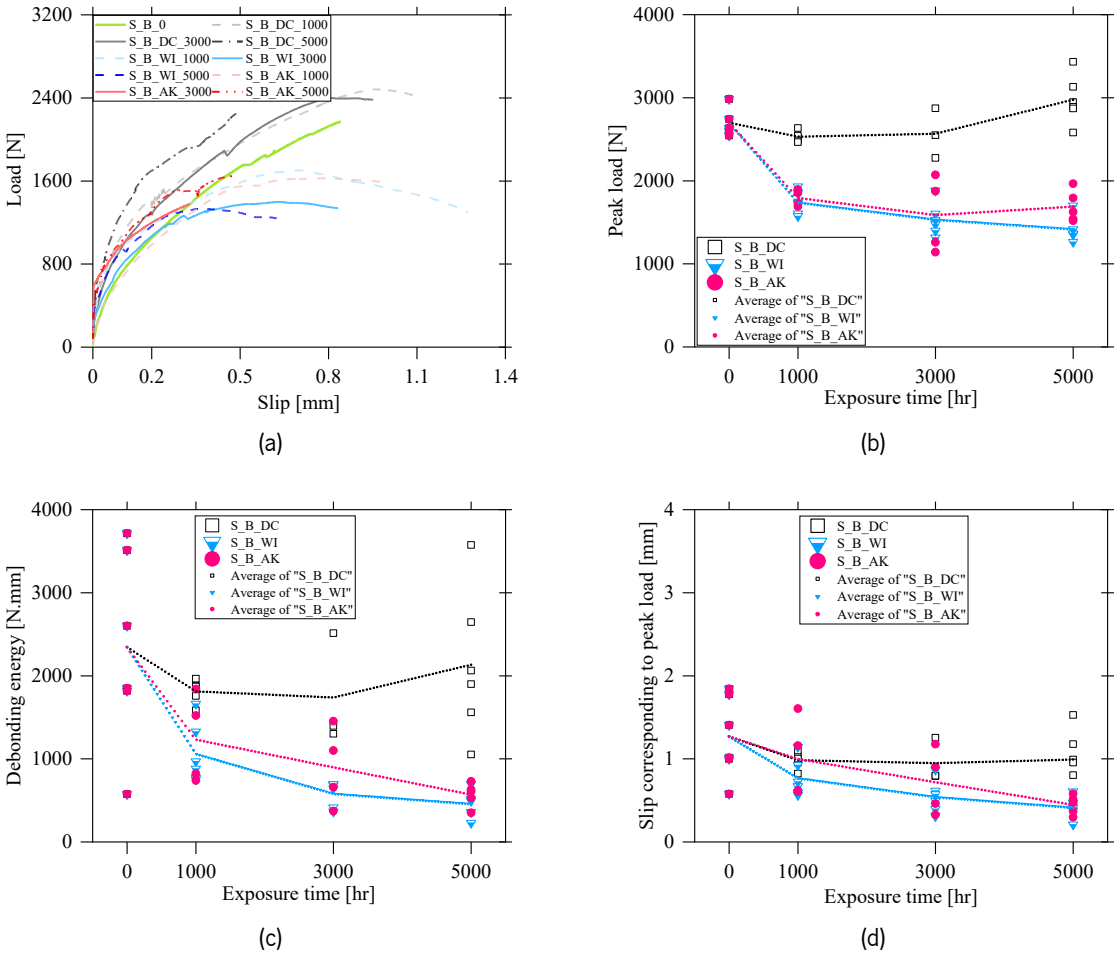

Figure 89 Single-lap behavior of basalt-TRM in different exposure durations and mediums; effect of alkaline environment: (a) average load-slip curve; (b) peak load; (c) debonding energy; (d) slip corresponding to peak load.

The slip corresponding to peak load, as presented in Figure 89d, exhibited a declining trend across all exposure durations for alkaline-aged specimens. A pronounced reduction was recorded at 1000 hours, which then stabilized over time. This suggests that the early pozzolanic reactions contribute to bond stiffening and constrain deformation at failure, consistent with an initially stronger and more rigid interface. The observed stabilization at later ages may indicate a saturation of the pozzolanic reaction or the onset of microstructural degradation, limiting further gains in interfacial stiffness. When compared to the other exposure environments, dry conditions led to the lowest slip values, reflecting maximum bond stiffness, while alkaline aging maintained intermediate slip levels, with water condition resulting in the highest ductility. Generally, the single-lap shear response of basalt-based TRM exposed to an alkaline environment demonstrated enhanced bond performance during early exposure, attributed to pozzolanic reactions, followed by stabilization in mechanical parameters over time. Although alkaline exposure improved both stiffness and strength relative to immersion in water, its long-term benefits remained below those achieved through carbonation in dry conditions. These observations are consistent with the trends reported in pull-out testing and are supported by mechanical and mineralogical characterizations, confirming the beneficial but time-limited nature of alkaline-induced chemical reactions in TRM systems incorporating basalt fibers.

6.6.3.2.4 Effect of saline condition

The mechanical behavior of basalt-based TRM subjected to saline aging was evaluated through single-lap shear testing. To illustrate the experimental variability and the representative nature of the average

curves, Figure 90 presents the individual load–slip responses for all specimens alongside their corresponding average trends. These curves reveal the characteristic three-phase behavior typical of TRM systems under shear: an initial linear response reflecting elastic bond behavior, followed by a nonlinear hardening segment, and concluding with a post-peak phase governed by fiber–matrix interaction and failure mechanisms. As shown in the subsequent average response (Figure 91a), the saline-aged specimens exhibited relatively stable initial stiffness up to 3000 hours, with a slight increase observed at 5000 hours. This moderate enhancement suggests that early chloride-induced hydration reactions may have promoted matrix densification and improved the fiber–matrix interface. Nevertheless, the expected acceleration effect of chloride exposure was not distinctly evident. This limited response may stem from the chemical resilience of basalt fibers and the role of the fired clay brick substrate, which potentially impeded chloride ingress or influenced the ionic environment near the bond interface.

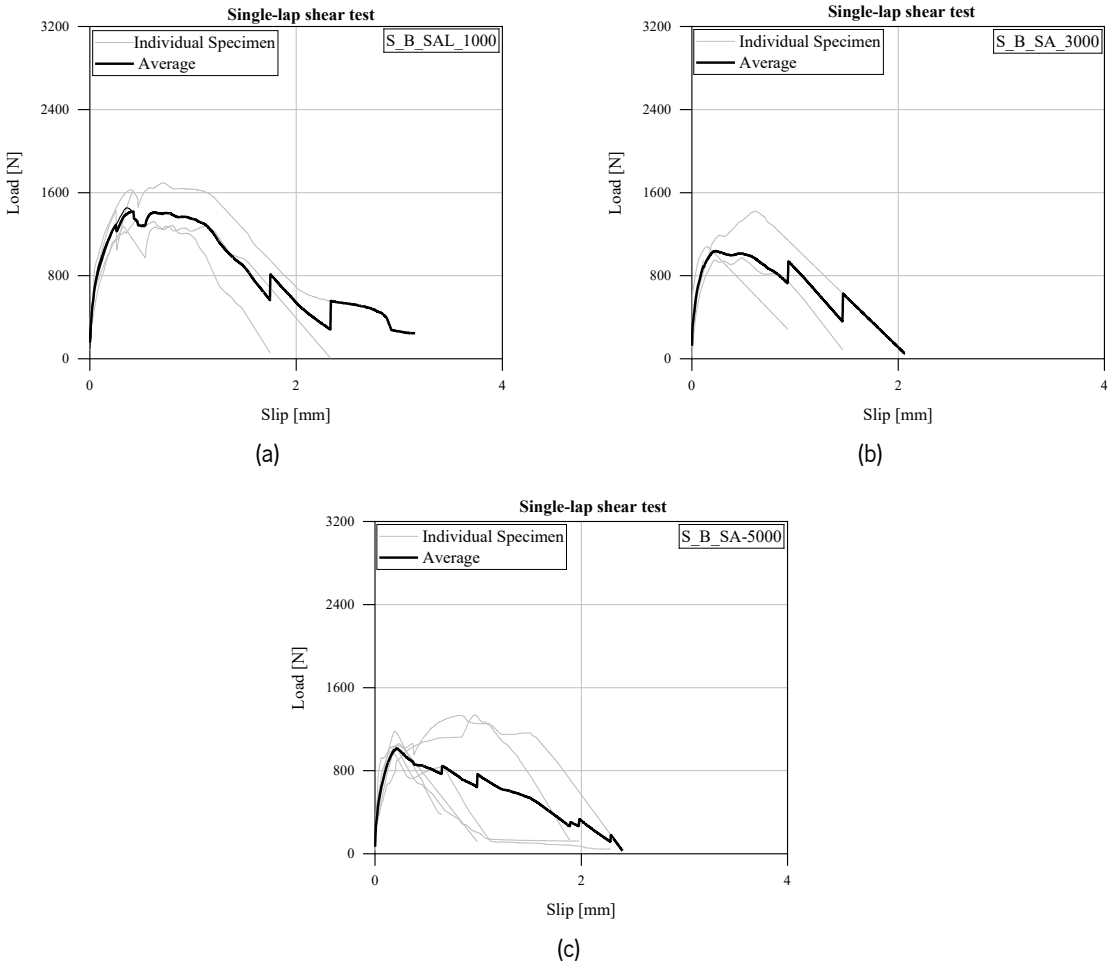

Figure 90 Load-slip curves from the single-lap shear tests of basalt fiber in saline environment, showing individual specimen results and the average curve for each aging duration: (a) S_B_SA_1000; (b) S_B_SA_3000; (c) S_B_SA_5000.

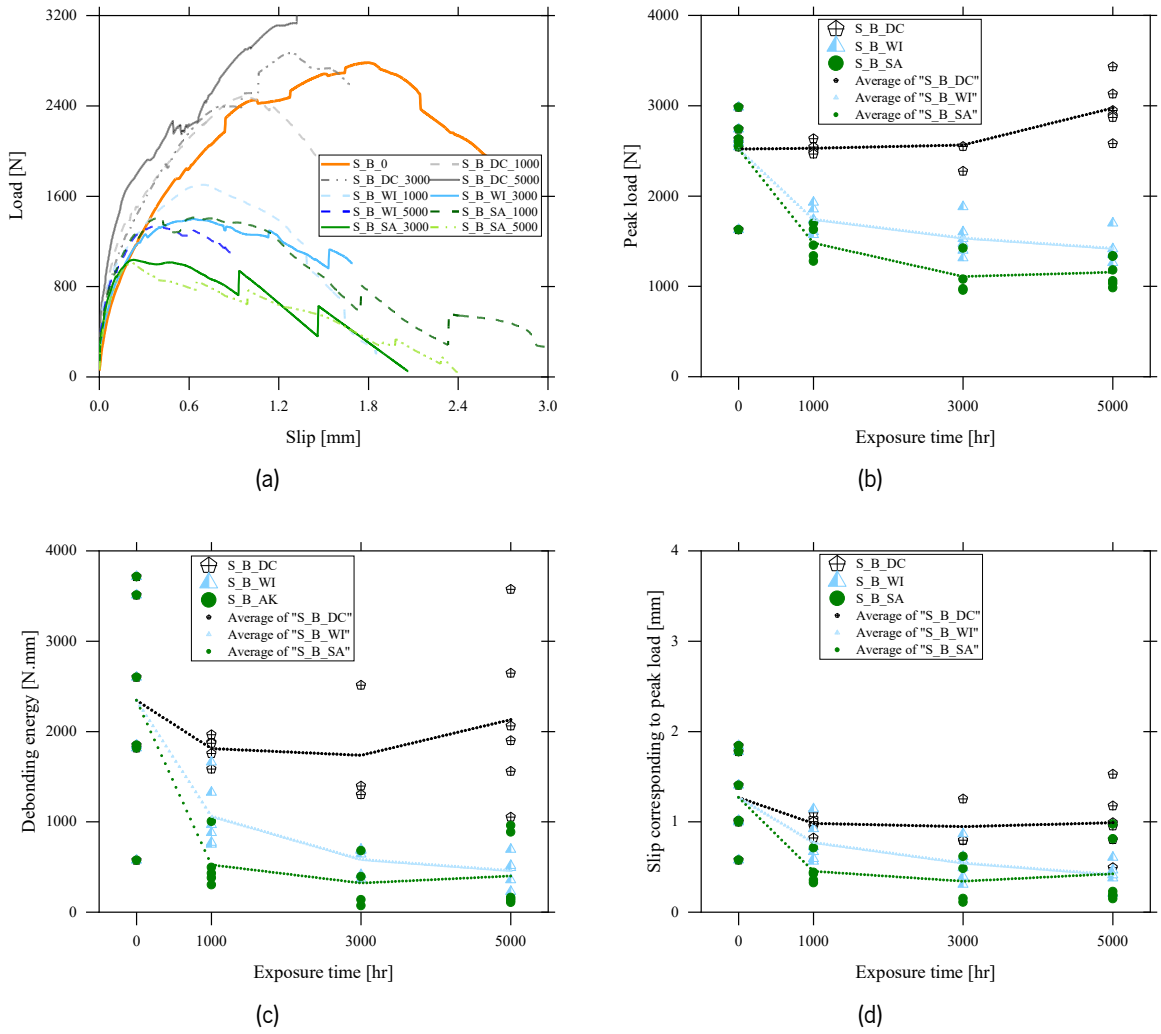

Figure 91 Single-lap behavior of basalt-TRM under various exposure durations and conditions; effect of saline environment: (a) average load-slip curve, (b) peak load, (c) debonding energy, (d) slip corresponding to peak load

In the nonlinear hardening regime, a decline in load-carrying capacity was noted up to 3000 hours of exposure, followed by partial recovery at 5000 hours. This behavior aligns with a two-stage response to chloride exposure: an initial degradation phase possibly induced by salt crystallization and microstructural damage, and a subsequent stabilization or slight improvement due to continued hydration or secondary reaction products. However, in comparison with glass-TRM, this recovery was less intense and delayed, likely reflecting the reduced reactivity and more resilient mechanical characteristics of basalt fibers. The fired clay substrate may also have played a role by buffering chloride concentrations and mitigating short-term damage. The trend in peak load values (Figure 91b) further supports this interpretation. A progressive reduction was observed up to 3000 hours, beyond which the values stabilized rather than recovering substantially. This contrasted with the trend observed in the pull-out test for glass-TRM, where a late-stage increase in peak load was recorded. The absence of such recovery in the basalt-based system suggests that the intrinsic chemical and mechanical stability of basalt fibers may lead to more inert behavior in saline environments but also limits the potential for performance gains through delayed hydration or secondary bonding. Furthermore, the brick substrate may have restricted the chloride mobility necessary to initiate such improvements.

Figure 91c presents the variation in debonding energy across exposure durations. A consistent reduction was observed at 1000 hours for all aging environments, after which the saline-aged specimens

showed minimal changes. By 5000 hours, the debonding energy values for saline and water-immersed specimens had converged, indicating a similar degree of degradation at the fiber–matrix interface. This lack of strong temporal evolution suggests that, after initial damage, the interfacial properties stabilized, likely due to saturation effects or the limited further progression of crystallization-induced microcracking. The subtlety of the response also implies that debonding energy in saline conditions may be dominated by early-stage mechanisms, with subsequent evolution constrained by the relatively inert behavior of the basalt yarn and the brick substrate's role in limiting ion transport.

The slip corresponding to the peak load (Figure 91d) exhibited a distinct pattern. All groups experienced a reduction at 1000 hours, consistent with stiffening effects or initial bond deterioration. Notably, the saline-aged specimens maintained the lowest slip values throughout the exposure period, indicating a stiffer and more brittle failure response. This behavior is consistent with salt crystallization at the interface, which can lead to embrittlement and sudden failure. However, a modest increase in slip was observed after 3000 hours, suggesting that either matrix microcracking or partial bond relaxation allowed slightly greater deformation before failure. Despite this, saline specimens remained more brittle compared to those aged in dry or water condition conditions. In general, saline aging induced a relatively stable yet degraded bond performance in basalt-based TRM systems. While early chloride-induced hydration effects appeared to marginally enhance interfacial properties, these were rapidly offset by microstructural damage, leading to lower energy absorption and reduced deformability. The delayed and subdued changes observed across mechanical parameters underscore the dual role of chloride exposure and the mitigating effects of the brick substrate. When compared to acidic conditions, the bond deterioration was less severe in saline environments, highlighting the greater durability of basalt yarns under non-acidic ionic exposures and supporting the suitability of basalt-TRM in chloride-prone applications, provided the long-term embrittlement risk is adequately addressed.

6.6.4 Comparison between the glass and the basalt TRM systems

A comparative assessment between glass- and basalt-based TRM systems offers critical insights into the role of textile material in the mechanical performance and durability of composite systems under different environmental exposures. Although both fiber types exhibited sufficient bond with lime-based mortar under dry conditions, their response to aggressive environments, especially acidic, alkaline, and saline, diverged significantly due to their respective microstructural and chemical stabilities. The following subsections outline the influence of each environmental condition on the mechanical and interfacial performance of glass- and basalt-TRM systems using the data obtained from pull-out and single-lap shear tests.

6.6.4.1 Effect of Acidic Condition

Under acidic exposure, a clear disparity emerged between the performance of glass and basalt TRMs. While glass-TRM demonstrated relatively stable performance, maintaining approximately 61% of its ultimate yarn capacity in the pull-out test after 5000 hours, basalt-TRM retained only 36%. This contrast was further emphasized in single-lap shear tests, where the peak load of glass-TRM after 5000 hours nearly reached the ultimate tensile strength of the bare fabric, whereas basalt-TRM retained only about 35% of its capacity. Additionally, glass-TRM exhibited more ductile post-peak behavior and higher energy absorption, as evidenced by the pull-out and debonding energies. In contrast, basalt-TRM showed more brittle failure patterns with reduced ductility and increased prevalence of fiber rupture over sliding, particularly in acidic samples with longer exposure durations. These performance disparities are likely related to the higher susceptibility of basalt fibers to acidic degradation, potentially due to their finer surface and greater calcium and aluminum content, which are more reactive with sulfuric compounds. The trend lines for peak load and slip consistently showed sharper declines for basalt than for glass, indicating a higher degradation rate. These findings underline the critical vulnerability of basalt-based

TRM systems to acidic environments, contrasting with the more stable and resilient performance of glass-based systems.

6.6.4.2 Effect of Alkaline Condition

In the alkaline environment, both TRM systems exhibited initial strength enhancements, attributed to pozzolanic activity and matrix densification. However, their long-term responses diverged. Glass-TRM maintained more consistent performance, with a 54% increase in pull-out capacity and only a 4% change in single-lap shear strength over 5000 hours. Basalt-TRM, although initially exhibiting a 34% increase in pull-out strength, experienced a substantial 37% reduction in single-lap shear strength by the end of the exposure. These results indicate that the pozzolanic-induced densification initially improved bonding, but the long-term effect was detrimental, especially for basalt fibers. Evidence of mineral accumulation and interface degradation was more prominent in basalt specimens, particularly at later stages, which may explain the discrepancy between pull-out and single-lap behavior. The sharper post-peak decline and the reduction in slip observed in basalt-TRM highlight increased brittleness and compromised interface resilience under prolonged alkaline exposure. These findings suggest that while basalt can exhibit superior short-term mechanical interlock, its durability under high-pH conditions is limited, possibly due to coating deterioration or the fiber's inherent reactivity with the alkaline medium. In contrast, glass fibers presented a more balanced bond evolution and retained sufficient integrity under prolonged alkaline influence.

6.6.4.3 Effect of Saline Condition

The response of TRM systems to saline exposure demonstrated further material-specific differences. In pull-out tests, glass-TRM specimens showed an initial decrease in bond performance followed by partial recovery at 5000 hours, likely related to chloride-induced acceleration of hydration. Basalt-TRM exhibited a more erratic response, with greater variability and weaker overall recovery, potentially due to localized interface degradation and higher fiber sensitivity. Single-lap shear test results reinforced these findings: glass-TRM experienced a modest increase in peak load at 5000 hours, while basalt-TRM maintained a declining or plateauing trend. The influence of the fired clay brick substrate likely moderated chloride availability at the interface, particularly for glass-TRM specimens, thereby altering early bond enhancement. Energy-based parameters such as debonding and pull-out energy also revealed higher scatter in basalt-TRM, pointing to more brittle failure and greater sensitivity to local imperfections. Slip at peak load was generally lower in basalt specimens, further supporting their reduced ductility and increased brittleness in saline conditions. Overall, while both fibers displayed some degradation, the glass-TRM system exhibited more predictable behavior and partial recovery, whereas basalt-TRM performance was marked by inconsistent trends and greater vulnerability to prolonged saline attack.

6.6.5 Comparison on the different aging environments

The mechanical performance of TRM systems across different aging conditions revealed that dry storage consistently enhanced both peak load and stiffness due to ongoing carbonation and matrix densification. In dry conditions, both basalt- and glass-based composites developed a strong interfacial bond, with glass TRM achieving peak loads close to the tensile capacity of the bare yarns. Basalt TRM also showed considerable performance improvement, albeit to a slightly lower extent. Water condition introduced moderate aging effects. While the matrix benefitted from continued hydration, the overall bond quality—particularly in basalt TRM—deteriorated over time. The weaker bond response in basalt systems was associated with moisture-sensitive degradation mechanisms and greater variability in slip and energy parameters. Glass TRM showed more stable behavior under water exposure, though minor strength loss and ductility reduction were still observed.

Saline exposure generated complex responses due to the dual effect of chloride ions. Early-stage acceleration of hydration contributed to transient improvements in bond strength, particularly in pull-out configurations. Over time, however, salt crystallization and leaching effects led to increased brittleness and reduced ductility, especially in basalt-based composites. Glass TRM exhibited more predictable performance trends, with a moderate reduction in energy parameters at later stages.

Alkaline environments produced initial gains in strength and stiffness, driven by enhanced pozzolanic reactions at the fiber–matrix interface. These benefits were more sustainable in glass TRM systems, where bond quality remained stable even after prolonged exposure. In contrast, basalt TRM experienced notable degradation beyond 3000 hours, marked by reduced peak loads and a shift in failure modes. This behavior was attributed to long-term chemical interactions at the interface, compromising mechanical interlock.

Acidic aging caused the most detrimental effects in basalt-based composites. Even though the lime-based mortar maintained its mineralogical integrity, basalt fibers demonstrated substantial loss in bond strength and ductility. Glass TRM preserved better mechanical response under the same conditions, indicating greater resistance to acidic degradation. The disparity between the two systems was particularly evident in energy absorption and post-peak behavior, where basalt systems showed a sharper decline.

Given the significant degradation observed under acidic exposure, especially for basalt textiles, and the limitations of moderate-intensity aging conditions explored so far, a deeper investigation is required. The next chapter addresses this gap by examining TRM durability under intensified acidic environments, with the goal of identifying the thresholds of performance decline and the governing degradation mechanisms.

6.7 Conclusion

The analysis presented in this chapter has demonstrated that environmental exposure significantly influences the durability and mechanical performance of TRM systems. Through an extensive experimental program of pull-out and single-lap shear testing, supported by mineralogical and microstructural characterization, the comparative behavior of glass and basalt fibers was assessed under dry, water, saline, alkaline, and acidic conditions. While both TRM systems exhibited enhanced performance in dry conditions due to carbonation, glass textiles consistently outperformed basalt fibers under all aggressive environments, showing lower susceptibility to interface degradation and more stable post-peak behavior. Acidic exposure emerged as the most detrimental condition for basalt TRM, underscoring the need for a focused examination of its mechanisms. The limitations of moderate-intensity exposure in fully capturing long-term deterioration trends justify a deeper investigation under more severe acidic conditions, which will be addressed in the following chapter. Key conclusions drawn from this chapter are as follows:

- Dry storage promoted the highest bond strength and stiffness in both glass and basalt TRM systems, driven by matrix densification from carbonation, and should be considered the reference condition for lime-based composites.
- Water condition induced moderate aging, with basalt TRM showing significant reductions in bond quality and ductility, whereas glass TRM exhibited more stable behavior with slight strength losses.
- Saline environments generated complex degradation trends, where chloride-induced hydration initially enhanced bonding, followed by increased brittleness and variable energy absorption, especially in basalt TRM systems.

- Alkaline exposure initially enhanced mechanical response due to pozzolanic reactions, but long-term exposure led to notable bond degradation in basalt TRM, while glass TRM maintained relatively stable performance.
- Acidic conditions caused the most severe degradation, particularly in basalt-reinforced TRM, which experienced substantial losses in peak load and ductility due to interfacial weakening and higher fiber vulnerability.
- Glass textiles demonstrated better long-term durability and more consistent performance across all environmental conditions, making them a reliable reinforcement choice in aggressive scenarios.
- Basalt textiles showed superior initial stiffness and mechanical interlock, but their long-term durability in wet and chemically aggressive environments was markedly lower.
- Failure modes and degradation trends were more variable in basalt TRM due to its finer yarn geometry and susceptibility to fiber rupture, particularly under acidic and saline exposures.
- Microstructural observations confirmed the limited mineralogical alteration in mortars; however, gypsum formation and localized damage were evident in acidic environments, influencing mechanical behavior.
- The need for intensified acidic aging studies is strongly supported by the observed sensitivity of basalt TRM and the limitations of current exposure regimes in capturing late-stage deterioration.

The findings of this chapter form the foundation for a targeted analysis of TRM performance under intensified acidic conditions in Chapter 7, aimed at defining critical thresholds and advancing predictive models for long-term durability.

Chapter 7
Multiscale analysis of TRM matrix aging in acidic environments: from experimental testing to chemo-mechanical and machine learning models

7.1 Introduction

In Chapter 6, a first experimental campaign, referred to as Durability Campaign I, was conducted to provide an initial understanding of the durability performance of TRM composites and their constituent materials under various mild environmental exposures. That study included saline, alkaline, and moderately acidic aging conditions, alongside reference media such as water immersion and dry storage. The findings of that chapter established the critical importance of further exploring the effects of acid attack, as the degradation of the lime-based mortar matrix under acidic environments emerged as one of the most severe and complex deterioration mechanisms observed.

Building upon these initial insights, this chapter focuses exclusively on the aging mechanisms of the lime-based mortar matrix in the presence of sulfuric acid. To address the existing knowledge gap, a new experimental program, Durability Campaign II, was established. This targeted campaign was specifically designed to investigate the multiscale effects of prolonged exposure to aggressive acidic environments, with the aim of understanding both the chemical transformations and the resulting mechanical degradation of the material. The selected experimental parameters included three acidic levels (pH 3.0, 2.0, and 1.5) and three exposure durations (1000, 3000, and 6000 hours), enabling a systematic evaluation of the progressive deterioration processes.

In parallel with the experimental campaign, two complementary modeling approaches were pursued. The first approach, based on machine learning, aimed to leverage existing data from Durability Campaign I, as preliminary research to predict flexural performance trends of acid-aged mortars, using advanced algorithms to capture non-linear dependencies between input variables and mechanical response. The second approach employed a chemo-mechanical model based on continuum damage mechanics, calibrated with the new experimental data from Durability Campaign II, to simulate the compressive behavior of the acid-aged mortar and establish predictive degradation trends. Together, these

experimental and modeling efforts aim to deliver a robust, multiscale understanding of the aging mechanisms governing lime-based mortar performance in acidic environments. The flowchart summarizing the methodological structure of this chapter is available in Figure 32.

7.2 Experimental program: durability campaign II

A dedicated experimental campaign was designed to investigate the aging behavior of lime-based mortar under acidic conditions. Over 500 specimens were prepared and exposed to three sulfuric acid solutions with pH levels of 3.0, 2.0, and 1.5, alongside reference conditions of distilled water immersion and dry storage in a controlled climatic chamber. Each exposure condition was evaluated at three durations: 1000, 3000, and 6000 hours, as well as unexposed condition. Following exposure, specimens were tested for compressive strength, flexural strength, and elastic modulus on cylindrical samples, besides of the ultimate compressive strength on the same cylindrical specimens. Microstructural and mineralogical changes will be assessed here in this section using micromechanical and mineralogical testing including XRD, FTIR, SEM, TGA, and ICP analysis to support the interpretation of degradation mechanisms.

7.2.1 Materials

The same mortar as introduced I Chapter 3, as a NHL mortar with eco pozzolan made of lime-cement-pozzolan, was selected for this study. The formulation of the mortar includes dispersed short polymeric fibers intended to mitigate shrinkage and enhance fiber-matrix adhesion, promoting mechanical interlocking suitable for TRM applications. The particle size distribution (PSD) of the dry mortar, analyzed by laser diffraction using a Mastersizer 2000 (Malvern Instruments), exhibited a bimodal pattern (Figure 93a), with peaks associated with binder fines and coarse aggregate fractions. Such a gradation is favorable for optimizing packing density and fresh-state workability.

FTIR and SEM were employed to characterize the short fibers embedded in the mortar. SEM imaging (Figure 93d) revealed that the fibers are formed by bundles of finer fillaments. The FTIR spectra (Figure 93b) identified strong C=O stretching vibrations at 1734 cm^{-1}, along with C-H bending modes at 1479 cm^{-1} and 1371 cm^{-1}, consistent with polyester-based materials, most probably polyethylene terephthalate (PET). Combustion tests confirmed the polymeric nature, and immersion tests in low-pH acidic solutions demonstrated the fibers' high chemical resistance with negligible dissolution. XRD analysis (Figure 93c) performed on unreacted mortar samples with fibers, identified quartz (SiO_2), calcite ($CaCO_3$), and portlandite ($Ca(OH)_2$) as the primary crystalline phases, with minor amounts of ettringite ($C_6A_6S_3H_{32}$). C_3S is also visible due to the addition of Portland cement.

The preparation of the mortar followed the procedure presented in Chapter 3. Two specimen geometries were cast: prismatic specimens (40 × 40 × 160 mm) for flexural and compressive strength tests, and cylindrical specimens (75 × 150 mm) for elastic modulus and ultimate strength evaluations. Immediately after casting, all specimens were covered with plastic sheets to minimize evaporation. Moisture retention was further ensured by placing damp burlap on the surface during the first three days. The specimens were demolded on the third day and then cured under controlled conditions (20°C, 80% RH) in a climatic chamber for 60 days.

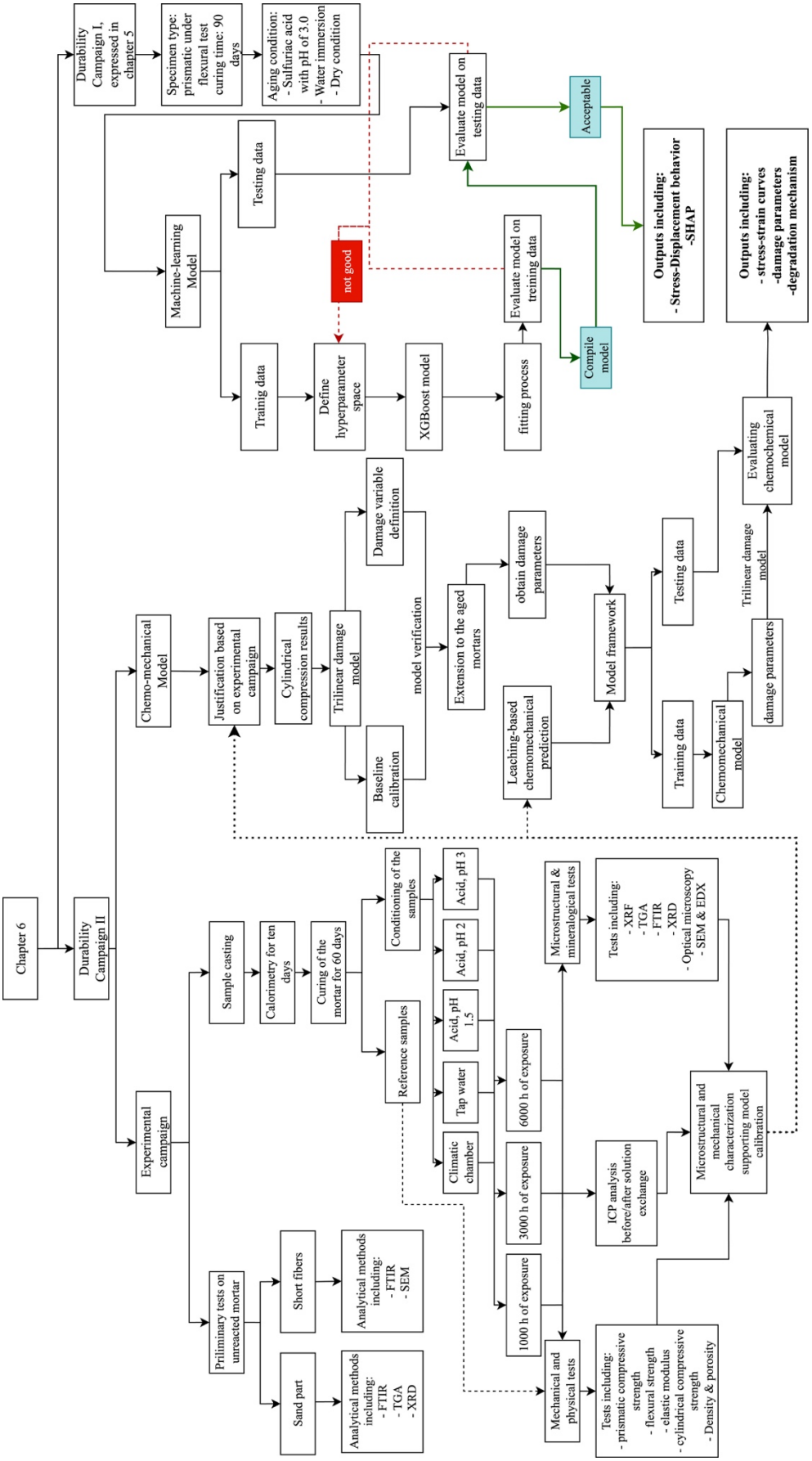

Figure 92 Overview of the experimental program, of the present chapter.

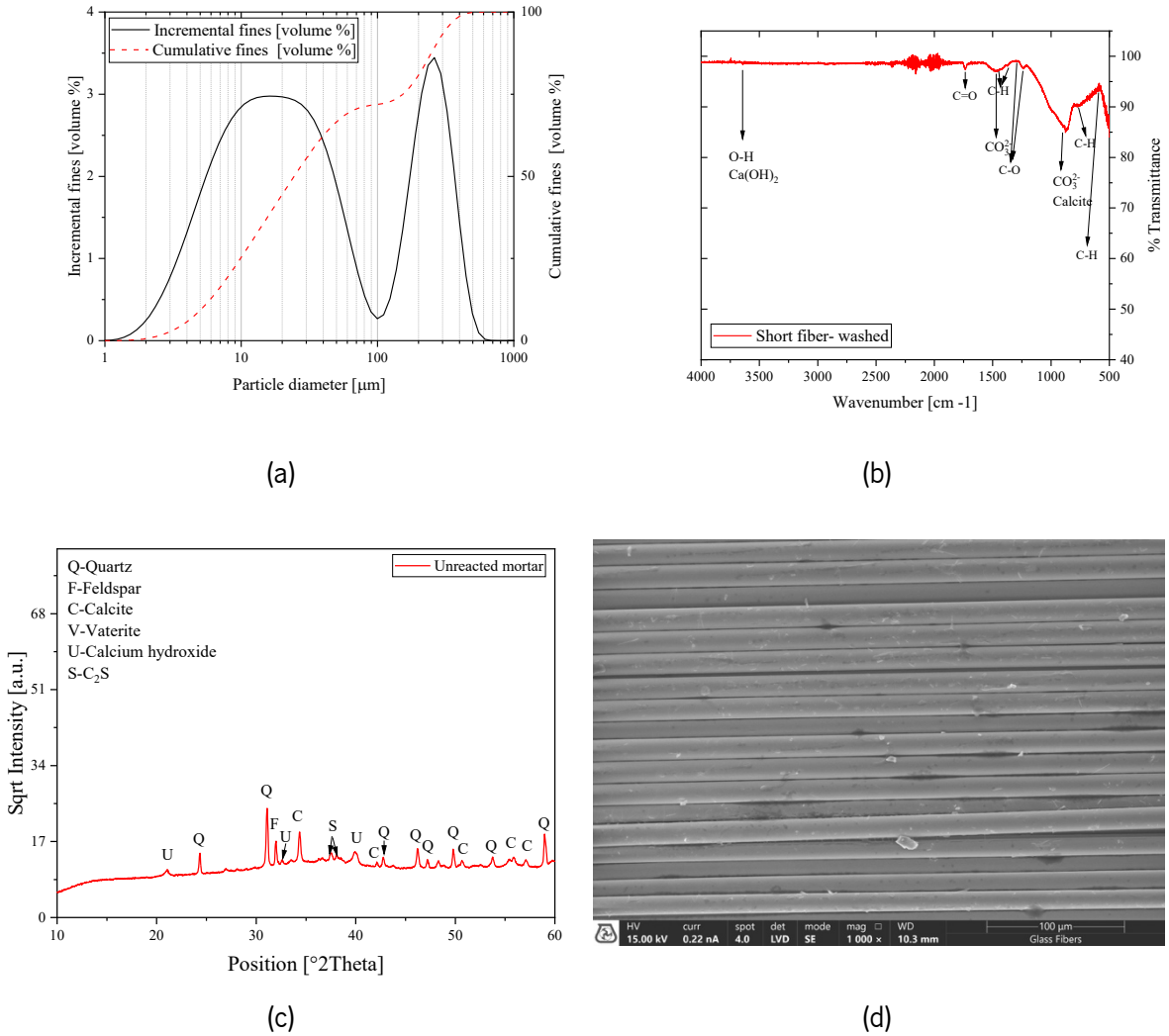

Figure 93 Characterization of the mortar: (a) particle size distribution of the dry mortar; (b) FTIR spectra of unreacted mortar, and isolated short fibers; (c) XRD patterns of unreacted mortar with fibers; (d) SEM image showing the morphology of bundled short fibers.

7.2.2 Aging method

In addition to the main aging campaign, a set of specimens was tested at intermediate curing durations (3, 7, 14, and 28 days) to monitor early-stage mechanical development. After the 60-day curing period, the specimens were exposed to accelerated aging under five environmental conditions: immersion in sulfuric acid solutions with pH 3.0, 2.0, and 1.5; continuous immersion in tap water; and dry storage in a climatic chamber. Each exposure condition was investigated at 1000, 3000, and 6000 hours, along with a reference group maintained unexposed.

The acidic solutions were prepared using sulfuric acid (H_2SO_4, 95–97% purity) and refreshed regularly to maintain chemical stability and control leaching effects. All immersion tanks were equipped with circulation systems, and the pH was monitored and adjusted twice weekly. A solid-to-solution mass ratio of 1:5 was maintained, and the solution temperature was held at 20°C throughout. Prior to mechanical testing, all aged specimens were conditioned in a climatic chamber for seven days to stabilize moisture content. The testing methodology adopted in this chapter mirrors that of the previous campaigns. Detailed descriptions of the mechanical test procedures, including flexural and compressive strength tests on prismatic specimens, and elastic modulus and ultimate strength on cylinders, were

provided in Chapter 3. Similarly, protocols for microstructural and mineralogical characterization (XRD, FTIR, SEM, TGA, and ICP analysis) have been described in Chapter 5.

7.2.3 Labeling schemes

To ensure systematic identification and traceability of all tested specimens, two complementary labeling schemes were adopted to differentiate curing durations and aging conditions. For specimens evaluated during the early-age curing phase, the classification format T_D was used, where T denotes the type of mechanical test, flexural (F), compressive (C), or elastic modulus (E), and D indicates the curing duration in days, expressed as 3D, 7D, 14D, or 28D. Specimens subjected to full curing for 60 days were labeled using C in place of the numerical duration.

For the main aging campaign conducted after full curing, a more detailed notation was adopted: T_C_E_A_R. In this format, T identifies the test type, C confirms that the specimen was fully cured, E specifies the exposure environment, RC for dry climatic chamber, RW for tap water, P15 for sulfuric acid at pH 1.5, P2 for pH 2.0, and P3 for pH 3.0, A indicates the exposure duration (1000, 3000, or 6000 hours), and R is the specimen number within its group. For example, the designation F_C_P3_3000_4 corresponds to the fourth flexural specimen tested after 60 days of curing and 3000 hours of immersion in a pH 3.0 acidic solution.

7.3 Experimental results and discussion

7.3.1 Early age curing effect

The early hydration kinetics of the mortar system were evaluated through calorimetric monitoring over a 240 hours (10-day) period. Figure 94 illustrates the heat flow (expressed in W/g of binder) and cumulative heat release for two mixes: one incorporating Part B, an activator solution, and the other using distilled water. The reported heat flow values are normalized to the binder mass to ensure comparability between the two systems. The water-based mix exhibited a more intense and sharply defined exothermic peak, reaching its maximum around 30 hours, indicative of a relatively rapid hydration process. In contrast, the mix containing Part B displayed a broader and delayed heat flow curve, with the peak shifted to approximately 42 hours and showing a lower intensity. This altered thermal behavior indicates that the chemical composition of Part B influenced the early hydration kinetics by moderating the initial reactivity and extending the overall reaction period. However, the exact mechanism remains complex and may involve multiple interacting factors within the activator system [309] .

Despite the more extended heat flow observed in the Part B system, the cumulative heat release after 240 hours was lower than that of the water-based mix. This finding suggests a less complete hydration reaction over the same period, potentially reflecting the slower dissolution and reaction rates associated with the silicate-rich formulation. Such thermal behavior may influence early-age properties like setting time and structural build-up, which are critical in the development of performance in lime-based mortars.

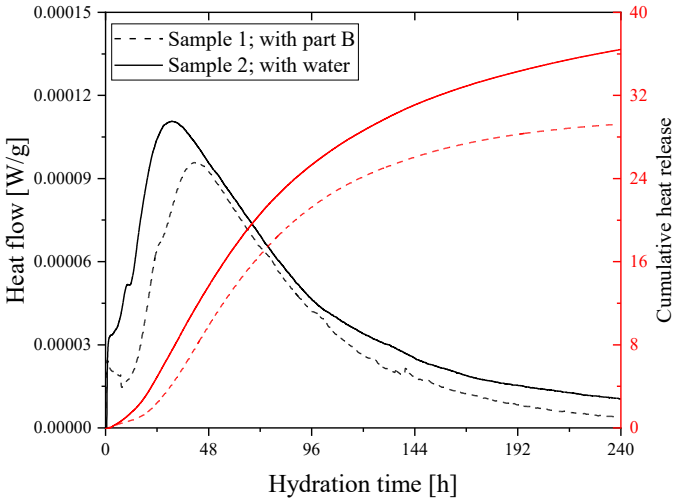

Figure 94 Heat flow and cumulative heat release over 10 days. Sample 1 contains mortar part B; Sample 2 is mixed with water only.

7.3.2 Evolution of lime-based mortars during reference aging

Up to 60 days of curing, the mortar exhibited a steady development of mechanical and physical properties, defining the baseline condition for later environmental exposure. As observed in Figure 95a–d, compressive strength, flexural strength, and elastic modulus consistently increased throughout the curing phase, driven by ongoing hydration and early-stage carbonation. Compressive strength on both prismatic and cylindrical specimens, along with flexural strength and modulus, followed comparable upward trends, though slight magnitude differences were evident due to specimen geometry. Porosity (Figure 96b) initially rose up to 28 days, a phenomenon likely attributed to the dissolution of early hydration products and the onset of carbonation reactions as well as the loss of free water. During carbonation, transformation into calcium carbonate with concurrent water release occured, which can temporarily enlarge the pore network before densification occurs [310]. Meanwhile, porosity may also be influenced by ongoing dissolution processes that contribute to transient pore enlargement.

After 28 days, porosity began to decline, which may be explained by the delayed pozzolanic reactions taking place [288]. Similarly, bulk density (Figure 96a) showed a slight decline until 14 days, likely due to mass loss associated with free water evaporation and carbonation-induced dehydration. Beyond this period, the density increased gradually, corresponding to matrix consolidation and the accumulation of carbonation and hydration products. These coupled mechanical and physical evolutions are consistent with the interplay between early-age hydration, carbonation, and latent pozzolanic activity, in agreement with prior observations in lime-rich systems [311]. The mortar at 60 days was thus considered fully cured and used as the reference condition for aging studies.

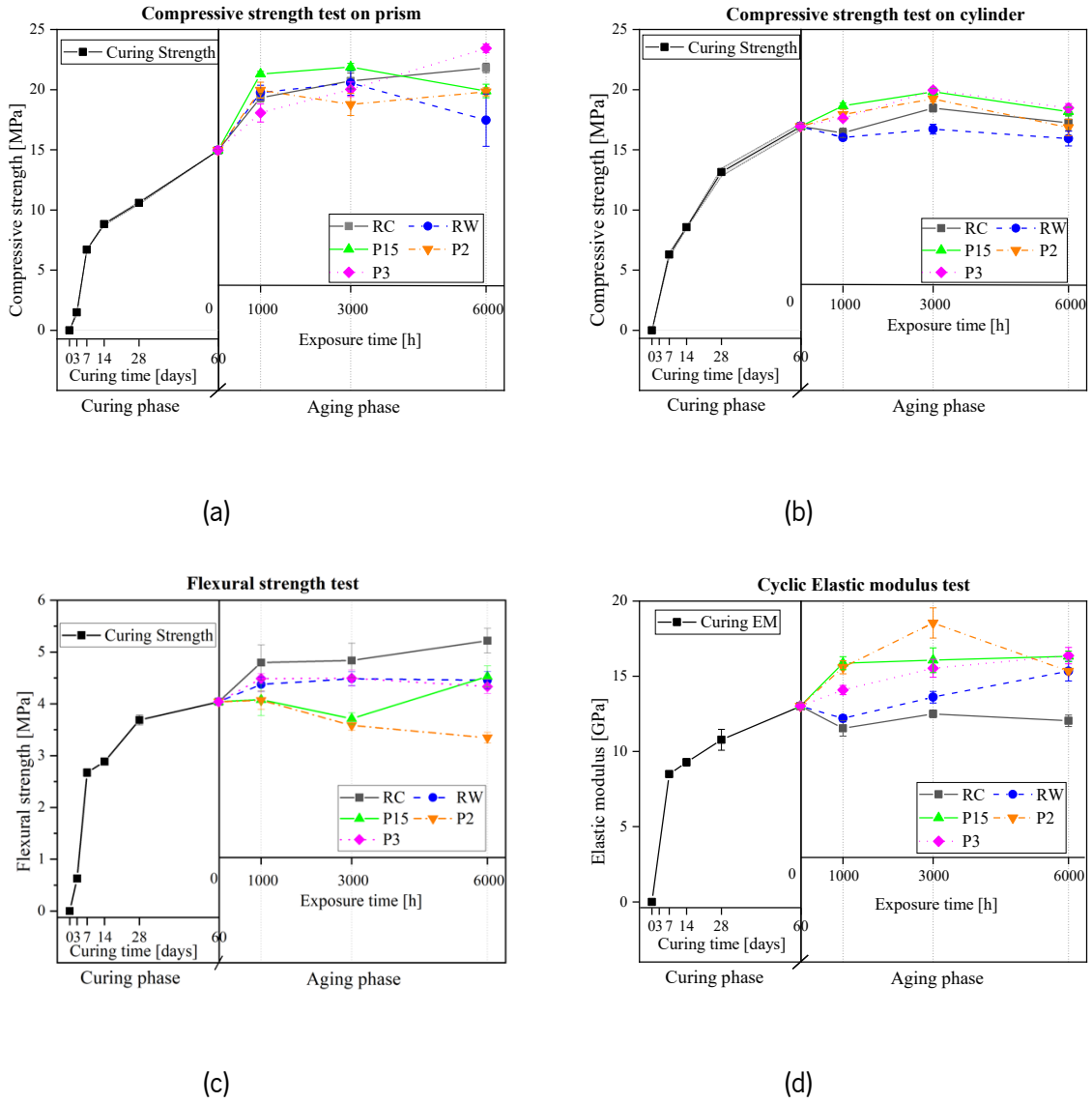

Figure 95 Mechanical performance of mortar specimens during curing and aging phases: (a) prismatic compressive strength; (b) cylindrical compressive strength; (c) flexural strength; (d) cyclic elastic modulus.

Following the 60-day reference curing, specimens subjected to standard dry condition and continuous water immersion exhibited divergent mechanical and microstructural evolutions. In the RC environment, mechanical tests (Figure 95a,b) demonstrated a slight but consistent improvement in compressive strength in prismatic samples, whereas cylindrical specimens displayed stabilization after initial curing. This progressive behavior is attributed to ongoing carbonation reactions within the mortar matrix, promoted by exposure to ambient CO_2 under moderate humidity [312]. Flexural strength and cyclic elastic modulus (Figure 95c,d) also remained stable or experienced modest increases, suggesting that the material continued to densify without significant deterioration. Porosity measurements (Figure 96b) revealed a slight reduction in RC specimens, supporting the hypothesis of pore refinement through carbonation [285], while density values (Figure 96a) showed minimal variation, indicating no substantial material loss during dry aging. Complementary XRD analyses and TG (Figure 97) show the increase of portlandite between 1000 and 6000 hours likely due to the continuous reaction of the compounds in the mortar, alongside an increase in calcite, consistent with carbonation of the sample.

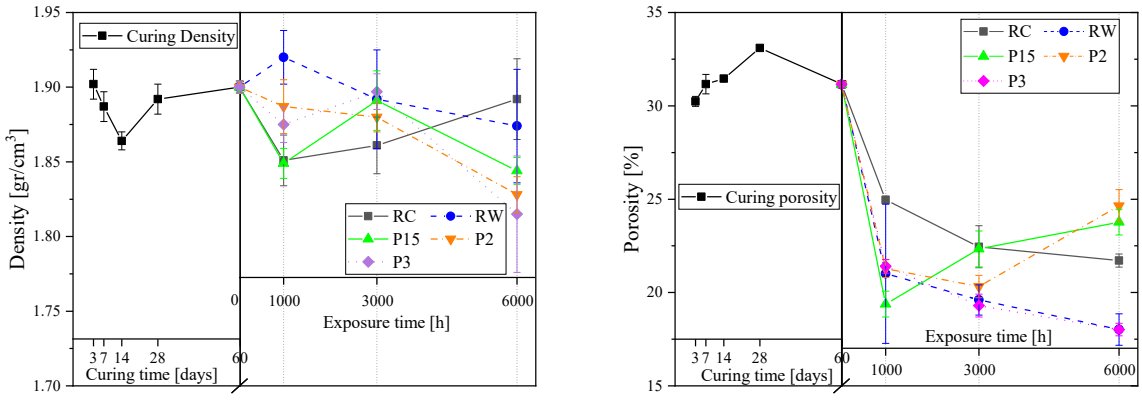

(a) (b)

Figure 96Physical properties of lime-based mortars in all environments: (a) bulk density and (b) open porosity evolution during curing and exposure.

In contrast, mortars immersed continuously in water exhibited more complex mechanical responses. The compressive strength of prismatic samples (Figure 95a) initially increased up to 3000 hours but subsequently declined toward 6000 hours, suggesting early matrix densification followed by microstructural degradation. Cylindrical specimens (Figure 95b) exhibited a slight reduction in compressive strength at 1000 hours, followed by a stabilization trend up to 6000 hours. Flexural strength (Figure 95c) showed a slight gain after 1000 hours and remained relatively stable thereafter, while cyclic elastic modulus (Figure 95d) experienced a minor decrease at 1000 hours but progressively recovered during prolonged immersion. While mechanical trends suggest evolving material behavior, direct evidence of significant microstructural alterations compared to the reference dry curing (RC) is not clearly observed in the available XRD and TGA data. XRD analysis (Figure 97a) shows no significant differences to the RC samples. Complementary TG results show that the calcite in the RC samples is slightly higher, due to the storage in air which allows a direct interaction of the air with the sample.

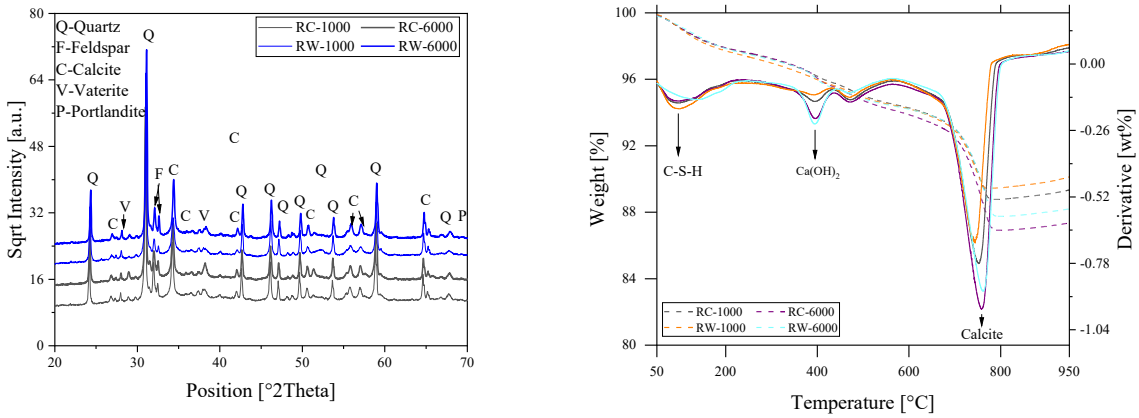

(a) (b)

Figure 97 Chemical and mineralogical test results on lime-based mortar samples exposed to climatic chamber and water immersion: (a) XRD patterns; (b) TGA thermograms.

7.3.3 Effect of acidic aging

The exposure of lime-based mortars to acidic environments induced complex and multiscale degradation processes, which differed significantly from the behaviors observed under reference curing and immersion conditions. Figure 98 and Figure 99 collectively illustrate the effects caused by prolonged immersion at studied pH levels up to 6000 hours. For prismatic specimens, compressive strength initially increased across all acidic environments (compared to unexposed reference samples) up to 1000 hours, likely due to continued curing and the the precipitation of secondary phases such as gypsum, which temporarily densified the microstructure (Figure 95a). This phenomenon was most prominent at pH 1.5 (P15 group), as confirmed by XRD (Figure 98a), which revealed an intense gypsum peak and the complete disappearance of portlandite in all acid-exposed samples. TGA results (Figure 98b) further corroborated these findings by showing clear gypsum-related mass loss and portlandite depletion in P15 samples, particularly at longer exposures. However, calcite content remained relatively stable across most groups, with more noticeable changes primarily observed in the P15 samples. These changes are consistent with the degradation of the lime and cementitious components, while the amorphous pozzolanic phase, although not directly visible in XRD, may have also contributed to matrix evolution. After 1000 hours, divergent trends were observed: specimens exposed to pH 2 stabilized, P3 samples continued strengthening, while P15 specimens exhibited a gradual strength decline beyond 3000 hours, indicating that prolonged sulfate crystallization and acid-induced microcracking outweighed any initial densification benefits.

In cylindrical specimens (Figure 95b), a different trend was observed compared to prisms ones. Compressive strength by the cylinder exhibited a slight reduction at 1000 hours, followed by a stabilization up to 6000 hours. This divergence from the prismatic results is primarily attributed to size effects: larger cylinders (7.5 cm × 15 cm) contained a thicker undamaged core, less exposed to surface degradation compared to the smaller prisms (4 × 4 × 16 cm), as evidenced by the altered zone thicknesses presented in Figure 98d. Such a size-dependent mitigation of acid attack has been previously reported in the literature [313]. In addition, the presence of dispersed short polymeric fibers within the mortar matrix, which were chemically resistant, played a key role in bridging cracks and maintaining mechanical integrity during acidic exposure. However, previous research has reported some variability in their performance depending on the solution, dosage, and exposure conditions [11,140]. Nonetheless, their contribution to maintaining cohesion in partially degraded zones likely supported the overall mechanical response under long-term aging.

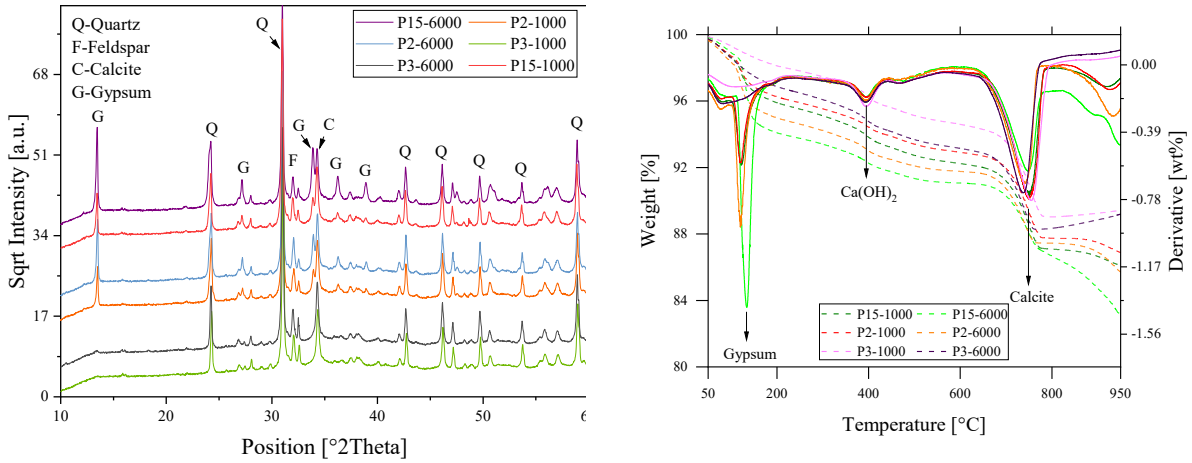

(a) (b)

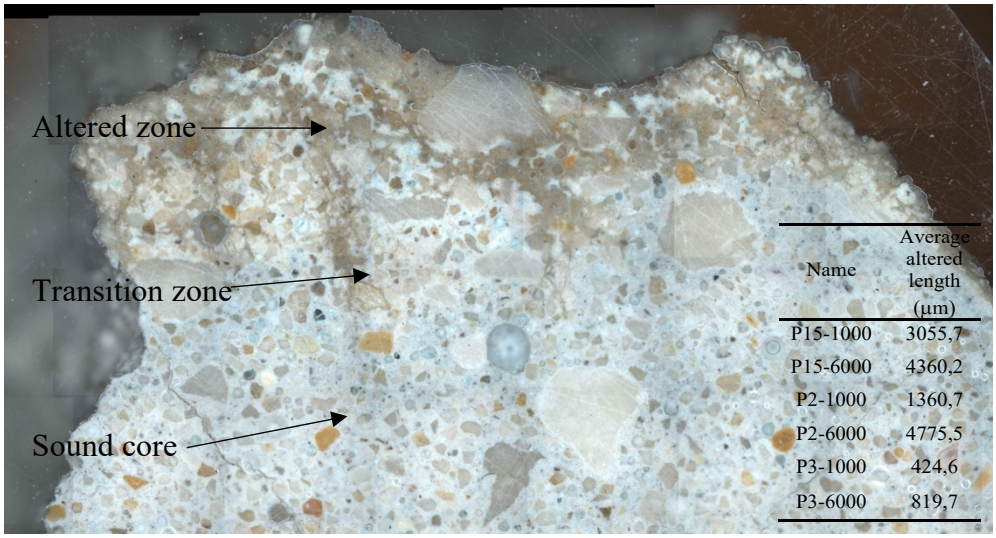

Name	Average altered length (µm)
P15-1000	3055,7
P15-6000	4360,2
P2-1000	1360,7
P2-6000	4775,5
P3-1000	424,6
P3-6000	819,7

(c) in mm

Figure 98 Chemical and mineralogical test results on lime-based mortar samples exposed to different acidic immersion: (a) XRD patterns; (b) TGA thermograms; (c) optical microscopy for P15_6000 group showing altered zone.

Flexural strength trends (Figure 95b and c) further emphasized the influence of acid intensity. Specimens exposed to pH 3 mirrored the behavior of water-immersed samples, suggesting minimal acid-induced deterioration. By contrast, P2 and P15 groups exhibited substantial reductions in flexural strength after 1000–3000 hours. Interestingly, a partial recovery was recorded for P15 specimens at 6000 hours, which may be attributed to the recrystallization of gypsum within surface-connected pores or microdefects, potentially contributing to localized densification, acting as a self-healing mechanism [314]. The evolution of the elastic modulus (Figure 95b,d) corroborated these trends, showing that long-term acidic exposure compromised stiffness, particularly at lower pH.

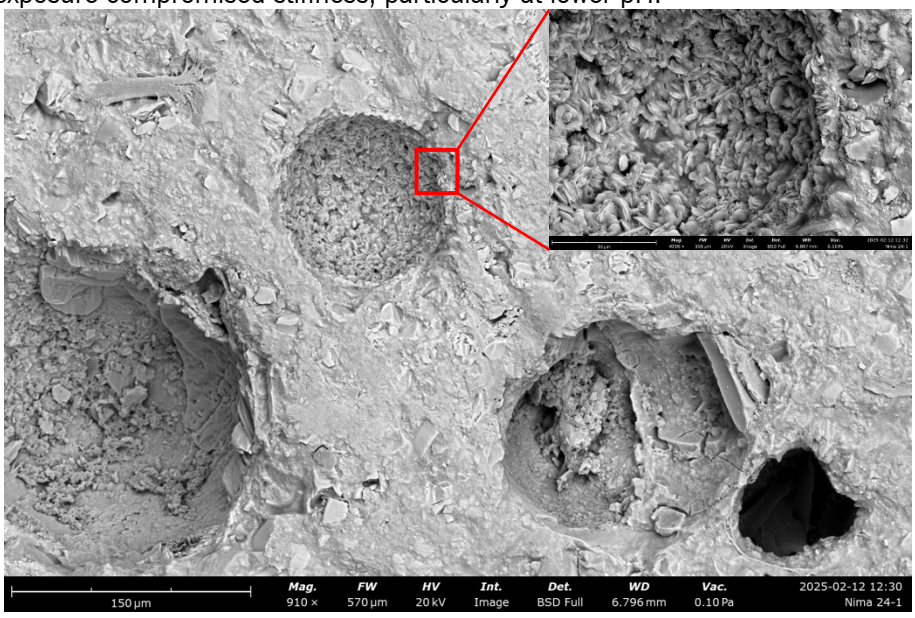

Figure 99 SEM image of the P15-6000 mortar group, showing pores filled with calcite crystals.

The ICP results in Table 8, were used to examine ionic concentrations in the exposure solutions prior to their second renewal. As expected, Ca^{2+} concentrations were substantially higher in all acidic environments (P15, P2, P3) compared to WI, suggesting that calcium release was facilitated by acid solubility, and possibly reached saturation levels as there is little difference in the Ca concentration for

all 3 acidic samples. This limits its suitability as a degradation index in predictive modeling. Conversely, elements such as Al, Fe, and Mn showed increasing concentrations with decreasing pH, in line with their known solubility behavior under acidic conditions. Among these, Fe exhibited the highest concentration increase, rising from undetectable levels in WI to over 350 mg/kg in P15, indicating its high sensitivity to acid exposure and potential value as a robust chemical indicator of degradation. This makes Fe a good candidate to correlate chemical leaching with mechanical behavior, offering a continuous and quantifiable representation of environmental severity. Si levels decreased with increasing acidity, consistent with the lower solubility of silica in low-pH environments. Na^+ and K^+ concentrations remained relatively stable across exposure types due to the generally high solubility of these elements independent of pH. [315].

Quantitative results of bulk density and porosity (Figure 96a and Figure 96b) show a clear relationship with mechanical performance. The decline in elastic modulus and flexural strength correlates with an increase in porosity and a decrease in density, especially for P15 specimens at 6000 hours, where both parameters reflect significant matrix degradation. These findings suggest that acid-induced leaching and phase transformation lead to the loss of solid volume and the development of a more porous structure. Although direct microcracking was not visible in the with the optical microscope, it is widely recognized that prolonged acid exposure promotes internal stresses from gypsum crystallization and matrix decalcification, which can lead to microcrack formation. The altered zone thickness observed under optical microscopy followed a clear pH-dependent trend (Figure 98d), with specimens exposed to pH 1.5 developing substantially thicker affected regions (~4.36 mm at 6000 hours) compared to those at pH 3 (~0.82 mm), highlighting the accelerating role of increased acidity on degradation depth.

Table 8 Elemental concentrations (ICP analysis) of the acidic and water immersion solutions after interaction with mortar specimens. Samples were collected before the second renewal cycle at one month of exposure.

Name	Na^+	K^+	Ca^{2+}	Mg^{2+}	Al	Fe	Mn	Si
	mg/kg of solid	mg/kg of solid	mg/kg of solid	mg/kg of solid	mg/kg of solid	mg/kg of solid	mg/kg of solid	mg/kg of solid
*WI	36,1	63,4	89,4	3,1	0,2	0,0	0,0	62,8
P3	32,6	65,3	1496,9	91,5	219,3	7,7	4,7	30,4
P2	54,1	127,3	1527,2	409,1	1100,4	70,0	13,7	13,2
P15	56,1	124,4	1499,1	480,8	1273,7	358,1	37,8	24,4

*The pH of the water immersion (WI) was measured as 8.5

Mineralogical and chemical analyses substantiate these mechanical observations. XRD patterns (Figure 98a) showed progressive disappearance of portlandite and intensification of gypsum peaks with increasing exposure severity. TGA results (Figure 98b) further confirmed this trend, with increased mass loss observed around 150°C, attributed to gypsum dehydration, and a marked decrease near 450°C, corresponding to the decomposition of portlandite ($Ca(OH)_2$). These findings are consistent with acid-induced dissolution of calcium hydroxide and carbonate phases, and subsequent formation of secondary sulfate minerals. SEM imaging (Figure 99) of the P15-6000 mortar group further supports these observations, showing pores filled with calcite crystals, likely formed through carbonation reactions likely occurring. From a chemical perspective, the primary governing reactions include Eq. (1a).

$$Ca(OH)_2 + 2H^+ \rightarrow Ca^{2+} + 2H_2O \quad (1a)$$

$$CaCO_3 + 2H^+ \rightarrow Ca^{2+} + CO_2 \uparrow + H_2O \quad (1a)$$

$$Ca^{2+} + SO_4^{2-} + 2H_2O \rightarrow CaSO_4 \cdot 2H_2O \text{ (Gypsum)} \quad (1a)$$

7.3.4 Discussion on aging mechanism

The evolution of lime-based mortars under varying environmental conditions revealed a distinct divergence in degradation mechanisms and mechanical outcomes. Under curing and reference exposures, including dry storage and water immersion, the materials exhibited strength development and matrix densification, primarily driven by hydration and carbonation. These conditions promoted the gradual transformation of portlandite to calcite, resulting in stable or slightly improved mechanical performance. In contrast, acidic environments induced fundamentally different deterioration patterns. The dissolution of portlandite and calcite, followed by gypsum precipitation, initially led to pore filling and transient strength gains. However, prolonged exposure resulted in internal stress accumulation, matrix softening, and strength loss. The evidence from TGA and XRD, corresponded with measurable reductions in stiffness, strength, and ductility, and were more pronounced at lower pH and longer durations. Given the clear correspondence between chemical transformations and mechanical degradation, a physically informed predictive approach is required. Such a model must be capable of incorporating both the time-dependent chemical alterations and their structural consequences, enabling durability forecasting under aggressive exposure scenarios.

7.4 Chemo-mechanical damage modeling

7.4.1 Damage modeling strategy

To complement the experimental campaign and support interpretation of mechanical degradation trends, a damage modeling framework based on CDM was implemented. The purpose of the model was to quantify stiffness reduction, strength degradation, and post-peak softening behavior observed in aged mortar specimens subjected to environmental conditioning. A smooth trilinear formulation was adopted to describe the full stress–strain response under uniaxial compression, segmented into elastic, hardening, and softening regimes. The model incorporates a scalar internal damage variable to represent the progressive deterioration of mechanical integrity, particularly in the post-peak region. For each exposure group, average stress–strain curves were used as input, and key mechanical parameters were extracted through nonlinear optimization, including the initial elastic modulus E_0, elastic limit strain γ, peak strain ε_u, peak stress σ_u, residual stress σ_{res}, and the damage energy threshold Ω. The model calibration and implementation were carried out in MATLAB using constrained optimization routines to ensure physical plausibility.

7.4.2 Damage model calibration and chemo-mechanical prediction

To translate the observed mechanical degradation of lime-based mortars into a predictive framework, a CDM model was calibrated using the experimental stress–strain envelopes obtained from uniaxial compression testing on the cylindrical specimens. This modeling step serves as a bridge between experimental observations and predictive performance assessment, especially in light of the progressive deterioration induced by chemical aging in acidic environments. The implementation of a trilinear damage model is grounded in the mechanical behavior of quasi-brittle lime mortars and justified by the need to capture the three characteristic phases observed in their response: elastic deformation, inelastic hardening, and post-peak softening. Microstructural investigations conducted in this study such as Ca leaching, gypsum formation and increased porosity demonstrated the progressive internal degradation of the mortar matrix. These changes correspond to reductions in stiffness, load-bearing capacity, and ductility. Thus, the adoption of a scalar damage variable $D(\varepsilon)$ governed by energy dissipation enables a meaningful translation of these microscale phenomena into a macroscopic constitutive law. The model not only reproduces the mechanical behavior of the material but is also calibrated to reflect the damage

mechanisms evidenced at the microstructural level. The constitutive formulation, inspired by Cui et al. [234] and adapted herein for chemically aged lime mortars, describes the stress–strain relationship using a smooth trilinear law as presented in Eq. (2).

$$\sigma(\varepsilon) = \begin{cases} E_0\,\varepsilon & \varepsilon \le \gamma \\ \sigma(\gamma) + \dfrac{\sigma_u - \sigma(\gamma)}{\varepsilon_u - \gamma}(\varepsilon - \gamma), & \gamma < \varepsilon \le \varepsilon_u \\ \sigma_{res} + (1 - D(\varepsilon))(E_0\,\varepsilon - \sigma_{res}), & \varepsilon > \varepsilon_u \end{cases} \quad (2)$$

where E_0 is the initial undamaged elastic modulus, γ is the elastic-to-inelastic transition strain, and σ_{res} is the residual stress, assumed to be 10% of the peak stress σ_u. The damage variable $D(\varepsilon)$ is defined as a function of the dissipated strain energy [234]:

$$D(\varepsilon) = 1 - \exp\left(-\frac{W(\varepsilon)}{\Omega}\right) \quad (3)$$

where Ω is the material parameter representing the characteristic energy threshold required to initiate and propagate damage, and $W(\varepsilon)$ is the accumulated strain energy density, defined as [234]:

$$W(\varepsilon) = \int_{\varepsilon_u}^{\varepsilon} \left(E_0\varepsilon' - \sigma_{exp}(\varepsilon')\right) d\varepsilon' \quad (4)$$

This energy-based damage function ensures that the material degradation initiates at peak stress and evolves progressively toward failure, capturing the gradual softening and stiffness reduction typical of lime-based mortars. Beyond fitting the stress–strain curves, the model enables the quantitative tracking of mechanical degradation indicators that were identified as key research objectives in the literature. These include: (i) the reduction in initial elastic modulus E_0 with increasing exposure severity, (ii) the decline in peak strength σ_u, and (iii) the evolution of the damage parameter $D(\varepsilon)$ as a function of exposure time and acidity level. Such parameters were extracted through nonlinear optimization against average experimental responses and provide a consistent framework for assessing the long-term mechanical deterioration of mortars subjected to acidic attack. The predictive capability of the model offers a physically interpretable and mechanistically consistent tool for durability analysis, directly connected to the experimentally observed microstructural transformations.

7.4.3 Model calibration and reference group validation

The model was first calibrated using the reference (unexposed) group, labeled E_C, which had been cured for 60 days but not subjected to any environmental exposure. For this group, the average stress–strain curve was computed by aggregating and interpolating the responses of all individual specimens. This interpolation was conducted over a common strain domain, ensuring a consistent and smooth representation of the mechanical behavior across all samples. The resulting average curve was used as the representative dataset for model calibration. As can be seen in Figure 100, the full experimental envelope of the E_C group was plotted as a shaded region, and the numerical prediction based on the average curve was overlaid to verify that the model accurately captured both the mean trend and the variability observed across replicates. Since no external LVDT or extensometer was installed during the experimental campaign, a compliance correction was applied to the raw displacement data, based on a linear fit through the initial portion of the stress–strain curve, ensuring that the apparent stiffness matched the material behavior rather than the combined stiffness of the system and the specimen.

Model calibration was conducted in MATLAB using the fmincon function to minimize the sum of squared differences between experimental and modeled stress values over the strain range. The initial elastic modulus E_0 was estimated via linear regression in the 4–8 MPa range of the pre-peak region,

reliably representing the undamaged stiffness. The elastic limit strain γ was approximated as 60% of the peak stress divided by E_0, corresponding to the observed onset of inelasticity. The post-peak behavior was governed by the damage energy parameter Ω, treated as a fitting variable. A parabolic transition ensured smooth stress and slope continuity around the peak. The residual stress σ_{res}, assumed as 10% of the peak strength σ_u, aligned with the stress stabilization observed at large strains. To ensure physical plausibility and numerical stability, constraints were applied during optimization: E_0 remained below the maximum experimental slope, the softening region was bounded within reasonable post-peak limits, and Ω was restricted to positive, realistic values. Though not central to the model structure, these bounds helped guide convergence and avoid unphysical fits. The final model successfully reproduced the full mechanical response of the E_C group, capturing the elastic rise, peak strength, and softening phase with residual stress. The fit achieved a high coefficient of determination ($R^2 = 0.95$), confirming strong agreement with the average curve and the experimental envelope.

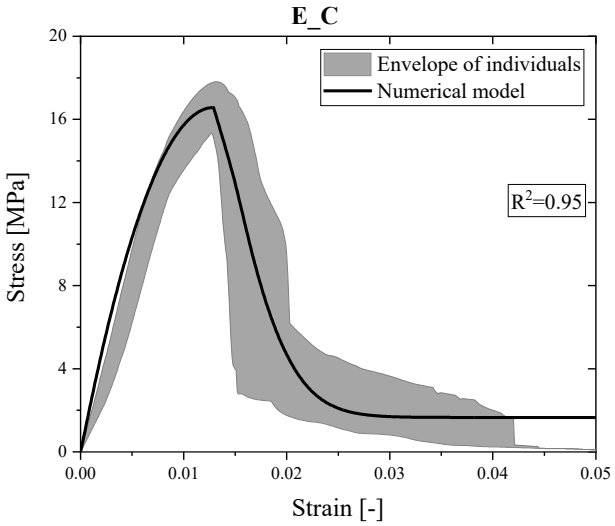

Figure 100 Trilinear damage model for the unexposed reference group (E_C), compared against the experimental stress–strain envelope.

7.4.4 Extension of the damage model to aged mortars

Following the successful calibration on the unexposed reference specimens, the trilinear damage model was systematically applied to specimens aged under various environmental conditions to evaluate progressive degradation. These included exposure to dry conditions (E_C_RC), water immersion (E_C_RW), and three levels of acid attack: pH 3.0 (E_C_P3), pH 2.0 (E_C_P2), and pH 1.5 (E_C_P15) and aging durations of 1000, 3000, and 6000 hours. Average stress–strain curves for each group were extracted following compliance correction and used to calibrate the trilinear model parameters. For every exposure group, the following parameters were determined through nonlinear fitting: the initial elastic modulus E_0, the elastic limit strain γ, the peak strain ε_u, the peak stress σ_u, the residual stress σ_{res}, and the energy-based damage parameter Ω. Model accuracy was quantified by the coefficient of determination R^2, and results are summarized in Table 9. The corresponding numerical stress–strain curves for each of these groups obtained using the fitted parameters are provided in the Figure 101-Figure 105 for reference and comparison with the experimental response envelopes.

Table 9 Model parameters for all aging environments

Sample_Name	E_0 (MPa)	γ (-)	ϵ_u (-)	σ_u (MPa)	σ_{res} (MPa)	Ω (MPa)	R^2 (-)
E_C	2375,81	0,001	0,013	16,57	1,66	0,13	0,958

E_C_RC_1000	1893,65	0,006	0,011	16,78	1,68	0,00	0,971
E_C_RC_3000	2360,25	0,003	0,013	18,13	1,81	0,10	0,975
E_C_RC_6000	1465,18	0,007	0,016	16,71	1,67	0,08	0,946
E_C_RW_1000	2560,31	0,001	0,012	16,00	1,60	0,15	0,953
E_C_RW_3000	1867,90	0,006	0,011	15,45	1,54	0,09	0,956
E_C_RW_6000	1188,38	0,012	0,014	15,13	1,51	0,01	0,966
E_C_P15_1000	2684,68	0,003	0,011	18,23	1,82	0,09	0,958
E_C_P15_3000	2142,33	0,006	0,012	19,08	1,91	0,07	0,959
E_C_P15_6000	1418,64	0,009	0,016	17,63	1,76	0,08	0,770
E_C_P2_1000	1903,33	0,007	0,011	17,10	1,71	0,00	0,971
E_C_P2_3000	2549,45	0,003	0,012	19,02	1,90	0,12	0,967
E_C_P2_6000	1087,02	0,013	0,016	15,75	1,57	0,01	0,976
E_C_P3_1000	1836,37	0,007	0,012	17,38	1,74	0,00	0,947
E_C_P3_3000	2222,42	0,006	0,011	18,95	1,89	0,11	0,958
E_C_P3_6000	1461,88	0,008	0,016	17,05	1,71	0,08	0,923

The evolution of these parameters with aging duration and pH revealed key degradation trends. A general reduction in stiffness (E_0) was observed as a function of exposure time and acidity, confirming progressive matrix weakening. The peak strength (σ_u) declined with time and severity, supporting the dissolution of calcium-bearing phases, including portlandite, calcite and potentially hydrated cement products, along with the formation of expansive by-products such as gypsum. Conversely, both the elastic limit γ and the peak strain ε_u tended to increase under more severe conditions, suggesting a transition from brittle to more ductile failure behavior, consistent with internal microcracking and the collapse of the binder network. The parameter Ω, which governs the post-peak energy dissipation, generally decreased at lower pH values, indicating a more abrupt softening response associated with chemically induced damage.

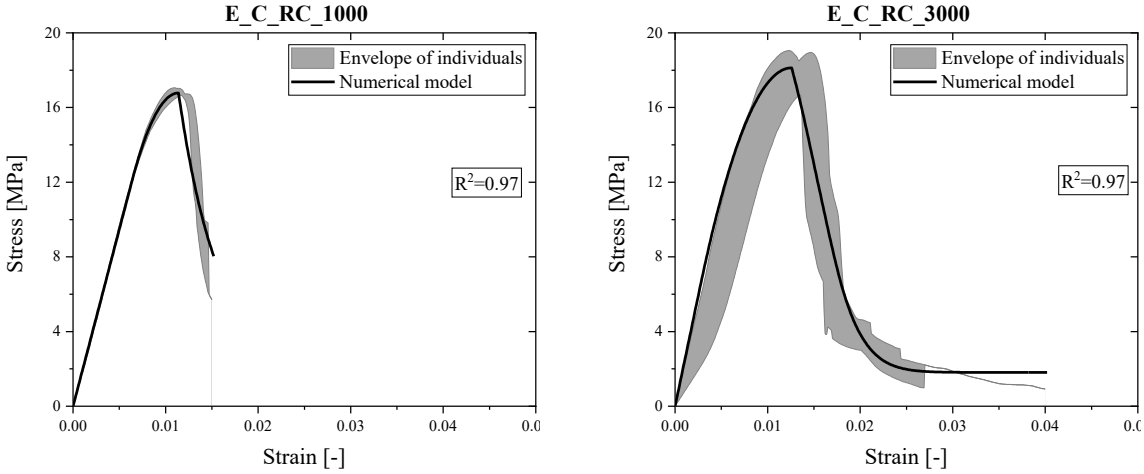

(a) (b)

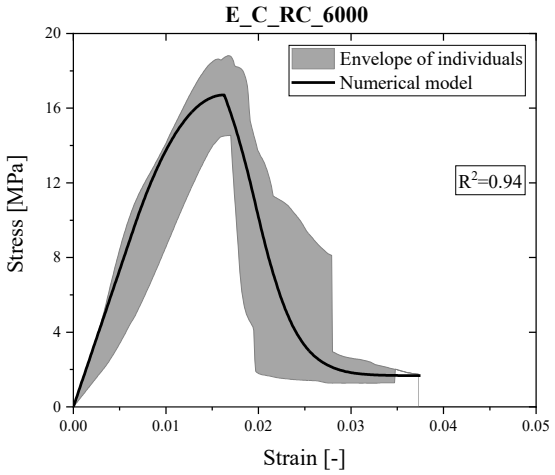

(c)

Figure 101 Stress–strain response of cylindrical specimens under compression: experimental envelope and numerical model for dry-conditioned samples aged (a) 1000 h; (b) 3000 h; and (c) 6000 h.

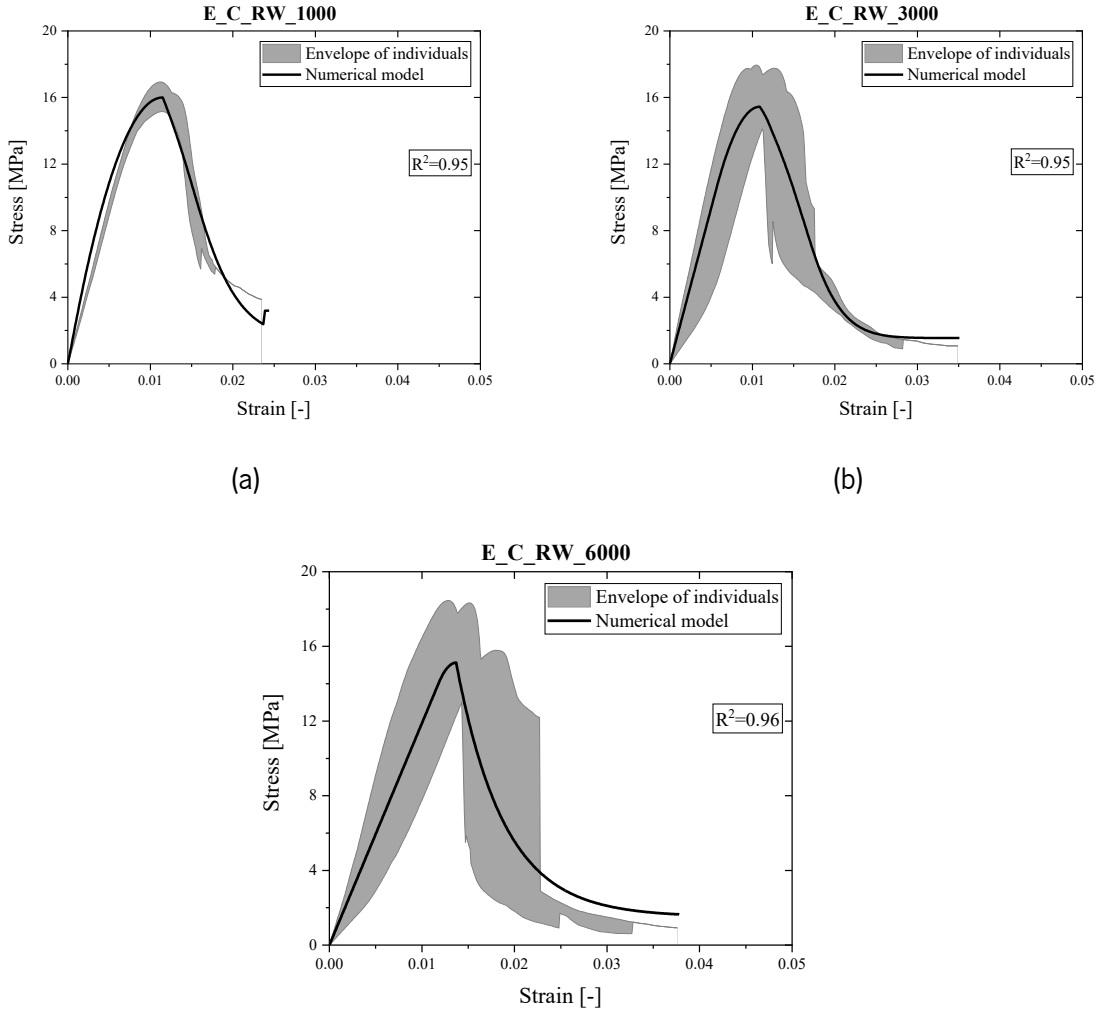

Figure 102 Stress–strain response of cylindrical specimens under compression: experimental envelope and numerical model for water-immersion samples aged (a) 1000 h; (b) 3000 h; and (c) 6000 h.

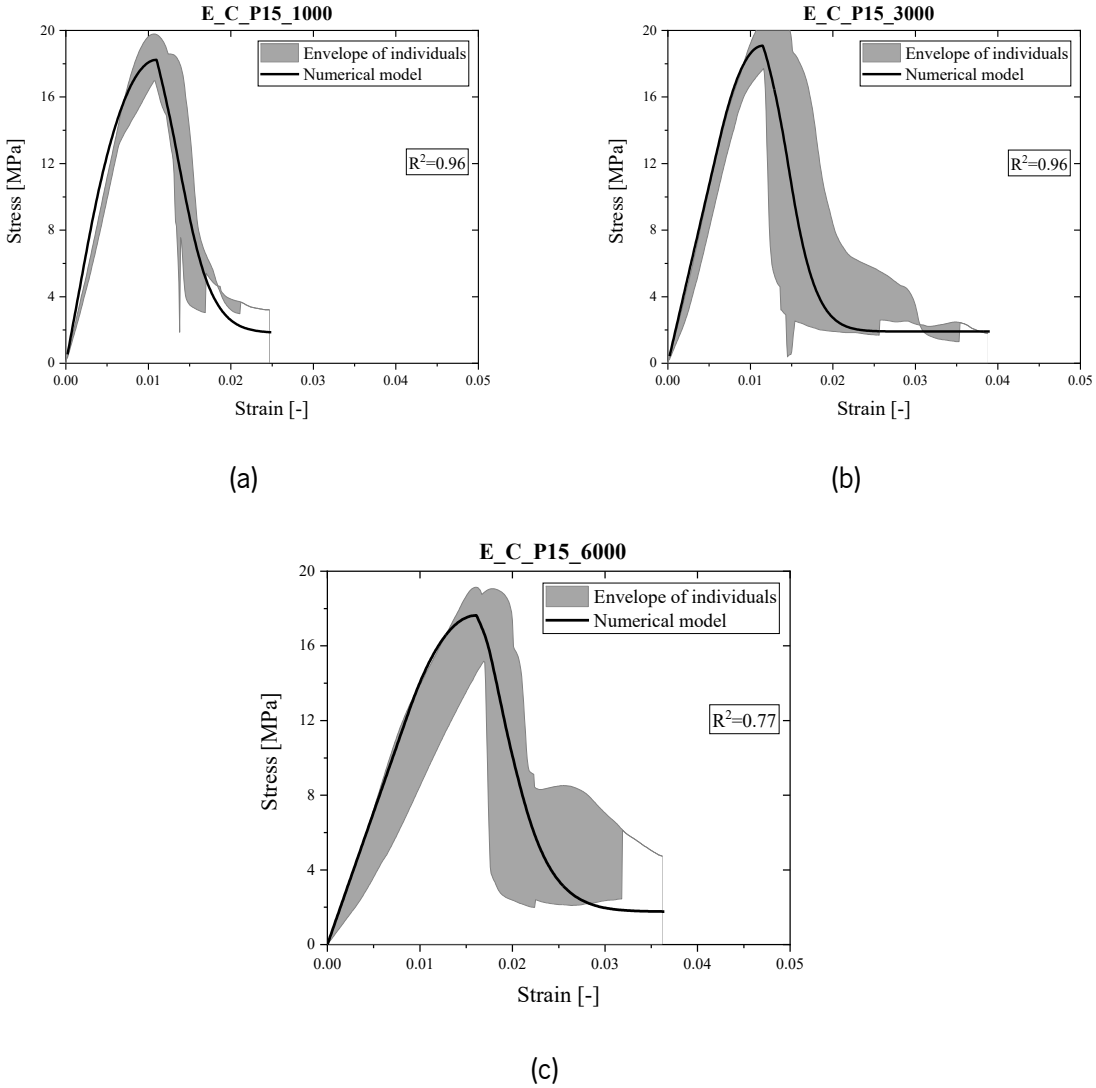

Figure 103 Stress–strain response of cylindrical specimens under compression: experimental envelope and numerical model for acidic solution with pH of 1.5 samples aged (a) 1000 h; (b) 3000 h; and (c) 6000 h.

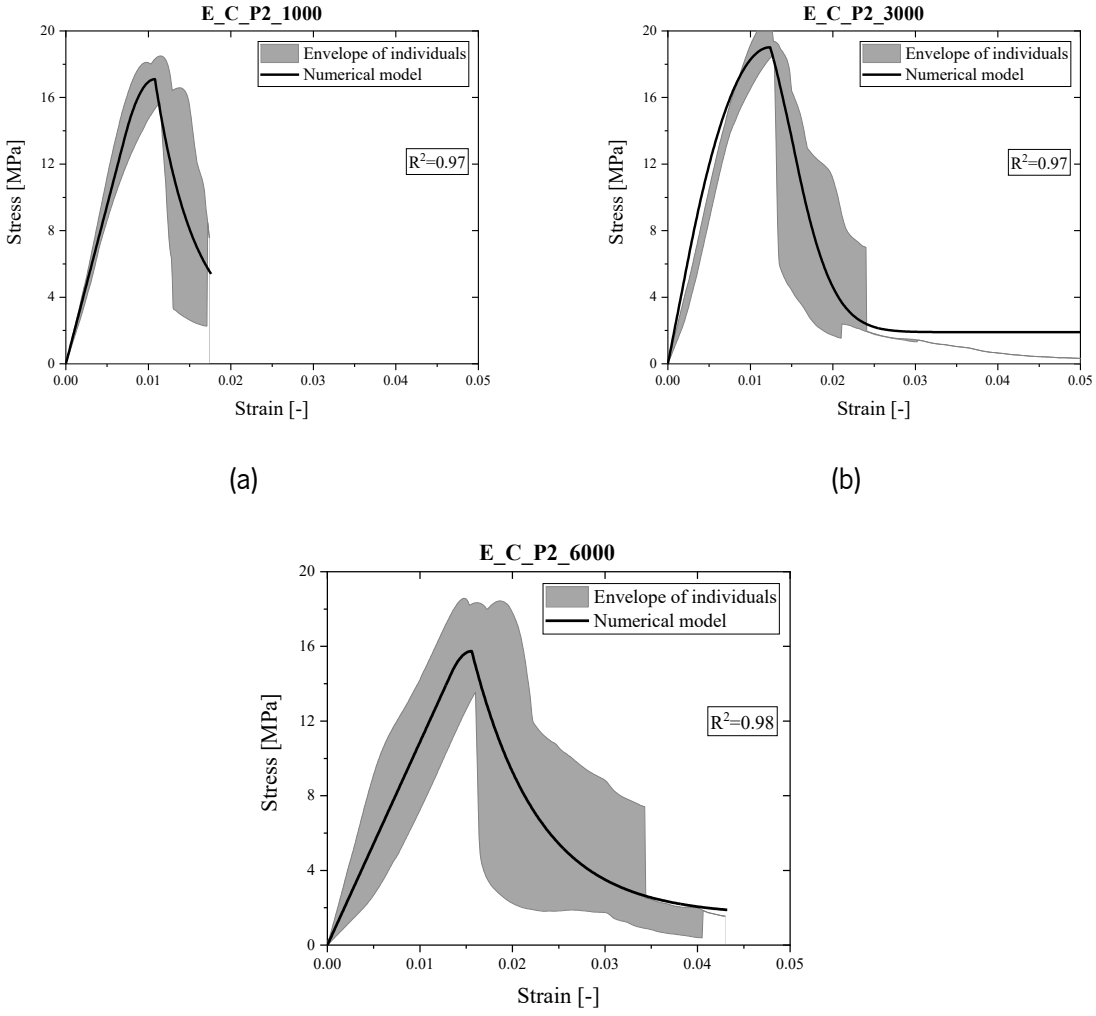

Figure 104 Stress–strain response of cylindrical specimens under compression: experimental envelope and numerical model for acidic solution with pH of 2 samples aged (a) 1000 h; (b) 3000 h; and (c) 6000 h.

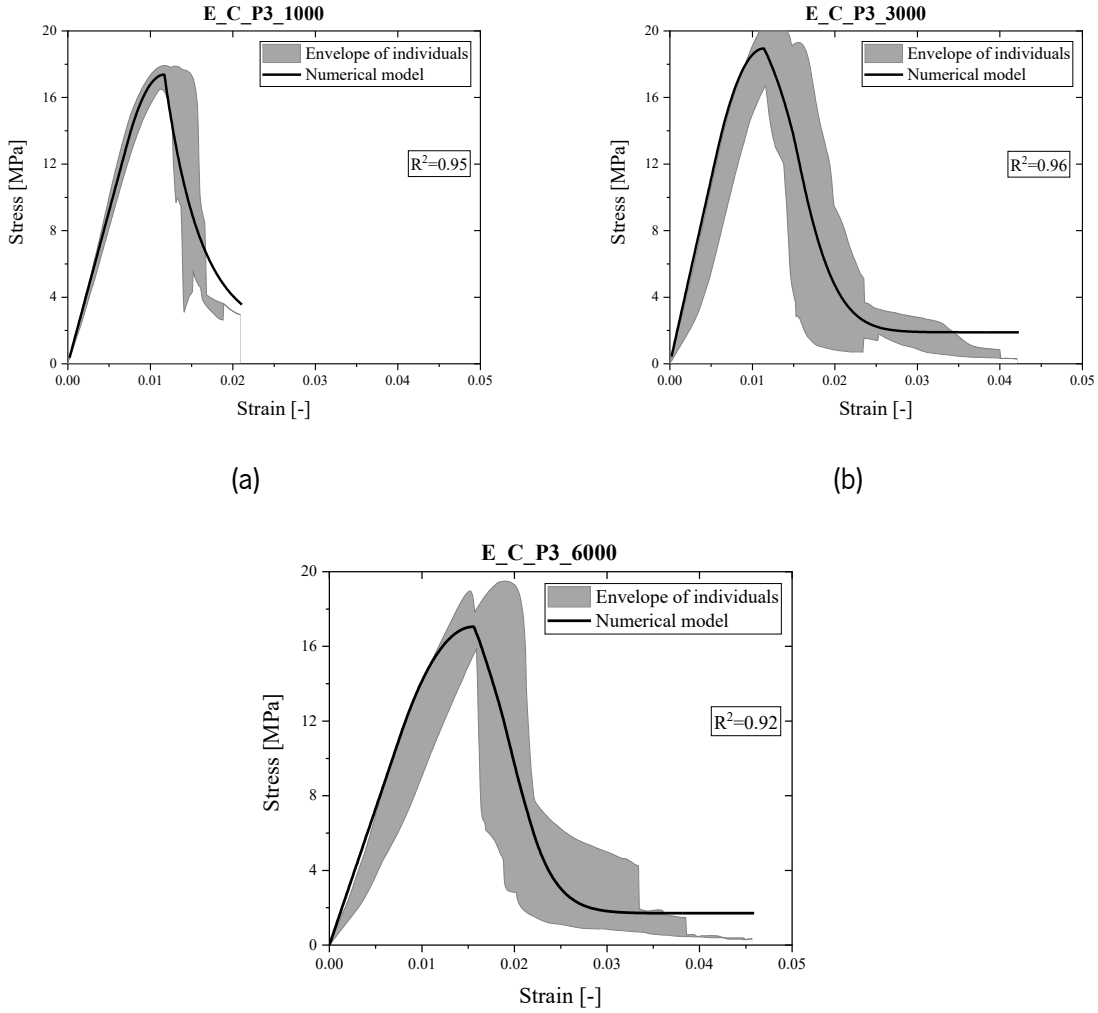

Figure 105 Stress–strain response of cylindrical specimens under compression: experimental envelope and numerical model for acidic solution with pH of 3 samples aged (a) 1000 h; (b) 3000 h; and (c) 6000 h.

Among all experimental groups, specimens exposed to pH 1.5 showed the most pronounced deterioration in stiffness, strength, and damage resistance. These findings are consistence with the extensive degradation of calcium-bearing phases within the hydraulic binder system and the formation of expansive reaction products such as gypsum. The mechanical degradation captured through the model reflects internal matrix weakening due to increased porosity and progressive microcrack development, which were confirmed via optical microscopy. In contrast, the behavior of water-immersed samples was characterized by only mild reductions in mechanical parameters, indicating limited ionic dissolution. Dry-conditioned specimens remained largely unaffected, with stable model parameters across all durations, validating their role as a durability baseline. The consistency between mechanical modeling outputs and previously reported mineralogical changes reinforces the robustness of the chemo-mechanical degradation framework proposed in this study.

7.4.5 Leaching-based chemo-mechanical prediction framework

To establish a predictive link between chemical degradation and mechanical performance, a chemo-mechanical framework was developed by integrating iron (Fe) leaching data into the trilinear damage model. The model is based on the hypothesis that Fe release, which increases sharply under acidic

exposure, serves as a sensitive proxy for binder degradation, reflecting cumulative chemical attack, microstructural destabilization, and progressive mechanical weakening. Among all monitored elements, Fe exhibited the clearest and most consistent solubility trend with pH, rising from undetectable levels in water-immersed samples to over 350 mg/kg in the most acidic environment (pH 1.5), and thus was selected as a reliable degradation index. The Fe concentration values were normalized by the maximum Fe leaching observed across all environments, yielding a relative degradation index defined as $L_{\text{rel}}(t,\text{pH}) = \frac{L_{\text{Fe}}(t,\text{pH})}{L_{\text{Fe,max}}}$ [316]. This index was then used to formulate empirical degradation laws for the three primary mechanical parameters of the trilinear damage model, as shown in Eq. (5a).

$$E_0(t,\text{pH}) = E_{0,\text{ref}} \cdot \left(1 - \alpha_E \cdot L_{\text{rel}}(t,\text{pH})\right) \quad (5a)$$

$$\sigma_u(t,\text{pH}) = \sigma_{u,\text{ref}} \cdot \left(1 - \alpha_\sigma \cdot L_{\text{rel}}(t,\text{pH})\right) \quad (5a)$$

$$\Omega(t,\text{pH}) = \Omega_{\text{ref}} \cdot \left(1 - \alpha_\Omega \cdot L_{\text{rel}}(t,\text{pH})\right) \quad (5a)$$

By Eq. (5a), $E_{0,\text{ref}}$, $\sigma_{u,\text{ref}}$, and Ω_{ref} denote the calibrated parameters from the unexposed reference group (E_C). The degradation coefficients α_E, α_σ, and α_Ω were obtained through linear regression between the mechanical properties and L_{rel}, capturing the influence of Fe-based degradation. The remaining model parameters, including the elastic limit strain γ, the peak strain ε_u, and the residual stress σ_{res}, were interpolated from the experimentally measured dataset and held constant during predictions to isolate the chemically driven deterioration captured by Fe leaching. capability under untested conditions is further explored and validated in the following section.

7.4.6 Predictive evaluation using the chemo-mechanical model

To assess the robustness and predictive capability of the leaching-based chemo-mechanical model, its performance was evaluated on four exposure groups excluded from the initial calibration phase: E_C_P15_3000, E_C_P2_1000, E_C_P2_6000, and E_C_P3_3000. These groups were specifically selected to represent intermediate durations within each acidic environment, enabling an interpolation-based validation of the model. For each group, the normalized ferric ion leaching index $L_{\text{rel}}(t,\text{pH})$, as defined by the previous section, was used to estimate the degradation of the key mechanical parameters: the initial elastic modulus E_0, peak stress σ_u, and damage energy threshold Ω. The additional model inputs, elastic limit strain γ, peak strain ε_u, and residual stress σ_{res}, were interpolated from reference data. Using these inputs, predicted stress–strain curves were generated using the smooth trilinear damage model and compared with experimental results. As illustrated in Figure 106, the predicted responses closely matched the experimental envelopes across all groups, particularly in terms of initial stiffness, peak load, and the overall softening profile. This agreement highlights the model's ability to capture deterioration behavior based on chemical exposure alone, without relying on mechanical fitting for new exposure conditions.

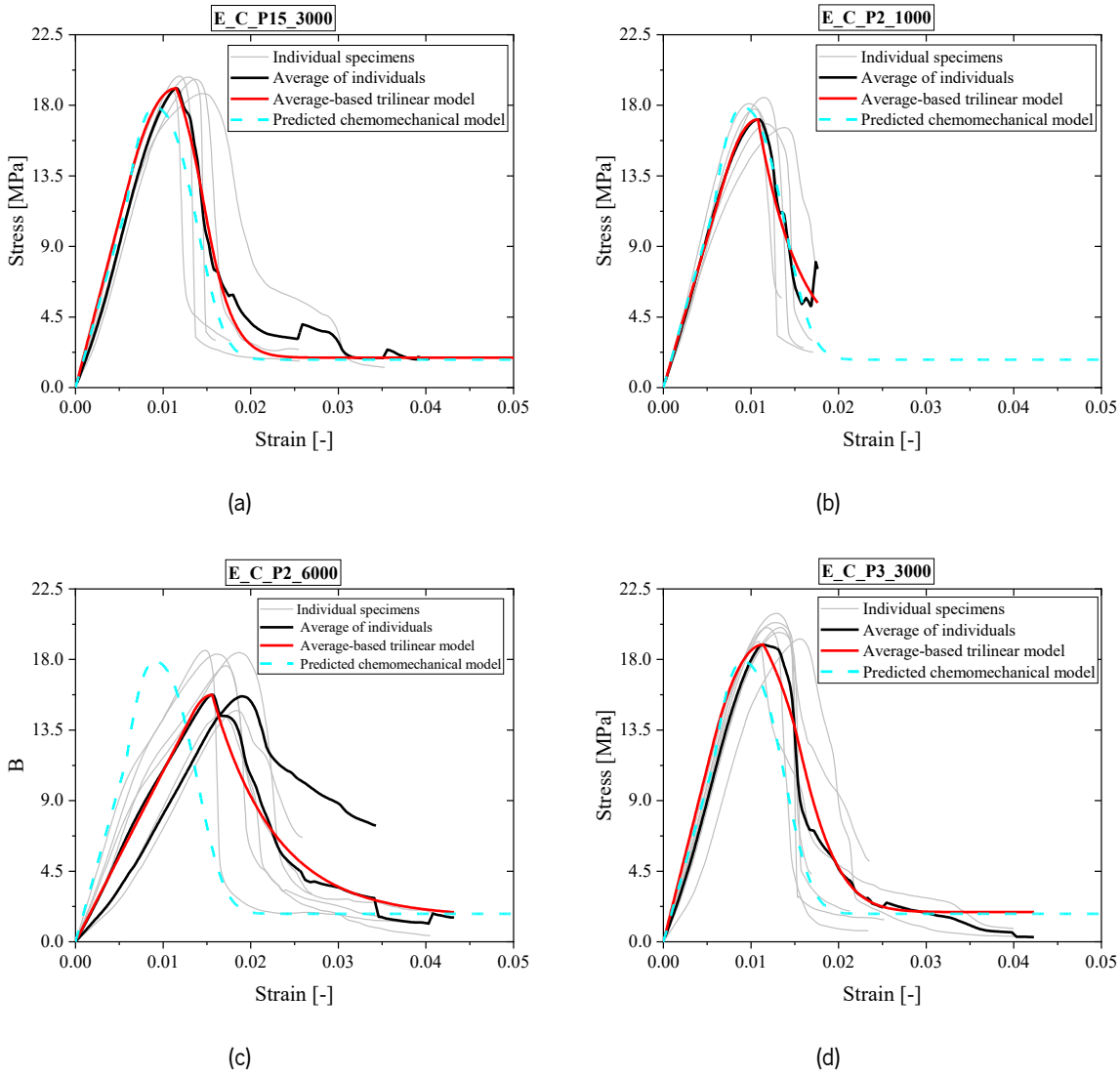

Figure 106 Stress–strain response of selected exposure groups: individual tests, average curve, fitted trilinear model, and predicted chemo-mechanical model for (a) EM_C_P15_3000, (b) EM_C_P2_1000, (c) EM_C_P2_6000, and (d) EM_C_P3_3000.

Table 10 presents the predicted mechanical parameters and their respective percentage deviations from the experimental values. Errors for both E_0 and σ_u remained within an acceptable 5–10% range, supporting the suitability of Fe^{3+} as a degradation indicator. Although predictions for the damage parameter Ω, exhibited higher variability, especially for longer exposure durations such as E_C_P2_6000, this is attributable to the inherent sensitivity of post-peak energy dissipation to local cracking behavior and microstructural heterogeneity. Nonetheless, these differences do not compromise the model's ability to reproduce the global stress–strain behavior with sufficient accuracy. Importantly, the trends captured by the chemo-mechanical model align well with the microstructural findings discussed earlier in the manuscript. The progressive deterioration in mechanical parameters corresponds with the observed increase in ferric ion leaching and corroborates mineralogical signatures such as portlandite consumption, gypsum formation, and microstructural fragmentation identified through XRD and TG. This convergence between chemical diagnostics and mechanical modeling validates the proposed framework and reinforces the potential of Fe-based leaching indicators for long-term durability forecasting of lime-based mortars in acidic environments.

Table 10 Predicted versus experimental model parameters for selected exposure groups using the leaching-based chemo-mechanical model.

Sample	E_0 (MPa)	γ (-)	σ_u (MPa)	Ω (MPa)
EM_C_P15_3000	1987,70 (7)	0,01 (8)	17,89 (6)	0,08 (15)
EM_C_P2_1000	1987,70 (4)	0,01 (19)	17,89 (5)	0,08 (1500)
EM_C_P2_6000	1987,70 (83)	0,01 (57)	17,89 (14)	0,08 (955)
EM_C_P3_3000	1987,70 (11)	0,01 (3)	17,89 (6)	0,08 (32)

7.4.7 Interpretation and integration

The chemo-mechanical modeling framework developed in this study serves as a critical link between experimentally observed microstructural deterioration and macroscopic mechanical behavior. By integrating leaching data with a trilinear continuum damage model, a robust methodology was established to quantify the influence of chemical aging, specifically acid attack, on the structural integrity of lime-based mortars. This approach bridges multiple scales, enabling the translation of chemical and morphological degradation processes into predictive mechanical parameters relevant for long-term durability assessments. At the microstructural level, results from TGA and XRD confirmed substantial portlandite depletion in specimens subjected to acidic environments. The observed decline in elastic modulus E_0 across all aged groups closely mirrored this chemical loss, supporting the interpretation that binder dissolution is a primary driver of stiffness reduction. These features are consistent with the decrease in peak strength σ_u observed under increasing exposure severity. In particular, the transition from a relatively compact matrix to one exhibiting internal fragmentation and reduced fiber-to-matrix bonding aligns with the mechanical softening captured by the model.

The damage energy parameter Ω, introduced as part of the energy-based damage law, reflects the energy required to initiate and propagate post-peak damage. It can be interpreted as a phenomenological representation of failure mechanisms such as crack coalescence and fiber rupture, both of which are exacerbated by microstructural weakening. Its systematic reduction with increasing exposure severity suggests that chemically aged mortars reach instability and failure under lower energy input, a conclusion supported by visual observations of crack morphology and gypsum crystallization along fracture planes. Beyond post-processing of experimental results, the developed model has demonstrable predictive capabilities. By calibrating empirical degradation laws against leaching data, the model was able to estimate the mechanical response of intermediate exposure groups—previously untested—solely based on chemical degradation indices. These predictions exhibited strong agreement with experimental trends, particularly for the elastic modulus and peak stress, validating the feasibility of using leaching measurements as surrogate indicators of performance loss. While larger discrepancies were noted for Ω in certain cases, this can be attributed to the cumulative and nonlinear nature of post-peak failure processes, which are more sensitive to local variability and harder to capture through global empirical scaling.

The leaching-based degradation index provides a robust foundation for simulating mortar performance across various environmental scenarios. Within the range of calibrated data, interpolation enables reliable predictions of mechanical degradation as a function of chemical aging. However, while the framework allows extrapolation to more aggressive conditions—such as lower pH levels or prolonged aging periods—these predictions should be interpreted with caution, as they extend beyond the experimental calibration domain. Despite this limitation, the chemo-mechanical model retains a strong physical basis, grounded in microstructural evidence including portlandite depletion, gypsum crystallization, and interfacial deterioration. The consistency observed across chemical, microstructural, and mechanical indicators affirms the internal validity and predictive utility of the proposed approach.

7.5 Machine learning-based modeling of flexural behavior

As an extension of the experimental findings from Durability Campaign II, this section explores the use of data-driven modeling to predict the flexural behavior of lime-based mortar subjected to acidic aging. Despite the widespread use of such mortars in structural strengthening applications, their long-term mechanical response under acidic conditions remains insufficiently characterized in the literature. To address this gap, a machine learning framework was developed, using experimental results obtained from specimens exposed to sulfuric acid at pH 3.0 in the durability campaign expressed described in Chapter 5, as well as reference conditions including water immersion and dry storage, for durations of 1000, 3000, and 5000 hours. The modeling approach employed the extreme gradient boosting (XGBoost) algorithm to capture the complex, nonlinear relationships between environmental and physical parameters, such as exposure time, bulk density, moisture content, and visual indicators of corrosion, and the corresponding flexural stress–displacement behavior. This section identifies the most important features affecting stress-displacement curve prediction in the utilized lime-based mortar. The following sections of the paper discuss the experimental testing procedure, as well as machine learning methods to enhance the predictive capabilities for material behavior analysis using an integrated approach. This methodology underscores the importance of combining robust experimental data with advanced computational techniques to achieve reliable and accurate predictions.

7.5.1 Model training and validation (XGBoost)

One of the most popular and effective machine learning techniques for regression problems is XGBoost, which stands for eXtreme Gradient Boosting. XGBoost is an ensemble method that combines multiple weak learners, usually decision trees, into a strong learner that can make accurate predictions on complex data sets. XGBoost uses a gradient boosting framework that iteratively updates the weights of the learners based on the residuals of the previous predictions, minimizing a predefined loss function. XGBoost has several advantages over mathematical regression methods, such as its scalability, robustness, and interpretability [317,318]. The symbolic mathematical formulation of XGBoost and its decision-making process is presented in the following paragraphs. XGBoost has an objective function, which combines a loss function that measures the difference between the predicted and actual values, and a regularization term to control the complexity of the model [224]. The objective function reads:

$$\Phi(\Theta) = \underbrace{\sum_{i=1}^{n} \mathcal{L}(y_i, \hat{y}_i)}_{Loss} + \underbrace{\sum_{k=1}^{K} \Omega(f_k)}_{Regularization} \quad (6)$$

where:

- $\Phi(\Theta)$ is the overall objective function.
- $\mathcal{L}(y_i, \hat{y}_i)$ is the loss function, often mean squared error for regression tasks.
- $\Omega(f_k)$ is the regularization term for the kth tree.
- y_i is the actual value for the ith input.
- $\hat{y}_i$ is the predicted value for the ith input.
- n is the number of inputs.
- K is the total number of trees.
- f_k represents the kth tree.

The loss function measures the difference between predicted and actual values, presented in Eq. (7):

$$\mathcal{L}(y_i, \hat{y}_i) = \frac{1}{n}\sum_{i=1}^{n}(y_i - \hat{y}_i)^2 \quad (7)$$

The regularization term $\Omega(f_k)$ is used to penalize the complexity of the model and can be expressed as:

$$\Omega(f_k) = \Upsilon \mathrm{T} + \frac{1}{2}\lambda\sum_{j=1}^{T}\omega_j^2 \quad (8)$$

where:

- Υ is the parameter that controls the complexity of the tree.
- T is the number of leaves in the tree.
- λ is the parameter that controls the regularization of the leaf weights.
- ω_j is the weight of the jth leaf.

The XGBoost algorithm, illustrated in Figure 107, is an advanced implementation of gradient boosting that enhances performance and speed. This ensemble learning method involves constructing a sequence of decision trees, each aiming to correct the errors of its predecessor by focusing on the residuals. Initially, the data from the database is fed into the first decision tree, $Tree\ (X, \theta_1)$. Within the XGBoost algorithm, the residuals of decision trees, which are the differences between predicted and actual values, are computed and used as input for all subsequent trees. For instance, the function $f_1(X, \theta_1)$ represents the output of the first decision tree, and its residuals are then fed into the next decision tree. This process of calculating residuals and feeding them into subsequent trees continues iteratively through the ensemble up to the $(n-1)-th$ tree, $f_{n-1}(X, \theta_{n-1})$. This iterative process ensures that each tree in the sequence improves upon the predictions of its predecessors such that each one learns to correct the errors made by the previous trees. After all the decision trees are culminated, a cumulative sum integrates the contributions of all trees, effectively capturing the complexities in the data. In the Figure 107, the white, red, yellow, and green nodes represent different stages of data processing within each decision tree. The white nodes typically represent the root nodes where the initial decision splits occur. The yellow nodes indicate the intermediate decision points where the chosen splits are made, guiding the flow of data based on specific criteria, while the red nodes represent the paths that were not selected at each decision point within the tree. Finally, the green nodes signify the leaf nodes where final predictions or residuals are computed.

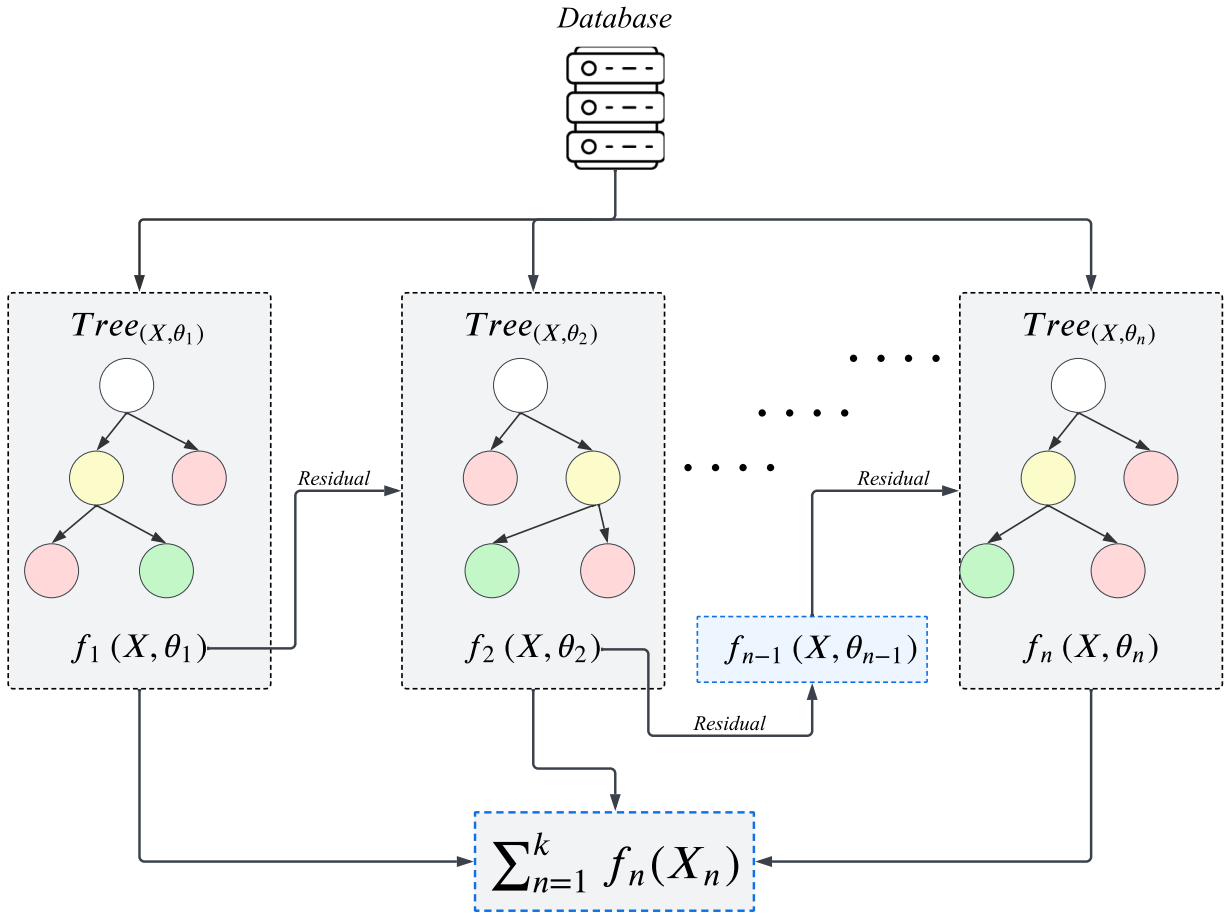

Figure 107 XGBoost algorithm flowchart, depicting a series of consecutive decision trees, initial split (yellow), resulting predictions (green), and the adjustment of residuals (equations).

One of the challenges of using machine learning models is to understand how the model makes predictions and what features are important for the model. A common way to measure feature importance is to use the number of times a feature is used to split a node in a tree, or the total reduction in the loss function due to splitting on a feature. However, these methods do not account for the interaction effects between features or the impact of a feature on the prediction for a specific instance. To address these limitations, a novel method called SHAP (SHapley Additive exPlanations) was proposed by Lundberg and Lee [319], which provides a unified framework to explain the output of any machine learning model. SHAP values are based on the concept of Shapley values from cooperative game theory, which measures the contribution of each player to the outcome of a game. The SHAP values interpretation for this study would be to measure the contribution of features to the prediction of a model, and the direction and magnitude of their effects, as well as the interactions and nonlinearities among them. A summary of the experimental database prepared for the machine learning model, as well as the histogram for each variable, is brought in Table 11 and Figure 108.

Table 11 Summary of the experimental database prepared for the machine learning model.

Statistic	Output		Input			
	Stress [MPa]	Displacement [mm]	Density [gr/cm³]	Aging Environment [pH]	Moisture [%]	Time [h]
count	12901	12901	12901	12901	12901	12901
mean	1.94	0.36	1.70	7.78	81.03	3075.58
std	1.93	0.27	0.06	2.78	19.98	1713.23
min	0.00	0.00	1.57	3.5	60	0
25%	0.32	0.14	1.66	3.5	60	1000
50%	1.34	0.29	1.69	8.5	100	3000
75%	3.23	0.52	1.74	10	100	5000
max	14.46	1.40	1.8	10	100	5000

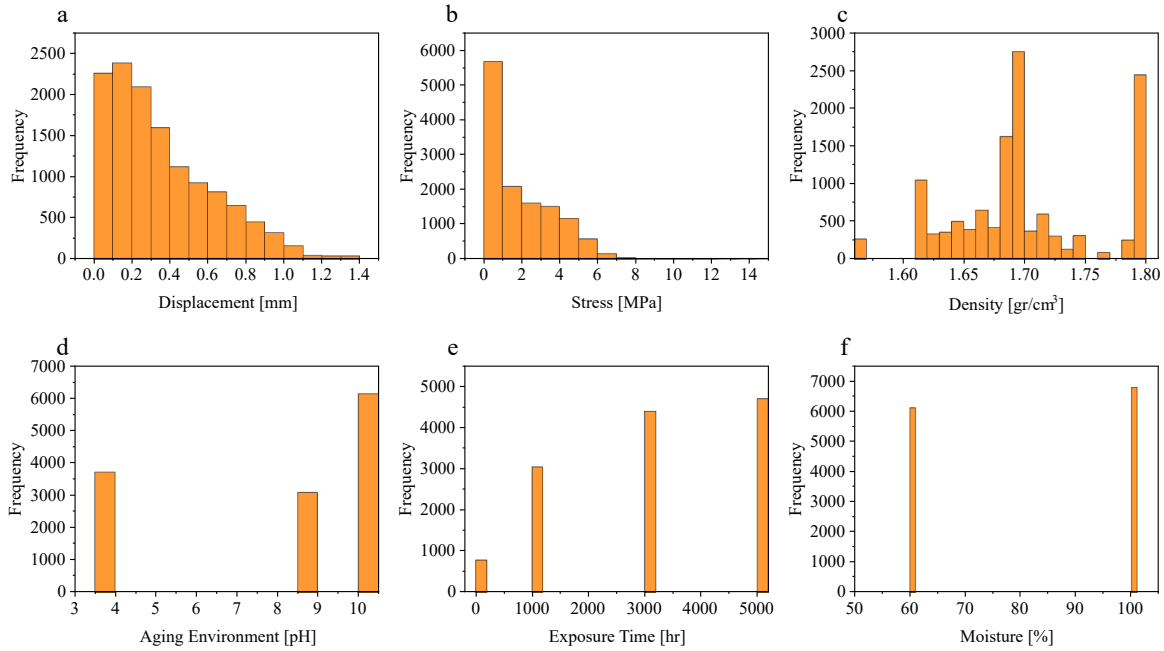

Figure 108 Histogram of the utilized experimental dataset.

7.5.2 Predictive results and interpretation

The following sections present and discuss the results of both the experimental and machine learning analyses. Initially, data was collected from the experimental process, as detailed in the materials and methods section.

7.5.2.1 Mechanical tests

The flexural strength tests provided valuable insights into the behavior of lime-based mortars subjected to various environmental conditions and exposure durations. The stress versus displacement response, as shown in Figure 109, highlights the bell-shaped curve typical of flexural tests. This curve generally comprises an initial elastic region, a peak corresponding to the maximum load capacity, and a post-peak region where the load gradually decreases. The width and shape of the curve, as well as the post-peak

behavior, depending on the exposure conditions. For instance, lime-based mortars tend to exhibit wider bell-shaped curves due to their ductile properties, while exposure to harsh environmental conditions can alter this behavior significantly [320]

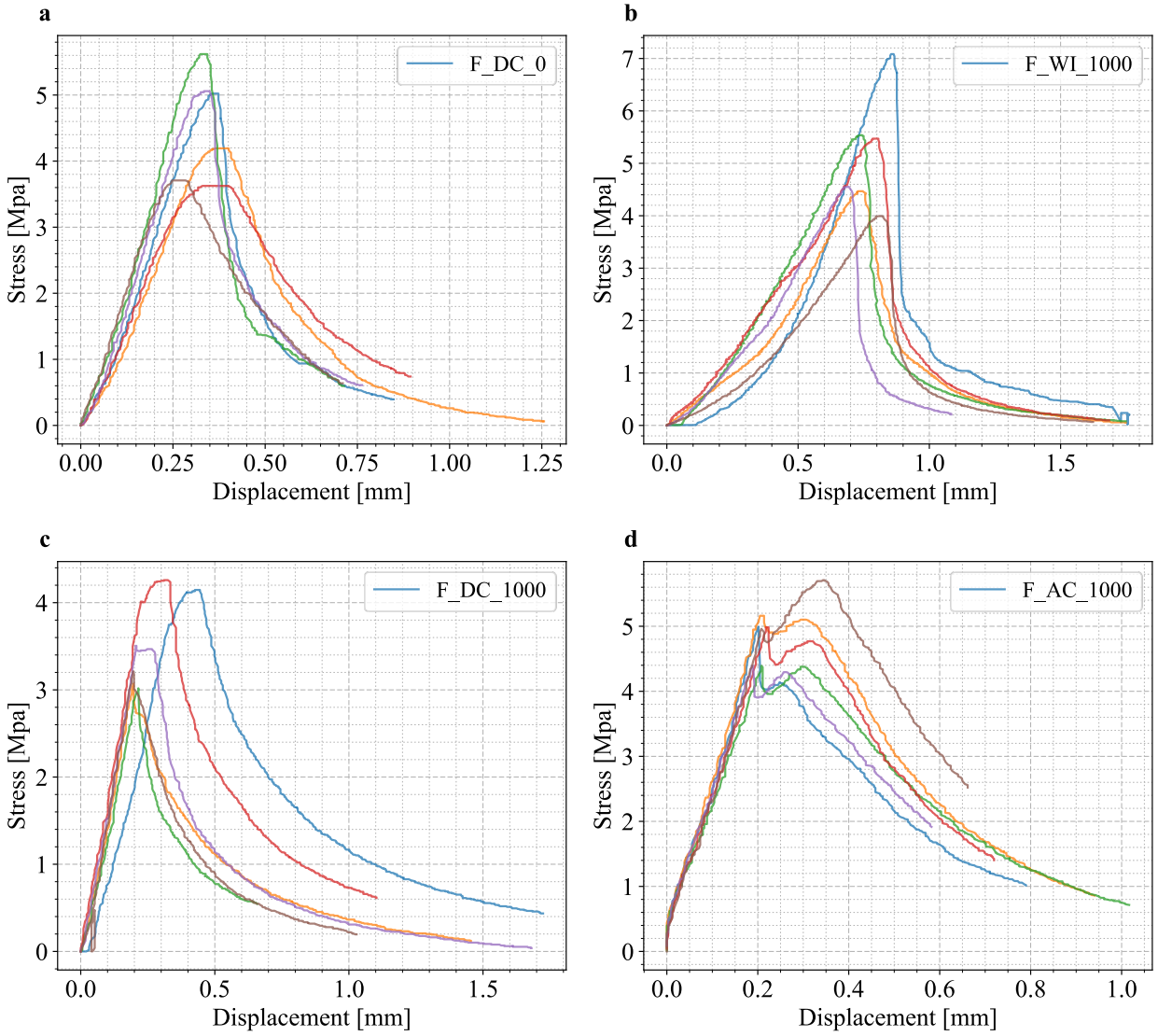

Figure 109 Stress vs. displacement diagram for each individual specimens from the experiments for: (a) F_0 group; (b) F_DC_1000; (c) F_WI_1000; (d) F_AC_1000.

According to the Figure 113, under dry curing conditions, the flexural strength showed a continuous increase up to 5000 hours. This improvement is likely due to ongoing hydration and limited carbonation, which enhanced the material's structural integrity over time. For specimens exposed to water immersion (WI), an initial drop in load capacity was observed at 1000 hours, likely due to saturation and the lubrication of short fibers within the mortar matrix. However, subsequent strength gains were recorded, suggesting that the prolonged hydration effect eventually outweighed the initial weakening. Specimens exposed to acidic conditions displayed a peak in flexural strength at 3000 hours before reaching a plateau. The enhanced strength observed in acidic environments can be attributed to ongoing hydration and carbonation processes, which contributed to improved mechanical performance up to this point. Beyond 3000 hours, however, the acidic exposure may have limited further strength development due to chemical interactions that could destabilize the mortar matrix.

The inclusion of short fibers in the mortar played a critical role in enhancing flexural strength across all conditions. These fibers effectively bridged cracks improved overall toughness, and reduced crack width during loading. Such mechanisms were particularly evident in the post-peak behavior, where the presence of fibers mitigated the rapid loss of load-bearing capacity [321]. As illustrated in Figure 109, the stress-displacement curves for different groups reveal varied mechanical responses based on exposure time and environmental conditions. Mortar samples exposed to distilled water demonstrated higher strength values compared to those in dry conditions. This can be attributed to continuous hydration and carbonation, particularly within the interfacial transition zone (ITZ), which contributed to the improved mechanical properties [11,151,322]. The contrasting behaviors depicted in Figure 109 underscore the significant influence of environmental conditions on the flexural performance of lime-based mortars, highlighting the need for tailored approaches in restoration and repair applications.

7.5.2.2 Machine Learning

following the process of the experimental results data, they fed into the machine learning model for further analysis. The analysis of the model's performance across different cross-validation folds reveals that the 4-fold cross-validation provided the highest R^2 score. However, while 10-fold cross-validation yields a marginally higher accuracy, it requires more computational resources. The decision to use 4-fold cross-validation was made to balance accuracy and efficiency, ensuring robust performance with fewer computational demands. The optimal learning rate of 0.01729, achieved at iteration 9 of Bayesian optimization, results the highest R^2 scores for both training and validation, indicating the best generalization performance.

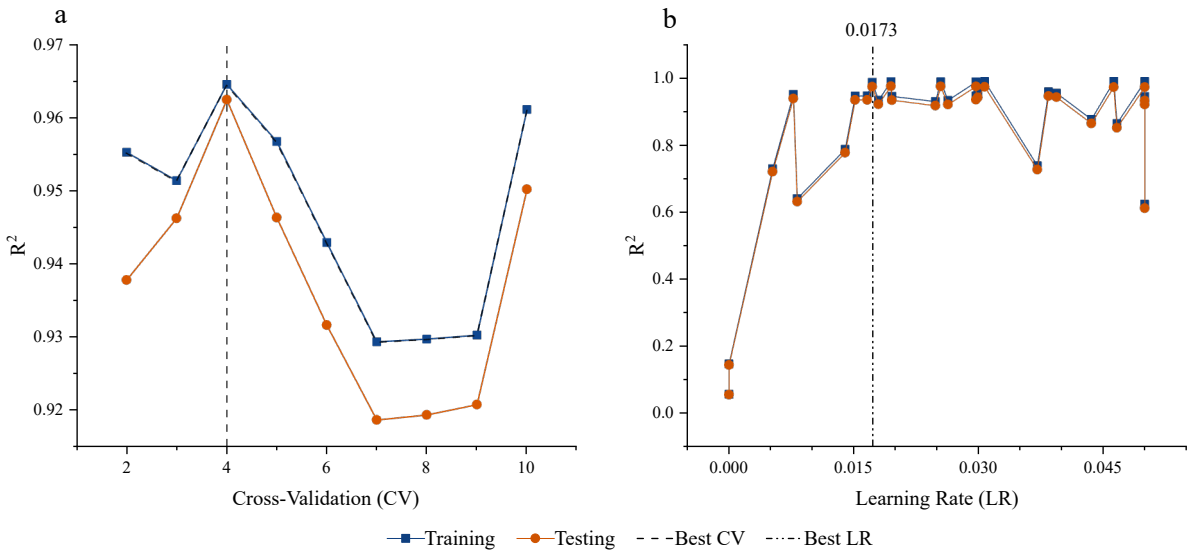

Figure 110 Results of XGBoost performance evaluation across various (a) cross-validation folds and (b) learning rates during Bayesian optimization for training and validation sets.

Additionally, detailed results of the stress-displacement diagram's prediction are provided, emphasizing the quantified effects of various explanatory variables. The experimental results involve mechanical tests conducted on the mortar samples, as described in the previous section and brought into by previous research, portraying each sample's outcome. Moreover, the machine learning results discussion encompasses comparative plots of actual versus predicted values for both training and testing datasets, along with kernel density estimation (KDE) plots to assess the distributions of actual-vs-predicted values visually. The close correspondence between the KDE plots of actual and predicted values indicates robust predictive performance. Additionally, SHAP plots are employed to identify the most significant input features and their respective impacts on the output. To validate the prediction accuracy

multiple mathematical metrics were employed and evaluated. Primarily, the coefficient of determination (R^2) measures the proportion of variance in the dependent variable that is predictable from the independent variables (Eq. (9)). Mean Absolute Error (MAE) represents the average absolute difference between observed and predicted values, highlighting the average magnitude of errors in the predictions (Eq. (10)). Root Mean Square Error (RMSE) assesses the magnitude of prediction errors, offering a measure of the model's predictive accuracy by evaluating the square root of the average squared differences (Eq. (11)). Together, these metrics provide a comprehensive assessment of the model's performance, capturing various aspects of prediction accuracy and error magnitude.

$$R^2 = 1 - \frac{\sum_{i=1}^{n}(y_i - \hat{y}_i)^2}{\sum_{i=1}^{n}(y_i - \bar{y}_i)^2} \quad (9)$$

$$MAE = \frac{1}{n}\sum_{i=1}^{n}|y_i - \hat{y}_i| \quad (10)$$

$$RMSE = \sqrt{\frac{1}{n}\sum_{i=1}^{n}(y_i - \hat{y}_i)^2} \quad (11)$$

where:

- y_i denotes actual values,
- $\hat{y}_i$ represents predicted values,
- $\bar{y}_i$ is the mean of actual values, and
- n is the number of observations.

As discussed in the methodology section, the XGBoost model is an optimized gradient-boosting algorithm that iteratively refines its predictions by building an ensemble of decision trees. Table 12 summarizes the hyperparameter tuning results for the XGBoost model using three different methods: Randomized Search, Grid Search, and Bayesian Optimization. The table shows that the Bayesian Optimization method achieved a maximum depth of 12, 950 estimators, a subsample of 0.60, and a learning rate of 0.0124, among other settings. This method used 10-fold cross-validation over 50 iterations, resulting in a total of 500 fits and a training time of 4 minutes. In comparison, Randomized Search and Grid Search used different parameter values and required more total fits and training time to optimize the model. Bayesian Optimization provided the best results for fine-tuning the model and is used for the results discussion.

Table 12 Hyperparameter tuning results of Bayesian optimization methods for the XGBoost model.

Hyperparameters	**Bayesian**
Maximum Depth	9
No. of Estimators	1500
Subsample	0.60

Min Child Weight	8
Learning Rate	0.0173
Gamma	0.0
Colsample-bytree	0.85
Cross Validation	4
No. of Iteration	50
Total fits	200
Training time	4 min

The results presented in Table 13 confirm that the XGBoost model performs exceptionally well in both training and testing phases. For the training dataset, the model achieves a MSE of 0.011, MAE of 0.042, RMSE of 0.105, and an R^2 score of 0.984, indicating a high level of accuracy and minimal error. Similarly, in the testing dataset, the model maintains strong performance with an MSE of 0.014, MAE of 0.050, RMSE of 0.116, and an R^2 score of 0.980. These metrics demonstrate that the model generalizes well to unseen data, maintaining low error rates and high explanatory power. The consistency between training and testing results underscores the model's reliability for predicting stress values in various time intervals.

Table 13 Comparing performance metrics of machine learning models on training and testing datasets for stress prediction.

Dataset	**MSE**	**MAE**	**RMSE**	**R^2**
Training	0.011	0.042	0.105	0.984
Testing	0.014	0.050	0.116	0.980

Figure 111 presents a comparative performance analysis of the XGBoost model. The KDE plots for the training (a) and testing (b) datasets reveal a close alignment between the distributions of predicted and actual values, indicating the model's accuracy in stress prediction. The scatterplots of actual vs. predicted values for training (c) and testing (d) datasets display a strong linear relationship, with most points closely aligned along the line of perfect fit (diagonal line). The comparison of scatter plots (a and b) suggests that the model is performing remarkably well in terms of predicting stress values based on the selected set of input features. The consistency across training and testing datasets suggests the model's robustness and reliability, demonstrating its effective generalization from training to unseen data.

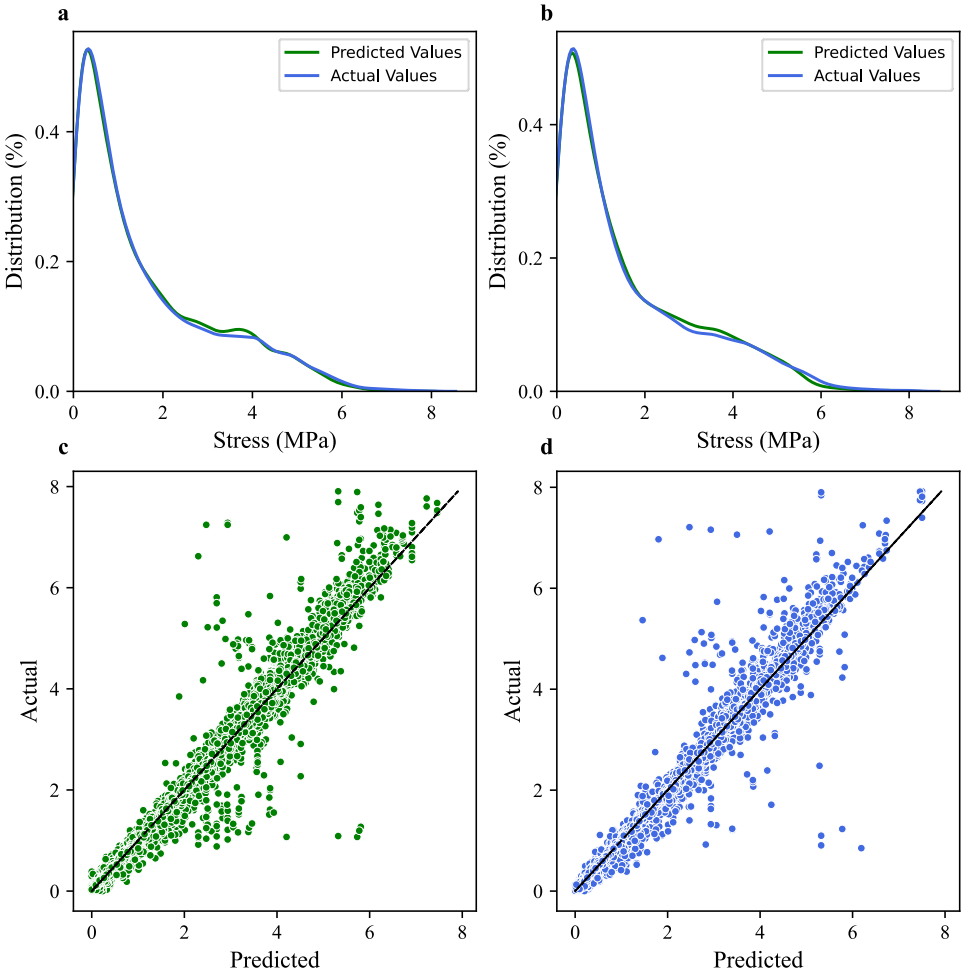

Figure 111 Comparative performance analysis of the XGBoost model representing (a) KDE for the training dataset, (b) KDE for the testing dataset, scatterplots of actual vs. predicted values for (c) training and (d) testing datasets.

Figure 112 illustrates the most important input features for predicting stress values of mortar, highlighting their impact on the model's output. Each point on the plot corresponds to a SHAP value for a particular instance, with the color indicating the feature value (red for high values and blue for low values). The “Displacement (mm)” feature has the most significant impact on stress prediction, showing a wide range of SHAP values. It’s important to note that to predict stress using the algorithm, a notional displacement, based on the observed displacement range, is used as the input, with stress then predicted accordingly. This underscores that variations in displacement greatly influence the predicted stress, consistent with experimental findings, where displacement is the most critical parameter in the flexural test. “Density” and “Time” also make substantial contributions, highlighting their importance in the model's predictions. While “Corrosion (pH)” and “Moisture (%)” have relatively smaller, yet noteworthy, negative and positive correlations with stress, they still play crucial roles. Overall, the plot provides insights into how each feature influences the model's output, shedding light on the factors driving stress predictions in the mortar samples

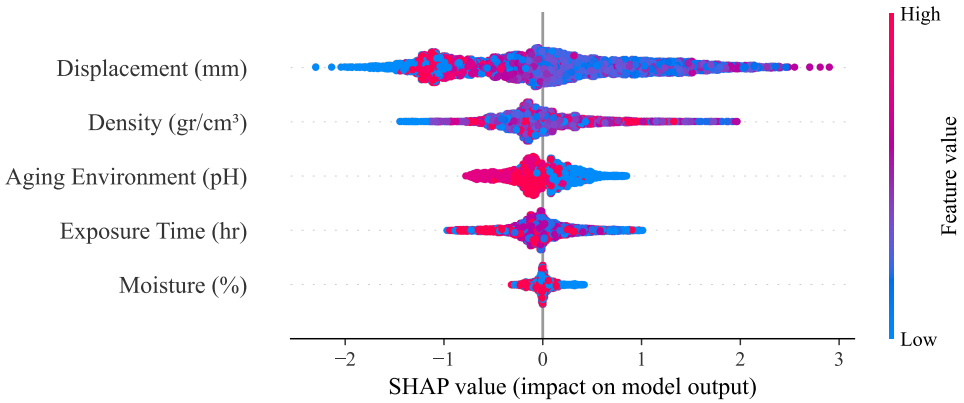

Figure 112 SHAP summary plot of the most important input features for predicting stress values of mortar.

7.5.3 Discussion

The variation of the flexural strength in different aging media is depicted in Figure 109. This figure illustrates the flexural strength of specimens under zero exposure, 1000-hour exposure, 3000-hour exposure, and 5000-hour exposure across three different environments: DC, WI, and AC. Figure 109 shows a significant variation in flexural strength depending on the aging medium and exposure duration. For instance, the flexural strength of specimens under zero exposure starts at 4.54 MPa for DC, with notable increases or decreases observed at subsequent exposure durations. Specifically, the strength in the DC environment shows a peak at 5000 hours with a value of 6.78 MPa, while the WI environment shows a decline over time, indicating the influence of water on material degradation. Conversely, the AC environment maintains a more stable flexural strength over time. The experimental results highlight the importance of environmental factors on the evolution of material properties, which the gradient boosting model aims to predict and interpret with high accuracy. By comparing the experimental data with the model predictions, there would be a better understanding of the reliability and applicability of machine learning in predicting material behavior under various conditions.

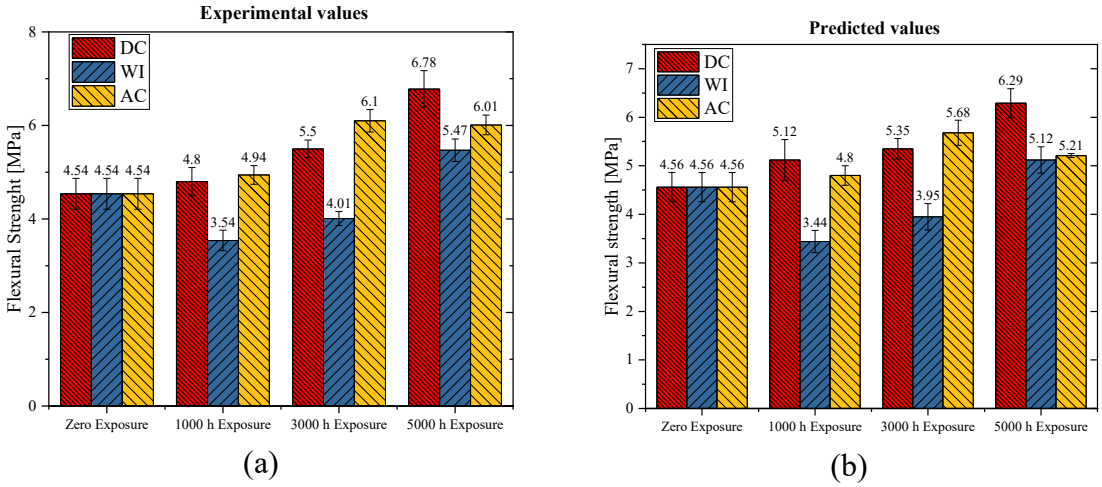

Figure 113 Variation of the flexural strength in different aging media from (a) experimental and (b) machine learning outputs.

Figure 109 and Figure 114 present the actual and predicted stress-displacement curves for specimens subjected to DC, WI, and AC environments after zero and 1000 hours of exposure. These graphs provide a detailed comparison of the behavior of different specimens under varying conditions.

Additionally, the area under the curve for each diagram was calculated, and the ratio of the predicted values' area to the tested values' area was measured. These ratios ranged from 0.957 to 1.007, with a CoV of 2, further highlighting the accuracy of the model. Subsequently, a XGBoost model was trained and evaluated based on the experimental data, enabling a comparison of the model's robustness and interpretability against different environmental conditions provided from the experimental results.

In Figure 109(a), the stress values for the F_0 condition demonstrate a rapid increase after approximately 0.15 mm of displacement, reaching a peak stress of around 6.0 MPa. This behavior is indicative of the material's initial stiffness and subsequent yielding. The corresponding graph in Figure 114(a) shows the predicted stress values following a similar trend. The predicted values closely align with the actual data, peaking around the same displacement range, with a rough margin of error of ±0.05 mm in displacement and ±0.2 MPa in maximum stress. This close alignment validates the accuracy of the XGBoost model in capturing the material's mechanical response under this condition.

As for the F_WI_1000 condition, Figure 109(b) illustrates the actual stress values, which initially increase sharply, peaking at approximately 6.5 MPa near 0.75 mm of displacement. In Figure 114(b) the predicted values also show a steep rise, albeit with slight deviations. The margin of displacement error is around ±0.05 mm, and the maximum stress difference is about ±0.3 MPa. Despite these minor discrepancies, the model successfully captures the overall trend, indicating its robustness in predicting stress-displacement behavior of specimens under water immersion after 1000 hours. For the F_DC_1000 condition depicted in Figure 109(c), the actual stress values rise steadily, reaching a peak around 4.0 MPa at 0.75 mm of displacement. Figure 114(c) shows the predicted stress values with a similar trend, with the model accurately reflecting the material's behavior after exposure to distilled conditions for 1000 hours. The estimated margin of error for displacement is ±0.1 mm, and for maximum stress, it is about ±0.3 MPa. This consistency further demonstrates the model's predictive reliability across varied conditions.

Finally, the F_AC_1000 condition in Figure 109(d) shows a more gradual increase in stress, peaking at around 4.5 MPa near 0.6 mm of displacement. The predicted stress values in Figure 114(d) mirror this pattern, with the XGBoost model effectively capturing the slower rate of stress increase associated with acidic exposure after 1000 hours. The rough margin of error for displacement here is ±0.05 mm, with a maximum stress difference of approximately ±0.2 MPa. The model's prediction accuracy under this condition highlights its ability to adapt to different environmental stressors and predict material degradation over time. These estimated margins of error indicate the model's overall effectiveness in predicting the stress-displacement curves across different exposure conditions. Indeed, the XGBoost model effectively captures the overall behavior of the material under prolonged acidic exposure, reflecting its capability for predicting the mechanical behavior of lime-based mortars under various environmental conditions.

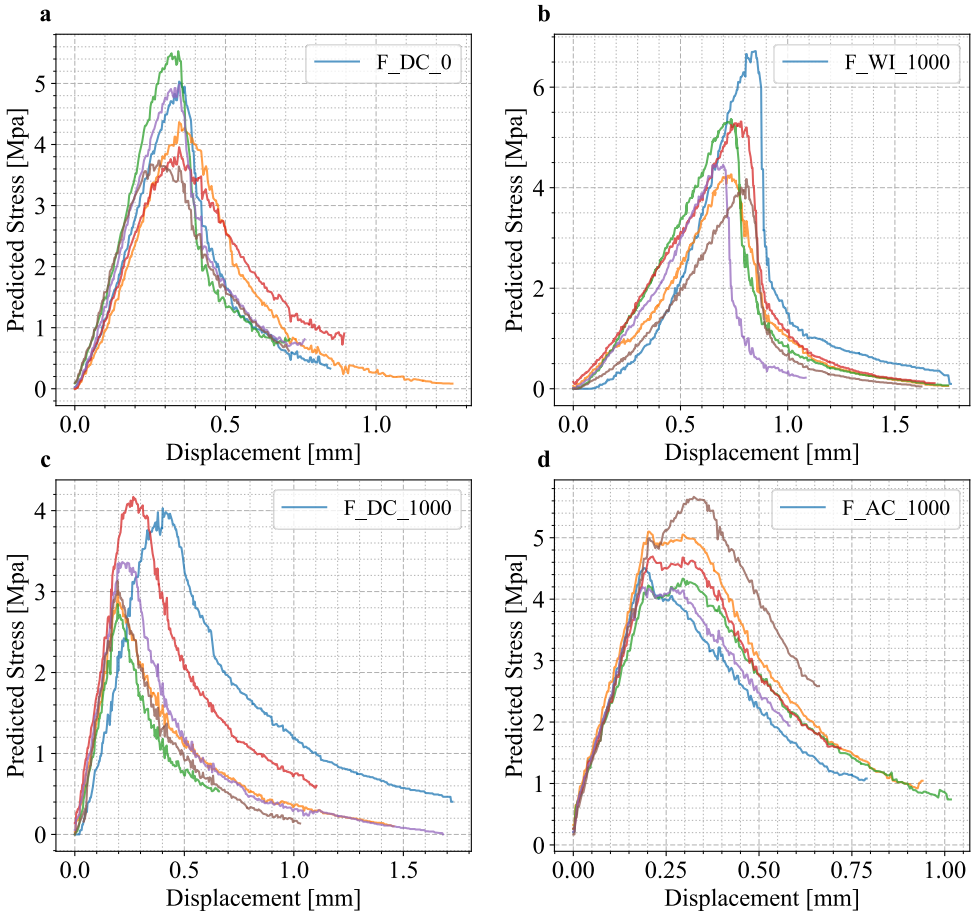

Figure 114 Predicted Stress vs. displacement diagram for each individual specimens from the XGBoost output for: (a) F_0 group; (b) F_DC_1000; (c) F_WI_1000; (d) F_AC_1000.

Figure 115 illustrates the comparison between the experimental results and the machine learning predicted flexural stress for different environments (DC, WI and AC) over time intervals of 1000, 3000, and 5000 hours. The actual average flexural stress values are represented by solid lines, while the predicted values are shown with dashed lines. The experimental results encompass the mechanical test outcomes for mortar samples subjected to various aging durations and conditions.

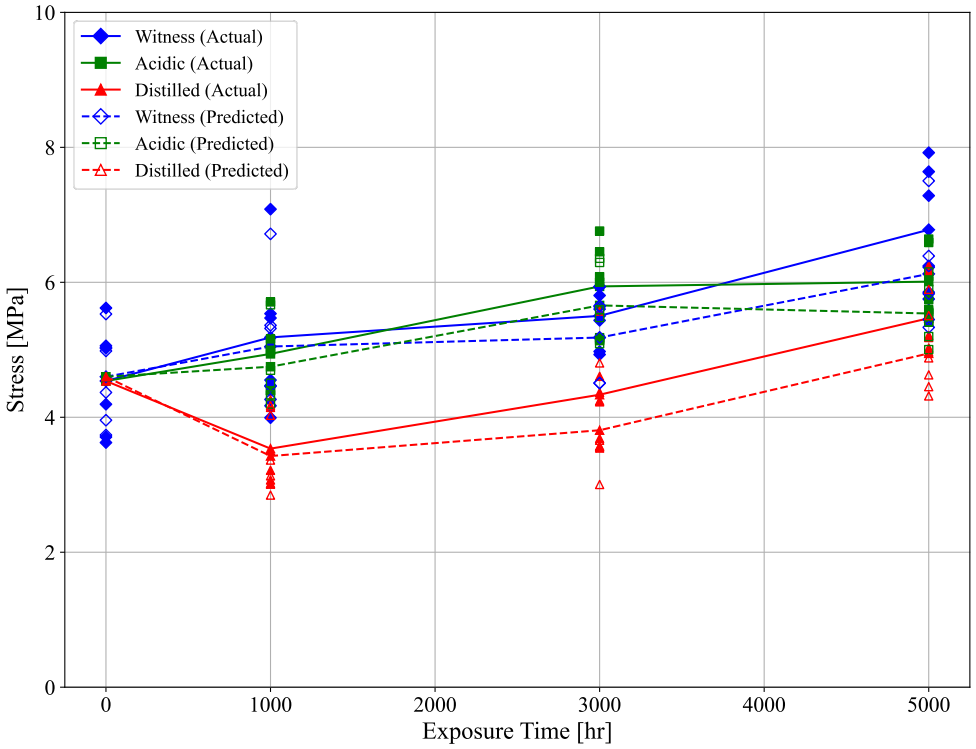

Figure 115 Comparative analysis of experimental versus machine learning prediction of flexural strength for different environments (DC, WI and AC) at intervals of 1000, 3000, and 5000 hours of exposure.

For all environments, there is a noticeable trend where the predicted values closely follow the actual values, although the XGBoost results slightly underpredict the actual stress values. The experimental results show that DC samples exhibit the highest flexural stress, followed by acidic and distilled samples. This pattern is similarly predicted by the machine learning model, demonstrating its reliability and robustness. The average predicted values for all environments closely align with the average actual values at different hour-marks, showcasing the generalizability of the model's predictive performance under varying environmental conditions. The model achieved an R^2 of 0.984 and an RMSE of 0.116 for the testing dataset using a 4-fold cross-validation approach, indicating excellent accuracy and consistency in capturing the complex relationships between input features (e.g., density, corrosion, moisture, and exposure duration) and the stress-displacement behavior of lime-based mortar. These metrics provide a standard measure of the model's error, allowing for direct comparison with other studies in the literature. While the model demonstrates robust predictive capabilities, slight increases in deviations are observed at higher time points, particularly under acidic exposure conditions. This suggests potential areas for refinement, such as incorporating more data points or leveraging additional machine learning techniques to further enhance the model's accuracy and reliability. Overall, the results underline the strength of the XGBoost model in delivering reliable predictions and its potential as a valuable tool for assessing material performance in adverse environmental conditions.

7.6 Conclusion

This chapter investigated the mechanical and chemical degradation of a commercial NHL mortar with pozzolan exposed to acidic conditioning, relevant to durability concerns in construction and conservation applications. A combined experimental and modeling approach was adopted to evaluate mortar performance under immersion in sulfuric acid solutions (pH 1.5, 2.0, 3.0), water storage, and dry curing for durations up to 6000 hours. The main findings of this chapter may be summarized as follows:

- Acidic environments significantly impaired mechanical properties, particularly at lower pH values and longer exposures. Mortars exposed to pH 1.5 for 6000 hours exhibited the greatest reduction in elastic modulus and compressive strength, in line with the observed depletion of portlandite and progressive gypsum formation.
- Chemical degradation followed a well-defined sequence involving portlandite and calcite dissolution, followed by gypsum precipitation. TGA and ICP analyses confirmed a clear correlation between calcium leaching and mechanical deterioration, especially in acid-exposed groups.
- Reference environments demonstrated distinct trends: dry storage led to moderate strength gains due to continued carbonation, while water immersion initially enhanced strength via ongoing hydration but ultimately induced moderate stiffness loss due to leaching effects.
- The inclusion of short polymeric fibers was beneficial under acidic conditions, particularly in delaying crack propagation and preserving post-peak structural integrity. Their impact on compressive strength was limited but significant for damage control and energy dissipation.
- A calibrated trilinear damage model effectively captured the compressive behavior of both unaged and aged mortars, reflecting the changes in elastic, peak, and post-peak response due to chemical degradation. The model also integrated porosity evolution and matrix embrittlement due to secondary phase formation.
- A leaching-based chemo-mechanical model, formulated using normalized iron concentration as a degradation indicator, was validated across multiple exposure conditions. It successfully predicted mechanical parameters for exposure groups not included in calibration, confirming its robustness for interpolating deterioration trends under acidic conditions.
- A machine learning model based on the XGBoost algorithm was developed to predict the flexural behavior of lime-based mortar under environmental exposure. Using a combination of material properties and environmental parameters as inputs, the model achieved strong agreement with experimental stress–displacement results (R^2 = 0.984, RMSE = 0.116), providing an efficient predictive tool for flexural performance under prolonged aging.

The Integration of experimental characterization with both chemo-mechanical and machine learning-based modeling offers a comprehensive framework for understanding and forecasting the durability of lime-based mortars in aggressive environments. These modeling approaches are not only capable of predicting untested exposure conditions with high fidelity but also serve as valuable tools for long-term performance evaluation and material optimization. Given the increasing use of lime-based mortars in TRM systems for structural strengthening, the predictive models developed in this chapter provide relevant insights into how acidic degradation affects the mechanical behavior of the matrix. These results serve as a foundation for the subsequent analysis in Chapter 7, where the behavior of full TRM systems exposed to acidic environments is investigated. The experimental campaign and the chemo-mechanical framework introduced here are extended in Chapter 7 to assess bond performance and the global response of TRM composites, offering a direct link between matrix deterioration and composite-level behavior.

This page is left blank on purpose

Chapter 8
Effect of acidic conditioning on TRM composites: experimental evaluation and mechanistic modeling of aging

8.1 Introduction

In continuation of the durability assessment presented in Chapter 7, the present chapter advances the investigation by shifting the focus from the mortar matrix to the performance of the TRM composite system. While Chapter 6 provided a comprehensive evaluation of the degradation mechanisms affecting the mortar phase, including mechanical deterioration, leaching phenomena, and the development of empirical damage models, this chapter aims to extend the durability analysis to the structural composite, integrating both experimental and analytical approaches.

This chapter is dedicated to the study of the TRM system subjected to acidic aging environments of varying severity, as part of the durability campaign II. Initially, the uniaxial tensile behavior of aged TRM specimens is evaluated to identify changes in cracking behavior, strength, and deformation capacity. Subsequently, a detailed mechanical characterization is carried out through pull-out and single-lap shear tests to assess bond degradation at the fiber–matrix and matrix–substrate interfaces. These results serve as the foundation for the development of an analytical model governed by a trilinear CML, calibrated using the shear bond data. The calibrated model is then extended to simulate the tensile behavior of TRM composites under different aging conditions, enabling a mechanistic interpretation of performance loss and the contribution of bond deterioration to overall composite degradation.

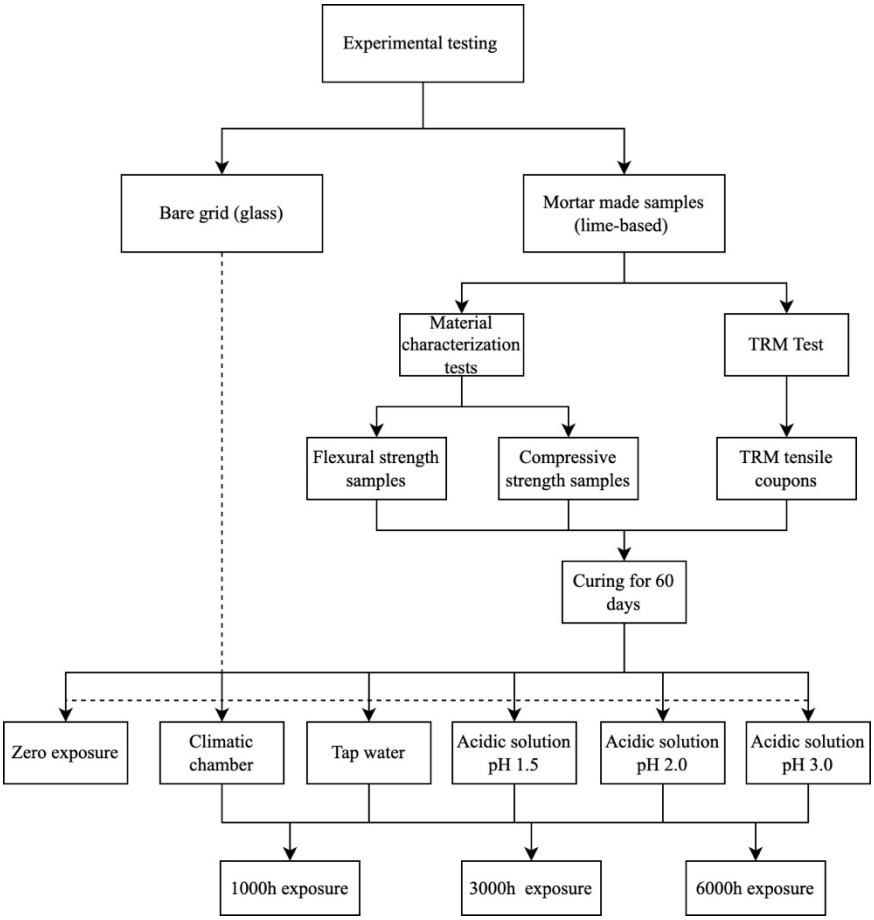

Figure 116 An overview flowchart of the experimental campaign.

8.2 Experimental program

The experimental methodology implemented in this chapter is based on durability campaign II, which follows the environmental aging protocols and curing regimes previously established in Chapter 6. While the earlier campaign focused on the characterization of mortar properties under different aggressive conditions, durability campaign II expands the investigation to the composite level, targeting the performance of the full TRM system and its constituents. The same controlled exposure environments, including dry reference, water immersion, and acidic solutions with varying pH levels (1.5, 2.0, and 3.0), were adopted to maintain consistency across the experimental phases and facilitate a mechanistic comparison between matrix-level and composite-level degradation phenomena.

Four types of specimens were prepared and tested to capture the evolution of mechanical behavior due to acidic exposure will be studied in this chapter: (i) TRM tensile coupons for evaluating the global tensile performance of the composite, (ii) single-lap shear specimens for assessing the bond performance between the TRM and the masonry substrate, (iii) pull-out specimens to isolate fiber–matrix bond degradation, and (iv) bare textile yarns for tensile testing to quantify any direct influence of the acidic environment on the reinforcement itself. This multi-scale testing strategy aimed to separate the effects of matrix deterioration, interface degradation, and fiber sensitivity, providing a comprehensive framework for mechanistic modeling.

Specimens were identified using a standardized four-part code, S_C_E_R. In this notation: “S” designates the type of test, T for TRM tensile coupon tests, S for single-lap shear test, P for pull-out test and X for textile tensile tests. The second character “C” defines the conditioning environment, RC for dry

climatic chamber reference, RW for water immersion reference, P15 for acidic immersion at pH 1.5, P2 for pH 2.0, and P3 for pH 3.0. The third term "E" corresponds to exposure duration, 0 for unaged specimens, 1000, 3000, and 6000 for the respective durations in hours. The last component "R" denotes the specimen number within each group. For instance, the code T_P15_3000_6 refers to a TRM tensile specimen that was exposed to a pH 1.5 acidic solution for 3000 hours and is the sixth specimen in its group. For each test group consisted of seven specimens were considered for testing. This ensured sufficient data for statistical reliability and model calibration. Detailed specimen information, environmental conditions, and test distributions are summarized in Table 14 and Table 15.

8.3 Experimental results and discussion

8.3.1 Mortar behavior overview

The results of mortar tests of this campaign are brought in the previous chapter. As a summary, in compressive strength, for the RC specimens, the compressive strength curve exhibits a smooth transition from a steep initial incline to a gradual increase, reaching peak compressive strength. The rate of strength gain is faster between age zero and 1000 h, indicating ongoing hydration and carbonation of the mortar over time, with a higher rate at earlier ages. In the case of the reference RW specimens, the compressive strength values increase until reaching a peak at 3000 h, after which they begin to decrease. The strength increases up to 1000 h is lower than that observed in the climatic chamber, likely due to inhibited carbonation in saturated environments, followed by leaching of portlandite and C–S–H phases, as noted in previous research [11,323]. Specimens immersed in acidic solutions exhibit different trends in compressive strength depending on the acidity levels. For samples immersed in a solution with pH 3.0, the compressive strength increases over time, suggesting that gypsum formation and mild acid-induced carbonation may contribute to matrix densification and strength gain. Specimens in pH 2.0 exhibit an initial increase followed by stabilization, while exposure to pH 1.5 leads to strength development up to 3000 h, followed by a marked reduction. This pattern resembles that of RW specimens, though pH 1.5 yields higher compressive values up to 3000 h. These short-term strength improvements in mildly to moderately acidic solutions can be attributed to gypsum precipitation and possible densification effects, but over time, ongoing acid attack results in portlandite and calcite dissolution, internal stress buildup, and matrix softening. The most severe degradation is observed at pH 1.5 after prolonged exposure, demonstrating that increased acidity accelerates deterioration mechanisms, particularly under longer durations.

Also, regarding the flexural strength, similar to the compressive strength trend, RC specimens exhibit overall increases in flexural strength with exposure time. RW specimens show a modest strength gain up to 3000 h, followed by a reduction between 3000 and 5000 h. It is important to note that short fibers are embedded in the mortar matrix, and their interaction with the evolving matrix critically influences flexural performance. The post-3000 h strength loss in RW specimens likely reflects the weakening of the fiber–matrix interface due to progressive leaching and loss of cohesion in the matrix gel [324]. The effect of acidic exposure on flexural strength similarly depends on acid intensity and time. Up to 3000 h, specimens in pH 3.0 display behavior comparable to RW samples, with slightly higher strength, likely due to initial gypsum formation that temporarily enhances matrix continuity and fiber bond quality [325]. With longer exposure, strength declines but remains above RW levels. In contrast, specimens in pH 2.0 and 1.5 exhibit similar strengths at 1000 h, but diverge thereafter. pH 2.0 specimens show gradual degradation, while those in pH 1.5 display a pronounced decline following early strength gains. This behavior can be attributed to an initial pore-filling phase from gypsum formation, followed by binder depletion, internal cracking, and weakening of fiber–matrix adhesion under more aggressive conditions. Ultimately, flexural performance under acidic environments is governed by a trade-off between early

chemical densification and long-term deterioration mechanisms, most pronounced at lower pH and longer exposure times.

Table 14 Characteristics of specimens tested

Specimen Name	Specimen type	Aging Medium	Exposure time	Specimen Name	Specimen type	Aging Medium	Exposure time
T_0	Tensile coupon	Climatic chamber	-	S_0	Single-lap	Climatic chamber	-
T_RC_1000			1000 h	S_RC_1000			1000 h
T_RC_3000			3000 h	S_RC_3000			3000 h
T_RC_6000			6000 h	S_RC_6000			6000 h
X_0	Tensile textile	Climatic chamber	-	P_0	Pull-out	Climatic chamber	-
X_RC_1000			1000 h	P_RC_1000			1000 h
X_RC_3000			3000 h	P_RC_3000			3000 h
X_RC_6000			6000 h	P_RC_6000			6000 h
T_RW_1000	Tensile coupon	Tap water immersion	1000 h	S_RW_1000	Single-lap	Tap water immersion	1000 h
T_RW_3000			3000 h	S_RW_3000			3000 h
T_RW_6000			6000 h	S_RW_6000			6000 h
X_RW_1000	Tensile textile	Tap water immersion	1000 h	P_RW_1000	Pull-out	Tap water immersion	1000 h
X_RW_3000			3000 h	P_RW_3000			3000 h
X_RW_6000			6000 h	P_RW_6000			6000 h
T_P15_1000	Tensile coupon	pH 1.5 immersion	1000 h	S_P15_1000	Single lap	pH 1.5 immersion	1000 h
T_P15_3000			3000 h	S_P15_3000			3000 h
T_P15_6000			6000 h	S_P15_6000			6000 h
X_P15_1000	Tensile textile	pH 1.5 immersion	1000 h	P_P15_1000	Pull-out	pH 1.5 immersion	1000 h
X_P15_3000			3000 h	P_P15_3000			3000 h
X_P15_6000			6000 h	P_P15_6000			6000 h
T_P2_1000	Tensile coupon	pH 2.0 immersion	1000 h	S_P2_1000	Single lap	pH 2.0 immersion	1000 h
T_P2_3000			3000 h	S_P2_3000			3000 h
T_P2_6000			6000 h	S_P2_6000			6000 h

Table 15 Characteristics of specimens tested (continued from Table 14)

Specimen Name	Specimen type	Aging Medium	Exposure time	Specimen Name	Specimen type	Aging Medium	Exposure time
X_P2_1000	Tensile textile	pH 2.0 immersion	1000 h	P_P2_1000	Pull-out	pH 2.0 immersion	1000 h
X_P2_3000			3000 h	P_P2_3000			3000 h
X_P2_6000			6000 h	P_P2_6000			6000 h
T_P3_1000	Tensile coupon	pH 3.0 immersion	1000 h	S_P3_1000	Single lap	pH 3.0 immersion	1000 h
T_P3_3000			3000 h	S_P3_3000			3000 h
T_P3_6000			6000 h	S_P3_6000			6000 h
X_P3_1000	Tensile textile	pH 3.0 immersion	1000 h	P_P3_1000	Pull-out	pH 3.0 immersion	1000 h
X_P3_3000			3000 h	P_P3_3000			3000 h
X_P3_6000			6000 h	P_P3_6000			6000 h

8.3.2 Grid performance

Table 16 provides detailed numerical results for tensile strength and elastic modulus, along with their variations relative to the reference sample (X_0). These values highlight the distinct effects of aging environments and exposure times. The average value of the tensile strength for the reference specimens was 1062 MPa. For RC samples, the tensile strength decreased by 13.9% at 1000 h (X_RC_1000), but since aging of the textile in a controlled climatic chamber is highly unlikely, such difference can be attributed to fluctuations arising from the manufacturing process rather than meaningful trends. The fluctuations observed for this series, both for tensile strength and elastic modulus, were within 15% threshold and should be considered insignificant. By 3000 h (X_RC_3000), a minor increase in strength of 0.4% was observed, and at 6000 h (X_RC_6000), a 5.7% strength decrease was recorded, which further reinforces the idea that these are random fluctuations rather than actual aging effects. RW samples exhibited a short-term increase in tensile strength (+9.7%, X_RW_1000), likely due to hydration or densification effects under immersion. However, over longer durations, tensile strength values converged with those of RC samples, suggesting that the observed differences are related to the CoV of the samples rather than significant trends. Elastic modulus for RW samples showed a reduction of 5% at 6000 h (X_RW_6000), shows fiber resistance under water immersion condition.

Figure 117 shows a graphical representation of these trends of tensile strength (Figure 117a) and elastic modulus (Figure 117b) over time for each aging environment. In Figure 117a, RC and RW specimens show minor fluctuations in tensile strength, as discussed as well as the elastic modulus according to the Figure 117b. Specimens exposed to acidic environments exhibited more meaningful trends. Specimens immersed in solutions with pH 1.5 and 3 showed an increase in tensile strength and fluctuation in the elastic modulus over time, indicating possible beneficial effects from acidic reactions, such as enhanced fiber-matrix interactions in the short term. Conversely, specimens exposed to pH 2 exhibited a slight increase in their strength values up to 3000 h followed by a decremental trend afterward, suggesting a different interaction mechanism that led to cumulative damage. This divergence highlights the complex role of acidic intensity in influencing textile performance, and relatively good resistance of them in such an environment.

Table 16 Mechanical properties of the exposed textiles under different aging conditions

Group Name	Tensile strength [MPa]	Tensile strength Variation [%]	Elastic modulus [GPa]	Elastic modulus variation [%]	Ultimate strain [%]
X_0	1062	-	63.7	-	18.5
X_RC_1000	914	-13.9	64.0	0.5	16.9
X_RC_3000	1067	0.4	61.3	-3.8	20.6
X_RC_6000	1002	-5.7	54.9	-13.8	17.8
X_RW_1000	1166	9.7	64.1	0.6	19.0
X_RW_3000	1034	-2.7	63.3	-0.5	19.3
X_RW_6000	1163	9.4	60.5	-5	20.6
X_P15_1000	1247	17.3	63.3	-0.6	24.6
X_P15_3000	1244	17	61.2	-3.9	25.0
X_P15_6000	1431	34.6	65.6	2.9	27.3
X_P2_1000	1202	13.1	66.8	4.9	20.7
X_P2_3000	1265	19.1	64.5	1.2	24.4
X_P2_6000	1032	-2.9	61.9	-2.7	19.6
X_P3_1000	1127	6.1	63.2	-0.8	20.9
X_P3_3000	1167	9.8	62.4	-1.9	23.0
X_P3_6000	1385	30.4	62.1	-2.5	24.4

Overall, the data suggest that RC and RW environments induce minor fluctuations in tensile strength and elastic modulus that are within the range of experimental variability. However, acidic environments result in more pronounced and meaningful trends, with the behavior depending on the acid intensity and exposure duration. While the increase in strength and stiffness under certain acidic conditions might reflect short-term beneficial reactions, the long-term behavior indicates material degradation, emphasizing the need for further investigation into the mechanisms at play.

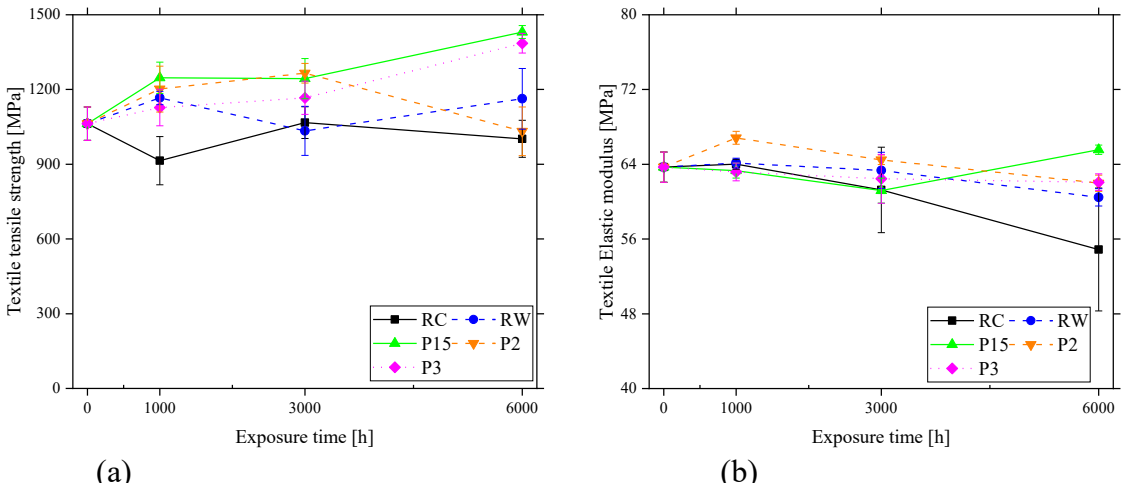

Figure 117 Variations in the mechanical properties of the textiles over exposure time under different aging environments: (a) Tensile strength variation across aging conditions; (b) Elastic modulus variation across aging conditions.

8.3.3 TRM tensile behavior

Many previous studies have categorized the tensile response of TRM composites into three stages: the uncracked stage, the crack development stage, and the post-cracking stage [75,110,111,251]. To accurately capture threshold strains and associated stresses in these stages, advanced techniques such as DIC have been proposed in combination with traditional load-displacement measurements [7]. However, these methods are time-consuming and costly, making them impractical for routine application with current technologies. In this study, threshold strains and stresses associated with the end of first (σ_1, ε_1) and second (σ_2, ε_2) stages were directly identified from the stress-strain curve of individual specimens, as recommended in previous investigations [75,110,111,251]. Using parameters of the first and the second thresholds, segmental moduli for each stage, E_1 (elastic), E_2 (post-first crack), and E_3 (post-crack stabilization), were calculated as the slopes of their respective portions of the stress-strain curve. Additionally, the tensile strength (f_t) and its corresponding strain ($\varepsilon_{(ft)}$) were identified. The values of these nine parameters, evaluated for the rectangular prism specimens, are summarized in Table 17 and Table 18, with average values and CoV provided to assess the reliability and variability of the results.

The axial stress–strain curves obtained from tensile tests are presented in Figure 119. Matrix cracks were observed to occur both within and outside the gauge length of the LVDTs, meaning that strain measurements did not always fully represent the behavior of the entire specimen. Nonetheless, consistency between specimens with matrix cracks inside and outside the LVDTs gauge length confirms that the overall σ–ε behavior was reliably captured using the employed instrumentation and experimental setup. This consistency aligns with observations reported in previous studies [75]. Based on the clamping method and gripping type used in the tests, three distinct failure modes were identified: (a) rupture of the fibers at a major crack far from the clamping area (Figure 118a) ; (b) opening of a major crack near the clamping area, accompanied by textile slippage within the matrix without failure of the yarn (Figure 118b); and (c) failure of the textile at the bare textile region. The third failure mode, attributed to potential damage in the resin-impregnated areas, was infrequent and such specimens were excluded from the analysis to ensure the reliability of the results.

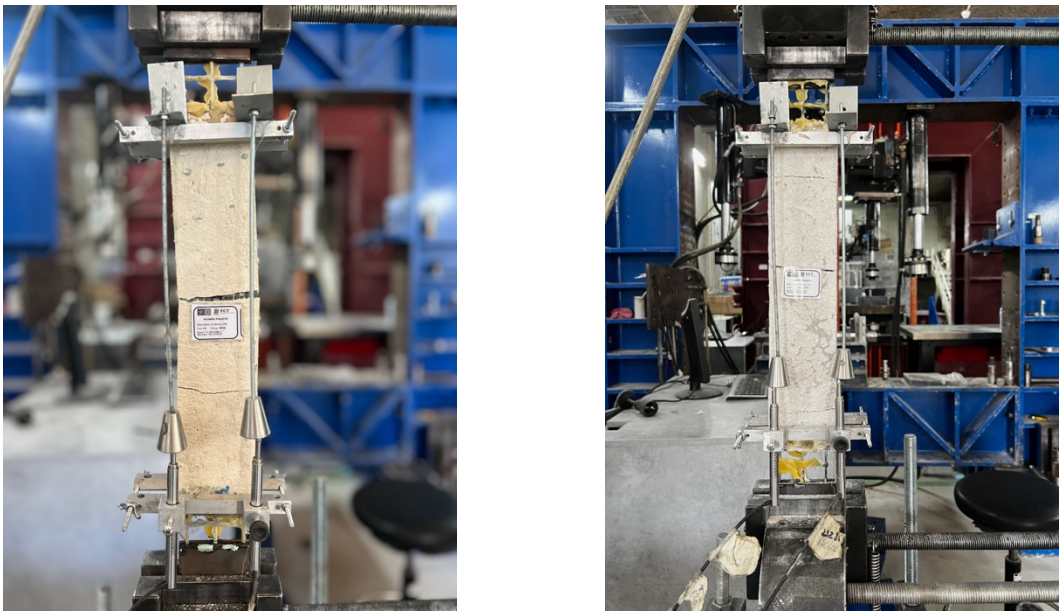

(a) (b)

Figure 118 (a) Failure mode "a" in specimen T_C_RW_6000_2; (b) failure mode "b" in specimen T_C_RC_1000_2

The concept of critical fiber volume content in the design of TRM, as discussed in prior research [326], emphasizes the balance between matrix and fiber contributions to tensile performance. In composites with fiber content below the critical volume, only a single crack forms, resulting in strain-softening behavior and limited ductility. In contrast, composites with fiber content above the critical volume exhibit crack-bridging behavior, where fibers effectively bridge multiple cracks under loading. This capability may allow the composite for carrying higher loads, leading to strain-hardening behavior characterized by multiple cracking. Such behavior significantly improves the tensile performance of TRM composites, as fibers provide additional resistance and stiffness after the matrix has first cracked [251]. In the context of aging, however, weakening of either the matrix or the textile can alter the critical fiber volume content, leading to changes in the cracking pattern. Ensuring that fiber content exceeds the critical volume is therefore essential to prevent catastrophic (brittle) failure of the matrix. This ensures the composite can sustain higher loads and maintain its structural integrity under deformation, even as aging-induced degradation affects the individual components.

8.3.3.1 TRM tensile behavior (RC condition)

Figure 119 illustrates the stress–strain curves for individual specimens and their group averages under RC conditions across different exposure times, while Table 17 summarizes the parameters associated with the loading stages and cracking patterns, reported as averages along with their CoV. For all specimens conditioned at 0, 1000, 3000, and 6000 h, the three loading stages were clearly observed. The tensile strength of the coupons (f_t) fluctuated over time without following a specific trend. Since the textile governs the capacity of the composite, and the tensile strength closely aligns with the textile's capacity (as shown in Figure 117a), these fluctuations are attributed to inherent variation in textile performance rather than environmental effects under RC conditions.

The strain corresponding to failure ($\varepsilon(f_t)$) exhibited a decreasing trend with increasing exposure time, [likely due to evolving mortar stiffness and reduced deformability, potentially related to carbonation or continued curing]. Parameters characterizing stage 1 were expressed relative to the textile cross-sectional area for consistency, though they fundamentally relate to the mortar's contribution. These parameters showed some scatter, but σ_1 increased over time, suggesting improved interfacial bond strength or more efficient load transfer between the mortar and textile. The strain at the end of stage 1 (ε_1) fluctuated slightly but remained generally stable, indicating limited variation in the cracking strain of the mortar. The segmental modulus for stage 1 (E_1) increased slightly between 0 and 1000 h, likely due to ongoing matrix consolidation or shrinkage effects], and remained relatively stable thereafter.

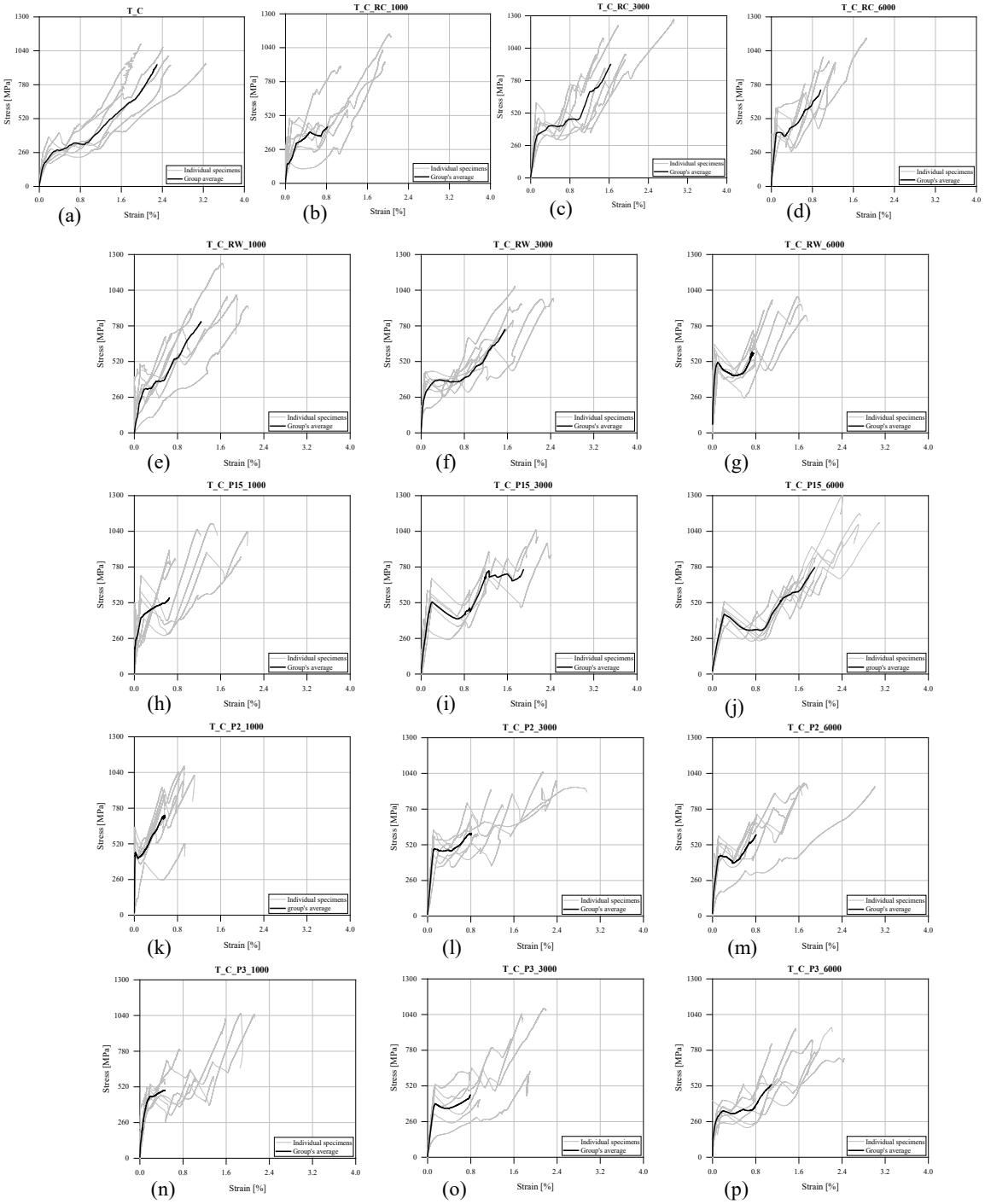

Figure 119 Stress-strain curves of individuals and group average for: (a) T_C; (b) T_C_RC_1000; (c) T_C_RC_3000; (d) T_C_RC_6000; (e) T_C_RW_1000; (f) T_C_RW_3000; (g) T_C_RW_6000; (h) T_C_P15_1000; (i) T_C_P15_3000; (j) T_C_P15_6000; (k) T_C_P2_1000; (l) T_C_P2_3000; (m) T_C_P2_6000; (n) T_C_P3_1000; (o) T_C_P3_3000; (p) T_C_P3_6000.

Table 17 Test results for characterization parameters of different coupon groups (CoV shown in parentheses)

Group name	ε_1 [%]	ε_2 [%]	$\varepsilon(f_t)$ [%]	σ_1 [GPa]	σ_2 [GPa]	f_t [GPa]	E_1 [GPa]
T_0	0.11 (29)	1.04 (34)	2.40 (21)	213.3 (22)	354.8 (18)	991.2 (7)	191.02 (39)
T_RC_1000	0.06 (41)	0.76 (46)	1.39 (37)	310.8 (43)	294.1 (20)	782.59 (34)	434.76 (36)
T_RC_3000	0.12 (33)	1.24 (17)	1.66 (14)	356.47 (15)	589.91 (25)	1059.76 (13)	362.86 (38)
T_RC_6000	0.10 (45)	0.55 (44)	1.158 (7)	477.58 (19)	358.33 (26)	959.13 (11)	452.96 (36)
T_RW_1000	0.05 (42)	0.51 (52)	1.425 (35)	324.02 (31)	390.64 (26)	883.94 (12)	746.49 (59)
T_RW_3000	0.08 (10)	1.07 (42)	1.78 (24)	382.82 (15)	436.14 (32)	866.43 (18)	469.24 (21)
T_RW_6000	0.11 (52)	0.68 (37)	1.22 (32)	532.42 (13)	424.19 (18)	872.38 (11)	694.61 (55)
T_P15_1000	0.08 (74)	0.44 (62)	1.25 (45)	487.45 (15)	295.59 (22)	942.22 (11)	1715.24 (52)
T_P15_3000	0.17 (18)	1.08 (50)	1.36 (55)	543.50 (16)	435.45 (37)	759.04 (31)	348.45 (25)
T_P15_6000	0.22 (6)	1.87 (23)	2.47 (15)	446.34 (12)	606.15 (24)	1053.82 (14)	211.34 (16)
T_P2_1000	0.01 (35)	0.46 (47)	0.83 (24)	543.55 (14)	557.88 (36)	978.54 (8)	4143.29 (55)
T_P2_3000	0.11 (17)	1.03 (45)	1.64 (43)	518.65 (16)	549.74 (20)	853.98 (18)	474.16 (25)
T_P2_6000	0.11 (14)	0.95 (45)	1.39 (26)	507.81 (10)	501.24 (17)	886.67 (11)	394.88 (34)
T_P3_1000	0.10 (61)	0.98 (43)	1.30 (43)	437.07 (17)	499.97 (19)	804.65 (26)	401.84 (26)
T_P3_3000	0.12 (13)	0.97 (44)	1.49 (36)	441.63 (18)	443.52 (23)	776.34 (31)	377.19 (4)
T_P3_6000	0.08 (21)	1.25 (23)	1.82 (23)	299.94 (23)	470.47 (11)	842.30 (10)	356.34 (19)

* All the reported values are the average of each group

The second loading stage, associated with crack development, exhibited higher scatter in the data. The segmental modulus E_2 followed a decreasing trend and became negative at 6000 h, indicating reduced load redistribution capacity during crack propagation. This may reflect altered fiber-matrix interaction, possibly due to slight changes in the matrix microstructure or bond deterioration at the interface over time. Regarding failure modes, Table 18 indicates that all specimens conditioned at 0 to 3000 h failed in mode “a”. At 6000 h, 2 out of 7 specimens failed in mode “b”, while the others retained mode “a”. This slight shift in failure behavior may be associated with evolving interfacial characteristics or changes in local stress concentrations near the clamping zones, rather than purely mortar strength. Figure 120 presents the average number of cracks and crack spacing over time. While the total number of cracks decreased with longer exposure durations, this trend is better attributed to changes in the fiber-matrix interface behavior rather than improvements in mortar strength alone, which cannot directly explain crack number or spacing. As the ability of the textile to bridge multiple cracks diminishes, whether due to reduced interfacial bond efficiency or increased localization of stress, the system transitions from multiple to fewer dominant cracks. Consequently, the fiber volume may become insufficient to activate multiple cracks once the critical bond condition is not met. Despite the reduced number of cracks, the average crack spacing and the distance from the nearest crack to specimen extremities remained largely unchanged over time, highlighting the importance of interface characteristics and composite geometry in governing crack pattern distribution under RC conditions.

Table 18 Test results on characterization parameters of different groups of coupons (continued from Table 17)

Group name	E_2 [GPa]	E_3 [GPa]	Number of failure in mode "a"/ mode "b"	f_t/textile strength [%]	Average number of cracks*	Average Distance of the closest crack to extremities* [mm]	Average crack spacing* [mm]
T_0	16.92 (55)	49.24 (24)	6/0	93.28	4.33 (22)	4.77 (17)	8.45 (24)
T_RC_1000	10.00 (72)	73.31 (17)	7/0	85.58	3 (31)	9.09 (35)	8.79 (24)
T_RC_3000	13.43 (65)	97.46 (13)	7/0	99.33	2.86 (12)	8.76 (25)	9.01 (13)
T_RC_6000	-32.89 (41)	112.56 (10)	5/2	95.75	1.57 (31)	9.66 (36)	8.43 (44)
T_RW_1000	24.79 (52)	70.45 (18)	5/2	75.81	2.71 (32)	10.39 (29)	8.48 (19)
T_RW_3000	15.78 (41)	65.92 (10)	4/3	83.78	2.57 (28)	8.38 (36)	12.17 (25)
T_RW_6000	-19.15 (63)	82.41 (16)	6/1	75.04	1.29 (54)	13.93 (26)	5.92 (64)
T_P15_1000	-113.88 (64)	93.03 (34)	4/3	75.56	1.28 (35)	16.01 (16)	3.38 (74)
T_P15_3000	-19.69 (74)	77.38 (25)	6/1	61.03	1.43 (63)	14.56 (22)	4.57 (71)
T_P15_6000	10.02 (49)	73.39 (15)	7/0	73.66	2.71 (17)	8.43 (29)	9.26 (46)
T_P2_1000	25.35 (72)	97.30 (16)	5/2	81.42	1.86 (34)	13.43 (24)	7.03 (64)
T_P2_3000	7.74 (62)	56.37 (37)	5/2	67.49	2.14 (39)	10.75 (44)	9.36 (85)
T_P2_6000	10.74 (52)	62.05 (31)	5/1	85.90	1.67 (47)	11.6 (30)	10.7 (50)
T_P3_1000	8.39 (61)	104.16 (13)	6/1	71.36	1.86 (53)	12.04 (26)	6.71 (64)
T_P3_3000	3.88 (32)	51.62 (26)	6/1	66.54	1.71 (51)	13.77 (16)	5.8 (49)
T_P3_6000	15.67 (26)	62.82 (37)	4/2	60.79	2 (36)	10.77 (18)	8.15 (35)

* All the reported values are the average of each group

8.3.3.2 TRM tensile behavior (RW condition)

TRM coupons exposed to RW conditions also exhibited the three distinct stages of loading during tensile testing. Generally, TRM coupons conditioned in RW showed a lower tensile strength (ft) compared to unexposed specimens. Despite the slight reduction in textile strength observed in the bare textile tests (Figure 117), the ft/textile strength ratio presented in Table 18 was lower than that of unexposed specimens. This observation highlights the aging effect of water immersion on the specimens, as previously reported in related research [11]. Interestingly, the ratio between the tensile strength of the coupons and the bare textile tensile strength peaked at 3000 h of exposure, followed by a reduction, a trend opposite to that observed in the bare textile strength. The strain corresponding to the tensile strength ($\varepsilon(f_t)$) followed a similar behavior, peaking at 3000 h and then decreasing, indicating changes in the interaction between the textile and mortar over time.

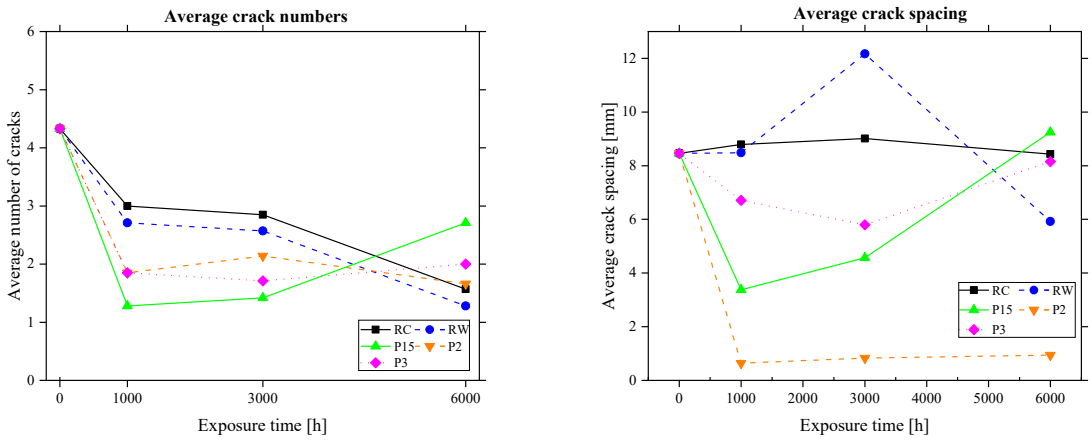

(a) (b)

Figure 120 Cracks properties: (a) average crack numbers; (b) average crack spacing.

The stress and strain values associated with the end of stage 1 displayed an increasing trend with exposure time. The increased stress is attributed to mortar strength development due to hydration, while the increased cracking strain is likely due to enhanced ductility of the mortar, also resulting from hydration over time. The elastic modulus during stage 1 (E_1) exhibited a minimum at 3000 h, followed by a gradual increase with prolonged exposure, suggesting an initial reduction in stiffness that later stabilized with further hydration and bond enhancement between the textile and mortar. During the second loading stage, the segmental moduli (E_2) followed a decreasing trend, becoming negative at 6000 h. This indicates a diminishing load redistribution capability within this phase as the exposure time increased, which is consistent with observations under RC conditions. The segmental moduli during stage 3 (E_3) showed slightly higher values than the bare textile, with a subtle increasing trend as exposure time increased, indicating continued mechanical improvements despite the prolonged immersion.

Failure modes showed significant variability across exposure times. For specimens aged 3000 h, the highest frequency of mode “b” failures was observed, with 3 out of 7 specimens failing in this mode. For specimens aged 1000 and 5000 h, mode “b” failures occurred in 2 out of 7 and 1 out of 7 specimens, respectively. This shift in failure behavior can be attributed to the interplay between mortar strength, hydration, and the textile tensile capacity, which change over time under RW conditions. The crack patterns further reflect these trends. The number of cracks consistently decreased with increased exposure time, dropping from 4.33 at 0 h to 1.28 at 6000 h. This reduction is likely due to the progressive tensile strength development of the mortar, which reduces the textile crack-bridging capacity as the critical fiber volume content increases. Crack spacing, as illustrated in Figure 120, exhibited some fluctuations without a clear trend, and the distance of the closest crack to the specimen extremities remained similarly inconsistent. These variations highlight the complex interplay between mortar strength and textile capacity governing the mechanical behavior of TRM composites under water immersion conditions.

8.3.3.3 TRM tensile behavior (acidic immersion)

The three stages of loading were clearly observed for all TRM coupons immersed in acidic solutions, regardless of exposure time or acidic concentration as can be found by the Figure 119. This indicates that the first matrix crack was distinguishable, and the system maintained its composite behavior throughout the test. The tensile strength values of f_t for all acidic concentrations exhibited a minimum at 3000 h, followed by an increase at 6000 h. For specimens immersed in pH 1.5 and pH 2.0 solutions, the tensile strength followed a similar trend as of bare textile test results. However, specimens immersed

in pH 3.0 showed a further reduction in ultimate strength after 3000 h, reaching the lowest value at 6000 h. Notably, this weakest performance at pH 3.0 and 6000 h was not reflected in the bare textile strength or the mortar mechanical properties, suggesting complex interactions between the mortar and textile under these conditions. The strain corresponding to the tensile strength ($\varepsilon(f_t)$) increased with prolonged exposure to all acidic environments, indicating enhanced ductility of the mortar over time. This behavior parallels that observed for specimens immersed in water (RW). Overall, despite strength gains observed in bare textile tests, immersion of TRM tensile coupons in acidic media reduced their tensile strength, with the most significant reduction occurring in samples exposed to pH 3.0 for 6000 h. This reduction highlights the detrimental effects of acidic environments on the composite performance, likely due to fiber-matrix interaction degradation and chemical leaching.

The stress and strain values at the end of stage 1, related primarily to mortar performance, exhibited varying trends across acidic environments. For pH 2.0 and pH 3.0, these values decreased with increased exposure time, whereas for pH 1.5, a peak was observed at 3000 h followed by a reduction at 6000 h. This behavior aligns with the flexural strength results of the mortar, which also showed a peak at 3000 h. The lowest stress value at the end of stage 1 was observed for specimens immersed in pH 3.0 at 6000 h. Strain values at this stage increased consistently for all acidic solutions with prolonged exposure, likely due to hydration effects and calcium hydroxide leaching into the acidic medium, which reduced the ductility of the mortar. The elastic modulus of stage 1 followed a decreasing trend across all acidic environments with increased exposure time, reflecting a weakening of the mortar stiffness.

A significant elongation of the second stage was observed for all acidic environments. The extent of this stage was most pronounced for specimens immersed in pH 1.5 at 6000 h, indicating substantial changes in the mechanical behavior of the mortar that prolonged the crack development phase. The segmental moduli of stage 3, which primarily reflects the elastic modulus of the textile, initially increased at 1000 h for all solutions. Over time, specimens immersed in pH 1.5 showed an overall reduction in E_3, whereas those in pH 2.0 and pH 3.0 exhibited a minimum at 3000 h, followed by an increase at 6000 h. These variations reflect the evolving interactions between the mortar and textile under prolonged acidic exposure. In terms of failure modes, prolonged exposure to acidic environments led to a reduction of mode “b” failures across all solutions, with mode “a” becoming predominant. For specimens immersed in pH 1.5, mode “b” failures were completely eliminated by 6000 h, with all specimens failing in mode “a.” This shift suggests that the mortar strength gain over time reduced the likelihood of textile slippage near the clamping area, improving the system composite behavior.

Crack behavior further illustrated the effects of acidic immersion. The number of cracks decreased significantly compared to reference samples, stabilizing after 1000 h for specimens immersed in pH 2.0 and pH 3.0. In contrast, specimens immersed in pH 1.5 showed an overall increase in crack spacing over time. Additionally, for specimens in pH 1.5, the distance of the nearest crack to the extremities consistently decreased with prolonged exposure, reflecting changes in crack propagation and distribution influenced by the mortar mechanical properties.

8.3.3.4 Discussion on the tensile behavior

The performance of TRM coupons immersed in different environmental conditions, RC, RW, and acidic solutions (pH 1.5, pH 2.0, and pH 3.0), is a result of the combined effects of mortar and textile properties, as well as the interactions between these two components. By analyzing mortar characterization tests, textile tensile tests, and TRM tensile coupon tests, the mechanical behavior under each condition can be better understood. The mortar exhibited distinct behavior under different environmental conditions, which significantly influenced the performance of TRM coupons. Under RC conditions, the mortar showed consistent strength development over time due to hydration and carbonation, resulting in higher compressive and flexural strength. This strength gain enhanced the bond between the mortar and textile,

improving the overall load transfer and crack-bridging capability of the composite. In RW conditions, the mortar compressive and flexural strength exhibited a peak around 3000 h, followed by a slight reduction at longer exposure times. This behavior can be attributed to water leaching processes, which initially promote hydration and strength gain but eventually cause minor weakening due to calcium hydroxide dissolution. The reduced ductility observed in the mortar under RW conditions is reflected in the cracking patterns and mechanical response of the TRM coupons. For acidic environments, the mortar performance was highly dependent on the acid concentration. Specimens immersed in pH 1.5 and pH 2.0 exhibited a similar strength trend, with a peak at 3000 h followed by a reduction at 6000 h, aligning with previous observations of chemical leaching and gypsum formation. However, for pH 3.0, the mortar mechanical properties were less affected, indicating that the milder acidic medium resulted in less aggressive chemical interactions. The ductility of the mortar increased consistently across all acidic conditions, likely due to prolonged exposure to moisture, which promotes hydration despite the chemical attack.

The tensile strength and stiffness of the textile showed distinct variations across the tested environments. Under RC conditions, the textile exhibited stable behavior with minimal changes over time. In RW conditions, a slight reduction in textile tensile strength and elastic modulus was observed, indicating minor degradation due to prolonged immersion. In acidic environments, the textile exhibited significant variations depending on the pH level. Specimens exposed to pH 1.5 experienced more pronounced degradation in tensile strength and stiffness, while those immersed in pH 2.0 and pH 3.0 showed relatively better performance, with pH 3.0 exhibiting the least reduction. These results align with the known effects of acidic environments on glass fibers, where higher acidity accelerates degradation through chemical etching [11,166].

The tensile behavior of TRM coupons reflects the combined effects of mortar and textile performance, as well as their interactions. In RC conditions, TRM coupons showed the highest tensile strength and better crack-bridging capability, as evidenced by higher numbers of cracks and lower crack spacing. This can be attributed to the mortar consistent strength development and the textile stable behavior, which maintained effective load transfer and crack distribution. In RW conditions, TRM coupons exhibited lower tensile strength compared to RC samples, even after accounting for the slight reduction in textile capacity. While water immersion initially enhanced the mortar properties due to ongoing hydration, prolonged exposure eventually led to strength reduction as a result of leaching effects. The strain corresponding to f_t peaked at 3000 h, reflecting the hydration-driven strength gain in the mortar during this period, but decreased at longer exposure times due to mortar leaching effects.

In acidic environments, the behavior of TRM coupons varied significantly with pH level. Specimens immersed in pH 1.5 showed a pronounced reduction in ultimate strength and segmental moduli of stage 2 E_2 over time, particularly at 6000 h. This indicates a diminished load redistribution capability due to the aggressive chemical attack on both the mortar and textile. Specimens in pH 2.0 exhibited a peak in strength at 3000 h, followed by a reduction at 6000 h, while those in pH 3.0 showed the lowest ultimate strength, with consistent reductions across all exposure times. The number of cracks decreased consistently across all acidic conditions, reflecting the mortar reduced crack-bridging capacity as its tensile strength approached that of the textile. However, crack spacing showed varying trends, with pH 1.5 exhibiting increased spacing over time. The tensile behavior of TRM coupons immersed in acidic environments is governed by the intensity of the acid and the duration of exposure. Higher acidity leads to significant degradation in both the mortar and textile, resulting in reduced strength, fewer cracks, and larger crack spacing. Moderate acidity allows for temporary strength gains due to hydration effects but ultimately results in degradation at prolonged exposure times. Mild acidity exhibits less aggressive behavior, but the cumulative effects of acidic exposure still reduce the composite tensile capacity. Overall, the combined effects of mortar hydration, chemical leaching, textile degradation, and fiber-matrix

interaction determine the tensile performance of TRM coupons under different environmental conditions. Acidic intensity and exposure time play critical roles in dictating the degree of degradation, with higher acidity and prolonged exposure amplifying the adverse effects. The results underscore the importance of considering both matrix and textile durability in the design and application of TRM composites for long-term performance in harsh environments.

8.3.4 TRM pull-out behavior

The pull-out behavior of individual glass textile yarns embedded in the lime-based matrix of the TRM system was investigated to assess the evolution of bond performance under different aging environments, as established in Durability Campaign II. This testing configuration is fundamental to isolate the response of the fiber–matrix interface from global composite behavior, thus allowing for a mechanistic interpretation of degradation processes occurring at the micro-scale. The load-slip responses recorded at the loaded end (Figure 121) reveal a variety of failure modes and bond characteristics, ranging from sharp interface debonding to progressive frictional sliding. These differences reflect the cumulative influence of environmental exposure on chemical, physical, and mechanical attributes of the interface.

To quantify this response and support comparative evaluation, three main parameters were extracted: the peak load, the debonding energy, and the pull-out energy. The peak load corresponds to the maximum force attained during the pull-out process and is commonly used as an indicator of the ultimate bond capacity. However, peak load alone may not fully capture the mechanical resilience or toughness of the interface, particularly under progressive degradation. For this reason, debonding energy, defined as the area under the load–slip curve up to the point of maximum load, was calculated to represent the energy required to initiate and propagate the debonding process. In contrast, pull-out energy, computed as the total area under the entire load–slip curve, represents the cumulative energy dissipated during full yarn extraction, including both adhesive and frictional contributions. These energy-based metrics provide a more comprehensive measure of interface performance, particularly under aging where peak load may remain relatively stable while ductility and energy absorption decline.

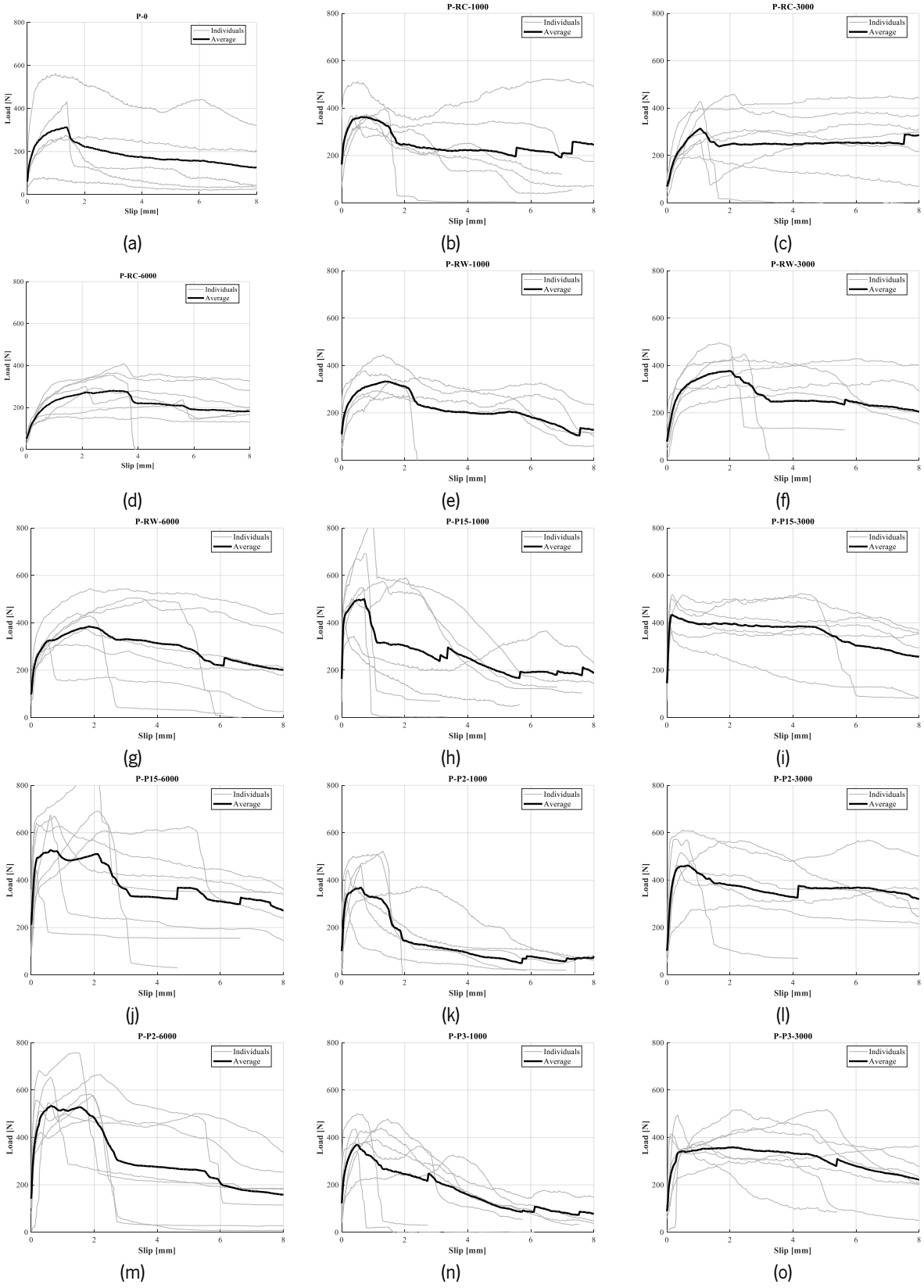
P-0
P-RC-1000
P-RC-3000
P-RC-6000
P-RW-1000
P-RW-3000
P-RW-6000
P-P15-1000
P-P15-3000
P-P15-6000
P-P2-1000
P-P2-3000
P-P2-6000
P-P3-1000
P-P3-3000
Individuals
Average
Load [N]
Slip [mm]
(a)
(b)
(c)
(d)
(e)
(f)
(g)
(h)
(i)
(j)
(k)
(l)
(m)
(n)
(o)

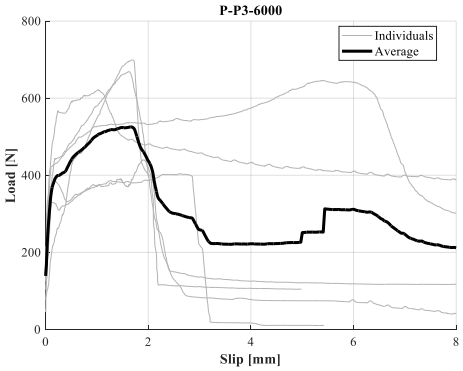

(p)

Figure 121 Load-slip curves of individuals and group average for: (a) P_0; (b) P_RC_1000; (c) P_RC_3000; (d) T_RC_6000; (e) P_RW_1000; (f) P_RW_3000; (g) P_RW_6000; (h) P_P15_1000; (i) P_P15_3000; (j) P_P15_6000; (k) P_P2_1000; (l) P_P2_3000; (m) P_P2_6000; (n) P_P3_1000; (o) P_P3_3000; (p) P_P3_6000.

8.3.4.1 TRM pull-out behavior (RC condition)

The specimens subjected to dry climatic chamber conditioning (P_RC) exhibited highly stable pull-out behavior throughout the aging duration. As seen in Figure 122b, the peak load remained nearly unchanged between 1000 and 3000 hours, with a slight reduction by 6000 hours. This minor decrease may be attributed to normal aging effects such as microcracking or interfacial friction loss due to drying shrinkage. However, the overall peak load values remained within a narrow range (~600–650 N), indicating sustained interfacial bond integrity in the absence of aggressive chemical or moisture-driven degradation. In terms of energy parameters, the debonding energy (Figure 122c) showed a slight increase at 3000 hours, followed by a decrease at 6000 hours. This trend suggests a possible transient improvement in bond adhesion due to continued internal hydration or microstructural densification during mid-term exposure, before eventual minor degradation effects began to appear. The pull-out energy (Figure 122d) also followed a similar pattern, peaking slightly at 3000 hours and reducing thereafter. These modest fluctuations, however, do not indicate significant damage or deterioration mechanisms and are consistent with the expected behavior of a reference condition. Thus, P_RC specimens confirmed the mechanical stability of the TRM bond in controlled indoor conditions and served as a reliable baseline for comparison against more aggressive environments.

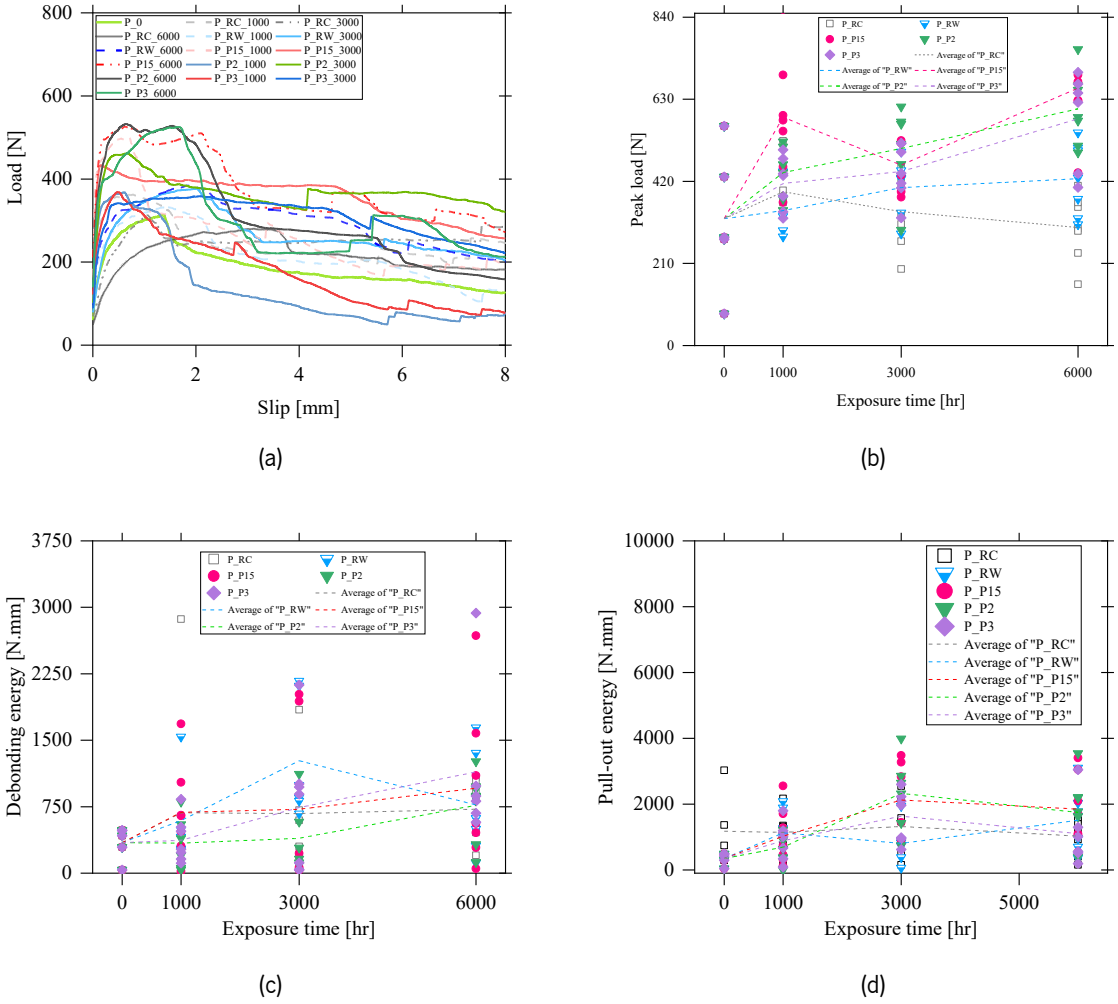

Figure 122 Pull-out parameters of single TRM glass yarn in different environments vs. exposure time: (a) average load-slip response at the load end; (b) peak load; (c) debonding energy; (d) pull-out energy.

8.3.4.2 TRM pull-out behavior (RW condition)

Under water immersion (P_RW), the TRM specimens demonstrated more pronounced trends in degradation over time. The peak load (Figure 122b) increased slightly from the unaged condition to 1000 hours, followed by a gradual and sustained increase up to 6000 hours, reaching values close to 700–750 N. This trend may appear counterintuitive but could be associated with temporary pore refinement or densification near the fiber–matrix interface due to extended hydration, particularly in lime-based matrices where slow pozzolanic reactions continue over time in the presence of moisture. Additionally, the progressive saturation may increase the contact area between the mortar and the fibers, contributing to enhanced frictional resistance. However, the energy metrics reveal a more nuanced picture. The debonding energy (Figure 122c) increased significantly at 3000 hours, nearly doubling compared to earlier durations, and then decreased slightly at 6000 hours. This behavior indicates a phase of increased energy absorption capacity at the interface, possibly due to delayed matrix hydration, followed by the onset of matrix softening, leaching, or interfacial microcracking. The pull-out energy (Figure 122d) displayed a parallel trend, with a peak at 3000 hours and a slight reduction at 6000 hours, although still maintaining higher values than the early exposures. These results suggest that while water immersion initially promotes interface densification and frictional engagement, the long-term effects begin to reduce bond ductility and energy dissipation, which could eventually lead to more brittle behavior in service conditions.

8.3.4.3 TRM pull-out behavior (acidic immersion)

The pull-out performance under acidic immersion showed the most distinct and variable behavior, highly dependent on pH level and exposure duration. For the most aggressive condition, pH = 1.5, the peak load (Figure 122b) was initially stable up to 1000 hours but then showed a sharp decline at 3000 and 6000 hours, dropping below 500 N. This significant reduction points to severe chemical degradation of the matrix and interface, driven by acid-induced leaching and decalcification, which compromise the bond strength and reduce the ability of the interface to sustain load. In parallel, the debonding energy (Figure 122c) also decreased notably with time, from approximately 2000 N·mm at 1000 hours to below 1000 N·mm at 6000 hours, indicating early bond failure with limited energy absorption. Interestingly, the pull-out energy (Figure 122d) for P15 showed a slight increase at 3000 hours before dropping significantly at 6000 hours. This might reflect a phase of increased interfacial friction during progressive deterioration where the loss of adhesion is partially compensated by increased roughness or fiber abrasion, before complete interface failure sets in. This behavior reveals that under severe acid attack, the durability of the fiber–matrix bond is severely compromised over time, with both strength and toughness affected.

The behavior of the P2 condition was more complex. The peak load (Figure 122b) increased significantly at 3000 hours and remained stable or even slightly higher at 6000 hours. Similarly, both the debonding and pull-out energy (Figure 122c and Figure 122d) peaked at 3000 hours, showing the highest values across all conditions and exposure times. This counterintuitive improvement might be explained by the formation of acid-induced byproducts, such as gypsum or ettringite, which could densify the interface temporarily. However, the long-term behavior still trends downward, suggesting this is an intermediate phase before full degradation dominates. For the P3 condition, the trends were more moderate. Peak load remained nearly stable across the entire exposure period, ranging between 600 and 650 N (Figure 122b). The debonding energy showed a consistent increase up to 6000 hours, indicating gradual improvements in bond ductility or interface densification, possibly due to limited acid penetration or carbonation reactions. Pull-out energy followed a similar trend, suggesting that mild acidity may not immediately impair the bond, and under some circumstances may even enhance short-term mechanical performance.

8.3.4.4 Discussion on the pull-out behavior

The comparative evaluation of pull-out performance under various environmental exposures reveals key insights into the durability mechanisms of TRM interfaces. The dry reference condition confirmed that in the absence of chemical or physical attack, the fiber–matrix bond remains stable, with minor variations attributed to internal hydration and drying effects. Water immersion demonstrated a time-dependent improvement in both strength and energy metrics at intermediate durations, likely due to matrix maturation. However, a reduction at 6000 hours suggests the onset of softening or microstructural breakdown due to sustained saturation or pore structure evolution. Acidic environments introduced the most critical and variable degradation patterns. Under acidic solution with the pH of 1.5, both bond strength and energy absorption capacity declined significantly over time, clearly indicating aggressive leaching, interfacial damage, and failure in adhesion mechanisms. For pH of 2.0, a transient phase of enhanced performance was detected, possibly due to acid reaction products or matrix re-compaction effects, but this trend did not persist. In contrast, the mild acidic condition (pH = 3.0) induced minimal damage and even slight performance enhancement, suggesting that a threshold pH exists below which damage progression is substantially slowed or reversible.

A key outcome of this study is the importance of energy-based metrics, debonding and pull-out energy, in assessing bond degradation. These parameters capture the cumulative energy dissipated throughout interface mobilization and failure, providing a more sensitive and integrative measure of interfacial

performance than peak load alone. Especially under progressive degradation scenarios, such as acid attack, peak load may remain deceptively stable for some time, whereas energy parameters reveal underlying ductility loss and interfacial weakening. Therefore, the use of these indicators is essential for the development of accurate durability models and the reliable prediction of TRM performance in service conditions. The trends identified here form the basis for calibrating the cohesive bond-slip model presented in subsequent sections.

8.3.5 TRM single-lap behavior

The single-lap shear test is a critical configuration for evaluating the bond between the TRM system and the masonry substrate, offering a representative assessment of the interface behavior under direct shear transfer. Compared to the pull-out test, this configuration accounts for the composite action of mortar–fiber interaction and its synergy with substrate adhesion. This section presents the experimental results of the TRM single-lap tests conducted under Durability Campaign II, including dry condition, water immersion, and acidic (P15, P2, P3) environments, evaluated at multiple exposure durations. Stress–slip curves (Figure 123) are used to describe the load-transfer capacity and deformation behavior of the interface. Average curves are complemented by quantitative indicators shown in Figure 124: the peak bond stress (Figure 124b), which represents the maximum shear stress attained before failure; the debonding energy (Figure 124c), defined as the area under the curve up to the peak stress, representing the energy required to initiate failure; and the slip corresponding to peak load (Figure 124d), which reflects the ductility of the interface and the extent of pre-peak deformation.

Throughout the tests, different failure modes were recorded, including progressive fiber–matrix debonding, cohesive failure within the mortar, and adhesion loss at the mortar–substrate interface. Notably, a complete detachment of the mortar layer from the masonry substrate was observed in the P15 group at 6000 hours, resulting in zero measurable load resistance and the absence of a valid stress–slip curve for that condition. This type of failure marks the critical limit of TRM bond durability under severe acidic exposure and is addressed in detail in the corresponding subsection.

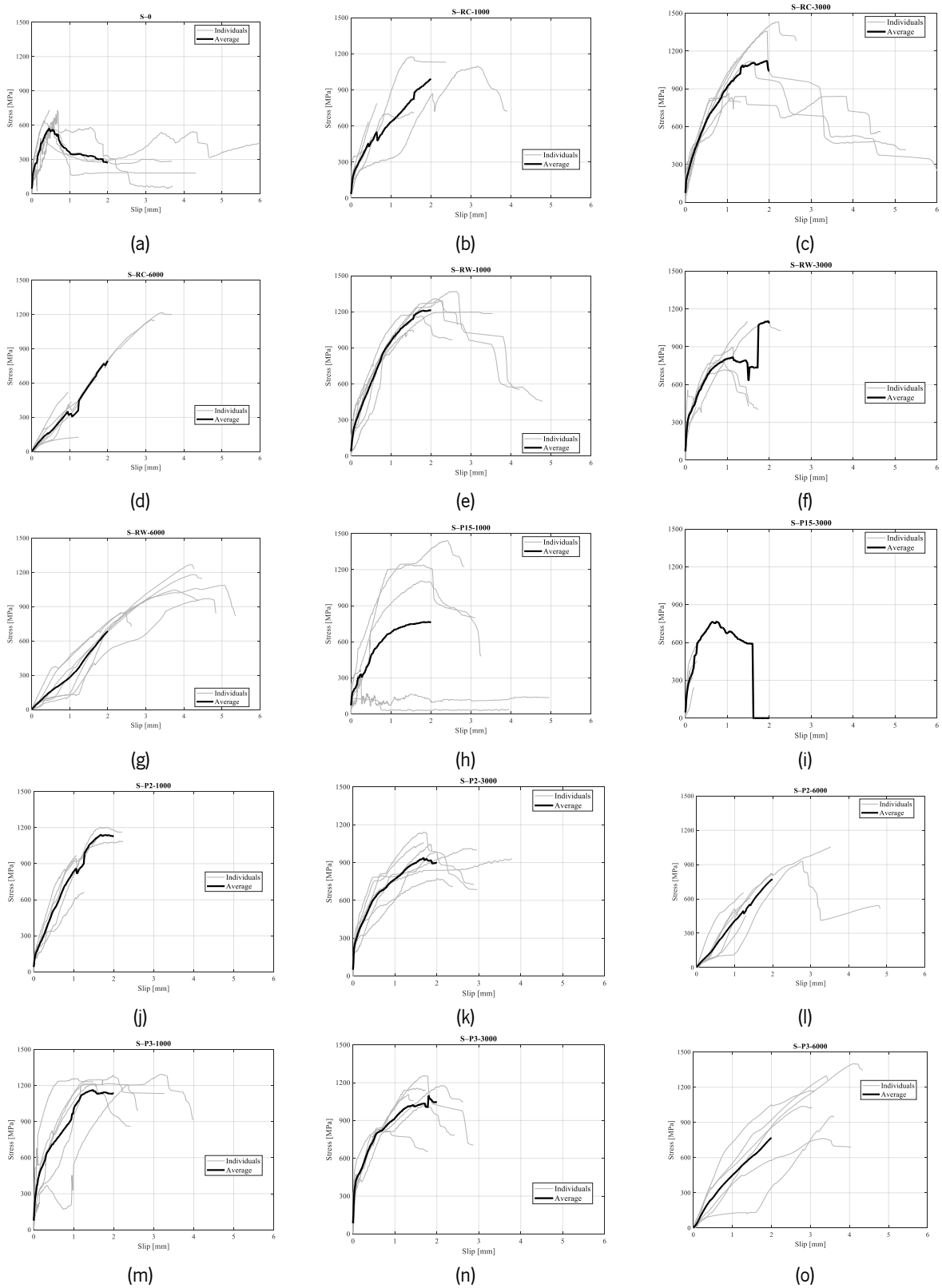

Figure 123 Stress-slip curves of individuals and group average for: (a) S_0; (b) S_RC_1000; (c) S_RC_3000; (d) S_RC_6000; (e) S_RW_1000; (f) S_RW_3000; (g) S_RW_6000; (h) S_P15_1000; (i) S_P15_3000; (j) S_P2_1000; (k) S_P2_3000; (l) S_P2_6000; (m) S_P3_1000; (n) S_P3_3000; (o) S_P3_6000.

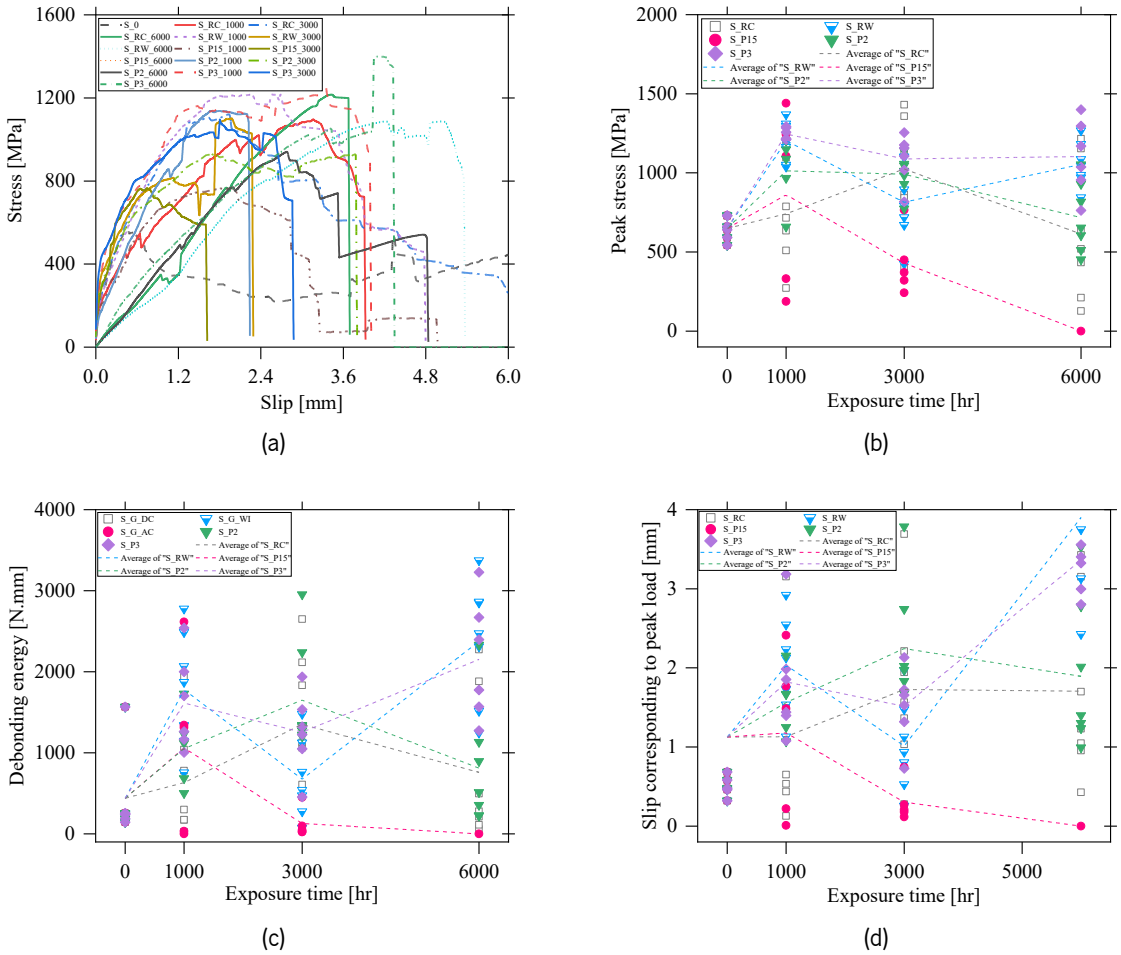

Figure 124 Single-lap behavior of glass-TRM in different exposure durations and mediums: (a) average stress-slip curve; (b) peak stress; (c) debonding energy; (d) slip corresponding to peak load.

8.3.5.1 TRM single-lap behavior (RC condition)

The single-lap behavior of specimens aged in the dry environment demonstrated highly stable performance across all exposure durations, providing a baseline for interpreting the impact of environmental aging. As shown in Figure 124b, the peak bond stress remained relatively constant across 1000, 3000, and 6000 hours, with values consistently exceeding 1200 MPa. This stability reflects the preservation of the fiber–matrix interface and the mortar–substrate adhesion under ambient indoor conditions, where neither moisture ingress nor chemical degradation mechanisms are active. The debonding energy values (Figure 124c) followed a similar trend. A modest increase was observed at 3000 hours, potentially attributable to ongoing internal curing or shrinkage-induced compaction near the interface. However, the changes remained within a limited range, indicating no adverse effect on bond toughness. The slip corresponding to peak load (Figure 124d) also showed limited variation, with values clustering between 2.0 and 2.5 mm, suggesting consistent pre-peak ductility across all durations. The failure modes observed in this group were predominantly characterized by progressive debonding along the fiber–matrix interface, with partial engagement of the mortar surface. No full interfacial delamination or brittle failure was detected. These results confirm that in the absence of external chemical agents, the TRM bond system maintains its structural integrity and deformation capacity even over extended time periods.

8.3.5.2 TRM single-lap behavior (RW condition)

The specimens exposed to water immersion (P_RW) presented more dynamic behavior, reflecting the time-dependent interaction between hydration-driven strengthening and moisture-induced degradation. According to Figure 124b, the peak stress increased from the unaged condition to 1000 hours, reaching values above 1400 MPa, the highest among all groups at that duration. This increase likely corresponds to continued pozzolanic reactions and the refinement of the matrix microstructure due to prolonged hydration, which is characteristic of lime-based mortars in moist environments. However, beyond 1000 hours, a decline in peak stress was observed. By 6000 hours, the peak stress had dropped to approximately 1000 MPa. This reduction indicates the emergence of long-term degradation mechanisms such as pore saturation, internal microcracking, and the leaching of calcium-rich phases, which weaken the matrix and interfacial zones.

Debonding energy (Figure 124c) followed a non-linear trend. It increased markedly at 3000 hours, surpassing 3000 N·mm, then decreased at 6000 hours. The initial rise suggests enhanced energy absorption during intermediate exposure, potentially due to frictional engagement at the fiber–matrix interface and increased matrix cohesion. However, the later decline points to cumulative damage impairing the system's ability to resist shear. The slip at peak load (Figure 124d) increased consistently across exposure durations, reaching values above 4.0 mm at 6000 hours. This observation implies that while peak strength was compromised, the interface transitioned to a more ductile failure mode over time. The failure mechanisms were characterized by extensive interfacial slip, and in some cases, partial mortar softening was evident near the substrate. These findings highlight the dual nature of water immersion: an initial phase of improved bond due to curing, followed by progressive degradation that reduces both strength and toughness in the long term.

8.3.5.3 TRM single-lap behavior (acidic immersion)

Acidic immersion resulted in the most severe impact on the TRM single-lap behavior, with the degradation patterns strongly influenced by pH level and exposure duration. Among all groups, pH of 1.5 exhibited the most dramatic deterioration. As illustrated in Figure 124b, the peak stress decreased significantly over time, dropping from approximately 800 MPa at 1000 hours to below 200 MPa at 6000 hours. The corresponding debonding energy (Figure 124c) also diminished sharply, approaching zero at the longest exposure. Most notably, a full detachment of the mortar layer from the masonry substrate occurred in this group after 6000 hours, precluding the recording of a stress–slip response. This catastrophic failure mode reveals a complete breakdown of adhesion at the interface, driven by acid-induced dissolution, decalcification, and loss of microstructural integrity. The slip at peak load for P15 specimens (Figure 124d) decreased with increasing exposure, reflecting a transition toward brittle failure. The loss of ductility further confirms the compromised performance of the bond zone under severe acid attack.

In contrast, the P2 group displayed a more complex evolution. Peak stress increased significantly at 3000 hours, reaching above 1500 MPa, followed by a reduction at 6000 hours. This intermediate enhancement may be attributed to the formation of secondary mineral phases such as gypsum or ettringite, which can transiently densify the interface. However, these phases may later disrupt the matrix due to volumetric instability, leading to long-term degradation. Debonding energy and slip values followed a similar pattern: peaking at 3000 hours before declining. These trends suggest that even under moderate acidity, degradation is time-dependent and may involve transient reinforcement followed by structural weakening.

For P3, the bond behavior remained comparatively stable. Peak stress values fluctuated within a narrow range (~1100–1300 MPa) across exposure durations. Debonding energy and slip values also remained high and consistent, indicating sustained interfacial strength and ductility. Failure modes in this group involved cohesive failure within the mortar layer and progressive slip, without signs of

delamination or abrupt failure. These results confirm that mildly acidic environments pose limited short-term threat to bond performance but may still warrant monitoring for long-term applications.

8.3.5.4 Discussion on the single-lap behavior

The TRM single-lap shear results underscore the central role of environmental severity in governing bond durability at the mortar–substrate interface. Under dry climatic conditions, both bond strength and energy dissipation were preserved over the entire exposure duration, confirming the mechanical robustness of the TRM system in non-aggressive settings. Water immersion initially enhanced interface performance through continued hydration, but long-term exposure led to strength reduction and interface softening due to chemical leaching and saturation. The acidic groups revealed a spectrum of degradation responses. The extreme pH 1.5 condition resulted in the most critical failure mode, complete mortar detachment from the substrate, marking the structural limit of durability. The pH 2.0 group exhibited a transient improvement in bond behavior, likely linked to chemical densification, followed by significant deterioration at extended durations. The pH 3.0 condition maintained mechanical integrity, showing that TRM systems may remain functional within mildly acidic environments up to 6000 hours of exposure.

The combination of peak stress, energy dissipation, and slip values provided a comprehensive understanding of interface strength, toughness, and ductility. Notably, energy-based parameters were more sensitive to early-stage degradation and ductility loss than peak stress alone, particularly in the P2 and P15 groups. These metrics capture the effects of interfacial friction, cohesion, and the progressive breakdown of the composite, substrate bond zone. Overall, these findings emphasize the importance of distinguishing between reversible (e.g., hydration-related) and irreversible (e.g., acidic dissolution) degradation mechanisms when assessing long-term TRM durability. The results presented here form a foundational dataset for the calibration of bond-slip laws and interface models that incorporate environmental deterioration, which will be further developed in subsequent sections.

8.4 Analytical modeling of the bond interface in single-lap shear test

The transfer of stress from textile reinforcement to the surrounding mortar in TRM systems is governed by the shear interaction along their interface. Accurate modeling of this interaction is critical to predicting the structural performance and long-term durability of TRM strengthening solutions. Among the different mechanical tests designed to investigate this bond mechanism, the single-lap shear test offers a well-controlled configuration in which the slip and stress development along the bonded length can be systematically studied. The resulting data enable the derivation of a local bond–slip relationship, typically expressed in terms of shear stress τ as a function of local slip s, which is referred to as the τ–s law.

The τ–s law serves as the foundational constitutive input to any analytical or numerical model aiming to simulate the mechanical behavior of TRM composites [18]. It captures the mechanisms of adhesion, friction, mechanical interlock, and progressive damage along the interface. When aging phenomena are involved, such as immersion in aggressive environments or long-term exposure to moisture or temperature, the τ–s law reflects the deterioration of bond quality. Therefore, establishing a model that integrates the τ–s relation into a mechanical framework is essential for both interpreting experimental results and projecting the performance of TRM systems under design or service conditions.

To this end, a one-dimensional mechanical model of the bonded interface is developed, starting from force equilibrium at the fiber and mortar levels. The geometry and notation of the system are schematically illustrated in Figure 125, where the fiber is embedded in the mortar matrix. The segment shown has length dx, and the fiber and matrix interact through a distributed interfacial shear stress τ_{zx}, which acts along a perimeter $p = 2b_f$ (Figure 125). The axial stress in the fiber varies as $\sigma(x)$, while

that in the matrix is $\sigma_m(x)$. The differential displacement between the two materials leads to the local slip $s(x)$, and the force equilibrium can be formulated based on these variables.

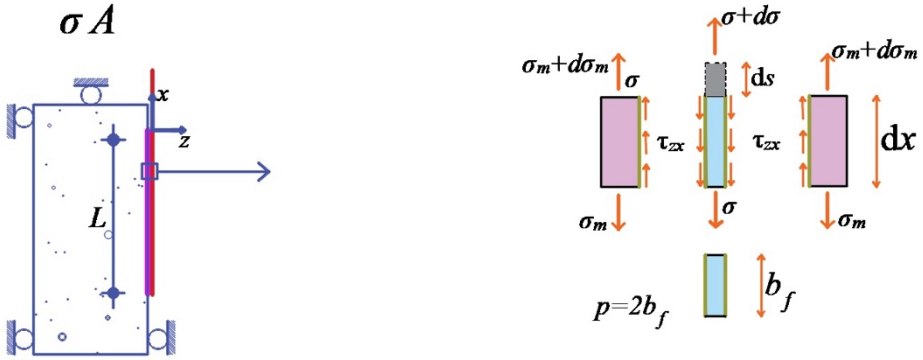

(a) (b)

Figure 125 (a) Single-lap shear setup with bonded length L; (b) differential free-body diagram illustrating internal forces and shear stress transfer through the interface.

The axial equilibrium of the fiber over an infinitesimal segment dx requires that the reduction in axial force be balanced by the interfacial shear stress as expressed in Eq. (*1*).

$$\frac{d\sigma_f(x)}{dx} \cdot A_f = -\tau(x) \cdot p \tag{1}$$

Where $\sigma_f(x)$ is the axial stress in the fiber at position x, A_f is the cross-sectional area of the fiber, $\tau(x)$ is the local shear stress, and p is the fiber perimeter in contact with the mortar, here defined as $p = 2b_f$.Assuming that the fiber behaves as a linearly elastic material, the stress–strain relation is expressed in Eq. (2).

$$\sigma_f(x) = E_f \cdot \varepsilon_f(x) = E_f \cdot \frac{du_f(x)}{dx} \tag{2}$$

where $u_f(x)$ is the axial displacement of the fiber at position x. The slip between the fiber and the matrix is defined as:

$$s(x) = u_f(x) - u_m(x) \tag{3}$$

with $u_m(x)$ being the displacement of the matrix. If the matrix is assumed to be rigid (or its deformation is negligible compared to the fiber), the slip becomes approximately equal to the fiber displacement according to the Eq. (4).

$$s(x) \approx u_f(x) \Rightarrow \frac{ds(x)}{dx} = \frac{du_f(x)}{dx} \Rightarrow \frac{d^2s(x)}{dx^2} = \frac{d^2u_f(x)}{dx^2} \tag{4}$$

Substituting Eqs. (2) and (4) into Eq. (*1*) yields the governing equation for slip:

$$E_f \cdot \frac{d^2s(x)}{dx^2} = -\frac{p}{A_f} \cdot \tau(s) \Rightarrow \frac{d^2s(x)}{dx^2} - \frac{p}{E_f A_f} \cdot \tau(s) = 0 \tag{5}$$

Eq. (5) represents the fundamental differential equation for slip evolution in TRM systems under single-lap shear loading. It is a second-order nonlinear ordinary differential equation, in which the nonlinearity arises from the dependency of the interfacial shear stress on the slip through the τ–s law. While the deformation of the matrix can be included through a similar equilibrium equation, expressed in Eq. (6).

$$\frac{d\sigma_m(x)}{dx} \cdot A_m = +\tau(x) \cdot p \tag{6}$$

In most TRM systems the matrix stiffness is sufficiently high or its deformation is absorbed in the calibration of τ(s), allowing it to be excluded from the governing formulation. The result is a single-field model based entirely on the behavior of the reinforcement and its interface with the surrounding mortar. To solve Equation (5), boundary conditions are applied depending on the specific test configuration. Typically, in single-lap tests, one end of the textile is loaded (prescribed displacement or force), and the other end is either free or embedded sufficiently to be considered fixed. The function τ(s) is defined using a cohesive law that reflects the experimental behavior of the interface under various exposure conditions. This constitutive law is presented in detail in the following section 8.4.1.

8.4.1 Definition of the rigid trilinear interfacial law τ(s)

To complete the solution of the governing Equation (4), which describes the evolution of interfacial slip along the bonded length in the single-lap shear configuration, it is necessary to define an explicit relation between the interfacial shear stress τ and the local slip s. The function $\tau(s)$ embodies the mechanical behavior of the interface and directly controls the transfer of axial force from the textile reinforcement to the mortar. In the present work, a rigid trilinear cohesive material law is adopted to model the $\tau(s)$ relationship. This form of cohesive law has been widely employed in TRM systems due to its ability to capture the sequential stages of interfacial response: initial elastic behavior, strain-softening due to interfacial damage, and residual frictional sliding. The choice of a trilinear law also facilitates analytical formulation, preserves continuity, and allows for direct calibration using key experimental parameters. The τ–s law is defined piecewise over three regimes, according to the Eq. (7) and can be seen by the Figure 126.

$$\tau(s) = \begin{cases} \tau_0 + k_e s & for\ 0 < s \leq s_{\tau max} \quad (elastic) \\ \tau_{max} + k_s(s_{\tau max} - s) & for\ s_{\tau max} < s \leq s_f \quad (softening) \\ \tau_f & for\ s > s_f \quad (debonding) \end{cases} \tag{7}$$

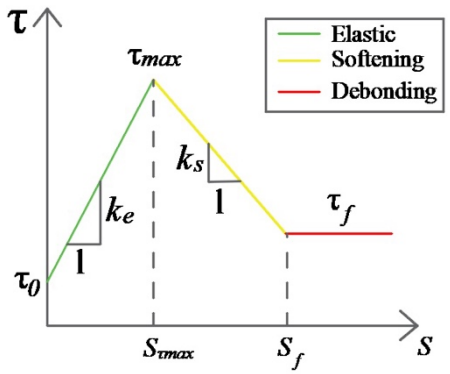

Figure 126 Trilinear cohesive law with distinct elastic, softening, and residual frictional branches.

The parameters introduced in Eq. (7) are defined as, k_e which is the initial shear stiffness $\left[\mathrm{N/mm^2}\right]$, governing the linear response prior to damage initiation; τ_{max} is the peak shear stress at the interface, marking the transition from elastic to inelastic behavior; $s_{\tau_{max}}$ is the slip corresponding to τ_{max}; k_s is the softening modulus (with $k_s > 0$), describing the degradation of shear strength with increasing slip; s_f is the slip value at the end of softening, beyond which the interface sustains only residual stress; τ_f is the residual shear stress representing post-debonding frictional resistance. The elastic and softening slopes are explicitly defined by Eq. (8).

$$k_e = \frac{\tau_{max}}{s_{\tau_{max}}}, \qquad k_s = \frac{\tau_{max} - \tau_f}{s_f - s_{\tau_{max}}} \tag{8}$$

Equation (7), when inserted into the governing equation (*5*), the key equation of (9) will be emerged.

$$\frac{d^2 s(x)}{dx^2} - \frac{p}{E_f A_f} \cdot \tau(s) = 0 \tag{9}$$

results in a nonlinear, piecewise-defined ordinary differential equation. In each of the three regions defined in the τ–s law, the ODE becomes a second-order linear equation with constant coefficients, allowing separate analytical treatment in each interval of slip, provided continuity conditions are enforced at the interfaces $s = s_{\tau_{max}}$ and $s = s_f$. The selection of a rigid trilinear law is particularly suited for this study for the following reasons. Primarily, the three regimes represent distinct physical mechanisms in TRM systems, uncracked elastic bond, progressive mortar degradation, and residual sliding after detachment. Secondly, the formulation is compatible with both experimental observations and closed-form analytical solutions over finite bonded lengths.

8.4.2 Identification of the τ–s law and CML calibration

The rigid trilinear cohesive material law introduced earlier describes the interfacial shear stress $\tau(s)$ as a function of local slip, distinguishing among elastic, softening, and debonding frictional regimes. This law is inserted into the governing differential equation for the bonded interface, as defined in Eq. (9), which characterizes the evolution of slip along the bond length. However, to utilize this formulation in the prediction of single-lap shear test responses, the parameters governing the τ–s relationship must first be identified based on experimental results. These parameters include τ_0, τ_{max}, $s_{\tau_{max}}$, s_f, and τ_f.

The experimental single-lap stress–slip curves provide the necessary data for the calibration of the τ–s law. In this identification approach, two key data points are extracted from each experimental response. The first corresponds to the end of the linear branch, which marks the transition from elastic to softening behavior. Although the shear stress τ_{max} at this point is not directly known, the corresponding slip value, denoted as $s_{\tau_{max}}$, is identified with the global slip g_1 measured at the loaded end, recorded via LVDT instrumentation. The second point is the peak of the stress–slip curve, where both the axial stress σ_2 and the associated global slip g_2 are directly available from the experiment. Therefore, while τ_{max} and τ_0 remain unknown, the governing analytical solutions at these two stages can be expressed as functions of the known global slip and axial stress at the loaded end. The values of s_f and τ_f, which define the onset and magnitude of the residual frictional phase, are obtained directly from the final portion of the experimental curves. In particular, s_f is selected at the inflection point where the descending branch stabilizes, and τ_f is computed as the average shear stress over the plateau associated with post-debonding sliding as it reaches the residue value. Environmental conditions, especially those involving acidic immersion, may significantly influence these parameters by reducing bond strength and

accelerating degradation, whereas water immersion may induce only marginal changes due to continued hydration.

To compute the two unknowns τ_0 and τ_{max}, a system of two equations is established by solving the governing equation of the bonded interface in its closed form. This is achieved through the application of the rigid trilinear cohesive material law in each of the corresponding regimes, where the analytical solution of Eq. (9) becomes tractable under the assumption of piecewise-linear interfacial behavior. In Stage I, the elastic region is defined by a linear bond–slip law expressed as $\tau(s) = k_e s$, where k_e is the initial shear stiffness. Substituting this into the governing equation leads to a homogeneous second-order linear differential equation with constant coefficients as brought in the equation (10).

$$\frac{d^2 s(x)}{dx^2} - \lambda_1^2 s(x) = 0 \tag{10}$$

where the characteristic parameter λ_1 is defined as of Eq. (11).

$$\lambda_1 = \sqrt{\frac{p k_e}{EA}} \tag{11}$$

The general solution of Eq. (10) takes the form of a hyperbolic function, and by applying the boundary conditions associated with the onset of the bonded interface, i.e., null slip and null axial stress at x = -a, the solution for the slip distribution becomes:

$$s_e(x \in I) = \frac{\tau_0}{k_e}\left[\cosh\left(\lambda_1 (x + a)\right) - 1\right] \tag{12}$$

Correspondingly, the axial stress and shear stress distributions in the elastic regime are given by:

$$\sigma_e(x \in I) = \frac{\tau_0 p}{A\lambda_1}\sinh\left(\lambda_1 (x + a)\right) \tag{13}$$

$$\tau_e(x \in I) = \tau_0 \cosh\left(\lambda_1 (x + a)\right) \tag{14}$$

These expressions define the complete solution of the mechanical field in the uncracked region of the bonded interface. In the subsequent stage, where interfacial damage has been initiated, the softening branch governs the stress–slip relationship. In this region, the τ–s law is characterized by a linearly degrading function, $\tau(s) = \tau_{max} - k_s\left(s - s_{\tau_{max}}\right)$, and when inserted into Eq. (9), the differential equation becomes non-homogeneous. The general solution is formulated as:

$$\frac{d^2 s(x)}{dx^2} - \lambda_2^2 s(x) = -\lambda_2^2\left(\frac{\tau_{max}}{k_s} - s_{\tau_{max}}\right) \tag{15}$$

where the softening parameter λ_2 is defined as:

$$\lambda_2 = \sqrt{\frac{p k_s}{EA}} \tag{16}$$

The closed-form solution of Eq. (15) includes both the homogeneous and particular parts and is derived subject to the continuity of axial stress and slip at the interface transition point x = -d. These continuity conditions are expressed as:

$$s_s(x=-d) = s_{\tau_{max}}, \quad \sigma_s(x=-d) = \sigma_e(x=-d) \tag{17}$$

The resulting expressions for slip, axial stress, and interfacial shear stress in the softening region are given by:

$$s_s(x \in II_L) = \frac{\tau_0 \lambda_2}{k_s \lambda_1} \sinh(\lambda_1 a_c) \sin[\lambda_2 (x+d)] - \frac{\tau_{max}}{k_s} \cos[\lambda_2 (x+d)] + \frac{\tau_{max}}{k_s} \tag{18}$$

$$\sigma_s(x \in II_L) = \frac{\tau_0 p}{A\lambda_1} \sinh(\lambda_1 a_c) \cos[\lambda_2 (x+d)] + \frac{\tau_{max} p}{A\lambda_2} \sin[\lambda_2 (x+d)] \tag{19}$$

$$\tau_s(x \in II_L) = -\frac{\tau_0 \lambda_2}{\lambda_1} \sinh(\lambda_1 a_c) \sin[\lambda_2 (x+d)] + \tau_{max} \cos[\lambda_2 (x+d)] \tag{20}$$

These expressions govern the distribution of local fields in the damaged regime and allow for the reconstruction of the interfacial behavior over the entire bonded length. The pair of experimental observations, namely the global slip at the end of Stage I (denoted as g_1) and the global slip at the peak load g_2, are substituted respectively into Eq. (13) and Eq. (19)at the loaded end x = 0, together with the corresponding axial stress values σ_1 and σ_2. This results in a nonlinear system of two equations in two unknowns, τ_0 and τ_{max}. The system is solved numerically using MATLAB through a nonlinear root-finding routine, which ensures that the closed-form analytical solution matches the experimental boundary data. Following the identification of $\tau_0$and τ_{max}, the complete τ–s law is defined for each exposure scenario. The value of τ_f, which governs the final residual plateau, is taken as the average shear stress observed in the stabilized tail of the experimental stress–slip response, where the slip reaches the terminal value s_f. In this friction-dominated regime, the governing equation reduces to a constant solution:

$$\tau(x) = \tau_f \quad \text{for all } x \in [0, L] \text{ in Stage III} \tag{21}$$

The final calibrated τ–s law is then used to reconstruct the complete response, enabling both the reproduction of experimental trends and the prediction of bond degradation behavior across varying environmental conditions.

8.4.3 Interfacial phases and model calibration

The bond behavior of TRM systems subjected to monotonic pull loading evolves through successive stages governed by interfacial mechanical interactions. The cohesive zone model adopted herein, as formulated in the framework of Bertolli and D'Antino [18], provides a piecewise analytical solution describing this evolution based on local slip s(x), interfacial shear stress $\tau(x)$, and axial stress $\sigma(x)$. One of the pivotal elements in this formulation is the concept of the effective bond length, denoted l_{eff}, which represents the minimum interface length required to fully mobilize bond stress before saturation. This parameter is defined by the sum of the elastic and softening front positions at critical loading:

$$l_{eff} = a_c + d_c^{II} \tag{22}$$

Here, a_c represents the extent of the elastic region prior to the onset of softening, and d_c^{II} denotes the softening region terminating at the point where frictional sliding initiates. The closed-form expressions for these two quantities are explicitly given as:

$$a_c = \frac{1}{\lambda_1} \operatorname{arcosh}\left(\frac{\tau_{max}}{\tau_0}\right) \tag{23}$$

$$d_c^{II} = \frac{2}{\lambda_2}\arctan\left(\frac{j+\sqrt{j^2-\tau_f^2+\tau_{max}^2}}{\tau_{max}+\tau_f}\right), \quad j = -\tau_0\frac{\lambda_2}{\lambda_1}\sinh(\lambda_1 a_c) \tag{24}$$

These expressions arise from the enforcement of equilibrium and compatibility conditions across the bonded interface and enable the effective bond length to be predicted based on material parameters and the τ–s cohesive law. Two configurations can be distinguished based on the relative magnitude of the actual bonded length L and the calculated l_{eff}. In cases where $L > l_{eff}$, only a portion of the interface is activated during loading, leading to bond saturation within a confined region. Conversely, for $L < l_{eff}$, the entire bonded length is engaged, and all mechanical regimes (elastic, softening, and frictional) are activated progressively. The current study investigates specimens exclusively falling under the $L < l_{eff}$ regime, which is the most informative for tracking full interfacial evolution. This progressive evolution is classified into four phases, denoted α, β, γ, and δ, based on the spatial extent of the internal degradation fronts a and d. Phase α corresponds to a fully elastic interface, phase β marks the onset of softening at the loaded end, phase γ describes a fully softening interface, and phase δ includes residual frictional sliding initiated at the loaded boundary and propagating toward the free end.

To demonstrate the implementation of this framework, specimen S-RC-1000-1 according to the Table 14 is selected for detailed evaluation. This specimen had a bonded length $L = 100$ mm and using the calibrated parameters $\tau_0 = 0.023$ MPa, $\tau_{max} = 2.599$ MPa, and $\tau_f = 0.223$ MPa, the computed effective bond length using Eqs. (11), (18), and (19) was $l_{eff} = 307.82$ mm. Thus, $L < l_{eff}$ was satisfied, placing the specimen within the complete interfacial degradation regime of Type A configuration. The calibrated cohesive material law (CML) for this specimen is graphically represented in Figure 127, where the elastic, softening, and frictional phases are clearly demarcated according to the rigid trilinear τ–s formulation.

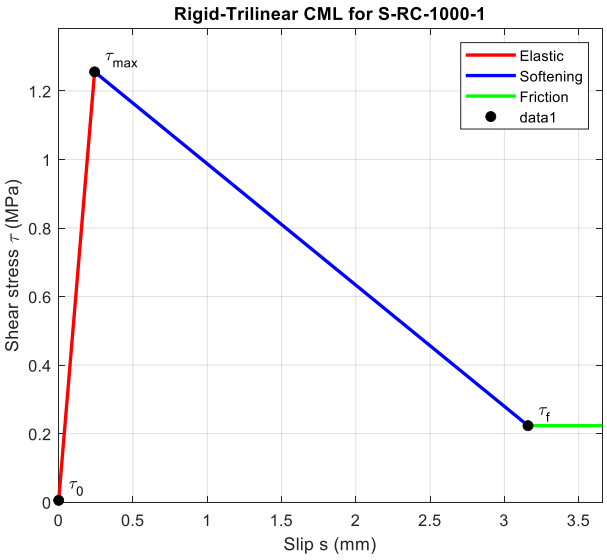

Figure 127 Calibrated rigid trilinear τ–s law for specimen S-RC-1000-1, showing elastic, softening, and frictional branches.

Within the $L < l_{eff}$ regime, four physically distinct response configurations, denoted as α, β, γ, and δ, can be identified depending on the relative magnitude and interaction of the elastic front a and the softening front d. These configurations describe the evolution of stress states along the bonded interface as damage progresses from elastic bonding to complete frictional sliding. The transitions among these configurations depend on the cumulative slip imposed at the loaded end and are governed by the position

of internal fronts, which in turn depend on the τ–s parameters and geometric properties of the specimen. In configuration α, the entire bonded interface remains elastic (a + d < L, with d = 0), and the shear stress follows the ascending linear branch of the τ–s law. This phase reflects the uncracked regime, with stress increasing uniformly from the free end toward the loaded end. Configuration β corresponds to the initiation of softening at the loaded boundary, while a portion of the interface remains elastic (0 < d < L, a + d < L). In this phase, shear stress progressively decays from τ_{max} at the loaded end through the softening branch, with continuity enforced at the elastic–softening transition. Configuration γ represents the exhaustion of the elastic zone (a = 0) with the entire interface governed by softening behavior, but still without frictional sliding. Finally, configuration δ corresponds to the simultaneous presence of softening and frictional regimes (d > 0, a = 0, residual stress τ_f reached at the loaded boundary), describing the fully degraded phase where the interface initiates post-peak sliding at constant friction.

The full bond degradation process for δ-type configurations, as exemplified by specimen S-RC-1000-1, unfolds across six sequential loading stages, each associated with a distinct combination of cohesive law regimes distributed along the bonded interface. The analytical derivation of shear stress $\tau(x)$, slip s(x), and axial stress $\sigma(x)$ fields throughout these stages was conducted in accordance with the formulation strategy developed by Bertolli and D'Antino [18]. Although only key expressions are reported here, the evolution of local fields and internal fronts is captured and illustrated at the end of each stage. The representative stress, slip, and shear distributions obtained for this case are displayed in Figure 128 through Figure 133.

8.4.3.1 Stage I of loading

In the initial stage, the bonded interface remains fully elastic and undamaged. The interfacial shear stress $\tau(x)$ progressively increases from the free end toward the loaded boundary, without exceeding the critical value τ_{max}. The local fields $\sigma(x)$ and s(x) follow analytical expressions provided by Eqs. (12) – (14), which are derived from the governing ODE under elastic conditions. The evolution in this phase is governed exclusively by the ascending elastic branch of the cohesive material law. The termination condition for this stage depends on the relative progression of the stress front and the τ–s profile classification. Specifically, for specimens exhibiting γ- or δ-type behavior, such as S-RC-1000-1, Stage I ends when the shear stress at the free end reaches the initial interfacial value τ_0, i.e., $\tau(-L) = \tau_0$, indicating full development of the elastic response throughout the interface. The internal front at this stage spans the entire bonded length $a = L$, while no softening or frictional sliding has been activated. The distributions of interfacial fields at the end of Stage I are presented in Figure 128.

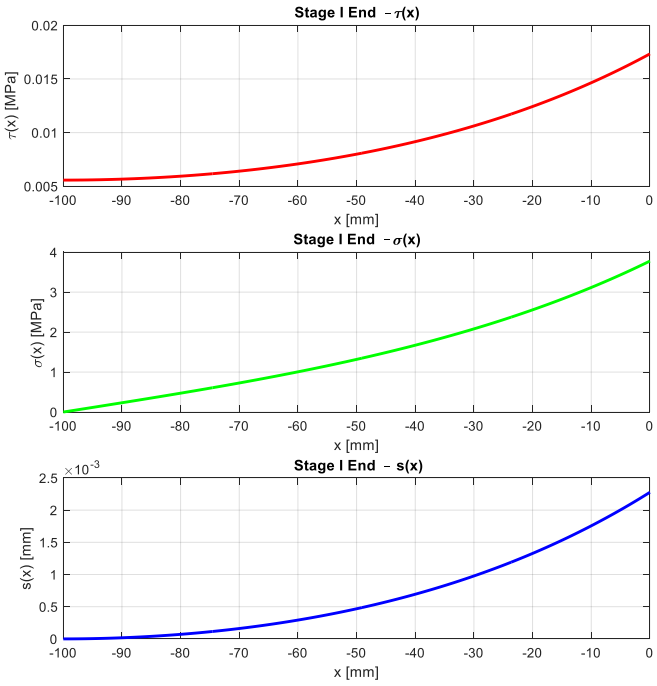

Figure 128 Distributions of $\tau(x)$, $\sigma(x)$, and s(x) at the end of Stage I.

8.4.3.2 Stage II of loading

In the second phase of interfacial evolution for δ-type joints—where the bonded length L is smaller than the characteristic elastic transfer length a_c, the response continues to be governed entirely by the elastic portion of the cohesive law. However, unlike Stage I where the shear stress distribution remains bounded below the threshold value τ_{max}, Stage II is defined by the attainment of τ_{max} at the loaded boundary, x = 0. The bonded interface remains fully elastic, with no regions of softening or frictional sliding, yet the applied axial stress at the loaded end imposes a different set of mechanical boundary conditions that require an updated analytical treatment. To describe the local response in this phase, the governing differential equation for slip evolution continues to be expressed as a second-order linear equation with constant coefficients:

$$\frac{d^2 s(x)}{dx^2} - \frac{p}{EA} \cdot \tau(x) = 0 \tag{25}$$

Since the cohesive law remains in its elastic branch, the interfacial shear stress $\tau(x)$ is linearly proportional to the local slip s(x) through the initial stiffness k_e, i.e., $\tau(x) = k_e \cdot s(x)$. Substituting this relation into the governing equation yields a homogeneous linear ordinary differential equation with hyperbolic solutions. Unlike Stage I, which assumes zero axial force at the loaded boundary, Stage II introduces a non-zero axial stress $\tilde{\sigma}$ at x = 0, while still satisfying the free-end condition $\sigma(-L) = 0$. These boundary constraints lead to the following closed-form solutions for slip, axial stress, and interfacial shear stress:

$$s(x) = \frac{\tilde{\sigma}}{E\lambda_1} \cdot \frac{1}{\sinh(\lambda_1 L)} \cosh[\lambda_1 (x + L)] - \frac{\tau_0}{k_e} \tag{26}$$

$$\sigma(x) = \tilde{\sigma} \cdot \frac{\sinh[\lambda_1(x+L)]}{\sinh(\lambda_1 L)} \tag{27}$$

$$\tau(x) = \frac{\tilde{\sigma} \cdot k_e}{E\lambda_1} \cdot \frac{1}{\sinh(\lambda_1 L)} \cosh[\lambda_1(x+L)] \tag{28}$$

In the expressions above, $\lambda_1 = \sqrt{\frac{pk_e}{EA}}$ represents the characteristic length scale associated with the elastic bond-slip interaction. The term $\tilde{\sigma}$ is determined from experimental data as the axial stress at the loaded end when the global response curve reaches the end of its elastic ascending branch. This value coincides with the point at which the shear stress at x = 0 reaches its peak value τ_{max}, thus defining the termination condition of Stage II. Throughout this stage, the full bonded length continues to contribute to stress transfer via elastic mechanisms, and no damage has yet occurred in the interface. The cohesive front remains at a = L, and neither softening (d = 0) nor frictional sliding (f = 0) regions have formed. Nevertheless, the mechanical fields have now fully developed under the elastic τ–s relationship, such that further loading will necessarily lead to local degradation and a transition to Stage III. The distributions of interfacial shear stress $\tau(x)$, axial stress $\sigma(x)$, and slip s(x) at the end of this stage, computed from the closed-form solutions in Eqs. (26) – (28), are illustrated in Figure 129. These distributions demonstrate a progressive increase in all field quantities toward the loaded end, with the peak shear stress coinciding with τ_{max}at x = 0, signaling the imminent onset of softening.

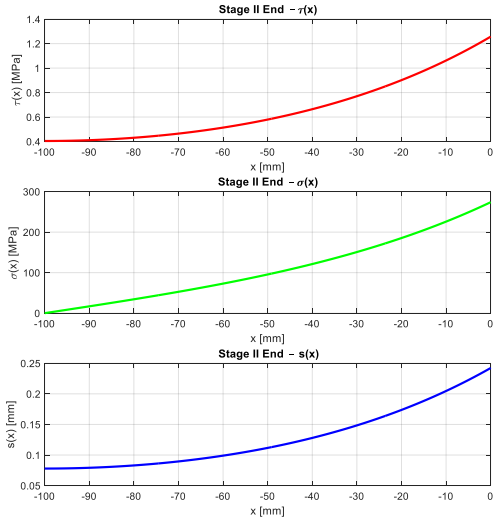

Figure 129 Distributions of $\tau(x)$, $\sigma(x)$, and s(x) at the end of Stage II.

8.4.3.3 Stage III of loading

During Stage III of the interfacial evolution, the elastic region is no longer sustained, and the entire bonded interface transitions into a combination of elastic and softening zones. This phase occurs once the stress at the loaded boundary reaches values beyond the peak τ–s threshold τ_{max}, and cohesive degradation initiates at the boundary. In this regime, two distinct zones coexist: an elastic domain near the free end and a progressively expanding softening region near the loaded end. The front $d_c^{IV(A)}$ marks the extent of the softening regime, and the two subdomains are coupled through continuity of stress and

displacement fields. The response in the elastic zone, defined over the interval $x \in \left[-L,\ -d_c^{\text{IV(A)}} - f\right]$, is described by the following closed-form expressions:

$$s_e\left(x \in \text{IV}_\text{L}(\text{A})\right) = \frac{\tau_{max}}{k_e} \cdot \frac{1}{\cosh(\lambda_1 a)} \cosh[\lambda_1 (x + L)] - \frac{\tau_0}{k_e} \tag{29}$$

$$\sigma_e\left(x \in \text{IV}_\text{L}(\text{A})\right) = \frac{p\tau_{max}}{A\lambda_1} \cdot \frac{1}{\cosh(\lambda_1 a)} \sinh[\lambda_1 (x + L)] \tag{30}$$

$$\tau_e\left(x \in \text{IV}_\text{L}(\text{A})\right) = \tau_{max} \cdot \frac{1}{\cosh(\lambda_1 a)} \cosh[\lambda_1 (x + L)] \tag{31}$$

These solutions capture the exponential decay of slip, axial stress, and shear stress toward the free end. The cohesive zone behavior within the softening region is governed by Eqs. (32) – (34), which are applied over $x \in \left[-d_c^{\text{IV(A)}} - f,\ 0\right]$, subject to the interface conditions defined in Eq. (31). These include the continuity of s(x) and $\sigma(x)$ at the transition point $x = -d_c^{\text{IV(A)}} - f$:

$$s_s\left(x \in \text{IV}_\text{L}(\text{A})\right) = \frac{\tau_{max}}{k_s}\left\{\frac{\lambda_2}{\lambda_1}\tanh(\lambda_1 a) \sin\left[\lambda_2\left(x + d^{\text{IV(A)}} c + f\right)\right] - \cos\left[\lambda_2\left(x + d^{\text{IV(A)}} c + f\right)\right] + 1\right\} + s\tau max \tag{32}$$

$$\sigma_s\left(x \in \text{IV}_\text{L}(\text{A})\right) = \frac{\tau_{max} p}{A\lambda_1}\tanh(\lambda_1 a) \cos\left[\lambda_2\left(x + d^{\text{IV(A)}} c + f\right)\right] + \frac{\tau max p}{A\lambda_2} \sin\left[\lambda_2\left(x + d_c^{\text{IV(A)}} + f\right)\right] \tag{33}$$

$$\tau_s\left(x \in \text{IV}_\text{L}(\text{A})\right) = -\tau_{max} \cdot \frac{\lambda_2}{\lambda_1}\tanh(\lambda_1 a) \sin\left[\lambda_2\left(x + d^{\text{IV(A)}} c + f\right)\right] + \tau max \cos\left[\lambda_2\left(x + d_c^{\text{IV(A)}} + f\right)\right] \tag{34}$$

The parameter f corresponds to the length of the frictional segment, which remains zero in Stage III. The transition from elastic to softening response proceeds without yet activating frictional resistance, as the minimum interfacial shear stress remains above τ_f. As illustrated in Figure 130, the field distributions s(x), $\sigma(x)$, and $\tau(x)$ reflect a coordinated decay in stress from the loaded end while cohesive mechanisms dominate energy dissipation throughout the bonded interface.

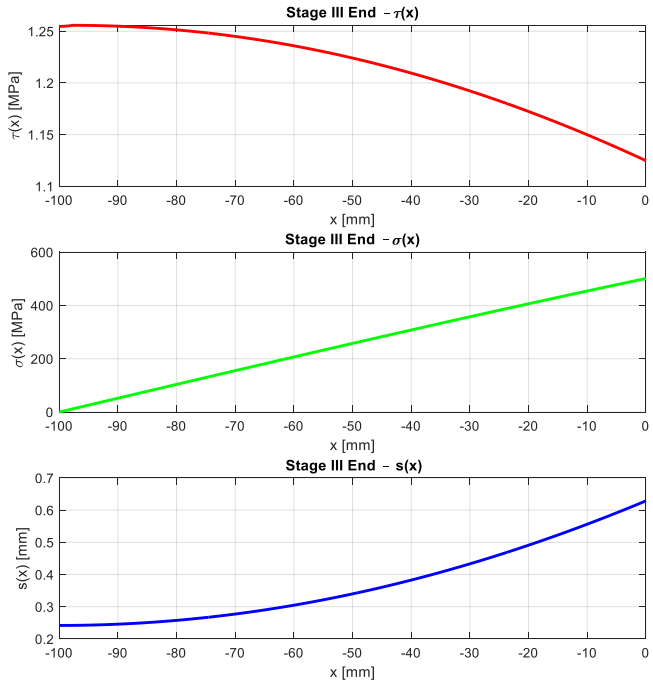

Figure 130 Distributions of $\tau(x)$, $\sigma(x)$, and s(x) at the end of Stage III.

8.4.3.4 Stage IV of loading

In Stage IV, the bonded interface undergoes a significant transition from cohesive softening to partial frictional engagement. This stage is triggered when the interfacial shear stress at the loaded boundary, x = 0, reaches the residual frictional stress value, τ_f, while the remainder of the bonded length remains in the softening regime. This condition marks the onset of sliding governed by friction at the loaded end, which progressively replaces the stress transfer previously carried by the softening mechanism. The interfacial domain is now partitioned into two distinct regions: a fully softening segment and a residual-frictional zone adjacent to the loaded boundary. To describe the stress, slip, and shear profiles in this stage, the boundary conditions are defined as follows:

$$\begin{cases} \sigma_s(x \in \text{IV}s^{\beta\delta}(A))|\{x = -L\} = 0 \\ \sigma_s\left(x \in \text{IV}s^{\beta\delta}(A)\right) x = 0 = \tilde{\sigma} \end{cases} \tag{35}$$

With these constraints applied to the governing equilibrium equation, the resulting analytical expressions for the slip s(x), axial stress $\sigma(x)$, and shear stress $\tau(x)$ across the bonded length are given by:

$$s_s\left(x \in \text{IV}s^{\beta\delta}(A)\right) = -\frac{\tilde{\sigma}}{E\lambda_2} \cdot \frac{1}{\sin(\lambda_2 L)} \cos[\lambda_2(x+L)] + \frac{\tau\text{max}}{k_s} + s_{\tau_{\text{max}}} \tag{36}$$

$$\sigma_s\left(x \in \text{IV}_s^{\beta\delta}(A)\right) = \frac{\tilde{\sigma}}{\sin(\lambda_2 L)} \sin[\lambda_2(x+L)] \tag{37}$$

$$\tau_s\left(x \in \text{IV}_s^{\beta\delta}(A)\right) = \frac{\tilde{\sigma}\, k_s}{E\lambda_2} \cdot \frac{1}{\sin(\lambda_2 L)} \cos[\lambda_2(x+L)] \tag{38}$$

These expressions describe the progressive transition from softening to frictional load transfer. The axial stress continues to increase linearly due to continued loading, but the rate of increase diminishes

as more of the interface is governed by the residual stress state. The shear stress profile decreases from an intermediate level to τ_f at the loaded boundary. This stage concludes when the entire bonded region reaches the critical residual shear threshold $\tau_s(x = 0) = \tau_f$, signaling the full mobilization of frictional resistance across the entire bonded interface. The distributions of $\tau(x)$, $\sigma(x)$, and s(x) at the end of Stage IV are shown in Figure 131, where the partial frictional behavior at the loaded end can be clearly observed. This stage represents the final phase before complete degradation and uniform frictional sliding.

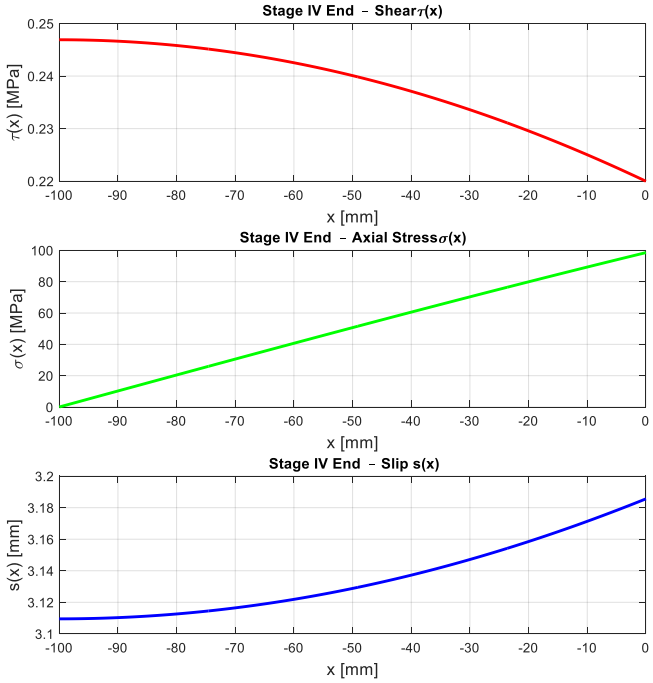

Figure 131 Distributions of $\tau(x)$, $\sigma(x)$, and s(x) at the end of Stage IV.

8.4.3.5 Stage V of loading

As interfacial degradation evolves, Stage V corresponds to the transitional regime in which the frictional front, initially nucleated near the loaded end, propagates progressively toward the free end. The interface is now characterized by a combination of two distinct regimes: a fully debonded zone governed by residual frictional resistance and a cohesive-softening region undergoing bond deterioration. This configuration is a hallmark of Type A joints, where the bonded length is shorter than the effective transfer length l_{eff}, and the transition from cohesive to frictional behavior is fully realized during the loading path. The frictional regime is modeled by enforcing constant shear stress τ_f along a growing segment of the interface, which satisfies the expressions:

$$s_s\big(x \in V(A)\big) = -\frac{\tilde{\sigma}}{E\lambda_2}\cos[\lambda_2(x+L)] + \frac{\tau_{\max}}{k_s} + s_{\tau_{\max}} \tag{39}$$

$$\sigma_s\big(x \in V(A)\big) = \frac{\tau_f p}{A\lambda_2}\sin[\lambda_2(x+L)] \tag{40}$$

$$\tau_s\big(x \in V(A)\big) = \frac{\tau_f}{\cos(\lambda_2 d)}\cos[\lambda_2(x+L)] \tag{41}$$

where the coordinate $x \in [-L, -f]$ spans the softening–frictional interface, and $\tilde{\sigma}$ is the axial stress at the loaded boundary. These fields satisfy the boundary conditions at the transition point x = -f. For the fully debonded region extending beyond x = -f, a separate set of expressions governs the slip, axial stress, and shear stress:

$$s_d\big(x \in V(A)\big) = \frac{\tau_f p}{2EA}(x+f)^2 + \frac{\tau_f p}{\lambda_2 EA}\tan(\lambda_2 d)\,(x+f) + s_f \tag{42}$$

$$\sigma_d\big(x \in V(A)\big) = \frac{\tau_f p}{A}(x+f) + \frac{\tau_f p}{A\lambda_2}\tan(\lambda_2 d) \tag{43}$$

$$\tau_d\big(x \in V(A)\big) = \tau_f \tag{44}$$

These equations, defined for $x \in [-f, 0]$, describe the mechanical behavior of the interface where only residual frictional stress contributes to load transfer. The internal variable $d^{V(A)}c$, which denotes the critical length of the residual phase, can be evaluated by enforcing the initiation condition of Stage V at x = -L, where $\tau_s(-L) = \tau\text{max}$ is satisfied. The complete interface during Stage V thus consists of a frictional region of length $d_c^{V(A)}$ adjacent to the loaded edge, followed by a gradually vanishing cohesive-softening zone, and ultimately a fully debonded segment characterized by residual sliding. This configuration leads to simplified but evolving stress and slip profiles, with the slip field increasing monotonically and the axial stress field reaching higher levels toward the end of loading. The distributions of $\tau(x)$, $\sigma(x)$, and s(x) at the end of this phase are illustrated in Figure 132.

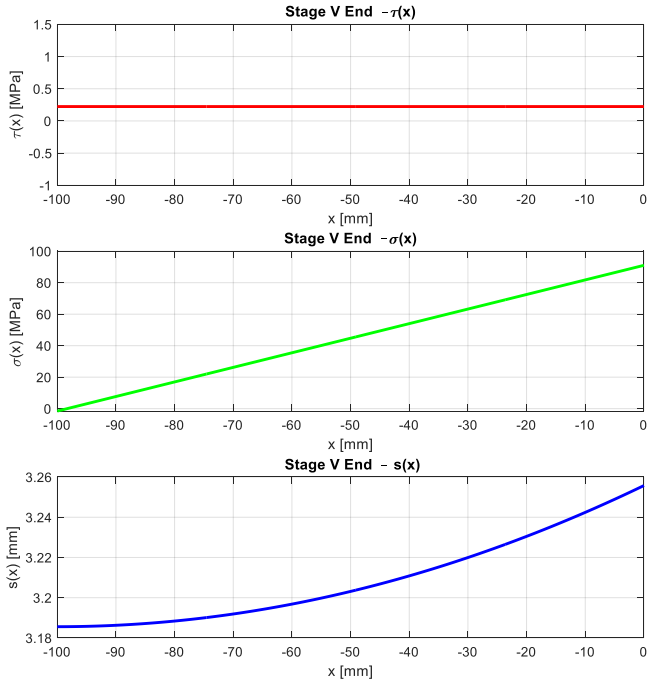

Figure 132 Distributions of $\tau(x)$, $\sigma(x)$, and s(x) at the end of Stage V.

8.4.3.6 Stage VI of loading

The final stage of bond-slip evolution, referred to as Stage VI, is characterized by the complete exhaustion of cohesive mechanisms along the bonded interface. At this point, the entire interface operates under frictional sliding conditions, meaning that the interfacial shear stress uniformly assumes the residual value τ_f along the full bonded length. This condition corresponds to the complete mobilization of the

post-debonding frictional resistance. The mechanical response in this stage is governed exclusively by the frictional branch of the trilinear cohesive law. Since the shear stress is constant, no additional resistance is offered beyond this plateau, and the slip field evolves in a quadratic form under steady-state sliding. The axial stress increases linearly with respect to the coordinate x, while the shear stress remains uniform and independent of the imposed slip level. This behavior indicates that although slip accumulation continues, no additional load-bearing contribution from the interface is provided.

The governing expressions for slip $s_d(x)$, axial stress $\sigma_d(x)$, and interfacial shear stress $\tau_d(x)$ are given by the following equations:

$$s_d\big(x \in \text{VI}(A)\big) = \frac{\tau_f p}{2EA}(x+L)^2 + s_f \tag{45}$$

$$\sigma_d\big(x \in \text{VI}(A)\big) = \frac{\tau_f p}{A}(x+L) \tag{46}$$

$$\tau_d\big(x \in \text{VI}(A)\big) = \tau_f \backslash tag53 \tag{47}$$

These relations are valid within the interval $x \in [-L, 0]$, under the assumption of a bonded length L and a constant residual friction stress τ_f. The boundary conditions applied for this stage are:

$$s_d(x=-L) = s_f, \quad \sigma_d(x=-L) = 0 \tag{48}$$

Figure 133 displays the distributions of shear stress \tau(x), axial stress \sigma(x), and slip s(x) at the end of Stage VI, highlighting the fully degraded interface where frictional behavior solely dictates the transfer mechanism.

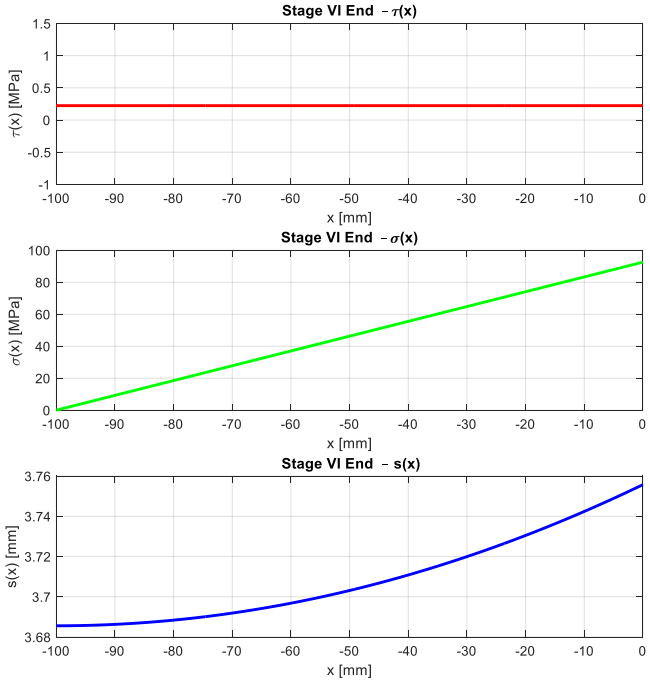

Figure 133 Distributions of $\tau(x)$, $\sigma(x)$, and s(x) at the end of Stage VI.

8.4.3.7 Global Stress–Slip Response and Stage Transitions

The cumulative response of the TRM system subjected to single-lap shear loading is effectively illustrated through the global stress–slip curve, which characterizes the applied axial stress $\sigma_{applied}$ as a function of

the global slip $s(0)$ measured at the loaded end. This macroscopic representation encapsulates the successive transitions between the six distinct loading stages defined earlier, thereby providing a synthetic overview of the interface evolution under increasing load and displacement demand. Figure 134 presents the full $\sigma_{applied} - s(0)$ profile for specimen S-RC-1000-1, with each phase distinctly color-coded to reflect its contribution within the cumulative response. The initial ascending branch, highlighted in blue and green, corresponds to Stages I and II, where the interface exhibits purely elastic and partially softening behavior. In Stage I, the entire bonded length is governed by the elastic stiffness k_e, leading to a nearly linear increase in applied stress with respect to slip. Upon reaching the maximum shear stress τ_{max} at the loaded boundary, the system enters Stage II, wherein a portion of the interface transitions to softening, while the remainder remains elastic. The gradual reduction of the elastic region is accompanied by a continued, though increasingly nonlinear, rise in stress. Stage II concludes when the entire bonded interface has entered the softening domain.

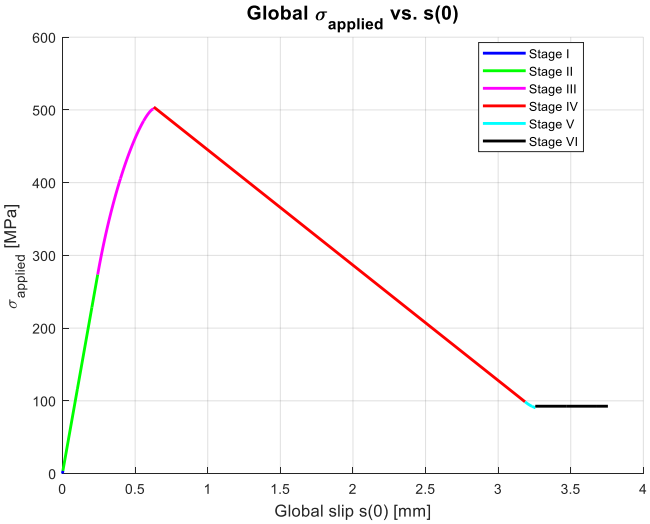

Figure 134 Global stress–slip curve for specimen GP79-1, showing transitions across all six loading stages with color-coded segments.

The peak of the global response, corresponding to the magenta-colored region (Stage III), marks the point at which the interface is fully governed by softening behavior. At this stage, the elastic front vanishes (a = 0), and the cohesive stress distribution spans the entire bond length, decaying sinusoidally from τ_{max} at the loaded end. The stress–slip trajectory transitions from rising to descending as the load-bearing capacity is gradually diminished due to bond degradation. Stage IV, indicated in red, initiates when the shear stress at the loaded end reaches the residual frictional value τ_f. A localized region adjacent to the loading point becomes governed by frictional sliding, while softening continues along the remaining interface. The global stress decreases more steeply in this stage as the frictional region grows in extent. Subsequently, Stage V (cyan) emerges when the frictional stress extends over a substantial portion of the bonded length, with the softening region shrinking accordingly. The stress continues to decline due to the limited resistance provided by the cohesive law and the fixed residual stress. This process culminates in Stage VI (black), where the entire interface exhibits constant frictional sliding. At this point, the applied axial stress remains nearly constant despite further increments in slip, indicating complete interfacial debonding and the loss of cohesive contribution.

8.4.4 Scaling-Based Transformation Between CMLs:

To establish a generalizable and mechanistically sound framework for comparing the interfacial behavior of TRM systems subjected to environmental degradation, a parametric mapping approach has been

adopted. This methodology is based on the assumption that the τ–s law of a deteriorated interface may be represented as a scaled version of the reference (unaged) cohesive law through the introduction of two non-dimensional parameters: φ (phi), which governs the vertical scaling of interfacial shear stress, and ψ (psi), which governs the horizontal stretching of slip. This concept is especially valuable when attempting to calibrate or reconstruct aged cohesive laws from limited experimental data or to establish empirical degradation trends in terms of measurable physical quantities. The general expression for the parametric transformation between the τ–s responses of the aged and control conditions is defined as:

$$\tau_{\text{aged}}(s) = \varphi \cdot \tau_{\text{ref}}\left(\frac{s}{\psi}\right) \tag{49}$$

where $\tau_{\text{ref}}(s)$ is the known cohesive shear stress–slip law of the reference material, and $\tau_{\text{aged}}(s)$ is the transformed (aged) law. The parameter φ modifies the amplitude of the shear stress, accounting for strength degradation, while ψ adjusts the slip axis, capturing changes in deformation capacity such as embrittlement or enhanced ductility. To ensure physical consistency of the transformation, particularly with respect to the spatial characteristics of load transfer, the effective bond length must also be included in the formulation. Based on the mechanics of shear stress transfer, the effective bond length of the aged configuration is analytically linked to that of the reference through the following relationship:

$$L_{\text{eff,aged}} = \sqrt{\frac{\psi}{\varphi}} \cdot L_{\text{eff,ref}} \tag{50}$$

Equation (15) emerges from closed-form derivations of interfacial stress decay in bonded systems and establishes a geometric constraint between the two cohesive laws. It guarantees that the scaled law will be not only pointwise equivalent but also consistent in terms of the global response and spatial transfer mechanics. In this framework, the simultaneous identification of φ and ψ is achieved by solving a system of coupled equations. Given a set of three slip–stress pairs $(s_i, \tau_i^{\text{aged}})$ obtained from the trilinear approximation of the aged τ–s response, the following residuals are defined:

$$R_i(\varphi, \psi) = \tau_i^{\text{aged}} - \varphi \cdot \tau_{\text{ref}}\left(\frac{s_i}{\psi}\right) \quad \text{for} \quad i = 1,2,3 \tag{51}$$

In parallel, the bond length constraint from Eq. (15) is enforced as an additional residual:

$$R_{\text{Leff}}(\varphi, \psi) = L_{\text{eff,aged}} - \sqrt{\frac{\psi}{\varphi}} \cdot L_{\text{eff,ref}} \tag{52}$$

This yields a system of four nonlinear equations with two unknowns, which is solved using numerical techniques. In the present study, the "fsolve" routine in MATLAB was employed with initial guesses based on the ratio of peak stresses and slip capacities observed experimentally. The reference system chosen for calibration was group S-0, which was not subjected to any environmental aging. For all other groups (single-lap shear test as of Table 14), the experimental trilinear τ–s parameters were extracted, and the corresponding effective bond lengths were computed from inverse modeling as described in previous sections. Using these values, φ and ψ were calibrated for each aged group. The fitted τ–s curves were then reconstructed using Eq. (49), and the quality of the transformation was evaluated through the coefficient of determination (R^2), with values generally exceeding 0.85 across the dataset, indicating excellent agreement. The physical interpretation of these parameters is also of interest. A reduction in φ indicates a loss in shear transfer capacity, consistent with damage or chemical deterioration at the interface. An increase in ψ typically implies an extended softening branch, often observed in systems that have undergone microcracking or weakening of the mortar matrix. Together, these parameters

provide a compact yet powerful representation of interfacial degradation. The next section will explore the variation of φ and ψ across different environmental exposures, particularly in terms of pH and aging duration. Their evolution will be used to formulate predictive empirical models suitable for inclusion in design and service-life assessment protocols.

8.4.5 Empirical Modeling of Interfacial Degradation Parameters

Following the identification of φ and ψ as cohesive law transformation parameters, this section explores their evolution as a function of environmental exposure severity. The objective is to establish predictive expressions for these parameters that capture the effects of both pH and exposure time, thus enabling a quantitative integration of environmental degradation into the bond–slip modeling framework for TRM systems. The control group for calibration was (S-0), representing unaged specimens tested under ambient laboratory conditions. For all other aged single-lap specimens listed in Table 19, the experimental trilinear cohesive law parameters,slip values s_0, s_1, s_2; shear stress values τ_0, τ_1, τ_2; and the measured effective bond length l_{eff} were used to calibrate φ and ψ through a constrained affine transformation. This transformation enforced both the pointwise consistency of the τ–s law, as described by Eq. (50), and the compatibility with bond length degradation according to Eq.(52).

Table 19 Experimental slip–stress data and effective bond lengths for all specimen groups.

Group Name	s_0	s_1	s_2	τ_0	τ_1	τ_2	l_{eff}
S-0	0	0,06	0,46	0,052	4,8	0,22	119,3
S-RC-1000	0	0,24	3,16	0,005	1,2	0,22	581,5
S-RC-3000	0	0,57	1,96	0,042	4,2	0,22	318,1
S-RC-6000	0	0,67	3,44	0,006	1,2	0,22	777,9
S-RW-1000	0	0,26	1,52	0,032	3,5	0,22	275,4
S-RW-3000	0	0,33	1,99	0,011	2,1	0,22	426,9
S-RW-6000	0	1,14	4,99	0,003	0,6	0,22	1316,1
S-P15-1000	0	0,19	1,96	0,013	2,7	0,22	329,5
S-P15-3000	0	0,08	0,74	0,068	6	0,22	128,8
S-P2-1000	0	0,51	1,71	0,013	2,1	0,22	451,4
S-P2-3000	0	0,17	1,97	0,017	2,2	0,22	338,8
S-P2-6000	0	0,97	2,79	0,005	0,8	0,22	998,1
S-P3-1000	0	0,31	1,90	0,047	4,5	0,22	215,5
S-P3-3000	0	0,14	1,70	0,058	5,1	0,22	160,1
S-P3-6000	0	0,66	2,84	0,006	1,2	0,22	731,0

A custom MATLAB script was implemented to automate this calibration procedure by minimizing residuals across the τ–s space and solving the coupled system of equations through nonlinear optimization. The outputs of this calibration process are presented in Table 2, which reports the calibrated values of φ and ψ, the R^2 goodness-of-fit indicator, and the comparison between experimental and reconstructed shear stress values at each of the three slip stages.

Table 20 Calibrated φ and ψ values with corresponding R^2 and τ predictions for aged groups.

Group	s_1	s_2	φ	φ	R^2	τ_0 –	τ_0 – pred	τ_1 _exp	τ_1 _	τ_2 _exp	τ_2 _

						exp			pred		pred
S-RC-1000	0,24	3,16	0,316	7,522	0,726	0,005	0,016	1,2	0,7	0,22	0,22
S-RC-3000	0,58	1,96	0,767	5,451	0,867	0,042	0,039	4,2	3,3	0,22	1,08
S-RC-6000	0,67	3,45	0,224	9,552	0,976	0,006	0,011	1,1	1,1	0,22	0,31
S-RW-1000	0,27	1,53	0,675	3,600	0,985	0,032	0,035	3,4	3,2	0,22	0,45
S-RW-3000	0,33	2	0,394	5,045	0,977	0,011	0,020	2,0	1,9	0,22	0,39
S-RW-6000	1,15	5	0,130	15,833	0,991	0,003	0,006	0,6	0,6	0,22	0,25
S-P15-1000	0,19	1,97	0,577	4,400	0,845	0,013	0,030	2,6	1,8	0,22	0,23
S-P15-3000	0,08	0,75	1,370	1,596	0,981	0,068	0,071	6,0	5,3	0,22	0,22
S-P2-1000	0,51	1,72	0,370	5,294	0,846	0,013	0,01	2,1	1,6	0,22	0,68
S-P2-3000	0,17	1,97	0,549	4,426	0,871	0,017	0,028	2,225	1,6	0,22	0,22
S-P2-6000	0,97	2,79	0,146	10,217	0,892	0,005	0,007	0,797	0,6	0,22	0,35
S-P3-1000	0,31	1,9	1,123	3,664	0,917	0,047	0,058	4,499	5,2	0,22	0,50
S-P3-3000	0,14	1,71	2,009	3,618	0,974	0,058	0,104	5,108	5,7	0,22	0,21
S-P3-6000	0,67	2,84	0,223	8,383	0,944	0,006	0,011	1,205	1,1	0,22	0,37

The trends revealed by the results demonstrate the sensitivity of interfacial behavior to environmental exposure. Degradation in acidic media led to a pronounced decrease in φ, with values dropping below 0.2 in the most aggressive conditions, indicating significant loss of load transfer capacity. Simultaneously, ψ exhibited considerable growth, often exceeding 7.5 for long-term exposure, signifying extended softening and delayed peak shear response. These transformations correspond to a flattening of the cohesive law, indicative of cohesive degradation in the mortar layer and damage at the fiber–matrix interface. The high R^2 values (generally >0.85) confirmed that the scaling procedure provided an accurate reconstruction of the observed experimental behavior across a diverse set of aging scenarios. To generalize these results into a predictive framework, multiple regression was performed using pH and logarithmic exposure time $\ln(t)$ as predictors. The regression included interaction terms to capture synergistic effects between chemical severity and exposure duration. The fitted empirical expressions for φ and ψ are provided as:

$$\varphi(pH,t) = -3.4173 + 1.7906 \cdot pH + 0.5926 \cdot \ln(t) - 0.2612 \cdot pH \cdot \ln(t) \quad (53)$$

$$\psi(pH,t) = 33.1867 - 17.1084 \cdot pH - 3.8622 \cdot \ln(t) + 2.3619 \cdot pH \cdot \ln(t) \quad (54)$$

Although the regression coefficients of determination were moderate (R^2 = 0.87 for φ and R^2 = 0.79 for ψ), the models accurately captured the degradation trajectory across different pH values and durations. These relationships are further illustrated in Figures X and Y, which show the evolution of φ and ψ versus exposure time at pH 1.5, 2.0, and 3.0. As evident from the plots, degradation tends to intensify rapidly within the first 3000 hours in more acidic environments, after which the parameters approach asymptotic values. This calibrated transformation strategy provides a practical and theoretically grounded method for representing environmental aging in TRM systems. By coupling Eqs. (*53*) and (*54*) with the known cohesive law of a reference system, the full degradation-modified τ–s behavior can be reconstructed for any combination of pH and exposure time. This enables the inclusion of durability effects into design-stage simulations and supports the development of performance-based, long-term strengthening solutions for masonry structures.

8.4.6 Discussion on the bond behavior modeling framework

The modeling framework adopted in this study offers a mechanistically rich and computationally efficient strategy for simulating the interfacial behavior of TRM systems subjected to monotonic pull loading. By incorporating a rigid trilinear CML, the framework enables the representation of the progressive degradation phenomena through distinct loading stages, each defined by closed-form solutions or piecewise analytical formulations. The identification of six distinct stages, ranging from elastic engagement to full frictional sliding, provides a robust basis for reconstructing the interfacial stress transfer mechanism. A key strength of the approach lies in its capacity to resolve the internal fields of axial stress, interfacial shear stress, and slip along the bonded length through calibrated τ–s relationships. These fields were validated against experimental and simulated responses for representative specimens, with results revealing consistent transitions between predicted stress fronts and observed load–slip behavior. Notably, the ability to distinguish between different degradation cases (α to δ) based on the bond length L, effective length l_{eff}, and the softening front d, enabled the accurate assignment of loading regimes for each specimen configuration.

The integration of φ and ψ scaling parameters into the modeling scheme further enhances its predictive capability by linking degradation-induced changes in the τ–s law to aging conditions. These parameters effectively condense complex chemo-mechanical alterations into interpretable shifts in peak stress and softening profile. When applied within the inverse modeling loop, this transformation enabled high-fidelity reconstruction of τ–s behavior for aged interfaces with R^2 values typically above 0.85. The coupled use of τ–s point scaling and bond-length transformation ensures internal consistency, thereby making the model applicable not only for back-analysis but also for forward simulations in service-life assessments.

Nevertheless, the model's assumptions should be recognized. The use of constant softening and frictional stiffnesses simplifies the actual behavior of aged mortars, particularly under extreme degradation scenarios where local heterogeneities may trigger premature interfacial detachment. Additionally, the absence of time-dependent phenomena such as creep or rate effects confines the present formulation to monotonic loading conditions. While suitable for most accelerated durability campaigns, future work may consider extending the framework to incorporate viscoelastic components or microcrack-induced interface evolution under sustained loads. Despite these simplifications, the present modeling methodology proves effective in capturing key features of TRM debonding and interfacial degradation. Its modular nature, analytical clarity, and compatibility with experimental calibration make it highly suitable for design applications and parametric degradation studies. Coupled with the empirical φ–ψ framework, it sets the foundation for a predictive model of long-term TRM bond performance across various environmental exposures.

8.5 Conclusion

This chapter presented a comprehensive investigation of the durability performance of TRM systems subjected to environmental degradation, with particular focus on acidic conditions of varying severity. The experimental program encompassed tensile, pull-out, and single-lap shear tests, performed on aged specimens conditioned in five different environments: climatic chamber, water immersion, and acidic solutions with pH values of 1.5, 2.0, and 3.0. These tests were supported by analytical modeling based on a cohesive material law and complemented by an empirical calibration framework. The main key findings can be summarized as follows:

- Tensile behavior was significantly affected by environmental exposure. In acidic conditions, especially at pH 1.5, reductions in strength, stiffness, and cracking capacity were observed,

attributed to combined mortar deterioration and textile degradation. Moderate acidity caused temporary strength gains due to hydration but eventually led to performance reduction. Water immersion induced strength decline at longer durations due to leaching of calcium hydroxide, while RC conditioning preserved mechanical properties.

- Mortar strength evolution showed a consistent trend across all environments: an initial increase in compressive and flexural strength at 3000 h followed by a decline due to chemical degradation or leaching. Under RC conditions, strength increased steadily due to ongoing hydration and carbonation. Ductility improved in all environments, particularly under acidic and RW conditions, likely driven by microstructural rearrangements.
- Textile performance was adversely affected in acidic environments due to fiber corrosion, especially at pH 1.5. In contrast, fibers remained largely unaffected under RC and only marginally weakened in RW. These changes directly influenced the tensile performance of the TRM composites.
- Cracking patterns changed with aging. Fewer cracks and larger crack spacing were observed in specimens exposed to aggressive environments. This indicated a reduction in the crack-bridging capability and load redistribution potential, especially in specimens aged at low pH levels for longer durations.
- Bond behavior, as assessed by pull-out and single-lap shear tests, revealed a progressive decrease in peak load, debonding energy, and slip capacity with increasing aging severity. Complete detachment of the mortar from the substrate was observed in single-lap specimens aged for 6000 h at pH 1.5. These results emphasized the critical role of bond degradation in limiting TRM durability.
- Analytical modeling of the single-lap shear test using a trilinear cohesive law successfully reproduced the evolution of local mechanical fields across six loading stages. These included the initiation and progression of softening and frictional sliding zones along the bonded length. A representative specimen (S-RC-1000-1) was modeled in detail, confirming the predictive capability of the approach.
- Affine transformation modeling was implemented to account for degradation through two scaling factors: φ (vertical scaling of stress) and ψ (horizontal scaling of slip). These parameters were calibrated from experimental τ–s curves and effective bond lengths. The fitted models achieved high accuracy, with most R^2 values exceeding 0.85.
- Empirical models for φ and ψ were formulated as functions of pH and exposure time using multivariate regression, enabling predictive representation of interface degradation. These relationships provide a simplified yet robust tool for incorporating aging effects into design and service-life estimation of TRM systems.

Chapter 9
Conclusions and future research

9.1 Introduction

This thesis aimed to address the existing knowledge gaps concerning the performance of TRM composites, with a particular focus on their durability under acidic environmental conditions. The research was structured into five main phases: (1) a comprehensive review of the existing literature, with an emphasis on the durability aspects of TRM systems; (2) the development of an experimental program to evaluate the short-term mechanical behavior of TRM composites; (3) preliminary investigations into the long-term performance of TRM, including both sustained loading and environmental degradation, to identify strengths and limitations; (4) implementation of an extensive durability campaign targeting acidic aging, incorporating mechanical testing alongside microstructural and mineralogical characterization to elucidate the aging mechanisms; and (5) development of predictive modeling approaches to describe the material behavior, which included analytical formulations, machine learning models, and chemo-mechanical frameworks, integrating the experimental insights. The following chapter present the main conclusions derived from this body of work and provide recommendations for future research directions.

9.2 Experimental research

Experimental investigations served as the backbone of this research, enabling the development, validation, and refinement of numerical and predictive models tailored to TRM systems. This section presents a synthesis of the main experimental findings across different stages of the research. The results of the TRM tensile tests clarified the cracking behavior and fiber contribution under direct tension. The long-term loading tests offered new perspectives on the creep behavior of TRM and its implications for structural reliability. In parallel, the exposure to mild aggressive environments allowed the identification of initial signs of degradation, laying the groundwork for more targeted aging campaigns. Lastly, the dedicated study on acidic exposure provided a deeper understanding of how varying levels of acidity influence TRM deterioration, integrating mechanical, microstructural, and mineralogical evidence to shed light on the underlying aging mechanisms.

9.2.1 Main outcomes of the TRM tensile testing

The tensile behavior of TRM composites was investigated through a comprehensive experimental campaign involving thirteen groups incorporating either glass or high-strength steel fabrics embedded within a lime-based mortar matrix. A total of seventy-eight tensile coupons were tested under direct tension to evaluate the influence of various parameters, including the gripping method, number and

arrangement of textile layers, and the thickness of the mortar. Two distinct gripping strategies were examined: one involving load application through the mortar and the other directly through the textile. The experimental outcomes highlighted the critical role of the gripping method in determining the reliability and mechanical response of the composite system. It was observed that applying the load directly to the textile, particularly when the bare textile segment was impregnated with resin, significantly enhanced the performance by reducing premature damage, minimizing scatter in the results, and facilitating a more accurate estimation of the composite strength. This approach mitigated the common issues observed when clamping the mortar, such as stress concentrations near the grips, delamination at the interface, and the influence of local cracking.

Furthermore, the use of resin impregnation in the clamping region proved highly beneficial for preserving the integrity of the textile during testing and promoting uniform stress transfer within the composite. This methodological refinement enabled the mobilization of tensile capacities close to those of the unembedded textile fabrics, thereby offering a more faithful representation of the composite behavior. In the case of multilayer configurations, the results demonstrated that, under an appropriate gripping setup, the tensile response remained independent of the reinforcement ratio. The presence of a thin mortar layer between textile plies was found to be effective in reducing variability in the measurements, contributing to a more reproducible response. Although a trilinear stress–strain behavior is theoretically expected for TRM composites under tension, the experimental curves often deviated from this ideal due to the complex nature of crack development and interaction. Digital Image Correlation (DIC) was identified as a valuable tool for capturing these stages with improved resolution, particularly in detecting the onset and progression of cracks, which are critical for interpreting the constitutive response. Overall, the outcomes of this experimental phase provided fundamental insights into the tensile performance of TRM composites and informed the methodological choices adopted in subsequent mechanical testing.

9.2.2 Creep behavior of the TRM

The long-term response of TRM composites under sustained loading was investigated through a detailed experimental campaign focused on creep behavior in a single-lap shear configuration. This study aimed to provide an in-depth understanding of how the interplay between curing time, load level, and bond characteristics influences the time-dependent deformation of TRM systems. The experimental program comprised material characterization of mortar and textiles at various curing stages, single-lap shear tests with different curing durations, and long-term creep tests performed on both single yarns and TRM specimens. The creep campaign extended over a duration of 250 days and involved twelve individual specimens subjected to a range of loading levels and curing conditions. The findings revealed that the creep performance of TRM is closely governed by the load intensity and the maturity of the mortar matrix. Specimens tested at higher loading levels, particularly those exceeding 60% of the short-term ultimate capacity, exhibited significant creep deformation and in some cases experienced premature failure. This behavior was largely attributed to microstructural degradation of the matrix and progressive bond deterioration at the textile–mortar interface.

In contrast, specimens subjected to lower sustained loads (e.g., 30–40% of U90) demonstrated considerably better resistance to creep, especially when the mortar was allowed to cure for extended periods. These samples retained high post-creep capacities and showed limited slip, even after prolonged loading durations. The beneficial effect of longer curing times was associated with improved mechanical properties of the matrix, which enhanced both load transfer and long-term stability. Although the intrinsic creep of glass yarns was found to be negligible within the tested range, frictional interaction with the mortar at higher loads may induce filament-level damage, which must be considered in future durability assessments. The study emphasized the importance of optimizing both the curing regime and the load-

carrying strategy in practical applications of TRM systems. It also underscored the need to incorporate considerations of long-term matrix aging beyond conventional curing periods to ensure the sustained mechanical integrity of the composite. Overall, these results provide a foundational understanding of the time-dependent behavior of TRM composites under sustained shear loading, offering valuable insights for the design of durable reinforcement systems in structural applications.

9.2.3 Effect of mild aggressive environments

The influence of mildly aggressive environments, including saline, alkaline, and weakly acidic exposures, on the performance of TRM composites was examined through an extensive experimental program incorporating mechanical testing, microstructural analyses, and mineralogical assessments. The objective was to evaluate the durability of TRM systems incorporating glass and basalt fibers in hydraulic lime mortar, while identifying degradation trends associated with long-term exposure to these environments. Each exposure condition was compared against reference media, namely dry curing and immersion in distilled water, to establish a baseline for performance evolution.

In the case of alkaline environments, specimens exhibited significant strength gains, particularly in compressive and flexural responses of the mortar, attributed to continued hydration and the formation of calcium-silicate-hydrate (C-S-H) and calcium-alumino-silicate-hydrate (C-A-S-H) phases. Despite the initial beneficial effects, prolonged exposure revealed a reduction in bond performance for basalt-based TRM systems, as observed in single-lap shear tests. This degradation was associated not with direct fiber breakdown but with interfacial weakening and excessive mineralization at the bond interface. Conversely, glass-TRM composites maintained or slightly improved their bond performance under the same conditions. These findings emphasize the importance of considering long-term chemical interactions at the textile–matrix interface when evaluating durability under alkaline conditions.

Under saline exposure, the mortar matrix initially benefitted from hydration acceleration and matrix densification, but over time, chloride ingress-initiated calcium leaching and salt crystallization, leading to increased brittleness and reduced ductility. The basalt TRM exhibited complex behavior, with an initial phase of bond degradation, followed by temporary strengthening and ultimately a pronounced brittleness, indicative of reduced long-term reliability. The glass TRM, while generally more stable, showed a steady decline in bond strength without phases of temporary improvement. These outcomes suggest that both matrix and fiber response to saline environments involve a combination of mechanical and chemical degradation mechanisms, necessitating protective strategies or material substitutions for long-term applications.

In weakly acidic environments, particularly in simulated acid rain conditions, the mechanical properties of the lime-based mortar demonstrated relative stability over extended immersion periods up to 5000 hours. While distilled water immersion acted as a mild aging mechanism, dry storage was identified as a more stable reference condition for lime-based mortars. Mineralogical analyses revealed minor changes in mortar composition across all environments, with gypsum formation being the primary indicator of chemical alteration under acidic exposure. Notably, glass textiles exhibited excellent durability under both water and acidic immersion, with minimal loss in mechanical performance. Basalt textiles, however, were significantly more susceptible to degradation, especially under prolonged acidic conditions, showing marked reductions in bond strength and overall performance. These observations underline the superior chemical resistance of glass over basalt in TRM applications exposed to acidic or saline conditions.

Altogether, the results from these campaigns provide valuable insights into how TRM composites respond to various mildly aggressive environments. The interplay between matrix hydration, fiber–matrix bonding, and environmental chemistry defines the long-term mechanical integrity of TRM systems.

Selection of the textile type and matrix composition must be carefully tailored to the expected exposure conditions to ensure sustained performance. These findings also highlight the necessity for future research under more severe or cyclic environmental conditions, particularly to understand the effects of repeated wet-dry cycles and cumulative chemical degradation over extended service periods.

9.2.4 Acidic intensity and aging mechanism

The influence of acidic severity on the mechanical performance and degradation mechanisms of TRM composites was investigated through a systematic experimental campaign that incorporated tensile, pull-out, and single-lap shear tests, alongside comprehensive mortar characterization. TRM systems were exposed to acidic environments with pH values of 1.5, 2.0, and 3.0 for up to 6000 hours, allowing the progressive deterioration of the composite constituents and interfaces to be assessed with increasing chemical aggressiveness. These results provided critical insight into the interaction between chemical degradation and mechanical integrity, revealing that both the intensity of the acidic environment and the duration of exposure play pivotal roles in defining the extent of damage and the failure mechanisms of the system. Tensile tests conducted on TRM coupons revealed clear trends associated with acid concentration. At pH 1.5, severe degradation was observed, including marked reductions in tensile strength, stiffness, and the segmental modulus of the second stage of loading (E_2), particularly at longer durations. These losses were attributed to the combined effects of mortar leaching, gypsum formation, and glass fiber deterioration due to chemical etching. The number of cracks consistently decreased across all acidic conditions, indicating a diminished crack-bridging capacity of the mortar as its tensile strength declined. Crack spacing increased under more aggressive conditions, notably at pH 1.5, reflecting a shift in damage localization driven by the progressive failure of the fiber–matrix interface. Intermediate acidity (pH 2.0) presented transient improvements in mechanical response, likely due to short-term matrix densification and secondary product precipitation, although degradation became apparent after extended exposure. Specimens aged at pH 3.0 showed relatively stable mechanical behavior, although cumulative damage still led to gradual performance loss, indicating that even mildly acidic conditions induce measurable long-term effects.

Bond degradation under acidic exposure was further examined through pull-out tests. The reference dry condition showed stable interfacial strength, while acidic immersion at pH 1.5 led to a pronounced decrease in both peak bond strength and energy dissipation capacity. These reductions were attributed to interfacial debonding, matrix softening, and fiber degradation. A short-lived enhancement in pull-out performance was observed at pH 2.0, again suggestive of matrix compaction or densification; however, this effect diminished over time. Mild acidic exposure at pH 3.0 had negligible impact on bond behavior and even showed slight improvements under specific conditions, suggesting a threshold below which acid-driven degradation is significantly delayed. Energy-based indicators, such as pull-out energy and debonding energy, proved particularly effective in capturing early-stage deterioration, outperforming peak load as a predictor of long-term interfacial damage.

Single-lap shear tests complemented these findings by providing insight into the behavior of the TRM–substrate interface. The extreme pH 1.5 condition produced the most severe outcome: complete detachment of the mortar from the substrate, indicative of catastrophic interfacial failure. At pH 2.0, initial improvements in bond performance were followed by pronounced declines with extended aging, consistent with acid-induced mineralogical transformation and loss of cohesion. In contrast, the pH 3.0 group retained mechanical integrity across all durations, reaffirming that mild acidic exposure results in limited bond degradation. Energy dissipation and slip measurements revealed that early-stage degradation was primarily characterized by ductility loss rather than strength reduction, underlining the importance of energy-based metrics in assessing the true progression of damage in TRM interfaces. The degradation of the hydraulic lime-based mortar under acidic attack was confirmed through

complementary microstructural and chemical analyses, including XRD, TGA, and ICP. Acid-induced deterioration followed a sequence involving calcium leaching, calcite breakdown, and gypsum formation. While the early stages of exposure led to temporary strength gains due to pore filling by gypsum, prolonged immersion caused internal stress accumulation, microstructural disruption, and strength decline. These changes were particularly evident at pH 1.5 and after 6000 hours of aging. The addition of polymeric fibers contributed to post-peak resilience, limiting crack propagation and enhancing ductility even in severely aged specimens. Nonetheless, the structural role of the mortar continued to diminish with increasing acid intensity.

Overall, the combined results across tensile, pull-out, and single-lap configurations demonstrated that acidic intensity exerts a substantial influence on both material degradation and composite performance. The degradation mechanisms involve simultaneous deterioration of the mortar matrix, chemical weakening of the fiber reinforcement, and progressive loss of interfacial cohesion. Higher acidity and prolonged exposure accelerate these mechanisms, whereas milder conditions permit partial preservation of mechanical capacity. These observations underscore the necessity of integrating chemical durability into design strategies for TRM systems intended for aggressive environments and provide a critical foundation for developing chemo-mechanical models capable of predicting long-term performance.

9.3 Numerical modeling

The numerical modeling efforts in this thesis were designed to complement and interpret the experimental findings through predictive and mechanistic simulations. Three distinct but interconnected modeling strategies were developed, each addressing a critical aspect of TRM durability. First, a data-driven machine learning model was trained to estimate the mechanical degradation of lime-based mortar as a function of environmental parameters, offering a rapid and adaptable prediction tool. Second, a chemo-mechanical model was formulated to explicitly capture the relationship between chemical degradation, particularly due to acidic exposure, and the mechanical deterioration of mortar, incorporating leaching dynamics and phase transformations. Finally, a physically grounded numerical framework was implemented to simulate the bond behavior of TRM systems under single-lap shear loading, supported by the calibration of a CML that reflects interface damage and slip evolution. These three modeling approaches provide complementary perspectives on degradation phenomena and enable long-term performance forecasting under varying environmental conditions. The following subsections detail the methodology, calibration, and key outcomes of each modeling component.

9.3.1 Machine learning-based prediction of mortar degradation

The application of machine learning in this thesis focused on developing a predictive framework for the degradation behavior of lime-based mortars subjected to different environmental aging conditions. An XGBoost algorithm was trained using an extensive dataset of experimentally measured flexural strengths and stress–displacement curves from mortars exposed to dry conditions, distilled water immersion, and acidic environments. The model inputs included environmental parameters such as pH level, exposure time, density, and moisture content, while the outputs consisted of mechanical indicators including flexural strength and stress–displacement response. The model achieved excellent predictive accuracy, with an R^2 value of 0.984 and a RMSE of 0.116 on the testing dataset, validated through 4-fold cross-validation. A comparison between experimental and predicted results revealed that the XGBoost model reliably captured both global strength trends and local mechanical behaviors. Specifically, the model effectively mirrored the stress–displacement response across all exposure scenarios, with deviations typically within ±0.05 mm for displacement and ±0.3 MPa for peak stress. This alignment was consistent across all exposure durations, with slight underprediction tendencies observed at higher exposure times

under acidic conditions, suggesting room for future enhancement through the inclusion of more complex descriptors or ensemble techniques. The model also demonstrated its ability to predict subtle environmental effects, such as the transient strength gain in acidic exposure at 3000 hours followed by a decline at 5000 hours. Moreover, energy-based indicators, such as the area under the stress–displacement curves, showed a predicted-to-experimental ratio within a narrow range of 0.957 to 1.007, with a coefficient of variation of 2%, reinforcing the model's robustness.

The machine learning approach developed herein offers a valuable, non-invasive tool for forecasting the mechanical degradation of lime-based mortars. By integrating experimental datasets with data-driven techniques, the model enables accurate and scalable assessments of material performance under diverse environmental conditions. This predictive capability holds direct implications for the service-life estimation and durability assessment of mortars used in TRM systems, particularly in conservation and retrofitting scenarios exposed to chemically aggressive environments.

9.3.2 Chemo-mechanical modeling of acidic damage in mortar

To complement the experimental investigation and interpret the mechanical degradation induced by acidic exposure, a chemo-mechanical model grounded in continuum damage mechanics was developed and calibrated. This modeling approach aimed to quantify the evolution of stiffness reduction, strength loss, and post-peak softening in lime-based mortars subjected to prolonged environmental conditioning. A smooth trilinear constitutive law was adopted to capture the full uniaxial compressive stress–strain response, encompassing elastic, hardening, and softening phases. The framework incorporates a scalar damage variable governed by energy dissipation to represent the progressive deterioration of the material's mechanical integrity. Model calibration was carried out using average experimental stress–strain envelopes obtained from cylindrical mortar specimens across a range of exposure durations and pH conditions.

Microstructural investigations provided the mechanistic foundation for the model's formulation. Chemical aging in acidic environments was shown to induce progressive portlandite depletion, gypsum formation, and increased porosity, as confirmed by TGA and XRD results. These transformations were reflected in the reduction of elastic modulus and peak compressive strength observed experimentally, aligning with the damage evolution predicted by the model. The scalar damage variable $D(\varepsilon)$ effectively captured the onset and propagation of mechanical degradation, while the parameter Ω served as an energetic descriptor of post-peak behavior, incorporating the effects of microcracking, crack coalescence, and fiber–matrix debonding. The systematic reduction of Ω with increasing acidic severity indicated a lower energy threshold for failure, consistent with visual evidence of interfacial disruption and gypsum crystallization along fracture planes.

In addition to reproducing measured stress–strain curves, the model was extended into a predictive framework by correlating mechanical degradation with leaching-based chemical indices. Empirical degradation laws were derived to relate the key mechanical parameters to chemical exposure metrics, enabling the model to estimate the mechanical behavior of intermediate exposure conditions not directly tested. These predictions showed strong agreement with the observed data for elastic modulus and peak stress, although greater variability was noted for post-peak parameters such as Ω, reflecting the complexity of localized damage mechanisms. Nevertheless, the integration of chemical and mechanical degradation into a unified modeling approach enables meaningful extrapolation across environmental scenarios. While caution is warranted when applying the model outside the calibration domain, such as to lower pH values or extended durations, the underlying physical consistency between microstructural deterioration and macroscopic mechanical response affirms the internal validity of the approach. This chemo-mechanical model thus provides a valuable tool for predicting long-term mortar performance in

aggressive environments, supporting durability assessments and informing design strategies for TRM systems exposed to acidic conditions.

9.3.3 Numerical simulation of TRM bond behavior under shear

The numerical simulation of TRM bond behavior under shear loading provided a comprehensive framework to interpret the influence of environmental degradation on the interfacial performance of TRM systems. By employing a trilinear cohesive material law to describe the shear stress–slip response, the model successfully reconstructed the complex progression of bond deterioration across different exposure conditions. A key contribution of the framework was the introduction of transformation parameters linked to aging severity, which enabled the prediction of degraded interface behavior using reference bond laws. This capability proved particularly effective in quantifying reductions in peak stress, interfacial stiffness, and slip capacity due to acidic exposure and prolonged conditioning.

The outcomes demonstrated consistent agreement between modeled and experimental responses, validating the framework's reliability in capturing stage-wise interfacial behavior, from elastic loading to full frictional sliding. Moreover, the model allowed for systematic classification of degradation severity and provided insights into the shifting location of softening and damage zones along the bonded length. These features are crucial for identifying the onset and extent of interfacial failure in practical applications. Beyond back-analysis, the model showed strong potential as a predictive tool for durability-based design. The ability to generalize environmental effects through empirical scaling laws makes the framework adaptable to a wide range of service conditions. While some limitations remain, such as the exclusion of time-dependent effects and localized heterogeneity, the analytical clarity and modular nature of the approach ensure its suitability for integration into broader design and life-cycle assessment methodologies. Overall, the modeling strategy presented in this work offers a physically consistent, experimentally validated, and computationally efficient approach for simulating and forecasting the long-term bond performance of TRM systems exposed to aggressive environments.

9.4 Suggestion for future works

The contribution of the present thesis to scientific knowledge and engineering practice marks a step forward in the broader objective of understanding the mechanism of aging in TRM systems, particularly under acidic environmental conditions. The combination of mechanical testing, microstructural characterization, and numerical modeling enabled a multi-scale investigation of degradation, supporting the development of a predictive framework. This approach can be transferred and adapted to other environmental exposures, such as alkaline, saline, or cyclic conditions, to achieve a more comprehensive and mechanistically grounded understanding of TRM aging. Ultimately, such integrated knowledge may contribute to the implementation of real-time durability models and LCA strategies for infrastructure strengthened with TRM. To build upon the outcomes of the present research, the following directions are proposed, grouped into thematic categories.

9.4.1 Experimental durability assessment

To expand the scope of environmental degradation scenarios and improve realism in durability evaluation, future experimental efforts should aim to:

- Investigate cyclic exposure regimes (e.g., wet–dry and freeze–thaw cycles), reflecting common service conditions.
- Extend acidic conditioning protocols to include more aggressive pH levels and prolonged durations to better define long-term deterioration thresholds.

- Couple mechanical loading with environmental exposure, examining simultaneous action effects on creep, bond, and fracture behavior.
- Explore biological degradation mechanisms, such as those caused by microbial activity or organic acids.
- Implement systematic leaching measurements throughout the exposure duration, with particular attention to calcium, aluminum, and iron release. This data would enhance the resolution and accuracy of the chemo-mechanical model by linking chemical depletion kinetics to mechanical property evolution.

9.4.2 Numerical modeling and predictive frameworks

Enhancement of the developed models should address both greater physical fidelity and broader applicability:

- Introduce time-dependent phenomena such as creep and viscoelasticity into bond-slip and damage models.
- Develop multi-physics formulations that couple ion transport, chemical reactions, and mechanical degradation at multiple scales.
- Apply probabilistic modeling techniques to account for uncertainties in material properties, environmental conditions, and measurement variability.
- Establish inverse modeling pipelines integrated with sensor data, enabling dynamic model updates and supporting the development of digital twins.

9.4.3 Materials and system optimization

The long-term durability of TRM systems may be significantly improved by innovations in constituent materials and reinforcement strategies:

- Evaluate the performance of alternative reinforcement textiles (e.g., carbon, basalt, PBO) in aggressive environments.
- Investigate durability-enhancing mortar compositions, including lime–pozzolan blends, supplementary cementitious materials, or polymer additives.
- Assess the role of textile surface treatments and impregnation resins in mitigating interfacial degradation.
- Promote the use of eco-efficient and recycled materials, while simultaneously monitoring their long-term mechanical and environmental performance.

9.4.4 Performance-based design and service life prediction

A long-term goal should be the integration of durability insights into engineering design and asset management frameworks:

- Formulate design-oriented degradation models based on environmental exposure class and material configuration.
- Derive predictive deterioration maps or empirical equations for use in performance-based design codes.
- Integrate chemo-mechanical models into LCA and reliability tools, offering real-time or scenario-based prediction of service life.
- Standardize test protocols and durability assessment methodologies across laboratories to ensure reproducibility and comparability.

REFERENCES

[1] N.A. Resketi, V. Toufigh, Enhancement of brick-mortar shear bond strength using environmental friendly mortars, Constr Build Mater 195 (2019) 28–40. https://doi.org/10.1016/j.conbuildmat.2018.10.118.

[2] R. Vicente, S. Lagomarsino, T.M. Ferreira, S. Cattari, J.A.R. Mendes da Silva, Cultural Heritage Monuments and Historical Buildings: Conservation Works and Structural Retrofitting, 2018. https://doi.org/10.1007/978-981-10-5858-5_2.

[3] G. Castori, A. Borri, A. De Maria, M. Corradi, R. Sisti, Seismic vulnerability assessment of a monumental masonry building, Eng Struct 136 (2017) 454–465. https://doi.org/10.1016/j.engstruct.2017.01.035.

[4] H. Maljaee, B. Ghiassi, P.B. Lourenço, D. V. Oliveira, Moisture-induced degradation of interfacial bond in FRP-strengthened masonry, Compos B Eng 87 (2016) 47–58. https://doi.org/10.1016/j.compositesb.2015.10.022.

[5] A. Bellini, C. Mazzotti, A review on the bond behavior of FRP composites applied on masonry substrates, RILEM Technical Letters 2 (2017) 74–82. https://doi.org/10.21809/rilemtechlett.2017.40.

[6] M. Grzegorczyk-Frańczak, D. Barnat-Hunek, W. Andrzejuk, J. Zaburko, M. Zalewska, G. Łagód, Physical properties and durability of lime-cement mortars prepared with water containing micro-nano bubbles of various gases, Materials 14 (2021) 1902.

[7] N. Azimi, A. Dalalbashi, D. V. Oliveira, B. Ghiassi, P.B. Lourenço, Tensile behavior of textile-reinforced mortar: Influence of test setup and layer arrangement, Constr Build Mater 394 (2023) 132185. https://doi.org/10.1016/j.conbuildmat.2023.132185.

[8] G. Ferrara, M. Pepe, R.D.T. Filho, E. Martinelli, Mechanical response and analysis of cracking process in hybrid TRM composites with flax textile and Curauá fibres, Polymers (Basel) 13 (2021) 1–14. https://doi.org/10.3390/polym13050715.

[9] T. D'Antino, C. Papanicolaou, Mechanical characterization of textile reinforced inorganic-matrix composites, Compos B Eng 127 (2017) 78–91. https://doi.org/10.1016/j.compositesb.2017.02.034.

[10] N. Nosrati, A. Zabett, S. Sahebian, Stress Dependency of Creep Response for Glass/Epoxy Composite at Nonlinear and Linear Viscoelastic Behavior, Int J Polym Sci 2022 (2022) 9733138. https://doi.org/https://doi.org/10.1155/2022/9733138.

[11] N. Azimi, K. Schollbach, D. V. Oliveira, P.B. Lourenço, Effect of Acidic Environment Exposure on Mechanical Properties of Trm Composites., Constr Build Mater 438 (2024) 1–24. https://doi.org/https://doi.org/10.1016/j.conbuildmat.2024.137142.

[12] X. Zeng, Y. Li, Y. Ran, K. Yang, F. Qu, P. Wang, Deterioration mechanism of CA mortar due to simulated acid rain, Constr Build Mater 168 (2018) 1008–1015. https://doi.org/https://doi.org/10.1016/j.conbuildmat.2018.03.033.

[13] D. Arboleda, S. Babaeidarabad, C. DiLaurenzio Hays, A. Nanni, Durability of Fabric Reinforced Cementitious Matrix (FRCM) composites, Proceedings of the 7th International Conference on FRP Composites in Civil Engineering, CICE 2014 (2014).

[14] M. Alma'aitah, B. Ghiassi, A. Dalalbashi, Durability of textile reinforced concrete: Existing knowledge and current gaps, Applied Sciences (Switzerland) 11 (2021). https://doi.org/10.3390/app11062771.

[15] M.R. Singh, R. Yadav, Microstructural analysis and characterization of lime mortar of seventeenth century Raigad hill fort from western India, Indian J Hist Sci 56 (2021) 217–227. https://doi.org/10.1007/s43539-021-00023-z.

[16] A. Taheri, N. Azimi, D. V. Oliveira, J. Tinoco, P.B. Lourenço, Integrating Experimental Analysis and Gradient Boosting for the Durability Assessment of Lime-Based Mortar in Acidic Environment, Buildings 15 (2025) 1–21. https://doi.org/10.3390/buildings15030408.

[17] M. Hosseinzadeh, S.S. Mousavi, A. Hosseinzadeh, M. Dehestani, An efficient machine learning approach for predicting concrete chloride resistance using a comprehensive dataset, Sci Rep 13 (2023) 15024.

[18] V. Bertolli, T. D'Antino, Modeling the behavior of externally bonded reinforcement using a rigid-trilinear cohesive material law, Int J Solids Struct 248 (2022) 111641. https://doi.org/10.1016/j.ijsolstr.2022.111641.

[19] V. Bertolli, C. Signorini, A. Nobili, T. D'Antino, Influence of severe thermal preconditioning on the bond between carbon FRCM and masonry substrate: Effect of textile pre-impregnation, Constr Build Mater 409 (2023) 134028.

[20] A. Monaco, G. Minafò, J. D'Anna, M.C. Oddo, L. La Mendola, Constitutive Numerical Model of FRCM Strips Under Traction, Front Built Environ 6 (2020) 1–10. https://doi.org/10.3389/fbuil.2020.00060.

[21] J. Scacco, B. Ghiassi, G. Milani, P.B. Lourenço, A fast modeling approach for numerical analysis of unreinforced and FRCM reinforced masonry walls under out-of-plane loading, Compos B Eng 180 (2020) 107553. https://doi.org/10.1016/j.compositesb.2019.107553.

[22] W. Graf, A. Hoffmann, B. Möller, J.U. Sickert, F. Steinigen, Analysis of textile-reinforced concrete structures under consideration of non-traditional uncertainty models, Eng Struct 29 (2007) 3420–3431. https://doi.org/10.1016/j.engstruct.2007.08.013.

[23] J.U.N. Wang, H.O.T.A. Gangarao, R. Liang, W. Liu, Durability and prediction models of fiber-reinforced polymer composites under various environmental conditions: A critical review, Journal of Reinforced Plastics and Composites 35 (2016) 179–211. https://doi.org/10.1177/0731684415610920.

[24] E. Franzoni, M. Santandrea, C. Gentilini, A. Fregni, C. Carloni, The role of mortar matrix in the bond behavior and salt crystallization resistance of FRCM applied to masonry, Constr Build Mater 209 (2019) 592–605. https://doi.org/10.1016/j.conbuildmat.2019.03.059.

[25] A. Aşıkoğlu, G. Vasconcelos, P.B. Lourenço, Overview on the nonlinear static procedures and performance-based approach on modern unreinforced masonry buildings with structural irregularity, Buildings 11 (2021) 147.

[26] V. Alecci, M. De Stefano, F. Focacci, R. Luciano, L. Rovero, G. Stipo, Strengthening masonry arches with lime-based mortar composite, Buildings 7 (2017) 1–11. https://doi.org/10.3390/buildings7020049.

[27] V. Rizzo, F. Micelli, M. Leone, A. Bonati, M.A. Aiello, Residual Strength and Durability of Glass fiber FRCM and CRM Systems Aged in Alkaline Environments, Current Topics and Trends on Durability of Building Materials and Components - Proceedings of the 15th International

Conference on Durability of Building Materials and Components, DBMC 2020 (2020) 1585–1592. https://doi.org/10.23967/dbmc.2020.156.

[28] A. Dushimimana, J. Sena-Cruz, L. Correia, J.M. Pereira, S. Cabral-Fonseca, R. Cruz, Effects of long-term exposure of NSM CFRP-to-concrete bond to natural and accelerated aging environments, Compos Struct 340 (2024) 118174.

[29] K. Al-Lami, T. D'Antino, P. Colombi, Durability of fabric-reinforced cementitious matrix (FRCM) composites: A review, Applied Sciences (Switzerland) 10 (2020). https://doi.org/10.3390/app10051714.

[30] M. Ramesh, M. Parente, M. Azenha, P.B. Lourenço, Influence of Lime on Strength of Structural Unreinforced Masonry: Toward Improved Sustainability in Masonry Mortars, Sustainability 15 (2023) 15320. https://doi.org/10.3390/su152115320.

[31] N. Bianchini, N. Mendes, P.B. Lourenço, C. Calderini, Modelling of the Dynamic Response of a Full-Scale Masonry Groin Vault: Unstrengthened and Strengthened with Textile-Reinforced Mortar (TRM), International Journal of Architectural Heritage (2024) 1–25.

[32] E. Franzoni, C. Gentilini, M. Santandrea, S. Zanotto, C. Carloni, Durability of steel FRCM-masonry joints: effect of water and salt crystallization, Materials and Structures/Materiaux et Constructions 50 (2017). https://doi.org/10.1617/s11527-017-1070-2.

[33] B.V.V. Reddy, C.V.U. Vyas, Influence of shear bond strength on compressive strength and stress--strain characteristics of masonry, Mater Struct 41 (2008) 1697–1712.

[34] J. Donnini, G. Maracchini, S. Lenci, V. Corinaldesi, E. Quagliarini, TRM reinforced tuff and fired clay brick masonry: Experimental and analytical investigation on their in-plane and out-of-plane behavior, Constr Build Mater 272 (2021) 121643. https://doi.org/10.1016/j.conbuildmat.2020.121643.

[35] C.G. Papanicolaou, T.C. Triantafillou, M. Papathanasiou, K. Karlos, Textile reinforced mortar (TRM) versus FRP as strengthening material of URM walls: Out-of-plane cyclic loading, Materials and Structures/Materiaux et Constructions 41 (2008) 143–157. https://doi.org/10.1617/s11527-007-9226-0.

[36] A. Aşıkoğlu, A. Barontini, N. Savalle, G. Vasconcelos, P.B. Lourenço, Experimental analysis of unreinforced masonry buildings through the quasi-static test: A half-scale two-story modern masonry building, in: North American Masonry Conference, 2023.

[37] A.J. Francis, C.B. Horman, L.E. Jerrems, The effect of joint thickness and other factors on the compressive strength of brickwork, in: Proceedings of 2nd International Brick Masonry Conference, Stoke-on-Trent, 1971: pp. 31–37.

[38] R.H. Atkinson, B.P. Amadei, S. Saeb, S. Sture, Response of masonry bed joints in direct shear, Journal of Structural Engineering 115 (1989) 2276–2296.

[39] C.J.W.P. Groot, Effects of water on mortar-brick bond, TU Delft, Delft University of Technology, 1993.

[40] B.V.V. Reddy, C.V.U. Vyas, Influence of shear bond strength on compressive strength and stress--strain characteristics of masonry, Mater Struct 41 (2008) 1697–1712.

[41] S.J. Lawrence, H.T. Cao, Microstructure of the interface between brick and mortar, Brick and Block Masonry(8 Th IBMAC) London, Elsevier Applied Science, 1 (1988) 194–204.

[42] S.J. Lawrence, H.T. Cao, An experimental study of the interface between brick and mortar, in: Proceedings 4th N Am Masonry Conference, Dublin, 1987: pp. 194–204.

[43] M.A. Hamad, I.A. Khattab, Effect of the combustion process on the structure of rice hull silica, Thermochim Acta 48 (1981) 343–349.

[44] F.M. Khalaf, New test for determination of masonry tensile bond strength, Journal of Materials in Civil Engineering 17 (2005) 725–732.

[45] P. Walker, Bond characteristics of earth block masonry, Journal of Materials in Civil Engineering 11 (1999) 249–256.

[46] H. Maljaee, B. Ghiassi, P.B. Lourenço, D. V. Oliveira, FRP-brick masonry bond degradation under hygrothermal conditions, Compos Struct 147 (2016) 143–154. https://doi.org/10.1016/j.compstruct.2016.03.037.

[47] P. Di Milano, Bond durability of FRP-concrete and FRCM-masonry joints under the effect of environmental conditions Doctoral Dissertation, (2021).

[48] H.A. Poornamazian, M. Izadinia, Prediction of compressive strength of brick columns confined with FRP, FRCM, and SRG system using GEP and ANN methods, Journal of Engineering Research 12 (2024) 42–55.

[49] S.M. Raoof, D.A. Bournas, Bond between TRM versus FRP composites and concrete at high temperatures, Compos B Eng 127 (2017) 150–165. https://doi.org/10.1016/j.compositesb.2017.05.064.

[50] N.H. Sadeghi, D. V. Oliveira, R.A. Silva, N. Mendes, M. Correia, H. Azizi-Bondarabadi, Experimental characterization of adobe vaults strengthened with a TRM-based compatible composite, Constr Build Mater 271 (2021) 121568. https://doi.org/10.1016/j.conbuildmat.2020.121568.

[51] A. Dalalbashi, B. Ghiassi, D. V. Oliveira, A multi-level investigation on the mechanical response of TRM-strengthened masonry, Materials and Structures/Materiaux et Constructions 54 (2021) 1–19. https://doi.org/10.1617/s11527-021-01817-4.

[52] G. Cai, K.D. Tsavdaridis, A. Si Larbi, P. Purnell, A simplified design approach for predicting the flexural behavior of TRM-strengthened RC beams under cyclic loads, Constr Build Mater 285 (2021) 122799. https://doi.org/10.1016/j.conbuildmat.2021.122799.

[53] H. Berg, H. Thiesies, N. Billström, Low-cost TRM technologies for phased array radars, Int J Microw Wirel Technol 1 (2009) 369–375. https://doi.org/10.1017/S1759078709990304.

[54] K. Audomvongseree, A. Yokoyama, S.C. Verma, Y. Nakachi, A Novel TRM Calculation Method by Probabilistic Concept, IEEJ Transactions on Power and Energy 124 (2004) 1400–1407. https://doi.org/10.1541/ieejpes.124.1400.

[55] N.A. Resketi, V. Toufigh, Enhancement of brick-mortar shear bond strength using environmental friendly mortars, Constr Build Mater 195 (2019). https://doi.org/10.1016/j.conbuildmat.2018.10.118.

[56] K. Toska, F. Faleschini, FRCM-confined concrete: Monotonic vs. Cyclic axial loading, Compos Struct 268 (2021) 113931. https://doi.org/10.1016/j.compstruct.2021.113931.

[57] K. Toska, F. Faleschini, FRCM-confined concrete: Monotonic vs. Cyclic axial loading, Compos Struct 268 (2021) 113931. https://doi.org/10.1016/j.compstruct.2021.113931.

[58] L. Ombres, Structural performances of PBO FRCM-strengthened RC beams, Proceedings of the Institution of Civil Engineers: Structures and Buildings 164 (2011) 265–272. https://doi.org/10.1680/stbu.2011.164.4.265.

[59] E. Franzoni, C. Gentilini, M. Santandrea, C. Carloni, Effects of rising damp and salt crystallization cycles in FRCM-masonry interfacial debonding: Towards an accelerated laboratory test method, Constr Build Mater 175 (2018) 225–238. https://doi.org/https://doi.org/10.1016/j.conbuildmat.2018.04.164.

[60] F. Micelli, G. Maddaloni, F. Longo, A. Prota, Axial Stress–Strain Model for FRCM Confinement of Masonry Columns, Journal of Composites for Construction 25 (2021) 04020078. https://doi.org/10.1061/(asce)cc.1943-5614.0001089.

[61] 2019 Gustavo Tumialan, FRP Composites for Masonry Retrofitting, Structure Magazine 53 (2019) 12–14.

[62] L.N. Koutas, Z. Tetta, D.A. Bournas, T.C. Triantafillou, Strengthening of Concrete Structures with Textile Reinforced Mortars: State-of-the-Art Review, Journal of Composites for Construction 23 (2019) 03118001. https://doi.org/10.1061/(asce)cc.1943-5614.0000882.

[63] G. de Felice, S. De Santis, L. Garmendia, B. Ghiassi, P. Larrinaga, P.B. Lourenço, D. V. Oliveira, F. Paolacci, C.G. Papanicolaou, Mortar-based systems for externally bonded strengthening of masonry, Materials and Structures/Materiaux et Constructions 47 (2014) 2021–2037. https://doi.org/10.1617/s11527-014-0360-1.

[64] Z. Dong, M. Deng, C. Zhang, Y. Zhang, H. Sun, Tensile behavior of glass textile reinforced mortar (TRM) added with short PVA fibers, Constr Build Mater 260 (2020) 119897. https://doi.org/10.1016/j.conbuildmat.2020.119897.

[65] N. Azimi, A. Dalalbashi, D.V. Oliveira, B. Ghiassi, P.B. Lourenço, Tensile behavior of textile-reinforced mortar: Influence of the number of layers and their arrangement, Key Eng Mater 916 (2022) 91–97. https://doi.org/10.4028/p-m6x658.

[66] M. Canestri, F. Ferretti, C. Mazzotti, Glass fibre-based FRCM systems under mild temperature exposures, Journal of Building Engineering (2025) 112072.

[67] G. Karanikoloudis, J.B. Serra, P.B. Lourenço, REPAIR OF PIERS AND SPANDREL MASONRY ASSEMBLIES WITH GROUTING AND FRCM SYSTEMS: AN EXPERIMENTAL AND ANALYTICAL STUDY, Journal of Building Engineering (2025) 112192.

[68] R. Joseph, A. Mwafy, M.S. Alam, Shake-table testing and numerical simulation to select the FRCM retrofit solution for flexure/shear deficient RC frames, Journal of Building Engineering 69 (2023) 106248.

[69] C.G. Papanicolaou, T.C. Triantafillou, K. Karlos, M. Papathanasiou, Textile-reinforced mortar (TRM) versus FRP as strengthening material of URM walls: In-plane cyclic loading, Materials and Structures/Materiaux et Constructions 40 (2007) 1081–1097. https://doi.org/10.1617/s11527-006-9207-8.

[70] C. Carloni, S. Verre, L.H. Sneed, L. Ombres, Open issues on the investigation of PBO FRCM-Concrete debonding, Compos Struct 299 (2022) 116062. https://doi.org/10.1016/j.compstruct.2022.116062.

[71] G.P. Lignola, C. Caggegi, F. Ceroni, S. De Santis, P. Krajewski, P.B. Lourenço, M. Morganti, C. (Corina) Papanicolaou, C. Pellegrino, A. Prota, L. Zuccarino, Performance assessment of basalt

FRCM for retrofit applications on masonry, Compos B Eng 128 (2017) 1–18. https://doi.org/10.1016/j.compositesb.2017.05.003.

[72] X. Wang, C.C. Lam, V.P. Iu, Bond behaviour of steel-TRM composites for strengthening masonry elements: Experimental testing and numerical modelling, Constr Build Mater 253 (2020) 119157. https://doi.org/10.1016/j.conbuildmat.2020.119157.

[73] A. Younis, U. Ebead, Bond characteristics of different FRCM systems, Constr Build Mater 175 (2018) 610–620. https://doi.org/10.1016/j.conbuildmat.2018.04.216.

[74] F. Roscini, M. Guadagnini, Bond Behavior of Steel Cords Embedded in Inorganic Mortars, Materials 15 (2022). https://doi.org/10.3390/ma15155125.

[75] T. D'Antino, C. Papanicolaou, Mechanical characterization of textile reinforced inorganic-matrix composites, Compos B Eng 127 (2017) 78–91. https://doi.org/10.1016/j.compositesb.2017.02.034.

[76] C.G. Papanicolaou, Textile Fibre Composites in Civil Engineering, 2016. http://www.sciencedirect.com/science/article/pii/B9781782424468000112.

[77] G.P. Lignola, C. Caggegi, F. Ceroni, S. De Santis, P. Krajewski, P.B. Lourenço, M. Morganti, C. (Corina) Papanicolaou, C. Pellegrino, A. Prota, L. Zuccarino, Performance assessment of basalt FRCM for retrofit applications on masonry, Compos B Eng 128 (2017) 1–18. https://doi.org/10.1016/j.compositesb.2017.05.003.

[78] Z. Dong, M. Deng, J. Dai, S. Song, Flexural strengthening of RC slabs using textile reinforced mortar improved with short PVA fibers, Constr Build Mater 304 (2021) 124613. https://doi.org/10.1016/j.conbuildmat.2021.124613.

[79] C.C. Lam, X. Wang, Z. Zhang, Y. Zhu, Experimental and numerical investigations of the tensile behaviour of steel-TRM prepared with recycled glass sands and lime, Constr Build Mater 280 (2021) 122512. https://doi.org/10.1016/j.conbuildmat.2021.122512.

[80] P. Sadrolodabaee, A. de la Fuente, M. Ardanuy, J. Claramunt, Mechanical performance of aged cement-based matrices reinforced with recycled aramid textile nonwoven fabric: Comparison with other FRCMs, Case Studies in Construction Materials 20 (2024) e02994. https://doi.org/https://doi.org/10.1016/j.cscm.2024.e02994.

[81] G.P. Lignola, C. Caggegi, F. Ceroni, S. De Santis, P. Krajewski, P.B. Lourenço, M. Morganti, C. (Corina) Papanicolaou, C. Pellegrino, A. Prota, L. Zuccarino, Performance assessment of basalt FRCM for retrofit applications on masonry, Compos B Eng 128 (2017) 1–18. https://doi.org/10.1016/j.compositesb.2017.05.003.

[82] A. Younis, U. Ebead, K. Shrestha, Tensile characterization of multi-ply fabric-reinforced cementitious matrix strengthening systems, Structural Concrete 21 (2020) 713–723. https://doi.org/10.1002/suco.201900076.

[83] P. Meriggi, C. Caggegi, A. Gabor, G. de Felice, Shear-compression tests on stone masonry walls strengthened with basalt textile reinforced mortar (TRM), Constr Build Mater 316 (2022) 125804. https://doi.org/10.1016/j.conbuildmat.2021.125804.

[84] M. Messori, A. Nobili, C. Signorini, A. Sola, Mechanical performance of epoxy coated AR-glass fabric Textile Reinforced Mortar: Influence of coating thickness and formulation, Compos B Eng 149 (2018) 135–143.

[85] F. Bompadre, J. Donnini, Fabric-Reinforced Cementitious Matrix (FRCM) Carbon Yarns with Different Surface Treatments Embedded in a Cementitious Mortar: Mechanical and Durability Studies, Materials 15 (2022). https://doi.org/10.3390/ma15113927.

[86] D. Arboleda, F.G. Carozzi, A. Nanni, C. Poggi, Testing procedures for the uniaxial tensile characterization of fabric-reinforced cementitious matrix composites, Journal of Composites for Construction 20 (2016) 1–11. https://doi.org/10.1061/(ASCE)CC.1943-5614.0000626.

[87] P. Larrinaga, C. Chastre, H.C. Biscaia, J.T. San-José, Experimental and numerical modeling of basalt textile reinforced mortar behavior under uniaxial tensile stress, Mater Des 55 (2014) 66–74. https://doi.org/10.1016/j.matdes.2013.09.050.

[88] G. de Felice, M.A. Aiello, C. Caggegi, F. Ceroni, S. De Santis, E. Garbin, N. Gattesco, Ł. Hojdys, P. Krajewski, A. Kwiecień, M. Leone, G.P. Lignola, C. Mazzotti, D. Oliveira, C. Papanicolaou, C. Poggi, T. Triantafillou, M.R. Valluzzi, A. Viskovic, Recommendation of RILEM Technical Committee 250-CSM: Test method for Textile Reinforced Mortar to substrate bond characterization, Materials and Structures/Materiaux et Constructions 51 (2018) 1–9. https://doi.org/10.1617/s11527-018-1216-x.

[89] C. Caggegi, F.G. Carozzi, S. De Santis, F. Fabbrocino, F. Focacci, Ł. Hojdys, E. Lanoye, L. Zuccarino, Experimental analysis on tensile and bond properties of PBO and aramid fabric reinforced cementitious matrix for strengthening masonry structures, Compos B Eng 127 (2017) 175–195. https://doi.org/10.1016/j.compositesb.2017.05.048.

[90] M. Leone, M.A. Aiello, A. Balsamo, F.G. Carozzi, F. Ceroni, M. Corradi, M. Gams, E. Garbin, N. Gattesco, P. Krajewski, C. Mazzotti, D. Oliveira, C. Papanicolaou, G. Ranocchiai, F. Roscini, D. Saenger, Glass fabric reinforced cementitious matrix: Tensile properties and bond performance on masonry substrate, Compos B Eng 127 (2017) 196–214. https://doi.org/10.1016/j.compositesb.2017.06.028.

[91] G. de Felice, T. D'Antino, S. De Santis, P. Meriggi, F. Roscini, Lessons Learned on the Tensile and Bond Behavior of Fabric Reinforced Cementitious Matrix (FRCM) Composites, Front Built Environ 6 (2020) 1–15. https://doi.org/10.3389/fbuil.2020.00005.

[92] M. Malena, M. Sangirardi, G. de Felice, Steel Reinforced Grout under uniaxial load: Experimental evidences and numerical modelling, Constr Build Mater 227 (2019) 116808. https://doi.org/10.1016/j.conbuildmat.2019.116808.

[93] B. Ghiassi, D. V. Oliveira, V. Marques, E. Soares, H. Maljaee, Multi-level characterization of steel reinforced mortars for strengthening of masonry structures, Mater Des 110 (2016) 903–913. https://doi.org/10.1016/j.matdes.2016.08.034.

[94] K. Al-Lami, T. D'Antino, P. Colombi, Durability of fabric-reinforced cementitious matrix (FRCM) composites: A review, Applied Sciences (Switzerland) 10 (2020). https://doi.org/10.3390/app10051714.

[95] R. Contamine, A. Junes, A. Si Larbi, Tensile and in-plane shear behaviour of textile reinforced concrete: Analysis of a new multiscale reinforcement, Constr Build Mater 51 (2014) 405–413. https://doi.org/10.1016/j.conbuildmat.2013.10.084.

[96] A. Si Larbi, R. Contamine, P. Hamelin, TRC and hybrid solutions for repairing and/or strengthening reinforced concrete beams, Eng Struct 45 (2012) 12–20. https://doi.org/10.1016/j.engstruct.2012.06.002.

[97] X. Wang, C.C. Lam, B.C. Sun, T. Noguchi, V.P. Iu, Effect of curing environment on the tensile behaviour of FRCM composites, Constr Build Mater 238 (2020) 117729. https://doi.org/10.1016/j.conbuildmat.2019.117729.

[98] M. Saidi, A. Gabor, Experimental analysis and analytical modelling of the textile/matrix interface shear stress in textile reinforced cementitious matrix composites, Compos Part A Appl Sci Manuf 135 (2020) 105961. https://doi.org/10.1016/j.compositesa.2020.105961.

[99] O. Homoro, M. Michel, T.N. Baranger, Dry mineral pre-impregnation for enhancing the properties of glass FRCM composites, Constr Build Mater 263 (2020) 120597. https://doi.org/10.1016/j.conbuildmat.2020.120597.

[100] J. Donnini, V. Corinaldesi, A. Nanni, Mechanical properties of FRCM using carbon fabrics with different coating treatments, Compos B Eng 88 (2016) 220–228. https://doi.org/10.1016/j.compositesb.2015.11.012.

[101] C. Signorini, A. Nobili, Targeting functionalised carbon nanotubes at the interphase of Textile Reinforced Mortar (TRM) composites, Compos Part A Appl Sci Manuf 144 (2021) 106330. https://doi.org/10.1016/j.compositesa.2021.106330.

[102] N. Trochoutsou, M. Di Benedetti, K. Pilakoutas, M. Guadagnini, Bond of Flax Textile-Reinforced Mortars to Masonry, Constr Build Mater 284 (2021) 122849. https://doi.org/10.1016/j.conbuildmat.2021.122849.

[103] N. Lior, G. Erez, P. Alva, Tensile behavior of fabric-cement-based composites reinforced with non-continuous load bearing yarns, Constr Build Mater 236 (2020) 117432. https://doi.org/10.1016/j.conbuildmat.2019.117432.

[104] N. Trochoutsou, M. Di Benedetti, K. Pilakoutas, M. Guadagnini, Mechanical Characterisation of Flax and Jute Textile-Reinforced Mortars, Constr Build Mater 271 (2021) 121564. https://doi.org/10.1016/j.conbuildmat.2020.121564.

[105] M.A. Aiello, F. Bencardino, A. Cascardi, T. D'Antino, M. Fagone, I. Frana, L. La Mendola, G.P. Lignola, C. Mazzotti, F. Micelli, G. Minafò, A. Napoli, L. Ombres, M.C. Oddo, C. Poggi, A. Prota, G. Ramaglia, G. Ranocchiai, R. Realfonzo, S. Verre, Masonry columns confined with fabric reinforced cementitious matrix (FRCM) systems: A round robin test, Constr Build Mater 298 (2021) 123816. https://doi.org/10.1016/j.conbuildmat.2021.123816.

[106] F. Ferretti, C. Mazzotti, FRCM/SRG strengthened masonry in diagonal compression: experimental results and analytical approach proposal, Constr Build Mater 283 (2021) 122766. https://doi.org/10.1016/j.conbuildmat.2021.122766.

[107] M. Angiolilli, A. Gregori, S. Cattari, Performance of Fiber Reinforced Mortar coating for irregular stone masonry: Experimental and analytical investigations, Constr Build Mater 294 (2021) 123508. https://doi.org/10.1016/j.conbuildmat.2021.123508.

[108] P. Valeri, M. Fernàndez Ruiz, A. Muttoni, Tensile response of textile reinforced concrete, Constr Build Mater 258 (2020) 119517. https://doi.org/10.1016/j.conbuildmat.2020.119517.

[109] F. Zhou, H. Liu, Y. Du, L. Liu, D. Zhu, W. Pan, Uniaxial tensile behavior of carbon textile reinforced mortar, Materials 12 (2019). https://doi.org/10.3390/ma12030374.

[110] J. Donnini, F. Bompadre, V. Corinaldesi, Tensile behavior of a glass FRCM system after different environmental exposures, Processes 8 (2020). https://doi.org/10.3390/pr8091074.

[111] S. De Santis, G. De Felice, Tensile behaviour of mortar-based composites for externally bonded reinforcement systems, Compos B Eng 68 (2015) 401–413. https://doi.org/10.1016/j.compositesb.2014.09.011.

[112] G. Loreto, S. Babaeidarabad, L. Leardini, A. Nanni, RC beams shear-strengthened with fabric-reinforced-cementitious-matrix (FRCM) composite, International Journal of Advanced Structural Engineering 7 (2015) 341–352. https://doi.org/10.1007/s40091-015-0102-9.

[113] M.T. De Risi, A. Furtado, H. Rodrigues, J. Melo, G.M. Verderame, A. António, H. Varum, G. Manfredi, Experimental analysis of strengthening solutions for the out-of-plane collapse of masonry infills in RC structures through textile reinforced mortars, Eng Struct 207 (2020) 110203. https://doi.org/10.1016/j.engstruct.2020.110203.

[114] A.S. Calabrese, T. D'Antino, P. Colombi, Experimental and analytical investigation of PBO FRCM-concrete bond behavior using direct and indirect shear test set-ups, Compos Struct 267 (2021) 113672. https://doi.org/10.1016/j.compstruct.2021.113672.

[115] Y. Du, M. Zhang, F. Zhou, D. Zhu, Experimental study on basalt textile reinforced concrete under uniaxial tensile loading, Constr Build Mater 138 (2017) 88–100. https://doi.org/10.1016/j.conbuildmat.2017.01.083.

[116] G. Minafò, M.C. Oddo, L. La Mendola, Formulation of a truss element for modelling the tensile response of FRCM strips, Constr Build Mater 315 (2021) 125576. https://doi.org/10.1016/j.conbuildmat.2021.125576.

[117] S. De Santis, G. De Felice, Tensile behaviour and durability of mortar-based strengthening systems with glass-aramid textiles, Key Eng Mater 624 (2015) 346–353. https://doi.org/10.4028/www.scientific.net/KEM.624.346.

[118] T. Trapko, K. Rogalski, M. Musiał, L. Ombres, Effectiveness of Concrete Elements Strengthening through PBO-FRCM Confinement with Various Types of Anchorage, Journal of Materials in Civil Engineering 33 (2021) 04020409. https://doi.org/10.1061/(asce)mt.1943-5533.0003510.

[119] F.G. Carozzi, A. Bellini, T. D'Antino, G. de Felice, F. Focacci, Ł. Hojdys, L. Laghi, E. Lanoye, F. Micelli, M. Panizza, C. Poggi, Experimental investigation of tensile and bond properties of Carbon-FRCM composites for strengthening masonry elements, Compos B Eng 128 (2017) 100–119. https://doi.org/10.1016/j.compositesb.2017.06.018.

[120] S. De Santis, F. Ceroni, G. de Felice, M. Fagone, B. Ghiassi, A. Kwiecień, G.P. Lignola, M. Morganti, M. Santandrea, M.R. Valluzzi, A. Viskovic, Round Robin Test on tensile and bond behaviour of Steel Reinforced Grout systems, Compos B Eng 127 (2017) 100–120. https://doi.org/10.1016/j.compositesb.2017.03.052.

[121] S.G. Kim, J.K. Park, D.J. Kim, Direct tensile responses of aramid fiber reinforced cementitious composites and textile reinforced cementitious composites with 3D spacer fabric at high strain rates, Constr Build Mater 168 (2018) 232–243. https://doi.org/10.1016/j.conbuildmat.2018.02.136.

[122] P. Larrinaga, C. Chastre, J.T. San-José, L. Garmendia, Non-linear analytical model of composites based on basalt textile reinforced mortar under uniaxial tension, Compos B Eng 55 (2013) 518–527. https://doi.org/10.1016/j.compositesb.2013.06.043.

[123] M. Tekieli, S. De Santis, G. de Felice, A. Kwiecień, F. Roscini, Application of Digital Image Correlation to composite reinforcements testing, Compos Struct 160 (2017) 670–688. https://doi.org/10.1016/j.compstruct.2016.10.096.

[124] R. Contamine, A. Si Larbi, Development of a textile reinforced concrete (TRC) to retrofit reinforced concrete structures, European Journal of Environmental and Civil Engineering 20 (2016) 626–642. https://doi.org/10.1080/19648189.2015.1030089.

[125] K. Kong, Z. Mesticou, M. Michel, A. Si Larbi, A. Junes, Comparative characterization of the durability behaviour of textile-reinforced concrete (TRC) under tension and bending, Compos Struct 179 (2017) 107–123. https://doi.org/10.1016/j.compstruct.2017.07.030.

[126] N. Trochoutsou, M. Di Benedetti, K. Pilakoutas, M. Guadagnini, Bond of Flax Textile-Reinforced Mortars to Masonry, Constr Build Mater 284 (2021) 122849. https://doi.org/10.1016/j.conbuildmat.2021.122849.

[127] N. Trochoutsou, M. Di Benedetti, K. Pilakoutas, M. Guadagnini, Bond of Flax Textile-Reinforced Mortars to Masonry, Constr Build Mater 284 (2021) 122849. https://doi.org/10.1016/j.conbuildmat.2021.122849.

[128] L.A.S. Kouris, T.C. Triantafillou, Design Methods for Strengthening Masonry Buildings Using Textile-Reinforced Mortar, Journal of Composites for Construction 23 (2019) 04018070. https://doi.org/10.1061/(asce)cc.1943-5614.0000906.

[129] C.-D. 200, Guide for the design and construction of an externally bonded frp system for strengthening existing structures, 2004.

[130] CNR-DT215, Istruzioni per la progettazione, l'esecuzione ed il controllo di interventi di consolidamento statico mediante l'utilizzo di compositi fibrorinforzati a matrice inorganica, in italian, Technical document, 2018.

[131] AC434, Acceptance criteria for masonry and concrete strengthening using fiber-reinforced cementitious matrix (frcm) composite systems, ICCEvaluation Service, Whittier, CA, 2013.

[132] ACI440, Guide for the design and construction of externally bonded fiberreinforced polymer systems for strengthening unreinforced masonry structures, Technical document, 2013.

[133] ACI Committee 549.4R-13, Guide to Design and Construction of Externally Bonded Fabric-Reinforced Cementitous Matrix (FRCM) Systems for Repair and Strengthening Concrete Structures, ACI Webinar Notes (2013) 1–18.

[134] ACI Committee 549, ACI 549.4R-20 Guide to design and construction of externally bonded fabric-reinforced cementitious matrix and steel-reinforced grout systems for repair and strengthening of concrete structures, 2020.

[135] A. 549.6R-20, Guide to Design and Construction of Externally Bonded Fabric-Reinforced Cementitious Matrix (FRCM) and Steel-Reinforced Grout (SRG) Systems for Repair and Strengthening Masonry Structures., (2020).

[136] C. Caggegi, E. Lanoye, K. Djama, A. Bassil, A. Gabor, Tensile behaviour of a basalt TRM strengthening system: Influence of mortar and reinforcing textile ratios, Compos B Eng 130 (2017) 90–102. https://doi.org/10.1016/j.compositesb.2017.07.027.

[137] M. De Munck, M. El Kadi, E. Tsangouri, J. Vervloet, S. Verbruggen, J. Wastiels, T. Tysmans, O. Remy, Influence of environmental loading on the tensile and cracking behaviour of textile reinforced cementitious composites, Constr Build Mater 181 (2018) 325–334. https://doi.org/10.1016/j.conbuildmat.2018.06.045.

[138] T. Tlaiji, X.H. Vu, E. Ferrier, A. Si Larbi, Thermomechanical behaviour and residual properties of textile reinforced concrete (TRC) subjected to elevated and high temperature loading:

Experimental and comparative study, Compos B Eng 144 (2018) 99–110. https://doi.org/10.1016/j.compositesb.2018.02.022.

[139] J. D'Anna, G. Amato, J.F. Chen, G. Minafò, L. La Mendola, Experimental investigation on BFRCM confinement of masonry cylinders and comparison with BFRP system, Constr Build Mater 297 (2021) 123671. https://doi.org/10.1016/j.conbuildmat.2021.123671.

[140] N. Azimi, K. Schollbach, D. V Oliveira, P.B. Lourenço, Effect of Exposure to Alkaline Environment on the Mechanical Properties of TRM Composites, Journal of Building Engineering (2025) 112468.

[141] H. Schreier, J.-J. Orteu, M.A. Sutton, Image Correlation for Shape, Motion and Deformation Measurements, Springer US, n.d. https://doi.org/10.1007/978-0-387-78747-3.

[142] D.M. Linn, D.G. Aggelis, E. Tsangouri, Single-lap shear tests of textile reinforced mortar retrofit systems bonded to masonry: revealing the fracture progress by digital image correlation and acoustic emission, Mater Struct 55 (2022). https://doi.org/10.1617/s11527-021-01850-3.

[143] A. Bilotta, F. Ceroni, G.P. Lignola, A. Prota, Use of DIC technique for investigating the behaviour of FRCM materials for strengthening masonry elements, Compos B Eng 129 (2017) 251–270. https://doi.org/10.1016/j.compositesb.2017.05.075.

[144] J. Lanas, J.L. Pérez Bernal, M.A. Bello, J.I. Alvarez, Mechanical properties of masonry repair dolomitic lime-based mortars, Cem Concr Res 36 (2006) 951–960. https://doi.org/10.1016/j.cemconres.2005.10.004.

[145] A. Dalalbashi, B. Ghiassi, D. V. Oliveira, Textile-to-mortar bond behaviour in lime-based textile reinforced mortars, Constr Build Mater 227 (2019) 116682. https://doi.org/10.1016/j.conbuildmat.2019.116682.

[146] T. D'Antino, A.S. Calabrese, C. Poggi, Experimental procedures for the mechanical characterization of composite reinforced mortar (CRM) systems for retrofitting of masonry structures, Materials and Structures/Materiaux et Constructions 53 (2020) 1–18. https://doi.org/10.1617/s11527-020-01529-1.

[147] M.J. Ahmed, K. Lambrechts, X. Ling, K. Schollbach, H.J.H. Brouwers, Effect of hydroxide, carbonate, and sulphate anions on the β-dicalcium silicate hydration rate, Cem Concr Res 173 (2023). https://doi.org/10.1016/j.cemconres.2023.107302.

[148] M. Shubaili, A. Elawadi, S. Orton, Y. Tian, Time-Dependent Behavior of Reinforced Concrete Beams under High Sustained Loads, Applied Sciences 12 (2022). https://doi.org/10.3390/app12084015.

[149] M.J. Watts, A. Amin, R.I. Gilbert, W. Kaufmann, Behavior of fiber reinforced concrete members under sustained axial/flexural load, Structural Concrete 21 (2020) 1441–1457. https://doi.org/https://doi.org/10.1002/suco.201900227.

[150] J. Yang, T. Guo, A. Li, Experimental investigation on long-term behavior of prestressed concrete beams under coupled effect of sustained load and corrosion, Advances in Structural Engineering 23 (2020) 2587–2596. https://doi.org/10.1177/1369433220919067.

[151] N. Azimi, D. V Oliveira, K. Schollbach, P.B. Lourenço, Effect of Alkaline Environment on the Bond Behavior of TRM Composites Through Single-lap Shear Tests, in: MATEC Web of Conferences, EDP Sciences, 2024: p. 5014.

[152] A.S. Calabrese, T. D'antino, P. Colombi, C. Poggi, Long-Term Behavior of PBO FRCM and Comparison with Other Inorganic-Matrix Composites, Materials 15 (2022). https://doi.org/10.3390/ma15093281.

[153] J. Donnini, Durability of glass FRCM systems: Effects of different environments on mechanical properties, Compos B Eng 174 (2019) 107047. https://doi.org/10.1016/j.compositesb.2019.107047.

[154] H. Akbari Hadad, A. Nanni, Fatigue Behavior of FRCM-Strengthened RC Beams, Journal of Composites for Construction 24 (2020) 1–10. https://doi.org/10.1061/(asce)cc.1943-5614.0001084.

[155] A. Bonati, A. Franco, L. Schiavi, A. Occhiuzzi, Experimental investigation of the long-term behaviour of fabric reinforced matrix systems, in: Brick and Block Masonry-From Historical to Sustainable Masonry, CRC Press, 2020: pp. 364–369.

[156] K. Li, Durability Design of Concrete Structures, John Wiley & Sons, 2016. https://doi.org/10.1002/9781118910108.

[157] F. Micelli, A. Franco, R. Greppi, M.A. Aiello, Durability of CRM reinforcements, Life-Cycle of Structures and Infrastructure Systems - Proceedings of the 8th International Symposium on Life-Cycle Civil Engineering, IALCCE 2023 (2023) 2820–2827. https://doi.org/10.1201/9781003323020-343.

[158] R.D. Toledo Filho, F. de A. Silva, E.M.R. Fairbairn, J. de A.M. Filho, Durability of compression molded sisal fiber reinforced mortar laminates, Constr Build Mater 23 (2009) 2409–2420. https://doi.org/10.1016/j.conbuildmat.2008.10.012.

[159] A. Izaguirre, J. Lanas, J.I. Álvarez, Ageing of lime mortars with admixtures: Durability and strength assessment, Cem Concr Res 40 (2010) 1081–1095. https://doi.org/10.1016/j.cemconres.2010.02.013.

[160] G. Crevello, I. Matteini, P. Noyce, Durability Modeling to Determine Long Term Performance of Historic Concrete Structures, in: R. Aguilar, D. Torrealva, S. Moreira, M.A. Pando, L.F. Ramos (Eds.), Structural Analysis of Historical Constructions, Springer International Publishing, Cham, 2019: pp. 1904–1913.

[161] J. Donnini, Durability of glass FRCM systems: Effects of different environments on mechanical properties, Compos B Eng 174 (2019) 107047. https://doi.org/10.1016/j.compositesb.2019.107047.

[162] J. Donnini, Durability of glass FRCM systems: Effects of different environments on mechanical properties, Compos B Eng 174 (2019) 107047. https://doi.org/10.1016/j.compositesb.2019.107047.

[163] C.M. Pederneiras, R. Veiga, J. de Brito, Incorporation of natural fibres in rendering mortars for the durability of walls, Infrastructures (Basel) 6 (2021). https://doi.org/10.3390/infrastructures6060082.

[164] B.Y. Pekmezci, E. Arabaci, C. Ustundag, Freeze-thaw durability of lime based FRCM systems for strengthening historical masonry, Key Eng Mater 817 KEM (2019) 174–181. https://doi.org/10.4028/www.scientific.net/KEM.817.174.

[165] N. Azimi, D. V. Oliveira, K. Schollbach, P.B. Lourenço, Effect of Acidic Environment on the Bond Behavior of TRM Composites Through Single-Lap Shear Tests, Springer Nature Switzerland, 2025. https://doi.org/10.1007/978-3-031-73310-9_47.

[166] N. Azimi, D. V Oliveira, K. Schollbach, P.B. Lourenço, Effect of Acidic Environment on the Bond Behavior of TRM Composites Through Single-Lap Shear Tests, in: G. Milani, B. Ghiassi (Eds.), 18th International Brick and Block Masonry Conference, Springer Nature Switzerland, Cham, 2025: pp. 666–679.

[167] N. Azimi, K. Schollbach, D. V. Oliveira, P.B. Lourenço, Effect of acidic environment exposure on mechanical properties of TRM composites, Constr Build Mater 438 (2024) 112468. https://doi.org/10.1016/j.conbuildmat.2024.137142.

[168] J. Donnini, F. Bompadre, V. Corinaldesi, Tensile behavior of a glass FRCM system after different environmental exposures, Processes 8 (2020). https://doi.org/10.3390/pr8091074.

[169] E. Franzoni, C. Gentilini, M. Santandrea, C. Carloni, Effects of rising damp and salt crystallization cycles in FRCM-masonry interfacial debonding: Towards an accelerated laboratory test method, Constr Build Mater 175 (2018) 225–238. https://doi.org/10.1016/j.conbuildmat.2018.04.164.

[170] M. Alma'aitah, B. Ghiassi, A. Dalalbashi, Durability of textile reinforced concrete: Existing knowledge and current gaps, Applied Sciences (Switzerland) 11 (2021). https://doi.org/10.3390/app11062771.

[171] J. Orlowsky, M. Raupach, Durability model for AR-glass fibres in textile reinforced concrete, Materials and Structures/Materiaux et Constructions 41 (2008) 1225–1233. https://doi.org/10.1617/s11527-007-9321-2.

[172] E. Franzoni, C. Gentilini, M. Santandrea, S. Zanotto, C. Carloni, Durability of steel FRCM-masonry joints: effect of water and salt crystallization, Materials and Structures/Materiaux et Constructions 50 (2017) 1–16. https://doi.org/10.1617/s11527-017-1070-2.

[173] G. Ferrara, M. Pepe, E. Martinelli, R.D. Tolêdo Filho, Tensile behavior of flax textile reinforced lime-mortar: Influence of reinforcement amount and textile impregnation, Cem Concr Compos 119 (2021). https://doi.org/10.1016/j.cemconcomp.2021.103984.

[174] T. D'Antino, C. (Corina) Papanicolaou, Comparison between different tensile test set-ups for the mechanical characterization of inorganic-matrix composites, Constr Build Mater 171 (2018) 140–151. https://doi.org/10.1016/j.conbuildmat.2018.03.041.

[175] A. Bellini, M.A. Aiello, F. Bencardino, C.B. de Carvalho Bello, G. Castori, A. Cecchi, F. Ceroni, M. Corradi, T. D'Antino, S. De Santis, M. Fagone, G. de Felice, M. Leone, G.P. Lignola, A. Napoli, M. Nisticò, C. Poggi, A. Prota, G. Ranocchiai, R. Realfonzo, E. Sacco, C. Mazzotti, Influence of different set-up parameters on the bond behavior of FRCM composites, Constr Build Mater 308 (2021). https://doi.org/10.1016/j.conbuildmat.2021.124964.

[176] M. Butler, V. Mechtcherine, S. Hempel, Durability of textile reinforced concrete made with AR glass fibre: Effect of the matrix composition, Materials and Structures/Materiaux et Constructions 43 (2010) 1351–1368. https://doi.org/10.1617/s11527-010-9586-8.

[177] D. Arboleda, S. Babaeidarabad, C. DiLaurenzio Hays, A. Nanni, Durability of Fabric Reinforced Cementitious Matrix (FRCM) composites, Proceedings of the 7th International Conference on FRP Composites in Civil Engineering, CICE 2014 (2014).

[178] A. Nobili, Durability assessment of impregnated Glass Fabric Reinforced Cementitious Matrix (GFRCM) composites in the alkaline and saline environments, Constr Build Mater 105 (2016) 465–471. https://doi.org/10.1016/j.conbuildmat.2015.12.173.

[179] A. Alatawna, L. Nahum, R. Sripada, M. Birenboim, O. Regev, A. Peled, Textile-reinforced mortar: Durability in salty environment, Cem Concr Compos 130 (2022) 104534. https://doi.org/10.1016/j.cemconcomp.2022.104534.

[180] S. Graus, G. Vasconcelos, C. Palha, Experimental characterization of the deterioration of masonry materials due to wet and dry and salt crystallization cycles, in: Structural Analysis of Historical Constructions: An Interdisciplinary Approach, Springer, 2019: pp. 687–695.

[181] C. Gentilini, E. Franzoni, S. Bandini, L. Nobile, Effect of salt crystallisation on the shear behaviour of masonry walls: An experimental study, Constr Build Mater 37 (2012) 181–189. https://doi.org/https://doi.org/10.1016/j.conbuildmat.2012.07.086.

[182] C. Tedeschi, S. Perego, P. Milano, Study on local effects of aggressive environmental conditions on masonry strengthened with FRCM, Brick and Block Masonry. Trends, Innovation and Challehgers; Modena, CF, Da Porto, MRV, Eds (2016) 441–449.

[183] V. Bertolli, A. Cagnoni, A.S. Calabrese, P. Colombi, T. D'Antino, Effect of salt crystallization on the bond behavior of glass FRCM-masonry joints, in: Life-Cycle of Structures and Infrastructure Systems, CRC Press, 2023: pp. 2804–2811.

[184] E.O. for Technical Approvals (EOTA), Guideline for European Technical Approval of Metal Injection Anchors for Use in Masonry, (2013). https://www.eota.eu/en-GB/content/etag-029/56/.

[185] A. International, Standard Test Method for Determining Tensile Breaking Strength of Glass Fiber Reinforcing Mesh for Use in Class PB Exterior Insulation and Finish Systems (EIFS), After Exposure to a Sodium Hydroxide Solution, (2002). https://www.astm.org/e2098-02.html.

[186] J.S. of Civil Engineers (JSCE), Recommendations for Upgrading of Concrete Structures with Use of Continuous Fiber Sheets, (2000). https://www.jsce.or.jp/committee/concrete/e/newsletter/newsletter01/recommendations.pdf.

[187] A. International, Standard Test Method for Alkali Resistance of Fiber Reinforced Polymer (FRP) Matrix Composite Bars Used in Concrete Construction, (2012). https://www.astm.org/d7705_d7705m-12.html.

[188] M. of Housing, U.-R.D. of the People's Republic of China, Standard for Test Methods of Long-term Performance and Durability of Ordinary Concrete, (2009). http://www.mohurd.gov.cn/wjfb/200906/t20090612_188098.html.

[189] A. Nobili, Durability assessment of impregnated Glass Fabric Reinforced Cementitious Matrix (GFRCM) composites in the alkaline and saline environments, Constr Build Mater 105 (2016) 465–471. https://doi.org/10.1016/j.conbuildmat.2015.12.173.

[190] S.J.C. Granneman, B. Lubelli, R.P.J. Van Hees, Lime mortar with mixed in crystallization modifiers to mitigate salt damage, in: Structural Analysis of Historical Constructions: Anamnesis, Diagnosis, Therapy, Controls, CRC Press, 2016: pp. 75–79.

[191] A.R.G. Azevedo, J. Alexandre, G.C. Xavier, E.B. Zanelato, M.T. Marvila, N.A. Cerqueira, B.C. Mendes, S.N. Monteiro, Study of durability of mortars with effluent sludge from paper industry exposed to salt spray, Minerals, Metals and Materials Series Part F8 (2018) 669–676. https://doi.org/10.1007/978-3-319-72484-3_71.

[192] G. Cardani, M.R. Valluzzi, M. Panizza, P. Girardello, L. Binda, Influence of salt crystallization on composites-to-masonry bond evaluated on site by pull-off tests, Key Eng Mater 624 (2015) 338–345. https://doi.org/10.4028/www.scientific.net/KEM.624.338.

[193] E. Franzoni, M. Santandrea, C. Gentilini, A. Fregni, C. Carloni, The role of mortar matrix in the bond behavior and salt crystallization resistance of FRCM applied to masonry, Constr Build Mater 209 (2019) 592–605. https://doi.org/10.1016/j.conbuildmat.2019.03.059.

[194] Z. Shi, M.R. Geiker, B. Lothenbach, K. De Weerdt, S.F. Garzón, K. Enemark-Rasmussen, J. Skibsted, Friedel's salt profiles from thermogravimetric analysis and thermodynamic modelling of Portland cement-based mortars exposed to sodium chloride solution, Cem Concr Compos 78 (2017) 73–83. https://doi.org/https://doi.org/10.1016/j.cemconcomp.2017.01.002.

[195] J. Machovec, P. Reiterman, Influence of aggressive environment on the tensile properties of textile reinforced concrete, Acta Polytechnica 58 (2018) 245–252. https://doi.org/10.14311/AP.2018.58.0245.

[196] Z. Makhloufi, T. Bouziani, M. Hadjoudja, M. Bederina, Durability of limestone mortars based on quaternary binders subjected to sulfuric acid using drying-immersion cycles, Comput Chem Eng 71 (2014) 579–588. https://doi.org/10.1016/j.conbuildmat.2014.08.086.

[197] G. da Silva Munhoz, M.E. Gomes Dobrovolski, B.L. Nenevê, R.L. Dias, J.P. Godinho, M.H.F. de Medeiros, The influence of fly ash and neutral sodium silicate on concretes submitted to sulfuric acid attack, Eng Fail Anal 141 (2022) 1–15. https://doi.org/10.1016/j.engfailanal.2022.106673.

[198] A. Izaguirre, J. Lanas, J.I. Álvarez, Ageing of lime mortars with admixtures: Durability and strength assessment, Cem Concr Res 40 (2010) 1081–1095. https://doi.org/10.1016/j.cemconres.2010.02.013.

[199] A. Nobili, C. Signorini, On the effect of curing time and environmental exposure on impregnated Carbon Fabric Reinforced Cementitious Matrix (CFRCM) composite with design considerations, Composites Part B 112 (2017) 300–313. https://doi.org/10.1016/j.compositesb.2016.12.022.

[200] C. Signorini, A. Nobili, Comparing durability of steel reinforced grout (SRG) and textile reinforced mortar (TRM) for structural retrofitting, Mater Struct 54 (2021). https://doi.org/10.1617/s11527-021-01729-3.

[201] G. Di Ruocco, Basalt Fibers: the green material of the xxi-century, for a sustainable restoration of historical buildings, VITRUVIO - International Journal of Architectural Technology and Sustainability 2 (2016) 25–39. https://doi.org/10.4995/vitruvio-ijats.2016.6984.

[202] R.L. Jones, J. Stewart, The kinetics of corrosion of e-glass fibres in sulphuric acid, J Non Cryst Solids 356 (2010) 2433–2436. https://doi.org/10.1016/j.jnoncrysol.2010.07.062.

[203] J. Donnini, Durability of glass FRCM systems: Effects of different environments on mechanical properties, Compos B Eng 174 (2019) 107047. https://doi.org/10.1016/j.compositesb.2019.107047.

[204] F. Ceroni, A. Bonati, V. Galimberti, A. Occhiuzzi, Effects of environmental conditioning on the bond behavior of FRP and FRCM systems applied to concrete elements, J Eng Mech 144 (2018) 04017144. https://doi.org/10.1061/(ASCE)EM.1943-7889.0001375.

[205] D. Arboleda, S. Babaeidarabad, C.D. Hays, A. Nanni, Durability of fabric reinforced cementitious matrix (FRCM) composites, in: 7th. International Conference of FRP Composites in Civil Engineering (CICE 2014), Vancouver, 2014: pp. 1–6.

[206] C.H. Koh, F. Gauvin, K. Schollbach, H.J.H. Brouwers, Upcycling wheat and barley straws into sustainable thermal insulation: Assessment and treatment for durability, Resour Conserv Recycl 198 (2023) 107161. https://doi.org/10.1016/j.resconrec.2023.107161.

[207] J.C.O. Zepper, S.R. van der Laan, K. Schollbach, H.J.H. Brouwers, Reactivity of BOF slag under autoclaving conditions, Constr Build Mater 364 (2023) 129957. https://doi.org/10.1016/j.conbuildmat.2022.129957.

[208] F. Iucolano, B. Liguori, C. Colella, Fibre-reinforced lime-based mortars: A possible resource for ancient masonry restoration, Constr Build Mater 38 (2013) 785–789. https://doi.org/10.1016/j.conbuildmat.2012.09.050.

[209] A. Moropoulou, A.S. Cakmak, G. Biscontin, A. Bakolas, E. Zendri, Advanced Byzantine cement based composites resisting earthquake stresses: The crushed brick/lime mortars of Justinian's Hagia Sophia, Constr Build Mater 16 (2002) 543–552. https://doi.org/10.1016/S0950-0618(02)00005-3.

[210] P.R. Rossi-Doria, Mortars for restoration: Basic requirements and quality control, Mater Struct 19 (1986) 445–448. https://doi.org/10.1007/BF02472148.

[211] M.J. Mosquera, D. Benítez, S.H. Perry, Pore structure in mortars applied on restoration: Effect on properties relevant to decay of granite buildings, Cem Concr Res 32 (2002) 1883–1888. https://doi.org/10.1016/S0008-8846(02)00887-6.

[212] W.Y. Peen, C.K. Keong, O. Hassanshahi, Behaviour of hollow circular section with multiple perforations under compression, flexure and torsion, Latin American Journal of Solids and Structures 16 (2019) e169.

[213] J. Lanas, R. Sirera, J.I. Alvarez, Compositional changes in lime-based mortars exposed to different environments, Thermochim Acta 429 (2005) 219–226. https://doi.org/https://doi.org/10.1016/j.tca.2005.03.015.

[214] H.A. Khan, A. Castel, M.S.H. Khan, A.H. Mahmood, Durability of calcium aluminate and sulphate resistant Portland cement based mortars in aggressive sewer environment and sulphuric acid, Cem Concr Res 124 (2019) 105852. https://doi.org/https://doi.org/10.1016/j.cemconres.2019.105852.

[215] S.N.R.G. Pallapothu, R.K. Pancharathi, R. Janib, Predicting concrete strength through packing density using machine learning models, Eng Appl Artif Intell 126 (2023) 107177. https://doi.org/10.1016/j.engappai.2023.107177.

[216] B. Cheng, L. Mei, W.-J. Long, Q. Luo, J. Zhang, C. Xiong, Y. Shu, Z. Li, S. Gao, Data driven multi-objective design for low-carbon self-compacting concrete considering durability, J Clean Prod 450 (2024) 141947. https://doi.org/10.1016/j.jclepro.2024.141947.

[217] E. Asadi Shamsabadi, N. Roshan, S.A. Hadigheh, M.L. Nehdi, A. Khodabakhshian, M. Ghalehnovi, Machine learning-based compressive strength modelling of concrete incorporating waste marble powder, Constr Build Mater 324 (2022) 126592. https://doi.org/10.1016/j.conbuildmat.2022.126592.

[218] L.T.M. Dat, T.L. Dmitrieva, V.N. Duong, D.T.N. Canh, An Artificial intelligence approach for predicting compressive strength of eco-friendly concrete containing waste tire rubber, IOP Conf Ser Earth Environ Sci 612 (2020) 012029. https://doi.org/10.1088/1755-1315/612/1/012029.

[219] Md. Habibur Rahman Sobuz, M.H. Khan, Md. Kawsarul Islam Kabbo, A.H. Alhamami, F.S. Aditto, Md. Saziduzzaman Sajib, U. Johnson Alengaram, W. Mansour, N.Md.S. Hasan, S.D. Datta, A. Alam, Assessment of mechanical properties with machine learning modeling and durability, and microstructural characteristics of a biochar-cement mortar composite, Constr Build Mater 411 (2024) 134281. https://doi.org/10.1016/j.conbuildmat.2023.134281.

[220] Z. Chen, Application of machine learning boosting and bagging methods to predict compressive and flexural strength of marble cement mortar, Mater Today Commun 39 (2024) 108600. https://doi.org/10.1016/j.mtcomm.2024.108600.

[221] P. Ravikanth, T.J. Saravanan, K.I.S.A. Kabeer, Supervised data-driven approach to predict split tensile and flexural strength of concrete with marble waste powder, Cleaner Materials 11 (2024). https://doi.org/10.1016/j.clema.2024.100231.

[222] M. Hosseinzadeh, M. Dehestani, A. Hosseinzadeh, Exploring elastic properties of fly ash recycled aggregate concrete: Insights from multiscale modeling and machine learning, Structures 59 (2024). https://doi.org/10.1016/j.istruc.2023.105720.

[223] A. Taheri, J. Sobanjo, Civil Integrated Management (CIM) for Advanced Level Applications to Transportation Infrastructure: A State-of-the-Art Review, Infrastructures (Basel) 9 (2024). https://doi.org/10.3390/infrastructures9060090.

[224] A. Taheri, J. Sobanjo, Ensemble Learning Approach for Developing Performance Models of Flexible Pavement, Infrastructures (Basel) 9 (2024). https://doi.org/10.3390/infrastructures9050078.

[225] A.A. Taheri, A. Abdali, A. Maboudi, K. Mazlumi, Thermal behavior investigation of installation orientation and color effect on distribution transformers using E-TRM method and its effect on loading, Engineering Science and Technology, an International Journal 24 (2021) 348–359. https://doi.org/10.1016/j.jestch.2020.09.004.

[226] C. Signorini, A. Nobili, Comparing durability of steel reinforced grout (SRG) and textile reinforced mortar (TRM) for structural retrofitting, Mater Struct 54 (2021) 131. https://doi.org/10.1617/s11527-021-01729-3.

[227] R. Cao, J. Yang, G. Li, F. Liu, M. Niu, W. Wang, Resistance of the composite cementitious system of ordinary Portland/calcium sulfoaluminate cement to sulfuric acid attack, Constr Build Mater 329 (2022) 127171. https://doi.org/https://doi.org/10.1016/j.conbuildmat.2022.127171.

[228] S. Marathe, N. Szemiot-Jankowska, S. Kumar, M. Muthu, Degradation Potential of Metakaolin-Based Geopolymer Composites Immersed in Real and Simulated Acidic Environments, Sustainability 17 (2025). https://doi.org/10.3390/su17020468.

[229] J. Wang, B. Du, M. Shen, Y. Li, S. Yuan, Damage constitutive model and mechanical properties of a concrete limestone composite after acid corrosion, Sci Rep 15 (2025) 1868. https://doi.org/10.1038/s41598-024-83364-w.

[230] R. Hay, K. Celik, Enhancing carbonation of magnesium oxide (MgO) cement (RMC)-based composites with calcined limestone, CEMENT 9 (2022) 100037. https://doi.org/https://doi.org/10.1016/j.cement.2022.100037.

[231] C. Mariam Ninan, K.P. Ramaswamy, R. Sajeeb, Influence of acid replenishment and concentration on the degradation kinetics of cement mortar exposed to acetic acid, Mater Today Proc 65 (2022) 908–914. https://doi.org/https://doi.org/10.1016/j.matpr.2022.03.524.

[232] C. De Nardi, S. Sayadi, I. Mihai, A. Jefferson, Simulation of autogenous self-healing in lime-based mortars, Int J Numer Anal Methods Geomech 49 (2025) 359–375.

[233] J.A.D. Fernandes Neto, T.N. Sombra, V.G. Haach, M.R.S. Corrêa, Effects of post-fire curing on the residual mechanical behavior of cement-lime masonry mortars, Constr Build Mater 327 (2022) 126613. https://doi.org/https://doi.org/10.1016/j.conbuildmat.2022.126613.

[234] T. Cui, H. He, W. Yan, D. Zhou, Compression damage constitutive model of hybrid fiber reinforced concrete and its experimental verification, Constr Build Mater 264 (2020) 120026. https://doi.org/10.1016/j.conbuildmat.2020.120026.

[235] X.-B. Zuo, Z.-K. Zheng, X.-N. Li, Y.-X. Zou, L. Li, Mesoscale numerical simulation on the deterioration of cement-based materials under external sulfate attack, Eng Fail Anal 151 (2023) 107419. https://doi.org/https://doi.org/10.1016/j.engfailanal.2023.107419.

[236] Y. Pang, H. Wang, Q. Tang, L. Yang, Q. Wang, Enhancing cement mortar hydrophobicity against dry-wet cycling sulfate attack using stearic acid modified mica powder via high-temperature stirring, Constr Build Mater 441 (2024) 137556. https://doi.org/https://doi.org/10.1016/j.conbuildmat.2024.137556.

[237] W.Q. Shen, J.F. Shao, N. Burlion, Z.B. Liu, A microstructure-based constitutive model for cement paste with chemical leaching effect, Mechanics of Materials 150 (2020) 103571. https://doi.org/https://doi.org/10.1016/j.mechmat.2020.103571.

[238] Q. Huang, H. Liu, Q. Wang, Y. Shan, D. Tang, Z. Zhang, X. Zhu, Electric field-induced deterioration of cement mortars owing to calcium leaching, Developments in the Built Environment 17 (2024) 100303. https://doi.org/https://doi.org/10.1016/j.dibe.2023.100303.

[239] X. Chen, X. Gu, X. Xia, X. Li, Q. Zhang, A chemical-transport-mechanics numerical model for concrete under sulfate attack, Materials 14 (2021) 7710.

[240] D. Chen, W. Guo, D. Chen, L. Guo, B. Cai, T. Ye, Mechanistic modeling for coupled chloride-sulfate attack in cement-based materials, Constr Build Mater 455 (2024) 139231. https://doi.org/https://doi.org/10.1016/j.conbuildmat.2024.139231.

[241] R. Ramirez, B. Ghiassi, P. Pineda, P.B. Lourenço, Hygro-Thermo-Mechanical Analysis of Brick Masonry Walls Subjected to Environmental Actions, Applied Sciences 13 (2023). https://doi.org/10.3390/app13074514.

[242] G. Ponce-Antón, A. Arizzi, M.C. Zuluaga, G. Cultrone, L.A. Ortega, J. Agirre Mauleon, Mineralogical, Textural and Physical Characterisation to Determine Deterioration Susceptibility of Irulegi Castle Lime Mortars (Navarre, Spain), Materials 12 (2019). https://doi.org/10.3390/ma12040584.

[243] F. Teklal, A. Djebbar, S. Allaoui, G. Hivet, Y. Joliff, B. Kacimi, A review of analytical models to describe pull-out behavior – Fiber/matrix adhesion, Compos Struct 201 (2018) 791–815. https://doi.org/10.1016/j.compstruct.2018.06.091.

[244] V. Bertolli, T. D'Antino, Modeling the behavior of externally bonded reinforcement using a rigid-trilinear cohesive material law, Int J Solids Struct 248 (2022) 111641. https://doi.org/10.1016/j.ijsolstr.2022.111641.

[245] T. Trapko, Stress-strain model for FRCM confined concrete elements, Compos B Eng 45 (2013) 1351–1359. https://doi.org/10.1016/j.compositesb.2012.07.001.

[246] A.H. Adheem, M.M.A. Kadhim, A. Jawdhari, A. Fam, Confinement model for concrete wrapped with fiber reinforced cementitious mortar, Constr Build Mater 312 (2021) 125401. https://doi.org/10.1016/j.conbuildmat.2021.125401.

[247] E. Bertolesi, F.G. Carozzi, G. Milani, C. Poggi, Numerical modeling of Fabric Reinforce Cementitious Matrix composites (FRCM) in tension, Constr Build Mater 70 (2014) 531–548. https://doi.org/10.1016/j.conbuildmat.2014.08.006.

[248] J.P. Plassiard, I. Alachek, O. Plé, Damage-based finite-element modelling of in-plane loaded masonry walls repaired with FRCM, Comput Struct 254 (2021) 106481. https://doi.org/10.1016/j.compstruc.2021.106481.

[249] F. Focacci, T. D'Antino, C. Carloni, The role of the fiber–matrix interfacial properties on the tensile behavior of FRCM coupons, Constr Build Mater 265 (2020) 120263. https://doi.org/10.1016/j.conbuildmat.2020.120263.

[250] A. Bellini, M.A. Aiello, F. Bencardino, C.B. de Carvalho Bello, G. Castori, A. Cecchi, F. Ceroni, M. Corradi, T. D'Antino, S. De Santis, M. Fagone, G. de Felice, M. Leone, G.P. Lignola, A. Napoli, M. Nisticò, C. Poggi, A. Prota, G. Ranocchiai, R. Realfonzo, E. Sacco, C. Mazzotti, Influence of different set-up parameters on the bond behavior of FRCM composites, Constr Build Mater 308 (2021). https://doi.org/10.1016/j.conbuildmat.2021.124964.

[251] A. Peled, B. Mobasher, A. Bentur, Textile reinforced concrete, CRC Press, 2017.

[252] E. Bertolesi, F.G. Carozzi, G. Milani, C. Poggi, Numerical modeling of Fabric Reinforce Cementitious Matrix composites (FRCM) in tension, Constr Build Mater 70 (2014) 531–548. https://doi.org/10.1016/j.conbuildmat.2014.08.006.

[253] F. Nerilli, S. Marfia, E. Sacco, Nonlocal damage and interface modeling approach for the micro-scale analysis of FRCM, Comput Struct 254 (2021) 106582. https://doi.org/10.1016/j.compstruc.2021.106582.

[254] G. Castori, M. Corradi, E. Sperazini, Full size testing and detailed micro-modeling of the in-plane behavior of FRCM–reinforced masonry, Constr Build Mater 299 (2021) 124276. https://doi.org/10.1016/j.conbuildmat.2021.124276.

[255] F.G. Carozzi, G. Milani, C. Poggi, Mechanical properties and numerical modeling of Fabric Reinforced Cementitious Matrix (FRCM) systems for strengthening of masonry structures, Compos Struct 107 (2014) 711–725. https://doi.org/10.1016/j.compstruct.2013.08.026.

[256] R. Contamine, A. Si-Larbi, N.Q. Than, P. Hamelin, Numerical modeling of reinforced concrete beams under shear stress with and without external textile-reinforced concrete reinforcement, Journal of Reinforced Plastics and Composites 30 (2011) 1293–1303. https://doi.org/10.1177/0731684411420189.

[257] B.E. 1015–11, Methods of test for mortar for masonry. Determination of flexural and compressive strength of hardened mortar, (2019).

[258] A. C109/C109M, Standard Standard test method for compressive strength of hydraulic cement mortars, (n.d.).

[259] BS EN 12390-13, Testing hardened concrete. Determination of secant modulus of elasticity in compression, (2013).

[260] ASTM-C307 – 18, Standard Test Method for Tensile Strength of Chemical-Resistant Mortar, Grouts, and Monolithic Surfacings, 2018. https://doi.org/10.1520/C0307-18.2.

[261] E. STANDARD, BS EN 1936 – Natural stone test methods — Determination of real density and apparent density, and of total and open porosity, BSI 3 (2006).

[262] International Organization for Standardization, ISO 11885:2007, Water quality — Determination of selected elements by inductively coupled plasma optical emission spectrometry, (2007). https://www.iso.org/standard/36279.html.

[263] A. Dalalbashi, B. Ghiassi, D. V. Oliveira, A. Freitas, Fiber-to-mortar bond behavior in TRM composites: Effect of embedded length and fiber configuration, Compos B Eng 152 (2018) 43–57. https://doi.org/10.1016/j.compositesb.2018.06.014.

[264] A. Dalalbashi, B. Ghiassi, D. V. Oliveira, A. Freitas, Effect of test setup on the fiber-to-mortar pull-out response in TRM composites: Experimental and analytical modeling, Compos B Eng 143 (2018) 250–268. https://doi.org/10.1016/j.compositesb.2018.02.010.

[265] A. Dalalbashi, B. Ghiassi, D. v. Oliveira, Aging of lime-based TRM composites under natural environmental conditions, Constr Build Mater 270 (2021). https://doi.org/10.1016/j.conbuildmat.2020.121853.

[266] RILEM Technical Committee 232-TDT (Wolfgang Brameshuber), W. Brameshuber, M. Hinzen, A. Dubey, A. Peled, B. Mobasher, A. Bentur, C. Aldea, F. Silva, J. Hegger, T. Gries, J. Wastiels, K. Malaga, C. Papanicolaou, L. Taerwe, M. Curbach, V. Mechtcherine, A. Naaman, J. Orlowsky, P. Hamelin, H.W. Reinhardt, S. Shah, R. Toledo, T. Triantafillou, A. Si Larbi, D. Garcia, L. Garmendia, S. Gopinath, F. Jesse, Recommendation of RILEM TC 232-TDT: test methods and design of textile reinforced concrete: Uniaxial tensile test: test method to determine the load bearing behavior of tensile specimens made of textile reinforced concrete, Materials and Structures/Materiaux et Constructions 49 (2016) 4923–4927. https://doi.org/10.1617/s11527-016-0839-z.

[267] F. Alhussainy, H.A. Hasan, S. Rogic, M. Neaz Sheikh, M.N.S. Hadi, Direct tensile testing of Self-Compacting Concrete, Constr Build Mater 112 (2016) 903–906. https://doi.org/10.1016/j.conbuildmat.2016.02.215.

[268] M.I. Khan, Direct tensile strength measurement of concrete, Applied Mechanics and Materials 117–119 (2012) 9–14. https://doi.org/10.4028/www.scientific.net/AMM.117-119.9.

[269] S.F. Resan, S.M. Chassib, S.K. Zemam, M.J. Madhi, New approach of concrete tensile strength test, Case Studies in Construction Materials 12 (2020) 1–13. https://doi.org/10.1016/j.cscm.2020.e00347.

[270] A. Dalalbashi, B. Ghiassi, D. v. Oliveira, Influence of freeze–thaw cycles on the pull-out response of lime-based TRM composites, Constr Build Mater 313 (2021) 125473. https://doi.org/10.1016/j.conbuildmat.2021.125473.

[271] N. Williams Portal, K. Lundgren, H. Wallbaum, K. Malaga, Sustainable Potential of Textile-Reinforced Concrete, Journal of Materials in Civil Engineering 27 (2015). https://doi.org/10.1061/(asce)mt.1943-5533.0001160.

[272] A. 549.6R-20, Guide to Design and Construction of Externally Bonded Fabric-Reinforced Cementitious Matrix (FRCM) and Steel-Reinforced Grout (SRG) Systems for Repair and Strengthening Masonry Structures, Technical document, 2020.

[273] S. De Santis, G. de Felice, Steel reinforced grout systems for the strengthening of masonry structures, Compos Struct 134 (2015) 533–548. https://doi.org/10.1016/j.compstruct.2015.08.094.

[274] E.A.D.-E. 340275-00-0104, Externally-bonded Composite Systems with inorganic Matrix for Strenghening OF Concrete and Masonry Structures, 208AD.

[275] L.N. Koutas, Z. Tetta, D.A. Bournas, T.C. Triantafillou, Strengthening of Concrete Structures with Textile Reinforced Mortars: State-of-the-Art Review, Journal of Composites for Construction 23 (2019) 1–20. https://doi.org/10.1061/(asce)cc.1943-5614.0000882.

[276] S. De Santis, H.A. Hadad, F. De Caso y Basalo, G. de Felice, A. Nanni, Acceptance Criteria for Tensile Characterization of Fabric-Reinforced Cementitious Matrix Systems for Concrete and Masonry Repair, Journal of Composites for Construction 22 (2018) 04018048. https://doi.org/10.1061/(asce)cc.1943-5614.0000886.

[277] H. Maljaee, B. Ghiassi, P.B. Lourenço, Bond behavior in NSM-strengthened masonry, Eng Struct 166 (2018) 302–313. https://doi.org/https://doi.org/10.1016/j.engstruct.2018.03.091.

[278] X. Wang, W. Wei, Y. Niu, C. Xia, L. Song, G. Han, Z. Zhu, Triaxial Creep Mechanical Behaviors and Creep Damage Model of Dolomitic Limestone Material under Multi-Stage Incremental Loading, Materials 16 (2023) 1918.

[279] T. Mäkinen, J. Koivisto, L. Laurson, M.J. Alava, Scale-free features of temporal localization of deformation in late stages of creep failure, Phys Rev Mater 4 (2020) 93606.

[280] J.H.S. Almeida Jr., H.L. Ornaghi Jr., N.P. Lorandi, B.P. Bregolin, S.C. Amico, Creep and interfacial behavior of carbon fiber reinforced epoxy filament wound laminates, Polym Compos 39 (2018) E2199–E2206. https://doi.org/https://doi.org/10.1002/pc.24537.

[281] A. Dalalbashi, B. Ghiassi, D. V. Oliveira, Aging of lime-based TRM composites under natural environmental conditions, Constr Build Mater 270 (2021) 121853. https://doi.org/10.1016/j.conbuildmat.2020.121853.

[282] V. Rizzo, A. Bonati, F. Micelli, M. Leone, M.A. Aiello, Influence of alkaline environments on the mechanical properties of FRCM/CRM and their materials, Key Eng Mater 817 KEM (2019) 195–201. https://doi.org/10.4028/www.scientific.net/KEM.817.195.

[283] J.M. Marangu, Effects of sulfuric acid attack on hydrated calcined clay–limestone cement mortars, J Sustain Cem Based Mater 10 (2021) 257–271. https://doi.org/10.1080/21650373.2020.1810168.

[284] J. Zhou, X. Chen, S. Chen, Durability and service life prediction of GFRP bars embedded in concrete under acid environment, Nuclear Engineering and Design 241 (2011) 4095–4102. https://doi.org/10.1016/j.nucengdes.2011.08.038.

[285] M. Jia, Y. Zhao, X. Wu, X. Ma, The effect of carbonation accelerator on enhancing the carbonation process and mechanical strength of air-hardening lime mortars, Constr Build Mater 425 (2024) 136067. https://doi.org/https://doi.org/10.1016/j.conbuildmat.2024.136067.

[286] O. Cazalla, C. Rodriguez-Navarro, E. Sebastian, G. Cultrone, M.J. De la Torre, Aging of lime putty: Effects on traditional lime mortar carbonation, Journal of the American Ceramic Society 83 (2000) 1070–1076. https://doi.org/10.1111/j.1151-2916.2000.tb01332.x.

[287] D. Padmaraj, D.N. Arnepalli, Carbonation in lime-stabilized clays: mechanism, effects, and future prospects, Bulletin of Engineering Geology and the Environment 82 (2023) 258.

[288] Ö. Cizer, K. Van Balen, D. Van Gemert, Competition between hydration and carbonation in hydraulic lime and lime-pozzolana mortars, Adv Mat Res 133 (2010) 241–246.

[289] S. Jain, B. Pradhan, Effect of cement type on hydration, microstructure and thermo-gravimetric behaviour of chloride admixed self-compacting concrete, Constr Build Mater 212 (2019) 304–316. https://doi.org/https://doi.org/10.1016/j.conbuildmat.2019.04.001.

[290] P. Li, W. Li, T. Yu, F. Qu, V.W.Y. Tam, Investigation on early-age hydration, mechanical properties and microstructure of seawater sea sand cement mortar, Constr Build Mater 249 (2020) 118776. https://doi.org/https://doi.org/10.1016/j.conbuildmat.2020.118776.

[291] Z. Yang, H. Peng, W. Wang, T. Liu, Crystallization behavior of poly(ε-caprolactone)/layered double hydroxide nanocomposites, J Appl Polym Sci 116 (2010) 2658–2667. https://doi.org/10.1002/app.

[292] J. kang Chen, M. qiang Jiang, Long-term evolution of delayed ettringite and gypsum in Portland cement mortars under sulfate erosion, Constr Build Mater 23 (2009) 812–816. https://doi.org/10.1016/j.conbuildmat.2008.03.002.

[293] Z. Makhloufi, T. Bouziani, M. Hadjoudja, M. Bederina, Durability of limestone mortars based on quaternary binders subjected to sulfuric acid using drying-immersion cycles, Comput Chem Eng 71 (2014) 579–588. https://doi.org/10.1016/j.conbuildmat.2014.08.086.

[294] B. Scrivener, Karen and Snellings, Ruben and Lothenbach, A practical guide to microstructural analysis of cementitious materials, CRC Press, 2018.

[295] Ö. Cizer, K. Van Balen, J. Elsen, D. Van Gemert, Real-time investigation of reaction rate and mineral phase modifications of lime carbonation, Constr Build Mater 35 (2012) 741–751. https://doi.org/10.1016/j.conbuildmat.2012.04.036.

[296] C. Groot, R. Veiga, I. Papayianni, R. Van Hees, M. Secco, J.I. Alvarez, P. Faria, M. Stefanidou, RILEM TC 277-LHS report: lime-based mortars for restoration–a review on long-term durability aspects and experience from practice, 2022. https://doi.org/10.1617/s11527-022-02052-1.

[297] A.M. Forster, L.P. Masson, B. Suryanto, P.F.G. Banfill, C. Torney, J. Valek, The binder-aggregate interface in NHL mortar with non-calcitic aggregate: Physical properties, Constr Build Mater 398 (2023) 132349.

[298] H. Mehdizadeh, X. Jia, K.H. Mo, T.-C. Ling, Effect of water-to-cement ratio induced hydration on the accelerated carbonation of cement pastes, Environmental Pollution 280 (2021) 116914. https://doi.org/https://doi.org/10.1016/j.envpol.2021.116914.

[299] A.M. Forster, E.M. Szadurski, P.F.G. Banfill, Deterioration of natural hydraulic lime mortars, I: Effects of chemically accelerated leaching on physical and mechanical properties of uncarbonated materials, Constr Build Mater 72 (2014) 199–207. https://doi.org/10.1016/j.conbuildmat.2014.09.015.

[300] Z. Slížková, M. Drdácký, A. Viani, Consolidation of weak lime mortars by means of saturated solution of calcium hydroxide or barium hydroxide, J Cult Herit 16 (2015) 452–460. https://doi.org/10.1016/j.culher.2014.09.003.

[301] P. Štukovnik, M. Marinšek, B. Mirtič, V. Bokan Bosiljkov, Influence of alkali carbonate reaction on compressive strength of mortars with air lime binder, Constr Build Mater 75 (2015) 247–254. https://doi.org/10.1016/j.conbuildmat.2014.11.024.

[302] S. Bellifa, N. Boumechra, Effects of calcium leaching on the physical and mechanical properties of aerial lime-cement mortars, Journal of Engineering, Design and Technology 17 (2019) 649–666. https://doi.org/10.1108/JEDT-11-2018-0199.

[303] A.M. Forster, E.M. Szadurski, P.F.G. Banfill, Deterioration of natural hydraulic lime mortars, I: Effects of chemically accelerated leaching on physical and mechanical properties of uncarbonated materials, Constr Build Mater 72 (2014) 199–207. https://doi.org/10.1016/j.conbuildmat.2014.09.015.

[304] S. Chen, Z. Du, Z. Zhang, H. Zhang, Z. Xia, F. Feng, Effects of chloride on the early mechanical properties and microstructure of gangue-cemented paste backfill, Constr Build Mater 235 (2020) 117504. https://doi.org/https://doi.org/10.1016/j.conbuildmat.2019.117504.

[305] B. Ozer, M.H. Ozkul, The influence of initial water curing on the strength development of ordinary portland and pozzolanic cement concretes, Cem Concr Res 34 (2004) 13–18. https://doi.org/https://doi.org/10.1016/S0008-8846(03)00185-6.

[306] F. Rendell, R. Jauberthie, Deterioration of mortar in sulphate environments, Constr Build Mater 13 (1999) 321–327. https://doi.org/10.1016/S0950-0618(99)00031-8.

[307] Z. Zhang, J. Zhou, J. Yang, Y. Zou, Z. Wang, Cracking characteristics and pore development in concrete due to physical attack, Mater Struct 53 (2020) 104. https://doi.org/10.1617/s11527-020-01541-5.

[308] CNR DT 215/2018, Guide for the Design and Construction of Externally Bonded Fibre Reinforced Inorganic Matrix Systems for Strengthening Existing Structures, ACI Committee 440 (2018) 144.

[309] L. Li, W. Sun, Z. Feng, Y. Li, T. Feng, Z. Liu, Hydration kinetics and apparent activation energy of cement pastes containing high silica fume content at lower curing temperature, Constr Build Mater 435 (2024) 136881. https://doi.org/https://doi.org/10.1016/j.conbuildmat.2024.136881.

[310] T. Chen, X. Gao, Effect of carbonation curing regime on strength and microstructure of Portland cement paste, Journal of CO2 Utilization 34 (2019) 74–86.

[311] X. Chen, T. Zhang, W. Bi, C. Cheeseman, Effect of tartaric acid and phosphoric acid on the water resistance of magnesium oxychloride (MOC) cement, Constr Build Mater 213 (2019) 528–536. https://doi.org/https://doi.org/10.1016/j.conbuildmat.2019.04.086.

[312] A. Pop, I. Ardelean, Monitoring the size evolution of capillary pores in cement paste during the early hydration via diffusion in internal gradients, Cem Concr Res 77 (2015) 76–81. https://doi.org/https://doi.org/10.1016/j.cemconres.2015.07.004.

[313] O. Çopuroğlu, E. Schlangen, Modeling of frost salt scaling, Cem Concr Res 38 (2008) 27–39.

[314] L.K. Mettler, F.K. Wittel, R.J. Flatt, H.J. Herrmann, Evolution of strength and failure of SCC during early hydration, Cem Concr Res 89 (2016) 288–296. https://doi.org/https://doi.org/10.1016/j.cemconres.2016.09.004.

[315] M.T. Bassuoni, M.L. Nehdi, Durability of self-consolidating concrete to sulfate attack under combined cyclic environments and flexural loading, Cem Concr Res 39 (2009) 206–226. https://doi.org/https://doi.org/10.1016/j.cemconres.2008.12.003.

[316] Y. Wang, Q. Yuan, D. Deng, Degradation of mechanical properties of CA mortar caused by calcium leaching, Constr Build Mater 208 (2019) 613–621. https://doi.org/https://doi.org/10.1016/j.conbuildmat.2019.02.164.

[317] V. Gulshan, L. Peng, M. Coram, M.C. Stumpe, D. Wu, A. Narayanaswamy, S. Venugopalan, K. Widner, T. Madams, J. Cuadros, R. Kim, R. Raman, P.C. Nelson, J.L. Mega, D.R. Webster, Development and Validation of a Deep Learning Algorithm for Detection of Diabetic Retinopathy

in Retinal Fundus Photographs, JAMA 316 (2016) 2402. https://doi.org/10.1001/jama.2016.17216.

[318] T. Chen, C. Guestrin, XGBoost: A Scalable Tree Boosting System, Proceedings of the 22nd ACM SIGKDD International Conference on Knowledge Discovery and Data Mining (2016) 785–794. https://doi.org/10.1145/2939672.2939785.

[319] S. Lundberg, S.-I. Lee, A Unified Approach to Interpreting Model Predictions, Artif Intell (2017). http://arxiv.org/abs/1705.07874.

[320] J. Lanas, R. Sirera, J.I. Alvarez, Study of the mechanical behavior of masonry repair lime-based mortars cured and exposed under different conditions, Cem Concr Res 36 (2006) 961–970. https://doi.org/https://doi.org/10.1016/j.cemconres.2005.12.003.

[321] E. Campello, M. V Pereira, F. Darwish, The Effect of Short Metallic and Polymeric Fiber on the Fracture Behavior of Cement Mortar, Procedia Materials Science 3 (2014) 1914–1921. https://doi.org/https://doi.org/10.1016/j.mspro.2014.06.309.

[322] W. Li, Q. Wei, Q. Chen, Z. Jiang, Effect of CO32- and Ca2+ on self-healing of cementitious materials due to “build-in” carbonation, Journal of Building Engineering 56 (2022) 104781. https://doi.org/10.1016/j.jobe.2022.104781.

[323] J. Lei, W.W. Law, E.-H. Yang, Effect of calcium hydroxide on the alkali-silica reaction of alkali-activated slag mortars activated by sodium hydroxide, Constr Build Mater 272 (2021) 121868. https://doi.org/https://doi.org/10.1016/j.conbuildmat.2020.121868.

[324] F.Z. Youssari, O. Taleb, A.S. Benosman, Towards understanding the behavior of fiber-reinforced concrete in aggressive environments: Acid attacks and leaching, Constr Build Mater 368 (2023) 130444. https://doi.org/https://doi.org/10.1016/j.conbuildmat.2023.130444.

[325] M. Vafaei, A. Allahverdi, P. Dong, N. Bassim, Acid attack on geopolymer cement mortar based on waste-glass powder and calcium aluminate cement at mild concentration, Constr Build Mater 193 (2018) 363–372. https://doi.org/https://doi.org/10.1016/j.conbuildmat.2018.10.203.

[326] R. Illampas, D. V Oliveira, P.B. Lourenço, Design of Strain-Hardening Natural TRM Composites: Current Challenges and Future Research Paths, Materials 16 (2023). https://doi.org/10.3390/ma16134558.